Advances in Polymer Science 286

Gert Heinrich
Reinhold Kipscholl
Radek Stoček *Editors*

Fatigue Crack Growth in Rubber Materials

Experiments and Modelling

Springer

286
Advances in Polymer Science

Aims and Scope

The series Advances in Polymer Science presents critical reviews of the present and future trends in polymer and biopolymer science. It covers all areas of research in polymer and biopolymer science including chemistry, physical chemistry, physics, and material science.

The thematic volumes are addressed to scientists, whether at universities or in industry, who wish to keep abreast of the important advances in the covered topics.

Advances in Polymer Science enjoys a longstanding tradition and good reputation in its community. Each volume is dedicated to a current topic, and each review critically surveys one aspect of that topic, to place it within the context of the volume. The volumes typically summarize the significant developments of the last 5 to 10 years and discuss them critically, presenting selected examples, explaining and illustrating the important principles, and bringing together many important references of primary literature. On that basis, future research directions in the area can be discussed. Advances in Polymer Science volumes thus are important references for every polymer scientist, as well as for other scientists interested in polymer science - as an introduction to a neighboring field, or as a compilation of detailed information for the specialist.

Review articles for the individual volumes are invited by the volume editors. Single contributions can be specially commissioned.

Readership: Polymer scientists, or scientists in related fields interested in polymer and biopolymer science, at universities or in industry, graduate students.

More information about this series at http://www.springer.com/series/12

Gert Heinrich • Reinhold Kipscholl •
Radek Stoček
Editors

Fatigue Crack Growth in Rubber Materials

Experiments and Modelling

With contributions by

F. Addiego · D. Berghezan · R. Bernhardt · J. J. C. Busfield · J. Caillard · J. Chanda · L. Chazeau · J. -M. Chenal · C. Creton · S. Dedova · Q. Demassieux · R. Eberlein · M. El Yaagoubi · E. Euchler · C. E. Federico · Y. Fleming · Y. Fukada · C. Gauthier · P. Ghosh · G. Heinrich · T. W. Hohenberger · M. Kaliske · J. Kallungal · J. Khodor · M. Klüppel · O. Kotecky · O. Kratina · B. Langer · M. Ludwig · A. Machů · Z. Major · J. Maloch · P. Mangiagalli · W. V. Mars · J. Meier · R. Mukhopadhyay · K. Oßwald · H. R. Padmanathan · L. Pasieka · B. N. J. Persson · M. M. Rahman · G. Rauchs · K. Reincke · C. G. Robertson · S. Robin · N. Rodriguez · R. Rommel · S. G. Sathi · K. Schneider · M. Stěnička · R. Stoček · M. Stommel · T. Tada · K. Y. Volokh · S. Westermann · S. Wießner · R. J. Windslow · M. Wunde · B. Yin · P. Zádrapa

Springer

Editors
Gert Heinrich
Leibniz-Institut für Polymerforschung
Dresden e.V. and Technische Universität
Dresden, Dresden, Germany

Reinhold Kipscholl
Coesfeld GmbH & Co. KG
Dortmund, Germany

Radek Stoček
PRL Polymer Research Lab, Centre of
Polymer Systems
Tomas Bata University in Zlín
Zlín, Czech Republic

ISSN 0065-3195 ISSN 1436-5030 (electronic)
Advances in Polymer Science
ISBN 978-3-030-68919-3 ISBN 978-3-030-68920-9 (eBook)
https://doi.org/10.1007/978-3-030-68920-9

Preface

Rubbers, several kinds of rubber-like materials like thermoplastic elastomers (TPE), thermoplastic vulcanizates (TPV), polyurethanes, etc. belong to widely used classes of polymer materials with critical technological applications. The number of industrial and daily life applications of these classes of polymer materials has been growing continuously within the last decades. Typical examples are synthetic and natural covalently cross-linked rubbers integrated into automobile tires or other applications like driving belts, seismic isolators, fuel system hoses, seals, turbocharger hoses, cooling system hoses, engine bushing, spring pads, and more. Other technological applications continue to emerge in new fields such as soft robotics, stretchable electronics, tissue engineering, and others. In such applications, the soft materials are often exposed to a very complex load profile arising from several external impacts and leading to permanent small and large cyclic (dissipative and nonlinear) multiaxial deformations in a wide range of frequencies and amplitudes. Furthermore, in many cases, the sliding contact with rough multiscale counter-faces (roads, engine mounts, etc.) leads to wear phenomena and, hence, to the reduction of the product's lifetime. When cracks propagate throughout a rubber solid, even catastrophic failure can be induced and the corresponding part completely loses its macroscopic load-bearing capacity which could have severe effects. It is clear that the failure of rubber materials in critical technological applications can lead to catastrophic events that must definitely be prevented. To achieve this, a sound understanding of the failure mechanisms in rubber materials and their computational predictions are of cardinal importance. A realistic prediction will help to identify potential problems that may arise and lead to the tailoring of specific, robust, and long-lasting materials via application-specific designs. Furthermore, a sound understanding of the failure mechanisms and suitable laboratory testing methods, together with data evaluation concepts and criteria, will aid in reducing efforts by producing prototypes, lab trials, and product design loops, i.e. lowering the costs and time-to-market. Furthermore, the generated data from the

new testing methods will guarantee a reliable and precise application of corresponding calculation methods.

We are convinced that the advanced testing methods, modeling tools, and findings presented in the different chapters of this book will support speeding up the fatigue characterization of rubbers under practice-like conditions which is a crucial industrial and scientific requirement for quickly assessing newly developed compounds.

Following a scientific review in the field of fracture mechanics of rubber materials, the energy balance approach has proved successful in treating a number of fracture phenomena. In this approach, the crack growth behavior is expressed in terms of the energy release rate T. The resistance to crack initiation and propagation has been recognized as a critical material property and has become the central topic of fracture mechanics according to the pioneering works of R. S. Rivlin and A. G. Thomas in the early 1950s (for example: Journal of Polymer Science (1953) **10**, 291–318). Moreover, G. J. Lake, A. G. Thomas, and D. Tabor explained that rupture is an energetic process at the molecular scale originating from the breakage of molecular bonds in the polymer network of the rubbers (Proceedings of the Royal Society of London. Series A. Mathematical and Physical Sciences (1967) **300**, 108–119). However, within the last decades, many additional insights, interesting facets, new experimental data, models, and predictive tools were added to the field of fracture mechanics of rubbers leading to a growing interest in this research branch due to the growing range of technological applications of soft rubber materials.

The present book offers 20 cutting-edge chapters devoted to a thorough understanding of the fracture behavior of soft rubber materials. These chapters cover the fields of new testing equipment (Stoček et al.) and testing concepts for industrial applications (Robertson et al.; Mars) as well as new discussions about intrinsically multi-scale physical problems and structural features in connection with new experimental findings for understanding of the crack phenomena in soft materials (Creton et al.; Persson et al; Chazeau et al.; Busfield et al.; Westermann et al.; Meier et al.; Klüppel et al.; Euchler et al.; Dedova et al.). Furthermore, new concepts regarding a theoretical and numerical analysis of nonlinear crack-tip mechanics (Kaliske et al.; Volokh) are considered. Industrial applications regarding fatigue phenomena and regarding rubber materials designed under consideration of crack/wear phenomena are included in this book (Ghosh et al.; Reincke et al.). Finally, it is shown how fracture concepts and lifetime predictive tools, originally developed for covalently cross-linked rubbers, are successfully transferred to the class of thermoplastic rubbers (Eberlein et al; Major et al.). At a glance, the main physical and structural problems of experimental investigations of fatigue crack growth, which are described, consider the influence of loading conditions, sample geometry, notching procedure, viscoelasticity and dissipation and adhesion phenomena of rubbers, heat build-up, materials development, specific

features of rubber types and their compound formulations, influence of reinforcing fillers as well as plasticizers, impact of crystallization phenomena in rubbers, etc. The book provides a comprehensive overview of the recent developments in this area and will be of interest to both academic researchers and industrial professionals in this field.

Dresden, Germany — Gert Heinrich
Dortmund, Germany — Reinhold Kipscholl
Zlín, Czech Republic — Radek Stoček

Acknowledgement

G. H. acknowledges the DFG (German Research Foundation) project 380321452/GRK2430 for financial support.

Contents

Adv Polym Sci (2021) 286: 1–18
https://doi.org/10.1007/12_2020_72

Published online: 27 November 2020

Some Revisions of Fatigue Crack Growth Characteristics of Rubber

R. Stoček

Contents

Abstract Fatigue crack growth (FCG) characteristic of rubber materials is a very important factor in determining the durability of the rubber products. Slight variations in compounding ingredients, mixing and the curing process or even in the loading conditions and several physical factors have an impact on the final FCG behaviour of rubber vulcanisates. Thus, possible inaccuracies in the experimentally determined FCG characteristics can have direct consequences on the development of durable rubber compounds. Therefore, the aim of this work is focused on the experimental validation of the FCG characteristics of rubber in comparison with the recently customary theoretical background and functions describing the relationship between the FCG rate and the tearing energy. From the literature survey, the weak points directly influencing the accuracy of the FCG characteristics in the experimental approach were identified. The first weak point is the transient point or discontinuity of the FCG characteristics within the region of the stable FCG. To

R. Stoček (✉)
PRL Polymer Research Lab, Zlin, Czech Republic

Centre of Polymer Systems, Tomas Bata University in Zlin, Zlin, Czech Republic
e-mail: stocek@utb.cz

follow on, a visible deviation of the experimentally determined data within the region of the stable FCG from the theoretical function is necessary to be validated. FCG analyses of plane strain tension samples based on ethylene propylene diene monomer (EPDM) rubber filled with a varied content of carbon black were performed using a Tear and Fatigue Analyzer (TFA©, Coesfeld GmbH & Co. KG, Germany). The FCG characteristics were plotted for a broad range of tearing energies. The intrinsic strength and the ultimate strength were determined. The region of the stable FCG was studied in detail. The continuous function of the stable FCG within the region was found, and thus, the presence of a transient point was refuted. Moreover, a specific equation was validated to fit the data into the region of the stable FCG compared to a previously preferred power-law with a higher accuracy.

Keyword Analyses · Characteristics · Crack · Fatigue · Fracture · Plane strain · Rubber · Tear and Fatigue Analyzer

1 Introduction

Because of the viscoelastic behaviour of elastomeric materials, rubber products are mainly used for dynamic applications in which the cyclic fatigue loading is applied and leads to a fatigue failure mechanism and, therefore, significantly influences the long-term durability.

Generally, the fatigue failure process involves three phases. The very first phase is crack nucleation associated with an endurance limit, whereas at an energy input below, the endurance limit no cracks are initiated. An energy input above the endurance limit causes the propagation of nucleated cracks, which is the second phase. At the final phase the failure of the rubber material proceeds. The crack nucleation, its growth, and finally the total failure are all considered to be factors describing the fracture mechanical behaviour of rubber under fatigue loading conditions. Therefore, Gent, Lindley and Thomas [1] experimentally described fatigue fracture behaviour with a general function of the fatigue crack growth (FCG) rate, $r = da/dn$ (in which da is the increment of crack growth and dn is the difference of the relevant cycle counts between which the crack increases by da). It depends on the energy release rate or tearing energy, T, correspondent to the rubber materials, which are loaded cyclically, whereas the original proposition for calculating the tearing energy, T, was made by Rivlin and Thomas in Ref. [2]. The FCG data in Ref. [1] were obtained due to cyclic loading until failure occurred by the sample rupturing, whereas the FCG rate, r, was observed to be linearly dependent on the tearing energy, T, in a range from minimal obtained value 10^{-7} up to 10^{-3} mm/cycle. Thus, in the pioneering work, published in Ref. [1], the data did not consider the crack nucleation, but are defining the total failure, which was determined at FCG rate

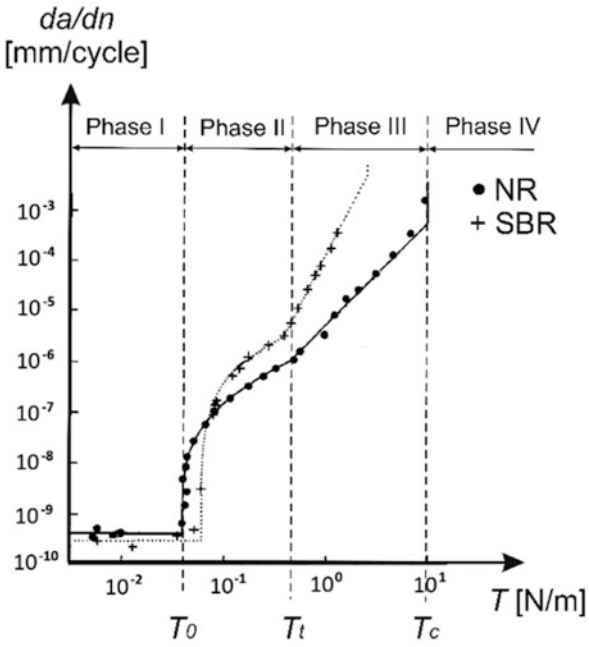

Fig. 1 Historical data describing FCG behaviour of unfiled rubbers, re-plotted from the Ref. [3] (logarithmic scale), where the phases are related to data representing NR

10^{-1} mm/cycle. Lake and Lindley in Ref. [3] performed a more detailed study of the FCG behaviour of natural rubber (NR) and styrene butadiene rubber (SBR), whereas the data are re-plotted in Fig. 1. They obtained the FCG rate data in a range from 10^{-10} up to10^{-3} mm/cycle. Thus, the FCG rate of the crack nucleation was firstly recorded and the absolute minimal value at which the crack nucleates was determined to be about 5E-10 mm/cycle for both analysed rubbers, whereas a slightly lower FCG rate was monitored for an SBR compared to an NR-based vulcanisate. Moreover, they firstly described the various phases in FCG behaviour and documented that the FCG rate, r, depends on the tearing energy, T, in each of the relevant phases in a characteristic manner.

In the first phase of the FCG behaviour shown in Fig. 1, there is a minimum energy requirement for the fracture process. For a simple unfilled cross-linked rubber, this minimum energy primarily depends on the details of the polymer network, such as the average molecular weight between the cross-links, and on the weakest bond strength in the main polymer chain [4]. It is largely independent of time, temperature and the degree of swelling. It is therefore often called the intrinsic strength, T_0, as it only reflects the polymer chemistry as well as the network and practically represents the endurance limit of the rubber material [5]. As long as the value of the tearing energy, T, is lower than T_0, the FCG proceeds at a constant rate, r, which is very close to zero, and it is solely attributable to ozone attack [3] and thus not caused mechanically. Therefore, the FCG is constant and independent from the applied T and formulated in Eq. (1):

$$\text{Phase I} : T \leq T_0 \rightarrow \frac{da}{dn} = r \rightarrow 0. \tag{1}$$

The mechanically caused and therefore relevant FCG proceeds in a broad range of tearing energies between the intrinsic energy, T_0, and the critical tearing energy respective ultimate strength, T_C. Within this range of energies, a transient point at a tearing energy, T_t, was found in the FCG curve. This transient tearing energy separates the region into two phases, whereas at the phase II the dependence of the FCG rate, r, on the tearing energy, T, is linear (Eq. 2) and above T_t changes into a fairly good approximation of the obtained data due to the power-law (Eq. 3), which defines the FCG behaviour in phase III:

$$\text{Phase II} : T_0 \leq T \leq T_\text{t} \rightarrow \frac{da}{dn} = \text{A}(T - T_0) + r. \tag{2}$$

$$\text{Phase III} : T_\text{t} \leq T \leq T_\text{c} \rightarrow \frac{da}{dn} = \beta \cdot T^m, \tag{3}$$

where β and m are material constants. Moreover, the FCG behaviour within phase III describes a stable crack growth. Finally, the crack proceeds to the unstable fatigue growth above the critical tearing energy, T_C, and the FCG rate becomes essentially infinite in phase IV. Many studies were concerned with the effect of sample geometry on the critical tearing energy, T_C, whereas the independence of sample geometry was verified and thus T_C can be regarded as a material property [6–8]:

$$\text{Phase IV} : T_c \leq T_c \rightarrow \frac{da}{dn} \rightarrow \infty. \tag{4}$$

The point T_t in Fig. 1 defines the so-called transient tearing energy. It is the tearing energy where the sloop of the FCG curve changes, which is a very interesting observation. The different authors have found a discontinuity in the FCG behaviour analysing various rubber materials. For example, in Ref. [9] Lindley found the presence of a transient point for mechano-oxidative FCG characteristics of a CB-filled SBR. Young in Ref. [10] determined the transient point in the FCG behaviour of NR as influence of various temperatures. Finally, Ghosh et al. in Ref. [11] defined a transient point between the regions of power-laws for carbon black-filled binary blends based on NR and butadiene rubber (BR). From these observations, the transient point occurs obviously in natural as well as in synthetic rubber, and thus the presence of the transient point can be considered as independent of the rubber type.

However, in natural processes, the continuity and gradual transitions are predominant. Thus, the continuous FCG process is expected and should be reflected in a continuous dependence between the FCG rate, r, and the tearing energy, T. Therefore, the presence of a transient point respective discontinuity in the FCG behaviour is highly spectacular even despite realising that it can never be shown by an experiment whether a function is continuously differentiable in certain point or not

due to estimation of measured data in a time interval. A possible approximation to determine whether the measured data correspond with a continuous function can be performed by using an approach based on minimising the increment in the sequence of individual measured values. Therefore, the possible reason for observing the transient points in the previous works can be assumed in an excessively large increment in the sequence of individual measured FCG data.

From Fig. 1 for the FCG behaviour of the NR in phase III, it is evident that the experimentally determined data points slightly deviate from the power-law fit. Especially in the part close to the T_C, the deviation increases significantly. The deviation of the experimentally determined FCG behaviour from the power-law is evident in many publications, e.g. in Refs. [4–16].

Therefore, it is of a very high scientific interest to perform a highly precise experimental investigation of FCG behaviour with the smallest possible increments of T to validate the shape of the function describing the relationship between the FCG rate and the tearing energy of rubber materials, which is the main aim of this study.

2 Experimental

The polymer used in this study was ethylene-propylene-diene-monomer rubber (EPDM) of the type Keltan® 4331A (Arlanxeo, Germany) extended with 33.3 wt. % of oil. Two rubber compounds varying in carbon black (CB) volume fraction, $\Phi = 0.24$ and 0.29, corresponding to 105 and 135 phr, respectively, whereas CB of the type N 550 has been used. A sulphur curing system was chosen. Table 1 lists the complete formulations of the rubber compounds.

These rubber compounds were prepared in a two-stage mixing process using a laboratory-scale internal mixer (SYD-2L, Everplast, Taiwan) of 1.0-L capacity. In the first stage, mixing the rubbers and chemicals (except for the curatives) was carried out at a rotor speed of 50 rpm (rotations per minute) for 4.0 min, and the chamber temperature was set at 90°C. The second stage of mixing was performed for a duration of 3.0 min at 35 rpm and a 90°C chamber temperature.

The pure-shear test specimen geometry is detailed in Fig. 2. The specimens were cured in a heated press (LaBEcon 300 from Fontijne Presses, Netherlands) at 160°C

Table 1 Rubber compound formulation

	Chemicals in [phr]						
Sample ID	EPDM	CB	IPPD	CBS	ZnO	Stearic acid	Sulphur
$EPDM_{\Phi(0.24)}$	150	105	2.25	3.75	4.5	1.5	2.55
$EPDM_{\Phi(0.29)}$		135					

IPPD: N-Isopropyl-N′-phenyl-1,4-phenylenediamine
ZnO: zinc oxide (ZnO)
CBS: N-cyklohexyl-2-benzo-thiazole-sulfenamide

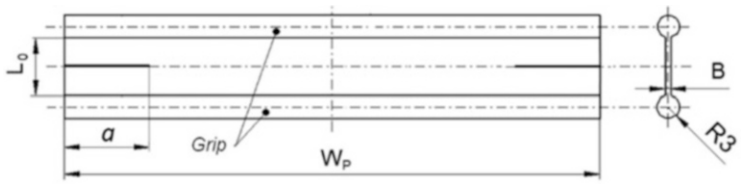

Fig. 2 Plane strain tension test specimen geometry

in accordance with an optimum curing time, *t90*, determined from cure rheometer curves evaluated at 160°C using a Moving Die Rheometer (MDR 3000 Basic from MonTech, Germany) in accordance with ASTM 6204.

Measuring the FCG characteristics were carried out with a Tear and Fatigue Analyzer (TFA©). A detailed description of the equipment is found in Refs. [17, 18]. The plane strain (PS) tension sample schematically shown in Fig. 2 (in the literature very often named as pure shear sample), having dimensions $L_0 = 4$ mm, $W_p = 40$ mm and $B = 1.0$ mm, was used for measuring the FCG characteristics. The PS samples were notched on both edges. A set of three samples per compound was analysed over the complete range of tearing energies, from T_0 to T_C. Finally, the fatigue loading at a given frequency was applied over the range of tearing energies, *T,* or strains. The analyses were performed at a fully relaxing mode, in which the R-ratio $=> R = 0$, which is the minimum applied stress divided by the maximum applied stress: $R = \sigma_{\min}/\sigma_{\max}$. Thus, within all steps of the analyses, the pre-force controlling system assured a stable constant value $R = 0$. The growth of both cracks at each sample was monitored in situ through an image processing system with a CCD camera. The crack growth increment determined from the crack contour (see Fig. 4) as well as the data for fatigue behaviour can be evaluated, whereas a resolution of the CCD system was 0.01 mm. Thus, a crack increment with an accuracy of ±0.01 mm can be determined.

A most exact and good repeatable investigation of FCG characteristics by using TFA is guaranteed by following five steps specified below.

2.1 1st Step: Sample Fixing

Each of the three un-notched PS samples is fixed to a separate upper clamp of the fixing system. Then the force, which the loading cell measured, is set to 0 N. The distance between the upper and bottom clamp is adjusted to the distance L_0, and the samples are afterwards fixed to the bottom clamps. The load cell will finally detect a non-zero force in most cases, caused by mounting of the samples. If that happens, the distance of the clamps has to be regulated until the required force of 0 N is achieved.

2.2 2nd Step: Sample Pre-conditioning

After the samples are fixed, they have to relax for 5 min immediately followed by a series of 3,000 loading cycles each with an increased strain at required test conditions (pre load/frequency/temperature/climate/atm).

2.3 3rd Step: Tearing Energy Determination

Firstly, the data required for calculating the tearing energy experimentally are determined. The data are captured while applying 3,000 loading cycles each at varied strains of 10, 30, 50, 70, and 90% under a given loading frequency. Additionally, the tearing energy relevant to each applied strain is calculated. Fundamentally, the tearing energy calculation is based on a simple formula for determining the PS sample as defined by Rivlin and Thomas [2]:

$$T = wL_0, \tag{5}$$

with L_0 being the initial length respective height of the sample and w being the stored energy density, in which its absolute value is an average from the data string determined in a range of 2,900 up to 3,000 cycles. Finally, the relationship between the tearing energy and the strain is plotted in Fig. 3 for both analysed rubbers, whereas the data are fitted with the polynomial 2. grade (see Fig. 3). Higher tearing energies at identical strains are evident for $EPDM_{\Phi(0.29)}$ due to a higher CB content.

Secondly, the relevant strains for pre-defined tearing energies are calculated from the determined polynomial quadratic functions relevant to each compound, in which the calculated strains are finally applied for the FCG analyses. Within this study, the FCG behaviour was analysed over a very broad range of tearing energies with varied increments, ΔT; the values are listed in Table 2.

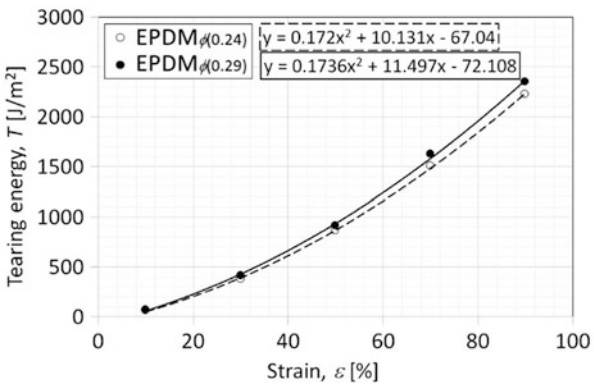

Fig. 3 Tearing energy, T at given strain, ε

Table 2 Tearing energies, T, and relevant increment, ΔT, applied for FCG analyses

Range of tearing energies, T [J/m^2]	Increment, ΔT [J/m^2]	Sample ID	
		EPDM $_{\Phi(0.24)}$	EPDM $_{\Phi(0.29)}$
50–90	5	Applied	Not applied
90–100	10		Applied
100–500	50		
500–1,900	100		
1900–2,500	100		Not applied

2.4 4th Step: Notching the Initial Crack

The samples were notched immediately after completing the tearing energy determination, because of the passed Mullins [18] and Payne effects [19] in the range of the applied strains for the future FCG analyses. Moreover, notching is strictly required to be performed on the mounted and pre-conditioned samples with the adjusted preload, to avoid any relaxation process during non-fixing. The pre-strain was kept to the controlled preload of 10 N applied to each sample. The samples were notched on both sides by manual cutting in the orthogonal direction to the strain (see Fig. 2) using stainless steel blades (Lutz GmbH, Germany) with varied thicknesses. The applied notch length, a, is required to be larger than the minimum notch length, $a_{\min}$, in accordance with Refs. [20, 21] defined for a PS sample. The minimum notch length, $a_{\min}$, for the given geometry was determined to be 7.29 mm, and therefore a notch length of, $a = 10$ mm, was realised, whereas firstly the notch length about 8 mm has been performed using a blade of 0.63 mm thickness and the remaining additional 2 mm have been notched with a blade of 0.1 mm thickness.

2.5 5th Step: FCG Analyses

The following parameters were chosen for the present FCG analyses:

- Load form sinusoidal
- Loading frequency 5 Hz
- Temperature of 28°C
- Preload 10 N
- Tearing energies, *T,* defined in Table 2 above

Photos of the samples used for the FCG rate evaluation were captured each 300 cycles via a CCD-camera synchronised triggered at a deformation of constant 0.50 mm strain, independent of the actually applied strain amplitude. The sample picture was then transferred to a frame grabber and stored as a grey-picture. Simultaneously, the picture was converted in a black/white picture (see Fig. 4). The software localises in situ the crack position and determines the crack contour, a_{cc} (red line) as well as the crack depth, a_{cd} (blue line), by following the black/white

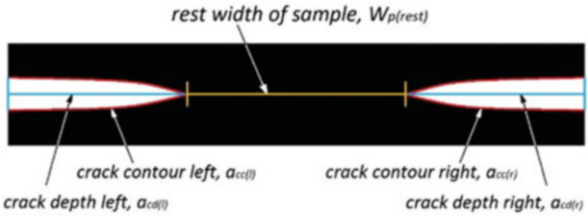

Fig. 4 Digitalised picture of sample during FCG analyses

border line of the crack. Further on the remaining rest width of sample, $W_{p(rest)}$ (yellow line) is evaluated. All the FCG data presented in this current work are related to the crack contour, a_{cc}. (Crack length = ½ Crack contour length).

3 Results and Discussion

In Fig. 5 the determined FCG behaviour of both analysed rubbers is shown. The plots contain all the original data based on the analysed set of three double notched PS samples each. As it can be seen, the plot for the rubber $EPDM_{\Phi(0.24)}$ bases from the FCG rate data over a broad range of tearing energies from 50 up to 2,500 J/m^2, while the FCG characteristics for the rubber $EPDM_{\Phi(0.29)}$ was evaluated by a smaller tearing energy range from 100 up to 1,900 J/m^2. Thus, the FCG characteristics for the $EPDM_{\Phi(0.24)}$ describes all the phases beside phase I of the fatigue failure process, whereas the $EPDM_{\Phi(0.29)}$ was characterised only in the stable crack growth region. From the characteristics, it is visible that a standard deviation of the FCG rate data significantly decreases by increasing the tearing energy.

The cracks growth of each sample was monitored in situ through an image processing system using a CCD camera. The crack growth increment, Δa, determined based on the crack contour length, a_{cc}, (see Fig. 4). The resolution of the CCD system allows to detect a minimum size of the distinguishable crack contour length, $a_{cc} = 0.01$, mm with an accuracy of ± 0.01 mm. The noise band of ± 0.01 mm is eliminated by statistics over numerous measurements per tearing energy value applied. In parallel the data to estimate the fatigue behaviour were measured and calculated. In Fig. 6 the relationship between the tearing energy, T, and the totally applied cycles, n (curve A), respective cycles required to reach a crack growth increment, $\Delta a = 0.01$ mm (curve B), for $EPDM_{\Phi(0.24)}$ (left) and $EPDM_{\Phi(0.29)}$ (right) are plotted. Independent of the analysed materials and over the complete range of the applied tearing energies, the realised total cycle count related to each value of the tearing energy is greater than that required for reaching the minimal differentiable length of crack growth. Therefore, it can be stated that all FCG data plotted in Fig. 5 were determined with a high safety factor beyond the minimum size of the distinguishable crack contour length. The total time currently expended to analyse each FCG characteristics in comparison with the time required to reach the minimal differentiable length of crack growth $\Delta a = 0.01$ mm are listed in Table 3

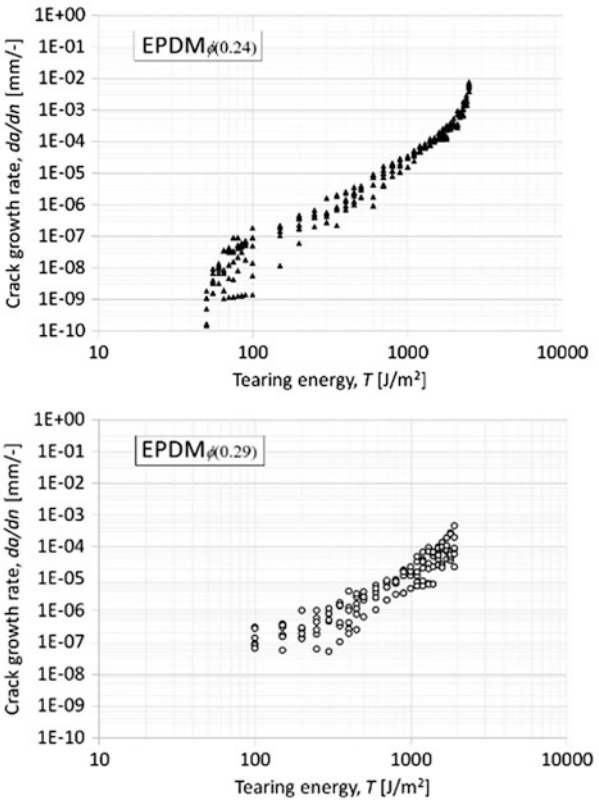

Fig. 5 Tearing energy vs. FCG rate for $EPDM_{\Phi(0.24)}$ (left) and $EPDM_{\Phi(0.29)}$ (right)

and are related to each phase of the FCG characteristics for both analysed rubbers. It is evident that the most time-consuming process is the determination of the FCG data described in beginning of phase II. Moreover, the minimum total time required to perform the determination of the complete FCG characteristics based on measuring the minimum size of the distinguishable crack growth length, $\Delta a = 0.01$ mm, would require 2,986 h ~ 125 days. On the other hand, for the high precise determination of FCG characteristics in the region of stable FCG, the measurement was realised in time lower than 1 day, which is a very efficient process.

In Fig. 7 the FCG characteristics for the $EPDM_{\Phi(0.24)}$ based on the average values of the FCG rate shown in Fig. 5 (left) are plotted. The characteristics are divided into the previously mentioned FCG phases. From the continuous progression of the FCG characteristics, it could be stated that there is no transient point within the complete curve respective within phase II and III, which was previously seen in Fig. 1, however for other rubber types.

In order to be able to describe the relationship between the tearing energy and the FCG rate with a continuous analytical function, moreover, with the highest possible accuracy, the specific function is necessary to be found. The specific functional dependence which governs the investigated quantities and which corresponds to the

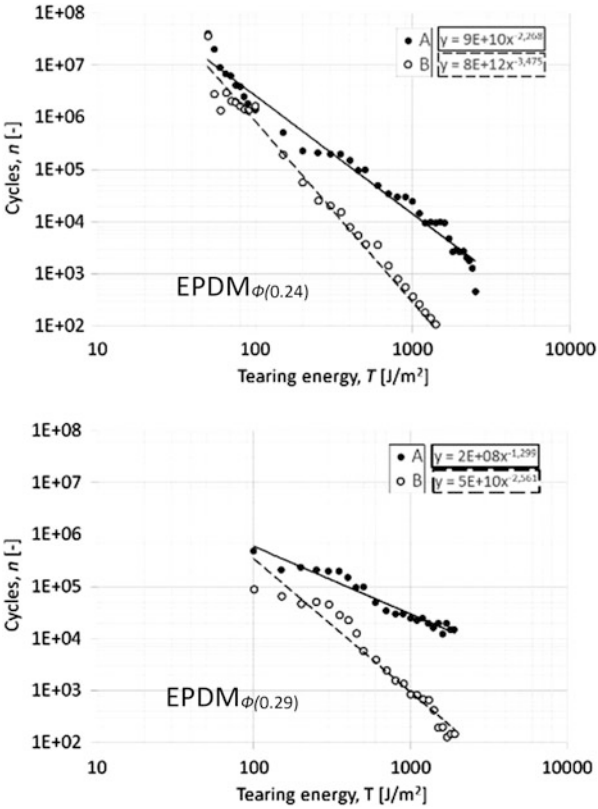

Fig. 6 Tearing energy related to totally applied cycles (curve A), respective cycles required to reach $\Delta a = 0.01$ mm of crack growth (curve B) for $EPDM_{\Phi(0.24)}$ (left) and $EPDM_{\Phi(0.29)}$ (right)

Table 3 Time required for determination of FCG characteristics

Analyses	Sample ID	Phase II	Phase III	Phase IV
		Time [h]		
Currently applied time	$EPDM_{\Phi(0.24)}$	5,365.0	108.0	1.0
	$EPDM_{\Phi(0.29)}$	–	134.0	–
Required time to reach 0.01 mm	$EPDM_{\Phi(0.24)}$	2,967.0	19.0	0.005
	$EPDM_{\Phi(0.29)}$	–	25.0	–

measured data is both given by the functional regulation and by its specific parameters respective coefficients. For each given functional rule, there are various procedures for finding its coefficients based on the determined data. Practically, the used procedure is based on searching from a set of given functions, $y = f(x)$, with two coefficients, in which one has the smallest sum of squares of deviation respective regression, R^2, with respect to the given set of data (x_i, y_i). Here, x and y are representing strings of general data. Thus, the general process is based on solving the specific function:

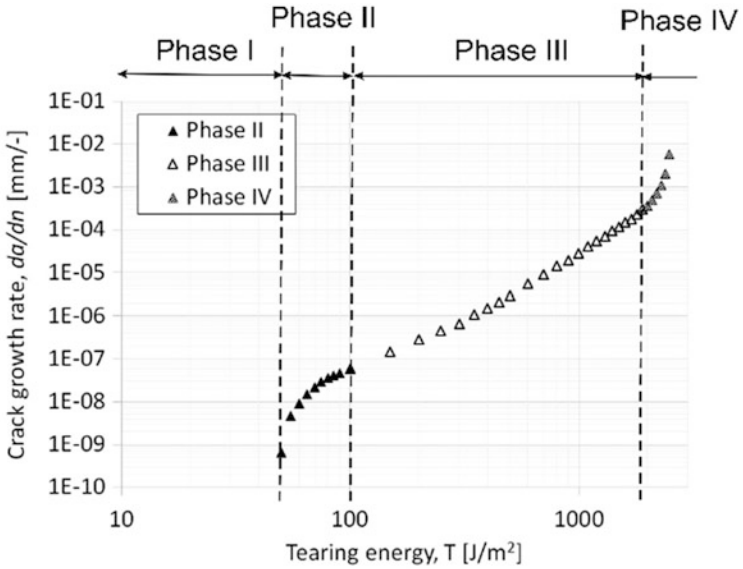

Fig. 7 FCG characteristics based on average values of FCG rate for $EPDM_{\Phi(0.24)}$

$$Y = c \cdot X + d, \tag{5}$$

in which $X = \alpha(x, y)$ and $Y = \beta(x, y)$. In the next step, the function will be modified to the function of one variable and thus Eq. (5) reads:

$$\beta(y) = c \cdot \alpha(x) + d. \tag{6}$$

Additionally, from Eq. (6), the parameter, y, can be derived to be:

$$y = \beta^{-1}(c \cdot \alpha(x) + d). \tag{7}$$

For this function the following set of two equations, which are necessary to be solved to find the unknown coefficients:

$$c \sum \alpha^2(x_i) + d \sum \alpha(x_i) = \sum \alpha(x_i)\beta(y_i) \tag{8}$$

$$c \sum \alpha(x_i) + d \cdot n = \sum \beta(y_i). \tag{9}$$

Its solution is the coefficients c, d of such a function $y = \mathrm{f}(x)$, which shows for the given set of data $\{\alpha(x_i); \beta(y_i)\}$, the minimum regression.

Because of the character of the FCG curves in the various regions, a set of specific and most fundamental functions were chosen: $y = x$; $y = 1/x$; $y = x^{1/3}$; $y = x^{1/2}$;

Table 4 Final fitting functions with the regression and related coefficients c, d

Function	Coefficient		Regression	Phase
	c	d	R^2	
$\frac{da}{dn} = \left[\left(\frac{c}{T^2} + d\right)^2\right]^2$	−31.4641	0.018604	0.9981	II $EPDM_{\Phi(0.24)}$
$\frac{da}{dn} = \left\{\left[c\left(\sqrt[3]{T}\right)^2 + d\right]^3\right\}^3$	0.001831	0.126593	0.9956	III $EPDM_{\Phi(0.24)}$
	0.001560	0.136132	0.9995	III $EPDM_{\Phi(0.29)}$
$\frac{da}{dn} = \left(\frac{1}{ce^{\sqrt[3]{T}} + d}\right)^3$	−0.000017	18.78814	0.9996	IV $EPDM_{\Phi(0.24)}$

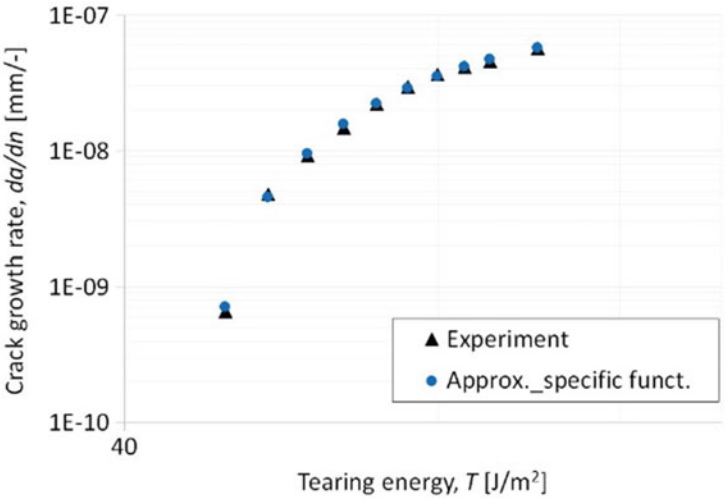

Fig. 8 The phase II of FCG characteristics for $EPDM_{\Phi(0.24)}$

$y = x^2$; $y = e^x$. Thus, $\alpha = f_p(x)$ and $\beta = f_q(y)$. Therefore, for the six selected functions, there are 36 different functions at disposal in shapes:

$$y = f_q^{-1}\left(c \cdot f_p(x) + d\right) \tag{10}$$

for $p \in <1.6>$, $q \in <1.6>$.

Finally, for each phase of the determined FCG characteristics in the case of the $EPDM_{\Phi(0.24)}$ and for phase III in the case of the $EPDM_{\Phi(0.29)}$, the functions with the minimum regression, R^2, as well as the numerically determined coefficients *c, d* are listed in Table 4. Moreover, the approximate best fits based on the listed functions are plotted in the next diagrams separately.

Figure 8 plots phase II of the FCG characteristics for $EPDM_{\Phi(0.24)}$, in which the data analysed are fitted with the functions listed in Table 2, with a regression, $R^2 = 0.9981$, plotted in Fig. 8 with blue data points. The intrinsic energy, T_0, can

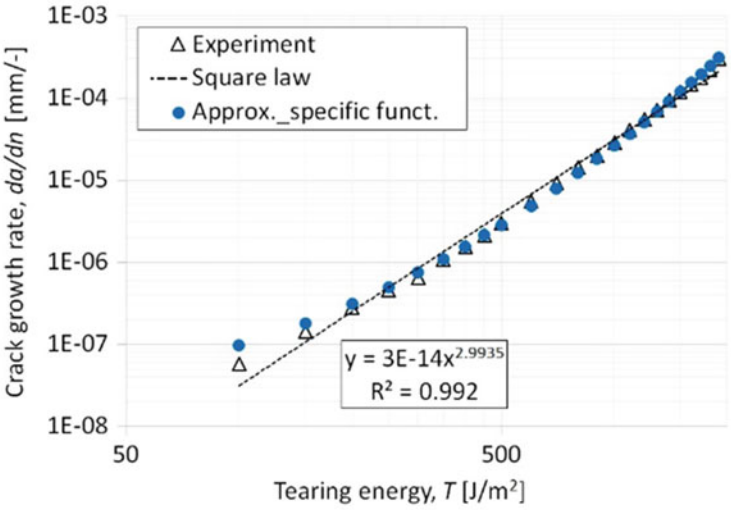

Fig. 9 The phase III of FCG characteristics for $EPDM_{\Phi(0.24)}$

additionally be calculated based on this function. From the data plotted in Fig. 1, the intrinsic energy, T_0, could be expected to be in the range of the FCG rate, $r \in <$1E-10; 1E-9$>$ mm/cycle. Moreover, due to realistic observations of the FCG, r = 6.57E-10 mm/cycle at the tearing energy 50 J/m^2, which seems to be very close to T_0, the intrinsic energy was calculated for the related FCG rate, r = 5E-10 mm/cycle, where finally $T_0 = 47.7$ J/m^2.

The full range of the FCG behaviours in phase III are shown in Figs. 9 and 10 for $EPDM_{\Phi(0.24)}$ and $EPDM_{\Phi(0.29)}$, respectively. Knowledge of the FCG characteristics in this phase directly implies an identical functional form of the curves for both analysed rubbers, which clearly achieved a non-linear function slightly deviating from the power-law in a double logarithmic scale. In Figs. 9 and 10, the experimentally determined data (triangles or circles for $EPDM_{\Phi(0.24)}$ and $EPDM_{\Phi(0.29)}$, respectively) are compared with the data given by the power-law (dashed line) as well as with the newly defined and numerically calculated fit respective approximation specific function (blue data points). Moreover, in Figs. 9 and 10, the power-law functions for both analysed materials are plotted, and the regression, R^2, are listed, whereas the regressions for the power-law functions $R^2 = 0.992$ for $EPDM_{\Phi(0.24)}$ and $R^2 = 0.9709$ for $EPDM_{\Phi(0.29)}$ were evaluated, which generally are lower than the regressions evaluated for the approximation-specific function applied ($R^2 = 0.9956$ for $EPDM_{\Phi(0.24)}$ and $R^2 = 0.9995$ for $EPDM_{\Phi(0.29)}$). It is worth mentioning that the power-law is a fairly good approximation for the data observed in the case of the $EPDM_{\Phi(0.24)}$; however for the $EPDM_{\Phi(0.29)}$, the approximation becomes significantly worst. Thus, the applied approximation-specific function fits the both experimentally determined data with a higher accuracy and respects the

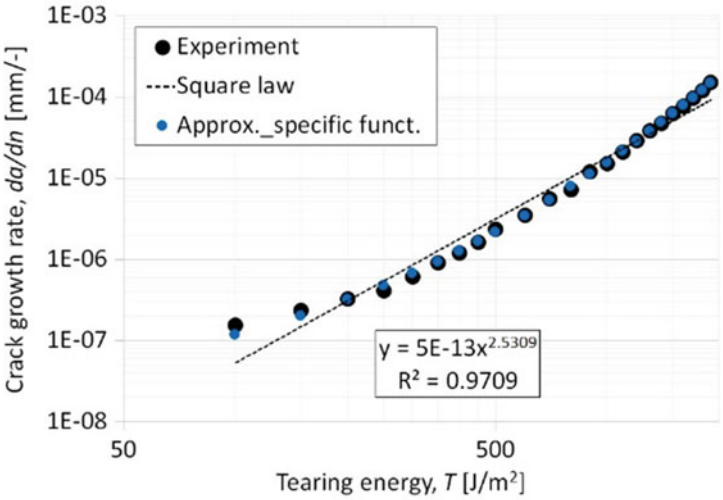

Fig. 10 The phase III of FCG characteristics for $EPDM_{\Phi(0.29)}$

non-linear character of the data in the double logarithmic scale, compared to the previously applied power-law.

The accelerated FCG process is defined in phase IV based on experimentally determined data (triangles), and numerically calculated fit respective approximation-specific function (blue data points) is plotted in Fig. 11 for the rubber $EPDM_{\Phi(0.24)}$. Here, the character of the data clearly implies the exponential functional form, which is exactly defined in Table 3. The defined function very precisely approximates the experimental data. The ultimate strength respective critical tearing energy, T_c, can additionally be calculated based on this function. From Fig. 1 generally, the critical tearing energy, T_c, could be expected to be in the range of the FCG rate, $r > 1.00\text{E-}3$ mm/cycle. Moreover, due to investigation of the FCG rate over this value, the critical tearing energy, T_c, was finally calculated for the related FCG rate, $r = 1.00\text{E-}2$ mm/cycle, as $T_c = 2{,}533.5$ J/m^2.

While comparing both of the FCG characteristics based on the experimentally determined data shown in Fig. 12, a very interesting phenomenon can be observed, where the curves are crossing each other approximately at the tearing energy, $T = 250$ J/m^2. The rubber loaded with a higher content of CB has a higher FCG rate for tearing energies below its characteristic value at the crossing point and a lower FCG rate beyond this value. This finding is different in comparison to previous works conducted by Lake and Lindley in Refs. [22, 23]. They strictly observed a horizontal shifting of the complete FCG characteristics to a higher tearing energy level with an increase in CB content without observing any data crossing. This observation leads to further consideration, e.g. if the form of the observed crossing of the FCG curves could indicate a slightly lower intrinsic strength, T_0, for rubbers reinforced with larger amounts of CB. This statement is contrary to observations by

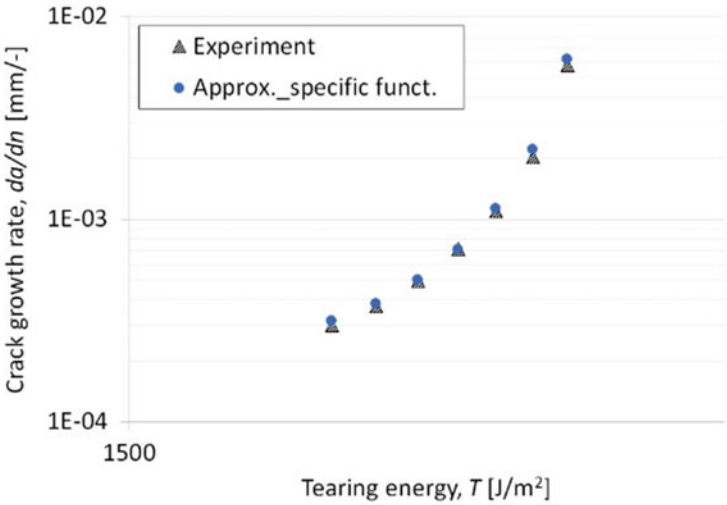

Fig. 11 The phase IV of FCG characteristics for $EPDM_{\Phi(0.24)}$

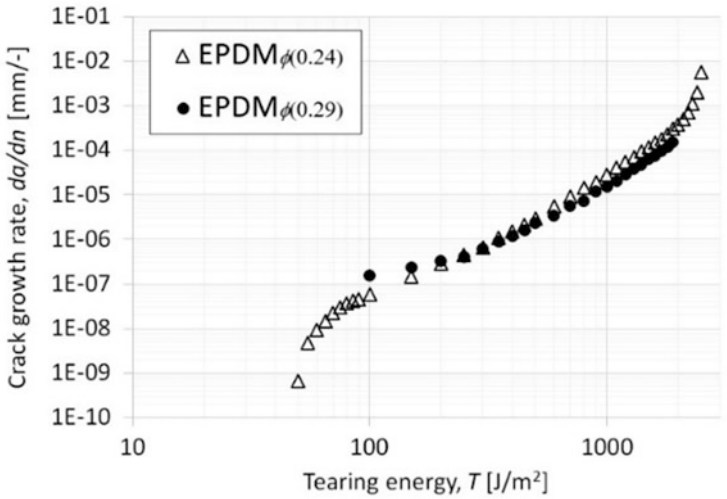

Fig. 12 FCG characteristics of both analysed rubbers

Bhowmick [24] who found an increasing trend of the endurance limit, directly proportional to the increase of CB loading. It is necessary to investigate this phenomenon and prove it in detail in future work for various rubbers as well as CB types.

4 Conclusion

The fatigue crack growth (FCG) characteristics of EPDM materials with a varied CB content have been determined and finally studied in detail in comparison to previous defined theoretical background as well as experimental analyses. Firstly, from the literature survey, weak points directly influencing the accuracy of the FCG characteristics were found in the experimental approach and described. To determine highly accurate FCG data, the exact experimental proceeding for the quantitative determination of FCG behaviour using Tear and Fatigue Analyzer has been described. From the obtained FCG characteristics, the related functions approximating the data in each of the phases of the FCG curve with the highest accuracy defining due to the regression have been found. It is worth mentioning that in the phase of the stable crack growth, the newly defined function is achieving a higher accuracy compared to the previously defined power-law for both analysed rubbers. From the continuous progression of the FCG characteristics, it is stated that there is no transient point within the complete curve respective within phases II and III, which has been observed in previous historical works. Following on from the FCG data and the related functional approximation, the exact values of the intrinsic strength as well as ultimate strength have been evaluated. A new phenomenon has been observed, in which the FCG characteristics are crossing each other due to the influence of different contents of CB, which has never been observed before. Thus, it is clearly visible that the highly accurate FCG analyses leads to an improvement in the FCG characteristics and strongly contributes to understanding the fatigue crack growth behaviour of rubber materials.

Acknowledgements This work was supported by the Ministry of Education, Youth and Sports of the Czech Republic – DKRVO (RP/CPS/2020/004).

References

1. Gent AN, Lindley PB, Thomas AG (1964) Cut growth and fatigue of rubbers. I. The relationship between cut growth and fatigue. J Appl Polym Sci:455–466
2. Rivlin RS, Thomas AG (1953) Rupture of rubber. I. Characteristic energy for tearing. J Polym Sci 10:291–318
3. Lake GJ, Lindley PB (1965) The mechanical fatigue limit for rubber. J Appl Polym Sci 9:1233–1251
4. Lake GJ, Thomas AG (1965) The strength of highly elastic materials. Proc R Soc Lond A 300:108–119
5. Gent AN, Mars WV (2013) Strength of elastomers, science and technology of rubber, 4th edn. Academic Press, Boston, pp 473–516
6. Thomas AG (1955) Rupture of rubber. II. The strain concentration at an incision. J Appl Polym Sci 18:177–188
7. Greensmith HW, Thomas AG (1955) Rupture of rubber. III. Determination of tear properties. J Appl Polym Sci 18:189–200
8. Thomas AG (1962) Rupture of rubber. Rheol Acta 2:63–66

9. Lindley PB (1974) Non-relaxing crack growth and fatigue in a non-crystallizing rubber. Rubber Chem Technol 47(5):1253–1264
10. Young DG (1986) Fatigue crack propagation in elastomer compounds: effects of strain rate, temperature, strain level and oxidation. Rubber Chem Technol 59:809–825
11. Ghosh P, Stoček R, Gehde M, Mukhopadhyay R, Krishnakumar R (2014) Investigation of fatigue crack growth characteristics of NR/BR blend based Tyre tread compounds. Int J Fract 188:9–21
12. Stoček R, Horst T, Reincke K (2017) Tearing energy as fracture mechanical quantity for elastomers. In: Stöckelhuber KW, Das A, Klüppel M (eds) Designing of elastomer nanocomposites: from theory to applications. Advances in polymer science, vol 275. Springer, New York, pp 361–398
13. Hintze C, Stoček R, Horst T, Jurk R, Wiessner S, Heinrich G (2014) Dynamic behavior of short aramid fiber-filled elastomer composites. Polym Eng Sci 54:2958–2964
14. Ghosh P, Mukhopadhyay R, Stocek R (2016) Durability prediction of NR/BR and NR/SBR blend tread compounds using tear fatigue analyser. Kautschuk-Gummi-Kunststoffe 69 (6):53–55
15. Stoček R, Stěnička M, Zádrapa P (2020) Future trends in predicting the complex fracture behaviour of rubber materials. Contin Mech Thermodyn. Article in press
16. Kaang S, Woong JY, Huh YI, Lee WJ, Im WB (2006) A test method to measure fatigue crack growth rate of rubbery materials. Polym Test 25(3):347–352
17. Eisele U, Kelbch SA, Engels H-W (1992) The tear analyzer – a new tool for quantitative measurements of the dynamic crack growth of elastomers. KGK 45:1064–1069
18. Mullins L (1969) Softening of rubber by deformation. Rubber Chem Technol 42:339–362
19. Payne AR (1962) The dynamic properties of carbon black-loaded natural rubber vulcanizates. Part I. J Appl Polym Sci 6(19):57–53
20. Stoček R, Heinrich G, Gehde M, Kipscholl R (2013) Analysis of dynamic crack propagation in elastomers by simultaneous tensile- and pure-shear-mode testing. In: Grellmann W et al (eds) Fracture mechanics & statistical mech., LNACM 70, pp 269–301
21. Stoček R, Heinrich G, Gehde M, Rauschenbach A (2012) Investigations about notch length in pure-shear test specimen for exact analysis of crack propagation in elastomers. J Plast Technol 01:2–22
22. Lake GJ, Lindley PB (1964) Ozone cracking, flex cracking and fatigue of rubber. 1. Rubber J 146(10):24–30
23. Lake GJ, Lindley PB (1964) Ozone cracking, flex cracking and fatigue of rubber. 2. Rubber J 146(11):30–36
24. Bhowmick AK (1988) Threshold fracture of elastomers. J Macromol Sci Polym Rev 28:339–370

Adv Polym Sci (2021) 286: 19–38
https://doi.org/10.1007/12_2020_78

Published online: 30 December 2020

Determining Parametrical Functions Defining the Deformations of a Plane Strain Tensile Rubber Sample

R. Stoček, M. Stěnička, and J. Maloch

Contents

Abstract The plane strain (PS) tensile sample, which is very often named as pure shear sample, featured prominently in classic studies of fracture mechanics of rubbers while investigating fatigue crack growth (FCG) behaviour. A PS sample is shaped as a thin, rectangular strip. For the FCG investigation it is held by rigid clamps along its long edges. While straining in-plane, deformation of the sample originates mainly along the loading direction except in the regions near the free edges. Thus, when using the PS sample for FCG characterization while applying simple fracture mechanics, the crack growth is required to be investigated within the region, where the deformation of the sample originates mainly along the loading direction. Parametrical functions defining the region of PS sample, where the

R. Stoček (✉)
PRL Polymer Research Lab, Zlin, Czech Republic

Centre of Polymer Systems, Tomas Bata University in Zlin, Zlin, Czech Republic
e-mail: stocek@utb.cz

M. Stěnička and J. Maloch
Centre of Polymer Systems, Tomas Bata University in Zlin, Zlin, Czech Republic

orientation of strain in the plane is in the loading direction or orthogonal to the crack growth, have experimentally been determined using a digital image correlation (DIC) system. In detail, the parametrical functions firstly describe the narrowing towards the edges and secondly the width of the region in which the FCG analysis should take place. This was observed over a broad range of the aspect ratio 'width/length' of the sample (<1/2, 10>) and the strain was varied in the interval ∈ <0, 0.5>. The strain over the complete horizontal axis across all applied aspect ratios has experimentally proven that no pure shear deformation (deformation strictly originating along the loading direction) is present in the PS sample in reality. Thus, thanks to the exponential character of the contraction over the complete horizontal axis of the PS sample, a novel criterion considering a deviation from the maximum achieved contraction in proportion ∈ <0.01, 0.05> has been established and it was included to the parametrical function defining the width of the region of deformation originating near the loading direction. Besides, it has been demonstrated that the deformation over the complete horizontal axis of sample is nearly independent of the applied rubber type. To conclude, based on the determined parametrical functions, the equation for calculating the minimal notch length required for FCG analyses within the region of deformation originating near the loading direction has been defined.

Keywords Crack · Fracture · Plane strain · Pure shear · Rubber · Sample

1 Introduction

Due to the unique viscoelastic behaviour of elastomeric materials, rubbers are used in a broad range of different engineering applications and require an understanding of their fracture behaviour to predict the service life of rubber products. The rapid advancement of simulation technology, which provides flexibility in applying a fracture mechanic analysis to determine the stresses, deformations and tearing energy for a rubber component of complex geometric and boundary conditions, is one way to do this, and it has created new opportunities to link lab testing materials to real-world rubber product performance. Fundamentally, finite element methods should relate the results from a lab experiment undertaken on simple sheet of cured rubber with realistic geometry and loading conditions, which occur in the actual rubber component used.

There are two general methods used to study the fracturing of rubber materials, namely the classic tearing energy method of Rivlin and Thomas [1] and the *J*-integral method introduced by Rice [2] and Cherepanov [3]. Both methods characterize the fracture behaviour by assuming that a critical amount of energy is required to advance a crack by a unit area. Both methods are based on an energy consideration; however, they differ in the methods of calculation and experimentation, whereas the sample geometry for investigating both methods remains identical.

Rivlin and Thomas [1] used three types of samples: the single-edge-notched tension (SENT), the trouser sample, and the plane strain (PS) tension sample, in which for each sample type specific formulas for determining the tearing energy were derived, using the identical assumption, which is inherent to the *J*-integral. Finally, the PS samples featured prominently in classic studies of fracture mechanics of rubber, in which the influence of different sample geometries compared to PS tension sample on fracture behaviour was studied, e.g., in Refs. [4–8]. The PS samples are commonly used for investigating fracture behaviour while applying both the loading quasi-static [9] and predominantly under fatigue conditions [10–24]. The PS behaviour with a dependence on varied rubber compositions is commonly studied using a PS sample and referenced, e.g., in [25, 26]. The future testing concepts based on PS samples for investigating the fracture behaviour of rubber under fatigue loading condition were studied in Refs. [27, 28] and these have successfully been implemented into standard experimental methods. Nowadays, the PS sample is the only one geometry, which is used for investigating endurance limits, intrinsic strength, based on a cutting method originally proposed in Ref. [29], where these studies are referenced [30–33].

In literature, the PS tension test pieces are very often named as pure shear samples, even though the resulting strain states that PS and pure shear are not identical [34]. PS samples consist of a thin, rectangular strip of rubber held by rigid clamps along its long edges (see Fig. 1). In deriving the approximation formulas for these samples, it is assumed that the sample volume can be divided into differently loaded regions firstly defined in Ref. [1], and here visualized in Fig. 1. When considering the un-notched PS sample (see Fig. 1, middle), there is a region D on both vertical edges which is influenced by the outer boundary and known as the edge effect. Between the regions D there is a region, in which the in-plane displacements are mainly along the loading direction and through the sample thickness, t, occurring in a region C. By assuming that the incompressibility of rubber, in the region C, since there should not be a contraction of the sample in its width, X-direction, respective, the thickness contraction would be similar in magnitude to the applied strain [34]. However, thanks to the application of a PS sample, in which the thickness, $t << L_0$, the displacement in the direction of the thickness can fully be neglected. Thus, the deformation state in the region C is expected to be near the deformation originating along the loading direction and fundamentally reads

$$\begin{bmatrix} x \\ y \end{bmatrix} = \begin{bmatrix} 1 & 0 \\ 0 & \varepsilon(y) + 1 \end{bmatrix} \cdot \begin{bmatrix} x_0 \\ y_0 \end{bmatrix} \tag{1}$$

When considering the notched PS sample (see Fig. 1, bottom), quite complicated stress and strain fields can be found in the vicinity of the crack tip (a region B). However, the remote fields are assumed to be homogeneous. Behind the crack tip there is a region A, and it is nearly unloaded. Nevertheless, in front of the crack tip, the region C can be found in which the deformation state again is near the deformation originating along the loading direction corresponding to Eq. (1).

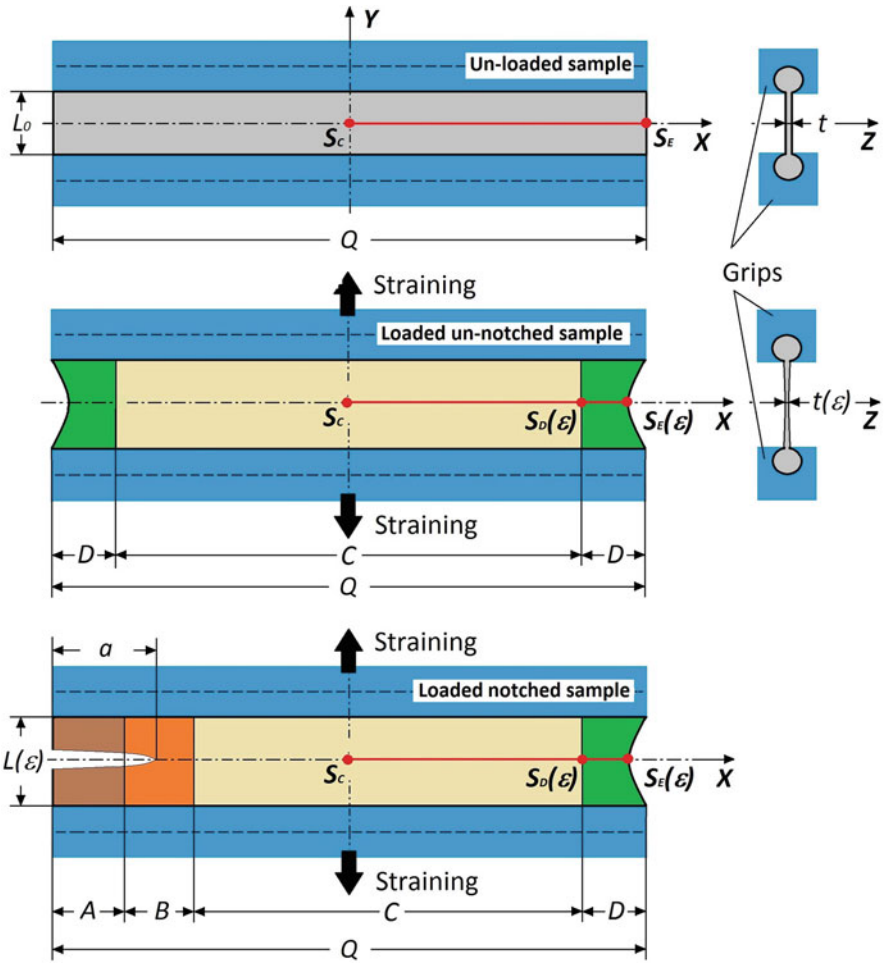

Fig. 1 The geometry of the plane strain tension sample

Finally, there is a region D which is identical with the region D in the un-notched sample. Considering infinitesimal crack propagation in such a sample, it is assumed that the complicated inhomogeneous state in the vicinity is translated with the crack tip. Consequently, the size of the region C is reduced increasing the unloaded region A.

Hence, the tearing energy can be determined via the elastic strain energy density, w in the homogeneous loaded region C, which is measured by the unloading curves from the un-notched PS sample at an identical boundary displacement, in which crack propagation occurred in the notched samples. This basic idea leads to the simple formula for determining the PS samples:

$$T = wL_0 \tag{2}$$

with the initial length of the sample, L_0 (corresponds to the initial distance of the clamps visible in the Fig. 1).

At the experimental investigation of the fracture behaviour of rubber, the deviation from the deformation originating strictly along the loading direction is usually neglected and the complete region C is associated with a non-deformation in the X-direction, orthogonally, respectively, to the main strain. However, the biggest advantage of the PS sample given by simple fracture mechanics (Eq. 2) requests a deep understanding of the influence of neglecting the deviation from the deformation originating strictly along the loading direction in the region C to be able to design the fracture experiment using the PS sample precisely. Moreover, the minimal notch length, $a_{0\min}$, corresponds with the width of the region D, in which the tip of the notch is requested to be located at the beginning or within the region C to be able to apply the simple fracture mechanics given by Eq. (2). Furthermore, the maximum width of PS sample given by the complete region C will be at disposal for fracture investigation. Thus, an investigation under a broader range of tearing energies could be realized in terms of the fatigue crack growth (FCG) analyses. Unfortunately, there is only limited information in literature regarding the width of the region of deformation originating strictly along the loading direction as well as the edge effect. The edge effect was studied from the numerical point of view in Refs. [35, 36]. Yeoh in Ref. [37] evaluated the effects of neglecting the deviation from the deformation originating strictly along the loading direction in the edge regions using non-linear finite element analysis. Stoček et al. in Ref. [28] firstly showed how the tearing energy, T, and the crack growth rate, r, depend on the PS sample's geometry defined with a varied aspect ratio given by 'width/length', Q/L_0, and the crack length, a. Moreover, Stoček et al. in Refs. [8, 38] firstly studied experimentally the minimal notch length, $a_{0\min}$, required for an FCG analysis using a PS sample at a crack growth within the region C for the aspect ratios, Q/L_0, in a range from 12 to 4, whereas they fully neglected the deviation from deformation originating strictly along the loading direction. Therefore, errors involved in neglecting this deviation from this deformation in the region C as well as the edge effect were neither experimentally investigated nor involved in the exact definition of each region of the PS sample as well as in defining the required minimal notch length.

Therefore, it is of very high scientific interest to perform a precise experimental investigation to determine the deformations of each of the regions of the PS rubber sample in dependence with a varied aspect ratio, Q/L_0, on strain, ε, as well as being influenced by various rubber types while considering the deviation from the deformation originating strictly along the loading direction. Finally, the main aim of this study is based on an experimental investigation to determine general parametrical functions considering the studied influences and defining the deformations of each region as well as the minimum notch length required for FCG analyses within the region C.

2 Experimental

The elastomers used in this study were a natural rubber (NR) SMR20 CV/BP1 (Lee Rubber Co. Pte Ltd. Malaysia) and a high-cis neodymium-catalysed butadiene rubber (BR, Trinseo, Germany), in which the NR represents a semi-crystalline and the BR is a typical representation of an amorphous type of elastomers. Both elastomers were filled with 50 phr of N330 type carbon black (CB). Table 1 lists the complete formulations of the rubber compounds.

Both rubber compounds were prepared in a two-stage mixing process using a laboratory scale internal mixer (SYD-2L, Everplast, Taiwan) of 1.5 L capacity. In the first stage, the master batches were prepared; mixing the rubbers and the chemicals (except for the curatives) was carried out at a rotor speed of 50 rpm (rotations per minute) for 5.0 min at a fill factor of 0.7, during which the initial chamber temperature was set at 100°C and finally reached 140–150°C. The prepared master batch was milled and sheeted with a two-roll mill at 60°C and stored for 4 h.

The second stage of the mixing was performed for a total time of 3.0 min at 35 rpm, with an initial chamber temperature of 90°C and the identical fill factor was 0.7. The master batches were mixed for 1 min, followed by adding the complete curing system and mixing for an extra 2 min, meanwhile the temperature was increased up to 100°C or 110°C. Then, the prepared final batch was milled and sheeted with the two-roll mill at 60°C and stored for 24 h before the rheological investigation and the sample curing.

The PS test sample (schematically shown in Fig. 1) of various geometry or aspect ratio, Q/L_0, respectively, listed in Table 2, was cured in a heated press (LaBEcon 300 from Fontijne Presses, the Netherlands) at 160°C in accordance with an optimum curing time, t_{90}, which was determined from rheometer curves using Moving Die Rheometer (MDR 3000 Basic from MonTech, Germany) with respect to ASTM 6204.

Table 1 The rubber compound formulation

Code	Ingredients	NR [phr]	BR [phr]
Master batch	SMR20 CV/BP1-NR	100	–
	High-cis Nd-BR	–	100
	N330 CB	50	50
Final batch	Zinc oxide	2	2
	Stearic acid	1	1
	Sulphur	2	2
	TBBS[a]	1	2
	MTBS[b]	0	0.5
	6PPD[c]	1	1
	Total	157	158.5

[a]N-tert-butyl-benzothiazole sulphonamide
[b]Benzothiazole disulphide
[c]N-1,3-dimethylbutyl)-N-phenyl-p-phenylenediamine

Table 2 PS sample geometry studied

Width, Q [mm]	5	10	20	30	40	50	60	70	80	90	100
Length, L_0 [mm]	10										
Aspect ratio, Q/L_0	0.5	1	2	3	4	5	6	7	8	9	10

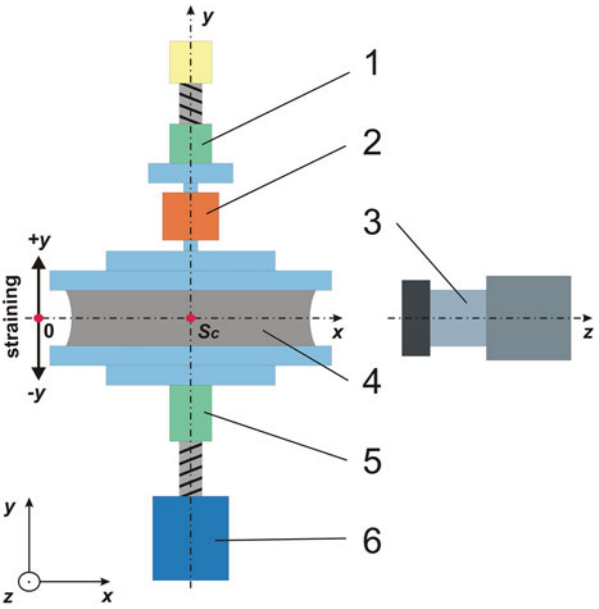

Fig. 2 The scheme of the experimental setup: 1 – upper clamps; 2 – loading cell in the y direction; 3 – CCD monochrome camera; 4 – PS sample; 5 – lower clamps; 6 – actuator for straining

The experimental investigation of the PS rubber sample deformation dependent on a varied aspect ratio, Q/L_0, was performed using a combination of two methods, based on the simultaneous straining and determining of complete sample deformation. The experimental setup is schematically shown in Fig. 2. The tensile loading was applied to the sample using an Intrinsic Strength Analyser (ISA™, Coesfeld GmbH & Co. KG, Germany) at a strain rate of 10.00 mm/min at a range of strains, $\varepsilon \in <0, 0.5>$. The ISA™ was used because it is a piece of equipment which can realize the tensile loading in both positive and negative Y-direction symmetrically to the X-axis. Thus, the X-axis remains unstrained in the direction of the main strain. Simultaneously, the complete process of sample deformation during tensile loading was recorded via CCD monochrome camera with a sampling rate of 10 Hz, during which the camera was located in the negative direction of the Z-axis. Finally, the captured photos were analysed with DIC software (GOM Correlate, Germany) to evaluate the displacement and the concave neck at the edges (Δx). For this purpose, prior to the experiment a stochastic pattern made by an anti-reflex spray, MR2000 Anti-Reflex L (MR Chemie GmbH, Germany) was created on the surface of all of the PS samples.

The data analysis was focused on the displacement distribution along the X-axis of the PS sample (Fig. 1), which is the path of future crack propagation. Thus, all of the data presented in the resulting part are related to that displacement only.

3 Results and Discussion

3.1 General Contractions of the PS Sample

For a general understanding of the experiment performed, the DIC results for the unloaded and the loaded PS sample are visualized in Fig. 3 for an exemplary test piece with an aspect ratio of 7 under strain, $\varepsilon = 0.5$ and the detail of the geometry used is described in previous paragraphs in line with the scheme of the sample geometry plotted in Fig. 1. It is noteworthy that an investigation and further quantification of the sample deformation can be achieved when an exact definition and the location of a coordinate system is undertaken. Here, the centre of the plane coordinate system, S_C, is identical with the centre of the rubber sample; therefore, the main axes of the plane coordinate system X and Y are associated with the main axes of the sample. Thus, the sample geometry can be additionally divided into four equal quadrants, in which the deformations act identically, whereas all points above the X-axis move up and vice versa, all points below it move equally, but in the opposite direction. The points, which are located directly on the X-axis, do not change their positions in the Y-direction; however, they are strictly contracted in the X direction only. The contraction in the X-direction intensifies from its minimum value close to the clamps to the centre of the sample, where it reaches its maximum and returns to the minimum contraction at the opposite clamps. Thus, all of the data evaluated and presented are related to measuring the displacement of the points located at the X-axis and associated with the abscissa $|S_C\ S_E|$, whereas at straining this region is divided into two separate zones given by the abscissa $|S_C\ S_D(\varepsilon)|$ for half of the

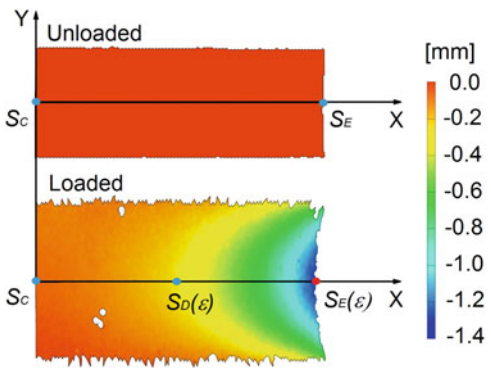

Fig. 3 An example of the deformation in the X-direction of the sample with an aspect ratio of 7 evaluated using DIC

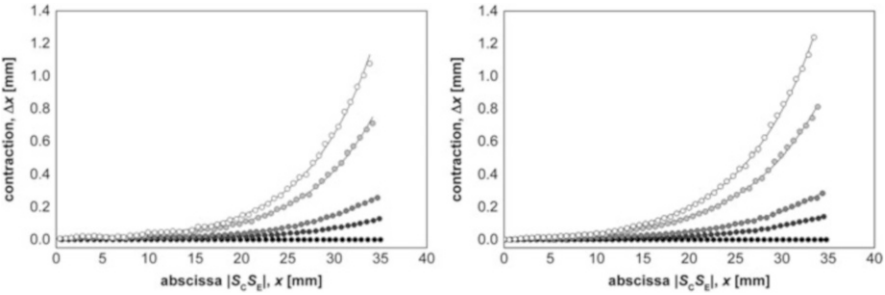

Fig. 4 The contraction and the Δx of the sample at the X-axis vs. the abscissa $|S_C\ S_E|$, x, of the BR (left) and the NR (right) samples for the aspect ratio of 7 at different strains, ε: 0 (black), 0.05 (dark grey), 0.10 (grey), 0.30 (light grey), and 0.50 (white)

region C, and $|S_D(\varepsilon)\ S_E(\varepsilon)|$ for the region D and the edge region, respectively. It is very challenging to define the location of the point $S_D(\varepsilon)$, because from the Fig. 3 there may be a visible slight change of the colour associated with the deformation in the X-direction around the complete X-axis. Thus, the location of $S_D(\varepsilon)$ seems to be ambiguous.

In the first step, a complete deformation around the X-axis defined with the abscissa $|S_C\ S_E(\varepsilon)|$ was performed depending on the varied strain applied in the Y-direction, the data for the strain values was evaluated, $\varepsilon = 0$, 0.05, 0.1, 0.3, and 0.5.

Simultaneously, the courses of the displacement, the contraction and the Δx respectively, over the abscissa $|S_C\ S_E(\varepsilon)|$ for both investigated compounds and all aspect ratios (see Tables 1 and 2) dependent on the various above-mentioned strains applied in the Y-direction were analysed. In Fig. 4, the courses of the contraction and the Δx for the aspect ratio of 7 exemplary are plotted. The originally determined data of the contraction and the Δx from DIC measurement are fitted with an exponential function with base e, which is the Euler no., using the software Origin™:

$$\Delta x = c + A \cdot e^{(b \cdot x)}, \tag{3}$$

in which x represents the investigated location at the abscissa $|S_C\ S_E|$, and A, b and c are varying parameters dependent on the applied strain.

Clearly, the exponential functions are firstly characterized with the growth over the complete real variable and secondly with their accelerated increase as x rises. Moreover, the regressions, $R^2_{\Delta x}$, of the exponential fits plotted in Fig. 4 are listed in Table 3. It is obvious that the functions are approximating the data excellently, and thus it is a fact that the exponential functions do not generally provide any constant contraction, $\Delta x = 0$. This is quite an interesting fact thanks to the definition of the region of deformation originating strictly along the loading direction or the region C, respectively, in which the contraction, $\Delta x = 0$ is expected [1, 34–38].

Table 3 Regression, $R^2_{\Delta x}$, for exponential approximation of the DIC data

Compounds	Strain, ε	0	0.05	0.10	0.30	0.50
BR	$R^2_{\Delta x}$	1.000	0.997	0.997	0.998	0.999
NR		1.000	0.998	0.998	0.999	0.999

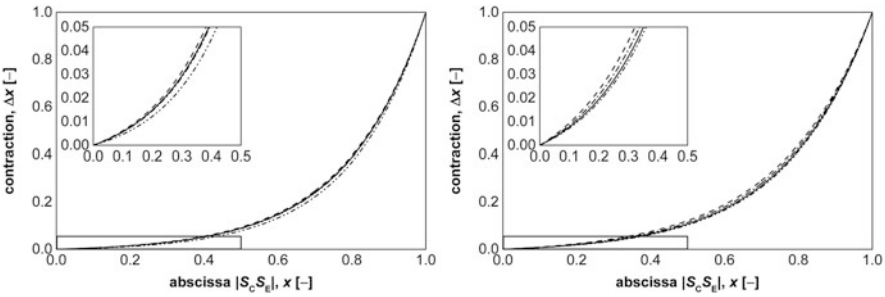

Fig. 5 The contraction and the Δx vs. the abscissa $|S_C\ S_E|$, x, of the BR (left) and the NR (right) samples for the aspect ratio of 7 at different strains, ε: 0.05 (solid line), 0.10 (dash line), 0.30 (dash dot line), and 0.50 (dash dot dot line) with a detailed view close to the centre of the coordinates, S_C

The contraction over the complete width of the PS sample as well as at the region very close to the vertical axis, respectively, close to the centre of the coordinates, S_C, exemplary is demonstrated in the sample with the aspect ratio of 7 for both of the analysed materials in Fig. 5. In these plots, both the contraction, the Δx, and the actual length of the abscissa $|S_C\ S_E(\varepsilon)|$, x, are normalized to '1' for all applied strains. Logically, this contraction is more intensive when the aspect ratio rises.

To finally define the width of the region, where the deformation originates near the loading direction, or the courses of contractions, Δx, over the abscissa $|S_C\ S_D|$ corresponding with half (un-notched sample, see Figure 1) of the region C, respectively, a criterion allowing a deviation from the contraction, $\Delta x = 0$ mm is required to be defined and implemented into the final equation.

Such criterion, K_{crit}, is based on a proportional deviation, D_{dev}, from the maximum observed contraction, Δx_{max}, achieved over the complete width, Q, of the PS sample and is finally defined as follows:

$$K_{crit} = D_{dev} \cdot \Delta x_{max}, \tag{4}$$

in which the proportional deviation, $D_{dev} \in <0.01,\ 0.05>$ in an increment $\Delta D_{dev} = 0.01$, which was applied within this study.

Thanks to the exponential character of the contraction over the complete horizontal axis of the PS sample, the contraction, $\Delta x > 0$ and thus no deformation originating strictly along the loading direction is present in the PS sample for the aspect ratios studied. The only reasonable way to exactly reach the deformation originating strictly along the loading direction in the rubber sample is to take the measurement while restraining the edges in the orthogonal direction to the main

strain. Such experiments are undertaken only by biaxial testing devices, e.g. Biaxial Tester (Coesfeld GmbH & Co. KG), and the results of which are presented, e.g., in Refs. [39, 40].

3.2 Contractions at the Edge of the Point, S_E

In Fig. 6, the length of abscissa $|S_C\, S_E(\varepsilon)|$, $x\,(S_E)$ which finally can be associated with the contraction of edge, $\Delta x\,(S_E)$, of the point, S_E for the previously defined various strains, ε, in relation to the aspect ratios of the analysed PS samples is plotted for both of the analysed rubber materials. Naturally, as the width, Q, of the samples increases the length of abscissa $|S_C\, S_E(\varepsilon)|$, $x\,(S_E)$ rise as well and represent an almost linear dependence defined as follows:

$$x(S_E) = k_{(S_E)} \cdot \left(Q/L_0\right) + q_{(S_E)} \Rightarrow \Delta x(S_E) = \frac{Q}{2} - x(S_E), \tag{5}$$

in which $k_{(S_E)}$ and $q_{(S_E)}$ correspond to the slope and the intercept at a given strain.

Moreover, only a minor influence from the applied strain on the contractions at the edge, $\Delta x(S_E)$, of the point, S_E is clearly visible from Fig. 6. The absolute value of the impact of the applied strain on the contractions at the edge, $\Delta x(S_E)$, is finally shown in Fig. 7, in which the slope, $k_{(S_E)}$ and the intercept, $q_{(S_E)}$, obtained from Eq. (3) are plotted dependent on the applied strain. Both the parameters $k_{(S_E)}$ and $q_{(S_E)}$ present an almost linear dependence on the strain and therefore, they can be written as follows:

$$k_{(S_E)} = k_{k(S_E)} \cdot \varepsilon + q_{k(S_E)} \tag{6}$$

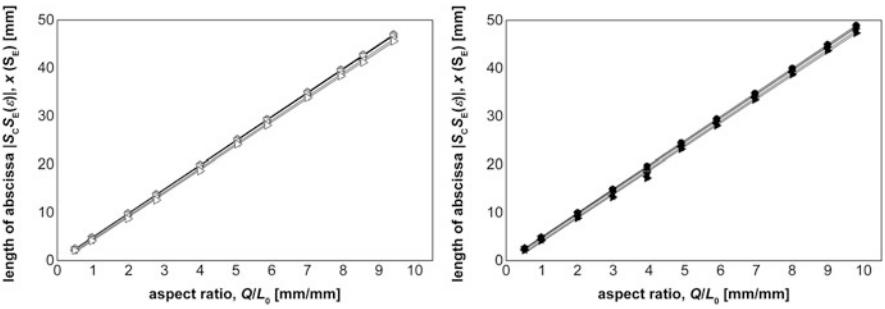

Fig. 6 The length of the abscissa $|S_C\, S_E(\varepsilon)|$, $x\,(S_E)$, vs. the aspect ratio, Q/L_0, for the BR (left, open symbols) and the NR (right, solid symbols) are plotted for the various strains, ε: 0 (○●), 0.05 (△▲), 0.1 (▽▼), 0.3 (◁◀), and 0.5 (▷▶)

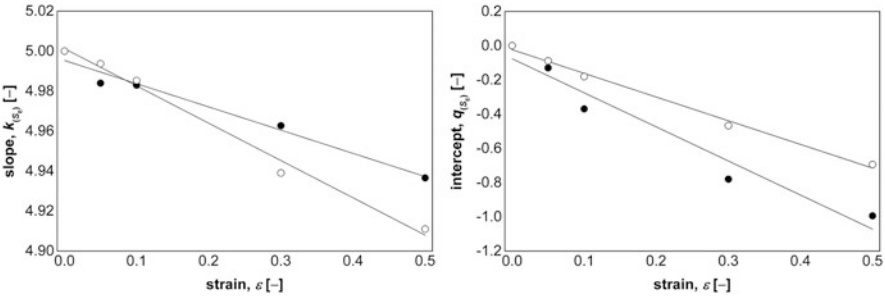

Fig. 7 The dependence of the slope, $k_{(S_E)}$ (left) and the intercepts, $q_{(S_E)}$ (right) on the strain, for the BR (open symbols) and the NR (solid symbols)

Table 4 The absolute values of the parameters defining the linear functions of Eqs. (6) and (7)

Material	Parameter			
	$k_{k(S_E)}$	$k_{q(S_E)}$	$q_{k(S_E)}$	$q_{k(S_E)}$
BR	−0.1866	−1.3837	5.0012	−0.0235
NR	−0.1162	−1.9909	4.9953	−0.0765
Average	−0.1514	−1.6873	4.9983	−0.0500
Deviation	±0.0498	±0.4293	±0.0042	±0.0375

$$q_{(S_E)} = k_{q(S_E)} \cdot \varepsilon + q_{q(S_E)} \tag{7}$$

Substituting Eq. (5) with Eqs. (6) and (7) results in a general formulation of the contraction at the edge, $\Delta x(S_E)$, dependent on the various strains, ε:

$$\Delta x(S_E) = \left(k_{k(S_E)} \cdot \varepsilon + q_{k(S_E)}\right) \cdot \left(Q/L_0\right) + \left(k_{q(S_E)} \cdot \varepsilon + q_{q(S_E)}\right) \tag{8}$$

In Table 4, the determined absolute values for the slopes $k_{k(S_E)}, k_{q(S_E)}$ as well as the intercepts $q_{k(S_E)}, q_{k(S_E)}$ are listed for both of the analysed rubber materials. From Fig. 7 and Table 4, the absolute values of the observed parameters for both the materials can be assumed to be very close to each other. Thus, the influence of the material on the monitored parameter, $\Delta x(S_E)$ could be neglected. Therefore, the final absolute values for the slopes $k_{k(S_E)}, k_{q(S_E)}$ as well as the intercepts $q_{k(S_E)}, q_{k(S_E)}$ are represented with average values from the values of both of the materials, actually representing an independence from the rubber material. The substitution of the relevant absolute values listed in Table 4 into Eq. (8) would finally represent the function describing the contraction at the edge, $\Delta x(S_E)$ of the point, S_E dependent on the various strains, ε, either for each of the analysed rubber materials or the function independent from the material type.

3.3 The Width of the Region of Deformation Originating Strictly along the Loading Direction

Within this chapter, a parametrical function, which generally defines the width, Q_C of the region C or the region of deformation originating near the loading direction given with the abscissa $|S_C\ S_D(\varepsilon)|$ dependent on the aspect ratio as well as in relation to the influence of the material and the strain is derived. Moreover, the above-mentioned statement regarding the exponential deviation from the contraction, $\Delta x = 0$ mm over the complete width, Q_C, of the PS sample the defined criterion, K_{crit} based on a proportional deviation, D_{dev} is implemented.

In Figs. 8 and 9, the dependences of half of the width, $Q_C/2$ of the region C on the aspect ratio, Q/L_0, for all the applied strains and both of the materials exemplary are plotted firstly at the implementation of the criterion, K_{crit}, in which the proportional deviation, $D_{dev} = 0.01$ (see Fig. 8), and secondly for the $D_{dev} = 0.05$ (see Fig. 9)

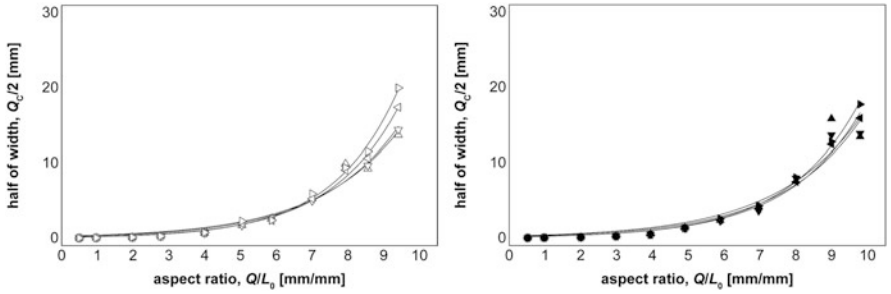

Fig. 8 The dependence of half of the width, $Q_C/2$ of the region C on the aspect ratio, Q/L_0 for all applied strains, ε: 0.05 (△▲), 0.1 (▽▼), 0.3 (◁◀), and 0.5 (▷▶) for the BR (open symbols) and the NR (solid symbols) at the implementation of the criterion, K_{crit} with a proportional deviation, $D_{dev} = 0.01$

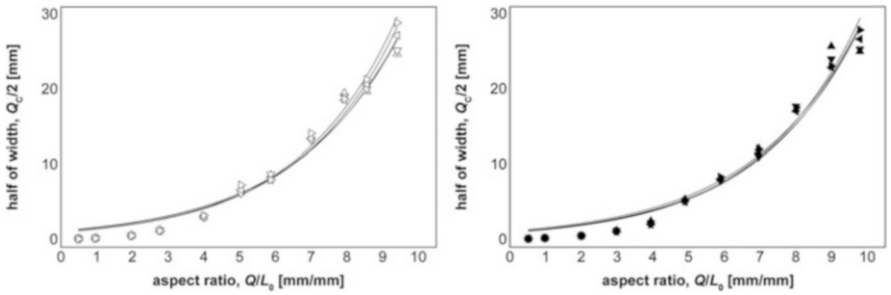

Fig. 9 The dependence of half of the width, $Q_C/2$ of the region C on the aspect ratio, Q/L_0 for all applied strains, ε: 0.05 (△▲), 0.1 (▽▼), 0.3 (◁◀), and 0.5 (▷▶) for the BR (open symbols) and the NR (solid symbols) at the implementation of the criterion, K_{crit} with a proportional deviation, $D_{dev} = 0.05$

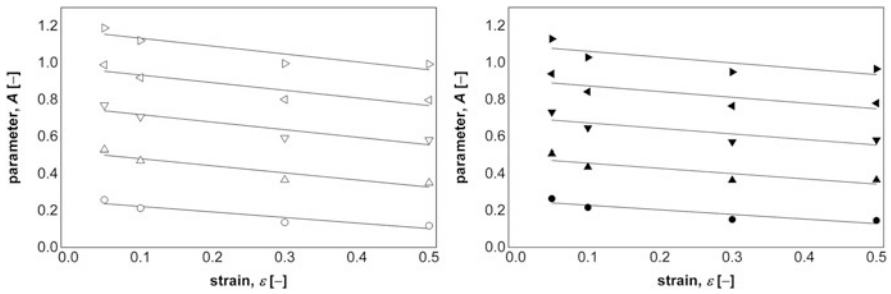

Fig. 10 The dependence of the parameter, A, on the strain, ε, for proportional deviations, $D_{\text{dev}} = 0.01$ (○●), 0.02 (△▲), 0.03 (▽▼), 0.04 (◁◀), and 0.05 (▷▶), in which the plot represents the BR (open symbols) and the NR (solid symbols)

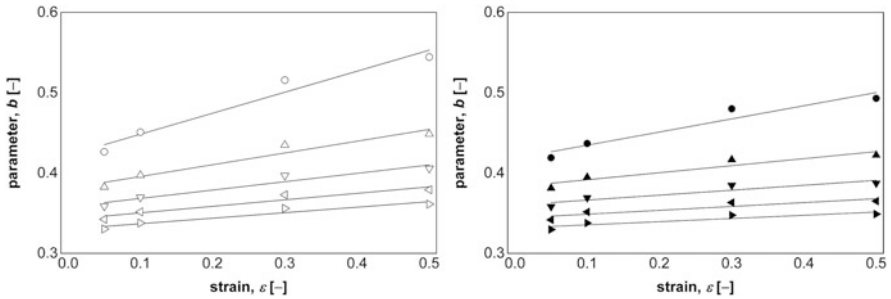

Fig. 11 The dependence of the parameter, b, on the strain, ε, for proportional deviations, $D_{\text{dev}} = 0.01$ (○●), 0.02 (△▲), 0.03 (▽▼), 0.04 (◁◀), and 0.05 (▷▶), in which the plot represents the BR (open symbols) and the NR (solid symbols)

were implemented. Thus, all values fulfilling the proportion $Q_C/2 \leq K_{\text{crit}}$ are associated with the contraction, $\Delta x = 0$ mm and therefore these are related to be part of the region C, whereas the value fulfilling the parity $Q_C/2 = K_{\text{crit}}$ is related to half of the width of the region C. It is worth mentioning that this dependence was calculated for a range of the proportional deviation, $D_{\text{dev}} \in <0.01, 0.05>$ in an increment, $\Delta D_{\text{dev}} = 0.01$. By comparing Figs. 8 and 9, the increase of the proportional deviation, D_{dev} to the absolute value of the width, $Q_C/2$, is significantly influenced.

Obviously, the dependence of half of the width, $Q_C/2$, of the region C on the aspect ratio, Q/L_0, presents an exponential character and can be defined as follows:

$$Q_C/2 = A.e^{b.\left(\frac{Q}{L_0}\right)}, \tag{9}$$

in which A and b are parameters at an applied strain, ε, and a relevant proportional deviation, D_{dev} of the criterion, K_{crit}. The dependences of parameter, A, in Fig. 10, and the dependences of parameter, b in Fig. 11, respectively, on various strains are plotted for all applied proportional deviations, D_{dev}, and for both of the investigated

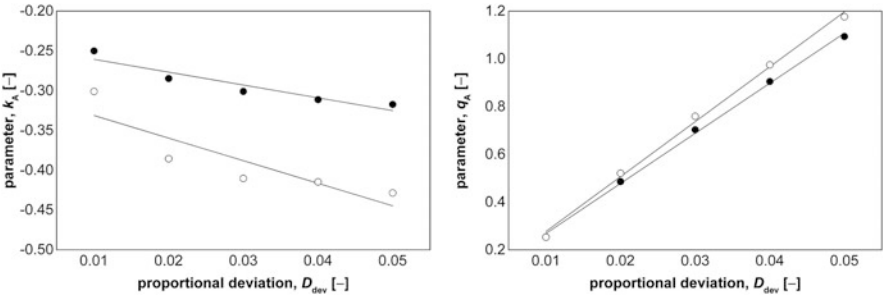

Fig. 12 The dependences of parameters k_A, q_A on proportional deviations, D_{dev}, for the BR (open symbols) and the NR (solid symbols)

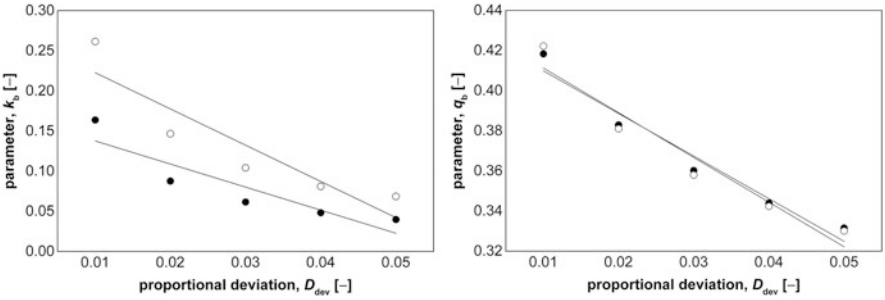

Fig. 13 The dependences of parameters k_b, q_b on proportional deviations, D_{dev}, for the BR (open symbols) and the NR (solid symbols)

rubber materials. The dependence of these parameters (A, and b) on the strain, ε, can be linearly approximated and written as follows:

$$A = k_A \cdot \varepsilon + q_A \tag{10}$$

$$b = k_b \cdot \varepsilon + q_b, \tag{11}$$

in which k_A, k_b and q_A, q_b correspond to the slopes and the intercepts at a given strain.

To properly determine a dependence of half of the width, $Q_C/2$, of the region C on the aspect ratio, Q/L_0, given by Eq. (10), the effect of the criterion, K_{crit} based on various proportional deviations, $D_{dev} \in <0.01, 0.05>$ on the parameters k_A, k_b and q_A, q_b corresponding to the slopes and the intercepts at a given strain is finally required to be taken into account and needs to be calculated. In Figs. 12 and 13, the dependences of parameters k_A, q_A, and k_b, q_b, respectively, on proportional deviations, D_{dev}, are plotted for both of the investigated rubber materials. The determined data were approximated with linear functions, as is visible in both Figs. 12 and 13, in which the linear approximations are generally expressed with Eqs. (12)–(15):

Table 5 The absolute values of parameters defining the linear functions of Eqs. (12) and (13)

Material	Parameters			
	$k_{k_{\text{Acrit}}}$	$k_{q_{\text{Acrit}}}$	$q_{k_{\text{Acrit}}}$	$q_{q_{Acrit}}$
BR	−1.6107	23.0089	−0.2445	0.0467
NR	−2.8394	20.9890	−0.3028	0.0587
Average	−2.2251	21.9990	−0.2737	0.0527
Deviation	±0.8688	±1.4283	±0.0412	±0.0085

Table 6 Absolute values of parameters defining the linear functions of Eqs. (14) and (15)

Material	Parameters			
	$k_{k_{\text{bcrit}}}$	$k_{q_{\text{bcrit}}}$	$q_{k_{\text{bcrit}}}$	$q_{q_{\text{bcrit}}}$
BR	−4.5159	−2.2294	0.2678	0.4336
NR	−2.8744	−2.1257	0.1664	0.4312
Average	−3.6951	−2.1776	0.2171	0.4324
Deviation	±1.1607	±0.0733	±0.0717	±0.0017

$$k_A = k_{k_{\text{Acrit}}}.D_{\text{dev}} + q_{k_{\text{Acrit}}}, \tag{12}$$

$$\mathrm{q_A} = \mathrm{k_{q_{Acrit}}}.\mathrm{D_{dev}} + \mathrm{q_{q_{Acrit}}}, \tag{13}$$

$$\mathrm{k_b} = \mathrm{k_{k_{bcrit}}}.\mathrm{D_{dev}} + \mathrm{q_{k_{bcrit}}}, \tag{14}$$

$$\mathrm{q_b} = \mathrm{k_{q_{bcrit}}}.\mathrm{D_{dev}} + \mathrm{q_{q_{bcrit}}}, \tag{15}$$

in which $k_{k_{\text{Acrit}}}, k_{q_{\text{Acrit}}}, k_{k_{\text{bcrit}}}, k_{q_{\text{bcrit}}}$ correspond to the slopes and $q_{k_{\text{Acrit}}}, q_{q_{\text{Acrit}}}, q_{k_{\text{bcrit}}}, q_{q_{\text{bcrit}}}$ to the intercepts.

After substituting Eqs. (12)–(15) for Eqs. (10) and (11) and the final substitution of these two equations for Eq. (9) gives the final general relationship for determining the width, Q_C, of the region C dependent on the aspect ratio, Q/L_0, which reads:

$$Q_C = 2 \cdot \left\{ \left[\left(k_{k_{Acrit}}.D_{dev} + q_{k_{Acrit}} \right) \cdot \varepsilon + \left(k_{q_{Acrit}}.D_{dev} + + q_{q_{Acrit}} \right) \right] .e^{\left[\left(k_{k_{bcrit}}.D_{dev} + \mathrm{q_{k_{bcrit}}} \right) \cdot \varepsilon + \left(k_{q_{bcrit}}.D_{dev} + q_{q_{bcrit}} \right) \right] . \left(\frac{Q}{L_0} \right)} \right\}, \tag{16}$$

In Tables 5 and 6, the determined absolute values for the slopes $k_{k_{Acrit}}, k_{q_{Acrit}}, k_{k_{bcrit}}, k_{q_{bcrit}}$ and the intercepts $q_{k_{Acrit}}, q_{q_{Acrit}}, q_{k_{bcrit}}, q_{q_{bcrit}}$ are listed for both of the analysed rubber materials. The linear approximations have a very close character to each other when comparing both the analysed rubber materials for all investigated parameters. Therefore, the final absolute values for all parameters are averaged to formulate one equation independent of the type of used rubber material. The substitution or the relevant absolute values listed in Tables 5 and 6 for Eq. (16) would finally represent width, Q_C, of the region C vs. the aspect ratio, Q/L_0, dependent on the various strains, $\varepsilon \in <0,\ 0.5>$ at a chosen criterion, K_{crit}, based on various proportional deviations, $D_{\text{dev}} \in <0.01,\ 0.05>$ either for each of the analysed rubber materials or the function independent of it.

Table 7 The calculated values representing the length of abscissa $|S_C\, S_E(\varepsilon)|$, $x\,(S_E)$, the contraction of edge, $\Delta x\,(S_E)$, of the point, S_E, the width of region C, Q_C, and the minimum notch length, a_{0min} as a percentage of the width, Q

Aspect ratio, Q/L_0	0.5	1	2	3	4	5	6	7	8	9	10
$x\,(S_E)$	62.7	80.6	89.5	92.5	94.0	94.9	95.5	95.9	96.2	96.5	96.7
$\Delta x\,(S_E)$	37.3	19.4	10.5	7.5	6.0	5.1	4.5	4.1	3.8	3.5	3.3
Q_C	6.4	4.1	3.4	3.7	4.6	6.1	8.4	11.9	17.1	25.1	37.3
a_{0min}	46.8	47.9	48.3	48.1	47.7	47.0	45.8	44.1	41.4	37.4	31.4

In conclusion, the difference between Eqs. (8) and (16) represents the strain, $\varepsilon = 0$ the original, whereas for the strain, $\varepsilon > 0$ the contracted width of the region D. Additionally, this difference corresponds to the parameter defining the minimum notch length, $a_{0\min}$ applied to the PS sample for FCG analyses in the region C and reads:

$$a_{0\,\min} = |S_D(\varepsilon)S_E(\varepsilon)| = x(S_E) - Q_C/2 \tag{17}$$

Finally, thanks mainly to the manual process of sample notching, which produces high inaccuracy, it is recommended to produce the real notch approximately 20% longer compared to the minimum notch length, $a_{0\min}$. Thus, the length of a finally real applied notch to the rubber sample is defined as follows:

$$a_{0\text{real}} = 1.2 \cdot a_{0\,\min}\,. \tag{18}$$

However, the more details about performing an exact notch using a manual process can be found in Ref. [41].

In the final part of this study, the numerical values were calculated using the parametrical functions (Eqs. (5), (16), and (17)) at the maximal strain, $\varepsilon = 0.5$ and proportional deviations $D_{\text{dev}} = 0.01$, whereas both parameters are representing the critical condition. Moreover, the calculation is based on application of average constants, which represent the behaviour independent of material type. Additionally, the values are expressed as a percentage of the width, Q of the PS sample to introduce the values independent of the absolute dimensions of sample geometry. In the Table 7, the values representing the length of abscissa $|S_C\, S_E(\varepsilon)|$, $x\,(S_E)$ the contraction of edge, $\Delta x\,(S_E)$ of the point, S_E the width of region C, Q_C, and the minimum notch length, $a_{0\min}$ are listed. Thus, Table 7 represents independent of PS sample geometry the values of each parameter, which are required to be taken into the account for the exact FCG characterization within the region of deformation originating near the loading direction deformation while applying simple fracture mechanics.

4 Conclusion

This study refers back to the previous works of Stoček et al. [8, 28], in which the minimum notch length in a plane strain PS tensile sample was experimentally defined for an exact analysis of the FCG of rubber for the first time. The current work extends the previous investigation for determining the deformation of a PS sample considering a broader range of the aspect ratios and the strains. Due to applying the DIC system for capturing the local strains, high accuracy of measured data was achieved. Firstly, the DIC analyses were performed on the PS samples based on the various aspects at a variety of strains for two, naturally very different rubber materials, namely NR and BR, both filled with CB. The local strains over the complete horizontal axis (the location of the crack growth) of the PS sample were evaluated. The achieved data clearly demonstrate that the contraction is >0 over the complete horizontal axis, whereas an exponential approximation was found to fit the data. Thus, it has been proved that no deformation originating strictly along the loading direction is present in the PS sample in reality. Therefore, to define an approximate region of deformation originating near the loading direction in a PS sample, a novel criterion considering a deviation from the maximum achieved contraction was established. The parametrical function defining the contraction of the edge, the width of the region of deformation originating near the loading direction and the minimum notch length required for FCG analyses in PS samples in relation to various aspect ratios and strains have been determined. As mentioned above, the parametrical function calculating the width of the region of deformation originating near the loading direction took into consideration the criterion admitting a deviation from the maximum achieved contraction in proportion $<0.01, 0.05>$.

This work firstly serves as the exact data describing the deviation of the deformation in the centre of the plane strain tensile sample from the deformation originating strictly along the loading direction for PS geometry, a range of aspect ratios $<1/2, 10>$ and a range of strain up to 0.5, respectively. Next, the novel criterion allowing to approximately establish the width of the region of deformation originating near the loading direction was implemented. It has been also demonstrated that the deformation over the complete horizontal axis of sample is nearly independent of the applied rubber type.

Finally, the set of parametrical functions offer mathematical bases for a simple and very fast determination of minimum notch length to apply the simple fracture mechanics approach for determining FCG behaviour in rubber materials using a PS sample.

Acknowledgments This work was supported by the Ministry of Education, Youth and Sports of the Czech Republic – DKRVO (RP/CPS/2020/004).

References

1. Rivlin RS, Thomas AG (1953) Rupture of rubber. I. Characteristic energy for tearing. J Polym Sci 10:291–318
2. Rice JR (1968) A path independent integral and the approximate analysis of strain concentration by notches and cracks. J Appl Mech 35:379–386
3. Cherepanov GP (1967) Crack propagation in continuous media. Appl Math Mech 31:503–512
4. Lee RF, Donovan JA (1987) J-integral and crack opening displacement as crack initiation criteria in natural rubber in pure shear and tensile specimens. Rubber Chem Technol 60:674–688
5. Kim W, Kim M, Chang YW, Shin JE, Bae JW (2003) Fatigue crack growth behavior of NR and HNBR based vulcanizates with potential application to track pad for heavy weight vehicles. Macromol Res 11:73–79
6. Stoček R, Gehde M, Heinrich G (2009) Analyse des dynamischen risswachstums von elastomeren-simultaner zug-(tensile) und pure-shear-prüfmodus bei optimierter risserfassung. Kautschuk Gummi Kunststoffe 62:170–176
7. Andreini G, Straffi P, Cotugno S, Gallone G, Polacco G (2013) Crack growth behaviour of styrene-butadiene rubber, natural rubber and polybutadiene rubber compounds: comparison of pure-shear versus strip tensile test. Rubber Chem Technol 86:132–145
8. Stoček R, Heinrich G, Gehde M, Kipscholl R (2013) Analysis of dynamic crack propagation in elastomers by simultaneous tensile- and pure-shear-mode testing. In: Grellmann W et al (eds) Fracture mechanics & statistical mech, vol 70. LNACM, pp 269–301
9. Marano C, Boggio M, Cazzoni E, Rink M (2014) Fracture phenomenology and toughness of filled natural rubber compounds via the pure shear test specimen. Rubber Chem Technol 87:501–515
10. Neubert D, Saunders DW (1958) Some observations of the permanent set of cross-linked natural rubber samples after heating in a state of pure shear. Rheol Acta 1(2–3):151–157
11. Yanyo LC (1989) Effect of crosslink type on fracture of natural rubber vulcanizates. Int J Fract 39:103–110
12. South JT, Case SW, Reifsnider KL (2002) Crack growth of natural rubber using a modified double cantilever beam. Mech Mater 34:451–458
13. Persson BNJ, Albohr O, Heinrich G, Ueba H (2005) Crack propagation in rubber-like materials. J Phys Condens Matter 17:R1071–R1142
14. Feichter C, Major Z, Lang RW (2006) Experimental determination of fatigue crack growth behavior and surface strain distribution of 'faint-waist pure shear' specimens with different crack tip RADII. Rubber Chem Technol 79(4):712–733
15. Major Z, Lang RW (2010) Characterization of the fracture behavior of NBR and FKM grade elastomers for oilfield applications. Eng Fail Anal 17:701–711
16. Stadlbauer F, Koch T, Planitzer F, Fidi W, Archodoulaki VM (2013) Setup for evaluation of fatigue crack growth in rubber: pure shear sample geometries tested in tension-compression mode. Polym Test 32:1045–1051
17. Rooj S, Das A, Morozov IA, Stöckelhuber KW, Stoček R, Heinrich G (2013) Influence of “expanded clay” on the microstructure and fatigue crack growth behavior of carbon black filled NR composites. Compos Sci Technol 76:61–68
18. Ghosh P, Stoček R, Gehde M, Mukhopadhyay R, Krishnakumar R (2014) Investigation of fatigue crack growth characteristics of NR/BR blend based Tyre tread compounds. Int J Fract 188:9–21
19. Hintze C, Stoček R, Horst T, Jurk R, Wiessner S, Heinrich G (2014) Dynamic behavior of short aramid fiber-filled elastomer composites. Polym Eng Sci 54:2958–2964
20. Ghosh P, Mukhopadhyay R, Stocek R (2016) Durability prediction of NR/BR and NR/SBR blend tread compounds using tear fatigue analyser. Kautschuk-Gummi-Kunststoffe 69 (6):53–55

21. Stoček R, Kratina O, Ghosh P, Maláč J, Mukhopadhyay R (2017) Influence of thermal ageing process on the crack propagation of rubber used for tire application, vol 247. Springer, Cham, pp 351–364
22. Stoček R, Horst T, Reincke K (2017) Tearing energy as fracture mechanical quantity for elastomers. In: Stöckelhuber KW, Das A, Klüppel M (eds) Designing of elastomer nanocomposites: from theory to applications. Advances in polymer science, vol 275. Springer, New York, pp 361–398
23. Stoček R, Kipscholl R (2017) Influence of test specimen thickness on the fatigue crack growth of rubber. In: Constitutive models for rubber X – proceedings of the 10th European conference on constitutive models for rubber, pp 347–350
24. Stoček R, Stěnička M, Zádrapa P (2020) Future trends in predicting the complex fracture behaviour of rubber materials. Contin Mech Thermodyn. (In press)
25. Benevides RO, Nunes LCS (2015) Mechanical behavior of the alumina-filled silicone rubber under pure shear at finite strain. Mech Mater 85:57–65
26. Schubert G, Harrison P (2015) Large-strain behaviour of magneto-rheological elastomers tested under uniaxial compression and tension, and pure shear deformations. Polym Test 42:122–134
27. Kaang S, Woong JY, Huh YI, Lee WJ, Im WB (2006) A test method to measure fatigue crack growth rate of rubbery materials. Polym Test 25(3):347–352
28. Stoček R, Heinrich G, Gehde M, Kipscholl R (2012) A new testing concept for determination of dynamic crack propagation in rubber materials. Kautschuk Gummi Kunststoffe 65:49–53
29. Lake GJ, Yeoh OH (1978) Measurement of rubber cutting resistance in the absence of friction. Int J Fract 145:509–526
30. Legorju Jago K, Bathias C (2002) Fatigue initiation and propagation in natural and synthetic rubbers. Int J Fatigue 24:85–92
31. Stoček R, Mars WV, Kratina O, Machů A, Drobilík M, Kotula O, Cmarová A (2017) Characterization of ageing effect on the intrinsic strength of NR, BR and NR/BR blends. In: Constitutive models for rubber X – proceedings of the 10th European conference on constitutive models for rubber, pp 371–374
32. Mars WV, Robertson CG, Stoček R, Kipscholl C (2019) Why cutting strength is an indicator of fatigue threshold. In: Constitutive models for rubber XI – proceedings of the 11th European conference on constitutive models for rubber 2019, pp 351–356
33. Robertson CG, Stoček R, Kipscholl C, Mars WV (2019) Characterizing the intrinsic strength (fatigue threshold) of natural rubber/butadiene rubber blends. Tire Sci Technol 47(4):292–307
34. Bergstrom JS (2015) Mechanics of solid polymers. Elsevier, London
35. Busfield JJC, Ratsimba CHH, Thomas AG (1999) Crack growth and predicting failure under complex loading in filled elastomers. In: Boast D, Coveney VA (eds) Finite element analyses of elastomers. Professional Engineering Publishing, London, pp 235–250
36. Lindley PB (1972) Energy for crack growth in model rubber components. J Strain Anal Eng Des 7:132–140
37. Yeoh OH (2001) Analysis of deformation and fracture of 'pure shear' rubber test piece. Plastics Rubber Compos 30:389–397
38. Stoček R, Heinrich G, Gehde M, Rauschenbach A (2012) Investigations about notch length in pure-shear test specimen for exact analysis of crack propagation in elastomers. J Plastics Technol 1:2–22
39. Dedova S, Schneider K, Heinrich G (2018) Biaxial testing system for high static and dynamic loading of elastomers and its application. Kautschuk Gummi Kunststoffe 6:85–90
40. Dedova S, Schneider K, Stommel M, Heinrich G (2021) Dissipative heating, fatigue and fracture behaviour of rubber under multiaxial loading. In: Heinrich G, Stoček R, Kipscholl R (eds) Fatigue crack growth in rubber materials: experiments and modelling. Springer, Cham
41. Stoček R (2021) Revision of fatigue crack growth characteristics of rubber. In: Heinrich G, Stoček R, Kipscholl R (eds) Fatigue crack growth in rubber materials: experiments and modelling. Springer, Cham

Adv Polym Sci (2021) 286: 39–56
https://doi.org/10.1007/12_2020_69

Published online: 11 December 2020

The Effect of Polyglycols on the Fatigue Crack Growth of Silica-Filled Natural Rubber

O. Kratina, R. Stoček, P. Zádrapa, and S. G. Sathi

Contents

Abstract Polyglycols are mainly used as plasticizers to enhance the incorporation of polar fillers in non-polar elastomers. Polyglycols can help to prevent the self-agglomeration of the filler particles and thereby improve their dispersion in the rubber matrix. It can also prevent undesired chemical reactions of the polar components in the curing system with the surface of the filler particles. Therefore, it is expected that polyglycols can play a crucial role as plasticizer and coupling agent in a silica-filled rubber compound. In this work, polyethylene glycol (PEG) and polypropylene glycol (PPG) in two different concentrations were applied in a silica-filled natural rubber (NR). Their effects are compared with the influence of

O. Kratina, P. Zádrapa, and S. G. Sathi
Centre of Polymer Systems, Tomas Bata University in Zlín, Zlín, Czech Republic

R. Stoček (✉)
Centre of Polymer Systems, Tomas Bata University in Zlín, Zlín, Czech Republic

PRL Polymer Research Lab, Zlín, Czech Republic
e-mail: stocek@utb.cz

the coupling agent bis[3-(triethoxysilyl)propyl]tetrasulfide (TESPT), which is widely used in rubber industry as silica coupling agent. Firstly, the cure characteristics and fundamental mechanical properties have been studied, whereas the ability of polyglycols to improve cure efficiency as well as filler-elastomer interactions has been confirmed. Moreover, polyglycols are improving the fundamental mechanical properties in general, whereas the polyglycols-treated silica-filled NR composites show lower tensile strength and modulus with a higher elongation at break compared to the TESPT-treated silica-filled NR. Finally, the effect of polyglycols on fatigue crack growth (FCG) resistance was investigated using a Tear and Fatigue Analyzer (TFA©, Coesfeld GmbH & Co. KG, Germany). It has been found that 2 phr of PEG leads to a higher improvement of FCG resistance in comparison with the corresponding content of TESPT. However, 4 phr of polyglycols significantly decreases this property again. Moreover, the application of PPG generally leads to decreasing FCG resistance. As conclusion, it was stated that the polyglycols act as agent leading to significant improvement of fundamental mechanical behaviour in general as well as to improvement of FCG behaviour using specific polyglycol.

Keyword Crack growth · Fatigue · Natural rubber · Polyglycol · Silane · Silica

1 Introduction

Fatigue failure is a critical issue which frequently arises in rubber components in service. This phenomenon widely exists in rubber products, such as tires, seals, dampers as well as conveyor belts, which are usually exposed to cyclic dynamic loading. During fatigue cyclic loading or flexing, the rubber components fail in service due to initiation and subsequent growth of cracks, which may lead to a catastrophic failure. The failure may be due to either the propagation of the already existing microcracks in the virgin rubber matrix or due to the environmental ageing by ozone and oxygen. Therefore, exploring the fatigue damage mechanism of rubber compounds has a great significance to estimate the service life of rubber products. Thus, to improve the performance of rubber materials to resist fatigue failure has always been a very important goal of the rubber industry since a long time. One of the methods to achieve this requirement is reinforcing the base elastomer with suitable reinforcing fillers. The reinforcing fillers generally improve various mechanical properties like tensile strength, abrasion resistance as well as fatigue and fracture behaviour [1].

It is well-known that the efficiency of filler reinforcement depends on factors like filler structure, surface area, grade of dispersion of the fillers and filler-elastomer interactions.

The reinforcing effect of carbon black (CB) which is the most used filler in rubber industry has predominantly been affected by particle size, structure, specific surface area and surface chemistry [2].

Nowadays silica finds its use in many industrial rubber products in particular in the tire industry [3] where the addition of silica leads to improve properties like wet grip [4] and low rolling resistance of tires resulting in a reduction of the overall vehicle's fuel consumption [5]. Moreover, silica reduces heat build-up as well and takes no negative influence on abrasion resistance and, hence, improves the service life of tires [6]. Silica technology fundamentally employs solution-polymerized synthetic elastomers like solution styrene-butadiene rubber (SSBR) and solution butadiene rubber (BR). On the other hand, the great majority of rubber polymers used for CB-reinforced passenger car tires (PCT) is emulsion styrene-butadiene rubber (E-SBR) and natural rubber (NR) in the case of truck, off-the-road (OTR), or multipurpose (MPTR) tires. However, the chemical nature of silica is quite different from CB due to the presence of polar silanol groups on the particle surface. Therefore, silica particles undergo self-association via hydrogen bonds, leading to the formation of a strong filler-filler network resulting in a poor dispersion in the elastomer matrix. In order to overcome those limitations, sulphur-containing silane coupling agents such as bis(3-triethoxysilylpropyl)tetrasulfide (TESPT) are commonly applied in conventional polar elastomers like SBR-based rubber compounds. The mixing of silica with silane in rubber, the so-called silanization, and the extent of the chemical reaction have a significant effect on the final compound respective cured rubber behaviour [7, 8]. Moreover, the poor dispersion in the elastomer matrix is predominant especially in non-polar elastomers like NR which is key elastomer for the abovementioned tire applications because of its outstanding mechanical strength, ability to withstand large deformations and resistance to fatigue crack growth [9–12]. Up until now, NR still is not fully utilized in silica technology due to postulation of its ineffectiveness with silane coupling agent. To solve this problem, an epoxidized natural rubber (ENR) has been used as a compatibilizer in silica-reinforced NR tire tread compounds, resulting in a substantial improvement in the properties when compared to a compound without ENR [13].

In a situation where there is no ENR content in the compound, it is necessary to perform a silica surface treatment that facilitates the dispersion of silica particles and their interaction with the matrix based on non-polar elastomers. One of the widely used methods to enhance the reinforcing efficiency of silica is the use of bifunctional organosilanes as coupling agents. Silane possesses a hydrolysable alkoxy group that reacts with silanol groups on the silica surface to form a stable siloxane linkage during mixing and later coupling with the elastomer during the curing process via nonhydrolyzable organic radicals [9, 14]. Another approach to reduce the self-association of silica particles and thereby to improve their dispersion and interaction with the matrix is the addition of plasticizers. Plasticizers lead to a reduction of the stiffness of agglomerates by weakening the intermolecular forces and improving the elastomer chain mobility [15]. Polyglycols are one of the widely used groups of plasticizers that have a large number of ether linkages. The etheric oxygens in the polyglycols can form hydrogen bonds with the silanol groups on the silica surface,

and thereby reducing its hydrophilicity consequently enhance the dispersion of silica in the elastomer matrix [16]. Moreover, this reduction in hydrophilicity prevents the formation of hydrogen bonds between silanol groups and polar additives such as cure accelerators and zinc oxide. If the components of the curing system react with the surface of the filler, the cure characteristics such as maximum torque, S'_{max}, and optimum cure time, t_{90}, may be significantly reduced. Thus, the addition of polyglycol increases the rubber curing rate [17]. An indisputable advantage of the use of polyglycols is the simplicity of the preparation of the rubber compounds, which eliminates the need to perform a silanization reaction.

It should be noted that the interactions established between silica and elastomer via polyglycols are based on less stable physical bonds that result in a lower strength compared to the silanized rubber, where the interactions formed by the silane coupling agents are mediated by covalent bonds. Figure 1a, b displayed schematic representations of chemical interactions between the silica and the elastomer with the aid of a silane coupling agent or with a suitable polyglycol, respectively.

Silane coupling agents were subjected to many scientific investigations, which predominantly described their effects on the mechanical properties, e.g. the strain

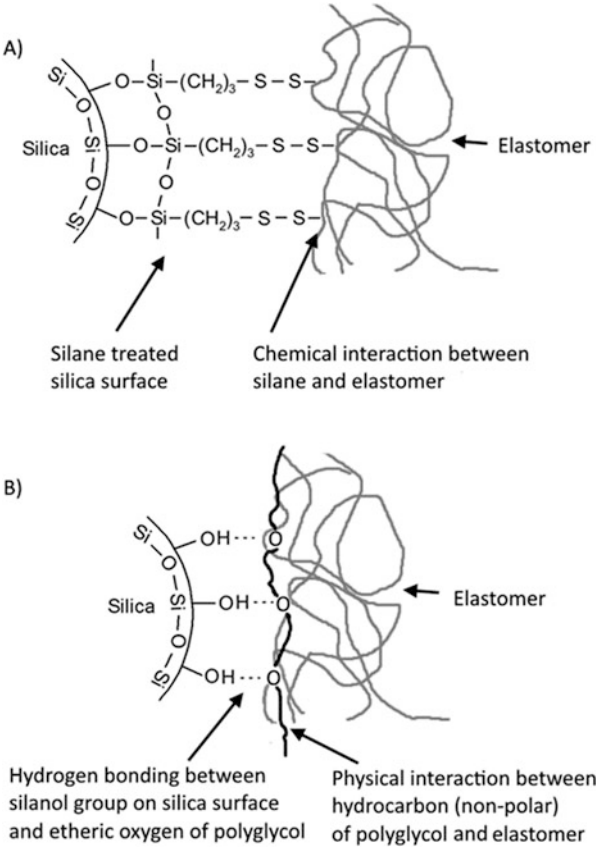

Fig. 1 Principle of silica surface treatment using silane (**a**) and polyglycol (**b**)

amplitude dependence of the dynamic modulus (Payne effect) and the tensile strength [2, 18–20]. However, fatigue and crack growth rate are rarely studied [21–23]. Moreover, the effect of polyglycols on fatigue crack growth (FCG) behaviour is neither studied theoretically nor experimentally. The primary aim of this study is to verify how useful are the polyglycols for improving the mechanical properties, especially the FCG resistance, of silica-filled natural rubber compounds.

2 Materials and Methods

Compounds based on NR (SVR CV60, Binh Phuoc, Vietnam) filled with 50 phr of silica (Ultrasil 7000 GR, Evonik, Germany) were prepared. 2 and 4 phr of polyethylene glycol (PEG 4000) and polypropylene glycol (PPG 4000) were used for improving the dispersibility of silica and its interphase adhesion with the elastomer matrix. Bis[3-(triethoxysilyl)propyl]tetrasulfide (TESPT) (Si69, Evonik, Germany) was used as the silane coupling agent. Additionally, zinc oxide (ZnO), stearic acid and N-(1,3-dimethylbutyl)-N'-phenyl-p-phenylenediamine (6PPD) (all from Sigma-Aldrich Chemie, Germany) were added. Masterbatch containing these ingredients were compounded in an internal mixer (SYD-2 L, Everplast, Taiwan) at a rotor speed of 40 rpm at 80°C. The dump temperature was 120°C. After the first step, the masterbatches were kept for 24 h at room temperature. In the second step, the silanization reaction for silane-treated compounds was performed in an internal mixer at a rotor speed of 10 rpm at 150°C for 5 min. The prepared rubber compounds were sheeted out using two-roll mill and stored at room temperature for 24 h.

Finally, the curatives were added into the masterbatches using a two roll-mill set at a temperature of 60°C for 5 min. Sulphur and accelerators N-cyclohexyl-2-benzothiazolesulfenamide (CBS) and diphenylguanidine (DPG) (all from Sigma-Aldrich Chemie, Germany) were used as curatives. The complete formulations of the compounds are given in Table 1.

Table 1 Rubber compounds formulations

	C0	CS2	CE2	CP2	CS4	CE4	CP4
	Phr						
SVR CV60	100.0						
Silica	50.0						
TESPT	–	2.0	–	–	4.0	–	–
PEG 4000	–	–	2.0	–	–	4.0	–
PPG 4000	–	–	–	2.0	–	–	4.0
Zinc oxide	3.0						
Stearic acid	1.0						
6PPD	1.5						
CBS	1.5						
DPG	1.0						
Sulfur	1.5						

The optimal quantities of TESPT and DPG were calculated based on the cetyltrimethylammonium bromide (CTAB)-specific surface area of the silica according to Guy et al. [24]:

$$\text{TESPT content (phr)} = 0.00053 \cdot Q_f \cdot \text{CTAB}, \tag{1}$$

$$\text{DPG content (phr)} = 0.00012 \cdot Q_f \cdot \text{CTAB}, \tag{2}$$

where Q_f is the filler content (phr) and CTAB is the specific surface area of silica (m^2/g).

The test specimens were cut out from sheets of vulcanizates that were cured in a heat press (LabEcon 300, Fontijne Presses, Netherlands) at 160°C according to optimum cure time, t_{90}.

2.1 Curing Efficiency

The cure characteristics were performed using a Moving Die Rheometer (MDR 3000 Basic, MonTech, Germany) at 0.50 arcs with a frequency of 100 cpm according to ASTM 6204 at 160°C for 0.3 h. The values of maximum torque, S'_{max} and optimum cure time, $t_{90,}$ obtained from the rheometer were used to evaluate the effect of type and amount of silica-treating agents on the vulcanization behaviour.

2.2 Mechanical Behaviour in Tension

The tensile properties were investigated by quasi-static tensile testing machine M350-5CT (Testometric, United Kingdom) according to ISO 37. S2 type rubber samples have been employed to perform the test at strain rate 500 mm/min. The obtained values of stress and elongation at break were used to evaluate the strength of the materials. Additionally, the stress values at 50, 100 and 300% elongation describing the stiffness of the material were also determined.

2.3 Fatigue Crack Growth Behaviour

The crack growth mechanism of rubber materials is highly complicated because it depends on the type of polymers, fillers, other ingredients, environmental conditions, etc. The fatigue crack growth (FCG) approach considers the existence of cracks (in the form of microcracks or flaws due to the presence of fillers, poor dispersion, ingredients, etc.) and their propagation under fatigue cyclic loading. The pioneering work of Rivlin and Thomas [25] is considered to be the foundation of fracture

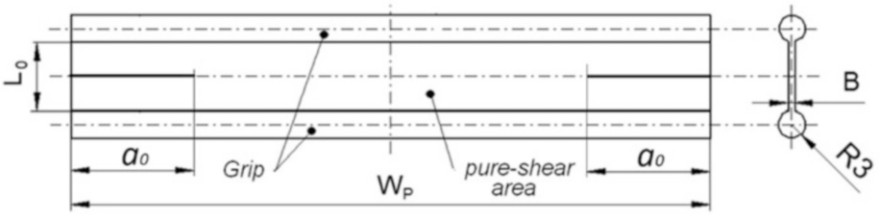

Fig. 2 Plane strain sample geometry

mechanics-based research to study the FCG behaviour of rubber materials. It proposes that the strain energy release rate is the controlling parameter for crack growth and can be mathematically defined as

$$T = -(\delta W/\delta A), \tag{3}$$

where T is tearing energy, W is the elastic strain energy and A is the interfacial area of crack, and the partial derivative denotes vanishing external work done on the system. It was demonstrated in [25] that the fracture property is the characteristics of the intrinsic material property and nearly independent of test piece geometry. Rivlin and Thomas in Ref. [25] used three types of specimens: the single-edge-notched tension (SENT), the trouser specimen and the plane strain (PS) specimen for fracture investigation. For each specimen type, specific formulas for the determination of the tearing energy, T, were derived. Finally, the PS samples (where the length of the sample is considerably lower than the width and the crack length is sufficiently long) (see Fig. 2) featured prominently in classical FCG studies of rubber [26–38], because of the quasi constant strain energy density in the middle region of the sample often labeled 'pure shear' [39, 40]. For the PS sample, the tearing energy, T, can be calculated from the strain energy density, w, stored in the unnotched test sample at its original length, L_o:

$$T = wL_0, \tag{4}$$

The detailed calculation of this expression can be found in Ref. [41]. This relationship shows that the tearing energy, T, is independent of crack length. Gent, Lindley and Thomas [41] experimentally determined the FCG rate, $r = \mathrm{d}a/\mathrm{d}n$, in dependence on the tearing energy, T, for rubber materials, where a is the actual crack length and n represents the current cycle count. The FCG is mainly defined by the relationship between FCG rate, r, over the range of tearing energies, where the crack grows steadily. This relation has firstly been derived and defined by Paris and Erdogan [42] and is well-known as a power law:

$$r = \frac{\mathrm{d}a}{\mathrm{d}n} = \beta\ T^m, \tag{5}$$

where β and m are material constants. The values of FCG rate, r, and tearing energy, T, for rubber material in this stable region are approximately among the following range:

$$10^{-9}\ \frac{\text{mm}}{\text{cycle}} < r \leq 10\ \frac{\text{mm}}{\text{cycle}}\ \text{and}\ T \approx 50\ \frac{\text{J}}{\text{m}^2} + 10,000\ \frac{\text{J}}{\text{m}^2}, \quad (6)$$

FCG measurements were carried out using a Tear and Fatigue Analyzer (TFA©, Coesfeld GmbH & Co. KG, Germany). The detailed description of the equipment can be found in [39, 43]. The minimalized plane strain (mPS) geometry having dimensions $L_0 = 4$ mm, $W_p = 40$ mm and $B = 1$ mm (length × width × thickness) is depicted in Fig. 2. The specimen has been notched on both the edges with an initial crack length $a_0 = 8$ mm based on the sample geometry ratio, L_0/W_p, reported in [39, 44]. Three samples per compound have been analysed over the complete range of applied tearing energies. The Gaussian pulse waveform (typical for the rubber loading during rolling of a tire) of the pulse frequency 10 Hz, which correspond with the pulse width 100 ms and loading frequency 5 Hz at the temperature 28°C, have been applied for the analyses. The analyses have been done at a fully relaxing mode, where the R-ratio ->$R = 0$, which is the minimum applied stress divided by the maximum applied stress: $R = \sigma_{\min}/\sigma_{\max}$). The crack growth of each sample has been monitored in situ through an image processing system with a CCD camera. The crack contour length and the crack growth increment as well as the data of fatigue behaviour in situ are evaluated. The resulting data were finally used to determine the power law defined by Eq. (5).

3 Results and Discussion

3.1 Effect of Surface-Treating Agents on Curing Efficiency

The cure characteristics of the rubber compounds with different concentrations of polyglycols are represented in Figs. 3 and 4. The compounds containing 2 phr of polyglycols PEG (CE2) or PPG (CP2) exhibit a significant increase of maximal torque, $S'_{\max}$. However, the effect was only marginal as the content of polyglycols increased from 2 to 4 phr. The higher value of S'_{max} can be considered as an indication of enhanced crosslink density. Thus, the influence of polyglycols up to 2 phr or slightly larger can be considered to be the optimum quantity for balanced mechanical properties of the rubber compounds. In contrast, a significant difference depending on the concentration of polyglycols is visible for t_{90} values. The t_{90} increases with increasing the quantity of polyglycols independent of its type. However, PEG exhibits a lower value of t_{90} for both the concentrations compared to PPG. Figure 5 represents the cure characteristics of the silane-treated rubber compounds. The addition of silane causes increased $S'_{\max}$ values of the compounds due to the formation of durable chemical filler-elastomer interaction. Moreover,

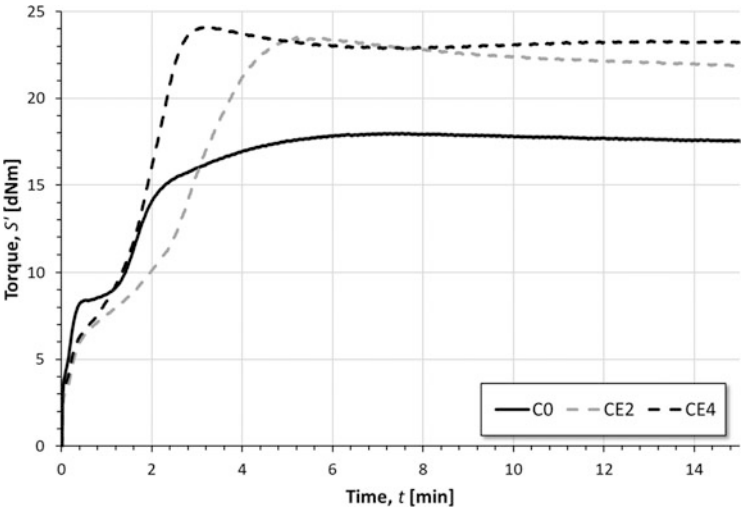

Fig. 3 Curing behaviour of rubber compounds with PEG

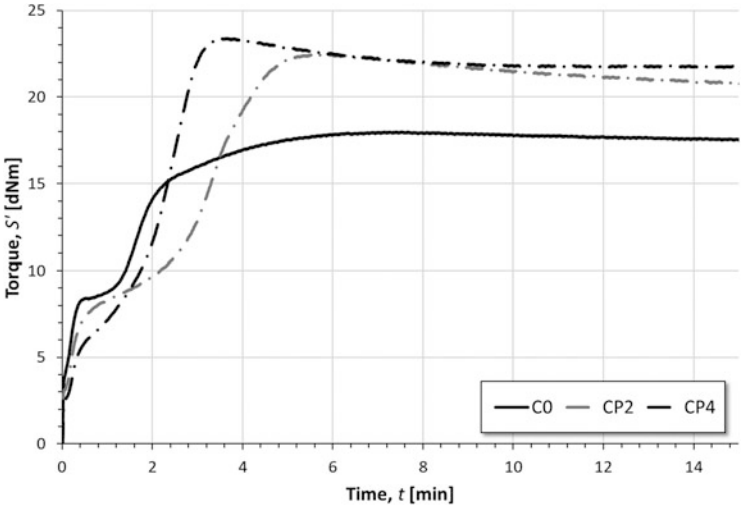

Fig. 4 Curing behaviour of rubber compounds with PPG

sulphur, that is a part of TESPT, participates on the curing process resulting in higher crosslink density. The lower values of S'_{max} of silane-treated rubber compared to polyglycols-treated rubber compounds could be explained by depressing the formation of a filler network resulting in higher degree of material flexibility.

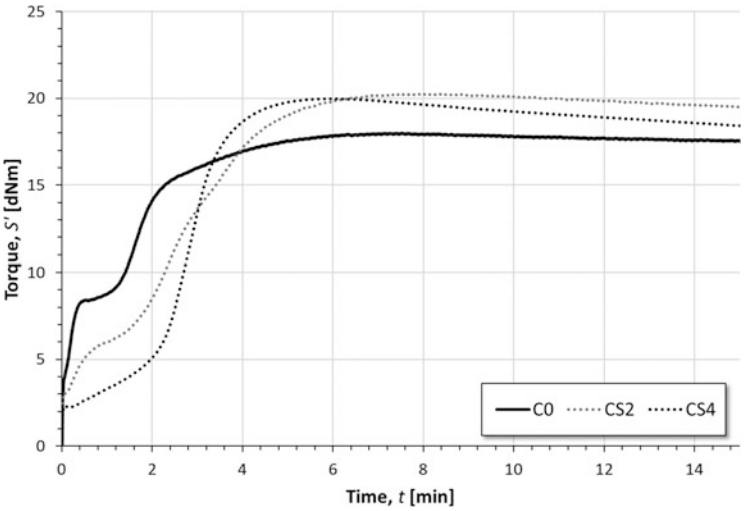

Fig. 5 Curing behaviour of the rubber compounds with silane coupling agent

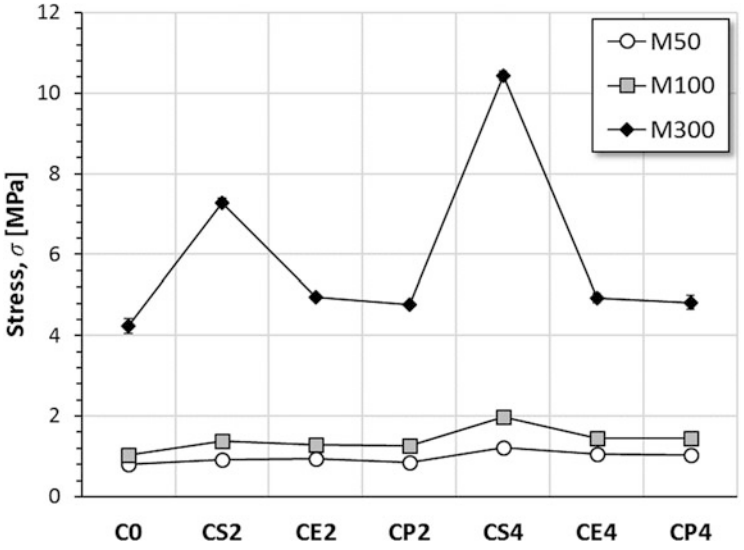

Fig. 6 Stress values of the compounds at 50% (M50), 100% (M100) and 300% (M300) elongation

3.2 Effect of Surface-Treating Agents on Mechanical Behaviour in Tension

The fundamental mechanical behaviour based on tensile tests of the vulcanizate is shown in Figs. 6 and 7. The effect of the surface-treating agents on the stress

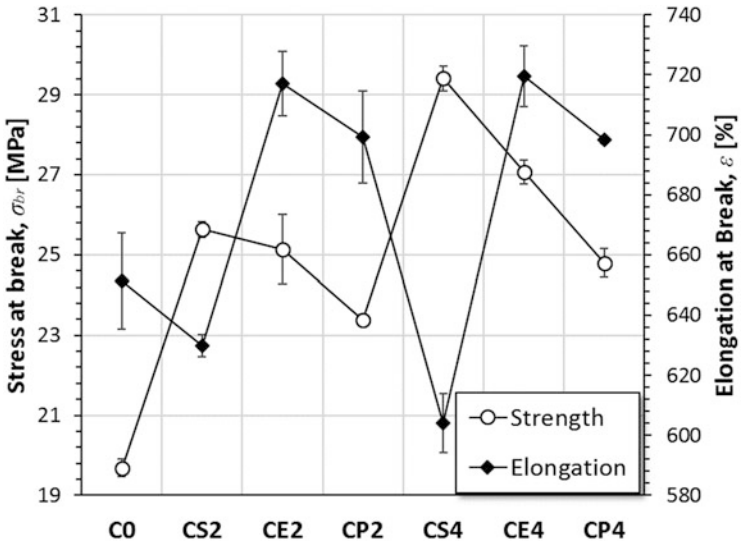

Fig. 7 Results of tensile strength and elongation at break

(modulus) at a different percentage of elongation is displayed in Fig. 6. The reference compound without any surface-treating agent exhibits the lowest stress values in comparison with the compounds containing the surface-treating agents. In addition polyglycols exhibit a slight increase of stiffness which is almost the same for both the concentrations. This stiffening is caused due to higher crosslink density and also due to a higher degree of dispersion of the particles in the matrix in comparison with the reference compound. However, for silanized rubber compounds, a significant increase of stiffness depending on silane concentration is visible. This trend is caused due to the high degree of silica dispersion and the formation of intermolecular chemical bonds between the silica particles and the elastomer matrix via the coupling agent bis-(3-triethoxysilylpropyl)tetrasulfide (TESPT).

Figure 7 depicts strength and elongation at break of the compounds with different content of the surface-treating agents. From these data, it is evident that the addition of polyglycols improves the strength and elongation under quasi-static loading in tension. It can be seen that the rubber with PEG achieves improved properties than rubber with the presence of PPG. However, the silanized rubber compounds show a higher stiffness due to the intermolecular chemical bonds established between the silica particles and the rubber chains. These chemical bonds are stronger than the weak physical bonds generated with the use of polyglycols. On the other hand, the elongation of silanized rubber compounds significantly decreased compared to the polyglycol-treated rubber compounds. This trend could be caused by limiting the mutual movement of the particles in the matrix due to the presence of strong intermolecular chemical bonds.

3.3 *Effect of Surface-Treating Agents on FCG Behaviour*

Table 2 summarizes the FCG rates, r, as well as the material constants β and m determined using the Eq. (5).

The effect of different types of silica-treating agents on the FCG behaviour at 2 phr loading is represented in Fig. 8. The addition of 2 phr PEG (CE2) and silane (CS2) leads to an improvement of FCG resistance, i.e. a decrease in the FCG rate, r. Moreover, both agents lead to decreasing values of m. Thus, both curves show enhanced stability of FCG behaviour, and the corresponding rubber materials are more resistant against crack propagation under cyclic loading over the complete range of tearing energies. A very interesting finding is that the PEG enhanced the FCG resistance of rubber more than silane. However, the slope representing the parameter m is marginally higher for PEG. The lowest FCG resistance has been observed for the compounds with the addition of PPG compared to the other two agents. Moreover, the PPG-treated rubber exhibits significantly higher FCG rates even in comparison with the reference compound.

Table 2 Power law describing the dependence of FCG rate on tearing energy, where x is meaning of the tearing energy, T

Compound	da/dn	β	m
C0	$6E\text{-}12x^{2.29}$	6E-12	2.29
CS2	$2E\text{-}08x^{0.87}$	2E-08	0.87
CE2	$3E\text{-}09x^{1.14}$	3E-09	1.14
CP2	$2E\text{-}11x^{2.19}$	2E-11	2.19
CS4	$1E\text{-}11x^{1.98}$	1E-11	1.98
CE4	$2E\text{-}14x^{3.04}$	2E-14	3.04
CP4	$2E\text{-}10x^{1.73}$	2E-10	1.73

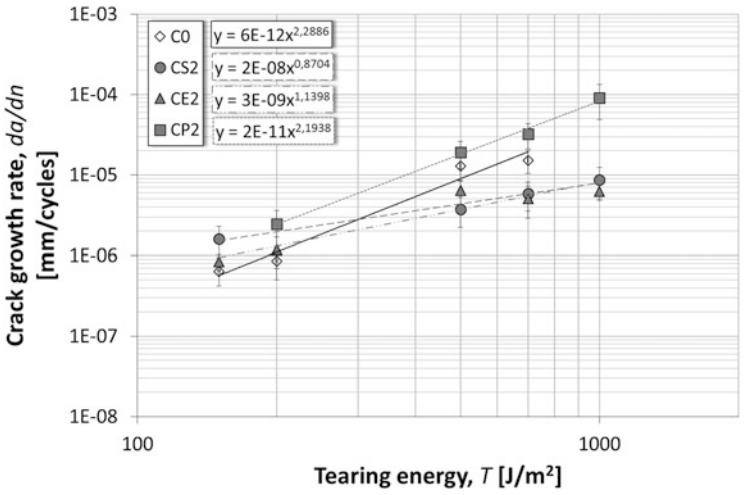

Fig. 8 FCG behaviour with different types of coupling agents at 2 phr loading

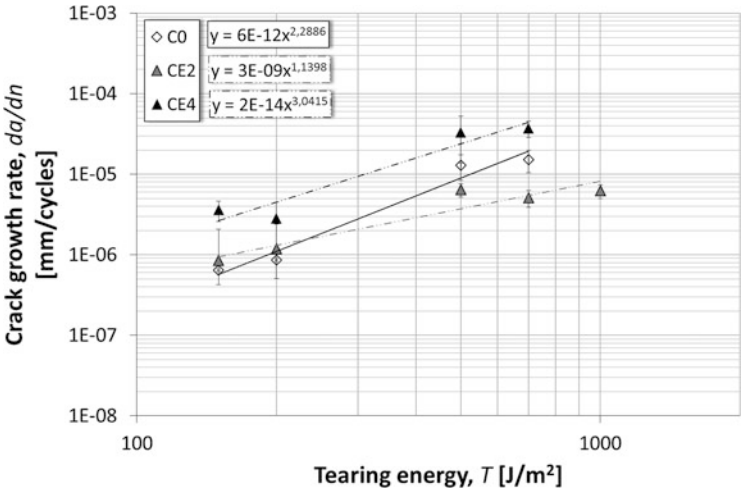

Fig. 9 FCG behaviour with different content of PEG

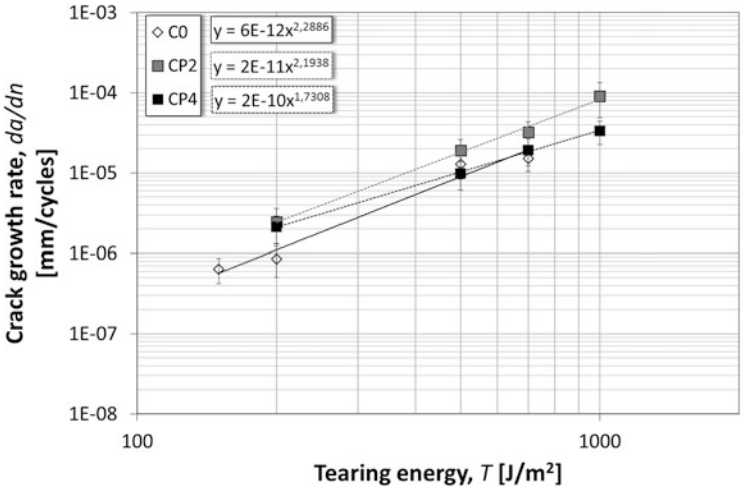

Fig. 10 FCG behaviour with different content of PPG

Figures 9, 10 and 11 represent the effect of different contents of the surface treating agents on the FCG rate. For a comparative purpose, the FCG rate of the reference compound was also incorporated in each figure. From Fig. 9, it is interesting to note that the addition of 2 phr PEG (CE2) improves the FCG resistance. However, a higher portion (4 phr) of PEG (CE4) leads to a significant decrease in the FCG resistance. From these experimental results, it is reasonable to assume that a higher concentration of PEG (over 2 phr) leads to a polarity mismatch between the NR and PEG because of the presence of higher amount of polar etheric oxygen in

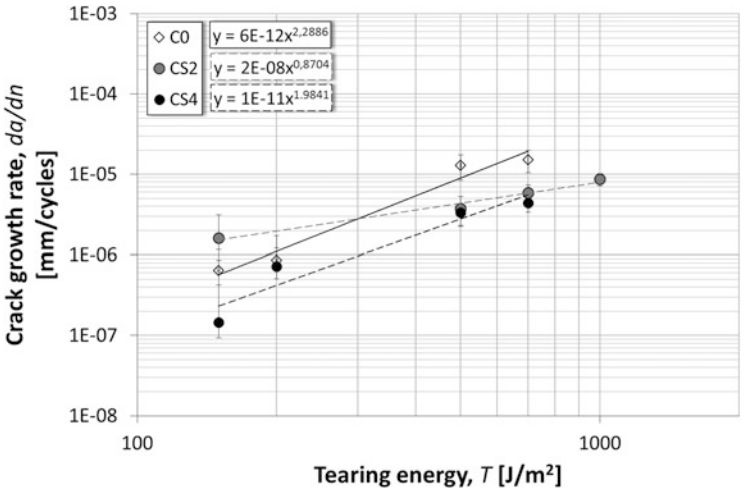

Fig. 11 FCG behaviour with different content of silane coupling agent

PEG. This polarity mismatch generates an incompatibility problem between silica coated with 4 phr PEG and the NR matrix, leading to a significant decrease in the FCG resistance. On the contrary, it is evident from Fig. 10 that even 2 phr PPG (CP2)-treated silica-filled NR exhibits a lower FCG resistance compared to the non-treated silica-filled NR (C0). The FCG resistance is further reduced as the content of PPG increased to 4phr. Figure 11 shows how the FCG resistance increases with increasing the content of TESPT. This might be due to a higher density of network between the TESPT-treated silica filler with the NR matrix.

4 Conclusion

The influence of two types of polyglycols (PEG and PPG) and one type of silane (TESPT) on the cure characteristics, mechanical and fatigue crack growth resistance properties of a silica-filled NR, have been explored. From the curing characteristics, it was confirmed that the addition of polyglycols significantly enhanced the rheometric torque. This indicates that the polyglycols can enhance the overall crosslink density of the silica-filled NR compound. Moreover, the addition of polyglycols significantly reduces the optimum cure time. The enhanced tensile strength and modulus of the polyglycol-treated silica-filled compounds, compared to the reference compound, support the fact that the polyglycols obviously lead to an increased crosslink density, here approximately related to an increase in the torque values during the curing process. However, compared to silane, polyglycols generate less durable physical interactions with the matrix. As a result, the compounds treated with polyglycols show lower mechanical properties. Among the polyglycols, the

compounds with PEG show improved fundamental mechanical properties under quasi-static loading than the compounds with PPG. A different situation was found in the case of FCG properties. It has been observed that 2 phr of PEG leads to an enhancement of FCG resistance, whereas the addition of 4 phr of PEG significantly decreases this property. Contrary to this observation, the addition of PPG generally decreases the FCG resistance for both applied concentrations. Overall, it can be concluded that the polyglycols, especially PEG, enhance the curing efficiency, mechanical and fatigue resistance properties. However, further study is still required in this line to establish the various utility of polyglycols in the rubber industry.

Acknowledgements This work was supported by the Ministry of Education, Youth and Sports of the Czech Republic – DKRVO (RP/CPS/2020/004).

References

1. Gheller Jr J, Ellwanger M, Oliveira V (2015) Polymer-filler interactions in a tire compound reinforced with silica. J Elastom Plast 48:217–226
2. Zafarmehrabian R, Gangali ST, Ghoreishy MHR, Davallu M (2012) The effects of silica/carbon black ratio on the dynamic properties of the tread compounds in truck tires. E-J Chem 9:1102–1112
3. Kim KJ, White JL (2000) Breakdown of silica agglomerates and other particles during mixing in an internal mixer and their processing character. J Ind Eng Chem 6:262–269
4. Saeed F, Ansarifar A, Ellis RJ, Haile-Meskel Y, Irfan MS (2012) Two advanced styrene-butadiene/polybutadiene rubber blends filled with silanized silica nanofiller for potential use in passenger car tire tread compound. J Appl Polym Sci 123:1518–1529
5. Liu X, Zhao SH, Zhang XY, Li XL, Bai Y (2014) Preparation, structure, and properties of solution-polymerized styrene-butadiene rubber with functionalized end-groups and its silica-filled composites. J Appl Polym Sci 55:1964–1976
6. Limper A (2012) Mixing of rubber compounds. Hanser Publishers, Munich. E-book ISBN 987-3-446-42865-2
7. Reuvekamp LAEM, ten Brinke JW, Van Swaaij PJ, Noordermeer JWM (2002) Effects of mixing conditions-reaction of TESPT silane coupling agent during mixing with silica filler and tire rubber. Kaut Gummi Kunst 55:41–47
8. Kaewsakul W, Sahakaro K, Dierkes WK, Noordermeer JWM (2012) Optimization of mixing conditions for silica-reinforced natural rubber tire tread compounds. Rubber Chem Technol 85:277–294
9. Kaewsakul W, Sahakaro K, Dierkes WK, Noordermeer JWM (2012) Factors influencing the flocculation process in silica-reinforced natural rubber compounds. In: Paper presented at MAMIP 2012, Penang, Malaysia, pp 980–989
10. Noriman NZ, Ismail H (2011) Properties of styrene butadiene rubber (SBR)/recycled acrylonitrile butadiene rubber (NBRr) blends: the effects of carbon black/silica (CB/Sil) hybrid filler and silane coupling agent, Si69. J Appl Polym Sci 124:19–27
11. Ghosh P, Stocek R, Gehde M, Mukhopadhyay R, Krishnakumar R (2014) Investigation of fatigue crack growth characteristics of NR/BR blend based tyre tread compounds. Int J Fract 188:9–21
12. Ghosh P, Mukhopadhyay R, Stocek R (2016) Durability prediction of NR/BR and NR/SBR blend tread compounds using tear fatigue analyser. Kaut Gummi Kunst 69:53–55

13. Sengloyluan K, Sahakaro K, Dierkes WK, Noordermeer JWM (2014) Silica-reinforced tire tread compounds compatibilized by using epoxidized natural rubber. Eur Polym J 51:69–79
14. Zheng J, Ye X, Han D, Zhao S, Wu X, Wu Y, Dong D, Wang Y, Zhang L (2017) Silica modified by alcohol polyoxyethylene ether and silane coupling agent together to achieve high performance rubber composites using the latex compounding method. Polymers 10(1):1
15. Laboulfie F, Hémati M, Lamure A, Diguet S (2013) Effect of the plasticizer on permeability, mechanical resistance and thermal behaviour of composite coating films. Powder Technol 238:14–19
16. Gonzalez J, Valentin JL, Arroyo M, Saalwächter K, Lopez-Manchado M (2008) Natural rubber/clay nanocomposites: influence of poly(ethylene glycol) on the silicate dispersion and local chain order of rubber. Eur Polym J 44:3493–3500
17. Bachmann JH, Sellers JW, Wagner MP (1959) Fine particle reinforcing silicas and silicates in elastomers. Rubber Chem Technol 32:1286–1391
18. Sattayanurak S, Noordermeer JWM, Sahakaro K, Kaewsakul W, Dierkes WK, Blume A (2019) Silica-reinforced natural rubber: synergistic effects by addition of small amounts of secondary fillers to silica-reinforced natural rubber tire tread compounds. Adv Mater Sci Eng 2019:1–8
19. Brinke JWT, Debnath SC, Reuvekamp LAEM, Noordermeer JWM (2003) Mechanistic aspects of the role of coupling agents in silica-rubber composites. Compos Sci Technol 63:1165–1174
20. Luginsland HD, Kalscheuren H (2000) Reactivity of the sulfur chains of the tetrasulfane silane Si 69 and the disulfane dilane TESPD. Kaut Gummi Kunst 53:10
21. Yao H, Weng G, Liu Y, Fu K, Chang A, Chen ZR (2015) Effect of silane coupling agent on the fatigue crack propagation of silica-filled natural rubber. J Appl Polym Sci 132:20
22. Bin D, Chang L, You-Ping W (2014) Fracture and fatigue of silica/carbon black/natural rubber composites. Polym Test 38:40–45
23. Saeed F (2011) Crack growth under dynamic loading in silanised silica filled rubber vulcanisates. A Doctoral thesis, Loughborough University, United Kingdom
24. Guy L, Daudey S, Cochet P, Bomal Y (2009) New insights in the dynamic properties of precipitated silica filled rubber using a new high surface silica. Kaut Gummi Kunst 63:383–391
25. Rivlin RS, Thomas AG (1953) Rupture of rubber. I. Characteristic energy for tearing. J Polym Sci 10:291–318
26. Neubert D, Saunders DW (1958) Some observations of the permanent set of cross-linked natural rubber samples after heating in a state of pure shear. Rheol Acta 1(2–3):151–157
27. Yanyo LC (1989) Effect of crosslink type on fracture of natural rubber vulcanizates. Int J Fract 39:103–110
28. South JT, Case SW, Reifsnider KL (2002) Crack growth of natural rubber using a modified double cantilever beam. Mech Mater 34:451–458
29. Persson BNJ, Albohr O, Heinrich G, Ueba H (2005) Crack propagation in rubber-like materials. J Phys Condens Matter 17:R1071–R1142
30. Feichter C, Major Z, Lang RW (2006) Experimental determination of fatigue crack growth behavior and surface strain distribution of 'faint-waist pure shear' specimens with different crack tip RADII. Rubber Chem Technol 79(4):712–733
31. Major Z, Lang RW (2010) Characterization of the fracture behavior of NBR and FKM grade elastomers for oilfield applications. Eng Fail Anal 17:701–711
32. Stadlbauer F, Koch T, Planitzer F, Fidi W, Archodoulaki V-M (2013) Setup for evaluation of fatigue crack growth in rubber: pure shear sample geometries tested in tension-compression mode. Polym Test 32:1045–1051
33. Rooj S, Das A, Morozov IA, Stöckelhuber KW, Stocek R, Heinrich G (2013) Influence of "expanded clay" on the microstructure and fatigue crack growth behavior of carbon black filled NR composites. Compos Sci Technol 76:61–68
34. Hintze C, Stoček R, Horst T, Jurk R, Wiessner S, Heinrich G (2014) Dynamic behavior of short aramid fiber-filled elastomer composites. Polym Eng Sci 54:2958–2964

35. Stoček R, Kratina O, Ghosh P, Maláč J, Mukhopadhyay R (2017) Influence of thermal ageing process on the crack propagation of rubber used for tire application. In: Springer series in materials science, vol 247. Springer, Cham, pp 351–364
36. Stoček R, Horst T, Reincke K (2017) Tearing energy as fracture mechanical quantity for elastomers. In: Stöckelhuber KW, Das A, Klüppel M (eds) Designing of elastomer nanocomposites: from theory to applications. Advances in polymer science, vol 275. Springer, New York, pp 361–398
37. Stoček R, Kipscholl R (2017) Influence of test specimen thickness on the fatigue crack growth of rubber. In: Constitutive models for rubber X – proceedings of the 10th European conference on constitutive models for rubber. CRC Press, Balkema, pp 347–350
38. Stoček R, Stěnička M, Zádrapa P (2020) Future trends in predicting the complex fracture behaviour of rubber materials. Continuum Mech Thermodyn. https://doi.org/10.1007/s00161-020-00887-z
39. Stoček R, Heinrich G, Gehde M, Kipscholl R (2013) Analysis of dynamic crack propagation in elastomers by simultaneous tensile- and pure-shear-mode testing. In: Grellmann W et al (eds) Fracture mechanics and statistical mechanics, LNACM 70, pp 269–301
40. Stocek R, Heinrich G, Gehde M, Kipscholl R (2012) A new testing concept for determination of dynamic crack propagation in rubber materials. Kaut Gummi Kunst 65:49–53
41. Gent AN, Lindley PB, Thomas AG (1964) Cut growth and fatigue of rubbers. I. The relationship between cut growth and fatigue. J Appl Polym Sci 8:455–466
42. Paris P, Erdogan F (1963) A critical analysis of crack propagation laws. J Basic Eng 85:528–534
43. Eisele U, Kelbch SA, Engels HW (1992) The tear analyzer – a new tool for quantitative measurements of the dynamic crack growth of elastomers. Kaut Gummi Kunst 45:1064–1069
44. Stocek R, Heinrich G, Gehde M, Rauschenbach A (2012) Investigations about notch length in pure-shear test specimen for exact analysis of crack propagation in elastomers. J Plast Technol 1:2–22

Adv Polym Sci (2021) 286: 57–84
https://doi.org/10.1007/12_2020_71

Published online: 27 November 2020

The Fatigue Threshold of Rubber and Its Characterization Using the Cutting Method

Christopher G. Robertson, Radek Stoček, and William V. Mars

Contents

Abstract Below a limiting value of tearing energy called the intrinsic strength or fatigue threshold (T_0), cracks will not grow in rubber due to fatigue; hence, this material characteristic is important to understand from both fundamental and practical perspectives. We summarize key aspects of the fatigue threshold, including the Lake-Thomas molecular interpretation of T_0 in terms of fracture of polymer network chains in crosslinked elastomers. The various testing approaches for quantifying T_0 are also discussed, with a focus on the classic Lake-Yeoh cutting method which was

C. G. Robertson (✉) and W. V. Mars
Endurica LLC, Findlay, OH, USA
e-mail: cgrobertson@endurica.com

R. Stoček
PRL Polymer Research Lab, Zlín, Czech Republic

Centre of Polymer Systems, Tomas Bata University in Zlín, Zlín, Czech Republic

recently revived by the introduction of a commercial testing instrument that applies this procedure, the Intrinsic Strength Analyser (ISA). A validation of the cutting method is also given by demonstrating that a 2-h test on the ISA yields a value of T_0 that is essentially identical to the T_0 from near-threshold fatigue crack growth (FCG) measurements that require 7.5 months of continuous testing. Compound formulation effects – polymer type, crosslink density, type and amount of reinforcing fillers, and addition of oils/plasticizers – are examined based on the limited published research in this area and our new results. At the end, some insights are offered into using the fatigue threshold to develop highly durable rubber products.

Keywords Durability · Elastomers · Fatigue crack growth · Intrinsic strength · Materials characterization · Polymer networks

1 Background

It is first essential to define the fatigue threshold which is also referred to as the endurance limit. We will also review the molecular interpretation of this material parameter which will be helpful later when considering the effects of various rubber compounding ingredients. Bhowmick published a nice review article on this topic in 1988 [1], and it is our intent to complement that summary in this section and throughout the chapter while presenting new experimental results and offering some fresh perspectives.

1.1 General Fatigue Crack Growth Response and the Fatigue Threshold

Cracks in rubber can grow when a cyclic mechanical deformation is applied, with a crack growth rate, r, that depends on the material, severity of the loading, temperature, and other conditions [2–4]. Although rubber can be formulated to have a wide range of fatigue crack growth (FCG) responses, the general shape of the FCG rate curve is essentially universal. This is shown in Fig. 1 where r is plotted on a log-log plot versus the tearing energy, T, which is also called energy release rate [5]. The FCG curve is a power law response that is bounded on both ends by T_0 and T_c. At the high-T end is the familiar tear strength or critical tearing energy (T_c) of the material. This chapter is focused on the limit at the low-T end of the response which is the fatigue threshold, T_0. This is an important parameter to quantify for a material. If loads remain below this threshold, then cracks cannot grow, and the material will

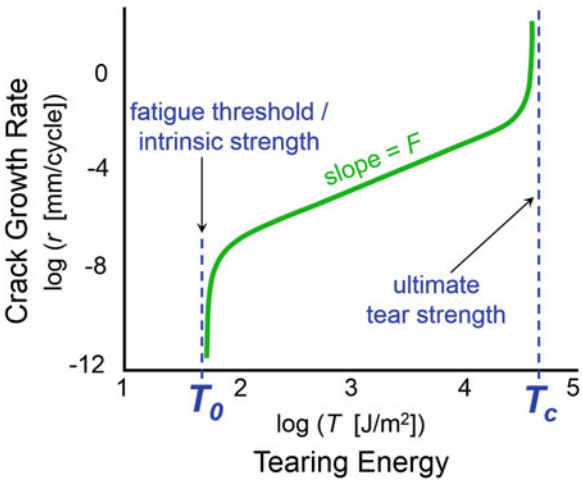

Fig. 1 Typical dependence of fatigue crack growth rate on tearing energy (energy release rate) for rubber under fully relaxing conditions (strain cycle oscillates between zero and a peak value at each value of T)

have an infinite fatigue lifetime, in the absence of ozone cracking, thermal-oxidative aging, or other life-limiting changes to the material [6].

In fatigue crack growth testing, the measured crack growth rate r diverges toward zero as T is decreased toward T_0. The rate is evaluated as $r = \mathrm{d}c/\mathrm{d}N$, where c is the crack length and N is the number of fatigue cycles. The r range where the FCG curve transitions downward, away from the power law slope, F, is from about 10^{-7} to 10^{-9} mm/cycle. To get a sense for the magnitude of testing time needed at these slow rates, if a typical testing frequency of 10 Hz is considered, it would take about 12 days of continuous testing to observe a tiny 0.1 mm of crack growth when $r = 10^{-8}$ mm/cycle for a material. Also, additional data points would be needed at even slower rates to define the FCG asymptote at T_0. Due to these generally prohibitive time requirements, it is common to see FCG results reported in the literature that only include the power law region and the upturn near T_c.

1.2 *Molecular Interpretation of Fatigue Threshold/Intrinsic Strength*

For a crosslinked elastomeric material, the minimum energy for a crack to grow is the energy required to break all the polymer chains that cross the path of the crack. This intrinsic strength is the reason for the divergence of the FCG curve toward $r = 0$ mm/cycle as tearing energy is decreased toward T_0; hence, fatigue threshold and intrinsic strength are synonymous. Lake and Thomas [7] derived an expression for intrinsic strength that includes details of the polymer backbone and the extent of crosslinking [1].

$$T_0 = \left[\left(\frac{3}{8}\right)^{1/2} \rho A U \gamma^{1/2} l M_0^{-3/2}\right] M_c^{1/2} = K M_c^{1/2} \quad (1)$$

The polymer backbone characteristics of importance are the chain stiffness (γ), molecular weight of a main chain bond (M_0), the bond length (l), and the bond dissociation energy (U; bond strength). These are averages across the polymer repeat unit. For example, 1,4-polybutadiene has a repeat unit with four main chain (backbone) bonds and molecular weight of 54 g/mol which leads to $M_0 = 13.5$ g/mol, with l, γ, and U taken as averages of the individual characteristics of the four bonds. Therefore, some of the microstructural details of the polymer backbone are lost in favor of a simpler molecular representation for predicting general trends. The density is represented by ρ, and A is Avogadro's number. For a given type of polymer, all of the molecular characteristics in Eq. 1 are fixed except for M_c and can be combined into a constant K. The molecular weight between crosslinks (M_c) – which is inversely related to crosslink density – is integral to the theory and influences T_0 in two opposite ways. All the bonds in the network chain need to be stretched until they are at the bond dissociation energy before one bond can break, so higher M_c means higher total energy required. The number of bonds in the network chain between two crosslinks is $n = M_c/M_0$, so the energy needed to break the network chain is nU. The other way that M_c plays a role is that longer network chains result in fewer chains that cross the path of the crack. The combination of these two conflicting contributions is a net positive effect leading to T_0 being proportional to $M_c^{1/2}$. Adding more crosslinks in a rubber compound is predicted to decrease the fatigue threshold. The type of polymer is also key, in particular the dependence $T_0 \sim M_0^{-3/2}$. Because the diameter of the chain is proportional to molecular weight per backbone bond, polymer chains with lower M_0 are thinner which means more chains have to be broken per area of crack.

A three-stage schematic is presented in Fig. 2 to illustrate molecular crack growth according to the Lake-Thomas theory: (a) the crack approaches the initially unperturbed network chain coil between crosslinks; (b) with the crosslinks fixed in their location, the advancing crack extends the network chain until it is taut (and all the bonds loaded up to the level of the bond dissociation energy); and (c) one bond in the network chain breaks, allowing the crack to advance and begin to deform the next chain it its path. Though helpful in rationalizing molecular effects on T_0, this is a highly simplified interpretation. Some limitations of the theory to point out are crosslinks are not allowed to move or break, trapped entanglements are not accounted for, and effects of filler particles are not included. These will be examined further in the later section on rubber formulation effects.

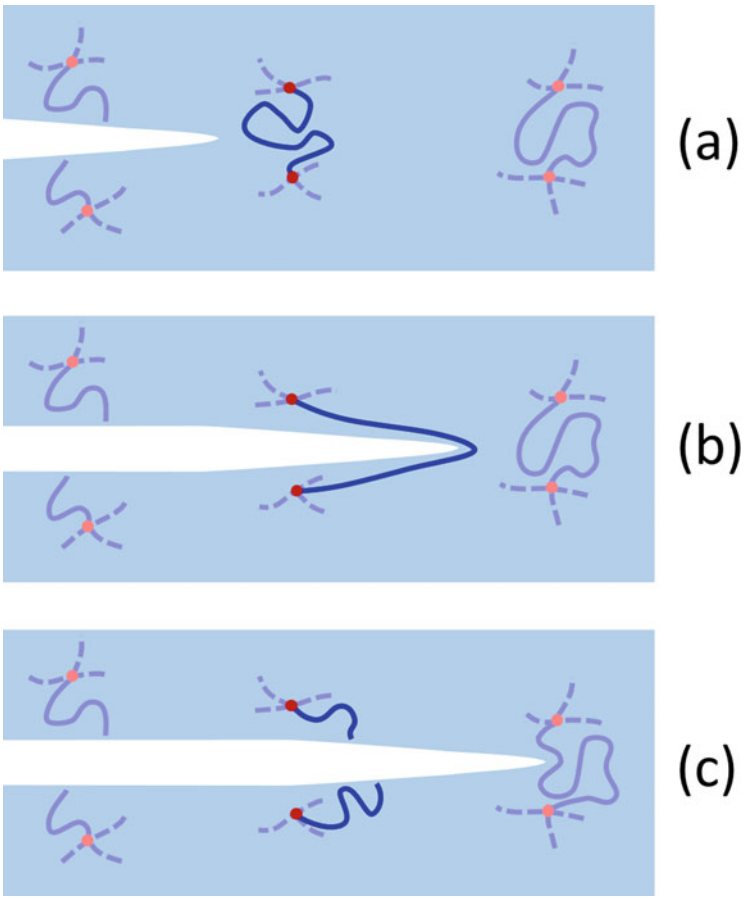

Fig. 2 Illustration of molecular crack growth progression from (**a**) to (**c**) for an elastomer network based on the Lake-Thomas model: (**a**) an initially unperturbed network chain (dark blue line) between two crosslinks (red dots) crosses the path of the advancing crack plane; (**b**) the advancing crack causes the network chain to become stretched until taut; and (**c**) the network chain breaks which allows the crack to grow further and begin to deform the next network chain in its path (**c**)

2 Characterization Methods

The actual energy needed to grow a crack in rubber can be significantly larger than T_0 due to viscoelastic dissipation in a process zone in front of the crack that prevents some of the mechanical energy from getting to the crack tip to break polymer chains. This is the reason that T_c of rubber can be 10 to 10,000 times larger than T_0 and explains the decrease in tear strength as rubber is heated [8]. The concept that tear strength is largely determined by the magnitude of the viscoelastic losses in the crack

tip region is supported by experiments [9, 10]. Rubber would be a weak material without this hysteresis, but it presents a challenge for measuring T_0.

The energy release rate T of a crack growing at a steady-state rate can be written as the sum of T_0 plus a dissipation-related term T_z [11].

$$T = T_0 + T_z(\dot{\varepsilon}, \theta) \tag{2}$$

The strain rate ($\dot{\varepsilon}$)- and temperature (θ)-dependent effects are contained entirely in the dissipation term, so that if the process zone dissipation can be eliminated, then the only remaining strength in the material is T_0. This is the general strategy of the testing methods employed for assessing the fatigue threshold.

2.1 Near-Threshold Fatigue Crack Growth

The direct way to quantify fatigue threshold is to make enough fatigue crack growth measurements near T_0 to define the low-T asymptote in Fig. 1. As T is decreased to values close to T_0, the size of dissipation zone and hence T_z naturally become small as the rate of crack growth approaches zero. Near-threshold FCG testing is discussed in detail in another chapter in this book by Stoček [12] who rigorously collected data across the entire FCG curve to define T_0, T_c, and the power law response between these limits for an ethylene-propylene-diene rubber (EPDM) material reinforced with N550 carbon black (CB) at a filler volume fraction (ϕ) of 0.24. The testing conducted in the range $T_0 < T \leq 100$ J/m^2 required 7.5 months of continuous instrument time and enabled a determination of $T_0 = 47.7$ J/m^2 for this material. This is the original method employed by Lake and Lindley [6] in their work on the fatigue limit. Zhang et al. [13] and Legorju-Jago and Bathias [14] also provide important examples of direct measurement of the fatigue threshold. Very few examples of such measurements are available, presumably due to the lengthy time requirements.

2.2 Tear Strength of Swollen Materials and/or at High Temperatures

It is widely understood that increasing the temperature of rubber causes the tear strength to decrease. The polymer network characteristics, such as bond strength and chain stiffness, are essentially insensitive to temperature, so T_0 does not change significantly as temperature is increased. In contrast, hysteresis decreases as rubber is heated, leading to a smaller T_z and thus a reduced T_c. The difference between T_c and T_0 diminishes with rising temperature which provides an opportunity to approximate T_0 from T_c measured at an elevated temperature. If this estimation approach is used,

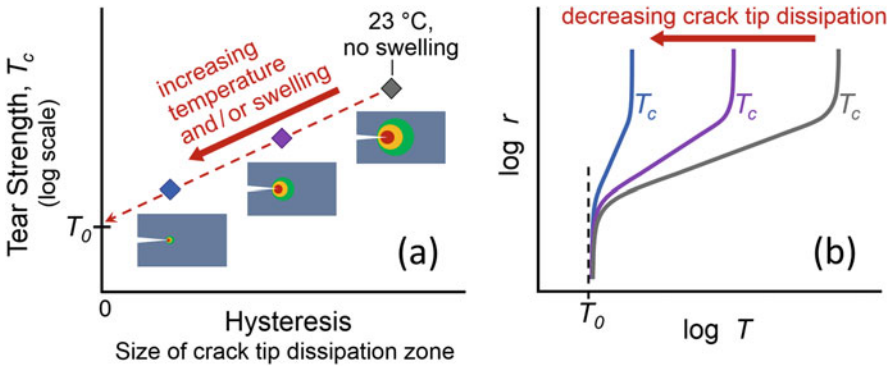

Fig. 3 Schematic of tear strength dependence on crack tip dissipation/hysteresis, as influenced by temperature and swelling (**a**) and the related crack growth rate curves (**b**). The dashed red arrow in (**a**) shows extrapolation to zero hysteresis to approximate T_0

we suggest making tear strength measurements at a few temperatures to generate a plot of T_c versus hysteresis – the latter determined from separate dynamic mechanical analysis testing – and extrapolating to zero hysteresis to evaluate T_0. This is schematically illustrated in Fig. 3a. It should be emphasized, however, that heating cannot completely eliminate dissipation, and there is a chance that thermal-oxidative aging can take place and change the behavior of the rubber if the temperature is too high. Also, it is not clear whether extrapolation should be performed on a linear or logarithmic T basis.

Another effective way to reduce the size of the crack dissipation process zone in an elastomer is to swell it in a liquid that is a good solvent for the polymer. When swollen, the energy to break a polymer chain is the same, but there are less chains per area of crack compared to the dry rubber. A correction for this chain dilution effect is accordingly required.

$$T_{0,\text{dry}} = \lambda^2 \, T_{0,\text{swollen}} \tag{3}$$

The λ is the one-dimensional swelling ratio that describes the change in volume (V) of the material from swelling.

$$\lambda = \left(\frac{V_{\text{swollen}}}{V_{\text{dry}}} \right)^{1/3} \tag{4}$$

Swelling and elevated temperatures have been used together to approximate T_0 by measuring tear strength at low hysteresis conditions [15–17].

2.3 Cutting Method of Lake and Yeoh

Lake and Yeoh [18] pioneered a cutting method for T_0 characterization that focuses the strain energy density at the crack tip and minimizes dissipation by slowly pushing a sharp blade into the open crack. Based on a crack tip energy balance, they introduced a material parameter called intrinsic cutting energy, $S_{0,c}$, which is equal to T plus an energy release rate for cutting, F.

$$S_{0,c} = T + F \tag{5}$$

Rearranging gives an equation for a line with slope of -1 and intercept $S_{0,c}$ for the dependence of F on T.

$$F = -T + S_{0,c} \tag{6}$$

When applied to the planar tension test specimen, the crack opening energy release rate is $T = Wh$, and the cutting energy release rate is $F = f/t$. W is the strain energy density, h is the gauge height of the specimen, t is the specimen thickness, and f is the cutting force.

Essential to implementing the Lake-Yeoh method is their key finding in Fig. 4 that the T_0 from lengthy near-threshold FCG testing is proportional to the measured $S_{0,c}$.

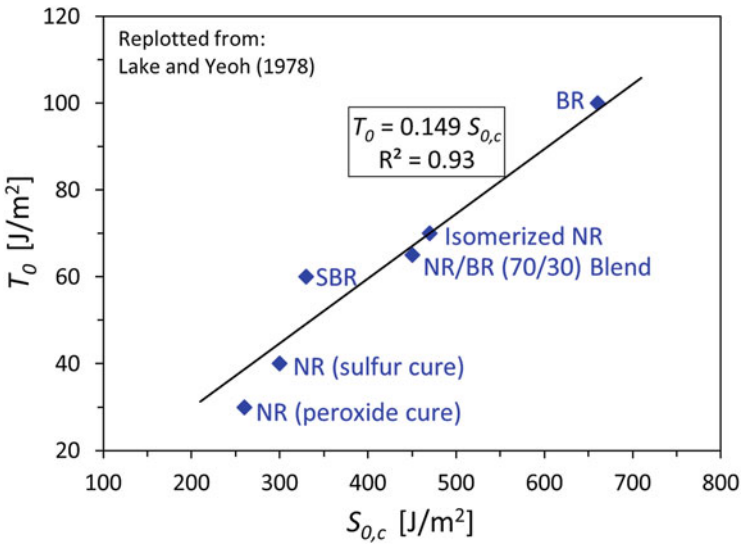

Fig. 4 Lake and Yeoh [18] results for various unfilled elastomers that show correlation between fatigue threshold from very lengthy FCG testing (Y-axis) and the intrinsic cutting energy from the much faster cutting method (X-axis)

$$T_0 = b\, S_{0,c} \tag{7}$$

Using the cutting method on a control material, for which T_0 is separately known from near-threshold FCG testing, allows the proportionality constant b to be determined. Measuring values of $S_{0,c}$ for both an experimental rubber and the control rubber thus allows T_0 to be quantified for the experimental material. The proportionality b is certainly influenced by the sharpness of the cutting blade. It should also be affected to some extent by the specific friction response between the elastomer material and the metal surface of the blade. This may explain why the linear correlation between T_0 and $S_{0,c}$ is not perfect in Fig. 4, where the unfilled styrene-butadiene rubber (SBR) and natural rubber (NR) materials have T_0 values that are slightly underpredicted and overpredicted, respectively, by the overall linear fit. The material dependence of b needs to be studied further. Application of the Lake-Yeoh cutting method requires a control material, and we use an unfilled SBR compound as a control material in the experiments that are discussed in the next section. For highly accurate measurements of T_0, for example, to use in developing rubber products with near-infinite fatigue lifetimes, it is recommended to employ a control compound that is similar to the experimental compounds being studied in terms of elastomer type and kind of filler.

2.3.1 Testing Protocol and Data Analysis

Figure 5 shows the experimental set-up of the Lake-Yeoh cutting method applied on the Intrinsic Strength Analyser (ISA) manufactured by Coesfeld GmbH & Co. (Dortmund, Germany). Cutting is performed using an ultra-sharp blade (see

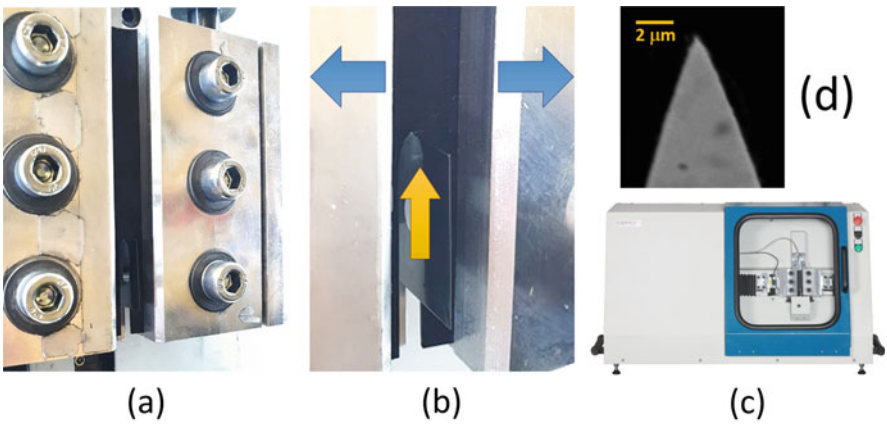

Fig. 5 Pictures of the Coesfeld Intrinsic Strength Analyser (ISA): (**a**) planar tension specimen in the grips being cut by the blade; (**b**) close-up view of ultra-sharp blade cutting the rubber specimen with stretching direction (blue arrows) and cutting direction (yellow arrow) indicated; (**c**) picture of the overall instrument; and (**d**) scanning electron microscopy image of blade tip

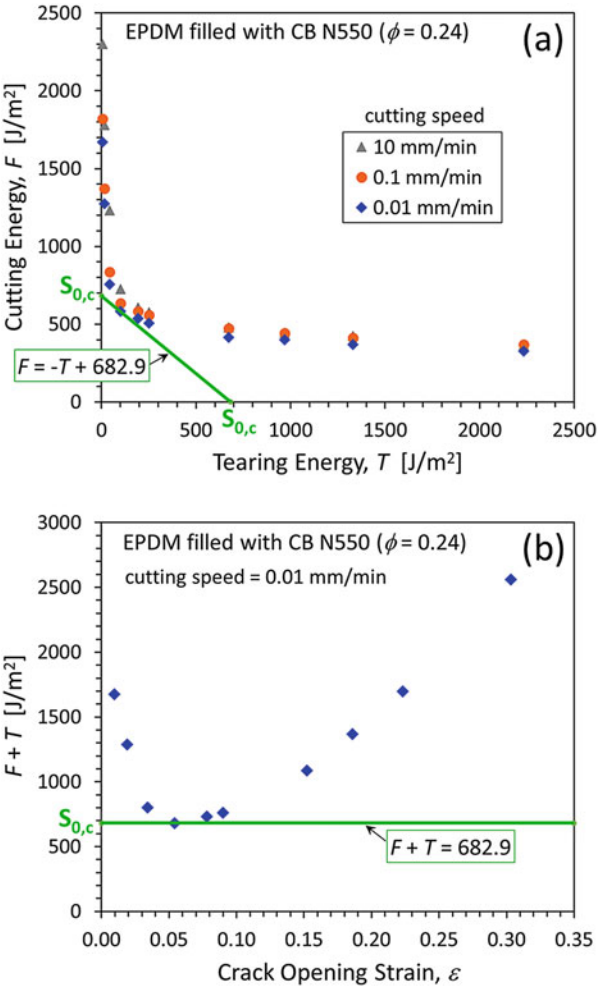

Fig. 6 Plot (**a**): F versus T cutting method data from the ISA at 23 °C for EPDM filled with CB N550 ($\phi = 0.24$); a line with slope $= -1$ (solid green line) according to Eq. (6) that contacts the data at the lowest point gives an intercept which is $S_{0,c}$. Plot (**b**): An alternate presentation of the same data at the lowest cutting speed, where the dependence of the total energy on the planar tension strain used to open the crack is shown, with $S_{0,c}$ defined by the minimum

Fig. 5d) that is attached to a sensitive force transducer. Cutting experiments are made for several crack opening strains (T is varied), and more details about the protocol for this series of measurements are given elsewhere [19]. For each T, a fast cutting rate of 10 mm/min is applied for a short time period to develop a well-defined crack path, and then the rate is sequentially slowed down to the rate of 0.01 mm/min to minimize hysteresis near the blade tip. The values of cutting energy release rate, F, used for determining $S_{0,c}$ are from this final slowest cutting rate. This procedure generates a series of F versus T points that are plotted in Fig. 6a for the same CB-filled EPDM ($\phi = 0.24$) studied by Stoček [12]. A line with slope $= -1$ (Eq. 6) that contacts the data at the lowest point gives the intercept $S_{0,c} = 683$ for this material. Experimental cutting forces are above this line at the lowest T values due to friction of the rubber against the sides of the blade when the crack is not opened much. Contributions from process zone dissipation (T_z becoming significant) explain the points above the line

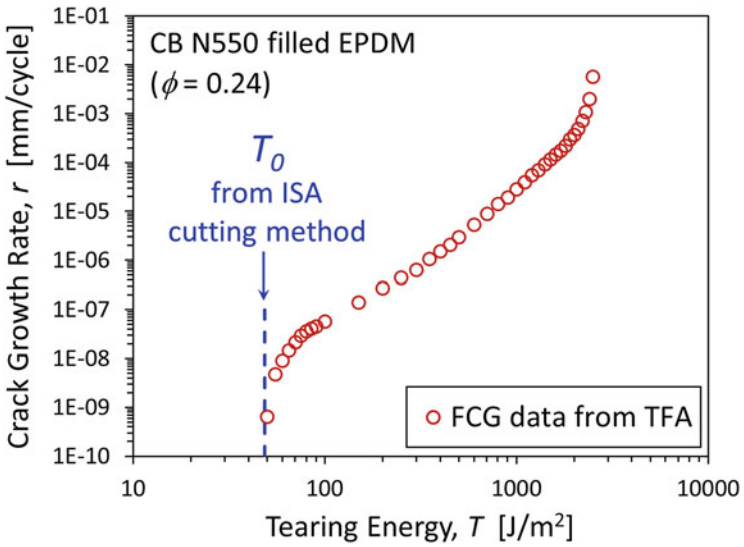

Fig. 7 Comparison of FCG data at 23°C for the CB-filled EPDM from the Tear and Fatigue Analyser (TFA) with separately determined T_0 from the Intrinsic Strength Analyser

Table 1 Fatigue threshold measurements for EPDM filled with CB N550 ($\phi = 0.24$)

Method	T_0 [J/m^2]	Testing time
Near-threshold fatigue crack growth	47.7	7.5 months
ISA cutting method	48.6	2 h[a]

[a]ISA can also be operated using a targeted testing protocol with total testing time of ~1 h

at the high-T end of the data set. An alternate way to view the results is a plot of the total energy, $F + T$, versus the crack opening strain, with $S_{0,c}$ defined by the minimum (Fig. 6b). An unfilled SBR control material [19] with known $T_0 = 60$ J/m^2 was also tested, giving a value of 844 J/m^2 for $S_{0,c}$. This information for the control rubber enabled the determination of $b = 0.0711$ from Eq. (7), then allowing the conversion of $S_{0,c}$ to T_0 for the EPDM compound to yield $T_0 = 48.6$ J/m^2.

2.3.2 Validation Using Experimental Results and Simulation

The 1978 investigation by Lake and Yeoh [18] showed that the cutting method can be used to assess T_0, as exemplified in Fig. 4. It is important to verify that our modern application of the cutting method on the Intrinsic Strength Analyser yields a T_0 which is similar to the fatigue threshold defined from fatigue crack growth testing. For this purpose, we consider the EPDM material just discussed with regard to ISA cutting results. EPDM is an appropriate elastomer choice for this comparison, because its largely saturated structure makes it a stable material against oxidation

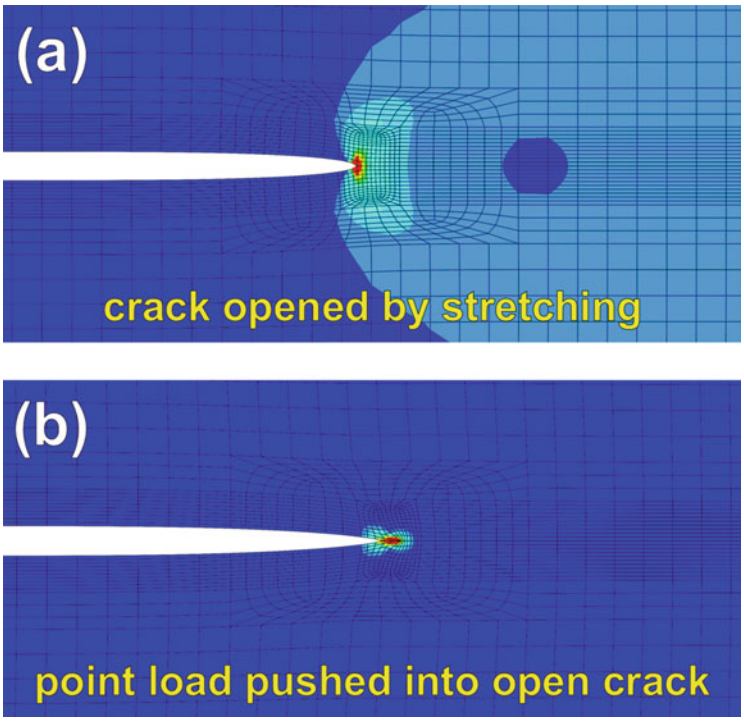

Fig. 8 Abaqus/Standard 2D finite element simulation of strain energy density for a crack in an elastomer that is opened by stretching to a planar tension strain of 0.09 (**a**) and the subsequent pushing of a point load into the open crack (**b**). The colors represent a map of different ranges of strain energy density from lower (dark blue) to higher (red) values. Results are from study by Mars et al. [20]

and ozone cracking during the long time period needed for the near-threshold FCG testing. The fatigue crack growth results from Stoček [12] for the EPDM material are presented in Fig. 7, and the data points represent average values from multiple measurements. Also indicated on this figure is the location of the T_0 separately determined using the ISA which is in close proximity to where the crack growth curve turns downward toward infinitesimally small rates. The T_0 from the cutting method test (48.6 J/m^2) is only 1% different than the T_0 from FCG measurements (47.7 J/m^2), as summarized in Table 1. The two characterization approaches produced essentially equivalent T_0 values, but the FCG method involved 7.5 months of testing in contrast to the 2-h ISA test.

A key premise of the Lake-Yeoh cutting approach is that the blade localizes the strain energy density at the crack tip to minimize the dissipation zone in front of the crack. Finite element analysis was recently performed [20] to investigate the validity of this assertion, and selected results from 2D modelling are shown in Fig. 8. When the simulated crack was opened by stretching, a sizeable process zone (i.e., region of magnified stress and strain) in front of the crack was evident. Then a point load was pushed into the open crack to model the effect of the sharp blade in the cutting

method, resulting in substantial reduction in the size of the process zone. This provided strong support for the scientific soundness of the cutting method for evaluating the intrinsic strength of rubber. This modelling research also generated F and T dependencies on crack opening strain and determined that the total process zone energy (sum of F and T) was minimized at a strain of 0.07 (7%). The minimum in Fig. 6b, representing the region of lowest total energy, occurred between the data points collected at strains of 0.054 and 0.078, quite comparable to the simulation minimum.

2.3.3 Combining Cutting Method and Tear Testing for Rapid Estimate of Fatigue Crack Growth Curve

After completion of the cutting procedure on the ISA, an optional standard tear test can be performed to determine T_c. The blade is retracted away from the rubber specimen, and then the crack is slowly opened until spontaneous tearing occurs. The ISA therefore can quantify for a rubber specimen the locations of the two ends of the FCG curve that bracket the intermediate power law behavior. Natural rubber (NR) and butadiene rubber (BR) have FCG power law responses that cross over each other. Examples for CB-filled compounds are shown in Fig. 9a [21]. Tear strength is significantly higher for NR (18,490 J/m^2) compared to BR (3,270 J/m^2), but the material ranking for T_0 is opposite (50.6 J/m^2 for NR and 99.6 J/m^2 for BR). We plot T_c and T_0 for both rubbers in Fig. 9a by assuming crack growth rates of $r_c = 10^{-2}$ mm/cycle for T_c and $r_0 = 10^{-8}$ mm/cycle for T_0. Connecting T_0 and T_c with a line on the log-log plot for each material gives a reasonable approximation for the FCG data between the two limits and reproduces the crossover for NR and BR. This approach can therefore estimate the FCG power law exponent, F, from the ratio of tear strength to intrinsic strength.

$$F \approx \frac{\log\left(r_c/r_0\right)}{\log\left(T_c/T_0\right)} \approx \frac{6}{\log\left(T_c/T_0\right)} \tag{8}$$

A good correlation between this F estimate and the actual F from rigorous FCG measurements is confirmed in Fig. 9b for 41 diverse rubber compounds spanning a large range of F. This quick approach is useful for screening materials and monitoring mixing quality in a rubber factory, but accurate FCG testing is still required for high fidelity fatigue analyses [22].

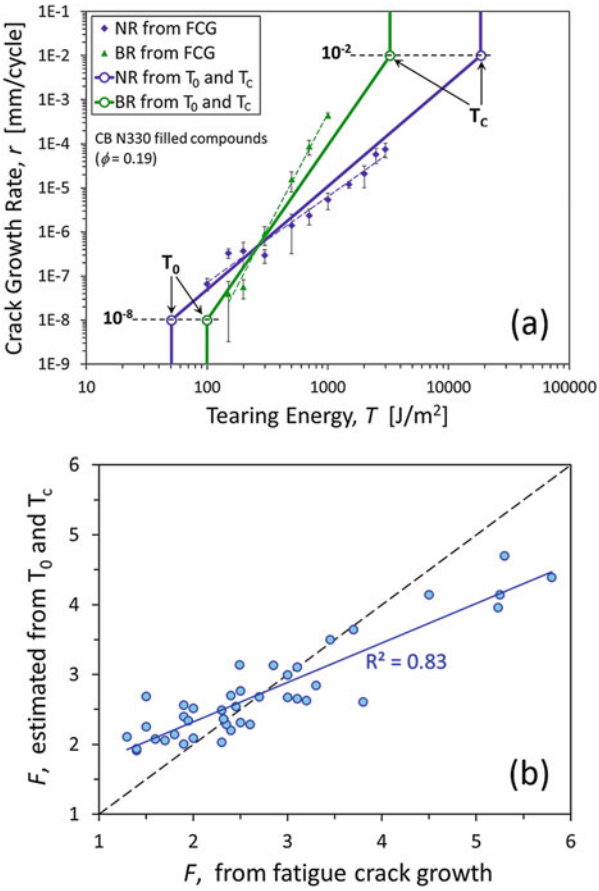

Fig. 9 Plot (**a**): Fatigue crack growth data from TFA (solid symbols) along with T_0 and T_c data from ISA (open symbols) plotted at r values of 10^{-8} and 10^{-2}, respectively; the thin lines are power law fits to the TFA data, and the thick lines connect the T_0 and T_c points on the log-log plot. Plot (**b**): Correlation between FCG power law slope determined by two point (T_0 and T_c) ISA method and from actual fitting to FCG data from TFA for data from 41 diverse rubber compounds. Results are replotted from Robertson et al. [21, 22]

3 Rubber Formulation Effects

Rubber formulations are complex mixtures of polymers, reinforcing fillers, curatives, oils/plasticizers, stabilizers, and other additives. The nature and amount of these ingredients, their interactions, and the quality of mixing will affect the compound's durability characteristics, including the fatigue threshold. This complexity gives materials engineers and compound developers the opportunity to create new materials to increase product lifetime. Despite the importance of T_0, there are only a few published studies that provide data for formulation effects on the fatigue threshold, likely due to the difficulty in measuring T_0 before the commercialization of the cutting method on the ISA. We review these prior investigations and share some of our recent findings in this section.

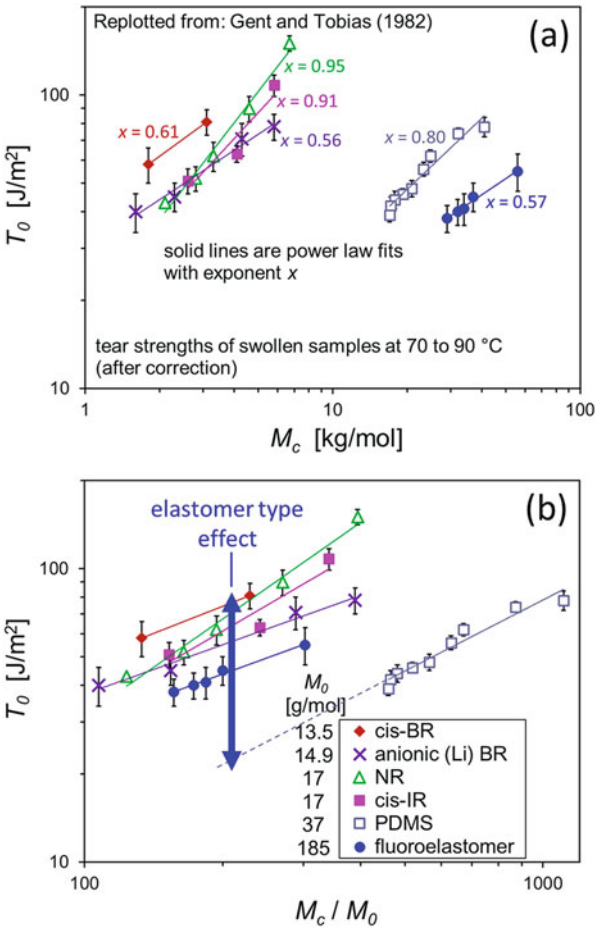

Fig. 10 Fatigue threshold estimated from swollen tear strength testing at elevated temperatures versus M_c (**a**) and versus M_c/M_0 (**b**) for the indicated unfilled elastomers crosslinked with dicumyl peroxide. The elastomer type effect manifests as a vertical shifting in (**b**) indicated by the blue double-headed arrow. The symbol legend in (**b**) also applies to (**a**). Replotted from Gent and Tobias [15]

3.1 Polymer Type

Gent and Tobias [15] used tear testing of swollen samples at temperatures from 70 to 90°C to approximate T_0 for a variety of unfilled polymer types, each studied across a range of M_c by varying the level of peroxide curative. Their results are replotted in Fig. 10a. It is more appropriate to compare crosslinked polymers at constant M_c/M_0 – which is the number of backbone bonds in a network chain between crosslinks (n) – so we compare the fatigue thresholds for the different elastomers as a function of M_c/M_0 in Fig. 10b. The elastomer type effect manifests as a vertical shifting in this plot. The polymer ranking does not exactly follow the Lake-Thomas expectation of $T_0 \sim M_0^{-3/2}$ due to other structural differences between the elastomer types, but the extremes make sense according to this scaling. The heaviest backbones are associated with the fluoroelastomer and poly(dimethylsiloxane) (PDMS) which have the

Table 2 Fatigue threshold values for CB-filled elastomers[a,b]

Parameter	T_0 [J/m^2]
Natural rubber (NR)	22.2 ± 2.0
Isoprene rubber (IR)[c]	25.7 ± 3.7
Butadiene rubber (BR)[c]	83.5 ± 7.7
Styrene-butadiene rubber (SBR)[d]	63.6 ± 4.7

[a]Data from our recent ISA cutting method study [23]
[b]60 phr CB N339 ($\phi \approx 0.23$) and 1.5 phr sulfur
[c]Predominantly cis-1,4 structure
[d]Emulsion SBR statistical copolymer with 23.5 wt.% styrene and 14% of butadiene polymerized in 1,2 (vinyl) structure

lowest fatigue thresholds at constant M_c/M_0. At the other extreme is the lightest backbone of cis-1,4-polybutadiene (cis-BR) which has the highest T_0. Polymer chains with lower M_0 have smaller diameters which translates into more network chains that have to be fractured per area for a crack to grow.

ISA testing of various general-purpose elastomers reinforced with carbon black demonstrated significant influence of polymer type on T_0 (Table 2) [23]. Consistent with the relative fatigue thresholds shown in Fig. 9a, these cutting method results showed that BR exhibited a significantly higher T_0 than was measured for NR. This difference can be qualitatively rationalized based on the Lake-Thomas theory prediction $T_0 \sim M_0^{-3/2}$ (Eq. 1). These two elastomers have similar chain stiffnesses and bond dissociation energies, so the main structural distinction leading to lower T_0 for NR is its higher M_0 (17 g/mol) compared to BR (13.5 g/mol). Also, it was found that the IR and NR materials had similar fatigue thresholds, reflecting their essentially identical cis-1,4-polyisoprene backbones. The T_0 for SBR was intermediate to BR and NR, evidently due to countervailing effects of higher chain stiffness and increased M_0. The composition of this emulsion SBR (see Table 2) yields $M_0 = 19.6$ g/mol. This is higher than the M_0 for NR and should cause T_0 to be lower for SBR relative to NR in the absence of other structural influences. However, the bulky styrene sidegroup in SBR increases the chain stiffness (γ parameter in Eq. 1) which apparently counters the effect of higher M_0. The fatigue threshold ranking of BR > SBR > NR in Table 2 agrees with the Lake and Yeoh [18] findings (Fig. 4).

3.2 Crosslinking Effects

The Lake-Thomas interpretation of intrinsic strength is based on the fracture of network chains, which leads to the key model prediction of $T_0 \sim M_c^{1/2}$. According to this anticipation, a higher density of crosslinks produced by adding more curatives in a rubber formulation will reduce M_c and decrease T_0. This is supported by the results from Gent and Tobias [15] in Fig. 10a which show power law exponents in the range from 0.56 to 0.95 for the different unfilled elastomers examined, reasonably close to the predicted exponent of 0.5. The materials consisted of model formulations with

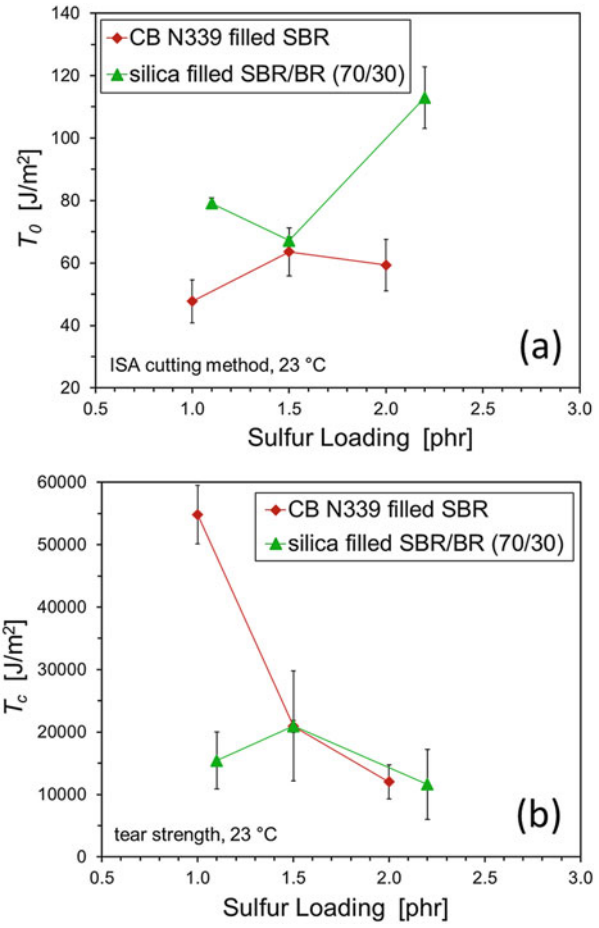

Fig. 11 Fatigue threshold (**a**) and tear strength (**b**) measured using the ISA for the indicated materials as a function of sulfur loading (accelerator-to-sulfur ratio kept constant). The CB N339 loading was $\phi = 0.23$ in the SBR material. For the silica-filled SBR/BR(70/30) compound, the loading of precipitated silica (165 m^2/g) was $\phi = 0.19$, and bis [3-(triethoxysilyl)propyl] disulfide (S2 silane; Si266) was added at 8 wt.% relative to the silica amount. Data replotted from our recent studies [23, 24]

only polymer plus dicumyl peroxide, the latter varied from 1 to 5 phr to vary the crosslink density. Their study approximated T_0 using tear strength measurements for swollen specimens at elevated temperatures.

Our recent cutting method evaluations of industrially relevant rubber compounds were less conclusive concerning the influence of crosslinking degree on fatigue threshold [23, 24]. The results are shown in Fig. 11a for two different rubber compositions wherein sulfur concentration was increased to generate different levels of crosslinking while keeping the ratio of accelerator to sulfur constant. There is no clear trend in T_0 versus sulfur level for either material, and the results considered in total are certainly not an endorsement for the Lake-Thomas prediction of a decrease in T_0 from adding more crosslinks. However, the compounds are more complex than the Gent and Tobias model materials and are instead close analogs of materials used in automotive rubber applications. The SBR compound includes CB N339 at a moderately high filler volume fraction, $\phi = 0.23$, and carbon black is known to

affect vulcanization [25, 26]. The silica-reinforced 70/30 blend of SBR and BR – which is similar to tread compounds used in improved fuel economy passenger car tires – has polymer-silica chemical linkages from bis[3-(triethoxysilyl)propyl] disulfide. This silica-SBR/BR material has a total of 250+ phr in the formulation, of which only 100 phr is the amount of dry elastomers, in clear contrast to 101–105 phr for the simple crosslinked elastomers in Fig. 10.

Crosslink type effects have been observed. Bhowmick, Gent, and Pulford [27] noted that intrinsic strengths of various unfilled elastomers with polysulfidic crosslinks were about two times higher than T_0 values for the same elastomers with monosulfidic or -C-C- crosslinks. That study assessed T_0 from tear strength of swollen samples at high temperatures. The same effect was found by Gent et al. [28] using the Lake-Yeoh cutting method. This can also be noted in the original Lake and Yeoh results for unfilled NR displayed in Fig. 4 where -C-C- crosslinks from peroxide curing have reduced fatigue threshold compared to polysulfidic crosslinks from sulfur vulcanization. Polysulfidic bonds are significantly weaker than -C-C- and -C-S-C- bonds. This allows polysulfidic crosslinks to break/reform/rearrange during elastomer deformation – which can be considered pseudo-self-healing behavior – to give the well-known advantage of increased tear strength, tensile strength, and fatigue lifetime [29]. Due to limited research, it is not known how the nature of polysulfidic crosslinks can increase the strength at threshold conditions. The Lake-Thomas theory does not allow for crosslink junctions to have lower bond strength than the bonds in the polymer backbone nor the possibility for crosslinks to reform after breaking.

3.3 *Influence of Reinforcing Fillers*

The majority of commercial applications of rubber employ compounds that contain reinforcing fillers such as carbon black and silica, and filler incorporation is known to increase tear strength and reduce fatigue crack growth rates [2, 10, 30–33]. Only a few studies have considered how filler affects fatigue threshold, however. Bhowmick and coworkers [16] discovered a strong positive influence of CB volume fraction on T_0 for NR and SBR compounds (Fig. 12), with a larger effect found for addition of the higher surface area N375 type of CB compared to N550. Kaolin clay gave a lower improvement in NR and nearly no change to T_0 in SBR. Up to this point in the chapter, the intrinsic strength data considered from several studies varied across the range from 20 to 150 J/m^2. The results in Fig. 12 exhibit T_0 in excess of 1,000 J/m^2 at the highest CB N375 concentrations. The authors discussed the general challenge in eliminating hysteresis in filled rubber by use of solvents and/or heating toward quantifying T_0, so it is possible that there were still T_z contributions to the measured tear strengths (Eq. 2). Using the Lake-Yeoh cutting method, Gent et al. [28] showed no effect of adding 50 phr ($\phi = 0.20$) of N330 carbon black to SBR compared to the unfilled material.

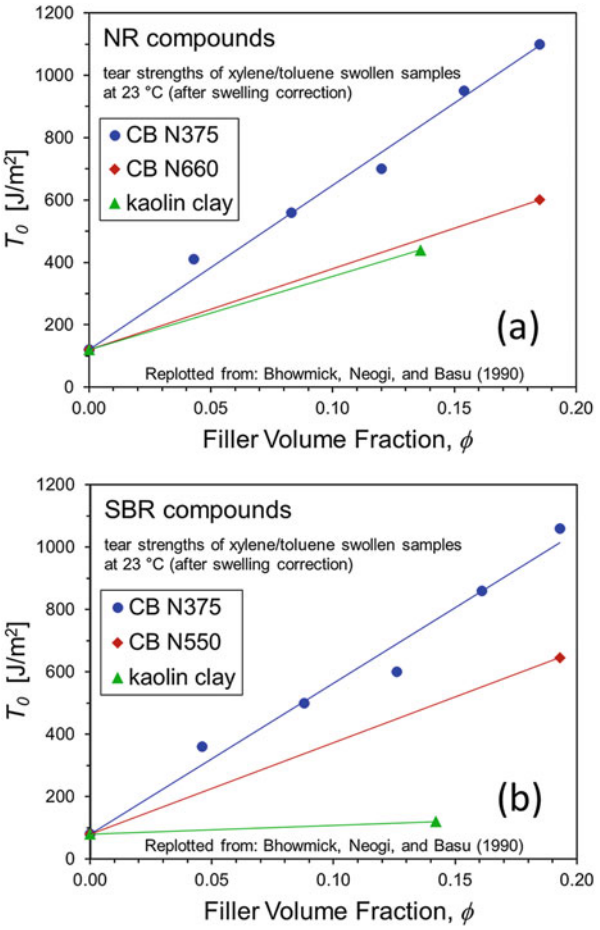

Fig. 12 Fatigue threshold estimated from swollen tear strength testing versus filler volume fraction for the indicated filler types in NR (**a**) and SBR (**b**). Replotted from Bhowmick, Neogi, and Basu [16]

In Table 3, we summarize new results from the ISA cutting method on the influence of carbon black volume fraction on fatigue threshold of EPDM, where it is evident that increasing CB N550 loading gives a slight decrease in T_0. These findings are compiled in Fig. 13a along with our recent data on the silica-SBR/BR (70/30) and CB-SBR materials [23, 24] discussed earlier with respect to crosslink density effects. With the exception of the highest silica level, the three filled rubber systems generally show moderately decreasing trends for T_0 as filler amount is increased in the formulation. Tear strength, T_c, increases as expected with filler concentration (Fig. 13b). In view of the opposite filler impacts on T_0 shown in Figs. 12 and 13a, additional research is needed to resolve this important aspect of formulation effects on fatigue threshold.

Before attempting to hypothesize about how to extend the molecular insights from the Lake-Thomas theory to address the roles of filler reinforcement and polymer-filler interactions, it is first useful to consider the relative size scales for

Table 3 T_0 results from ISA testing for EPDM filled with CB N550[a]

Filler volume fraction, ϕ	T_0 [J/m^2]
0.19	52.2
0.24	48.6
0.29	46.1

[a]Same rubber compounds described by Stocek [12]

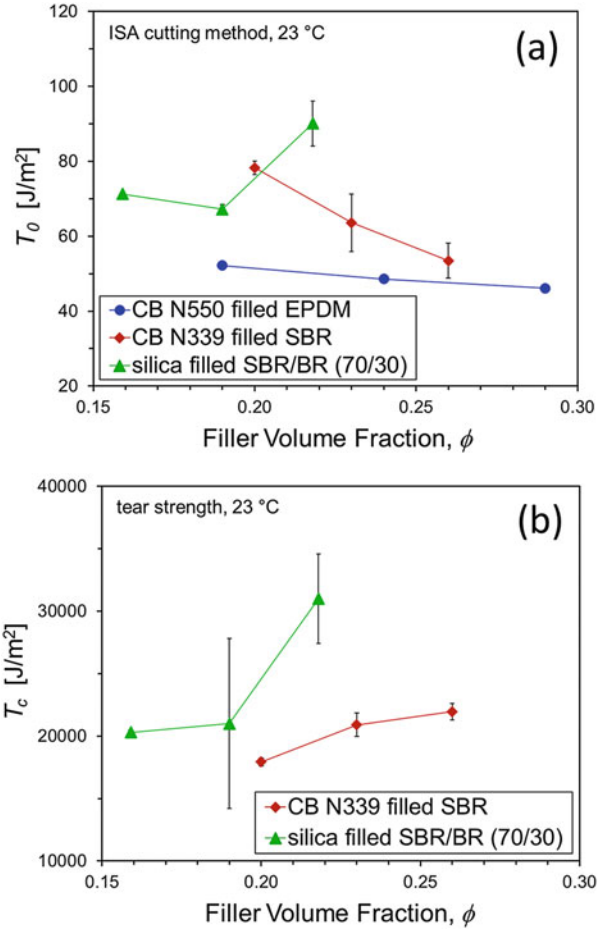

Fig. 13 Fatigue threshold (**a**) and tear strength (**b**) measured using the ISA for the indicated materials as a function of filler volume fraction. Data from our recent studies [23, 24] and new data for CB-filled EPDM. The crosslinking levels for the CB-SBR and silica-SBR/BR materials are the intermediate concentrations in Fig. 11a. The precipitated silica used in the silica-SBR/BR system had a specific surface area of 165 m^2/g, and bis [3-(triethoxysilyl)propyl] disulfide (S2 silane; Si266) was added at 8 wt.% relative to the silica amount

network chains and filler particles. Typical crosslink densities in elastomers are associated with distances between crosslinks that are less than 10 nm in the unstretched state [34, 35]. Measured chain dimensions in theta conditions for 1,4-polyisoprene (NR, IR) and 1,4-polybutadiene (BR) are characterized by essentially the same expression for the dependence of hydrodynamic radius on molecular

weight [36]: $R_H \approx 0.03\ M^{1/2}$, with M expressed in g/mol and R_H in units of nm. This can be used to estimate the size of the chain coil between crosslinks by substituting M_c for M. This gives coil diameters from 3 to 6 nm for M_c values in the common range from 2,000 to 10,000 g/mol (see data ranges in Fig. 10a). Comparable end-to-end distances of 3–7 nm can be determined using chain statistics for BR across the same span of M_c [34]. The standard N110, N339, and N550 grades of carbon black have average primary particle diameters of 17, 26, and 53 nm, respectively, and aggregate diameters of 54, 75, and 139 nm [37]. Therefore, even the smallest nanostructured carbon blacks that are used to reinforce rubber (e.g., N110) are characterized by primary particles that are more than twice the size of the network chain coil, and the aggregates of fused primary particles have diameters that are about ten times the distance between crosslinks. The size mismatch is depicted in Fig. 14. This greatly complicates the crack growth process beyond the simple Lake-Thomas molecular interpretation illustrated previously (Fig. 2). Certainly, physical adsorption or chemical bonding of a portion of the polymer chain to the surface of a particle will affect the mechanics of near-threshold crack growth. Perhaps more important to address is how the crack – which is able to progress forward between crosslink points that are a few nanometers apart according to the Lake-Thomas view – navigates around or through a much larger rigid filler aggregate. Another complexity is that swelling of a particle-reinforced elastomer network is not a simple chain dilution effect [38–40], and temperature affects filler networking and polymer-filler

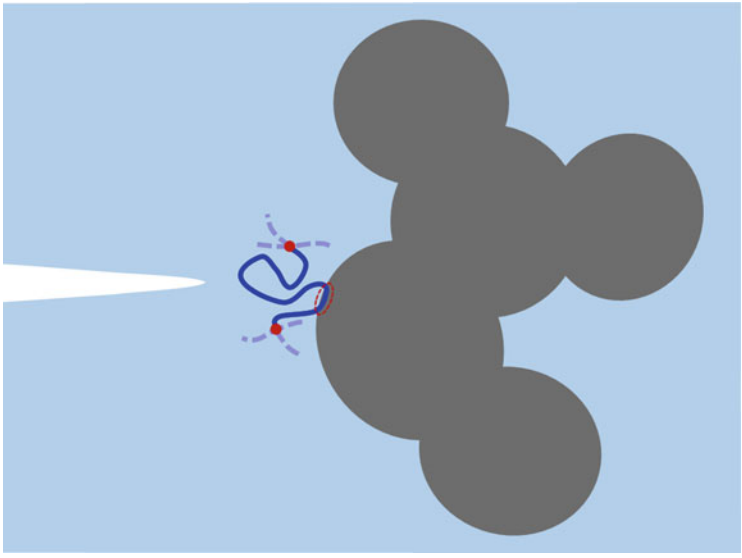

Fig. 14 Depiction of polymer network chain (dark blue line) between two crosslinks (red dots) that is in front of an advancing crack. The chain is adsorbed or bonded onto the surface of a filler aggregate (gray) which is composed of five primary particles fused together, with the region of polymer-filler interaction circled (red dashed line). See discussion text for relative sizes of polymer network chain and filler aggregate

interactions [41–44], so quantifying T_0 from tear strength testing of swollen samples at elevated temperatures may not be appropriate for filled rubber.

3.4 Oils/Plasticizers

To our knowledge, there have not been any systematic studies of the impacts of process oils, plasticizers, or other low molecular weight liquid additives on the fatigue threshold of rubber. We can get some insights by treating oil in a formulation in the same manner as the swelling correction in Eqs. 3 and 4, since oil has a comparable effect of diluting the polymer network chains. The one-dimensional swelling ratio for adding an oil to a dry polymer can be expressed as:

$$\lambda = \left(1 + \frac{w_o/\rho_o}{w_p/\rho_p}\right)^{1/3} \tag{9}$$

The w_o and w_p represent the weights in phr of the oil and dry polymer within the formulation, and ρ_o and ρ_p are their respective densities. Elastomers such as SBR and EPDM are often blended with oil by synthetic rubber manufacturers. A common oil concentration for oil extended elastomers is 37.5 phr per 100 phr of dry polymer. This amount of oil dilution causes a 19% reduction in T_0 according to Eqs. (3) and (9) if the oil and polymer have the same density. To increase fatigue threshold, the levels of process oils and other non-reactive low molecular weight liquids in a compound should be decreased, provided that reducing/eliminating these ingredients can be accomplished while still maintaining proper filler dispersion and acceptable rubber processability.

4 Using Fatigue Threshold to Develop Highly Durable Rubber Products

The main industrial interest in quantifying crack growth properties of elastomers is to use those insights to develop durable products. For product application conditions where $T > T_0$ and fatigue cracking will occur in a rubber component, modern fatigue analysis software for finite element analysis can be used to predict lifetime by incorporating concepts of critical plane analysis and integrated fatigue crack growth rate function [45–47]. The development approach is to create a material and design geometry combination that will give predicted cycles to failure in excess of the desired product lifetime for the complex application loading cycle and other use conditions. In this context, knowledge of the fatigue threshold is also useful for identifying non-damaging events in lengthy road load signals experienced by automotive rubber components. Sub-threshold events can be removed from consideration during testing and simulation efforts [45, 48].

An alternative, very conservative strategy is to produce a combination of design and material behavior that interplay with the loading situation to operate at sub-T_0 conditions where fatigue crack growth cannot take place. Accurate values of T_0 for the material and the effective tearing energy (T) associated with the rubber component operation must both be known in order to ensure $T < T_0$. The tearing energy can be expressed as [47, 49–52]:

$$T = 2\,k\,W\,c \tag{10}$$

Detailed discussions about the precise value of k are found in the chapters of Wunde et al. and Windslow et al. in this book [51, 52]. For simplicity, we use the approximate value $k = \pi$ [47]. The strain energy density (W) is the area under the stress versus strain response for the material experiencing the applied duty cycle in the product, so it is a combination of hyperelastic stress-strain behavior of the material, the part geometry, and deformation conditions. Finite element analysis is invaluable for assessing W throughout a rubber product design experiencing the loading conditions. At the start of fatigue, the crack size, c, of importance is the crack precursor size, c_0. The goal is then to find a material and design combination that satisfies:

$$2\,\pi\,W\,c_0 < T_0 \tag{11}$$

Crack precursors are sometimes called intrinsic flaws or defects, and they can come from undispersed filler agglomerates, hard contaminants in raw materials, and other aspects of the compound and its morphology/microstructure [53–55]. Crack precursor size is not a single number but rather a distribution [55] which should be considered with respect to failure statistics when selecting which c_0 to use in the product engineering criterion represented by Eq. (11). The possibility that fatigue threshold deteriorates with aging needs to be explored by testing T_0 of the material candidate after aging at relevant conditions. Also, any aging-induced changes to the rubber stiffness will affect W and should be included in the analysis toward keeping $T < T_0$ throughout the intended product lifetime.

5 Conclusions

We summarized key aspects of the fatigue threshold of rubber. Knowledge of this important material parameter can be used to develop rubber products with infinite fatigue lifetime, not considering other possible life-limiting changes to the material from aging, ozone cracking, and the like. The various testing approaches were discussed, with a focus on the well-established Lake-Yeoh cutting method that is implemented on the ISA. The cutting method was validated by demonstrating that a 2-h test on the ISA yields a T_0 that is nearly identical to the T_0 value from near-threshold fatigue crack growth measurements that require 7.5 months of continuous

testing. Finite element analysis of the cutting method provided support for the key premise that the blade localizes the strain energy density near the crack tip, and the simulations predicted a minimum in the total energy (tearing plus cutting) at a crack opening strain of 0.07 which matched the minimum in the experimental results.

The limited number of published studies on rubber formulation effects was reviewed, and the results were compared with our new data. The elastomer type has a clear impact on T_0, and lighter, smaller-diameter polymer chains have an advantage. Conflicting results exist for the dependencies of fatigue threshold on crosslink density and filler reinforcement, possibly due to differences in results from the cutting method versus tear testing of swollen specimens at high temperatures. For the latter characterization approach, it is particularly challenging to reach vanishing hysteresis conditions for rubber compounds that contain reinforcing fillers. More research is needed to clarify the various influences of rubber compound ingredients on T_0.

The Lake-Thomas model interprets T_0 in terms of fracture of elastomer network chains and is useful in rationalizing impacts of polymer structure, addition of oils/plasticizers to a compound, and crosslink density. Extending the Lake-Thomas conceptual framework to particle-reinforced rubber will require more than just adding polymer-filler interactions and related mobility effects into the physics. The size scales of common carbon black and precipitated silica particles are significantly larger than the size of a polymer network chain between crosslinks, which requires cracks to either go around the nano-structured filler aggregates or fracture them.

There are many interesting and innovative materials technologies such as sacrificial bonds [56], designer microstructures [57], self-healing functionalities [58], and double networks [59] that can increase intrinsic strength and retard crack growth in elastomeric materials. The translation of these basic research concepts and other materials science ideas into commercial rubber products with enhanced durability will require fast, reliable characterization of the fatigue threshold, and the Lake-Yeoh cutting method on the Intrinsic Strength Analyser will undoubtedly play an important role.

Acknowledgments This research was supported in part by the Ministry of Education, Youth and Sports of the Czech Republic – DKRVO (RP/CPS/2020/004). We thank Joshua R. Goossens from DriV Inc. (Milan, OH) and Dr. Nihat Isitman from Goodyear Tire & Rubber Company (Akron, OH) for collaborating in the ISA investigations of compounding effects that are described in previous works [23, 24] and replotted in this chapter.

References

1. Bhowmick AK (1988) Threshold fracture of elastomers. J Macromol Sci Part C Polym Rev 28:339–370
2. Mars WV, Fatemi A (2004) Factors that affect the fatigue life of rubber: a literature survey. Rubber Chem Technol 77:391–412
3. Harbour RJ, Fatemi A, Mars WV (2007) The effect of a dwell period on fatigue crack growth rates in filled SBR and NR. Rubber Chem Technol 80:838–853

4. Stadlbauer F, Koch T, Archodoulaki V-M, Planitzer F, Fidi W, Holzner A (2013) Influence of experimental parameters on fatigue crack growth and heat build-up in rubber. Materials 6:5502–5516
5. Stoček R, Horst T, Reincke K (2016) Tearing energy as fracture mechanical quantity for elastomers. Adv Polym Sci 275:361–398
6. Lake GJ, Lindley PB (1965) The mechanical fatigue limit for rubber. J Appl Polym Sci 9:1233–1251
7. Lake GJ, Thomas AG (1967) The strength of highly elastic materials. Proc R Soc Lond A 300:108–119
8. Sakulkaew K, Thomas AG, Busfield JJC (2013) The effect of temperature on the tearing of rubber. Polym Test 32:86–93
9. Tsunoda K, Busfield JJC, Davies CKL, Thomas AG (2000) Effect of materials variables on the tear behaviour of a non-crystallising elastomer. J Mater Sci 35:5187–5198
10. Bhattacharyya S, Lodha V, Dasgupta S, Mukhopadhyay R, Guha A, Sarkar P, Saha T, Bhowmick AK (2019) Influence of highly dispersible silica filler on the physical properties, tearing energy, and abrasion resistance of tire tread compound. J Appl Polym Sci 136:47560
11. Andrews EH (1963) Rupture propagation in hysteresial materials: stress at a notch. J Mech Phys Solids 11:231–242
12. Stoček R (2021) Some revision of fatigue crack growth characteristics of rubber. In: Heinrich G, Stoček R, Kipscholl R (eds) Fatigue crack growth in rubber materials: experiments and modelling. Springer, Berlin
13. Zhang E, Bai R, Morelle XP, Suo Z (2018) Fatigue fracture of nearly elastic hydrogels. Soft Matter 14:3563–3571
14. Legorju-Jago K, Bathias C (2002) Fatigue initiation and propagation in natural and synthetic rubbers. Int J Fatigue 24:85–92
15. Gent AN, Tobias RH (1982) Threshold tear strength of elastomers. J Polym Sci Polym Phys Ed 20:2051–2058
16. Bhowmick AK, Neogi C, Basu SP (1990) Threshold tear strength of carbon black filled rubber Vulcanizates. J Appl Polym Sci 41:917–928
17. Mazich KA, Samus MA, Smith CA, Rossi G (1991) Threshold fracture of lightly crosslinked networks. Macromolecules 24:2766–2769
18. Lake GJ, Yeoh OH (1978) Measurement of rubber cutting resistance in the absence of friction. Int J Fract 14:509–526
19. Robertson CG, Stoček R, Kipscholl C, Mars WV (2019) Characterizing the intrinsic strength (fatigue threshold) of natural rubber/butadiene rubber blends. Tire Sci Technol 47:292–307
20. Mars WV, Robertson CG, Stoček R, Kipscholl C (2019) Why cutting strength is an indicator of fatigue threshold. In: Huneau B, Le Cam J-B, Marco Y, Verron E (eds) Constitutive models for rubber XI. CRC Press, Taylor & Francis Group, London, pp 351–356
21. Robertson CG, Suter JD, Bauman MA, Stoček R, Mars WV (2020) Finite element modeling and critical plane analysis of a cut-and-chip experiment for rubber. Tire Sci Technol. https://doi.org/10.2346/tire.20.190221
22. Robertson CG, Stoček R, Kipscholl R, Mars WV (2019) Characterizing durability of rubber for tires. Tire Technol Int Ann Rev:78–82
23. Robertson, C.G., Goossens, J.R., Mars, W.V. (2019) Using the laboratory cutting method for predicting long-term durability of elastomers. In: Paper D15, presented at the fall 196th technical meeting of the rubber division, ACS, Cleveland, OH, Oct 10–12, 2019
24. Isitman N, Stoček R, Robertson CG (2020) Influences of compounding attributes on intrinsic strength and tearing behavior of model tread rubber compounds. In: Paper scheduled to be presented at the 197th technical meeting of the rubber division, ACS, Independence, OH, April 28–30, 2020 (Presentation slides made available online due to meeting cancellation for COVID-19 precaution)

25. Hosseini SM, Razzaghi-Kashani M (2018) Catalytic and networking effects of carbon black on the kinetics and conversion of sulfur vulcanization in styrene butadiene rubber. Soft Matter 14:9194–9208
26. Blokh GA, Melamed CL (1961) The interaction of carbon black with sulfur, MBT and TMTD in vulcanization. Rubber Chem Technol 34:588–599
27. Bhowmick AK, Gent AN, Pulford CTR (1983) Tear strength of elastomers under threshold conditions. Rubber Chem Technol 56:226–232
28. Gent AN, Lai S-M, Nah C, Wang C (1994) Viscoelastic effects in cutting and tearing of rubber. Rubber Chem Technol 67:610–618
29. Rader CP (2001) Chapter 7. Vulcanization of rubber – A. sulfur and non-peroxides. In: Baranwal KC, Stephens HL (eds) Basic elastomer technology. The rubber division. ACS, Akron, pp 165–190
30. Klüppel M (2009) The role of filler networking in fatigue crack propagation of elastomers under high-severity conditions. Macromol Mater Eng 294(2):130–140
31. Vaikuntam SR, Bhagavatheswaran ES, Xiang F, Wießner S, Heinrich G, Das A, Stöckelhuber KW (2020) Friction, abrasion and crack growth behavior of in-situ and ex-situ silica filled rubber composites. Materials 13:270
32. Sridharan H, Guha A, Bhattacharyya S, Bhowmick AK, Mukhopadhyay R (2019) Effect of silica loading and coupling agent on wear and fatigue properties of a tread compound. Rubber Chem Technol 92:326–349
33. Rooj S, Das A, Morozov IA, Stöckelhuber KW, Stoček R, Heinrich G (2013) Influence of "expanded clay" on the microstructure and fatigue crack growth behavior of carbon black filled NR composites. Compos Sci Technol 76:61–68
34. Heinrich G, Vilgis TA (1993) Contribution of entanglements to the mechanical properties of carbon black-filled polymer networks. Macromolecules 26:1109–1119
35. Robertson CG, Wang X (2004) Nanoscale cooperative length of local segmental motion in polybutadiene. Macromolecules 37:4266–4270
36. Fetters LJ, Hadjichristidis N, Lindner JS, Mays JW (1994) Molecular weight dependence of hydrodynamic and thermodynamic properties for well-defined linear polymers in solution. J Phys Chem Ref Data 23:619–640
37. Hess WM, McDonald GC (1983) Improved particle size measurements on pigments for rubber. Rubber Chem Technol 56:892–917
38. Kraus G (1963) Swelling of filler-reinforced vulcanizates. J Appl Polym Sci 7:861–871
39. Busfield JJC, Thomas AG, Yamaguchi K (2004) Electrical and mechanical behavior of filled elastomers 2: the effect of swelling and temperature. J Polym Sci B Polym Phys 42:2161–2167
40. Elhaouzi F, Mdarhri A, Brosseau C, El Aboudi I, Almaggoussi A (2019) Effects of swelling on the effective mechanical and electrical properties of a carbon black-filled polymer. Polym Bull 76:2765–2776
41. Arai K, Ferry JD (1986) Temperature-dependence of viscoelastic properties of carbon-black-filled rubbers in small shearing deformations. Rubber Chem Technol 59:592–604
42. Mujtaba A, Keller M, Ilisch S, Radusch HJ, Beiner M, Thurn-Albrecht T, Saalwächter K (2014) Detection of surface-immobilized components and their role in viscoelastic reinforcement of rubber–silica Nanocomposites. ACS Macro Lett 3:481–485
43. Sternstein SS, Amanuel S, Shofner ML (2010) Reinforcement mechanisms in Nanofilled polymer melts and elastomers. Rubber Chem Technol 83:181–198
44. Warasitthinon N, Genix A-C, Sztucki M, Oberdisse J, Robertson CG (2019) The Payne effect: primarily polymer-related or filler-related phenomenon? Rubber Chem Technol 92:599–611
45. Barbash KP, Mars WV (2016) Critical plane analysis of rubber bushing durability under road loads. SAE technical paper, no. 2016-01-0393
46. Mars WV, Wei Y, Hao W, Bauman MA (2019) Computing Tire component durability via critical plane analysis. Tire Sci Technol 47:31–54
47. Mars WV (2021) Critical plane analysis of soft materials. In: Heinrich G, Stoček R, Kipscholl R (eds) Fatigue crack growth in rubber materials: experiments and modelling. Springer, Berlin

48. Mars WV, Suter JD (2019) Breaking the computational barrier to simulating full road load signals in fatigue. In: Paper C08, presented at the fall 196th technical meeting of the rubber division, ACS, Cleveland, OH, Oct. 10–12, 2019
49. Aït-Bachir M, Mars WV, Verron E (2012) Energy release rate of small cracks in hyperelastic materials. Int J Non-Linear Mech 47:22–29
50. Mars WV (2002) Cracking energy density as a predictor of fatigue life under multiaxial conditions. Rubber Chem Technol 75:1–17
51. Wunde M, Klüppel M (2021) The role of phase morphology and energy dissipation around the crack tip in fatigue crack propagation of filler reinforced elastomer blends. In: Heinrich G, Stoček R, Kipscholl R (eds) Fatigue crack growth in rubber materials: experiments and modelling. Springer, Berlin
52. Windslow RJ, Hohenberger TW, Busfield JJC (2021) Determination of the loading mode dependence of the proportionality parameter for the tearing energy of embedded flaws in elastomers under multiaxial deformations. In: Heinrich G, Stoček R, Kipscholl R (eds) Fatigue crack growth in rubber materials: experiments and modelling. Springer, Berlin
53. Huneau B, Masquelier I, Marco Y, Le Saux V, Noizet S, Schiel C, Charrier P (2016) Fatigue crack initiation in a carbon black-filled natural rubber. Rubber Chem Technol 89:126–141
54. Ludwig M, Alshuth T, El Yaagoubi M, Juhre D (2015) Lifetime prediction of elastomers based on statistical occurrence of material defects. In: Marvalová B, Petríková I (eds) Constitutive models for rubber IX. CRC Press, Taylor & Francis Group, London, pp 445–448
55. Robertson CG, Tunnicliffe LB, Maciag L, Bauman MA, Miller K, Herd CR, Mars WV (2020) Characterizing distributions of tensile strength and crack precursor size to evaluate filler dispersion effects and reliability of rubber. Polymers 12:203
56. Ducrot E, Chen Y, Bulters M, Sijbesma RP, Creton C (2014) Toughening elastomers with sacrificial bonds and watching them break. Science 344:186–189
57. Xiang C, Wang Z, Yang C, Yao X, Wang Y, Suo Z (2020) Stretchable and fatigue-resistant materials. Mater Today 34:7–16
58. Das A, Sallat A, Böhme F, Suckow M, Basu D, Wießner S, Stöckelhuber KW, Voit B, Heinrich G (2015) Ionic modification turns commercial rubber into a self-healing material. ACS Appl Mater Interfaces 7:20623–20630
59. Zhang W, Liu X, Wang J, Tang J, Hu J, Lu T, Suo Z (2018) Fatigue of double-network hydrogels. Eng Fract Mech 187:74–93

Adv Polym Sci (2021) 286: 85–108
https://doi.org/10.1007/12_2020_73

Published online: 3 December 2020

Critical Plane Analysis of Rubber

W. V. Mars

Contents

Abstract Durability is an essential feature of most elastomer products, directly linked to safety and to perceptions of brand quality. Product designers must therefore consider the impact on product durability of typical and abusive end-user loading scenarios. This can be accomplished using critical plane analysis (CPA). CPA starts by acknowledging that a small crack precursor might exist at any point in a part, and in any orientation, and that the potential development of all crack precursors must be evaluated. The analysis produces a full accounting of which location and orientation maximizes crack growth (or, equivalently, minimizes fatigue life) at each point, the energy release rate history experienced, and of course the worst-case fatigue life across all possible orientations. This review provides an account of the development

W. V. Mars (✉)
Endurica LLC, Findlay, OH, USA
e-mail: wvmars@endurica.com

of the method over the last two decades and the validation case that has accumulated. This review also suggests directions for further development of the method.

Keyword Damage · Durability · Fatigue life · Multiaxial

1 Introduction

The growth of cracks is often the chief limiter of a product's useful life [1, 2]. Product designers must therefore make allowance via their selections of material, design, and loads for a sufficient margin between the demands of a given application and the capacity of the product to resist crack growth. Given that microscopic crack precursors exist [3–5] at nearly every point in a rubber part, and that they may have any orientation, a thorough analysis is required of a product's use and abuse in order to ensure adequate durability.

The growth of crack precursors is driven by the load inputs to a part. Load inputs may come from one direction or from several. They may be steady with a constant amplitude or random with variable amplitudes. The required analysis must account for how loading inputs to the part are experienced by each possible crack at each possible point of failure in a part, as well as the rate at which each possible crack grows.

Implementing such an analysis for practical use requires the computational resources of a sufficient computer, as well as fatigue solver software that is properly formulated to embody the many details and physical effects that come into play. In this review, we shall take for granted that the computer is sufficiently powerful, and we shall focus on a specific calculation framework: critical plane analysis (CPA).

2 The Critical Plane Method

Critical plane methods for rubbery materials were first proposed and developed independently and nearly simultaneously by Mars [6–9] and by Saintier [10–11] and have since been explored and validated by many others [12–21]. Both original implementations build upon precedents from the metal fatigue community [22–23]. The key idea is that cracks develop on a particular material plane, specifically the most critical material plane, and that their localized experience drives their evolution.

Although the key idea of CPA was the same for Mars and Saintier, there were also important differences between respective implementations (see Table 1 for a summary). Major differences include (1) how the critical plane is selected, (2) what criterion is used to quantify the severity of loading experience on the critical plane,

Table 1 Comparison of CPA methods of Mars and Saintier

	Mars	Saintier
Critical plane selection method	Minimum life across all planes	Maximum principal stress
Multiaxial criterion	Energy release rate estimated via cracking energy density	Stress traction on assumed critical plane
Damage evolution law	Crack growth rate law	Wohler curve
Strain crystallization law	R ratio dependence of crack growth rate law	Modifier of stress experienced on critical plane

and (3) how damage on the critical plane evolves under solicitation. The Mars framework has been implemented in the commercial fatigue solvers fe-safe/Rubber and Endurica CL.

2.1 Critical Plane Selection

In the Mars analysis framework, which is the basis of the Endurica CL fatigue solver, the critical plane is identified on the basis of minimizing the fatigue life, N_f, with respect to the orientation (specified by spherical coordinates θ and φ) of the crack plane normal vector, $\vec{N}$. The life is obtained by integrating the fatigue crack growth (FCG) rate law $\frac{da}{dN} = r(T)$ from the initial crack precursor size, a_o, to the end of life size, a_f, as shown in Eq. (1). T is the energy release rate of the assumed crack:

$$N_f(\theta, \varphi) = \int_{a_o}^{a_f} \frac{1}{r(T(\theta, \varphi, a))} da \tag{1}$$

The set of all orientations (θ, φ) can be represented via a sphere as in Fig. 1. The sphere is colored according to the life, N_f, so that red is the shortest life and blue is the longest.

The above framework offers significant accuracy advantages over alternative approaches because it makes no presumption about the orientation of the critical plane. The critical plane is rather a consequence of the calculations.

Other approaches assume a plane selection rule prior to evaluating damage. For example, Saintier's Wohler curve-based approach used a maximum principal stress direction to identify the critical plane [10, 11]. While it is sometimes true that the most critical plane coincides with the normal to the maximum principal stress, this is not always the case and cannot be taken for granted. Well-known exceptions [8] include simple compression (where planes that maximize shearing will see the most damage), nonrelaxing cycles for strain crystallizing materials (where nonrelaxing cycles can cause off-axis cracks [24]), and nonproportional loading histories (where a unique maximum principal stress direction may not even exist).

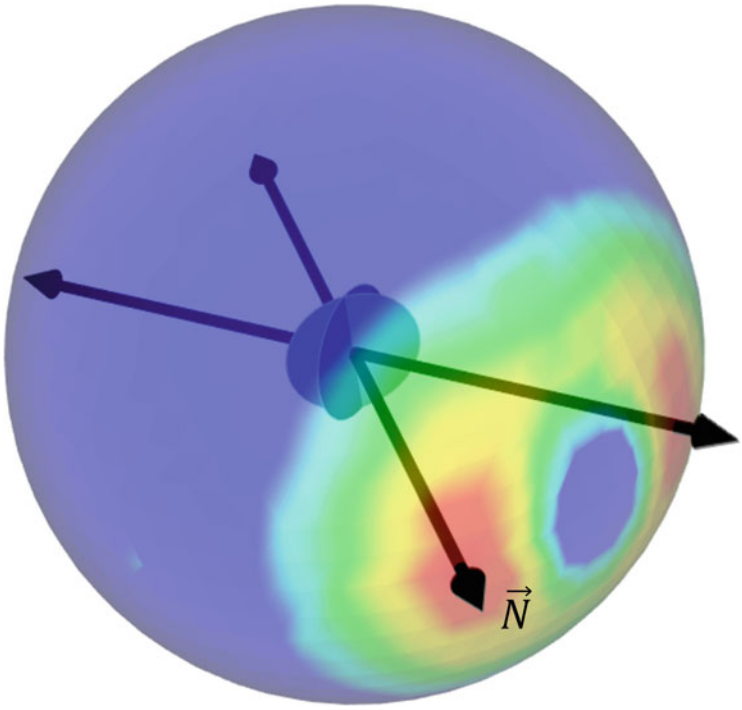

Fig. 1 Contours of fatigue life plotted on the sphere representing all possible critical plane orientations. The planes with normal $\vec{N}$ that minimize life are the critical planes

2.2 Multiaxial Criterion

Once a potential plane (θ, φ) is specified for consideration, either as a search iteration (as in Mars) or as an orientation resulting from an assumed selection rule (as in Saintier), some criterion must be applied to quantify the driving forces that cause precursor development. The criterion that is used will correspond with its associated damage evolution law.

In the Mars framework, the energy release rate of an idealized crack undergoing self-similar growth is taken as the multiaxial criterion, so that the FCG rate law may be used as the damage evolution law. The energy release rate of a small crack in this case is proportional to the size a of the crack [25], as follows:

$$T = 2kW_c a \tag{2}$$

The parameter k is a nondimensional factor that may depend on mode and magnitude of deformation and on the material constitutive law. Through experimentation, Greensmith [26] showed that for simple tension, it was loosely dependent upon the far-field principal stretch, λ, decreasing from $k = 3$ at small strains to k

($\lambda = 3$) $= 2$. Later, Lindley [27] used finite element analysis (FEA) to find $k = (2.95 - 0.08(1 - \lambda))\lambda^{-1/2}$. Lake [28] attempted to use symmetry conditions to adapt Rivlin and Thomas' test sample with a short crack solution to the tearing energy at a centrally positioned flaw in a thin sheet under uniaxial tension. He found the proportionality parameter related to the far-field principal stretch through π. This led to the simpler form, $k = \pi/\sqrt{\lambda}$ for both edge and central cracks. Klüppel and coworkers [29] published experimental data from SENT test pieces that suggests the factor of π is too high. They identified a value that ranged from 1.2 to 3.1. Chang et al. [30] and Yeoh [31] studied the effect of multiaxial states of deformation on k, as did Aït Bachir et al. [25]. Mars [32] showed that the value of k can evolve with the Mullins effect. To date, nobody has given a complete reckoning of this factor across all of its dependencies. In spite of these varied reports, experience [33] has shown that satisfactory correlation between measured and calculated fatigue lives for a broad range of multiaxial cases is obtained with the assignment $k = \pi$, which is used in this work.

W_c is the cracking energy density [7, 8]. This quantity is the portion of the strain energy density that is available for release by a crack growing in the specified plane. It can be calculated by considering the material plane with normal $\vec{N}$ in the undeformed configuration. In the deformed configuration with deformation gradient $\boldsymbol{F}$, this material plane has unit normal $\vec{n}$, given by the transform rule [14]:

$$\vec{\boldsymbol{n}} = \frac{\vec{\boldsymbol{N}}\boldsymbol{F}^{-1}}{\left|\vec{\boldsymbol{N}}\boldsymbol{F}^{-1}\right|} \tag{3}$$

Knowing $\vec{n}$, the instantaneous traction $\vec{S}$ on the plane can be determined by the rule:

$$\vec{S} = \bar{\bar{\boldsymbol{\sigma}}} \cdot \vec{n} \tag{4}$$

After computing the traction vector, the vector components normal and shear to the plane should be resolved so that crack closure effects can be checked and taken into account. Crack closure occurs when the normal component has a negative value.

A deformation increment $\overrightarrow{d\varepsilon}$ of a line element originally normal to the plane can also be defined via the rule:

$$\overrightarrow{d\varepsilon} = \bar{\bar{\mathbf{d\varepsilon}}} \cdot \vec{n} \tag{5}$$

The dot product of the traction vector $\vec{S}$ and the deformation increment vector $\overrightarrow{d\varepsilon}$ may then be taken to obtain the cracking energy density, as follows:

$$dW_c = \vec{S} \cdot d\vec{\varepsilon} \tag{6}$$

The cracking energy density represents that portion of the elastically stored strain energy density that may be said to be available for release when the crack in orientation $\vec{n}$ grows.

In other CPA frameworks, varied parameters have been used. Saintier [10, 11] used the traction vector on the selected plane together with a Wohler curve-based damage evolution law. In addition to the cracking energy density, Harbour [16] used strain-based criteria. Verron used the Eshelby tensor [12].

2.3 Damage Evolution Law

The choice of multiaxial criterion determines the form of the damage evolution law.

In the Mars framework, the FCG rate law governs the relationship between the solicitation and the damage evolution (i.e., crack length increase). The FCG rate law may take several forms [34]. The simplest is the Thomas law [2], given by

$$\frac{da}{dN} = r_c \left(\frac{T}{T_c} \right)^F \tag{7}$$

T_c is the rupture strength of the material. r_c is the rate of FCG at the point where Eq. (7) intersects the rupture strength. F is the power-law slope of the rate law. The Thomas law is similar to the Paris law known from metal fatigue, in that both involve an energy release rate raised to some power. However, where the Paris law is written as a function of the range of energy release rate, the Thomas law is written as a function of the peak energy release rate at the top of the stroke.

The Lake-Lindley form [35] of the FCG rate law imposes a lower bound [36–41] – the fatigue limit T_0 – on the energy release rate that will produce positive crack growth. Below this limit, no cyclic crack growth occurs. Above the limit, the following rules govern:

$$\begin{aligned} T_0 < T < T_t \quad & \frac{da}{dN} = A(T - T_0) \\ T > T_t \quad & \frac{da}{dN} = r_c \left(\frac{T}{T_c} \right)^F \end{aligned} \tag{8}$$

T_t is a transition point between the two branches of the rate law definition. The parameter A can be determined from the requirement of continuity across the branches as $A = \frac{r_c T_t^F}{T_c^F (T_t - T_o)}$.

In the Saintier framework, a power-law-based Wohler curve is used to correlate the stress amplitude magnitude on the critical plane to a total fatigue life. Two

drawbacks of Wohler curves are that (1) they are not universal with respect to different modes of deformation (e.g., simple tension, biaxial tension, and simple compression do not form a single curve) and (2) they are more expensive to generate experimentally than the FCG rate law.

2.4 Strain Crystallization Law

Under nonrelaxing cycles, materials that strain crystallize exhibit markedly different behavior from materials that do not crystallize [42–47].

Without strain crystallization, nonrelaxing cycles in rubbery materials follow a Paris law much the same as other engineering materials, where the crack growth rate depends primarily on the range ΔT of the energy release rate. This leads to the following equivalence rule between nonrelaxing cycles (i.e., cycles whose lower extreme energy release rate is greater than zero) operating with peak T_{max} and valley T_{min} and fully relaxing cycles operating at the same equivalent (i.e., same FCG rate) energy release rate T_{eq}:

$$T_{eq} = \Delta T = T_{max} - T_{min} = T_{max}(1 - R) \tag{9}$$

The ratio R is defined as $R = T_{min}/T_{max}$. The Paris law is recovered when using this rule with the Thomas law.

With strain crystallization, nonrelaxing cycles in rubbery materials show behavior in which the equivalent fully relaxing (i.e., cycles whose lower extreme energy release rate is zero) energy release rate T_{eq} is shifted according the following rule:

$$T_{eq} = \left(\frac{T_{max}}{T_c^{x(R)}} \right)^{\frac{1}{1-x(R)}} \tag{10}$$

$x(R)$ is a shift function relating the shift factor x (see Fig. 2) to its corresponding R ratio. The shift factor gives the log fraction by which the fully relaxing FCG rate curve must be shifted to give the nonrelaxing FCG rate curve. For example, when $x = 0$, the nonrelaxing curve is coincident with the fully relaxing curve. When $x = 0.5$, the nonrelaxing curve is shifted halfway between the fully relaxing curve and the vertical asymptote at T_C. When $x = 1.0$, the curve becomes coincident with the asymptote at T_C. Typical results for the shift function $x(R)$ are shown in Fig. 3.

As an example, the Haigh diagram [45] (a contour map showing the dependence of the fatigue life under uniaxial loading on mean strain and strain amplitude) for simple tension/compression corresponding to each of the above rules has been computed and plotted in Fig. 4. The noncrystallizing material is on the top, and the strain-crystallizing material is on the bottom. It can be appreciated from these examples that strain crystallization tends to retard crack growth when R ratio is increased at fixed peak energy release rate. Equivalently, for a crystallizing rubber,

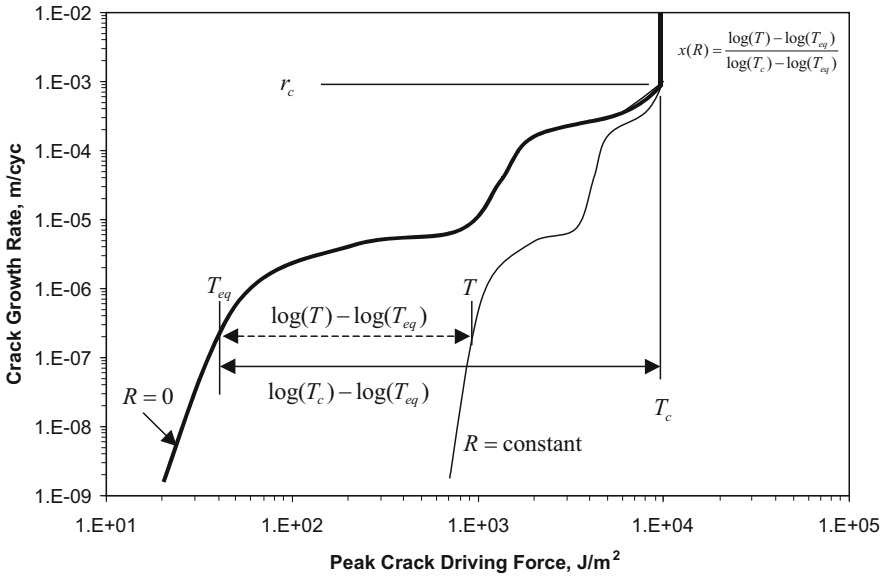

Fig. 2 Schematic showing definition of the shift function *x(R)* for a strain-crystallizing, nonrelaxing ($R > 0$) FCG rate curve relative to the fully relaxing rate curve ($R = 0$)

increasing the mean strain at constant strain amplitude can increase fatigue life, so long as the mean strain does not become large enough to approach ultimate limits.

In the Saintier framework, strain crystallization is treated as a modification of the stress experienced by the critical plane.

3 Incremental Procedure

The procedures outlined above serve well when it is desired to compute the life for a fixed history that repeats continually until failure. There are many circumstances, however, in which the load cases that occur in one period are different from the load cases that occur in another period. The block cycle schedules often prescribed as qualification tests for automotive components are a key example. Standard regulatory durability tests in the tire industry are another example. To solve the broadest range of problems, including these, it is necessary to extend the calculations using an incremental procedure.

In an incremental fatigue solver (Endurica DT is a commercial example), damage accrual is accomplished using the following reformulation [48–50] of Eq. (1). This utilizes the same crack growth rate laws and input variables as before, but it integrates over cycles from time N_i to time N_{i+1}, rather than over crack size a:

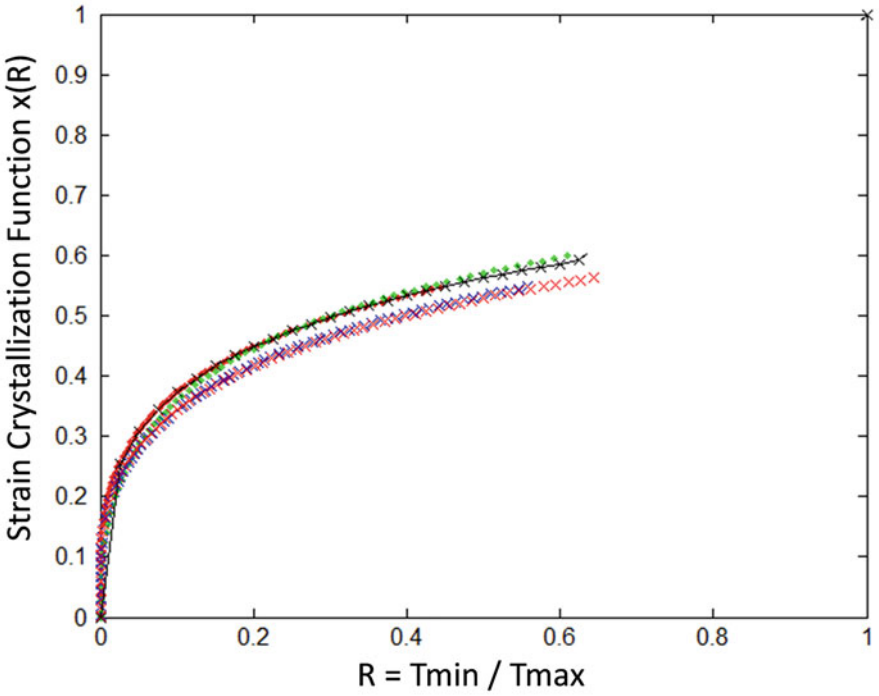

Fig. 3 Typical experimentally determined shift function *x(R)* defining the crystallization law for a natural rubber

$$\Delta a_{i \to i+1,j,k} = \int_{N_i}^{N_{i+1}} r(T(\varepsilon_{mn}(N), \theta(N), a(N)))dN \tag{11}$$

The result of the integration is the change of length $\Delta a_{i \to i+1,j,k}$ of a crack for each finite element *j* and each potential failure plane *k* of the model. The accumulated crack lengths for each element are written to a file during the analysis, so that future additions of load history may begin at the point at which the prior increment concluded. The basic incremental workflow for three successive periods is shown in Fig. 5. Additional load cases can be added ad infinitum until the crack length finally reaches its end of life size.

Incremental fatigue analysis has many important applications. It enables a proper accounting to be made of block cycle or multistep fatigue testing schedules, including sequence effects. At any stage of an incremental analysis, the workflow also admits the calculation of residual strength or residual life. This is useful if it is desired to visualize how life is decremented as a function of time or per event. The incremental analysis also enables an account to be made of the evolution of material properties [51] with cycles or time. For example, if cyclic softening effects or ageing effects evolve the elastic properties, then incremental analysis enables the stresses and strains in the finite element model to be updated periodically so that mode of

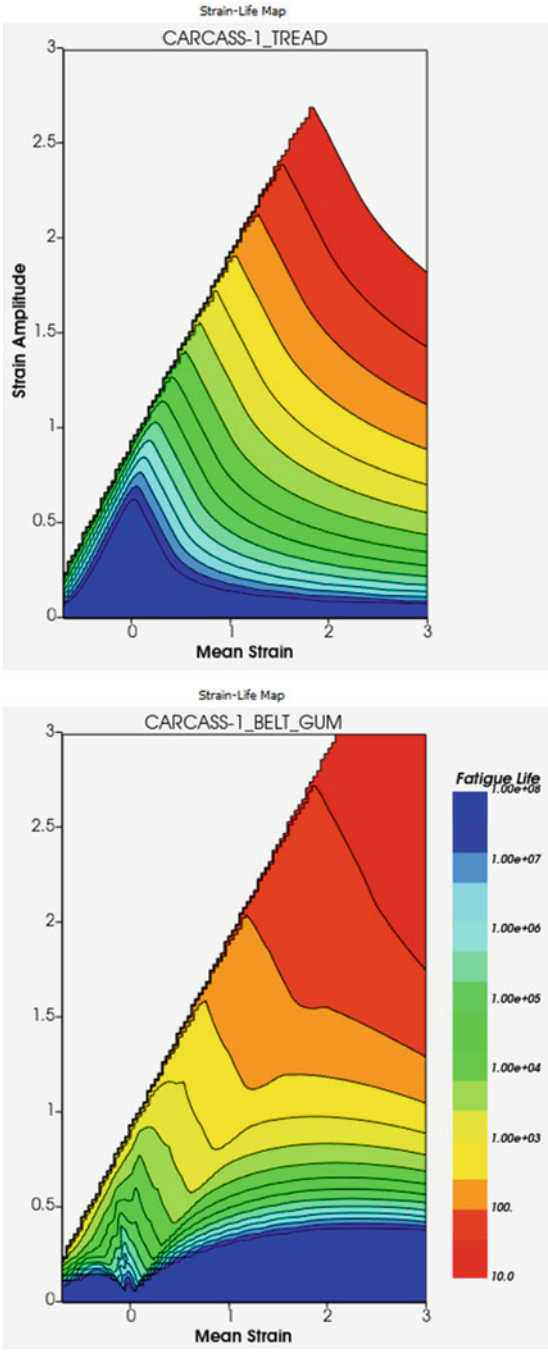

Fig. 4 Typical Haigh diagrams computed via critical plane analysis for noncrystallizing (top) and crystallizing (bottom) rubbers

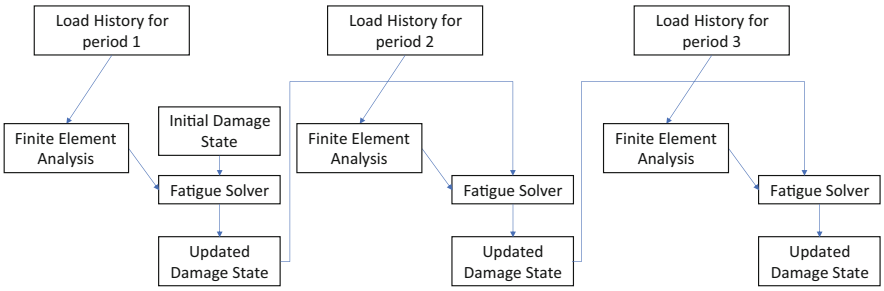

Fig. 5 Incremental fatigue analysis workflow

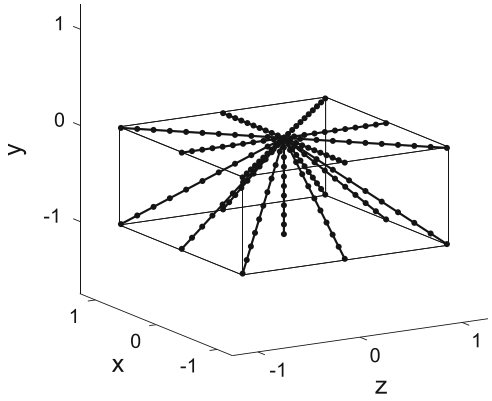

Fig. 6 Nonlinear case vector map of a three-channel load space used for rapidly interpolating stress and strain values from a set of pre-computed finite element solutions

control (displacement control vs. force control) effects can be accurately represented. The incremental analysis is useful for digital twin applications also [50, 52].

4 Managing Lengthy Loading Signals

Road load histories are sometimes so lengthy that the corresponding finite element solutions cannot easily be computed. In order to obtain strain history for fatigue analysis in such cases, a much faster computational strategy is needed. Endurica EIE (Efficient Interpolation Engine) accomplishes this by means of a nonlinear map relating the rubber part input channels (as many as three channels are supported, so far) to a set of pre-computed finite element solutions that span the mapped space [53, 54]. This approach assumes that there is a unique one-to-one mapping between points in the load space and stress/strain states in each element of the model. Since rubber is often treated via hyperelasticity, the assumption is often effective.

The workflow first involves computing the finite element model over the set of case vectors used to map the loading space. As an example, Fig. 6 shows a 3 channel (x, y

and z displacement) case vector map having 17 case vectors. Each vector is a finite element solution containing a series of increments. The stresses and strains in every element are known at each grid point along each vector. Interpolation is used to estimate solution values at points in between case vectors and grid points. Next, the set of pre-computed finite element solutions are used as the basis for an interpolation such that given a point (x, y, z) within the load space is assigned its stress and strain values by interpolating from the pre-computed nearest neighbor solutions. For lengthy road load signals, this process has been demonstrated [55] to generate accurate strain histories 100–10,000× faster than direct solution of the finite element model. An additional benefit of this method is that once the nonlinear map has been generated for a rubber component, many different load signals may be rapidly computed.

5 Some Applications

The methods described above have been successfully applied to many examples.

5.1 Critical Plane Analysis of Nonrelaxing Simple Tension

It was recently demonstrated [24] in simple tension fatigue tests, where cracks normally initiate perpendicular to the loading direction, that other crack initiation directions can occur. The tests were run on filled NR and filled SBR compounds. The results are summarized in Fig. 7.

When the strain cycle in the test was fully relaxing (0–100%), cracks initiated perpendicular to the loading direction for both the NR and SBR compounds.

However, when the strain cycle in the test was nonrelaxing (50–150%), the initiated crack orientation was found to depend on the material. For SBR, the crack appeared perpendicular to the load, as before. For NR, the crack appeared at a sharp angle to the loading axis.

The crack orientations occurring for all of the cases are accurately predicted by CPA using Endurica CL; see Figs. 8 and 9. The fatigue simulations showed that for the fully relaxing cases, and for the SBR under nonrelaxing conditions, the perpendicular crack orientation is favored because it maximizes the energy release rate experienced by a crack precursor on the critical plane. The simulation also showed that for NR under nonrelaxing loading, cracking occurs at a sharp angle (~17°) to the load due to competition between strain crystallization (which favors crack growth on planes experiencing lower R ratios) and energy release rate maximization (which favors crack growth on planes perpendicular to the load). A key advantage of CPA over prior art approaches is its ability to predict failure plane.

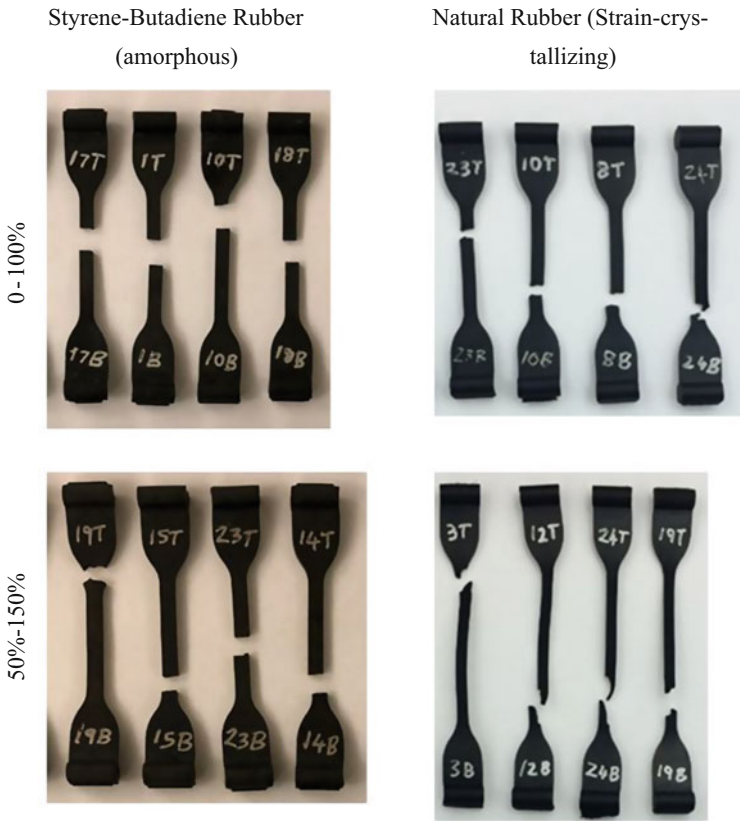

Fig. 7 Observations of critical plane dependence on material and strain cycle

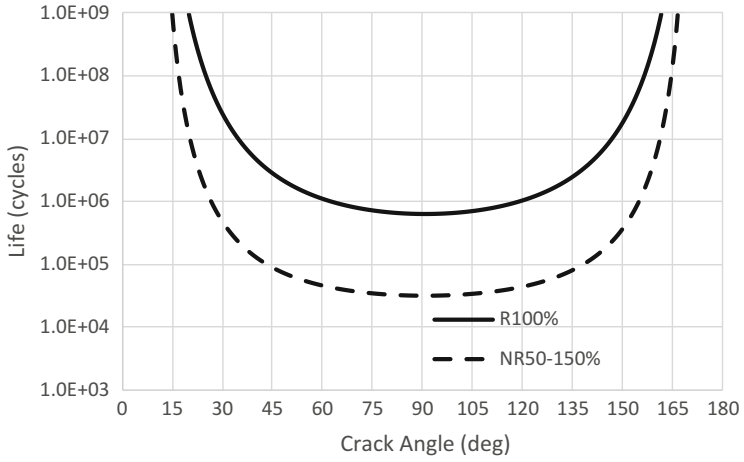

Fig. 8 CPA of SBR for relaxing and nonrelaxing cases

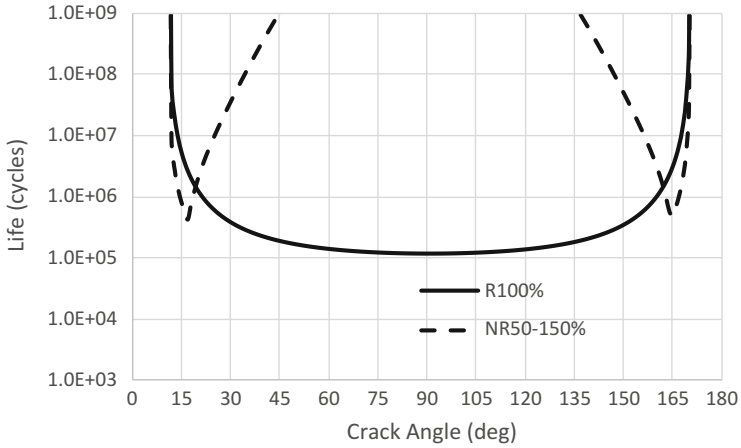

Fig. 9 CPA of NR for relaxing and nonrelaxing cases

5.2 *Incremental Analysis of Sequence Effects*

Sequence effects sometimes occur when the order of small and large events in a loading schedule is reversed. For example, Sun et al. showed [56], on fatigue experiments on simple tension strips, that a step-up sequence of loads is more damaging than a step-down sequence of loads. This was established by comparing the residual tensile energy to break after cycling for two cases: (1) the step-up case consisting of 300 cycles each of 250% and 300% peak strain, fully relaxing, and (2) the step-down sequence consisting of 300 cycles each of 300% and 250% peak strain, fully relaxing. Although Miner's rule predicts no difference for these cases, a small but measureable difference was in fact observed, as shown in Fig. 10. Using Endurica DT's incremental fatigue analysis, and considering the crack size at the end of each case, the residual breaking energy W_b in simple tension for each case was computed as $W_b = T_C/(2\ ka)$, where T_C is the critical tearing energy, a is the crack size following all fatigue cycles, and k is Greensmith's nondimensional factor. The Endurica DT computed results are shown in Fig. 11.

5.3 *Transmission Mount*

To further illustrate the capabilities of incremental fatigue analysis, when combined with nonlinear loads interpolation, consider the transmission mount shown in Fig. 12. The mount must endure a loading schedule comprising three-channel (x, y, and z displacements) signals, as shown in Fig. 13. The material property definition for the Endurica CL fatigue analysis of the mount is specified in Table 2. It consists of a specification of the stress-strain behavior (neo-Hookean in this case) and of the

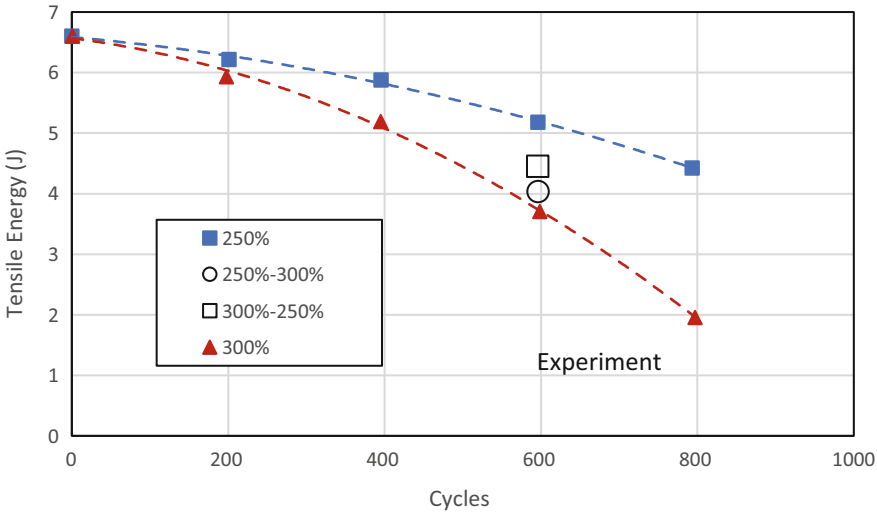

Fig. 10 Measured [56] residual tensile breaking energy following step-up (circle) and step-down (square) fatigue cycles

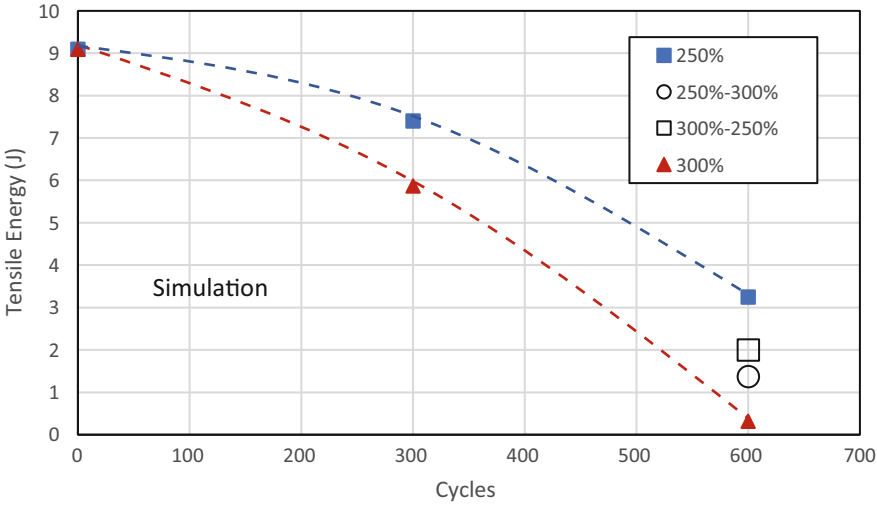

Fig. 11 Endurica DT computed residual tensile breaking energy following step-up (circle) and step-down (square) fatigue cycles

fatigue behavior (Thomas law). The signals are applied as the boundary condition to the mount, following the schedule given in Table 3. Rather than directly computing each signal via FEA, a three-channel nonlinear map was generated for use by EIE by running finite element models for each of the 17 case vectors shown in Fig. 6. The

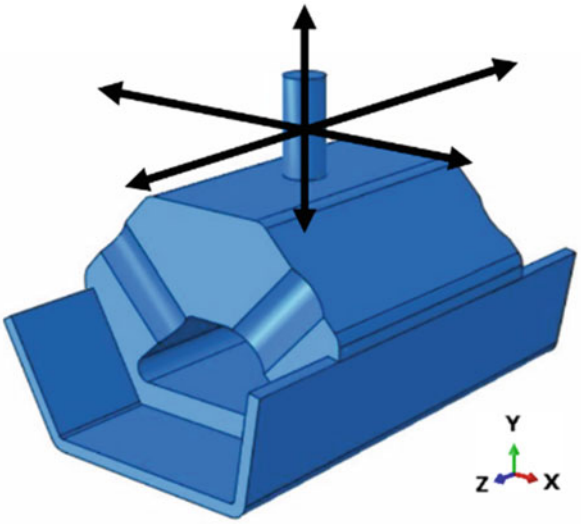

Fig. 12 Automotive transmission mount

results of these models were then interpolated via EIE. Each signal computes for the entire FE model in about 20 s.

In order to determine whether the mount qualifies with adequate durability under the duty cycle, the residual life was computed at each step of the schedule. The residual life is defined as the number of repeats of the city driving case required to fail the mount. After running the complete schedule from Table 3, about 30% of the original residual life remains, as shown in Fig. 14.

5.4 Tire Durability Testing

Commercial truck tires must qualify for durability following the FMVSS 119 testing regulation [57]. The regulation specifies a three-step test as given in Table 4. Changes to tire materials or geometry must be evaluated against this standard in order to certify tires for production.

The present example considers a 1200R20 TBR tire operating under 837 kPa inflation. The tire cross section geometry and 3D geometry are shown in Fig. 15. Material properties for this analysis have been published elsewhere [58].

For each step of the FMVSS testing schedule, a steady-state rolling analysis was performed [59]. The analysis included computation of the steady-state temperature field for each load step [60]. The strain and temperature fields for each step were then used to perform an incremental fatigue analysis with Endurica DT. Residual life was computed at time zero, and following each step of the procedure. The element with shortest life was shown to be the #3 belt edge of the tire. Contour plots showing residual fatigue life are given in Fig. 16. The residual fatigue life is reported in terms of repeats of the 101% loading case. The fatigue life of the shortest lived element –

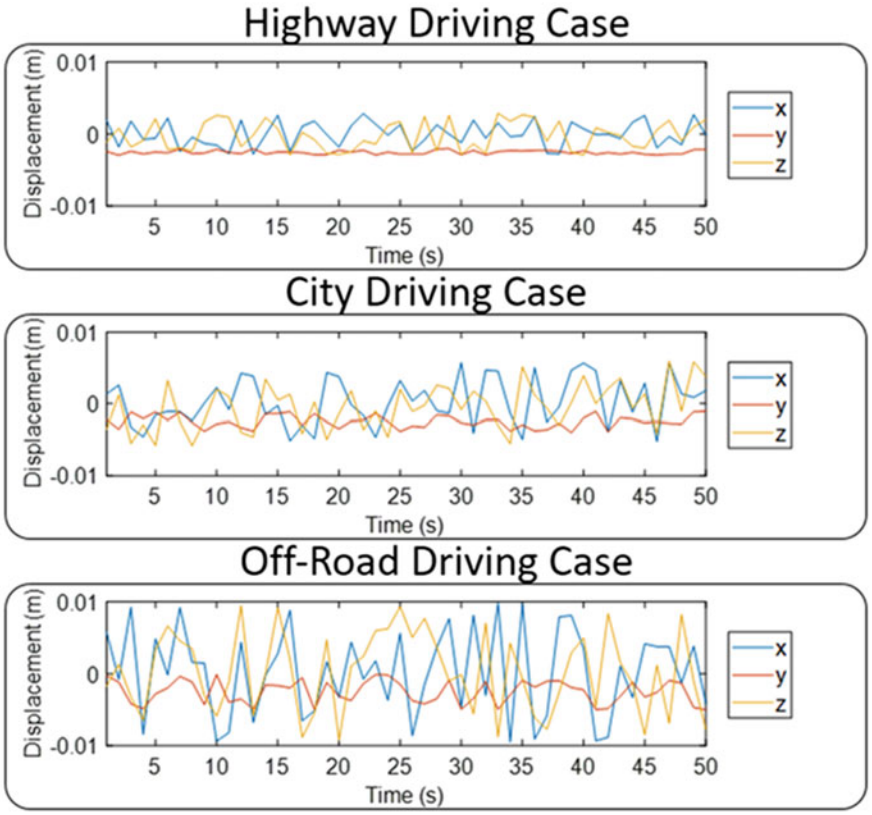

Fig. 13 Signals used for mount duty cycle

Table 2 Material property definition syntax for Endurica CL analysis of transmission mount fatigue analysis

```
ELASTICITY_TYPE=NEOHOOKEAN
SHEAR_MODULUS=5e6 ! Pa
BULK_MODULUS=3000e6 ! Pa
FATIGUE_TYPE=THOMAS
SIZE_PRE=100E-6  ! M
SIZE_EOL=1E-3  ! M
RC=5E-6   ! (M/CYCLE)
TCRITICAL=10000 ! J/m^2
F0=2
FEXP=3.7
```

Table 3 Durability schedule for transmission mount qualification

Time	Load case	Signal (see Fig. 13)	Repeats
t_A	A	City driving	100k
t_B	B	Off-road driving	50k
t_C	C	Highway driving	1000k
t_D	D	City driving	100k

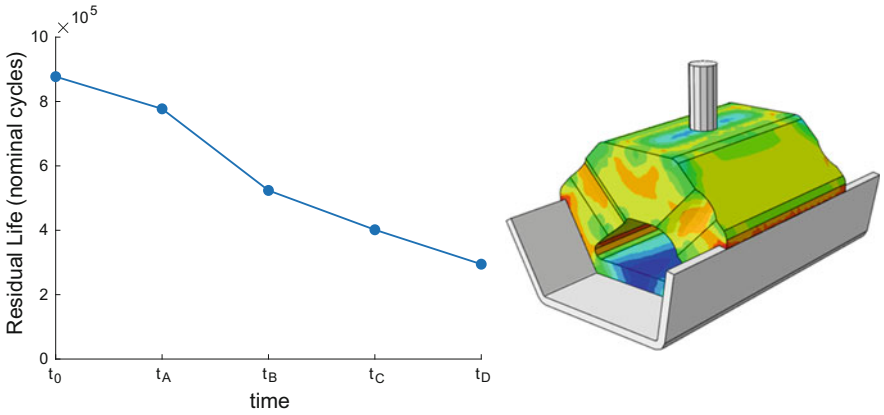

Fig. 14 Residual life as repeats of the city driving signal vs. duty cycle endpoints (left). Contours of fatigue life showing failure mode of mount following application of the scheduled load cases. (right)

Table 4 FMVSS 119 durability schedule

Step	Distance, km	Rated load (%)	Duration, h
1	630	66	7
2	1,440	84	16
3	2,160	101	24

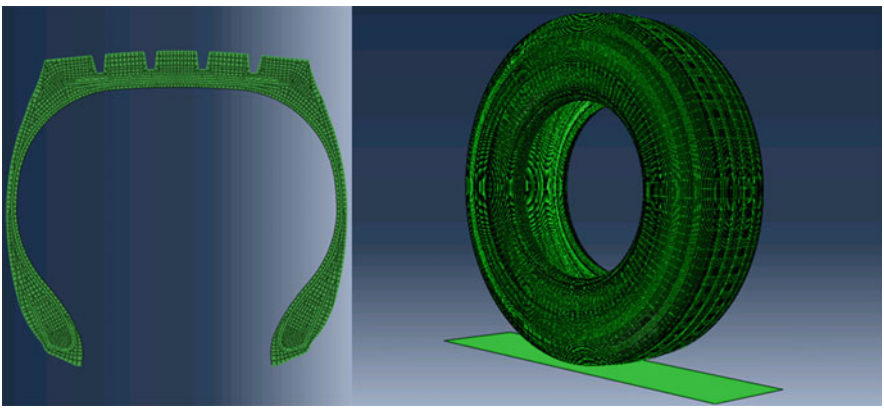

Fig. 15 Cross section and 3D geometry of 1200R20 TBR tire

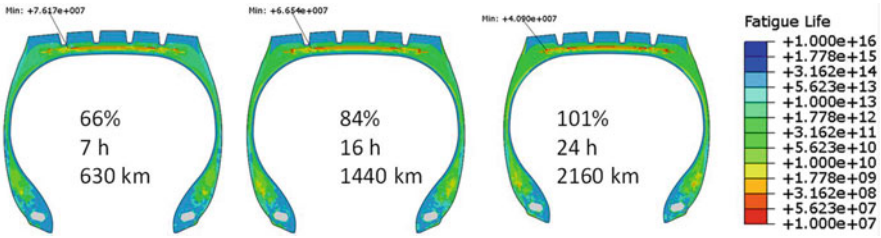

Fig. 16 Fatigue life contours of remaining life following each FMVSS 119 test step

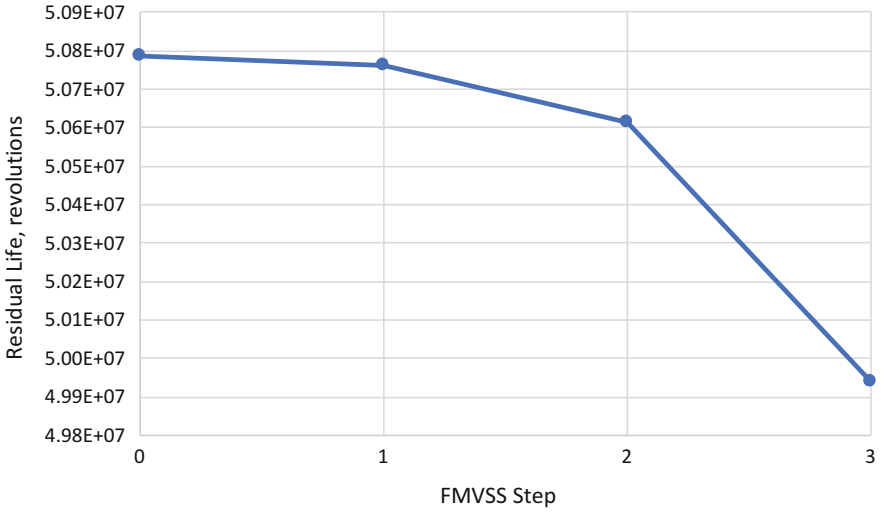

Fig. 17 Belt edge #3 remaining fatigue life following each FMVSS step

near the belt #3 ending in the tire cross section – is plotted in Fig. 17. Damage accrued during the FMVSS procedure is seen to be very light in this case – the residual life is seen to be reduced by only 1.7% relative to its original value. Here we have only considered the damaging effects of the required durability schedule. The incremental analysis is also suited to computing the damaging effects of multi-step high speed testing and abuse cases [61].

6 Future Developments

What do the next 20 years hold? We are going to see a transition in how fatigue analysis is used. OEM organizations that manage durability and risk across rubber component supply chains will transition away from receiving fatigue simulation results on an optional basis toward requiring fatigue simulations by default on every part at the inception of new programs. Expectations and achievement of cost

reduction, light weighting, and sustainability initiatives will increase as product optimization begins to fully account for actual product use cases.

CPA has already laid a foundation for these things to happen, having been commercialized successfully for more than a decade now. Older fatigue analysis methods that do not compete well against critical plane methods will become obsolete, except perhaps as hand calculations. There will be further development of material models for use in the critical plane framework. Ageing, cyclic softening, inelasticity, rate, and anisotropy effects still need further development, for example.

7 Conclusion

Engineering the durability of elastomer products requires proper, efficient, general-purpose analysis methods suited to the physics inherent in realistic applications and the workflows mandated by the engineering requirements. Fortunately, great strides have been made in the last decade along these lines and now include:

- Total and incremental fatigue solvers based upon CPA for simulation of the damaging effects of multiaxial strain histories and for calculation of residual life.
- Nonlinear load mapping for the efficient generation of full strain histories from multichannel input road load signals

In 20 years, durability will be just one more thing that engineers do well every day, whether or not they know that CPA was how they did it.

References

1. Gent AN, Mars WV (2013) Chapter 10 - Strength of elastomers. In: Mark E, Erman B, Roland M (eds) The science and technology of rubber, 4th edn. Academic Press, Boston, pp 473–516. https://doi.org/10.1016/B978-0-12-394584-6.00010-8
2. Rivlin RS, Thomas AG (1953) Rupture of rubber. I. Characteristic energy for tearing. J Polym Sci 10(3):291–318
3. Gent AN, Lindley PB, Thomas AG (1964) Cut growth and fatigue of rubbers. I. The relationship between cut growth and fatigue. J Appl Polym Sci 8(1):455–466
4. Li F, Liu J, Mars WV, Chan TW, Lu Y, Yang H, Zhang L (2015) Crack precursor size for natural rubber inferred from relaxing and non-relaxing fatigue experiments. Int J Fatigue 80:50–57
5. Huneau B, Masquelier I, Marco Y, Le Saux V, Noizet S, Schiel C, Charrier P (2016) Fatigue crack initiation in a carbon black–filled natural rubber. Rubber Chem Technol 89(1):126–141
6. Mars WV (2001) Multiaxial fatigue of rubber. PhD dissertation, University of Toledo, Toledo
7. Mars WV (2001) Multiaxial fatigue crack initiation in rubber. Tire Sci Technol 29(3):171–185
8. Mars WV (2002) Cracking energy density as a predictor of fatigue life under multiaxial conditions. Rubber Chem Technol 75(1):1–17
9. Mars WV (2003) Method and article of manufacture for estimating material failure due to crack formation and growth. US Patent No. 6,634,236

10. Saintier N (2001) Fatigue multiaxiale dans un élastomère de type NR chargé: mécanismes d'endommagement et critère local d'amorçage de fissure. PhD dissertation, Ecole des Mines de Paris
11. Saintier N, Cailletaud G, Piques R (2006) Crack initiation and propagation under multiaxial fatigue in a natural rubber. Int J Fatigue 28(1):61–72
12. Andriyana A, Saintier N, Verron E (2010) Configurational mechanics and critical plane approach: concept and application to fatigue failure analysis of rubberlike materials. Int J Fatigue 32(10):1627–1638
13. Wang Y, Yu W, Chen X, Yan L (2008) Fatigue life prediction of vulcanized natural rubber under proportional and non-proportional loading. Fatigue Fract Eng Mater Struct 31(1):38–48
14. Zine A, Benseddiq N, Nait Abdelaziz M (2011) Rubber fatigue life under multiaxial loading: numerical and experimental investigations. Int J Fatigue 33(10):1360–1368
15. Zarrin-Ghalami T, Fatemi A (2013) Multiaxial fatigue and life prediction of elastomeric components. Int J Fatigue 55:92–101
16. Harbour RJ, Fatemi A, Mars WV (2008) Fatigue life analysis and predictions for NR and SBR under variable amplitude and multiaxial loading conditions. Int J Fatigue 30(7):1231–1247
17. Nyaaba W, Frimpong S, Anani A (2019) Fatigue damage investigation of ultra-large tire components. Int J Fatigue 119:247–260
18. Belkhiria S, Hamdi A, Fathallah R (2020) Cracking energy density for rubber materials: computation and implementation in multiaxial fatigue design. Polym Eng Sci
19. Ruellan B, Le Cam J-B, Jeanneau I, Canévet F, Mortier F, Robin E (2019) Fatigue of natural rubber under different temperatures. Int J Fatigue 124:544–557
20. Tobajas R, Elduque D, Ibarz E, Javierre C, Gracia L (2020) A new multiparameter model for multiaxial fatigue life prediction of rubber materials. Polymers 12(5):1194
21. Oman S, Nagode M (2013) On the influence of the cord angle on air-spring fatigue life. Eng Fail Anal 27:61–73
22. Brown MW, Miller KJ (1973) A theory for fatigue failure under multiaxial stress-strain conditions. Proc Inst Mech Eng 187(1):745–755. https://doi.org/10.1243/PIME_PROC_1973_187_161_02
23. Fatemi A, Socie DF (1988) A critical plane approach to multiaxial fatigue damage including out-of-phase loading. Fatigue Fract Eng Mater Struct 11(3):149–165
24. Ramachandran A, Wietharn RP, Mathew SI, Mars WV, Bauman MA (2018) Experimental validation of crystallizing & non-crystallizing models of rubber fatigue behavior. In: Presented at the 2018 Great Lakes Simulia regional user meeting, October 10–12, 2018
25. Aït-Bachir M, Mars WV, Verron E (2012) Energy release rate of small cracks in hyperelastic materials. Int J Non-Linear Mech 47(4):22–29
26. Greensmith HW (1963) Rupture of rubber. X. The change in stored energy on making a small cut in a test piece held in simple extension. J Appl Polym Sci 7(3):993–1002
27. Lindley PB (1971) Plane-stress analysis of rubber at high strains using finite elements. J Strain Anal 6(1):45–52
28. Lake GJ (1970) Application of fracture mechanics to failure in rubber articles, with particular reference to groove cracking in tyres. In: International Conference Yield, Deformation and Fracture of Polymers. Plastics and Rubber Institute, Cambridge
29. Klüppel M, Huang G, Bandow B (2008) Evaluation of tearing energy of elastomer materials. Kautschuk Gummi Kunststoffe 61:656–659
30. Chang YW, Gent AN, Padovan J (1993) Strain energy release rates for internal cracks in rubber blocks. Int J Fract 60:363–371
31. Yeoh OH (2002) Relation between crack surface displacements and strain energy release rate in thin rubber sheets. Mech Mater 34:459–474
32. Mars WV, Cheng XZ, Yang H, Zhang LQ (2013) Influence of cyclic softening on the energy release rate of an edge crack under simple tension. In: Constitutive models for rubber VIII, p 371

33. Mars WV, Fatemi A (2005) Multiaxial fatigue of rubber: part II: experimental observations and life predictions. Fatigue Fract Eng Mater Struct 28(6):523–538
34. Mars WV (2007) Fatigue life prediction for elastomeric structures. Rubber Chem Technol 80 (3):481–503
35. Lake GJ, Lindley PB (1965) The mechanical fatigue limit for rubber. J Appl Polym Sci 9 (4):1233–1251
36. Lake GJ, Thomas AG (1967) The strength of highly elastic materials. Proc R Soc Lond Ser A Math Phys Sci 300(1460):108–119
37. Bhowmick AK (1988) Threshold fracture of elastomers. Polym Rev 28(3–4):339–370
38. Robertson CG, Stoček R, Kipscholl C, Mars WV (2019) Characterizing the intrinsic strength (fatigue threshold) of natural rub-ber/butadiene rubber blends. Tire Sci Technol TSTCA 47:292–307
39. Robertson CG, Stoček R, Kipscholl R, Mars WV (2019) Characterizing durability of rubber for tires. Tire Technol Int Ann Rev:78–82
40. Robertson CG, Goossens JR, Mars WV (2019) Using the laboratory cutting method for predicting long-term durability of elastomers. In: Paper presented at the 196th technical meeting of the rubber division, ACS, Cleveland, OH, Oct 10–12, 2019
41. Mars WV, Robertson CG, Stoček R, Kipscholl C (2019) Why cutting strength is an indicator of fatigue threshold. In: Huneau B, Le Cam J-B, Marco Y, Verron E (eds) Constitutive models for rubber XI. CRC Press, Taylor & Francis Group, London, pp 351–356
42. Lake GJ, Lindley PB (1965) Cut growth and fatigue of rubbers. II. Experiments on a noncrystallizing rubber. Rubber Chem Technol 38(2):301–313
43. Lindley PB (1973) Relation between hysteresis and the dynamic crack growth resistance of natural rubber. Int J Fract 9(4):449–462
44. Mars WV, Fatemi A (2003) A phenomenological model for the effect of R ratio on fatigue of strain crystallizing rubbers. Rubber Chem Technol 76(5):1241–1258
45. Mars WV (2009) Computed dependence of rubber's fatigue behavior on strain crystallization. Rubber Chem Technol 82(1):51–61
46. Ramachandran A, Wietharn RP, Mathew SI, Mars WV, Bauman MA (2017) Critical plane selection under nonrelaxing simple tension with strain crystallization. In: Fall 192nd technical meeting of the rubber division, pp. 10–12
47. Brüning K, Schneider K, Roth SV, Heinrich G (2012) Kinetics of strain-induced crystallization in natural rubber studied by WAXD: dynamic and impact tensile experiments. Macromolecules 45(19):7914–7919
48. Mars WV, Suter JD, Bauman M (2018) Computing remaining fatigue life under incrementally updated loading histories. No. 2018-01-0623. SAE technical paper
49. Mars WV (2019) System for tracking incremental damage accumulation. US patent application 16/149,738, filed April 4, 2019
50. Mars WV, Castanier M, Ostberg D, Bradford W (2017) Digital twin for tank track elastomers: predicting self-heating and durability. In: Proceedings of the 2017 ground vehicle systems engineering and technology symposium (GVSETS)
51. Mars WV, Isasi M, Arriaga A, Plaza J (2015) Relationship between displacement and force controlled fatigue tests. In: Constitutive models for rubber IX. CRC Press, pp 433–438
52. Mars WV (2020) Digital twin prototype and concept for EV mount integrity monitoring (recorded live demo), tinyurl.com/riegelec. Accessed 6 Aug 2020
53. Barbash KP, Mars WV (2016) Critical plane analysis of rubber bushing durability under road loads. No. 2016-01-0393. SAE technical paper
54. Mars WV (2017) Interpolation engine for analysis of time-varying load data signals. US patent 9,645,041, issued May 9, 2017
55. Mars WV, Suter JD (2019) Breaking the computational barrier to simulating full road load signals in fatigue. In: Fall 2019 ACS rubber division meeting
56. Sun C, Gent A, Marteny P (2000) Effect of fatigue step loading sequence on residual strength. Tire Sci Technol 28(3):196–208

57. NHTSA, Department of Transportation (2011) FMVSS 119 § 571.119 Standard No. 119; New pneumatic tires for motor vehicles with a GVWR of more than 4,536 kilograms (10,000 pounds) and motorcycles. https://www.govinfo.gov/content/pkg/CFR-2011-title49-vol6/pdf/CFR-2011-title49-vol6-sec571-119.pdf. Accessed 8 Feb 2019
58. Mars WV, Wei Y, Hao W, Bauman MA (2019) Computing tire component durability via critical plane analysis. Tire Sci Technol 47(1):31–54
59. Qi J, Herron JR, Sansalone KH, Mars WV, Du ZZ, Snyman M, Surendranath H (2007) Validation of a steady-state transport analysis for rolling treaded tires. Tire Sci Technol 35 (3):183–208
60. Nyaaba W, Bolarinwa EO, Frimpong S (2019) Durability prediction of an ultra-large mining truck tire using an enhanced finite element method. Proc Inst Mech Eng Part D J Automob Eng 233(1):161–169
61. Mars WV, Paudel G, Suter JD, Robertson CG (2019) Incremental, critical plane analysis of standing wave development, self-heating, and fatigue during regulatory high-speed tire testing protocols. Tire Sci Technol

Adv Polym Sci (2021) 286: 109–130
https://doi.org/10.1007/12_2020_70

Published online: 4 December 2020

Cavitation Micro-mechanisms in Silica-Filled Styrene-Butadiene Rubber Upon Fatigue and Cyclic Tensile Testing

C. E. Federico, H. R. Padmanathan, O. Kotecky, R. Rommel, G. Rauchs, Y. Fleming, F. Addiego, and S. Westermann

Contents

C. E. Federico, G. Rauchs, F. Addiego, and S. Westermann (✉)
Luxembourg Institute of Science and Technology, Materials Research and Technology, Hautcharage, Luxembourg
e-mail: stephan.westermann@list.lu

H. R. Padmanathan
Luxembourg Institute of Science and Technology, Materials Research and Technology, Belvaux, Luxembourg

University of Luxembourg, Esch-sur-Alzette, Luxembourg

O. Kotecky and R. Rommel
Goodyear Innovation Center Luxembourg, Colmar-Berg, Luxembourg

Y. Fleming
Luxembourg Institute of Science and Technology, Materials Research and Technology, Belvaux, Luxembourg

Abstract A multiscale approach was proposed to investigate cavitation micro-mechanisms developing in silica-filled styrene-butadiene rubber exposed to fatigue and cyclic tensile testing. At the macro-/mesoscopic scale, a decrease in load amplitude observed in fatigue was corroborated with cavitation micro-mechanisms initiated by silica agglomerate-rubber debonding and silica agglomerate breakdown. In the case of cyclic tensile testing, a gradual decrease of Poisson's ratio was correlated at the microscopic scale by similar cavitation micro-mechanisms than in fatigue. Both fatigue and cyclic tensile behaviors were considerably affected by an applied thermal treatment of the compound enhancing cavitation (especially agglomerate breakdown).

Keyword Cavitation · Fatigue · Filled rubber · Filler agglomerate · Tension · Thermal treatment

1 Introduction

The identification and understanding of crack mechanisms are of fundamental interest to maximize rubber material fatigue life by tuning and/or optimizing material composition, processing, and design. In general, fatigue-induced cracking can be regarded as a result of two successive mechanisms that are crack initiation and crack propagation [1, 2]. In rubber materials, approaches to predict crack propagation have been developed and intensively used, while such approaches for crack initiation have received less attention [1]. This is due to the complexity of the rubbers' mechanical behavior (viscoelasticity [3], strain hardening [4], Mullins [5, 6], and Payne effects [7, 8]) and their composition with multiple chemical components and several additives dispersed within the rubber matrix (e.g., presence of filler agglomerates and even filler networks). It is generally admitted that a crack is initiated by cavitation defined as the process of void nucleation under a given stress state [2]. Voids initially have a spherical shape of nanometer size [9]. With an increasing number of fatigue cycles, voids grow to reach a micrometer size and their shape becomes oblate. At this stage, they are oriented perpendicular to the main strain axis and are considered as cracks. Crack initiation has been investigated in natural rubber (NR) highly filled with carbon black (CB) and containing a small fraction of zinc oxide (ZnO) as curing activator [10]. In particular, void/filler/surface crack nature, localization, spatial distribution, and evolution as a function of fatigue life were investigated by scanning electron microscopy (SEM). The main results indicate that due to the sample shape multiple cracks formed at the surface of the tested specimen from agglomerate-matrix debonding and from the parting line. Cracks generated from agglomerate-matrix debonding were noted for both CB and ZnO. With respect to CB agglomerates, the authors observed three successive steps of cavitation. These are debonding at a pole, propagation of the debonding to the equator, as well as crack

formation. Cavitation in ZnO-filled rubber occurred either by debonding or by internal fracture of the agglomerates, without or with very limited crack formation. Importantly, the authors also demonstrated that the number of fatigue cycles until the end of life increased with decreasing average CB agglomerate size.

In tire applications, silica nanoparticles provide both a high reinforcement effect of the rubber matrix and a decrease of rolling resistance compared to CB nanoparticles [11]. To our best knowledge, the micro-mechanisms of crack initiation upon fatigue in SBR/silica nanocomposite have never been quantitatively investigated by a comprehensive study, as done for neat rubber materials [12]. In a pioneering work [13], it was qualitatively shown that silica-filled styrene-butadiene rubber (SBR) exhibited similar cavitation mechanisms as CB-filled NR, i.e., silica agglomerate-SBR matrix debonding, and internal silica agglomerate breakdown is followed by internal fibrillation due to the presence of rubber within the silica agglomerate.

The objective of this work is to analyze in detail the cavitation micro-mechanisms at the origin of cracks in SBR filled with silica nanoparticles upon uniaxial cyclic fatigue loading. Fatigue loading will be performed prior to and after thermal treatment. To this end, the behavior of material exposed to the first fatigue cycles will be analyzed at macro-/mesoscopic scales to determine relevant mechanical parameters reflecting cavitation. The origin and characteristics of cavities developing during the crack initiation stage will be studied by structural characterization tools, in particular SEM and micro-computed x-ray tomography (μCT).

2 Experimental Section

2.1 Materials

The compound used in the study is a silica-filled solution styrene-butadiene rubber. It was prepared with an internal mixer based on the formulation given in Table 1.

To form hourglass-shaped specimen for fatigue testing (see Fig. 2), the compounds were transfer molded at 170°C and cured for 10 min. The resulting specimens were specifically designed to fit into clamps of a customized miniature tensile/compression machine from Kammrath and Weiss (Dortmund, Germany) and the scanning electron microscope described later in the text.

To form tensile specimens, the compound was transferred in a roll-mix to form uniform sheets (2 mm of thickness) and finally cured in a hot-press using the same curing conditions as hourglass specimens. The dumbbell-shaped (ISO 37-2 sample type 2) specimens were subsequently carefully prepared by punching the sheets with a press. The fact that the same curing conditions were used for specimens having different thicknesses may imply that the crosslink density may be higher in the thinnest specimen type (dumbbell specimen) compared to the thickest specimen type (hourglass specimen).

Table 1 Compound formulation

Ingredients	Amount (phr)
SBR SE SLR 4602	100
Antioxidant	2.5
Oil vivetic 500	25
Stearic acid	3
Silica Zeosil 1165 MP	90
Silane 266	7.2
ZnO	2.5
Sulfur	1.4
CBS[a]	2.3
DPG[b]	3.2

[a]CBS = N-cyclohexyl-2-benzothiazole sulfonamide
[b]DPG = diphenylguanidine

The investigated compounds were referenced as C1 (untreated) and C1-T (thermally treated) for both specimen types. The treatment consisted in an accelerated thermal treatment procedure keeping the samples in an oven at 120°C for 2 days. A change in color (from black to brown) was observed in the case of the two specimen types. This allows the qualitative and quantitative evaluation of the effect of thermal treatment on both specimen types. Furthermore, as the crosslink density of the dumbbell-shaped specimen may be higher, the obtained results would give a more complete view of possible crack mechanisms that can take place.

2.2 Mechanical Testing

Uniaxial tensile testing was carried on an electromechanical universal testing machine Instron 5967 (Norwood, MA), equipped with a load cell of 1 kN. Tests were carried out at 21°C and relative humidity of 30% RH.

The true stress and stretch ratios were taken as an average of the measured values from the initial gauge and width lengths (20 × 3 mm) of the sample. Specimens were tested under cyclic loading conditions. The speed was constant and set to 500 mm/min (corresponding to 0.4 s^{-1} based on an initial gauge length of 20 mm). The loading history included 20 successive loading stages up to displacements of 20, 50, and 70 mm for C1 and 15, 20, and 30 mm for C1-T. The unloading stages were set for reaching a load of 0.2 N (to avoid buckling).

In order to determine the strain level, Digital Image Correlation (DIC) [14] was employed using the GOM Aramis software (GOM, Braunschweig, Germany) for cyclic tensile testing. The displacement field data obtained from DIC measurements were transformed into the stretch ratio, λ; the engineering strain, ε; or the Hencky or true strain, ε^H, as follows:

$$\begin{cases} \lambda_i = \dfrac{l_i(t)}{l_0} \\ \varepsilon_i = 1 + \lambda_i \\ \varepsilon_i^H = \ln \lambda_i \quad i \in \{1, 2, 3\} \end{cases} \tag{1}$$

where $l_i(t)$ is the instantaneous length. We defined λ_1 and ε_1^H as the stretch ratio and true axial strain in the loading direction, λ_2 and ε_2^H as the transversal stretch ratio, and true strain, λ_3 and ε_3^H as the thickness stretch ratio and true strain. Due to the difficulty of measuring the strain in the thickness, a transverse isotropy hypothesis, i.e., $\lambda_2 = \lambda_3$, and $\varepsilon_2^H = \varepsilon_3^H$, is accounted [15–17]. This hypothesis may however lead to an overestimation of the true stress and underestimation of the volume strain [18]. For characterizing the mechanical response of the material, we computed the true stress as:

$$\sigma_T = \frac{F}{A(t)} = \frac{F}{A_0 \lambda_2 \lambda_3} = \frac{F}{A_0 {\lambda_2}^2} \tag{2}$$

where $A(t)$ is the instantaneous cross-section. Additionally, having access to the principal strains allows determining Poisson's ratio (ν) that is defined as:

$$\nu = -\frac{\varepsilon_2^H}{\varepsilon_1^H} = -\frac{\ln \lambda_2}{\ln \lambda_1} \tag{3}$$

Fatigue testing was performed with a hydraulic testing machine Instron 8872 (Norwood, MA) equipped with a load cell of 5 kN. As the tests were fully relaxation displacement controlled, the sample was exposed to tension-compressive deformation by applying a sinusoidal waveform. The measurements were performed at room temperature of 21°C and at a frequency of 2 Hz. Note that this relatively low frequency was chosen to limit self-heating of the material. The load amplitude as a function of the number of cycles was plotted, and based on the first derivate, the number of cycles to the end of life, N_i, was determined [10].

As the local maximum engineering surface strain,$\varepsilon_{\text{local}}$, along the loading direction of the hourglass sample in the median section differs from the global strain due to the sample geometry, the maximum engineering strain applied locally is chosen to figure on the strain life plot. The latter's mean value was estimated using 3D-DIC. For this, samples were subjected to monotonic loading coupled with DIC to measure the local engineering strain amplitude and the local stretch ratio amplitude (stretch speed, 500 mm/min; DIC sampling rate, 23 fps maximum). Prior to this, all samples were subjected to ten sinusoidal cycles with an amplitude of 10 mm to reduce Mullin's effect [5]. Then, the local maximum stretch ratio, λ_{local}, is calculated from the local strain according to Eq. (1). As described in [19] , the constant stretch ratio amplitude, $\Delta\lambda = \lambda_{\max} - \lambda_{\min,}$ is applied during cyclic testing, where $\lambda_{\max}$ and $\lambda_{\min}$ are the maximum and minimum locally applied stretch ratios, respectively.

Wöhler curves were generated by testing hourglass samples to failure at four local nominal strain amplitudes, namely, 50, 65, 75, and 100%, and plotting the number of cycles required for the sample to their end of life, N_i, against the local strain amplitude. A power law function ($y = a \times b$) was used to fit the data.

To identify the root cause for the crack initiation, interrupted fatigue tests were performed. From the generated Wöhler curve, the number of cycles and the strain needed for the interrupted testing were obtained. The fatigue tests were interrupted after a number of cycles corresponding to 40 and 80% of N_i, and the specimens were subsequently investigated using SEM and micro-computed tomography in order to detect and characterize the flaws generated at the surface and in the bulk, respectively.

2.3 Structural Characterization

2.3.1 Micro-computed X-Ray Tomography

The internal structure of the materials before and after mechanical testing was analyzed by micro-computed x-ray tomography (μCT). To this end, an RX Solutions (Chavanod, France) equipment model EasyTom 160 was used. Images were recorded at a voltage of 70 kV by means of a micro-focused tube equipped with a tungsten filament. The source-to-detector distance (SDD) and the source-to-object distance (SOD) were adjusted in such a way to obtain a voxel size of around 2 μm in the case of the initial material, 6.5 μm in the case of the pre-deformed material under tension, and 6 μm in the case of the hourglass sample fatigued up to a given percentage of N_i. The lower resolution of the deformed material is due to the utilization of miniature tensile machine Deben CT5000 utilized to reopen the voids in the pre-deformed materials. In particular, samples are re-stretched and left to recover for 30 min before μCT imaging. The volume reconstruction was performed with the software Xact64 (RX Solutions) after applying inherent treatments of the technique such as geometrical corrections and ring artifact attenuation.

The commercial software Avizo (Thermo Fisher Scientific, Waltham, MA) was used for image treatment and analysis of μCT results. First, a sub-volume was extracted from the scanned samples. Next, images were de-noised by using a median filter option [20], and heterogeneities in the material were segmented by thresholding the grayscale intensity histogram. After segmentation, objects whose dimensions were 2.5 times smaller than the voxel size were discarded for eliminating the uncertainty caused by the small objects beyond the resolution of our equipment [21, 22]. Finally, images were statistically characterized through different morphological parameters. These parameters are the equivalent diameter, D_{eq}, corresponding to the diameter of a sphere of the same volume of the studied object; the sphericity, S ($S = 1$ for a sphere); the relative volume between the studied phase and the total studied volume, $V_{fraction}$; and the number of heterogeneities per unit volume, ρ_h. The definitions of these expressions are:

$$D_{\text{eq}} = \sqrt[3]{\frac{6V}{\pi}} \tag{4}$$

$$S = \frac{\pi^{1/3}(6V)^{2/3}}{A_S} \tag{5}$$

$$V_{\text{fraction}} = \frac{\sum_{i=1}^{n} V_i}{V_{\text{total}}} \tag{6}$$

$$\rho_h = \frac{N_o}{V_{\text{total}}} \tag{7}$$

where N_o is the number of detected objects, V and A_S are the volume and area of the object, and V_{total} is the total analyzed volume.

2.3.2 Scanning Electron Microscopy

The SEM observations of interrupted fatigue samples were carried using FEI Quanta FEG 200 instrument (Thermo Fisher Scientific, Eindhoven, Netherlands) in low vacuum mode. This method involving a low water pressure enables the visualization of nonconductive materials without the use of a coating. Cavities in hourglass samples were re-opened by gripping the samples on a miniature tensile machine and applying a displacement of 2 mm. SEM images were recorded at 20 kV using backscattered electron detector to optimize void visualization. Images were analyzed by means of the software ImageJ (National Institutes of Health, Bethesda, MD) to measure the length of the voids. Besides, the elemental composition of the agglomerates was analyzed by energy-dispersive x-ray spectroscopy (EDS) using a Genesis XM 4i system (EDAX, Mahwah, NJ).

3 Results and Discussion

3.1 Material Initial Structure and Properties

The size analysis of the agglomerates detected in C1 by μCT is shown in Fig. 1. In particular, the sphericity is plotted as a function of the equivalent diameter in Fig. 1a, and the distribution of the equivalent diameter is represented in Fig. 1b. Note that the volume fraction of the agglomerates corresponds to (0.37 ± 0.03) % . Their median equivalent diameter was determined to be (12.84 ± 0.44) μm. The figures reveal that the agglomerates present a non-Gaussian distribution of their size, ranging from 6 μm to 140 μm with sphericities from 0.35 to 1. These results may provide information about the agglomerates, which are potential sites of cavitation onset, i.e., with a size above 40 μm and a nonspherical shape ($S < 0.9$) [23–25]. Indeed, measurements reveal that 16.65 % of the fillers are considered as large

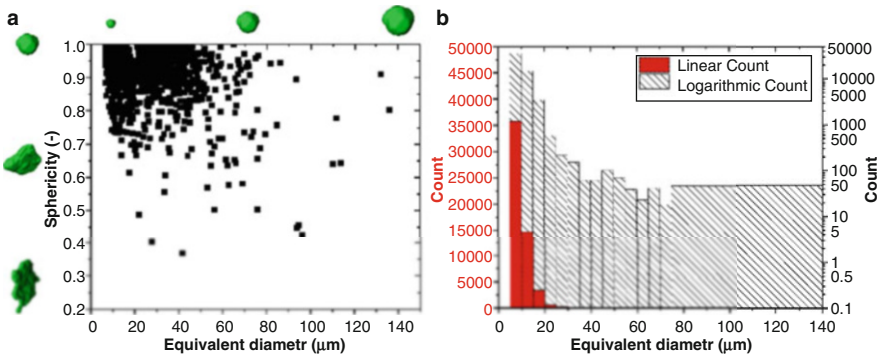

Fig. 1 Sphericity (**a**) and agglomerate distribution (**b**) as a function of the equivalent diameter

agglomerates (equivalent diameter above 40 μm), and 14.56% are nonspherical heterogeneities (sphericity below 0.9). The same procedure was carried out of the thermally treated compounds, finding that all morphological parameters of fillers remained unchanged.

The crosslink density results of C1 and C1-T have been determined to be $(2.35 \pm 0.13) \times 10^{-4}$ mol/cm3 and $(2.58 \pm 0.11) \times 10^{-4}$ mol/cm^3, respectively. Thus, the crosslink density of C1-T was higher than the one of C1, suggesting that the thermal treatment increases the matrix stiffness. Note that those measurements have only been done in the case of hourglass geometry type.

3.2 Fatigue-Induced Cavitation Micro-mechanisms

3.2.1 Macroscopic Mechanical Behavior

The Wöhler curves for materials C1 and C1-T, presented in Fig. 2, show that the number of cycles to the end of life of the compounds decreases as the local strain amplitude increases. Additionally, the non-treated samples provide a higher number of cycles to the end of life than the thermally treated ones. Obviously, one reason for this difference is the limited chain flexibility of the rubber matrix in C1-T due to the increase in stiffness by thermal treatment (as suggested by Hainsworth et al. [23, 26]). Also, thermal exposure may induce a hard skin at the rubber surface, facilitating cracks at the surface during fatigue cycling [27].

3.2.2 Cavitation Micro-mechanisms

μCT observations with a moderate resolution have been performed in the case of C1 hourglass samples prior to and after fatigue testing, observing the same specimen (Fig. 3). It can be observed that cavitation is present at the surface and in the bulk of

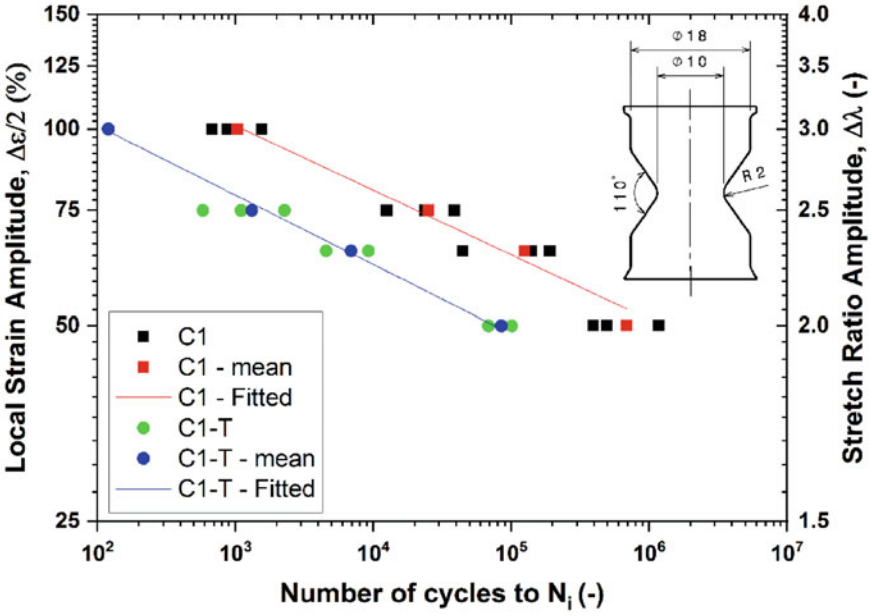

Fig. 2 Strain plotted against fatigue life for C1 and C1-T in case of hourglass specimen. Measurements were performed for four levels of local strain amplitude corresponding to stretch ratio amplitudes of 2, 2.3, 2.5, and 3. The inset shows the hourglass specimen geometry used for fatigue testing. Dimensions are in millimeters

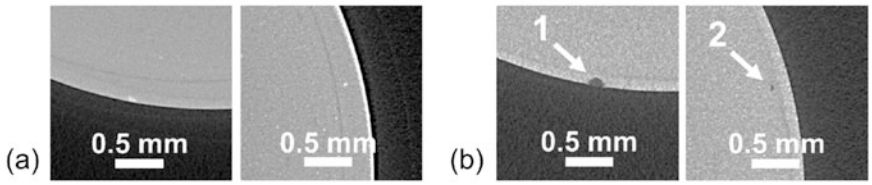

Fig. 3 Origin of cavitation in hourglass sample of C1 induced by fatigue observed by μCT (2D slices perpendicular to the deformation direction). (**a**) Undeformed case and (**b**) deformed case at 30% of N_i with a strain amplitude of 75 N. (1), Surface cavity and (2) bulk cavity, both types of cavity being linked to the presence of agglomerates

the specimen. Furthermore, the observed cavities are related to the presence of agglomerates, and surface cavity is not linked to the parting line as previously noted [10]. SEM investigation provided a more detailed observation of the cavities.

The SEM backscattered images of the cavities formed at the surface of the hourglass sample in the vicinity of silica agglomerate in C1 and C1-T are represented in Figs. 4 and 5. Two types of cavitation initiation micro-mechanisms were identified. In Fig. 4, debonding occurred between the silica agglomerate and the SBR

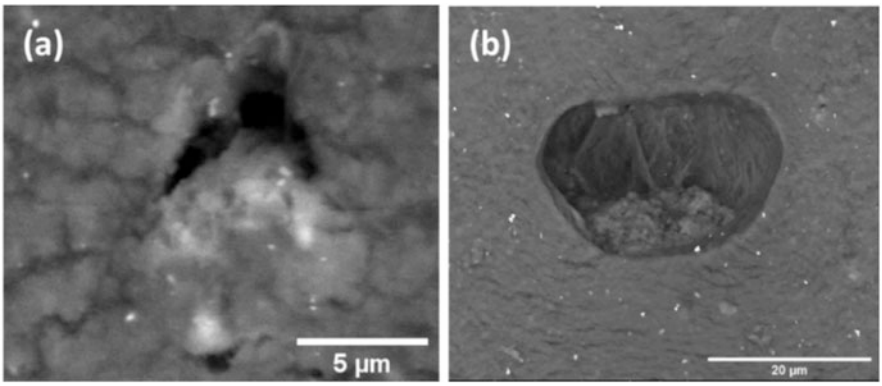

Fig. 4 Surface cavity in the vicinity of a silica agglomerate responsible for crack initiation: (**a**) debonding in C1 and (**b**) debonding at one pole in C1-T

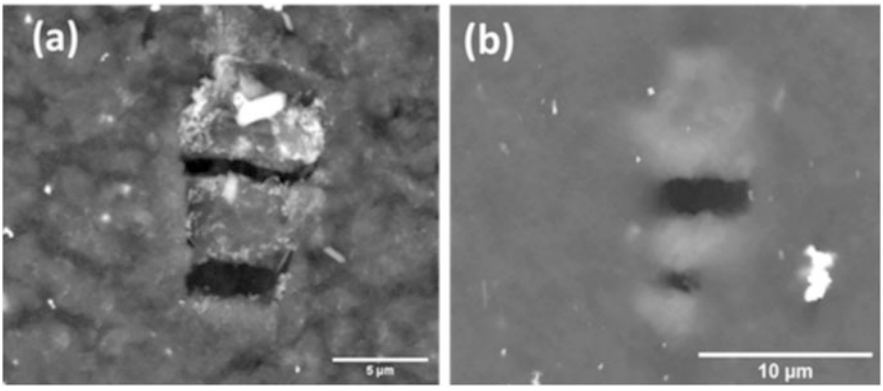

Fig. 5 Surface cavities formed due to the breakdown of a silica agglomerate observed with backscattered electron detection mode in the case of (**a**) C1 and (**b**) C1-T

matrix, and in Fig. 5, the initiation of cavity is due to the breakdown of silica agglomerate.

Figure 5 shows that the breaking of silica agglomerates also induces cavities and, hence, may have an impact on crack initiation. Silica agglomerates form by hydrogen bonding which is stronger than the van der Waals-London force of attraction. In general, melt-processing elongational forces do not enable to fully disperse silica into single nanoparticles, explaining the presence of agglomerates. The breakdown of silica agglomerates under the action of strain has been reported, e.g., by Suzuki et al. [28]. For confirming if the elemental nature of agglomerates was either silica or zinc oxide, EDX analysis has been performed. The EDX mappings confirmed the presence of carbon, silicon, and zinc of SEM image (Fig. 5b). Moreover, the

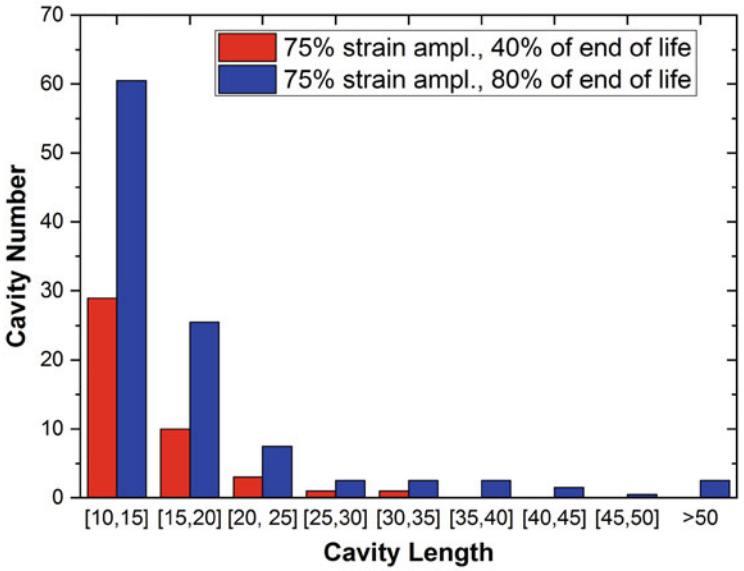

Fig. 6 Cavity length as a function of silica agglomerate size triggering the cavity (75% of applied local strain amplitude, 40% and 80% N_i)

elemental mapping confirms the agglomerates around the surface cavities are comprised of silica agglomerates, and the brighter particles seen on the SEM image are comprised of zinc oxide particles.

The impact of the increase in the number of fatigue cycles on fatigue crack initiation and propagation was studied on a single sample cycled with a strain amplitude of 75% (see Fig. 6). Here, the cavity length, which is represented as a function of the cavity number, is shown for 40% and 80% of the end of life. As can be seen from the figure, the number of initiated cracks increased with the increasing number of fatigue cycles. In addition, the length of the initiated cracks also increased.

Overall, for C1 and C1-T compounds, two major micro-mechanisms for crack initiation were identified with respect to silica agglomerates on the sample surface, i.e., debonding and filler agglomerate breakdown (broken filler). These results were obtained in the cases of C1 and C1-T after fatigue testing to 40% *N*i at a local strain amplitude of 100%. On the center slice (0.3×6.4 mm^2), a total of 80 and 46 cavities were determined and analyzed for C1 and C1-T, respectively. At the surface of C1, 73% of the cavities are initiated by debonding and 27% by filler agglomerate breakdown (broken filler). In the surface of C1-T, the number of cavities initiated due to a broken filler was found to be almost 76%. The remaining cavities (about 24%) were initiated by debonding.

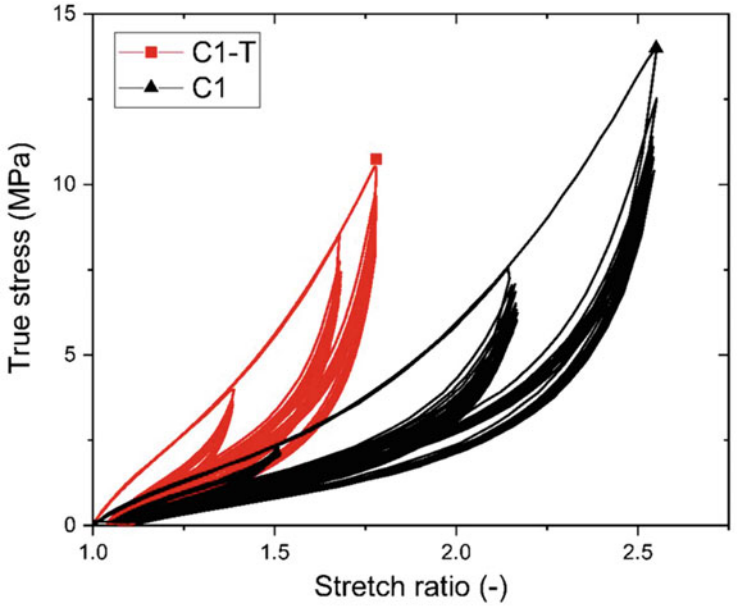

Fig. 7 True stress-stretching ratio obtained by non-monotonic tensile testing for C1 thermally treated and C1

3.3 Cyclic Tension-Induced Cavitation Micro-mechanisms

3.3.1 Macroscopic Mechanical Behavior

True stress-stretching ratio loading-unloading curves at various maximum stretch ratios for both materials are presented in Fig. 7. Both materials exhibit a hyper-elastoplastic response with strain hardening, residual strain, and an important hysteresis on the first cycle, followed by a hyperelastic behavior with low hysteresis in the next cycles. The important hysteresis loop observed in the first cycle of the material can be related to the Mullins effect [6, 29, 30] and/or to potential cavitation in the material induced by the imposed elongation. Thermal treatment increases the stiffness of the compound at all levels of stretching. Moreover, it can be seen that C1-T exhibits a stress two times higher than the pristine compound, but deformability is reduced. These observations confirm that the thermal treatment increases the stiffness of the compound due to the higher crosslink density (as displayed in the swelling testing), which also induces a loss in stretch ability.

To verify any potential structural change with deformation, we account for two macroscopic indicators: the hysteresis (ϕ^{cycle}) and Poisson's ratio. The hysteresis during a complete cycle corresponds to the mechanical energy dissipated due the viscous component in the matrix and/or due to the rearrangement or breakdown of

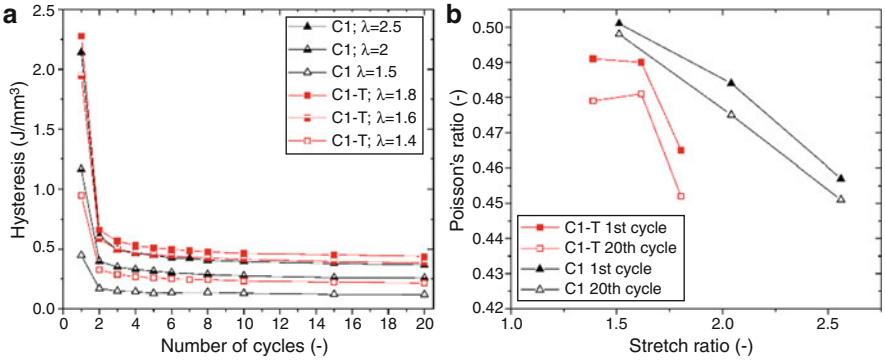

Fig. 8 Evolution of the hysteresis as a function of the number of cycles at different stretch ratios (**a**); Poisson's ratio versus stretch ratio for C1 and C1-T at the 1st and 20th cycles (**b**)

the fillers [8, 31–34]. To determine the hysteresis, we integrated the true stress-true strain data at each cycle for the different stretch ratios:

$$\phi^{\text{cycle}} = \phi^{\text{load}} - \phi^{\text{unload}} = \int_{\varepsilon_1^H}^{\varepsilon_{1,\max}^H} \sigma d\varepsilon_1^H \tag{8}$$

The evolution of the hysteresis with the number of cycles is shown in Fig. 8a, including results for the different tested stretch ratios, i.e., $\lambda = 2.5$, $\lambda = 2$, and $\lambda = 1.5$ for compound 1 and $\lambda = 1.8$, $\lambda = 1.6$, and $\lambda = 1.4$ for thermally treated compound 1. For both compounds, hysteresis drops drastically between the first and second cycle, followed by a gradual convergence to an asymptote. Additionally, there is an increase in the hysteresis with the imposed stretch ratio. With thermal treatment, compound dissipates more energy at lower stretch ratios. For instance, C1-T exhibits a larger hysteresis at $\lambda = 1.8$ than C1 at $\lambda = 2.5$ (which matches with C1-T at $\lambda = 1.6$). The same occurs for C1-T at $\lambda = 1.6$ and C1 at $\lambda = 1.4$, where hysteresis for thermally treated compound is nearly two times higher for a similar level of deformation.

Furthermore, the dependency of Poisson's ratio with strain at the 1st and 20th cycles (Fig. 8b) reveals analogue observations as for the hysteresis, i.e., a gradual decrease of Poisson's ratio from 0.5 (incompressible behavior [35]) to lower values (related to volume changes) with increasing number of cycles. A similar trend is observed with the stretch ratio, where Poisson's ratio passes from incompressible to compressible with increasing stretching. Moreover, thermal treatment impacts the material's behavior since compound C1 exhibits a gradual decrease of Poisson's ratio with stretching, whereas C1-T has an abrupt drop of ν at lower deformations.

The results obtained by cyclic tensile testing are suggesting that the increase in the stiffness induced by the thermal treatment is increasing the energy dissipation and volume changes. Having a larger crosslink density reduces the polymer chains' mobility upon deformation, which induces higher viscous dissipation. Additionally,

having a lower chain mobility also favors potential cavitation mechanisms such as chain scission [36, 37] and matrix/filler debonding [10, 38, 39]. Additionally, the hysteresis and Poisson's ratio evolve with the number of cycles in a similar trend, i.e., as an asymptotic decrease. Thus, we may assume that the C1-T is undergoing more viscous dissipation and cavitation.

3.3.2 Cavitation Micro-mechanisms

In situ μCT scans were performed on the postmortem dumbbell specimens at different pre-stretching to assess morphological changes induced by the cyclic tensile testing. This was carried out for C1 deformed at $\lambda = 2.5$ and C1-T deformed at $\lambda = 1.8$. In situ pre-stretching in a miniature tensile/compressive stage (Deben, Suffolk, UK) ranged from $\lambda = 1.2$ up to $\lambda = 1.4$. The purpose of this is to reopen all the potential cavities induced in the mechanical testing. Various pre-stretching were used to have a tracking of the cavitation history. With this protocol, we detected several cavities within the bulk of the material. These cavities were homogeneously distributed within the volume, and coalescence between them was observed. Therefore, the presence of cavities provides evidence of the physical source of hysteresis as well as the decrease in Poisson's ratio, i.e., part of the mechanical energy is dissipated due to the creation of new internal surfaces.

When increasing the in situ stretching in the μCT, there is an augmentation of the detected number of cavities and their total volume fraction, as depicted in Fig. 9a, b. When comparing both compounds, C1 exhibits a larger number of cavities but of smaller volume than the thermally treated compound. This could mean that C1-T experiences less cavitation sites, but with a faster growth.

The morphology evolution distribution, in terms of size and shape of voids, is presented in Fig. 10a, b for two stretch ratios. Both compounds exhibit most of their

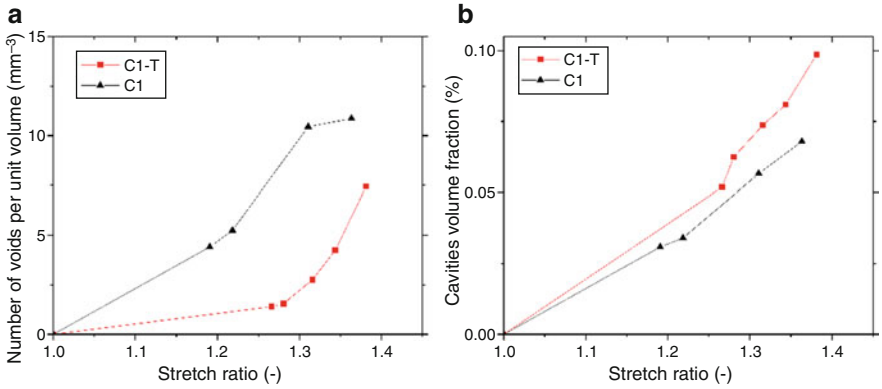

Fig. 9 Evolution of (**a**) number of voids per mm^3 and (**b**) volume fraction of voids as a function of the in situ stretch ratio

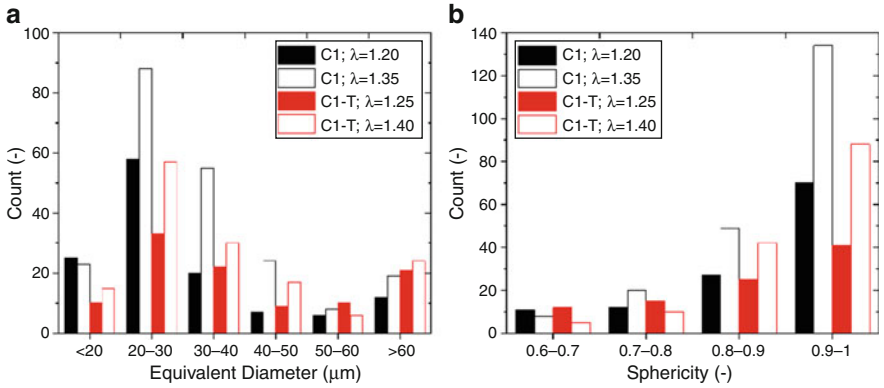

Fig. 10 Count of voids' size (**a**) and sphericity (**b**) at two different stretching ratios

voids between 20 μm and 30 μm. The number of cavities below 20 μm decreases, whereas the number of larger cavities increases with increasing stretching. Additionally, the number of voids above 60 μm is higher for C1-T. Concerning the sphericity, half of the detected cavities (around 48%) exhibit a spherical shape, i.e., with a sphericity between 0.9 and 1, whereas the other half presented an oblate shape (sphericity below 0.9). When increasing the stretching, we observe an increase in the relative number of spherical voids. For C1, there are 91% more spherical voids when passing from $\lambda = 1.20$ to $\lambda = 1.35$, whereas C1-T has an increase of 112% when stretching from $\lambda = 1.25$ to $\lambda = 1.40$. These changes suggest that voids are passing from an oblate to a more spherical shape due to their propagation in the rubber matrix. The fact that C1-T exhibits a larger number of voids, whose shape changed, indicates that the void's propagation in the stiffer matrix occurs faster.

An individual inspection of the cavities-agglomerates interaction revealed three types of micro-mechanisms for cavitation, as displayed in Fig. 11: (a) internal agglomerate breakdown, (b) debonding at the poles, and (c) combination of internal agglomerate breakdown and debonding at the poles. Agglomerates that suffered internal breakdown possessed (in the majority) a low sphericity ($0.6 < S < 0.7$) and large size (>80 μm), with their main orientation axis almost aligned to the loading direction.

Debonding was observed mainly in medium-size agglomerates ($40\ \mu m < D_{eq} < 80\ \mu m$) with a sphericity below 0.9. Additionally, a population of small cavities (<15 μm) was also detected, but with not clear evidence of their origin. This is likely due to the limited resolution of in situ μCT. These small cavities could be generated either by the mechanisms presented in the previous section (SEM observations) or due to chain scission in the rubber matrix. We will refer to these mechanisms as "uncertain."

The percentage of cavitation micro-mechanisms for both compounds is presented in Fig. 12. Both compounds exhibit around 25% voids with an "uncertain" origin, linked to an instrumental limitation. Moreover, the main micro-mechanism of

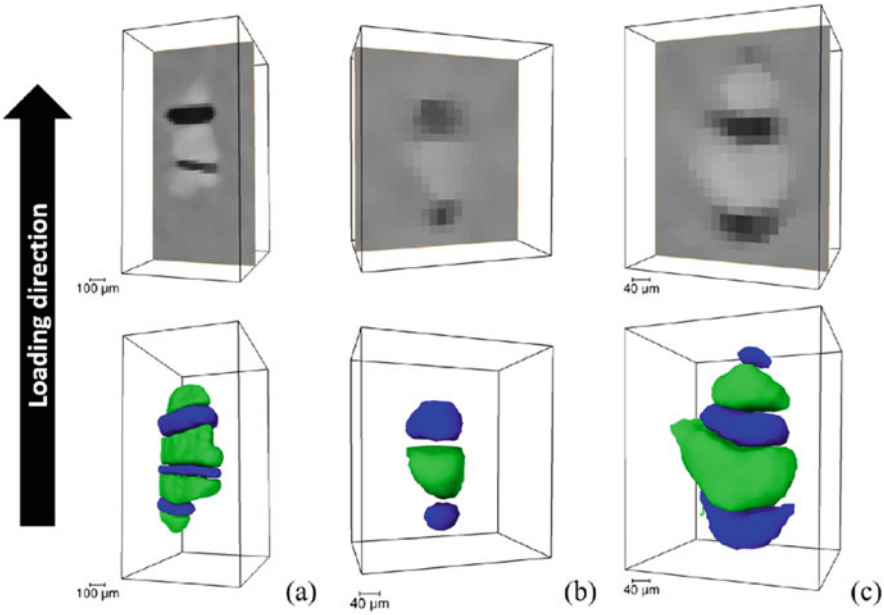

Fig. 11 2D representation (first row) and 3D representation (second row) of the three micro-mechanisms of cavitation: (**a**) Agglomerate breakdown, (**b**) debonding at the agglomerate poles, and (**c**) debonding at the poles combined with the agglomerate breakdown. The color green is assigned to the agglomerates and the blue to the voids

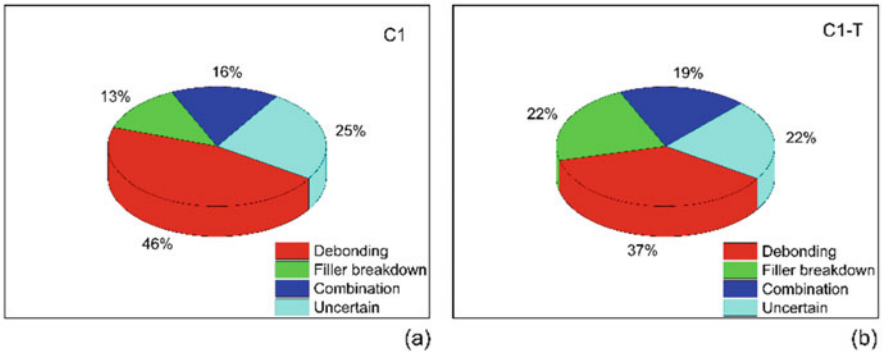

Fig. 12 Percentage of cavitation micro-mechanism for (**a**) C1 and (**b**) C1-T

cavitation in both materials consists in debonding, being more pronounced in C1. With the thermal treatment, we can observe an increase in the percentage of cavities due to agglomerates breakdown and also due to a combination of debonding and filler rupture. This is in good agreement with SEM observations. Therefore, it seems that thermally treated samples have an almost similar chance of undergoing

cavitation by debonding and agglomerate breakdown. The increase in stiffness of the matrix after thermal treatment (due to more crosslinks) may (1) facilitate stress transfer from the rubber matrix to the agglomerates due to more chain interconnections and/or (2) induce more lateral contraction at the agglomerate level during the drawing. These hypotheses may explain the increase of agglomerate breakdown after thermal treatment. Nevertheless, the stiffer matrix after thermal treatment may induce a faster cavitation propagation.

By extracting the total volume fraction of voids (V_f) from μCT observations, and assuming transversal isotropy $\left(\varepsilon_2^H = \varepsilon_3^H\right)$, we can then compute Poisson's ratio at a given deformation as:

$$V_f = \frac{\Delta V}{V_0} = \varepsilon_{yy} + 2\varepsilon_{xx} = \varepsilon_{yy}(1 - 2\nu) \tag{9}$$

Hence:

$$\nu = \frac{1}{2}\left(1 - \frac{V_f}{\varepsilon_1^H}\right) \tag{10}$$

A quantitative comparison between Poisson's ratios determined by DIC and μCT is presented in Fig. 13. Both approaches display comparable tendency of cavitation growth, which consisted in a decrease of ν with increasing stretching. The gap

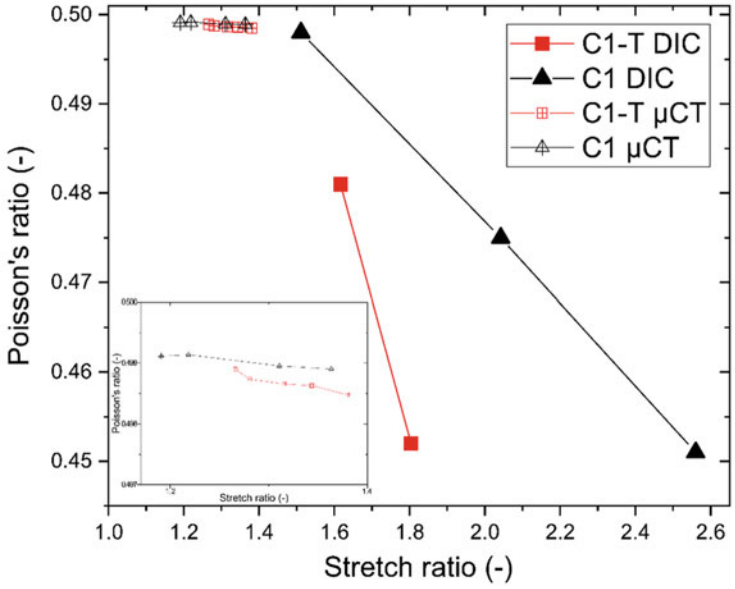

Fig. 13 Poisson's ratio determined from μCT analysis on postmortem compounds. The inset corresponds to a zoom of μCT measurements

between the experimental data of both techniques (represented with dotted lines) is due to the limited displacement allowed in the Deben stage. Additionally, the difference in Poisson's ratio determined by μCT for both compounds is relatively low. Nevertheless, we can observe that C1-T has lower values of Poisson's ratio due to larger cavities as previously mentioned. This finding suggests that the cavitation produced in the material has a permanent nature. The use of DIC and μCT techniques is then of great relevance since it confirms the role of Poisson's ratio as an indicator of cavitation and gives new insights of cavitation mechanisms involved in the material rupture.

4 Conclusions

Cavitation micro-mechanisms occurring in silica-filled styrene-butadiene rubber (SBR) nanocomposites upon fatigue and cyclic tensile testing have been analyzed in detail by a multiscale approach.

By micro-computed x-ray tomography (μCT), the spatial and size distributions of silica agglomerates were first analyzed. It was found that agglomerates were homogeneously distributed within the overall volume of the materials. Besides, the agglomerates exhibited a non-Gaussian distribution of their size, ranging from 6 μm to 140 μm with sphericities ranging from 0.35 to 1. Large and nonspherical agglomerates were expected to be sites of cavitation initiation.

In fatigue, cavitation is initiated from silica agglomerates at the surface or in the bulk of the hourglass specimen, as shown by μCT. Cavities having the most important influence on fatigue life formed at the surface of the sample, giving rise to fast crack formation and propagation probably dictating the number of cycles to the end of life, N_i. Scanning electron microscopy (SEM) imaging of the sample surface revealed that the initiation of cavitation micro-mechanisms relies on silica agglomerate-SBR matrix debonding, and by internal silica agglomerate breakdown, debonding mechanisms being more numerous.

Cyclic tensile testing showed a decrease of Poisson's ratio (initially at 0.5) with increasing the number of cycles, indicating that silica-filled SBR evolves from an incompressible to a compressible material. At the same time, the hysteresis of each cycle decreased with increasing the number of cycles, demonstrating a decrease of the viscous dissipation contribution and potential structural transformations. At the micrometer scale, this decrease of Poisson's ratio and hysteresis was characterized by cavitation micro-mechanisms homogeneously distributed within the dumbbell sample volume, whose initiation is largely similar to fatigue testing.

The influence of thermal treatment (120°C for 2 days) on cavitation was also characterized. Upon fatigue testing, N_i decreased for an equivalent applied strain amplitude after thermal treatment, while cavitation is predominately initiated by the agglomerate breakdown. Upon cyclic tensile testing, the compound exhibited a higher initial stiffness and a lower ductility. In addition, Poisson's ratio decreased faster at the low strain levels, which is corroborated with a faster increase of the

volume occupied by the cavities. The influence of thermal treatment on fatigue and cyclic tensile behaviors was discussed based on an increase in the crosslink density of SBR matrix, as revealed by swelling testing. The matrix stiffness was hence increased by the thermal treatment, which was expected to facilitate the stress transfer at the silica agglomerate-matrix interface and increase lateral contraction of the agglomerate during the drawing. These two phenomena may explain the increase of agglomerate breakdown after thermal treatment, but at the same time, the higher matrix stiffness was expected to enhance cavitation propagation within the matrix.

To go further, it would be relevant to analyze the transition between the initial cavity growing and the effective formation of cracks by investigating more fatigue life steps. The influence of the testing temperature on cavitation micro-mechanisms is also of high interest.

Acknowledgments This work was carried out within the framework of IBPG program supported by the Luxembourg National Research Fund (FNR), Project IPBG16/11514551/TireMat-Tech.

References

1. Mars W, Fatemi A (2002) A literature survey on fatigue analysis approaches for rubber. Int J Fatigue 24:949–961. https://doi.org/10.1016/S0142-1123(02)00008-7
2. Saintier N, Cailletaud G, Piques R (2006) Crack initiation and propagation under multiaxial fatigue in a natural rubber. Int J Fatigue 28:61–72
3. Guo Q, Zaïri F, Ovalle Rodas C, Guo X (2018) Constitutive modeling of the cyclic dissipation in thin and thick rubber specimens. ZAMM Zeitschrift fur Angew Math und Mech 98:1878–1899. https://doi.org/10.1002/zamm.201800087
4. Chen L, Zhou W, Lu J, Li J, Zhang W, Huang N, Wu L, Li L (2015) Unveiling reinforcement and toughening mechanism of filler network in natural rubber with synchrotron radiation X-ray nano-computed tomography. Macromolecules 48:7923–7928. https://doi.org/10.1021/acs.macromol.5b01301
5. Mullins L (1969) Softening of rubber by deformation. Rubber Chem Technol 42:339–362. https://doi.org/10.5254/1.3539210
6. Diani J, Fayolle B, Gilormini P (2009) A review on the Mullins effect. Eur Polym J 45:601–612. https://doi.org/10.1016/j.eurpolymj.2008.11.017
7. Payne AR (1962) The dynamic properties of carbon black loaded natural rubber vulcanizates. Part II. J Appl Polym Sci 6:368–372. https://doi.org/10.1002/app.1962.070062115
8. Heinrich G, Klüppel M (2007) Recent advances in the theory of filler networking in elastomers. Fill Elastomers Drug Deliv Syst 160:1–44. https://doi.org/10.1007/3-540-45362-8_1
9. Weng G, Chang A, Fu K, Kang J, Ding Y, Chen Z (2016) Crack growth mechanism of styrene-butadiene rubber filled with silica nanoparticles studied by small angle X-ray scattering. RSC Adv 6:8406–8415. https://doi.org/10.1039/c5ra26238k
10. Huneau B, Marco Y, Saux VL, Charrier P (2016) Fatigue crack initiation in a carbon black-filled natural rubber. Rubber Chem Technol 89:126–141. https://doi.org/10.5254/rct.15.84809
11. Byers JT (2002) Fillers for balancing passenger tire tread properties. Rubber Chem Technol 75:527–548. https://doi.org/10.5254/1.3547681
12. Gent AN, Lindley PB, Thomas AG (1964) Cut growth and fatigue of rubbers. I. The relationship between cut growth and fatigue. J Appl Polym Sci:455–466. https://doi.org/10.1002/app.1964.070080129

13. Robisson A, Laraba-Abbès F Laïarinandrasana L, Piques R, Chaverot JL (2000) Fatigue lifetime of a silica filled rubber. Application to a SBR shoe sole under bending. In: 13th European conference on fracture. San Sebastian
14. Sutton MA, Orteu J-J, Schreier HW (2009) Image correlation for shape, motion and deformation measurements: basic concepts, theory and applications. Springer, Boston. https://doi.org/10.1007/978-0-387-78747-3
15. G'Sell C, Hiver JM, Dahoun A (2002) Experimental characterization of deformation damage in solid polymers under tension, and its interrelation with necking. Int J Solids Struct 39:3857–3872. https://doi.org/10.1016/S0020-7683(02)00184-1
16. Billon N (2012) New constitutive modeling for time-dependent mechanical behavior of polymers close to glass transition: fundamentals and experimental validation. J Appl Polym Sci. https://doi.org/10.1002/app.36598
17. Federico CE, Bouvard JL, Combeaud C, Billon N (2018) Large strain/time dependent mechanical behaviour of PMMAs of different chain architectures. Application of time-temperature superposition principle. Polymer (Guildf) 139:177–187. https://doi.org/10.1016/j.polymer.2018.02.021
18. Candau N, Pradille C, Bouvard JL, Billon N (2016) On the use of a four-cameras stereovision system to characterize large 3D deformation in elastomers. Polym Test 56:314–320. https://doi.org/10.1016/j.polymertesting.2016.10.017
19. Narynbek Ulu K, Huneau B, Le Gac P-Y, Verron E (2016) Fatigue resistance of natural rubber in seawater with comparison to air. Int J Fatigue 88:247–256. https://doi.org/10.1016/j.ijfatigue.2016.03.033
20. Schörne K (2012) Development of methods for scatter artifact correction in industrial X-ray cone-beam computed tomography. Technical University of Munich, Munich
21. Gu J, Hacker GW (1994) Modern methods in analytical morphology. Springer, Boston. https://doi.org/10.1007/978-1-4615-2532-5
22. Cromey DW (2010) Use and manipulation of scientific digital images. Sci Eng Ethics 16:639–667. https://doi.org/10.1007/s11948-010-9201-y
23. Hainsworth SV (2007) An environmental scanning electron microscopy investigation of fatigue crack initiation and propagation in elastomers. Polym Test 26:60–70. https://doi.org/10.1016/j.polymertesting.2006.08.007
24. Glanowski T, Huneau B, Marco Y, Le Saux V, Champy C, Charrier P (2018) Fatigue initiation mechanisms in elastomers: a microtomography-based analysis. MATEC Web Conf 165:1–7. https://doi.org/10.1051/matecconf/201816508005
25. Tee YL, Loo MS, Andriyana A (2018) Recent advances on fatigue of rubber after the literature survey by Mars and Fatemi in 2002 and 2004. Int J Fatigue. https://doi.org/10.1016/j.ijfatigue.2018.01.007
26. Ismail H, Muniandy K, Othman N (2012) Fatigue life, morphological studies, and thermal aging of rattan powder-filled natural rubber composites as a function of filler loading and a silane coupling agent. Bioresources 7:841–858. https://doi.org/10.15376/biores.7.1.0841-0858
27. Ngolemasango FE, Bennett M, Clarke J (2008) Degradation and life prediction of a natural rubber engine mount compound. J Appl Polym Sci 110:348–355. https://doi.org/10.1002/app.28424
28. Suzuki N, Yatsuyanagi F, Ito M, Kaidou H (2002) Effects of surface chemistry of silica particles on secondary structure and tensile properties of silica-filled rubber systems. J Appl Polym Sci 86:1622–1629. https://doi.org/10.1002/app.11050
29. Merckel Y, Brieu M, Diani J (2012) A Mullins softening criterion for general loading conditions. J Mech Phys Solids 60:1257–1264
30. Diaz R, Diani J, Gilormini P (2014) Physical interpretation of the Mullins softening in a carbon-black filled SBR. Polymer (Guildf) 55:4942–4947. https://doi.org/10.1016/j.polymer.2014.08.020
31. Chrysochoos A (2012) Thermomechanical analysis of the cyclic behavior of materials. Proc IUTAM 4:15–26. https://doi.org/10.1016/j.piutam.2012.05.003

32. Loukil MT, Corvec G, Robin E, Miroir M, Le Cam JB, Garnier P (2018) Stored energy accompanying cyclic deformation of filled rubber. Eur Polym J 98:448–455. https://doi.org/10.1016/j.eurpolymj.2017.11.035
33. Ilseng A, Skallerud BH, Clausen AH (2017) An experimental and numerical study on the volume change of particle-filled elastomers in various loading modes. Mech Mater 106:44–57. https://doi.org/10.1016/j.mechmat.2017.01.007
34. Klüppel M (2009) The role of filler networking in fatigue crack propagation of elastomers under high-severity conditions. Macromol Mater Eng 294:130–140. https://doi.org/10.1002/mame.200800263
35. Starkova O, Aniskevich A (2010) Poisson's ratio and the incompressibility relation for various strain measures with the example of a silica-filled SBR rubber in uniaxial tension tests. Polym Test 29:310–318. https://doi.org/10.1016/j.polymertesting.2009.12.005
36. Howse S, Porter C, Mengistu T, Pazur RJ (2018) Experimental determination of the quantity and distribution of chemical crosslinks in unaged and aged natural rubber, part 1: peroxide vulcanization. Polym Test 70:263–274. https://doi.org/10.1016/j.polymertesting.2018.07.002
37. Candau N, Oguz O, Peuvrel-Disdier E, Bouvard JL, Pradille C, Billon N (2019) Strain-induced network chains damage in carbon black filled EPDM. Polymer (Guildf) 175:329–338. https://doi.org/10.1016/j.polymer.2019.05.017
38. Zhang B, Yu X, Gu B (2018) Modeling and experimental validation of interfacial fatigue damage in fiber-reinforced rubber composites. Polym Eng Sci 58:920–927. https://doi.org/10.1002/pen.24646
39. Gauthier C, Reynaud E, Vassoille R, Ladouce-Stelandre L (2004) Analysis of the non-linear viscoelastic behaviour of silica filled styrene butadiene rubber. Polymer (Guildf) 45:2761–2771. https://doi.org/10.1016/j.polymer.2003.12.081

Adv Polym Sci (2021) 286: 131–152
https://doi.org/10.1007/12_2020_64

Published online: 11 December 2020

New Approaches to Modeling Failure and Fracture of Rubberlike Materials

K. Y. Volokh

Contents

Abstract In this chapter we review some recent approaches to modeling failure and fracture of soft materials. By failure we mean the onset of damage via material instability. By fracture we mean further localization of damage into cracks with their subsequent propagation.

Mathematical description of failure is simple and it only requires some bounding of the strain energy density. The bounded strain energy automatically implies the bounded achievable stress, which is an indicator of material failure. By bounding the strain energy via energy limiters we show, for instance, how to explain cavitation, analyze strength of soft composites, and predict direction of possible cracks.

Mathematical description of fracture is more involved because it requires regularized formulations suppressing the so-called pathological mesh sensitivity. Most existing approaches utilize purely formal regularization schemes that lack physical grounds. We discuss a more physically based approach rooted in the idea that bulk

K. Y. Volokh (✉)
Faculty of Civil and Environmental Engineering, Technion – Israel Institute of Technology, Haifa, Israel
e-mail: cvolokh@technion.ac.il

cracks are not a peaceful unzipping of adjacent atomic layers but rather a catastrophic explosion of bonds localized within a finite characteristic area.

1 Introduction

Failure and fracture are the central unsolved problems in solid mechanics generally and in mechanics of soft materials particularly. In this chapter we present some recent developments towards the solution of the problem. We emphasize the distinction between the concept of failure, which we interpret as the onset of material instability and damage, and the concept of fracture, which we interpret as the localization of damage into cracks and their dynamic propagation. We strongly believe that the only consistent description of failure and fracture should be the one incorporated in constitutive equations. For the general theoretical background and notation we refer to [1].

2 Failure as Onset of Damage

Traditional strength-of-materials approach defines material strength as the maximum stress achievable in uniaxial tension experiments. Various other criteria can be imposed on stresses or strains to define the state of failure. Importantly, such criteria are not a part of the constitutive laws. Rather, they are extra conditions or constraints that should be obeyed in analysis and design in order to provide reliable mechanical behavior of materials and structures. The strength-of-materials approach is seemingly simple yet it can be dangerous. For example, the critical strains of highly stretchable elastomers are much lower in equibiaxial as compared to uniaxial tension. Thus, the criterion of the critical uniaxial stretches is not applicable to structures under biaxial deformation. The latter notion is not always appreciated and understood by designers.

More convincing would be a description of failure which is directly incorporated in the constitutive law. In the latter case, there is no need to search for and obey extra constraints and the onset of failure naturally comes out of the stress analysis. We note that the traditional constitutive laws for elastomers do not describe failure: numerous hyperelastic models describe the intact mechanical behavior of materials. Moreover, various restrictions (e.g. poly-convexity, strong ellipticity, Baker–Ericksen inequalities, etc. [2]) are usually imposed on the hyperelastic constitutive laws in order to provide material stability. Such restrictions preclude from a description of material failure. Obviously, that is not physical because all materials fail.

To describe material failure the approach of continuum damage mechanics (CDM) was developed in which a damage variable was used [3–12]. The damage variable is an internal parameter whose physical meaning is open to debate.

Mathematically, the internal variable is utilized to reduce material stiffness during the damage process. The additional variable requires extra evolution equation and a threshold condition for its activation. This approach is especially appealing when the accumulation of damage is gradual. In the case of the abrupt damage a simpler approach is available [13] which does not require any internal variables. The latter approach of energy limiters and its implications are considered below.

2.1 Elasticity with Energy Limiters

We assume that the local deformation of material is described by the deformation gradient: $\mathbf{F} = \mathrm{Grad}\mathbf{y} = \partial \mathbf{y}/\partial \mathbf{x}$; where $\mathbf{x} \in \Omega_0$ and $\mathbf{y}(\mathbf{x}) \in \Omega$ denote the referential and current positions of a generic material point accordingly. The linear and angular momenta balance and the hyperelastic constitutive law read

$$\rho_0 \ddot{\mathbf{y}} = \mathrm{Div}\mathbf{P}, \quad \mathbf{P}\mathbf{F}^{\mathrm{T}} = \mathbf{F}\mathbf{P}^{\mathrm{T}}, \quad \mathbf{P} = \partial \psi / \partial \mathbf{F}, \tag{1}$$

where ρ_0 is the referential mass density; $\ddot{\mathbf{y}}$ is the acceleration; $\mathbf{P}$ is the first Piola–Kirchhoff stress tensor; $(\mathrm{Div}\,\mathbf{P})_i = \partial P_{ij}/\partial x_j$; and ψ is the strain energy density.

The corresponding natural boundary condition expresses this same linear momentum balance law on the boundary $\partial\Omega_0$,

$$\mathbf{P}\mathbf{n}_0 = \bar{\mathbf{t}}_0, \tag{2}$$

where $\bar{\mathbf{t}}_0$ is the given surface traction and $\mathbf{n}_0$ is a unit outward normal to $\partial\Omega_0$.

Alternatively to (2), essential boundary conditions for placements can be prescribed on $\partial\Omega_0$

$$\mathbf{y} = \bar{\mathbf{y}}. \tag{3}$$

In addition, initial conditions in Ω_0 complete the formulation of the problem

$$\mathbf{y}(t = 0) = \mathbf{y}_0, \quad \dot{\mathbf{y}}(t = 0) = \mathbf{v}_0. \tag{4}$$

We note again that a traditional strain energy function describes material that never fails. Such a description directly contradicts reality. Indeed, the number of atoms/molecules is limited within any material volume and, consequently, their bond energy is limited. The latter notion implies that the macroscopic strain energy density must also be limited. We emphasize that the latter conclusion is a direct consequence of the structure of matter. Introduction of the limited strain energy is not a matter of choice – it is a physics demand.

Table 1 Material constants

c_1 [MPa]	c_2 [MPa]	c_3 [MPa]	Φ [MPa]	m
0.298	0.014	0.00016	82.0	10

One can imagine various ways to introduce the limited strain energy. We use the upper incomplete gamma function, $\Gamma[s,x]=\int_x^\infty t^{s-1}e^{-t}dt$, for the following definition of the generic bounded strain energy density [14, 15]

$$\psi(\mathbf{F})=\psi_{\mathrm{f}}-\psi_{\mathrm{e}}(\mathbf{F}), \tag{5}$$

where

$$\psi_{\mathrm{e}}(\mathbf{F})=\Phi m^{-1}\Gamma[m^{-1},W(\mathbf{F})^m\Phi^{-m}],\quad \psi_{\mathrm{f}}=\psi_{\mathrm{e}}(\mathbf{1}). \tag{6}$$

Here, we designated failure energy by ψ_{f}; elastic energy by $\psi_{\mathrm{e}}(\mathbf{F})$; strain energy without failure by $W(\mathbf{F})$; the energy limiter (average bond energy) by Φ; identity tensor by $\mathbf{1}$; and material parameter by m.

We note that the increase of deformation beyond some critical threshold will lead to the decrease of the elastic energy: $\psi_{\mathrm{e}}\to 0$, which will numerically vanish. In this case, the strain energy will approach the failure energy: $\psi\to\psi_{\mathrm{f}}$, indicating a fixed energy dissipation. To make the process irreversible it is possible to slightly modify (5) – see [16]. However, the irreversibility is important when damage localization is considered and we postpone its discussion to the section on fracture.

Substitution of (5) in $(1)_3$ yields a simple form of the constitutive law

$$\mathbf{P}=\exp\left[-W^m\Phi^{-m}\right]\partial W/\partial\mathbf{F}. \tag{7}$$

Remarkably, the latter constitutive equation does not include any gamma function and only the exponential factor makes difference between the present formulation and traditional hyperelasticity with the intact material behavior. The exponential term has two major modes. It equals one for the intact material behavior and it goes to zero for damage. The subtle transition between these two modes provides a description of the onset of failure.

By way of illustration, we specify the intact strain energy for natural rubber as follows [15]:

$$W=c_1(I_1-3)+c_2(I_1-3)^2+c_3(I_1-3)^3, \tag{8}$$

where $I_1=\mathbf{F}:\mathbf{F}$ is the first principal invariant and material is incompressible: $J=\det\mathbf{F}=1$.

Material constants were fitted [15] to the experimental data from [17] and they are given in Table 1.

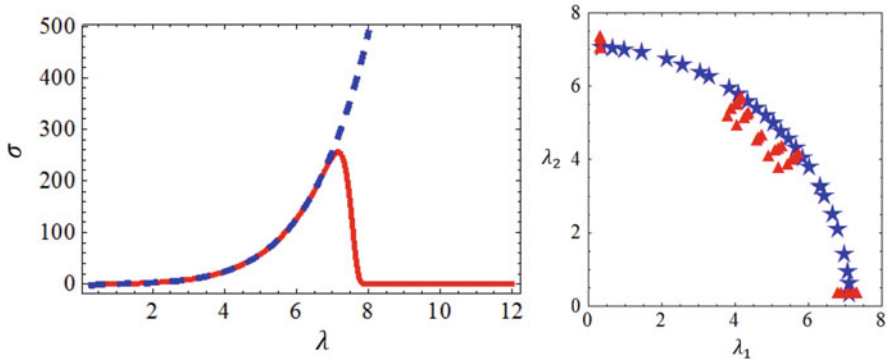

Fig. 1 Left: Cauchy stress [MPa] versus stretch: dashed line denotes the intact model; solid line denotes the model with failure. Right: Failure envelope for biaxial tension: theory (stars) versus experiment (triangles)

The stress–stretch curve for uniaxial tension is shown on the left of Fig. 1. The bounded strain energy automatically provides the bounded stress and the limit point on the diagram.

This same model was also used to create the failure envelope in biaxial tension – Fig. 1 right. The theoretical critical points were calculated from the condition of the vanishing determinant of the Hessian of strain energy [15].

In summary, we showed a simple way to account for material failure in the constitutive law without introducing internal variables. In this case, all material constants can be fitted in macroscopic experiments. Despite its simplicity, the proposed formulation allows attacking various interesting problems related with the onset of damage. Some of them are considered in the next three subsections.

2.2 *Cavitation*

Cavitation is the phenomenon of a sudden *irreversible* expansion of micro-voids into the visible macroscopic voids. Gent and Lindley [18] nicely demonstrated this phenomenon in tension experiments on the poker-chip rubber samples – Fig. 2 left. Such thin samples exposed to uniaxial tension in out-of-plane direction exhibit highly triaxial deformation – hydrostatic tension. The hydrostatic tension, in its turn, leads to the void expansion – cavitation.

Mathematically the void expansion can be described by the following integral formula [1]:

$$p(\lambda_a) = \int_1^{\lambda_a} \frac{1}{\lambda^3 - 1} \frac{d\psi}{d\lambda} d\lambda, \tag{9}$$

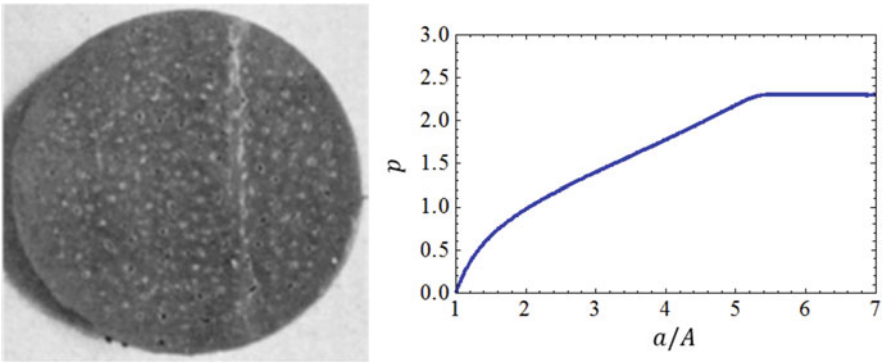

Fig. 2 Left: Grown voids in the poker-chip test [18]. Right: Hydrostatic tension [MPa] versus hoop stretch for void growth

where p is the hydrostatic tension; λ is the hoop stretch; $\lambda_a = a/A$ with A and a denoting the initial and current radius of the void accordingly; and the strain energy is expressed in terms of the principal stretches for incompressible material

$$\psi(\lambda_1, \lambda_2, \lambda_3) = \psi(\lambda^{-2}, \lambda, \lambda). \tag{10}$$

Ultimately $\lambda_a \to \infty$ and (9) should converge to the critical tension [19]

$$p_{\text{cr}} = \int_1^{\infty} \frac{1}{\lambda^3 - 1} \frac{d\psi}{d\lambda} d\lambda. \tag{11}$$

In the case of neo-Hookean material model we define the strain energy as follows:

$$\psi = (\mu/2)(I_1 - 3), \quad I_1 = \lambda^{-4} + 2\lambda^2, \tag{12}$$

where μ is the shear modulus.

Then, substitution of (12) in (11) yields

$$p_{\text{cr}} = (5/2)\mu. \tag{13}$$

The latter result was used by Gent and Lindley [18] to explain the cavitation phenomenon theoretically. Such explanation proliferated in the subsequent literature and it tacitly relies upon the following assumptions:

(a) cavitation is a purely elastic phenomenon;
(b) neo-Hookean material model is applicable for analysis of large stretches;
(c) the obtained critical hydrostatic tension (13) is universal for all materials with the given initial shear modulus μ.

All these assumptions are incorrect:

[a] if the cavitation phenomenon was purely elastic, then we would not observe it after unloading while we do observe it;
[b] Neo-Hookean model is only relevant for very moderate stretches not exceeding values of 1.4 while the critical hydrostatic tension is achieved for much greater stretches;
[c] the integral in (11) converges to the finite critical tension for the neo-Hookean material model while it does not converge for more realistic material models [20].

We emphasize that the very fact of irreversibility of the void growth clearly indicates that cavitation is related to damage and only theories describing damage can be used for the explanation of the phenomenon. Particularly, the model with energy limiters presented in the previous subsection can be used in (9). The tension–stretch curve for this model is presented in Fig. 2 right [21]. The horizontal line gives the critical tension of ~ 2.3 MPa that can be calculated from (11). The experimental estimate of the critical tension of about ~ 2.7 MPa [18] is encouraging for the theoretical analysis. Various models without failure can be enhanced with energy limiters to provide convergence to critical tensions [20, 22]. Without the limiters such models would not be able to explain the cavitation phenomenon.

The role of inertia forces and viscosity in cavitation was uncovered in [23] while the thermal effects were considered in [24] for the first time.

We note, in passing, that the specific constitutive model for natural rubber described in the previous subsection nicely fits experimental data in uniaxial, biaxial, and triaxial (cavitation) states of deformation including failure.

2.3 Strength of Soft Composites

Soft composites comprise soft matrix and reinforcements of various shapes. They are used in various applications ranging from rubber bearings to soft robots and advanced biomedical devices. Soft biocomposites can be created, for example, by the natural process of tissue calcification, etc. The reinforcement stiffens a soft ground matrix. What is the effect of reinforcement on the strength of the composite? The answer is not evident at all.

We developed micromechanical approach to analysis of the onset of failure in soft composites combining the elasticity with energy limiters and high fidelity generalized method of cells (HFGMC) [25].

We used the approach to study strength of an idealized calcified aneurysmal tissue [26]. Particularly, we analyzed the effect of the varying amount of calcification (10%, 40%, and 70%), i.e. the relative volume of the hard inclusion within the periodic elementary cell, on the tissue stiffness and strength. We found that the increase of the relative volume of calcium particles unconditionally led to the stiffening of the tissue. At the same time, the strength did not increase in the most considered cases – it could significantly decrease. Quantitatively, the strength

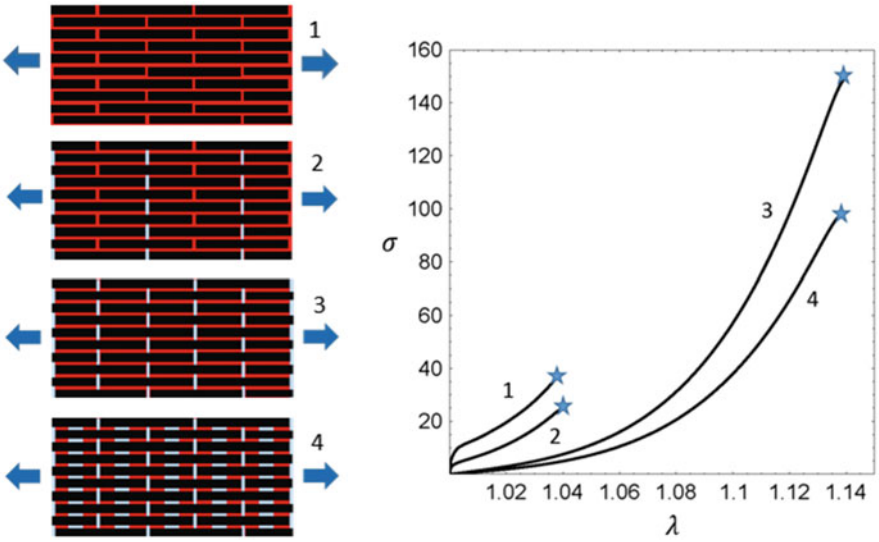

Fig. 3 Staggered soft composites comprising matrix (red) and reinforcing platelets (black) and pre-existing cracks (white) under uniaxial tension are shown on the left. Corresponding Cauchy stress – stretch curves in uniaxial tension are shown on the right. Stars designate critical points beyond which static solution does not exist – strength [27]

decrease could vary from 10% to 40% and more. One might find it contrary to intuition that the strength can decrease while the stiffness always increases with calcification. This interesting finding emphasizes the difference between the concepts of stiffness and strength which is not always appreciated. The strength of a composite is significantly affected by the locally nonuniform state of deformation. Small hard particles rather than big ones can be stress concentrators amplifying the likelihood of the local material failure. Also the hard particles restrain deformation in their vicinity creating the state of hydrostatic tension which, in its turn, may trigger cavitation with the subsequent fracturing. The obtained results have limitations because an ideally periodic distribution of calcified particles was assumed in computations while in reality the distribution is random. Thus, additional research in stochastic mechanics of failure analysis is required.

The approach developed in [25] was also used in [27] to simulate strength of bioinspired soft composites with the staggered alignment of hard platelets in a soft matrix. The strength was analyzed for different cases of the composite material with various amounts of hard inclusions and various pre-existing cracks – Fig. 3.

We found, for example, that the soft matrix material placed between short edges of platelets with high aspect ratio was the weakest link of the composite. In these areas the strength was reached. Amazingly, by deleting soft material or introducing pre-existing cracks in these dangerous areas it was possible to significantly increase (~ 4 times) the strength of the composite. Such finding might seem contrary to intuition at first glance. However, the pre-existing cracks actually relieved the stress

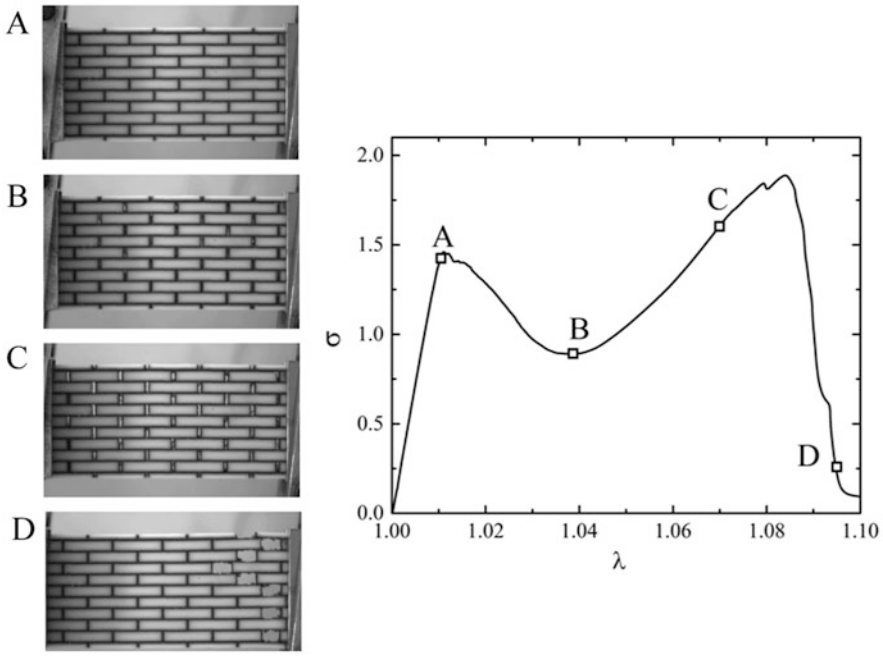

Fig. 4 Experiments with 3D printed soft composite: snapshots on the left correspond to the points on the stress – stretch curve on the right [27]

and strain concentrators providing greater material resistance. The main load bearing area of the matrix became the region connecting long edges of platelets. This region was predominantly in the state of shear. The failure of the soft matrix in shear was responsible for the overall strength of the composite. Importantly, the overall strength did not exceed the strength of the matrix material in the uniaxial tension.

In order to validate the computational analysis described above, we performed experiments on 3D printed composites – Fig. 4.

Unfortunately, the 3D printing procedure did not allow to create the natural rubber material used in simulations. Instead, soft interfaces were printed in soft hyperelastic digital material and stiff platelets were printed in rigid VeroWhite polymer. Samples were fabricated by using a multi-material Polyjet technique with a help of the 3D-printer Objet Connex 260. Performing the uniaxial tension test shown in Fig. 4, we observed that after reaching the critical level of loading – point A, the soft matrix at the short platelet edges ruptured. This led to a significant drop in stress level during the following loading up to point B. Then the shear deformation in the soft matrix along the lengthy edges of platelets dominated until approximately point C soon after which the ultimate stress – strength – was reached and material started disintegrating as at point D. This observation qualitatively supported the numerically predicted phenomena – Fig. 3 – showing that the catastrophic failure originated in the soft interface phase, and it had a significant

influence on the overall strength of the composite. We emphasize the qualitative rather than quantitative resemblance in view of the different matrix materials used in simulations and experiments. The resemblance is encouraging.

2.4 Prediction of Crack Direction

In this subsection, we show how to predict the onset of cracks including their direction by using the elasticity with energy limiters and strong ellipticity condition.

We start with a brief description of the underlying theory [28]. Designating increments with tildes it is possible to derive incremental equations of momenta balance and constitutive law

$$\rho_0\ddot{\tilde{\mathbf{y}}} = \mathrm{Div}\tilde{\mathbf{P}}, \quad \tilde{\mathbf{P}}\mathbf{F}^{\mathrm{T}} + \mathbf{P}\tilde{\mathbf{F}}^{\mathrm{T}} = \left(\tilde{\mathbf{P}}\mathbf{F}^{\mathrm{T}} + \mathbf{P}\tilde{\mathbf{F}}^{\mathrm{T}}\right)^{\mathrm{T}}, \quad \tilde{\mathbf{P}} = \partial^2\psi/\partial\mathbf{F}\partial\mathbf{F} : \tilde{\mathbf{F}}. \tag{14}$$

Alternatively, these incremental equations can be reformulated in the Eulerian form where the current configuration Ω is referential

$$\rho\ddot{\tilde{\mathbf{y}}} = \mathrm{div}\tilde{\boldsymbol{\sigma}}, \quad \tilde{\boldsymbol{\sigma}} + \boldsymbol{\sigma}\tilde{\mathbf{L}}^{\mathrm{T}} = \left(\tilde{\boldsymbol{\sigma}} + \boldsymbol{\sigma}\tilde{\mathbf{L}}^{\mathrm{T}}\right)^{\mathrm{T}}, \quad \tilde{\boldsymbol{\sigma}} = \mathbb{A} : \tilde{\mathbf{L}}, \tag{15}$$

where $\rho = J^{-1}\rho_0$; $\boldsymbol{\sigma} = J^{-1}\mathbf{P}\mathbf{F}^{\mathrm{T}}$ is the Cauchy stress tensor and $(\mathrm{div}\tilde{\boldsymbol{\sigma}})_i = \partial\tilde{\sigma}_{ij}/\partial y_j$; $\tilde{\boldsymbol{\sigma}} = J^{-1}\tilde{\mathbf{P}}\mathbf{F}^{\mathrm{T}}$ is the incremental Cauchy stress; $\tilde{\mathbf{L}} = \tilde{\mathbf{F}}\mathbf{F}^{-1}$ is the incremental velocity gradient; $\mathbb{A}$ is the fourth order elasticity tensor with Cartesian components

$$A_{ijkl} = J^{-1}F_{js}F_{lr}\frac{\partial^2\psi}{\partial F_{is}\partial F_{kr}}. \tag{16}$$

For the strain energy defined by (5), we further calculate

$$\frac{\partial\psi}{\partial F_{is}} = \frac{\partial\psi}{\partial W}\frac{\partial W}{\partial F_{is}} = \exp\left[-W^m\Phi^{-m}\right]\frac{\partial W}{\partial F_{is}}, \tag{17}$$

and

$$\frac{\partial^2\psi}{\partial F_{is}\partial F_{kr}} = \left(\frac{\partial^2 W}{\partial F_{is}\partial F_{kr}} - mW^{m-1}\Phi^{-m}\frac{\partial W}{\partial F_{kr}}\frac{\partial W}{\partial F_{is}}\right)\exp\left[-W^m\Phi^{-m}\right]. \tag{18}$$

Substitution of (18) in (16) yields

$$A_{ijkl} = J^{-1} F_{\ js} F_{lr} \left(\frac{\partial^2 W}{\partial F_{is} \partial F_{kr}} - m W^{m-1} \Phi^{-m} \frac{\partial W}{\partial F_{kr}} \frac{\partial W}{\partial F_{is}} \right) \exp\left[- W^m \Phi^{-m} \right]. \quad (19)$$

We look for a plane wave solution of the incremental initial boundary value problem

$$\tilde{\mathbf{y}} = \mathbf{r} g(\mathbf{s} \cdot \mathbf{y} - vt), \quad (20)$$

where $\mathbf{r}$ and $\mathbf{s}$ are the unit vectors in the directions of wave polarization and wave propagation, respectively; and v is the wave speed.

Substituting for $\tilde{\mathbf{L}} = \text{grad}\tilde{\mathbf{y}} = \partial \tilde{\mathbf{y}} / \partial \mathbf{y}$ from (20) to $(15)_3$, we get the incremental stress $\tilde{\boldsymbol{\sigma}}$. Then, substituting for $\tilde{\mathbf{y}}$ from (20) and $\tilde{\boldsymbol{\sigma}}$ to the linear momentum balance $(15)_1$, we get

$$\rho v^2 \mathbf{r} = \boldsymbol{\Lambda}(\mathbf{s}) \mathbf{r}, \quad (21)$$

where $\boldsymbol{\Lambda}(\mathbf{s})$ is the acoustic tensor with Cartesian components

$$\Lambda_{ik} = A_{ijkl} s_{\ j} s_l. \quad (22)$$

Taking scalar product of (21)with $\mathbf{r}$, we obtain for the wave speed

$$J \rho v^2 = J \mathbf{r} \cdot \boldsymbol{\Lambda} \mathbf{r} = f_1 f_2, \quad (23)$$

where

$$\begin{aligned} f_1 &= f_3 - m W^{m-1} \Phi^{-m} f_4^2, \\ f_2 &= \exp\left[- W^m \Phi^{-m} \right], \\ f_3 &= s_{\ j} s_l r_i r_k F_{\ js} F_{lr} \partial^2 W / \partial F_{is} \partial F_{kr}, \\ f_4 &= r_k s_l F_{lr} \partial W / \partial F_{kr}. \end{aligned} \quad (24)$$

The positive wave speed corresponds to the mathematical condition of the strong ellipticity of the incremental initial boundary value problem. Zero wave speed mathematically means violation of the strong ellipticity condition and, physically, it means inability of the material to propagate a wave in direction $\mathbf{s}$. The latter notion can also be interpreted as the onset of a crack perpendicular to $\mathbf{s}$.

Consider, for example, longitudinal wave (P-wave) and transverse wave (S-wave) in plane of a material sheet. Denoting the unit vectors in the plane by $\mathbf{e}_1$ and $\mathbf{e}_2$, we can write

Fig. 5 Great East Japan Earthquake in 2011: bridge rubber bearings on the left and the horizontal crack is observed on the right [33]

$$\mathbf{s} = \mathbf{r} = \cos\alpha\mathbf{e}_1 + \sin\alpha\mathbf{e}_2 \tag{25}$$

for the P-wave and

$$\begin{aligned} \mathbf{s} &= \cos\alpha\mathbf{e}_1 + \sin\alpha\mathbf{e}_2, \\ \mathbf{r} &= -\sin\alpha\mathbf{e}_1 + \cos\alpha\mathbf{e}_2 \end{aligned} \tag{26}$$

for the S-wave, where α is unknown angle in plane.

Then, we have from (23) for the vanishing wave speed

$$J\rho v^2(\mathbf{F},\alpha) = f_1(\mathbf{F},\alpha)\, f_2(\mathbf{F}) = 0. \tag{27}$$

This condition can be explained mathematically as follows. The Rayleigh quotient rule for the given $\mathbf{s}$ states that $\mathbf{z}\cdot\boldsymbol{\Lambda}(\mathbf{s})\mathbf{z}/(\mathbf{z}\cdot\mathbf{z})$ is minimized by the first eigenvector $\mathbf{z}=\mathbf{r}$ and $\zeta=\mathbf{r}\cdot\boldsymbol{\Lambda}(\mathbf{s})\mathbf{r}/(\mathbf{r}\cdot\mathbf{r})$ is its minimum value, which is the smallest eigenvalue of $\boldsymbol{\Lambda}(\mathbf{s})$. Obviously, this eigenvector $\mathbf{r}$ might not obey conditions of the longitudinal ($\mathbf{r}=\mathbf{s}$) or transverse ($\mathbf{r}\cdot\mathbf{s}=0$) waves. However, the situation changes when we assume the minimum value in advance: $\zeta=\mathbf{r}\cdot\boldsymbol{\Lambda}(\mathbf{s})\mathbf{r}=0$. In this particular case both longitudinal and transverse waves can be found by the direct solution of $\mathbf{r}\cdot\boldsymbol{\Lambda}(\mathbf{s})\mathbf{r}=0$. Any $\mathbf{r}$ providing the zero minimum eigenvalue becomes the corresponding eigenvector. The very existence of the longitudinal ($\mathbf{r}=\mathbf{s}$) or transverse ($\mathbf{r}\cdot\mathbf{s}=0$) waves comes directly from the computation itself.

The described approach was used to predict the onset of cracks and their direction in a series of publications [29–32].

Bridge rubber bearings undergo a simultaneous compression and shear under earthquakes and cracks appear in them in the direction of shear – Fig. 5. Such shear cracks were predicted by the analysis described above [29].

This analysis included the assumption of material incompressibility. However, the incompressibility constraint suppresses longitudinal waves and, thus, valuable information about cracks can be missed. The latter issue was explored in [30] where the incompressibility constraint was abandoned. It was found, indeed, that the

constraint could turn into a Trojan Horse in the analytical calculations and an important information about cracks could be missed. Particularly, in the cases of uniaxial tension and pure shear, it was found that namely longitudinal waves helped to predict cracks perpendicular to the direction of tension. Amazingly, it was also found that the transverse wave led to the prediction of cracks whose direction was close to the direction of tension. The latter prediction seemed unrealistic; however, such cracks in the direction of tension were found in recent experiments [34]!

The onset of cracks in anisotropic soft materials – arterial wall – was considered in [31, 32]. Particularly in [32], we developed two constitutive models with 16 and 8 structure tensors to account for anisotropy and failure of the wall. The intact material behavior was calibrated based on the experimental data for human adventitia and energy limiters were introduced to describe failure. These models were used in analysis of the loss of strong ellipticity in uniaxial tension and pure shear in circumferential and axial directions of the artery and in biaxial tension. Directions of possible cracks were obtained from the condition of the vanishing speed of the superimposed longitudinal and transverse waves. The vanishing longitudinal wave speed predicted the appearance of cracks in the direction perpendicular to tension in uniaxial tension and pure shear. As in the case of isotropic material discussed above, such prediction would be suppressed by the incompressibility constraint. The vanishing transverse wave speed predicted the appearance of cracks in the direction inclined to tension in uniaxial tension and pure shear. Equibiaxial stretching can lead to the appearance of cracks in any direction despite the anisotropy of material. The inclined cracks oriented along the bundles of collagen fibers have been found in experiments [35].

3 Fracture as Damage Localization

Fracture in the form of cracks was first considered by Griffith [36]. Analogously to the strength-of-materials approach, he suggested a criterion of growth of pre-existing cracks based on the global energy balance. Such integral balance ignores the role of the strain and stress concentrations at the tip of the crack and, therefore, it is open to criticism [37]. There are various conceptual approaches to fracture in the literature. We believe that fracture should be incorporated in the constitutive description of materials and crack initiation and propagation should be an outcome of the solution of the clearly formulated initial boundary value problems. In this spirit, there are two main approaches to modeling fracture – surface and bulk crack models.

Surface crack models, or cohesive surface models (CSM), consider continuum enriched with discontinuities along surfaces with additional traction-displacement-separation constitutive laws [37–47]. If the location of the separation surface is known in advance (e.g. fracture along weak interfaces), then the use of CSM is natural. Otherwise, the insertion of cracks in the bulk in the form of separation surfaces remains an open problem, which includes definition of criteria for crack nucleation, orientation, branching, and arrest. Besides, the CSM approach presumes

the simultaneous use of two different constitutive models: one for the cohesive surface and another for the bulk, for the same real material. Certainly, a correspondence between these two constitutive theories is desirable yet not promptly accessible.

Bulk crack models, or continuum damage mechanics (CDM), introduce failure in constitutive laws in the form of the falling stress–strain curves [48–55].[1] Damage nucleation, propagation, branching, and arrest naturally come out of the constitutive laws. Unfortunately, numerical simulations based on bulk failure laws show the so-called pathological mesh sensitivity, which means that finer meshes lead to narrower damage localization areas. In the limit case, the energy dissipation in damage tends to zero with the diminishing size of the computational mesh. This physically unacceptable mesh sensitivity is caused by the lack of a characteristic length in the traditional formulation of continuum mechanics. To surmount the latter pitfall gradient- or integral-type nonlocal continuum formulations are used where a characteristic length is incorporated to limit the size of the spatial damage localization [56–60]. In the gradient-type approaches, for example, an additional internal damage variable is introduced together with additional differential equation of reaction-diffusion type. This equation has a small parameter – the characteristic length – as a scaling factor for the highest spatial derivatives of the damage variable. The characteristic length provides solution of the boundary layer type. This layer is interpreted as a diffused crack of finite thickness rather than a surface of discontinuity.

A special choice of the additional regularizing equation, called phase-field approach, gained popularity in recent years [61–63]. It is claimed that the phase-field formulation provides convergence of the diffused crack to the surface of discontinuity under the decrease of the characteristic length. Thus, the characteristic length is interpreted as a purely numerical parameter which can be varied. However, the case of the uniform uniaxial tension shows that, in the phase-filed formulation, the characteristic length is a physical parameter linked to material strength[2] and it cannot be varied. Thus, the phase-field approach is a possible yet not superior regularization of the gradient type.

The regularization strategy rooted in the nonlocal continua formulations is attractive because it is lucid mathematically. Unluckily, the generalized nonlocal continua theories are based (often tacitly) on the physical assumption of long-range particle interactions while the actual particle interactions are short-range – on nanometer or angstrom scale. Therefore, the physical basis for the nonlocal models appears disputable. A more physically based treatment of the pathological mesh sensitivity of the bulk failure simulations should likely include multi-physics coupling. Such a

[1] These works were not devoted to soft materials per se.

[2] For example, the authors of [63] rightfully note that "although the length-scale parameter associated with the phase-field approximation is introduced as a numerical parameter it is, in fact, a material parameter that influences the critical stress at which crack nucleation occurs."

Fig. 6 Left: idealized crack with zero thickness; middle: visible closed crack in unloaded tire; right: realistic bulk crack with finite thickness l

theory coupling mass flow (sink) and finite elastic deformation is considered in the next subsections.

3.1 Material Sink Formulation

We can see crack surfaces and we rightfully conclude that these surfaces are a result of material separation. However, people usually and tacitly make one more logical step and assume that the separation is a result of debonding of two adjacent atomic or molecular layers – Fig. 6 left. At the first thought, the latter assumption is the simplest one and it appeals to intuition. At the second thought, it is possible to realize that the assumption is wrong because cracks are visible by a naked eye – Fig. 6 middle. Indeed, if the separation was between two adjacent atomic layers, then we would not see closed cracks because our eye can only distinguish objects on the scale of microns and not angstroms. Thus, the crack surfaces are not created by two adjacent atomic layers – they are created by a massive bond breakage spread over a region with characteristic length l – Fig. 6 right.

It is crucial to realize that the process of the bond breakage is diffusive rather than confined to one atomic plane. Some atoms fly out of the bulk material. Generally, we cannot see them because of their very small amount (as compared to the bulk). Sometimes, we can see them – remember the dust which comes out of cracks in brittle concrete. The characteristic length of the damage region is so big in the latter case that we can see small pieces of concrete that left the bulk during fracture.

Summarizing the qualitative picture of the crack formation we note that material sinks within the characteristic small region of damage. Such notion gives rise to the mathematical formulation in which momenta and mass balance are coupled [64].

Thus, the mass balance equations should be coupled with $(1)_{1,2}$ in Ω_0

$$\mathrm{Div}\mathbf{s}_0 + \xi_0 = 0, \tag{28}$$

where $\mathbf{s}_0$ and ξ_0 are the referential mass flux and source (sink) accordingly.

The corresponding natural boundary condition expresses this same mass balance law on the boundary $\partial\Omega_0$

$$\mathbf{s}_0 \cdot \mathbf{n}_0 = 0. \tag{29}$$

We note that we use the mass balance in the reduced form: $\mathrm{Div}\mathbf{s}_0 + \xi_0 = 0$; instead of the general form: $\dot{\rho}_0 = \mathrm{Div}\mathbf{s}_0 + \xi_0$; because we are only interested in pre- and post-cracked states while the transition – bond rupture – process is so fast that it can be ignored. Such simplification is analogous to consideration of the buckling process in thin-walled structures. In the latter case, pre- and post-buckled states of a structure are usually analyzed by using a time-independent approach while the very process of the fast dynamic transition to the buckled state is ignored in analysis by dropping the inertia terms from the momentum balance equation.

We define constitutive equations for the stress [64]

$$\mathbf{P} = (\rho_0/\overline{\rho}_0)\partial W/\partial \mathbf{F}, \tag{30}$$

mass sink

$$\xi_0 = \beta\overline{\rho}_0 H(\gamma)\exp\left[-W^m\Phi^{-m}\right] - \beta\rho_0, \tag{31}$$

and mass flux

$$\mathbf{s}_0 = \kappa H(\gamma)\exp\left[-W^m\Phi^{-m}\right]J(\mathbf{F}^{\mathrm{T}}\mathbf{F})^{-1}\mathrm{Grad}\rho_0, \tag{32}$$

where $\overline{\rho}_0 = \rho_0(t=0)$ is the initial referential density; $\beta > 0$ and $\kappa > 0$ are material constants; $H(\gamma)$ is a unit step function, i.e. $H(\gamma) = 0$ if $\gamma < 0$ and $H(\gamma) = 1$ otherwise; the switch parameter $\gamma \in (-\infty, 0]$ is necessary to prevent from material healing and it is defined by the evolution equation $\dot{\gamma} = -H(\varepsilon - \rho_0/\overline{\rho}_0)$, $\gamma(t=0) = 0$ where $0 < \varepsilon \ll 1$ is a dimensionless precision constant.

It is important to emphasize that the formulation presented in this subsection is a generalization of elasticity with energy limiters described above. Indeed, the elasticity with energy limiters emerges as a particular case where there is no damage localization via diffusion of broken bonds. In the latter case, we have the vanishing mass flux: $\mathbf{s}_0 = \mathbf{0}$; and sink: $\xi_0 = 0$. In view of the zero material sink we calculate from (31): $\rho_0/\overline{\rho}_0 = H(\gamma)\exp\left[-W^m\Phi^{-m}\right]$. Since the irreversibility of the process is not important in this case and $H(\gamma) \equiv 1$, we further simplify: $\rho_0/\overline{\rho}_0 = \exp\left[-W^m\Phi^{-m}\right]$. Substitution of the latter formula in (30) yields: $\mathbf{P} = \exp\left[-W^m\Phi^{-m}\right]\partial W/\partial \mathbf{F}$, which coincides with (7).

3.2 Dynamic Crack Propagation

Most works on modeling cracks consider quasi-static crack propagation. Yet in reality, most cracks propagate dynamically unless they are highly restrained. Indeed, the onset and localization of damage are usually related to the loss of the static

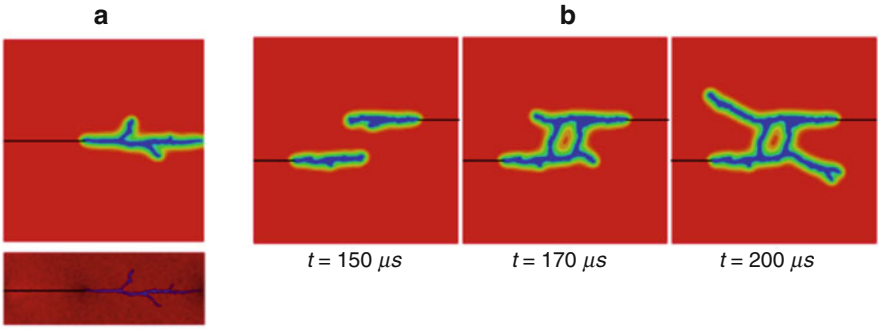

Fig. 7 (**a**) Propagation of Mode 1 crack in aneurysm material in current (top) and referential (bottom) configurations; (**b**) crack bridging and kinking

stability of a structure. The process of crack propagation becomes dynamic. The latter notion is not properly appreciated in the literature and many authors prefer static analysis over the dynamic one because of its relative simplicity rather than physical adequacy. A review of the crack propagation in rubberlike materials can be found in [65].

We implemented the material sink formulation presented above in analysis of dynamic crack propagation in aneurysm material and we refer to [66] for details. Nevertheless, we note that substitution of constitutive equations (31) and (32) in the mass balance law (28) yields the following second order partial differential equation with respect to the referential mass density, ρ_0,

$$\begin{aligned} l^2 \mathrm{Div}\{H(\gamma)\exp\left[-W^m\Phi^{-m}\right]J(\mathbf{F}^{\mathrm{T}}\mathbf{F})^{-1}\mathrm{Grad}\rho_0\} \\ +\overline{\rho}_0 H(\gamma)\exp\left[-W^m\Phi^{-m}\right]-\rho_0=0. \end{aligned} \tag{33}$$

Remarkably, we do not need to know material constants κ and β separately anymore. We only need to know their ratio, which gives us the characteristic length

$$l=\sqrt{\kappa/\beta}. \tag{34}$$

Such length serves as a small multiplier for the highest (second) spatial derivative of the mass density and, consequently, it causes solution of the boundary layer type. This boundary layer regularizes the crack width suppressing the pathological mesh sensitivity.

Some results of modeling propagation of a single crack and bridging of two cracks are shown in Fig. 7. These simulations led to the following interesting conclusions.

First, the inertia forces play crucial role at the tip of the propagating crack. If inertia is not canceled together with the material stiffness, then cracks tend to nonphysically widen with the increasing speed of their propagation. Most existing

models of cracks completely ignore this fact and they do not cancel inertia when they cancel stiffness. Remarkably, the very recent works based on the phase-field formulations [67, 68] started recognizing the importance of canceling inertia. Needless to say, the simultaneous cancellation of stiffness and inertia are a direct consequence of the material sink formulation presented in this chapter.

Second, the proposed material sink formulation allows suppressing the *strong* or the classical pathological mesh-dependence linked to the zero energy fracture. The latter is due to the fact that the augmented initial boundary volume problem enforces characteristic length and solutions of the boundary layer type. The boundary layer, associated with the crack thickness does not vanish under the mesh refinement.

Third, we observed a *weak* mesh-dependence, which we defined as the effect of the mesh shape and size on the specific crack pattern. We observed that various meshes caused slightly different crack patterns for the same amount of dissipated energy. The weak mesh-dependence remained even after a significant mesh refinement, which showed that the regularized formulations were not a universal solution for any mesh sensitivity as many would expect. The weak mesh-dependence is similar to the effect of structural inhomogeneities in real materials, which affect the crack path depending on the specific sample under consideration. Though all samples are made of the same material they have various microstructural patterns and, consequently, slightly different propagating cracks.

4 Final Remarks

We presented review of our recent developments concerning analysis of failure and fracture in soft materials. Approaches for modeling failure and fracture are different. Failure is identified with the onset of material instability and damage. We considered such instability as a direct consequence of the bounded strain energy density. The bounded strain energy, in its turn, follows from the fact that the number of physical particles and their integral bond energy are limited. We presented a general formula allowing for the enforcement of energy bounds in the known hyperelastic models of soft materials and we called it elasticity with energy limiters.

After the onset, material damage localizes into cracks and they propagate. We call this process fracture. To model fracture, we introduced an augmented formulation, in which momenta and mass balance are coupled. The mass balance equation reflects upon the physical fact that broken bonds are diffused in the area of characteristic size rather than confined to a single atomic plane. The mass balance equation regularizes numerical simulations creating solutions of the boundary layer type and suppressing the pathological mesh-dependence. The latter means that refining the mesh one would not be able to reduce fracture energy to zero.

It is remarkable that the approaches described in the present work are based on two physical observations only: bond energy is bounded and broken bonds are diffused. Based on these observations it was possible to formulate theories of failure and fracture without introducing any internal variables.

Acknowledgment This research was supported by the Israel Science Foundation (grant No. 394/20).

References

1. Volokh KY (2019) Mechanics of soft materials. Springer, Singapore
2. Truesdell C, Noll W (2004) The non-linear field theories of mechanics. Springer, Berlin
3. Simo JC (1987) On a fully three-dimensional finite strain viscoelastic damage model: formulation and computational aspects. Comp Meth Appl Mech Eng 60:153–173
4. Govindjee S, Simo JC (1991) A micro-mechanically based continuum damage model of carbon black-filled rubbers incorporating the mullins effect. J Mech Phys Solids 39:87–112
5. Johnson MA, Beatty MF (1993) A constitutive equation for the Mullins effect in stress controlled in uniaxial extension experiments. Cont Mech Therm 5:301–318
6. Miehe C (1995) Discontinuous and continuous damage evolution in Ogden-type large-strain elastic materials. Eur J Mech A/Solids 14:697–720
7. De Souza Neto EA, Peric D, Owen DRJ (1998) Continuum modeling and numerical simulation of material damage at finite strains. Arch Comp Meth Eng 5:311–384
8. Ogden RW, Roxburgh DG (1999) A pseudo-elastic model for the Mullins effect in filled rubber. Proc Roy Soc Lond Ser A 455:2861–2877
9. Menzel A, Steinmann P (2001) A theoretical and computational framework for anisotropic continuum damage mechanics at large strains. Int J Solids Struct 38:9505–9523
10. Guo Z, Sluys L (2006) Computational modeling of the stress-softening phenomenon of rubber like materials under cyclic loading. Eur J Mech A/Solids 25:877–896
11. De Tommasi D, Puglisi G, Saccomandi G (2008) Localized vs diffuse damage in amorphous materials. Phys Rev Lett 100:085502.
12. Dal H, Kaliske M (2009) A micro-continuum-mechanical material model for failure of rubber-like materials: application to ageing-induced fracturing. J Mech Phys Solids 57:1340–1356
13. Volokh KY (2013) Review of the energy limiters approach to modeling failure of rubber. Rubber Chem Technol 86:470–487
14. Volokh KY (2007) Hyperelasticity with softening for modeling materials failure. J Mech Phys Solids 55:2237–2264
15. Volokh KY (2010) On modeling failure of rubberlike materials. Mech Res Commun 37:684–689
16. Volokh KY (2014) On irreversibility and dissipation in hyperelasticity with softening. J Appl Mech 81:074501
17. Hamdi A, Nait Abdelaziz M, Ait Hocine N, Heuillet P, Benseddiq N (2006) A fracture criterion of rubber-like materials under plane stress conditions. Polym Test 25:994–1005
18. Gent AN, Lindley PB (1959) Internal rupture of bonded rubber cylinders in tension. Proc Roy Soc A 2:195–205
19. Ball JM (1982) Discontinuous equilibrium solutions and cavitation in nonlinear elasticity. Phil Trans Roy Soc Lond A 306:557–610
20. Lev Y, Volokh KY (2016) On cavitation in rubberlike materials. J Appl Mech 83:044501
21. Volokh KY (2011) Cavitation instability in rubber. Int J Appl Mech 3:29311
22. Volokh KY (2015) Cavitation instability as a trigger of aneurysm rupture. Biomech Model Mechanobiol 14:1071–1079
23. Faye A, Rodrguez-Martnez JA, Volokh KY (2017) Spherical void expansion in rubber-like materials: the stabilizing effects of viscosity and inertia. Int J Non-Linear Mech 92:118–126
24. Lev Y, Faye A, Volokh KY (2019) Thermoelastic deformation and failure of rubberlike materials. J Mech Phys Solids 122:538–554

25. Aboudi J, Volokh KY (2015) Failure prediction of unidirectional composites undergoing large deformations. J Appl Mech 82:071004
26. Volokh KY, Aboudi J (2016) Aneurysm strength can decrease under calcification. J Mech Behav Biomed Mater 57:164–174
27. Slesarenko V, Volokh KY, Aboudi J, Rudykh S (2017) Understanding the strength of bioinspired soft composites. Int J Mech Sci 131–132:171–178
28. Volokh KY (2017) Loss of ellipticity in elasticity with energy limiters. Eur J Mech A Solids 63:36–42
29. Mythravaruni P, Volokh KY (2018) Failure of rubber bearings under combined shear and compression. J Appl Mech 85:074503
30. Mythravaruni P, Volokh KY (2019) On incompressibility constraint and crack direction in soft solids. J Appl Mech 86:101004
31. Volokh KY (2019) Constitutive model of human artery adventitia enhanced with a failure description. Mech Soft Mater 1:8
32. Mythravaruni P, Volokh KY (2020) On the onset of cracks in arteries. Mol Cell Biomech 17:1–17
33. Takahashi Y (2012) Damage of rubber bearings and dumpers of bridges in 2011 great East Japan earthquake. Proceedings of the International Symposium on Engineering, Lessons Learned from the 2011 Great East Japan Earthquake, March 1–4, Tokyo, Japan
34. Lee S, Pharr M (2019) Sideways and stable crack propagation in a silicone elastomer. PNAS 116:9251–9256
35. Sugita S, Matsumoto T (2017) Local distribution of collagen fibers determines crack initiation site and its propagation direction during aortic rupture. Biomech Model Mechnobiol 17:577–587
36. Griffith AA (1921) The phenomena of rupture and flow in solids. Philos Trans R Soc Lond A 221:163–198
37. Volokh KY, Trapper P (2008) Fracture toughness from the standpoint of softening hyperelasticity. J Mech Phys Solids 56:2459–2472
38. Barenblatt GI (1959) The formation of equilibrium cracks during brittle fracture. General ideas and hypotheses. Axially-symmetric cracks. J Appl Math Mech 23:622–636
39. Needleman A (1987) A continuum model for void nucleation by inclusion debonding. J Appl Mech 54:525–531
40. Rice JR, Wang JS (1989) Embrittlement of interfaces by solute segregation. Mater Sci Eng A 107:23–40
41. Tvergaard V, Hutchinson JW (1992) The relation between crack growth resistance and fracture process parameters in elastic-plastic solids. J Mech Phys Solids 40:1377–1397
42. Camacho GT, Ortiz M (1996) Computational modeling of impact damage in brittle materials. Int J Solids Struct 33:2899–2938
43. de Borst R (2001) Some recent issues in computational failure mechanics. Int J Numer Meth Eng 52:63–95
44. Xu XP, Needleman A (1994) Numerical simulations of fast crack growth in brittle solids. J Mech Phys Solids 42:1397–1434
45. Moes N, Dolbow J, Belytschko T (1999) A finite element method for crack without remeshing. Int J Num Meth Eng 46:131–150
46. Park K, Paulino GH, Roesler JR (2009) A unified potential-based cohesive model of mixed-mode fracture. J Mech Phys Solids 57:891–908
47. Gong B, Paggi M, Carpinteri A (2012) A cohesive crack model coupled with damage for interface fatigue problems. Int J Fract 137:91–104
48. Kachanov LM (1958) Time of the rupture process under creep conditions. Izvestiia Akademii Nauk SSSR, Otdelenie Teckhnicheskikh Nauk 8:26–31
49. Gurson AL (1977) Continuum theory of ductile rupture by void nucleation and growth: part I-yield criteria and flow rules for porous ductile media. J Eng Mat Tech 99:2–151

50. Voyiadjis GZ, Kattan PI (1992) A plasticity-damage theory for large deformation of solids—I. Theoretical formulation. Int J Eng Sci 30:1089–1108
51. Gao H, Klein P (1998) Numerical simulation of crack growth in an isotropic solid with randomized internal cohesive bonds. J Mech Phys Solids 46:187–218
52. Klein P, Gao H (1998) Crack nucleation and growth as strain localization in a virtual-bond continuum. Eng Fract Mech 61:21–48
53. Lemaitre J, Desmorat R (2005) Engineering damage mechanics: ductile, creep, fatigue and brittle failures. Springer, Berlin
54. Volokh KY (2004) Nonlinear elasticity for modeling fracture of isotropic brittle solids. J Appl Mech 71:141–143
55. Benzerga AA, Leblond JB, Needleman A, Tvergaard V (2016) Ductile failure modeling. Int J Fract 201:29–80
56. Pijaudier-Cabot G, Bazant ZP (1987) Nonlocal damage theory. J Eng Mech 113:1512–1533
57. Lasry D, Belytschko T (1988) Localization limiters in transient problems. Int J Solids Struct 24:581–597
58. Peerlings RHJ, de Borst R, Brekelmans WAM, de Vree JHP (1996) Gradient enhanced damage for quasi-brittle materials. Int J Num Meth Eng 39:3391–3403
59. de Borst R, van der Giessen E (1998) Material instabilities in solids. Wiley, Chichester
60. Silling SA (2000) Reformulation of elasticity theory for discontinuities and long-range forces. J Mech Phys Solids 48:175–209
61. Francfort GA, Marigo JJ (1998) Revisiting brittle fracture as an energy minimization problem. J Mech Phys Solids 46:1319–1342
62. Hofacker M, Miehe C (2012) Continuum phase field modeling of dynamic fracture: variational principles and staggered FE implementation. Int J Fract 178:113–129
63. Borden MJ, Verhoosel CV, Scott MA, Hughes TJR, Landis CM (2012) A phase-field description of dynamic brittle fracture. Comp Meth Appl Mech Eng 217–220:77–95
64. Volokh KY (2017) Fracture as a material sink. Mater Theory 1:3
65. Persson BNJ, Albohr O, Heinrich G, Ueba H (2005) Crack propagation in rubber-like materials. J Phys Condens Matter 17:R1071–R1142
66. Faye A, Lev Y, Volokh KY (2019) The effect of local inertia around the crack tip in dynamic fracture of soft materials. Mech Soft Mater 1:4
67. Chen CH, Bouchbinder E, Karma A (2017) Instability in dynamic fracture and the failure of the classical theory of cracks. Nat Phys 13:1186
68. Agrawal V, Dayal K (2017) Dependence of equilibrium Griffith surface energy on crack speed in phase-field models for fracture coupled to elastodynamics. Int J Fract 207:243–249

Adv Polym Sci (2021) 286: 153–178
https://doi.org/10.1007/12_2020_82

Published online: 11 December 2020

Influence of Filler Induced Cracks on the Statistical Lifetime of Rubber: A Review

Jens Meier, Stefan Robin, Marvin Ludwig, and Mohammed El Yaagoubi

Contents

J. Meier (✉)
Deutsches Institut für Kautschuktechnologie e. V., Hannover, Germany
e-mail: jens.meier@dikautschuk.de

S. Robin
Semperit Profiles Leeser GmbH, Hückelhoven, Germany

M. Ludwig
Meteor Elastomer Solutions GmbH, Bockenem, Germany

M. El Yaagoubi
MS-Schramberg GmbH and Co. KG, Schramberg, Germany

Abstract A concept for the estimation of lifetime cycles is discussed assuming non-dispersed filler particles as origins of initial cracks which propagate under dynamic load according to fatigue crack growth (FCG) characteristics until failure occurs. Reference EPDM compounds with glass spheres of well defined size show strong correlation of the fatigue to failure analysis (FFA) behavior of dumbbells with largest incorporated particles, but dependence on polymer filler interaction, too. For NR and EPDM compounds, the occurrence of incorporated large particles is investigated by computed tomography and evaluated to a flaw size statistic. Based on the assumption of initial crack sizes matching the flaw diameters and together with the characteristic material parameters from FCG analysis, a statistical concept for the prediction of FFA lifetime analysis is presented. Predictions for near-homogeneously deforming dumbbell samples with carbon black (CB) reinforced NR display a particle size distribution which in combination with FCG results allows to calculate quantitative lifetime accordant to experimental findings, i.e. compounding dependency by shorter lifetime for worse dispersion and geometry dependency by longer lifetime for smaller specimens. An extension of the prediction concept for non-homogeneous deformation states is shown through a Monte Carlo simulation varying the positions of flaws inside the sample together with a Finite Element Analysis based calculation of the accordant local J-integral value. The simulations of lifetime statistics for rotational-parabolic buffer samples made of CB filled NR or EPDM show significant effects in average value and distribution width similarly found in experiment. This lifetime prediction concept has the unique capability to take into account not only recipe controlled matrix properties as cyclic crack propagation resistivity but volume dependency and processing related dispersion state, too in a quantitative manner.

Keywords Crack initiation · Elastomer · Fatigue crack growth · Fatigue to failure · Filler dispersion · Flaw size statistic · Lifetime simulation

1 Introduction

The service life properties of rubber components are still not fully understood with regard to the underlying mechanisms. Based on the work of August Wöhler on the fracture mechanics of steel [1], more recent FFA studies for technical rubber consider that any crack has its origin on an initiating flaw and grows driven by subsequent cyclic load up to the ultimately catastrophic failure [2, 3]. Characteristic material parameters supposed to connect the FCG behavior with the service life performance are polymer microstructure, molecular mass distribution, long chain branching, crosslinking structure, filler dispersion as well as size and probability of flaws in the compound. Flaws may origin from hard or soft inclusions, from polymer inhomogeneity, recipe ingredients or molding [2]. Here, we focus on filler dispersion and the assumptive identification of the relevant flaws with largest filler particles

occurring with diameters 50–500 μm, as found within many optical investigations [4].

The reinforcement of rubber compounds by fillers, e.g. carbon black is a well-established technique, but one known problem during the incorporation of the filler is the acquired state of particle size dispersion, which has been found to correlate with endurance of articles under cyclic loading [3, 5, 6]. Recent investigations show that the well-known correlation of rubber parts fatigue lifetime with both, FCG resistivity and particle size distribution can be combined quantitatively to suggest a unification of fracture mechanics and the Wöhler concept [5].

1.1 Reinforcement of Elastomers

Technical rubber compounds in many cases contain active filler to reinforce the mechanical properties of the elastomer matrix and of the vulcanized rubber, too. The term reinforcement refers to specific requirement of application, but in many cases simultaneous increase of modulus, elongation at break and wear resistance can be achieved with respect to the unfilled compound [7–10].

At micrometer scale, the increase of the small strain modulus of a vulcanized rubber with higher filler volume fraction was explained by Einstein and Smallwood [11, 12], arguing with infinite stiff particles. At smaller scales, reinforcement efficiency is related to the filler-polymer interaction attributed to the specific surface and to the surface activity of the filler [13]. Active fillers, such as carbon blacks or silica, interact with the rubber matrix, bind the polymer chains to their surface and thus restrict their mobility. A layer of immobilized polymer (bound rubber) forms around the filler particles, and with filler concentrations above the percolation limit two significant effects can be observed. First, a pronounced rise of the material stiffness is found, which can be explained with the assumption of the establishment of a filler network, e.g. within the dynamic flocculation network model (DFM) introduced by Klüppel et al. [14, 15]. Second, the stiffness ceases with repetitive loading under successively increase of the amplitude as reported by Payne [16], Mullins [17, 18], and Bueche [19]. Generally, filler reinforcement of elastomers results in a change in the viscoelastic properties and in an improvement of both, breakage or abrasion behavior and crack propagation resistivity, too [20–23].

1.2 Filler Dispersion

In rubber technology, the mixing process is found as highly relevant for the quality of a compound, with respect to both chemical and physical homogeneity and it influences basic as well as ultimate properties of the elastomer [9, 24, 25]. Apart from the intended network formed by fine filler particles of sub-micrometer size, undispersed particles of size 50–500 μm can be found within technical rubber

compounds [26, 27]. Such particle size origins from the production process where a specific size distribution is generated. During compound mixing, sufficiently high shear stress can break large particles and the size distribution shifts towards smaller values [28]. Through examinations by scanning electron microscopy and computed tomography, it is known that the largest particles are often found as the starting point for material failure [29–31]. Aims to enhance particle breakage with further increase of shear rate during mixing are often limited by the associated higher energy-dissipative heat build-up causing unwanted polymer chain degradation [32].

1.3 Origins of Cracks

In globally homogeneous loading, e.g. uniaxial conditions a non-homogeneous material consisting of ingredients with different stiffness will locally display inhomogeneous strain and stress distribution at the interphase of ingredients. Hence, hard filler particles incorporated into a soft matrix can be considered as stress raisers for the surrounding matrix material [33]. Initial cracks in filler reinforced vulcanizates can occur due to binding failure between polymer and filler. This motivates the assumption to identify the filler particles as flaws and their diameter as the sizes of initial cracks [5].

2 Modeling

Here, at first the fracture mechanical concept is outlined. Moreover the statistical concept for the estimation of particle sizes in a specimen is described and the combination of both to predict a lifetime for a homogeneous loadcase. Finally a general consideration for an inhomogeneous loadcase is formulated.

2.1 Linear Fracture Mechanics

The basic energy concept of fracture mechanics by Griffith [34] and Irwin [35] argues that a crack grows exactly when the energy released while the crack length and the crack surface increase is larger than the energy that must be used to create a new crack surface or crack length, referred to as the tearing energy T or G. Here a pure tensile stress of a purely linear-elastic material is assumed, only valid limited for rubber but found to allow for good approximations in the estimation of the material failure behavior [36, 37]. Determination of the energy release rate was done according to Rivlin [38] for a the single edge notch tensile (SENT) stripe shown in Fig. 1 left, characterized by initial specimen length, L, width, W, and thickness, H. A cyclically applied displacement amplitude, ΔL, results in a reaction force, F, and in

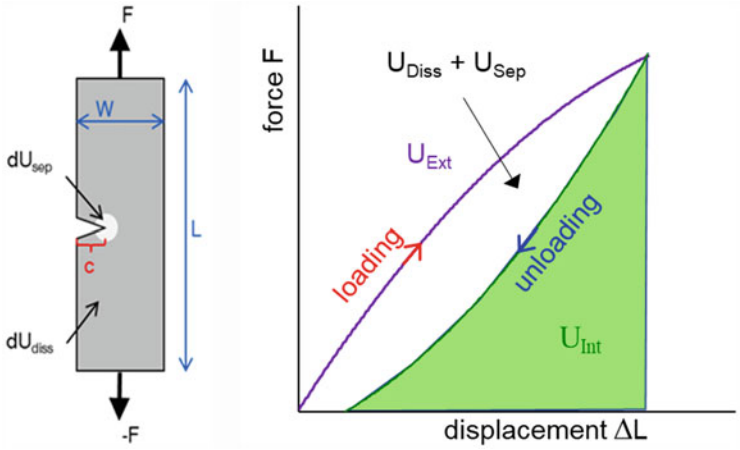

Fig. 1 Single edge notch tensile (SENT) stripe under uniaxial load; left: energy contributions, right: force-deflection curve

growth of the crack length, c. With the total mechanical potential, U_{Ext}, consisting of internally stored energy, U_{Int}, dissipated energy, U_{Diss}, and the separation energy, U_{Sep}, associated to an increase, dc, of the crack length, c, the energy balance is given as in Eq. (1).

With the cycle count n, an infinitesimal fatigue crack growth rate $r = \frac{dc}{dn}$, occurring at constant displacement ΔL can be considered. In this case, the right side of (1) gives the Griffith criterium for the minimal required energy release rate G necessary for crack growth [39].

$$\frac{dU_{\mathrm{Ext}}}{dA} - \frac{dU_{\mathrm{Int}}}{dA} = \frac{dU_{\mathrm{Sep}}}{dA} + \frac{dU_{\mathrm{Diss}}}{dA} \tag{1}$$

$$G = -\frac{dU_{\mathrm{Int}}}{dA} > \frac{dU_{\mathrm{Sep}}}{dA} \tag{2}$$

Thomas and Rivlin derived that crack propagation depends only on the tearing energy, T correlated to the energy density and the specimen geometry [38]. Lake and Thomas proved that the energy release rate is a material parameter independent of test specimen geometry [40]. The local tearing energy at the crack tip of a SENT specimen depends on the elastic part of the global energy density [2, 41]:

$$T = 2kW_{\mathrm{el}}c \quad (a), \quad k = \frac{\pi}{(1+\varepsilon)^{0.5}} \quad (b) \tag{3}$$

With global strain, ε, and elastic energy density, W_{el}.

Here, the simplifying assumption is made that the elastic energy determined via the integral of the unloading half-cycle of the force-deflection curve as indicated by

the shaded area in Fig. 1, right is used completely for the FCG evaluation [42]. For many materials, there is an amplitude regime where the dependence of the FCG rate on the tearing energy can be fitted according Paris-Erdogan with [36]:

$$\frac{dc}{dn} = B \cdot T^{\beta} \tag{4}$$

where B and β are material constants to be determined by FCG experiments.

The integrated form of (4) allows for a calculation of the number of cycles n necessary for a crack with the initial crack length, c_0, to grow to the length of c_n:

$$n = \frac{1}{\beta - 1} \cdot \frac{1}{B(2kW)^{\beta}} \cdot \left(\frac{1}{c_0^{\beta-1}} - \frac{1}{c_n^{\beta-1}} \right). \tag{5}$$

2.2 Statistical Modeling of Lifetime for Homogeneous Load Case

2.2.1 Particle Size Distribution

If a specimen contains only one particle as single flaw, for well definded loading a lifetime cycle number is predictable using Eq. (5). This can be done by identifying the initial crack length with the diameter of that particle and the final crack length with the specimen diameter. But for a technical compound grade with particles of non-unique size, the specific particle size density distribution is required to evaluate the specimen specific probability of particle size content and hence the probability of FFA cycle numbers. For this, a phenomenologically chosen logarithmic normal distribution function was chosen to represent the particle size distribution density.

$$f(c_0) = \frac{A}{\sigma c_0 \sqrt{2\pi}} \mathrm{e}^{\left(-\frac{\ln\left(\frac{c_0}{\mu}\right)^2}{2\sigma^2} \right)} \tag{6}$$

2.2.2 Estimation of Fatigue Lifetime

The lifetime prediction concept considers a specimen exposed to a homogeneous periodic load case, where the diameter of each incorporated particle is identified as the length of an associated crack. Such a crack grows during each cycle according to the material specific dynamic crack propagation resistivity until failure of the specimen. Particles size distributions found with any method have to be seen with respect to the investigated volume. Hence, a density function can be considered. In

estimations of occurrence of bigger flaws in a given sample the actual volume is to be considered. To estimate the occurrence of differently sized particles in a sub-volume V_{test} taken for specimens, here a multinomial distribution concept is assumed as shown by Ludwig [43].With the volume V_{CT} investigated by CT for particle size distribution, the probability function for specimen failure at cycle number n is found as:

$$P(n) = 1 - \left(\frac{V_{\text{CT}} - V_{\text{test}}}{V_{\text{CT}}}\right)^{V_{\text{CT}} f(c_0(n))} \tag{7}$$

In the exponent, by conversion of Eq. (5) the particle size c_0 associated with the cycle number is given as:

$$c_0(n) = \left(n(\beta - 1)B(2kW_{\text{el}})^{\beta} + \frac{1}{c_n^{\beta-1}}\right)^{\frac{1}{1-\beta}} \tag{8}$$

In Eq. (7), the explicit reference to the volume, V_{CT}, is relevant, since sampling V_{Test} from a larger volume reduces the probability of rare particles occurring in the test volume. Since the biggest flaws typically are the most seldom, it can be assumed that for a given specimen the probability of containing a particle depends on the volume of the specimen, as is visualized in Fig. 3. The final crack length c_n is now a free-of-choice failure criterium and is chosen as sample center diameter in the following. From the derivative of Eq. (7) with respect to cycle number, the failure probability density function $p(n)$ results, allowing to calculate the expected value $E_{\text{n}}(n)$ [43]:

$$p(n) = \frac{dP(n)}{\mathrm{d}n} \tag{9}$$

$$E_n(n) = \int n\, p(n) dn \tag{10}$$

2.3 Constitutive Modeling for Non-homogeneous Load Case

Lifetime evaluation for non-homogeneous deformation states can be done with three-dimensional FEA simulation of the cyclic behavior for the full specimen. Since the considered rubbers display effects like stress softening, hysteresis, and permanent set, for FEA calculations the inelastic material model "Model of Rubber Phenomenology" (MORPH) developed by Besdo and Ihlemann [44] was chosen to describe this effects typically found for filled rubber. The model considers a decomposition of the Cauchy stress $\boldsymbol{\sigma}$ into three tensorial terms:

$$\boldsymbol{\sigma} = \left(2\alpha\mathbf{b} + \boldsymbol{\sigma}^{Z}\right)' - p\mathbf{I} \tag{11}$$

With the basic stress $2\alpha\mathbf{b}$ which is similar to the Neo Hookean stress definition, the auxiliary stress for nonlinear elastic and inelastic effects $\boldsymbol{\sigma}^{Z}$ and the hydrostatic pressure $p\mathbf{I}$. Material parameters were fitted based on quasistatic measurements in cyclic multi-step mode with increasing maxima for uniaxial, equibiaxial, and shear mode. An in-depth discussion of the MORPH model and the acquirement of parameters for the material NR 1 defined in the experimental part is given in [45].

Simulation results were evaluated at each element for stress and energy density distribution taking into account only the cyclic turning points of the investigated specimen. The elastic energy in Eq. (3) is substituted by the total energy W_{tot}. Additionally, a relationship between the J-integral and the total energy density found by Yaagoubi et al. from FEA simulation of SENT-specimens of NR is used [45]:

$$J = \eta \cdot c_0 \cdot W_{\text{tot}} \tag{12}$$

with a material specific constant η, fitted according uniaxial tension measurements with SENT specimens and simulations to the value 2.20 for NR 1.

3 Experimental

3.1 Material and Sample Preparation

3.1.1 Model Compounds with Glass Spheres

To validate the assumption that the biggest flaw is the main source of crack initiation, the design of a technical elastomer compound with a well-defined maximum flaw in the form of spherical glass particles has already be considered by Abraham et al. [3, 46]. Here, in contrast, the first compound series was done as relevance study for particle–polymer interaction, too by using glass spheres with and without surface silanization [47].

The reference compound E-Ref is based on a polymer Ethylene Propylene Diene M-type rubber (EPDM) Buna EPG 5450 comprising 48 to 56 wt.% ethylene and 3.7 bis 4.9 wt.% ethylidene norbonene. The other ingredients are 40 phr oil Sunpar 2,280, 50 phr CB N-550, 4 phr ZnO, 2 phr stearic acid, 0.7 phr Sulfur, 1 phr TBBS, 3.5 phr TBzTD. This series was compounded with internal mixer Haake Polylab System with Rheomix 600 attachment, all with starting temperature of 40°C, rotation speed 40 rpm, and mixing time of 4 min. Based on the reference compound, variations are with sieved glass spheres of size 110 µm (E-G110), and with same glass spheres functionalized with silane (E-G110-Si). Another variation contains glass spheres of size 180 µm (E-G180).

3.1.2 Technical Compound Grades

The compound recipes of the main investigated materials are listed in Table 1. The polymers types are ethylene propylene diene monomer Keltan 4450 (EPDM) and natural rubber TSR CV 60 (NR). Reinforcing filler is carbon black N347 (CB) with 50 phr. Crosslinking is based on semi-efficient sulfur systems together with additives stearic acid and ZnO. Other ingredients are IPPD as aging protection, Oil type Sunpar 2,280, antioxidant N-Isopropyl-N-phenyl-4-phenylenediamine (IPPD), Zinc Oxide (Zn O). The crosslinking system comprises Sulfur, together with N-tert-butyl-2-benzothiazole sulfenamide (TBBS) and accelerator Tetrabenzyl thiuram disulphide Thiuram (TBzTD) for the EPDM compound and with N-cyclohexyl benzothiazyl sulphenamide (CBS) and Tetramethylthiuram disulfide (TMTD) for the NR compounds, ozone, and weathering protection (Antilux 500). Mixing was done with Werner & Pfleiderer GK 1,5 E. For each compound, the mixing parameters were chosen to achieve fine dispersion. Curing was done at appropriate temperature considering t_{90} time from rheometer curve plus additional 1 min per millimeter of sample thickness or diameter. Compounds NR 1 and NR 2 are with the same recipe but different mixing. Total mixing time is 5 min, but CB is added to NR 1 and NR 2 after 2 min and after 4 min, respectively.

3.2 *Test Methods*

3.2.1 Computed Tomography

Compound analysis for statistical filler size distribution was done with 3-D computed tomography (CT) by use of Phoenix Nanotom 1,400 [48]. As computed tomography is non-destructive, the same specimen can be investigated as they are scheduled for further fatigue lifetime investigation. Each measurement was done in

Table 1 Compound recipes of the main material used

EPDM 1		NR 1/NR 2	
Component	phr	Component	phr
EPDM	100	NR	100
N347	50	N347	50
Oil	40	IPPD	2
Zn O	4	TMQ	1
Stearic acid	2	Antilux 500	2
		Zn O	5
		Stearic acid	2
Crosslinking system			
Sulfur	0,7	Sulfur	1,5
TBBS	1	CBS	2
TBzTD	3,5	TMTD	0,2

Fig. 2 Density contrast for a CT investigation reconstruction for CB filled NR material, voxel size 9 µm [29]

parallel with a graphite standard for calibration of gray value evaluation referring to density. By CT analysis of at least 5 dumbbell specimens, a totally tested volume, V_{CT}, of at least 15.000 mm^3 is realized, with a resolution limit of 15 µm. A reconstruction for the density distribution of a CB filled NR compound is shown in Fig. 2, where areas of higher density are in blue color.

Based on CT generated gray scale data, particle size statistics were evaluated with the use of the software ImageJ from U. S. National Institutes of Health [49]. The evaluation of particle size distribution by CT cannot be considered as absolute. Machine specification, choice of X-ray beam intensity parameters, material ingredient densities, sample size, and positioning effect on the result [29]. Hence, all such parameters are kept constant for this evaluation.

For the model compounds with glass sphere, particle size fractions was evaluated by inspection of vulcanizate cutting planes with optical Dispersion Index Analysis System (DIAS) [4].

3.2.2 Fatigue Crack Growth Analysis

FCG was investigated with Tear and Fatigue Analyser (TFA©, Coesfeld GmbH & Co. KG, Germany) on Single Edge Notched Tensile (SENT) specimens (L: 60 mm, W: 16 mm, H: 1.6 mm, initial crack length 1 mm). The detailed description of the TFA equipment can be found in [50, 51]. Loading was done in non-relaxing conditions with a 50 ms Gauss pulse loading which is the pulse width and a repeating frequency of 10 Hz together with a static underload of 2 N (approx. 0.1 MPa). The temperature was ambient room temperature (RT). A minimum of 3 specimens per material and deformation stage was tested [43, 47].

Tearing energy according to Eq. (3) is evaluated with elastic part of the Energy density taking into account the unloading force-deflection data from machine. Only from the linear range of the crack growth, the crack growth rate with respect to cycle number is taken for parameter fitting according to Eq. (4).

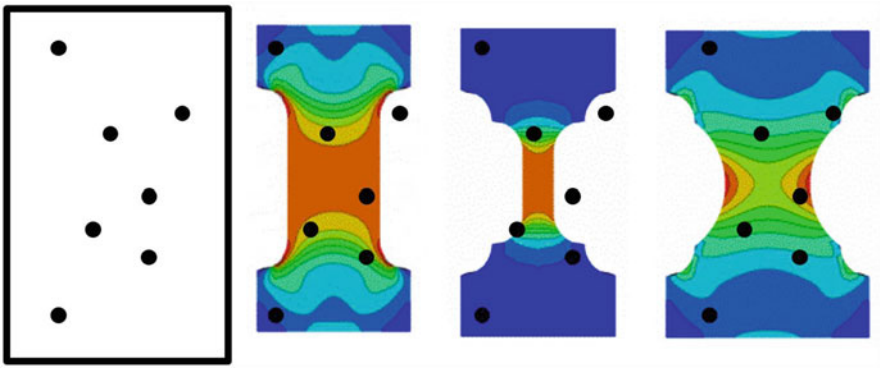

Fig. 3 Shape of rotational symmetric specimen with similar scaling; colors indicate stress distribution; points symbol large particles; compound with large particles, standard dumbbell, slim dumbbell, buffer (left to right)

3.2.3 Fatigue Lifetime Testing

FFA was carried out at room temperature with servo hydraulic testing systems MTS 831.50 Teststar Classic and MTS-322.21 Biaxial System in sinusoidal force excitation in full relaxing conditions at frequency 1 Hz pronounced heat build-up.

All samples are rotational symmetric and with similar full height 50 mm (Fig. 3). The nominal stress maximum σ_{max} is respective to the center cross section area, where the diameter is 15 mm for standard dumbbell and buffer but 5 mm for slim dumbbell. The ends with larger diameter are used for clamping. Exemplary, the time dependency of the surface temperature due to dissipative heat build-up has been recorded by means of an infrared camera. Quasi-stable surface temperature conditions was found after 1,000 cycles for all specimen shapes.

4 Results

At first, experimental findings for model compounds with varying glass sphere content will be discussed. Particle size fractions evaluated with optical method Dispersion Index Analysis System (DIAS) [4] are shown in Fig. 4. The largest particle size found is 50 µm for the unfilled compound whereas the E-G110 contains particles of size 110 µm and smaller. The diameter 165 µm of the largest particle surpasses the nominal width 110 µm of the mesh, which hence must be considered as having irregularities.

FCG rates of vulcanizates from these materials can be seen in Fig. 5. In comparison to the reference E-Ref, for E-G180 the addition of glass spheres results in similar slope of the Paris-Erdogan fitting curve, but with an offset indicating an increased FCG rate by a factor 2. Results for E-G110-Si display slightly higher rates

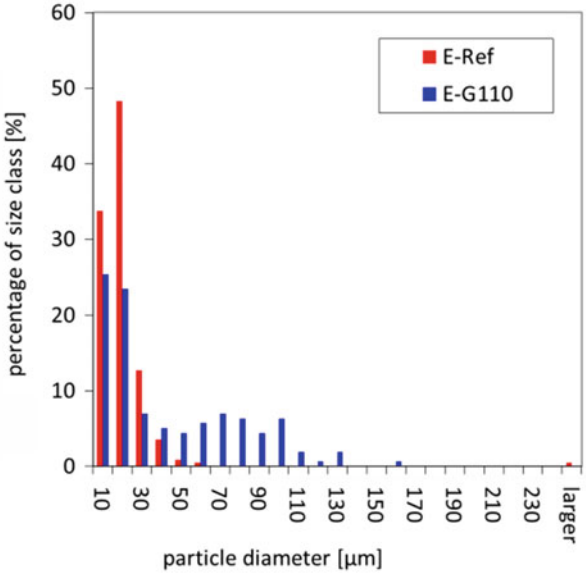

Fig. 4 Particle size fractions from optical method DIAS for E-Ref and E-G110

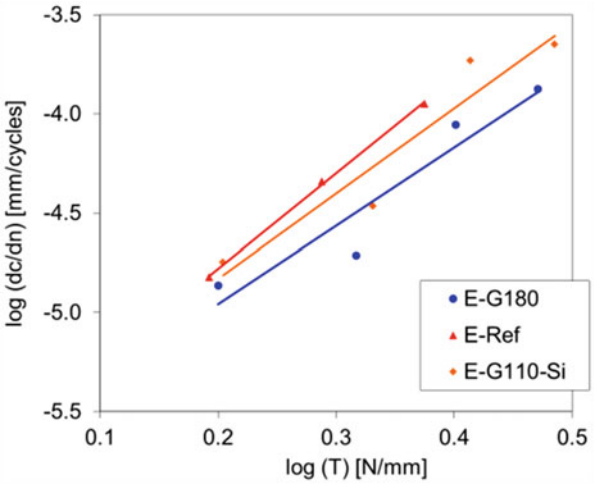

Fig. 5 Fatigue crack growth rate dependency on tearing energy for EPDM compounds with varying glass sphere content and silane bonding

than E-G180. This indicates first, that the presence of the glass spheres does not give pronounced rise to crack propagation and second, that the chemical binding of the silanized glass spheres' surface to the polymer matrix does not significantly influence FCG.

Wöhler curves as results from FFA with standard dumbbells from this material can be seen in Fig. 6. The highest cycle numbers are achieved with the reference E-Ref, but with a pronounced scattering especially at lowest amplitude. The cycle numbers found with the glass sphere containing material E-G110 are lower, at lowest

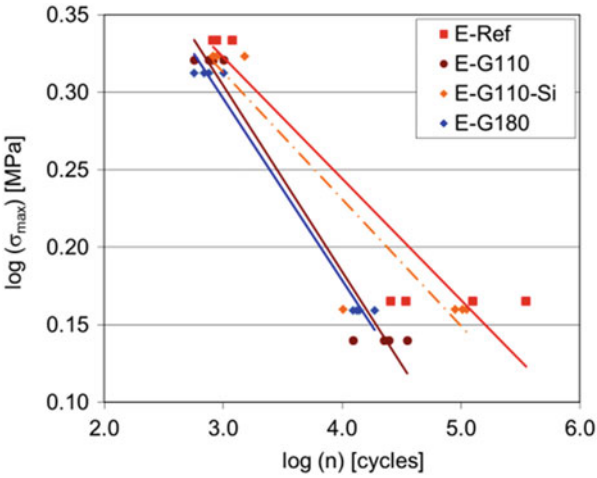

Fig. 6 Stress-load dependent fatigue life for EPDM compounds in variations of glass sphere content and silane bonding, full relaxing conditions

amplitude by a factor 10 and display significantly less scattering. This reduction in fatigue life cannot be contributed to the FCG rate. But it can be assumed that the lifetime limiting size of the biggest particle in the E-Ref specimens are varying due to filler particle size statistic, whereas in E-G110 the biggest particle diameter is about 110 μm due to the glass spheres so that high cycle numbers are suppressed resulting in only small cycle numbers with small scattering. This effect can be reduced if the glass spheres are silane-bound to the polymer as visible from the Wöhler data for E-G110-Si, even containing an outlier which reaches only 10,000 cycles. In comparison to E-G110, E-G180 with bigger glass spheres at same volume fraction shows again a slightly reduction of lifetime together with most narrow scattering.

From this experiment, it can be deduced, that lifetime in FFA depends on the matrix crack propagation resistivity, on the largest flaws – here identified as filler particle sizes and on the filler-polymer interaction.

4.1 Lifetime of Dumbbells in Near-Homogeneous Uniaxial Strain

In the following, for an CB reinforced NR with a distribution of particle size and consequently with a probability to find such particles in a specific specimen, the lifetime prediction concept is demonstrated and discussed considering the influence of filler dispersion, specimen volume, and load amplitude.

4.1.1 Particle Size Distribution

In Fig. 7a the particle size distribution from CT investigation of 10 dumbbell specimens each is shown for two grades of CB reinforced NR. The size classes are with width 10 µm. Generally, large sized particles are more seldom for both compounds, but for each size class, NR 1 contains less particles than the short-mixed NR 2. But within all size classes the short-mixed compound NR 2 contains more particles as NR 1. This can be explained by the longer time for CB incorporation for NR 1 according to the mixing procedure, resulting in higher probability of braking large particles into smaller ones and finally in an all-over better dispersion state, i.e. less particles on any of the scales visible with CT. This correlates with well-known experience about the influence of compounding method on dispersion state [9].

The total amount of detected CB reflects only a few percent of the total filler according the recipe. It is known from investigation by transmission electron microscopy that particle sizes of 50–200 nm occur quite frequently and this is supposed to be the most effective size for reinforcement. Otherwise the large particles are of interest for the estimation of crack initiators.

In Fig. 7 it can be seen, that with a phenomenologically chosen logarithmic normal distribution function given by Eq. (6) a fair fitting of the particle size distribution can be achieved by weighing logarithmic values resulting in the following parameter values for NR 1: $A = 0.034$, $\sigma = 0.640$, $\mu = 0.037$, correlation $R^2 = 0.9954$, and for NR 2: $A = 0.040$, $\sigma = 0.614$, $\mu = 0.050$, correlation $R^2 = 0.985$.

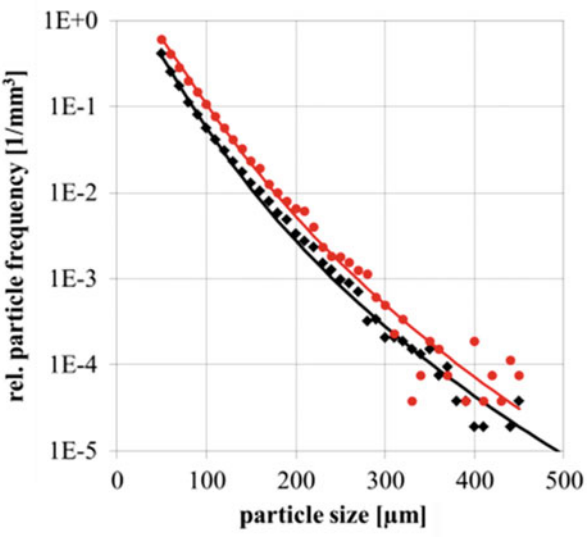

Fig. 7 Particle size distribution of NR compounds with size class width 10 µm; black: NR 1, red: NR 2; points: experimental, curves: fitting

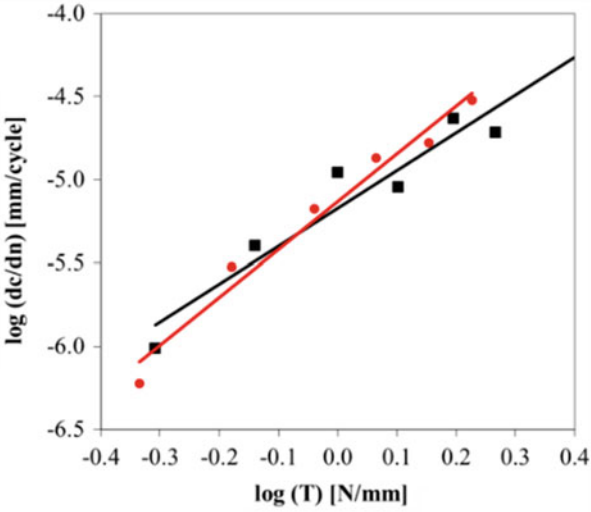

Fig. 8 Fatigue crack growth rate for SENT specimens of NR compounds; black: NR 1, red: NR 2; experimental medians (symbols) and Paris-Erdogan fitting (line) [6]

4.1.2 Fatigue Crack Growth Resistivity

In Tear Analyser experiments, NR 1 and NR 2 show nearly the same FCG rate "dc/dn" [9]. Obviously, the different flaw size distributions have just minimal impact on the FCG characteristics of both materials. For NR 1, the Paris-Erdogan parameters according Eq. (4) are: B [mm/cycle] = 6.730E-6, β = 2,271; and for NR 2: B = 7.396E-6, beta = 2.870 (Fig. 8).

4.1.3 Prediction for Load Amplitude Dependency

For standard dumbbells of NR1, in Fig. 9 a comparison of the experimentally determined failure cycle numbers with the numerically calculated failure probability density function (Eq. 9) is given for four load stages of elastic energy density. It can be seen that the simulations match reasonably with the scattering of the experimental values, with a mismatch of mean values less than 20%. The width of the simulated distributions reflects the probability of largest particle diameters in the specimen and is hence correlated with the particle size distribution (Fig. 7). Possible contributions to the deviations might come from FCG parameters strain or energy density, CT test volume, CT measurement parameters, and fitting procedure for the particle size distribution. Moreover, the local strains are not fully homogeneous, but with an excess strain in the curvature as can be seen from Fig. 3.

4.1.4 Prediction for Filler Dispersion Dependency

The effect of dispersion state on dumbbell lifetime can be seen in Fig. 10, where experimental fatigue life cycle and expected value (Eq. 10) from simulation for

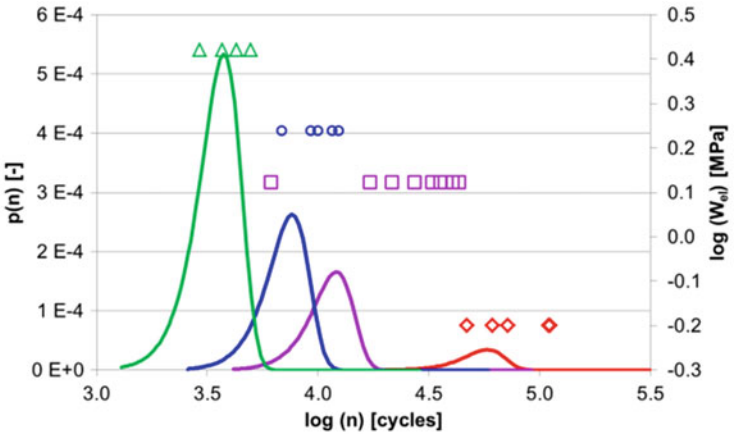

Fig. 9 FFA cycle numbers for NR 1 standard dumbbells at four elastic energy density amplitudes; experimental cycles (symbols); simulated probability density (curves)

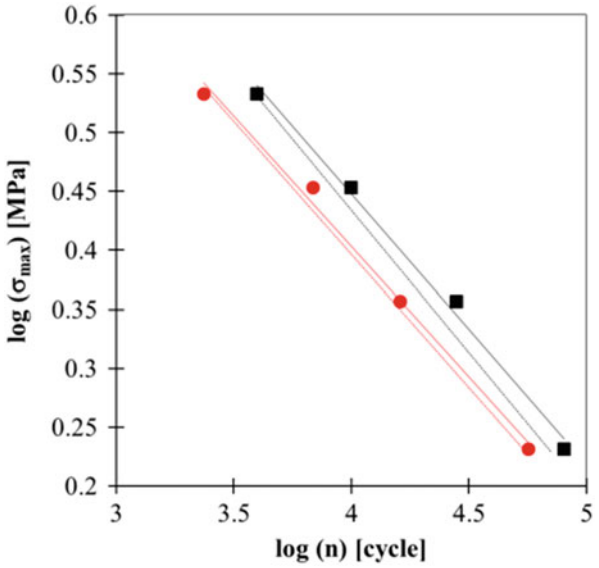

Fig. 10 FFA for two dispersion states: fine, NR1 (black) and coarse, NR2(red); experimental average (symbol) with Wöhler fit (continuous line), simulated expected values (dashed line) [43]

compounds varying in particle size statistics as shown in Fig. 7 are compared. The short-mixed NR 2 compound displays failure at significantly lower cycle numbers than the reference. This finding can be contributed to the higher probability of big particles which give rise to accordingly larger initial cracks and hence more early failure. Individual test specimens of the shorter mixed NR 2 achieve the service life

level of the longer mixed variant NR 1. This indicates the absence of major defects because of the statistical nature of the largest particle size, but overall the more thorough mixed compounds shows higher life cycle numbers.

4.1.5 Prediction for Test Volume Dependency

The choice of specimen shape affects the probability of large particle content. For experimental verification of such a volume selective effect on lifetime, the standard dumbbell type 1 is compared in contrast to a volume-reduced slim dumbbell type 2 which can be assumed as having less probability to contain large sized particles in the slim cylindrical area of highest load, as shown in Fig. 3 where blue and red colors indicate the areas to lowest and highest stress, respectively. Fatigue life results acquired for the two specimen geometries both of material NR 1 are shown in Fig. 11. Obviously due to the lower probability for occurrence of larger particles, the slim dumbbells reach larger cycles.

It should be noticed that the slim dumbbell displays less dissipation generated heating during the test because of the larger surface to volume ratio. At ambient temperature RT, maximum temperatures at surface are found with 33°C for the slim dumbbell and 45°C for the standard dumbbell. For comparison, three specimens of the slim dumbbell were tested at ambient temperature 45°C, resulting in slightly reduced lifetime cycles which are still larger by a factor 2 in comparison with the performance of the standard dumbbell at RT [43]. Recent investigations of Maanaoui et al. indicate the possibility to extend the evolved lifetime concept to consider temperature dependency, too [52]. For the temperature dependency of crack

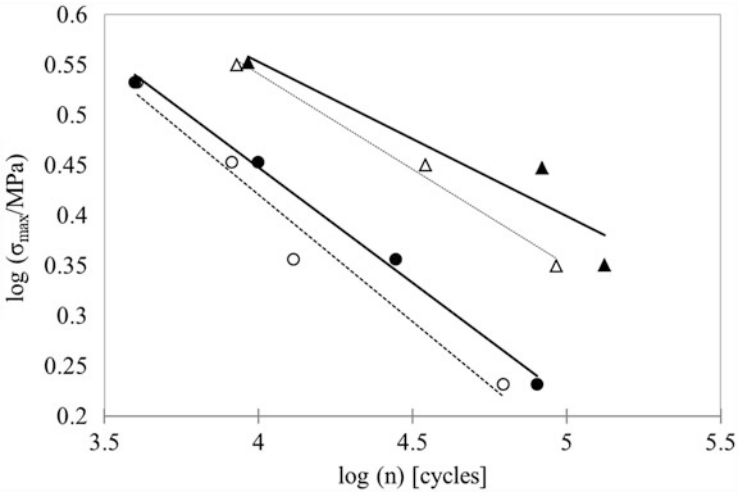

Fig. 11 FFA results for compound NR 1; dumbbell shape: standard (▲ Δ) and slim (● ○); full symbols: experiment; open symbols: simulation [43]

propagation behavior, Wunde et al. have shown that in principle a superposition concept can be applied [53].

4.2 Simulation for Non-homogeneous Deformation State

The dumbbell type 3 is larger in volume and should contain a higher amount of material defects than the standard dumbbell. Through the non-cylindrical design the local stress is not homogeneous. Only a small area with near-toroidal shape in the middle is excited critically. Despite the higher number of material defects in the whole specimen the probability to find big material defects in the critical volume is small compared to the other dumbbell types. Such a constitution-load-combination cannot be treated within the lifetime concept discussed so far.

But ongoing advances in computational performance during the last decades nowadays allow for numerical simulation of complex shaped rubber parts and investigation of transient development of crack growth up to fatigue failure is possible. Several paths have been followed, e.g. virtual crack extension [54], X-FEA [55, 56], and the development of concepts for crack nucleation [57, 58]. Following the line in this chapter, we now consider how to applicate the lifetime concept based on dispersion-caused crack nucleation and dynamic crack growth for non-homogeneously deforming rubber parts by means of finite element analysis (FEA) with estimation.

4.2.1 Validation for Non-homogeneous Deformation State

For non-homogeneous deformation states, the probability of presence of large particles in each load area must be considered. Hence, Monte Carlo simulation for Wöhler lifetime of NR 1 compound buffer samples is done in a post-processing manner. In each run first, a Weibull distribution of particles according the material specific particle size statistic is realized by assigning each particle an arbitrary element of the full specimen mesh position (Fig. 12a). Within the region of interest, it can be seen that particles smaller than 80 µm are much more frequent than particles larger than e.g. 160 µm.

In a second step, energy density and J-integral values are locally evaluated, the latter according Eq. (12) by taking the biggest particle in the actual element as initial crack size (Fig. 12b). The material specific constant η has been taken from the evaluation of SENT stripes as approximation, which of course does not reflect exactly the load situation in the buffer sample. Apparently, the highest J-integral values are at the waistline, directly on the sample surface.

As failure criteria, the final crack length, c_n, is chosen as the center diameter of the buffer sample which is 12 mm. The lifetime limit due to the actual element is calculated according Eq. (5) as shown in Fig. 12c. In comparison to Fig. 12b it can be seen that the shortest prospected lifetimes are not fully located at the

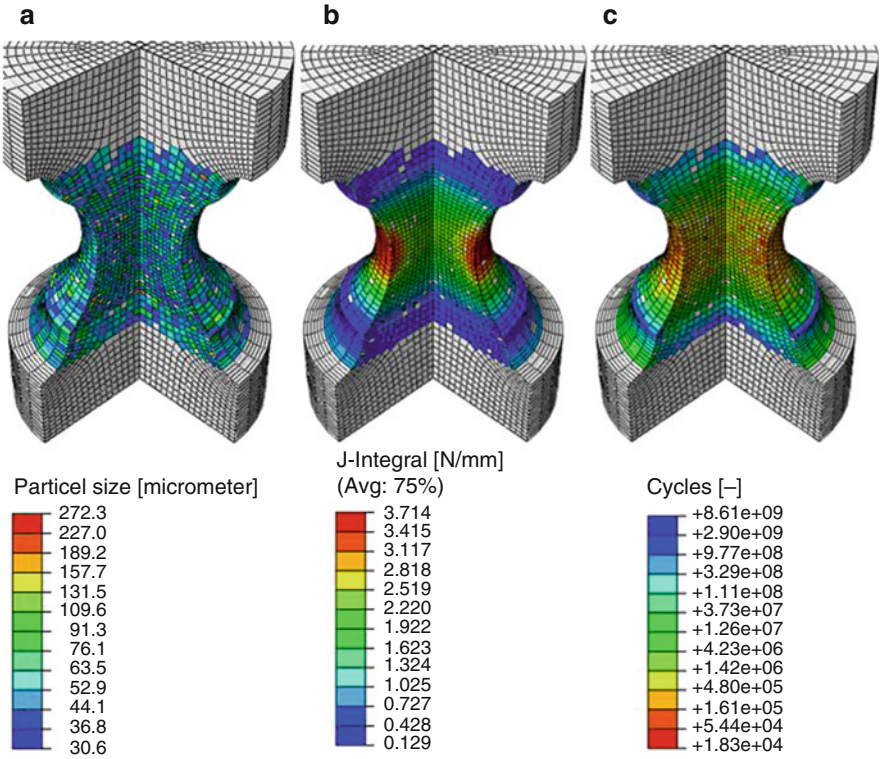

Fig. 12 Results from Monte Carlo FEA for the lifetime of an NR 1 buffer sample; (**a**) locally evaluated maximum particle size in elements; (**b**) Locally evaluated J-integral value in elements; (**c**) Locally evaluated full sample lifetime cycle limit due to single element

waistline. This is, because the lifetime values reflects now not only the local load situation but the diameter of the largest local flaw, too. But generally, volume areas of higher stress values are more selective for lifetime relevance of particles.

For each Monte Carlo run, the lifetime of the full sample is set to the minimum of locally evaluations form each element. After 1,000 Monte Carlo runs, a statistical consideration of lifetimes by a fitting with a logarithmic normal distribution can be done. The comparison of such predicted and measured life cycles is shown in Fig. 13. It can be seen that each prediction does not result only in a single value but in a distribution of lifetime. This is because of the double-inhomogeneity nature of the loaded buffer specimen. First, the local stresses and strains vary due to the curved shape of the buffer. Second, the probability density function for the particle size distribution has to be realized only within the actual volume of the buffer.

The predictions match the average lifetime at the different load stages quite well. Additionally, the spread of each distribution is of reasonable order. Recent studies on the influence of constitutive material law on such lifetime predictions show that with first invariant dependent Yeoh model [59] predictions can be made too but the

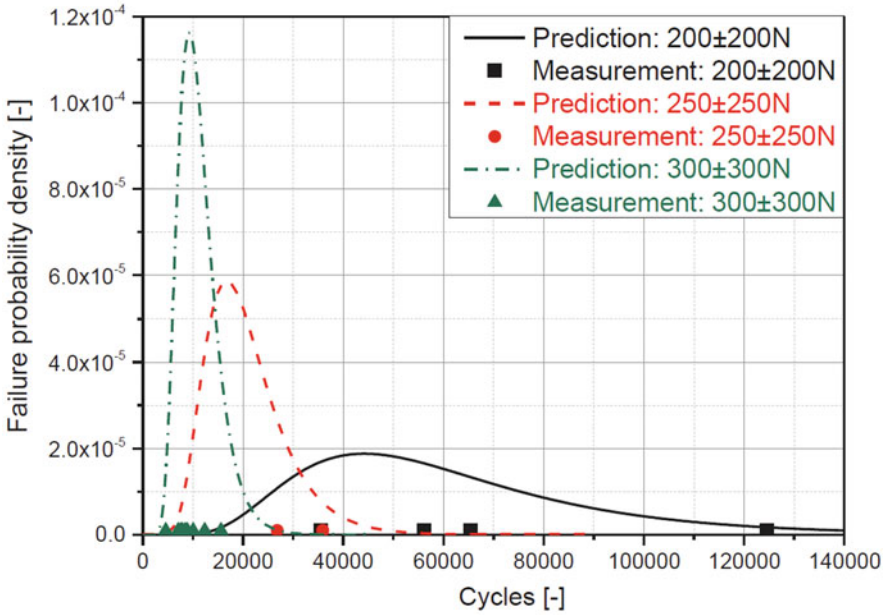

Fig. 13 Comparison between the lifetime prediction curves and the lifetime of measured buffer samples for NR 1; Reprint with permission, Copyright Elsevier (2018) [45]

selection of the amplitudes chosen for material parameter fitting affects the life cycle results by a factor of 2 to 3 [60].

As can be seen from Fig. 14, a similar investigation with CB reinforced EPDM 1 provides predictions in strong correlation with experimental findings at multiple load stages, as well as for NR 1. For both materials the simulations show a tendency for overestimation at higher loads. This might be contributed to the according more pronounced heat build. This effect is more pronounced for EPDM 1, which can be due to a larger full cycle hysteresis [45].

Of course, for the application of this method for more complex rubber parts, e.g. automotive bushings, the critical crack length must be adjusted to meet technical security requirements.

4.3 Limits of Concept

Here, the lifetime concept has been demonstrated by relying only on data generated with SENT stripes and evaluation of average elastic energy density or local J-integral value. Gehrmann et al. showed, that predictions for simple shear deformation are possible, too by determination of the material specific constant η from Eq. (12) for this mode [61]. But for general a strong relation between this constant and arbitrary

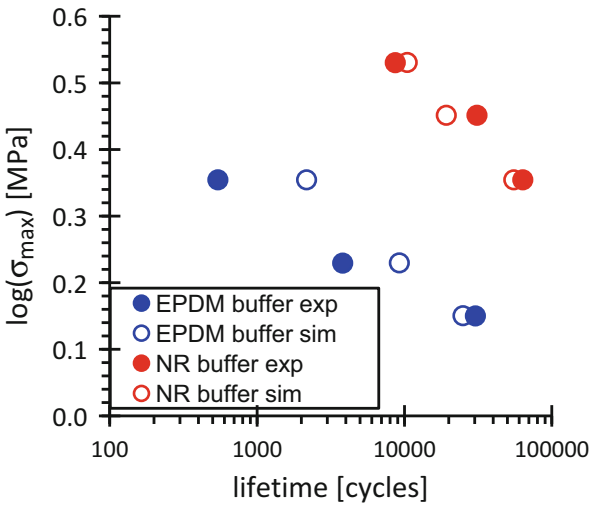

Fig. 14 Wöhler results for buffer dumbbells, experimental (full circles), and simulation (open circles) for compounds NR 1 (red) and EPDM 1 (blue); with numerical values from [45]

deformation mode is still desirable, especially in the application of FEA-postprocessing. For a more general consideration of local load cases a critical plane evaluation has been suggested by Fatemi [62] and applied, e.g. for rubber bushings by Barbash and Mars [63].

The influence of a static underload on FCG resistivity was reported by Abraham [64, 65]. El Maanaoui has shown that the prediction concept for FFA cycle numbers based on particle size statistics and crack propagation characteristics can be extended with a phenomenological approach for such non-relaxing conditions, at least for dumbbell specimens with cylindrical test area in uniaxial deformation mode [42].

The failure accumulation discussed does not take into account coalescence of multiple cracks which would reduce lifetime [58]. Polymer-filler interaction is not considered in explicit form as well as crosslinking inhomogeneities, energy-dissipative heating viscoelasticity [66] or chemical aging [67, 68].

Other lifetime concepts take into account local stress raising due to initial flaws origining from production process or specimen surface faults [58]. In principle, such defects can also taken into account within the presented concept, namely by an appropriately resolved FEA meshing.

In spite of this restriction, the unification concept of failure mechanics and the Wöhler fatigue by statistical considerations of flaws allows for more in-depth understanding of ultimate cyclic-dynamic properties of rubber materials.

5 Conclusions

By means of glass spheres as model flaws in an EPDM compound the impact of the initially largest flaw size on FFA lifetime was shown, which can be diminished by bonding of the glass spheres to the polymer matrix. CT has proven as useful for the evaluation of particle size distributions, although with not yet fully quantified uncertainty. Interpretation of particles larger than 50 μm as crack nucleation together with FCG properties allow for reasonable lifetime predictions for CB reinforced NR and EPDM compounds,

With an FEA based Monte Carlo approach for non-homogeneously deforming buffer sample it comes apparent, that the volume areas of higher stress values are selective for relevance of particles occurrence as crack initiators. This finding is of high relevance for lifetime optimization in article design.

The presented concept does only take into account the loading in the vicinity of the actual flaw and a preset fatal crack length. Hence, the estimated lifetime by accumulation of locally evaluated failure probabilities is not applicable for cases where crack propagation would diminish the energy density at the crack tip as might occur in complex shaped articles. Here, other approaches like X-FEM might be useful.

For more precise calculations, consideration of viscoelastic effects and filler-polymer interaction as well as an according refinement of the J-integral concept seem promising. The concept of fatigue life by crack propagation starting at initial flaws might be extended for other flaws, e.g. crosslinking density inhomogeneity or surface distorsions from molding or abrasion.

Acknowledgements The authors like to thank Dr. Thomas Alshuth for initialization, cooperation and many fruitful discussions through main parts of this research. Financial support is gratefully acknowledged from: Anvis Deutschland GmbH, Continental Reifen Deuschland GmbH, Freudenberg New Technologies SE & Co. KG, GMT Gummi-Metall-Technik GmbH, Henniges Automotive GmbH & Co. KG, Kaco GmbH & Co. KG, Parker Hannifin Manufacturing Germany GmbH & Co. KG, Polymer-Technik Elbe GmbH, Robert Bosch GmbH, Veritas AG.

References

1. Wöhler A (1870) Ueber die Festigkeits-Versuche mit Eisen und Stahl. Zeitschrift für Bauwesen Band XX:73–106
2. Gent A, Lindley P, Thomas A (1964) Cut growth and fatigue of rubbers I. The relationship between cut growth and fatigue. J Appl Polym Sci 8:455–466. (Reprinted in Rubber Chem Technol 38 (1965) pp 292–300)
3. Abraham F (2005) Testing and simulation of the influence of glass spheres on fatigue life and dynamic crack propagation of elastomers. In: Austrell PE, Kari L (eds) Constitutive models for rubber IV. Taylor & Francis, London, pp 71–76
4. Schuster RH, Geisler H, Bußmann D (1992) In: 2nd conference on carbon Black, Mulhouse 9

5. Robin S, Alshuth T (2013) Lifetime prediction- a unification of the fracture mechanics and the Wöhler concept. In: Gil-Negrete N, Alonso A (eds) Constitutive models for rubber VIII. Taylor & Francis, London, pp 405–407
6. Ludwig M, Alshuth T, El Yaagoubi M, Juhre D (2015) Lifetime prediction of elastomers based on statistical occurrence of material defects. In: Marvalova B, Petrikova I (eds) Constitutive models for rubber IX. Taylor & Francis, London, pp 445–448, Copyright (2015), with permission from Taylor and Francis Group, LLC, a division of Informa PLC. Rescaled reprint from
7. Medalia AI (1973) Rubber Chem Technol 46:877–896
8. Schuster RH (1989) Verstärkung von Elastomeren durch Ruß – Teil 1: Morphologie & Charakterisierung von Rußen; Wechselwirkung zw. Ruß und Kautschuk; Mechanisches Verhalten gefüllter Vulkanisate, W.d.K. (ed.), Grünes Buch Nr. 40
9. Schuster RH (1990) Verstärkung von Elastomeren durch Ruß – Teil 2: Dispersion, Hysterese & Reißverhalten; Zugfestigkeit, Bruchenergie und Abrieb, W.d.K. (ed.), Grünes Buch Nr. 41 (1990)
10. Donnet JB, Custodero E (2013) Reinforcement of elastomers by particulate fillers. In: Mark JE, Erman B, Roland CM (eds) The science and technology of rubber4th edn. Academic Press, New York, pp 383–416
11. Einstein A (1906) Eine neue Bestimmung der Moleküldimensionen. Ann Phys 19:289
12. Smallwood HM (1945) Rubber Chem Technol 18:292–305
13. Schröder A (2000) A. Charakterisierung verschiedener Rußtypen durch systematische statische Gasadsorption. Thesis, Gottfried Wilhelm Leibniz Universität Hannover, Hannover
14. Klüppel M (2003) The role of disorder in filler reinforcement of elastomers on various length scales. Adv Polym Sci 164:1–86
15. Lorenz H, Meier J, Klüppel M (2010) Micromechanics of internal friction of filler reinforced elastomers. In: Besdo D, Heimann B, Klüppel M, Kröger M, Wriggers P, Nackenhorst U (eds) Elastomere friction. LNACM, vol 51. Springer, Heidelberg, pp 27–52
16. Payne A (1962) The dynamic properties of carbon black-loaded natural rubber vulcanizates, part I. J Appl Polym Sci 6:57–63
17. Mullins L, Tobin NR (1965) Stress softening in rubber vulcanizates. Part I: use of a strain amplification factor to describe the elastic behaviour of filler-reinforced vulcanized rubber. J Appl Polym Sci 9:2293–3009
18. Mullins L, Tobin NR (1965) Stress softening in rubber vulcanizates. Part II: stress softening effects in pure cum and filler loaded rubbers. J Appl Polym Sci 9:3011–3021
19. Bueche F (1962) Mullins effect and rubber-filler interaction. Rubber Chem Technol 35:259–273
20. Dannenberg EM (1975) The effects of surface chemical interactions on the properties of filler-reinforced rubbers. Rubber Chem Technol 48:410–444
21. Lorenz H, Steinhauser D, Klüppel M (2013) Morphology and micro-mechanics of filled elastomer blends. In: Grellmann W et al (eds) Fracture mechanics and statistical mechanics of reinforced elastomeric blends. Springer, Berlin, pp 81–128
22. Müller M (2002) Einflussgrößen der Verstärkung elastomerer Werkstoffe durch Polymere und klassische Füllstoffe. Leibniz Universität Hannover, Hannover
23. Batzer H (1985) Polymere Werkstoffe. Thieme, Stuttgart
24. Limper A (2012) Mixing of rubber compounds. Hanser Verlag, München
25. Cotten G (1984) Mixing of carbon black with rubber I. measurement of dispersion rate by changes in mixing torque. Rubber Chem Technol 57:118–133
26. Edwards DC (1990) Polymer-filler interactions in rubber reinforcement. J Mater Sci 25:4175–4185
27. Tunnicliffe LB, Busfield JJC (2017) Reinforcement of rubber and filler network dynamics at small strains. In: Stöckelhuber KW, Das A, Klüppel M (eds) Designing of elastomer nanocomposites: from theory to applications. Springer, Cham, pp 71–102
28. Coran A, Donnet JB (1992) The dispersion of carbon black in rubber part I. rapid method for assessing quality of dispersion. Rubber Chem Technol 65:973–997

29. Robin S, Alshuth T (2010) Hochauflösende 3D-Röntgen-computertomographie (CT), Kautsch. Gummi Kunstst, pp 383–387
30. Robin S, Alshuth T (2012) Lifetime prediction- a unification of the fracture mechanics and the (Wöhler-) s-n-concept. In: Kautschuk Herbst Kolloquium, Hannover
31. Masquelier I (2014) Influence de la formulation Sur les propriétés en fatigue d'élastmères industriels. Université de Bretagne Occidentale, Brest
32. Eisele U (1990) Introduction to polymer physics. Springer, Berlin
33. Lake GJ (1983) Prog Rubber Technol 45:81
34. Griffith AA (1920) Philos Trans R Soc Lond Ser A 221:163
35. Irwin GR (1957) Analysis of stress and strain near the end of a crack fracture mechanics. J Appl Mech 24:361–364
36. Paris P, Gomez M, Anderson W (1961) A rational analytic theory of fatigue. Trend Eng 13:9–14
37. Paris P, Erdogan F (1963) A critical analysis of crack propagation laws. J Basic Eng 85:528–534
38. Rivlin RS, Thomas AG (1952) J Polym Sci 10(3):291
39. Griffith AA (1921) The phenomena of rupture and flow in solids. Philos Trans R Soc A 221:582–593
40. Lake GJ (1983) Prog Rubber Technol 45:102
41. Lake G, Lindley P (1964) Cut growth and fatigue of rubbers II. Experiments on a noncrystallizing rubber. J Appl Polym Sci 8:707–721
42. El Maanaoui H, Meier J (2019) Influence of the tensile preload variation on the lifetime prediction of technical materials. In: Huneau B et al (eds) Constitutive models for rubber XI. Taylor-Francis, London
43. Ludwig M (2017) Entwicklung eines Lebensdauer-Vorhersagekonzepts für Elastomerwerkstoffe unter Berücksichtigung der Fehlstellenstatistik. Thesis, Gottfried Wilhelm Leibniz Universität Hannover, Hannover
44. Besdo D, Ihlemann J (2003) A phenomenological constitute model for rubberlike materials and its numerical applications. Int J Plastic 19:1019–1036
45. El-Yaagoubi M, Juhre D, Meier J, Kröger N, Alshuth T, Giese U (2018) Lifetime prediction of filled elastomers based on particle distribution and the J-integral evaluation. Int J Fatigue 112:341–354
46. Abraham F, Clauß G, Alshuth T, Kroll J (2005) Kautsch Gummi Kunstst 11:595–599
47. Robin S. Thesis in progress
48. Robin S, Alshuth T (2008) Anwendung der hochauflösenden Computertomografie zur Untersuchung von Elastomeren und Elastomerbauteilen, proceedings of 8. Kautschuk-Herbst-Kolloquium, Hannover
49. Rasband WS (1997-2018) ImageJ, U.S. National Institutes of Health, Bethesda. https://imagej.nih.gov/ij/
50. Eisele U, Kelbch SA, Engels H-W (1992) The tear analyzer – a new tool for quantitative measurements of the dynamic crack growth of elastomers. KGK 45:1064–1069
51. Stoček R, Heinrich G, Gehde M, Kipscholl R (2013) Analysis of dynamic crack propagation in elastomers by simultaneous tensile- and pure-shear-mode testing. In: Grellmann W et al (eds) Fracture mechanics and statistical mech., LNACM, vol 70. Springer, Berlin, pp 269–301
52. El Maanaoui H, Meier J, Abdulghani A, El Yaagoubi M (2020) Dissipation-equivalent load control in dynamic fatigue testing of EPMD and NR elastomers (in submission)
53. Wunde M, Klüppel M (2018) Viscoelastic response during crack propagation of unfilled and filled SBR. Rubber Chem Technol 91(4):668–682
54. Parks DM (1977) Comput Method Appl Mech Eng 12:353
55. Belytschko T, Black T (1999) Int J Num Method Eng 45:601
56. Kaliske M, Dal H, Fleischhauer R, Jenkel C (2010) Comput Mech 122:1
57. Mars WV, Fatemi A (2002) A literature survey on fatigue analysis approaches for rubber. Int J Fatigue 24(9):949–961

58. Mars WV, Fatemi A (2006) Nucleation and growth of small fatigue cracks in filled natural rubber under multiaxial loading. J Mater Sci 41:7324–7332
59. Yeoh OH (1993) Some forms of strain energy function for rubber. Rubber Chem Technol 66:754–771
60. El Yaagoubi M, Meier J, Juhre D (2020) Lifetime prediction of carbon Black filled elastomers based on the probability distribution of particle using an inelastic and Hyperelastic material model (in submission)
61. Gehrmann O, El Yaagoubi M, El Maanaoui H, Meier J (2019) Lifetime prediction of simple shear loaded filled elastomers based on the probability distribution of particles. Polym Test 75:229–236
62. Fatemi A, Socie D (1988) A critical plane approach to multiaxial fatigue damage including out-of-phase loading. Fatig Fract Eng Mater Struct 11(3):149–165
63. Barbash K, Mars W (2016) Critical plane analysis of rubber bushing durability under road loads. SAE technical paper. 2016-01-0393
64. Abraham F (2002) The influence of minimum stress on the fatigue life of non-cristallising elastomers. Thesis, Coventry University, Conventry
65. Abraham F (2012) Definition and use of an effective flaw size for the simulation of elastomer fatigue. In: Jerrams S, Murphy N (eds) Constitutive models for rubber VII. Taylor-Francis, London
66. Kerchman V, Shaw C (2003) Rubber Chem Technol 76:386
67. Kingston J, Muhr A (2012) Determination of effective flaw size for fatigue life prediction. In: Jerrams S, Murphy N (eds) Constitutive models for rubber VII. Taylor & Francis, London, pp 337–342
68. Musil B, Johlitz M, Lion A (2018) On the ageing behaviour of NBR: chemomechanical experiments, modelling and simulation of tension set. Continuum Mech Thermodyn

Adv Polym Sci (2021) 286: 179–202
https://doi.org/10.1007/12_2020_68

Published online: 7 December 2020

Fatigue Life Analysis of Solid Elastomer-Like Polyurethanes

Robert Eberlein, Yuta Fukada, and Lucian Pasieka

Contents

Abstract The material behaviour of polymeric materials under cyclic fatigue loads is complex and forms a vast field of research activities. Elastomer-like polyurethane materials form an excellent fit for cyclically loaded system components in many cases. The present work aims to quantify fatigue crack growth (FCG) in a high-performance, commercially available hydrolysis-resistant thermoplastic polyurethane (TPU). This TPU material is often used in water or oil hydraulics and applications in mining, tunneling, etc. due to its high resistance to abrasion and tear strength. For those heavy-duty applications, the critical lifetime is reached as

R. Eberlein (✉)
Zurich University of Applied Sciences, Winterthur, Switzerland
e-mail: robert.eberlein@zhaw.ch

Y. Fukada
Sophia University, Tokyo, Japan

L. Pasieka
Eugen Seitz AG, Wetzikon, Switzerland

soon as cracks reach a critical threshold in the TPU material. The first part of the current work illustrates the FCG analysis of the TPU material, i.e. crack propagation measurements on a Tear and Fatigue Analyzer (TFA, Coesfeld GmbH & Co. KG, Germany). Based on the TFA measurements, it is shown how the tearing energy and the FCG rate have a certain regularity at different strain levels and quite a different behaviour compared to standard rubber material. Secondly, a lifetime prediction of the TPU material is derived by means of advanced finite element analysis (FEA). By using Abaqus simulation software (Dassault Systèmes) with advanced material modeling concepts, simulations are performed under the identical conditions as the TFA experiments. The results are plotted in terms of total elastic strain energy density per element (ESEDEN) over FCG rate in the vicinity of the crack tip. In a third step, the lifetime prediction concept ESEDEN is cross-validated by comparing experimental results from a test bench that applies cyclic high strain rate loading to the TPU material with corresponding FEA. As demonstrated the ESEDEN data proves being a promising criterion for lifetime prediction of critical TPU components under cyclic loading conditions.

Keywords Crack growth · Fatigue · FEM · Lifetime prediction · Polyurethane

1 Introduction

Polymeric materials such as rubber and polyurethanes are used for a broad range of applications, e.g. tires, seals, bushings, boots and so on. The characteristics of rubber and TPU materials are similar; both are elastic and flexible. However, TPUs are typically chosen instead of rubber due to their rubber-like characteristics combined with their high resistance to fatigue under recurring stress loadings. There are many publications on the material behaviour of rubber under cyclic loading conditions, compare with [1–6] among others, although fatigue life analysis including lifetime prediction of solid TPU under cyclic loading conditions is either described theoretically or experimentally. Up to now research on solid TPU materials has been mainly focused on the relationship between the morphology and the mechanical stress-strain behaviour [7–9]. For a detailed account on mechanical modeling of solid polymers, refer to [10]. Just a few studies were carried out to characterize the fracture resistance of solid TPU under cyclic loading conditions despite its widespread use in engineering applications [11, 12]. Like for rubber the current study deploys the analysis of crack propagation under cyclic loading to study fatigue life of TPU. For a comprehensive account on fatigue analysis approaches for rubber, it is referred to [13]. FCG analysis originates from fracture mechanics concepts first described in [14, 15] and firstly adapted to rubber materials in [16]. In the latter approach, a pre-notched sample is typically tested, and the crack propagation rate is characterized as a function of the applied tearing energy T. In a recent study published in [17], crack

propagation behaviour of solid TPU in cyclic fatigue loading was addressed for the first time in literature. The current work steps in the same direction employing crack propagation measurements on a Tear and Fatigue Analyzer (TFA). However, it additionally postulates a lifetime prediction concept that is based on the total elastic strain energy density per element (ESEDEN). The authors observed from various experimental investigations that ESEDEN is a reasonable measure to predict failure in solid polymers under cyclic loading conditions. The concept of using strain energy densities for failure prediction is not new and was thoroughly discussed in literature [18–20]. However, to our knowledge this concept has not been applied to solid TPU materials before. Failure prediction is eventually based on ESEDEN analyses employing results from TFA measurements and correlating finite element analyses (FEA). In a last step, the lifetime prediction concept is cross-validated by means of high strain rate experimental investigations which demonstrate its effectiveness.

2 Test Equipment and Material

A Tear and Fatigue Analyzer (TFA, Coesfeld GmbH & Co. KG, Germany) was used for the main experimental analyses. The TFA realizes a fully automated measurement of crack growth under cyclic fatigue loading, whereas up to ten samples are measured simultaneously. The technical specifications of a TFA can be found in literature [15, 21]. A sketch describing the measuring process as well as a picture of the TFA are visualized in Fig. 1.

For TFA tests plane-strain tension test specimens were used having the option to do simple fracture mechanics analysis as described in more detail, e.g. in [15, 22]. In literature plane-strain tension tests are very often named as pure shear (PS) tests, even though the resulting strain states for plane-strain tension and pure shear are not identical at large strains. Regarding the exact correlation in between plane-strain tension tests and pure shear tests, the interested reader is referred to [10]. For simplicity the term “PS specimen” is applied throughout this article, despite the

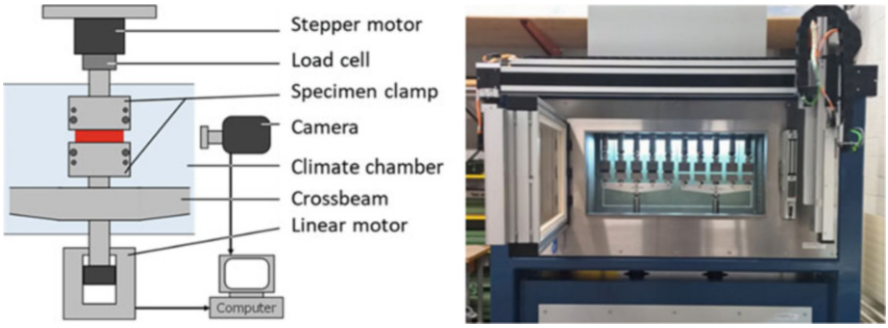

Fig. 1 Sketch and picture of the TFA

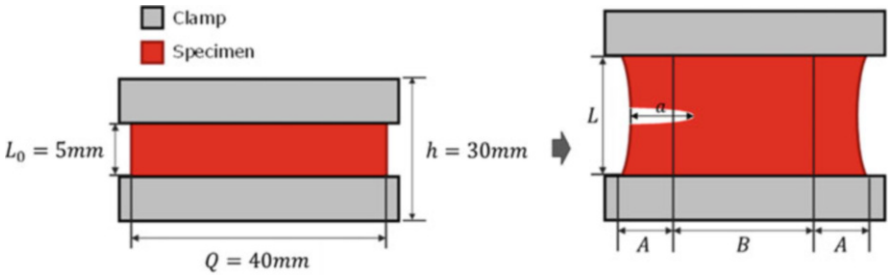

Fig. 2 PS specimen

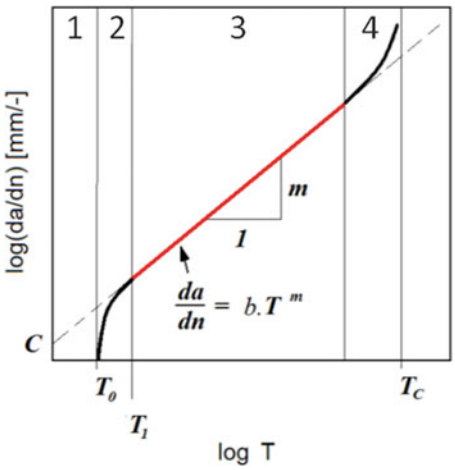

Fig. 3 Double logarithmic plot of crack growth rate over tearing energy as reported in [15]

fact that plane-strain tension tests were performed, instead. The used "PS specimen," visualized in Fig. 2, is a thin rectangular strip clamped by its long edges inside the test machine. The geometry ratio is defined as $L_0 : Q \ll 1$ where L_0 is the distance between the clamps and Q is the width of the specimen. This makes it possible to ignore the edge effect that occurs in the region A of Fig. 2 and ensure region B is at a pure plane-strain tension state [15, 23, 24].

There is a typical relationship for a rubber material between FCG rate, $r = da/dn$ and tearing energy, T, on a double logarithmic plot shown in Fig. 3, where a is the crack length (see Fig. 2) at actual cycle count. This plot can be divided into four regions that have different behaviours of tear which firstly have been determined by Lake and Lindley in [25] and simplified, e.g. in [15].

Without going into details here, region III, red curve is utilized as the region that corresponds most closely to crack growth rates found in the engineering fatigue range. It is characterized by stable crack growth, and the relationship between FCG rate, r, and tearing energy, T, has been defined by square law in [26] and reads

$$r = \frac{da}{dn} = b \cdot T^m, \tag{1}$$

where b and m are material-specific constants defining crack growth. For this work the solid TPU was tested in the same way under different strain conditions to create corresponding FCG characteristics. Single notching of the specimens was applied to ensure optimum use of the stable crack growth in region III.

The solid TPU material used for this work is an injection moulded, hydrolysis-resistant TPU. It combines outstanding engineering properties as high abrasive resistance, low compression set and high physical properties and tear strength, with high resistance to hydrolysis which is rarely found in TPUs. The detailed material formulation is confidential industrial information and therefore not subject for disclosure.

3 FCG Analysis

The main objective for the experimental analysis on the TFA is to acquire the data needed to create FCG characteristics as shown in Fig. 3. The TPU was tested at two different temperatures: room temperature (RT) about +24°C and +60°C.

3.1 Determination of the Tearing Energy

For PS specimens the tearing energy, T, is firstly considered in Ref. [23] to be independent of crack length:

$$T = \mathrm{w} \cdot L_0 \tag{2}$$

where w is the total elastic strain energy density. The tearing energy needs to be calculated using Eq. (2). The strain energy density, w, used in Eq. (2) is obtained from the total elastic strain energy, W, that can be acquired from tests using unnotched specimens. To acquire the necessary data for RT and 60°C, respectively, a wide variety of tests were carried out with three specimens for each test. Preloads were applied to all tests, and the stress ratio (R ratio) for cyclic loading was varying in a range from 0.1 to 0.9. The geometry of the specimens is depicted in Fig. 2; the average thickness d of the specimens is 2.3 mm. Based on results from pretests, the test parameters for the TPU material were fixed. Table 1 illustrates these parameters for a preload force $F_p = 100$ N. A sinusoidal loading waveform was used for all tests.

For the determination of the tearing energy, L_0^{100} serves as reference, i.e. L_0, when the preload force of 100 N is applied. In order to use the strain energy, W, in Eq. (2), it can be divided by the specimen volume:

Table 1 Basic test parameters for the crack fatigue tests

Parameters	Values
Frequency, f [Hz]	10
Preload force, F_p [N]	100
Sample length, L_0 [mm]	5
Notch length, $a_{\min}$ [mm]	5 ~ 20

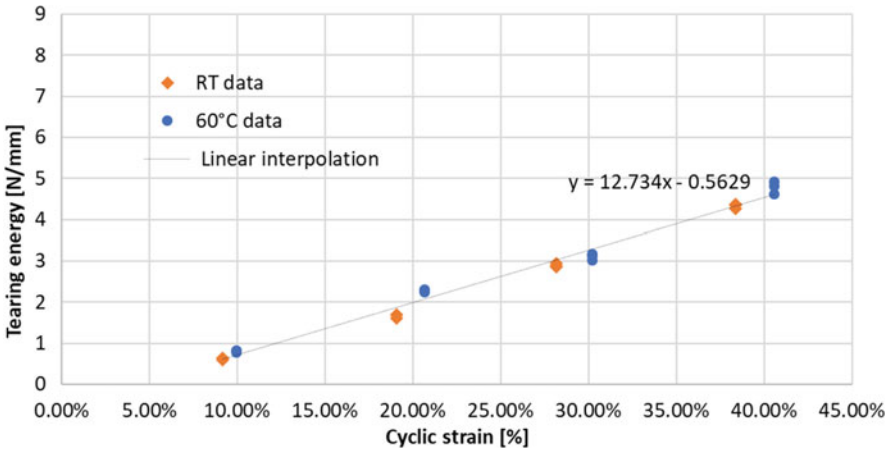

Fig. 4 Tearing energy vs. cyclic strain

$$T = \mathrm{W}/V \cdot L_0^{100} \tag{3}$$

where the volume, V, is defined as:

$$V = L_0^{100} \cdot Q \cdot d. \tag{4}$$

The parameter d indicates the sample thickness measured for each sample individually. The resulting plots for tearing energy over cyclic strain (i.e. 2× strain amplitude) with respect to L_0^{100} are shown in Fig. 4 for RT and 60°C, respectively.

3.2 Room Temperature Experiments

The FCG analysis is briefly explained by means of Fig. 5. The explanation is also valid for the experiments at 60°C. Figure 5 shows a picture that was captured by the TFA camera. The top and bottom parts are the clamps, and the part in the middle is the specimen. It is shown how the TFA software recognizes the crack contour (red line), determines the crack tip and calculates the crack length (blue line) to record the crack growth. The yellow line indicates the length of the rest of the specimen. It is important to notice that crack blunting can be observed in the TPU. This confirms the

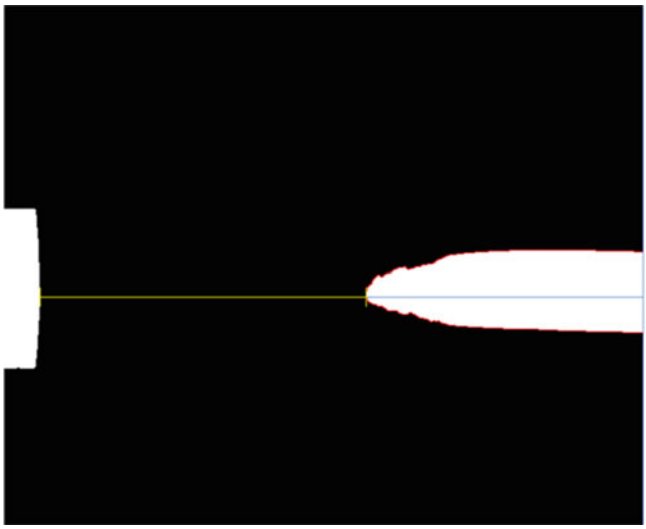

Fig. 5 A picture of the specimen taken by the CCD camera

statement by [17] that the details of the TPU's architecture resulting in a microphase separation can result in a very good resistance to crack propagation in cyclic conditions.

The tests were performed with five identical specimens for the lower range of tearing energy and three identical specimens for the tests with high range of tearing energy in order to not overload the linear drives due to real absolute force value. The width Q and the thickness d of the notched PS specimens were remeasured for each specimen, and the values were put into the TFA software. All experimental results reported are based on a preload force of 100 N and a tearing energy range in accordance to Fig. 4 and above for which the linear interpolation function was extrapolated. The resulting FCG characteristic is shown in Fig. 6. The plot illustrates a qualitatively different shape from typical rubber materials. Basically the plot can be separated into three distinct regions. In region I, there is only a slight increase in the crack growth rate as the tearing energy T for a cyclic strain of 12.3% increases to 0.93 N/mm or 933.25 J/m^2, respectively (corresponding to log$T = -0.03$ N/mm). In region II, the crack growth rate accelerates significantly up to a cyclic strain level of 25.1%. At this level the tearing energy T reaches 2.51 N/mm or 2511.89 J/m^2, respectively (corresponding to log$T = 0.4$ N/mm). Above that strain level in region III, the FCG rate decelerates again. Interestingly, all three regions are characterized by a linear increase of the crack growth rate but at different slopes. That sets the TPU material at test apart from typical rubber compounds. Again, severe crack blunting in region III might be an explanation for the enhanced tear strength of the material.

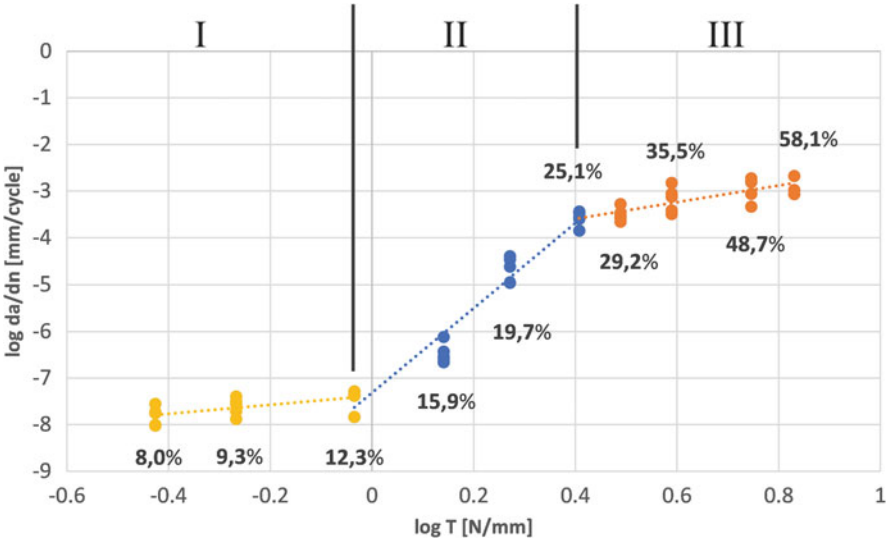

Fig. 6 FCG characteristic at RT

3.3 60°C Experiments

The experiments at 60°C were basically performed in the same way as for RT. Before testing, the specimens were put into the testing chamber for 1 h at 60°C. This is to ensure that the specimens were heated properly and evenly to 60°C. The FCG characteristic at 60°C is very similar to the results at RT with the plot being able to be separated in three regions as shown in Fig. 7. By comparing the results with Fig. 6 for RT, the crack growth rate at 60°C at low strains seems to be similar or a little higher, but at high cyclic strains, the FCG rate is even lower than at RT. Again, all three regions in Fig. 7 are characterized by a linear increase of the FCG rate.

4 Fatigue Life Concept

This section motivates a fatigue life or lifetime prediction concept for solid TPU under cyclic loading conditions. By means of advanced FEA, the TFA experiments are simulated in order to quantify the strain field in the vicinity of the crack tip. The TPU under test needs to be calibrated in terms of its mechanical material behaviour at RT and +60°C, respectively. The lifetime prediction concept is eventually illustrated by analysing the total elastic strain energy density per element (ESEDEN) in the vicinity of the crack tip over the FCG rate.

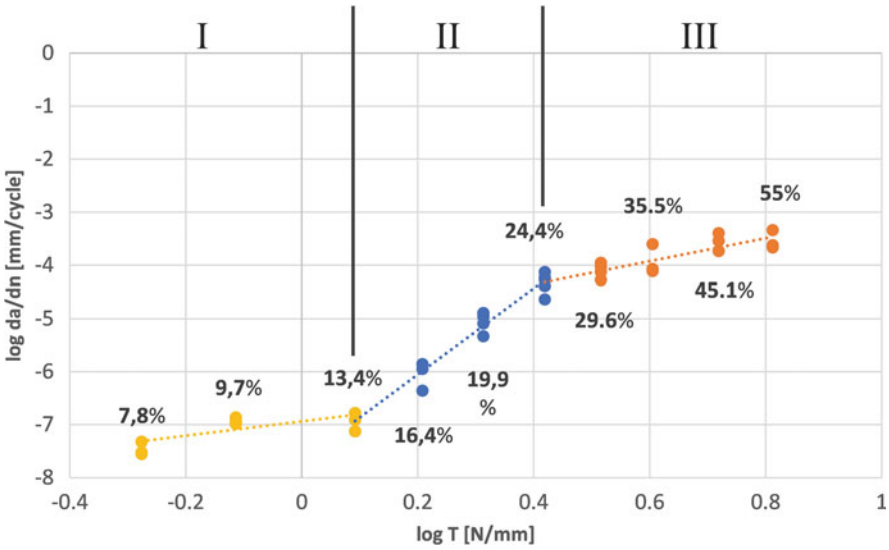

Fig. 7 FCG characteristic at 60°C

4.1 Material Model Calibration

To have a proper behaviour of the simulation model in FEA, the material parameters need to be acquired for the TPU under test. To achieve this, cyclic tensile tests were performed with the TPU material to gain experimental data needed for material model calibration. The material testing was done at comparable strain rates as employed in the TFA (see Table 1).

A customized biaxial testing machine was used for the tests. The machine can be used for uniaxial, equibiaxial and plane-strain tension tests. Like the TFA it is equipped with a temperature-controlled chamber which allows for low- and high-temperature testing, basically in the same range as the TFA. The tests were performed for PS specimens with identical geometries as shown in Fig. 2 and tensile specimens (type S2) with geometries shown in Fig. 8. For both PS and tensile specimens, tests were performed at RT (24°C and 60°C) with each condition containing three specimens.

For PS specimens at RT, the clamp distance was set to 5 mm just like on the TFA. Each specimen was stretched to the point where the total strain was around 20%, and then it was unloaded and finally stretched to around 40% to complete the test. For the 60°C tests, the specimens were heated for 1 h and put through the same test procedure.

For tensile specimens at RT, the specimens were stretched until the total strain was around 50%, unloaded, and stretched again to around 100% to complete the test. For the 60°C tests, the specimens were heated for 1 h as well before testing. All tests were done with displacement-controlled loading parameters. The mean average

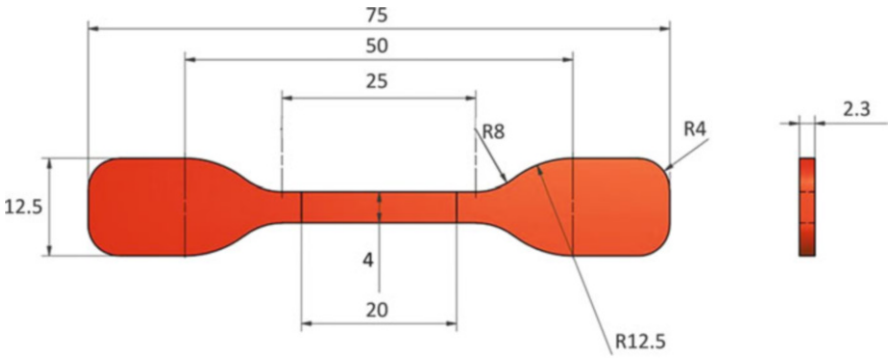

Fig. 8 Geometry of the tensile specimen

results of the three specimens for each load condition and specimen type were eventually used for the calibration.

The software used for material model calibration was MCalibration (Veryst Engineering, LLC). This software allows for extraction of pertinent material parameters from the experimental data described above.

The material model selected for calibration is the three network model (TNM) as described in [27], which was specifically developed for thermoplastic materials but also yields good results for PURs. The rheological representation of the TNM is given by three parallel networks: two nonlinear spring/damper networks A and B and a nonlinear spring network C. Using this framework, the total Cauchy stress in the system is given by $\boldsymbol{\sigma} = \boldsymbol{\sigma}_A + \boldsymbol{\sigma}_B + \boldsymbol{\sigma}_C$. The governing equations for the stress in each element of the model are as follows:

Cauchy stress in network A:

$$\boldsymbol{\sigma}_A = \frac{\mu_A}{J_A^e \overline{\lambda_A^{e*}}} \left[1 + \frac{\theta - \theta_0}{\widehat{\theta}}\right] \frac{\mathcal{L}^{-1}\left(\overline{\lambda_A^{e*}}/\lambda_L\right)}{\mathcal{L}^{-1}(1/\lambda_L)} \operatorname{dev}\left[\mathbf{b}_A^{e*}\right] + \kappa\left(J_A^e - 1\right)\mathbf{1}. \tag{5}$$

Cauchy stress in network B follows by swapping A to B. Cauchy stress in network C reads as:

$$\boldsymbol{\sigma}_C = \frac{1}{1+q}\left\{\frac{\mu_C}{J\lambda_{\text{chain}}}\left[1 + \frac{\theta - \theta_0}{\widehat{\theta}}\right] \frac{\mathcal{L}^{-1}\left(\frac{\lambda_{\text{chain}}}{\lambda_L}\right)}{\mathcal{L}^{-1}\left(\frac{1}{\lambda_L}\right)} \operatorname{dev}[\mathbf{b}^*] + \kappa(J-1)1 \right.$$

$$\left. + q\frac{\mu_c}{J}\left[I_1^* \boldsymbol{b}^* - \frac{2I_2^*}{3} I - (\boldsymbol{b}^*)^2\right]\right\}. \tag{6}$$

Without going into further details here, the model parameters and assumptions can be found in literature [27].

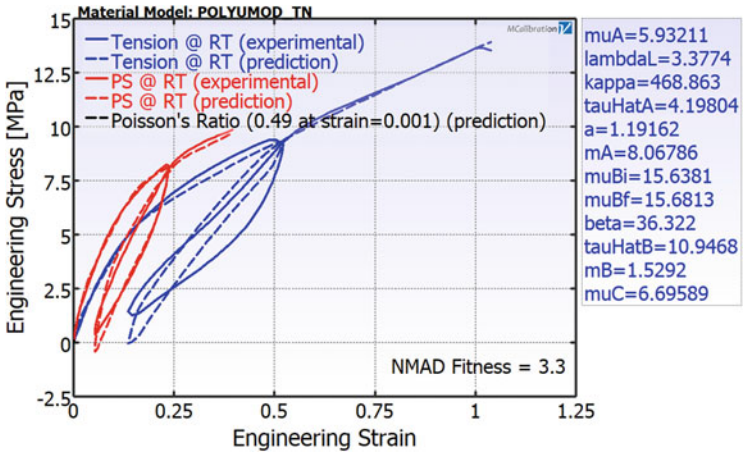

Fig. 9 MCalibration result for RT

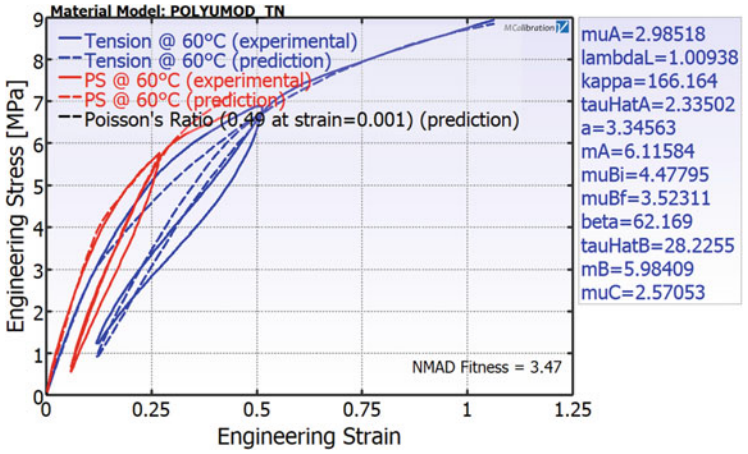

Fig. 10 MCalibration result for 60°C

The TNM was separately calibrated for both applied temperatures. For each temperature condition, the PS test data and the tensile test data are used by simultaneously assuming quasi-incompressible material behaviour of the TPU. The results are shown in Fig. 9 for RT and in Fig. 10 for 60°C with the imported material test data as solid lines (experimental) and the calibrated prediction as dotted lines. The results are depicted in engineering stress versus engineering strain.

To see how good the TPU material calibrations are compared to the test data, MCalibration uses a so-called fitness function. Normalized mean absolute difference (NMAD) is used for this case which is the average error in percent between the experimental data and the model predictions. If the NMAD fitness is below 10(%), the calibration represents in most cases a reasonably good fit. Figures 9 and 10 show

the calibrated material model parameters and the overall NMAD values. The material model data can be exported as a Python script for later use in FEA.

4.2 TNM Validation

For validating the calibrated TNM data, FE models of the PS specimen and the tensile test specimen were made to simulate the corresponding tests in Abaqus. The simulation results were compared to the experimental data. The geometry of the FE model for the PS specimen is identical to the geometry shown in Fig. 2. For the tensile specimen, the geometry of the FE model corresponds to Fig. 8 with a free specimen length of 50 mm. In both FE models, the loading is applied via specimen clamps which are directly comparable to the experiments.

The clamps are tied to the specimen, and the bottom clamps are fixed in space. The employed TPU material mass density is 1,200 kg/m^3. The material for the clamps is comparably stiff (e.g. steel) with a mass density of 7,900 kg/m^3, a Young's modulus of 200GPA and a Poisson's ratio of 0.4.

As loading a displacement is applied to the top clamps. For the PS specimen simulations, the maximum displacement is 2.5 mm which is a total strain of 50%. For the tensile specimen simulations, the maximum displacement is 50 mm which is a total strain of 100%. The actual strain measurements are done by means of a video extensometer in the free range of the specimens. For both cases the FE simulation time is chosen according to the material testing times in order to account for proper transient material response.

The stress and strain data obtained from Abaqus are given as true stress and strain data. For comparison with the experimental results reported in Figs. 9 and 10, the numerical stress and strain data needs to be converted to engineering stress and strain data first. The converted data is finally compared with the experimental results. As an example, results for 60°C are illustrated in Figs. 11 and 12, respectively. Qualitatively similar results are also obtained at RT, which are not shown here. The agreement in between experimental and FE data is reasonable for practical applications. Please note that for validation, only the loading path was calculated by FEA.

4.3 ESEDEN for Lifetime Prediction

As mentioned in the introduction, strain energy densities are a reasonable measure for failure prediction. Based on the TFA fatigue analysis and the TNM calibration results, the lifetime prediction concept for the total elastic strain energy density per element (ESEDEN) is outlined for 60°C data.

Advanced FEA of the TFA experiments were performed using the TNM calibration data. A FE model was generated as shown in Fig. 14. In order to assess the TPU failure by means of ESEDEN, a proper resolution of the ESEDEN distribution at the

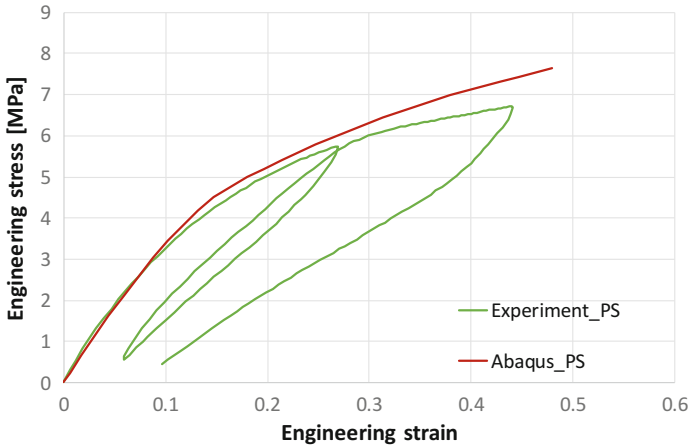

Fig. 11 TNM validation for plane-strain tension test at 60°C

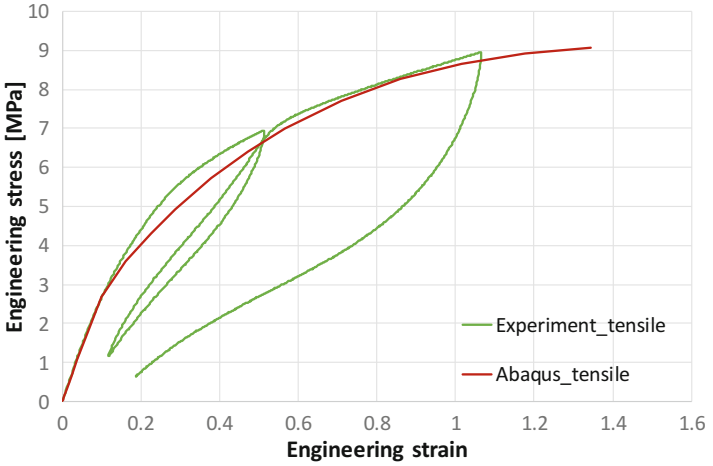

Fig. 12 TNM validation for tensile test at 60°C

crack tip is mandatory. Unlike for linear elastic material models usually employed for metals, the material response of the TPU under test is highly nonlinear with significant inherent material damping (see Figs. 11 and 12, respectively). In addition, crack blunting was observed during the TFA fatigue analysis (see Fig. 5). Therefore, the FE mesh resolution at the crack tip must be studied carefully. The actual FE discretization at the crack tip belongs to the proprietary rights of the involved industry partner and cannot be displayed here.

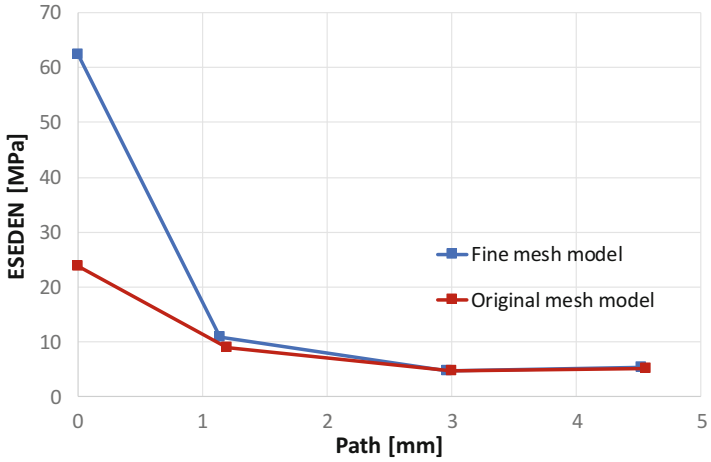

Fig. 13 Mesh convergence study for ESEDEN at the crack tip

4.3.1 Mesh-Independent Characterization of ESEDEN

To illustrate the lifetime prediction concept, it is presented in the vicinity of the crack tip where it is independent of mesh refinement. Before simulating all load cases, it is important to demonstrate how FE mesh refinement affects ESEDEN values at the vicinity of the crack tip. For this purpose, the load case preload force of 100 N plus a cyclic strain of 55.0% was simulated with various mesh refinements.

The results of this mesh convergence study are illustrated in Fig. 13 for two different FE mesh discretizations. They indicate that although there is a steep gradient for ESEDEN at the crack tip as expected, this effect disappears at 3 mm horizontal distance from the crack tip (compare with Fig. 2). Therefore all results reported for ESEDEN (i.e. the maximum value of ESEDEN during cyclic loading) below are taken at 3 mm horizontal distance from the crack tip. Thus, all results will be reproducible without infringing proprietary rights.

The overall boundary conditions for FEA are depicted in Fig. 14. The model components and dimensions were previously defined in Fig. 2. Figure 14 does additionally illustrate the initial notch length (grey line), the crack tip location (red dot) and the ESEDEN reference point (green dot) as described above.

4.3.2 ESEDEN Analysis and Correlation with Crack Growth Rate

The FEA loading conditions relevant for ESEDEN analysis are summarized in Table 2. Two load steps are defined as shown in Fig. 15. The (quasi-)static step is basically used for applying the preload of 100 N by means of an averaged displacement of 1.67 mm within 10 s. Quasi-static means that inertia terms in the governing

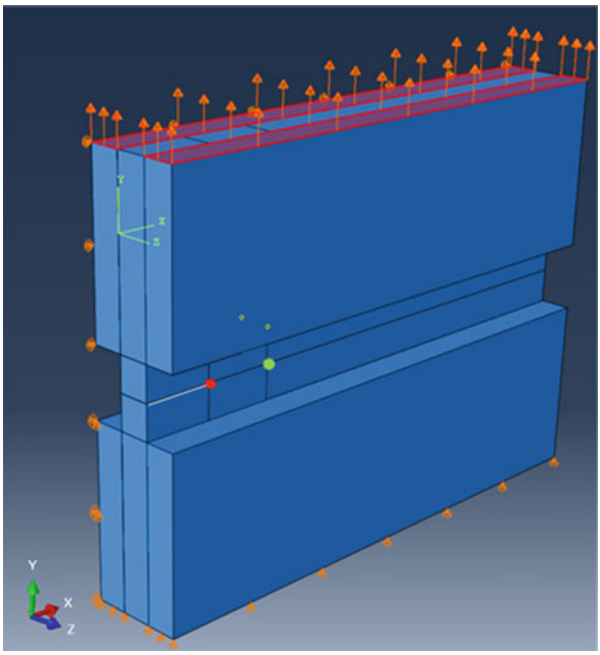

Fig. 14 Boundary conditions for FEA

equations are neglected but transient material behaviour is still considered. The preload is controlled by displacement which is applied to the top clamps shown in Fig. 14. Additionally, 1/2 of the stroke (1/2A) is added to the preload value within the static step due to a difference in between the TFA analysis and FEA analysis. The TFA keeps the preload force at 100 N throughout the cyclic load, which means the whole amplitude of the cyclic deformation is occurring on top of the preload. To replicate this in Abaqus, 1/2 of the stroke (1/2A) needs to be added before the cyclic step may start.

The cyclic step is for the fatigue loading. The frequency is set to 10 Hz, and it is defined to simulate ten cycles to account for potential stress relaxation during cyclic loading. This step applies displacement to the top clamps as shown in Fig. 14. The loading conditions are shown in Table 2.

After FEA the maximum values for ESEDEN in each load case are correlated with the FCG rate according to Fig. 7. It was also observed that the maximum values of ESEDEN are not significantly influenced by stress relaxation during cyclic loading. Therefore the peak value of the first cycle is chosen for reporting in each load case. The final result is shown in Fig. 16.

The same procedure can be applied at RT. The corresponding loading conditions are depicted in Table 3, and the maximum ESEDEN values vs. crack growth rate data are printed in Fig. 16.

For the TPU under test, the plots of maximum ESEDEN over FCG rate form a basis to determine the lifetime for critical TPU components under cyclic and primarily tensile (mode 1) loading conditions. The curves denoted in Fig. 16

Table 2 Loading conditions for FEA at 60°C

Parameters	Values									
Cyclic strain [%]	7.8	9.7	13.4	16.4	19.9	24.4	29.6	35.5	45.1	55.0
Preload displacement [mm]	1.67									
1/2A [mm]	0.28	0.33	0.475	0.535	0.645	0.8	0.955	1.18	1.42	1.835
Preload +1/2A [mm]	1.95	2.0	2.145	2.205	2.315	2.47	2.625	2.85	3.09	3.505

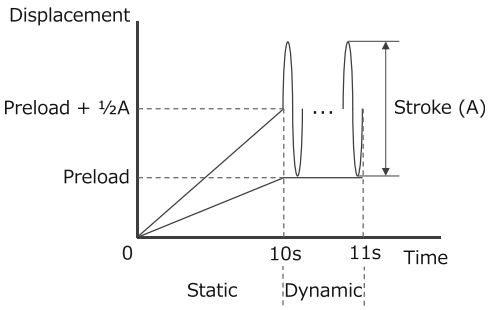

Fig. 15 Diagram of the load steps in FEA

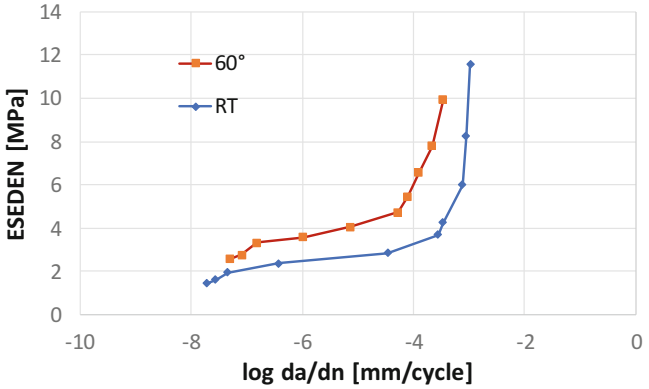

Fig. 16 Maximum ESEDEN values vs. FCG rate at 60°C and RT, respectively

illustrate the basic lifetime prediction concept. Nevertheless, the maximum ESEDEN values in this plot represent the elastic strain energy density values in the vicinity of the actual crack tip for reasons mentioned above. So, at this point these results can be interpreted qualitatively only. A quantitative analysis will be discussed in the subsequent section. It is important to note that the FCG rate for the tested TPU approaches is an asymptotic limit which is especially evident for the results at RT. But also for an elevated temperature at 60°C, this trend is still detectable. Again, these findings underline the exceptional tear strength of the current material.

5 Cross-Validation of Lifetime Prediction Concept

After deriving the lifetime prediction concept for TPU in the previous section and discussing it there in a qualitative manner, it will be demonstrated in this section that the concept yields reasonable results in industry-relevant applications. The

Table 3 Loading conditions for FEA at RT

Parameters	Values									
Cyclic strain [%]	8	9.3	12.3	15.9	19.7	25.1	29.2	35.5	48.7	58.1
Preload displacement [mm]	0.822									
1/2A [mm]	0.24	0.28	0.365	0.465	0.565	0.73	0.83	1.03	1.39	1.655
Preload +1/2A [mm]	1.06	1.1	1.187	1.287	1.387	1.55	1.652	1.85	2.21	2.477

effectiveness of the lifetime prediction concept is assessed via the cross-validation principle (test used for validation is different to these used for material model calibration). To achieve so, a dedicated high strain rate test bench was used to measure "implicitly" the high strain rate behaviour of the TPU under test (Fig. 17). In parallel, this test-bench system is FE-based model employing the aforementioned material models for TPU, respectively. Via comparing the simulated to the experimentally obtained counterparts, the ability of each corresponding material model to reproduce in good terms the real high strain rate behaviour of the TPU under test can be independently assessed.

To execute a high strain rate test on the test bench, the TPU under test is firmly clamped on the base (Fig. 17). The lightweight metallic piston (mass < 32 g), while lying on its "starting position" (Fig. 17a), is getting ejected towards the TPU under test. When the piston establishes contact with the TPU under test, it has velocity v_1 (Fig. 17b). During contact, the TPU under test is deformed at high strain rate due to the momentum of the piston. Finally, the piston bounces backward with velocity v_2.

During the test, the vertical movement and the proper alignment of the piston are achieved by two low friction bearings (friction force <1 N – Fig. 17). Right before and during and right after the contact of the piston with the TPU under test, three external forces act on the piston. These are the friction (<1 N), its weight (<0.5 N) and the reaction force from the TPU under test. The first two are negligible compared to the latter (to establish boundary conditions for the FE model simulation later). Practically speaking the only significant force acting on the piston during the contact is the reaction force, which its counterpart being responsible for the high strain rate deformation on TPU under test.

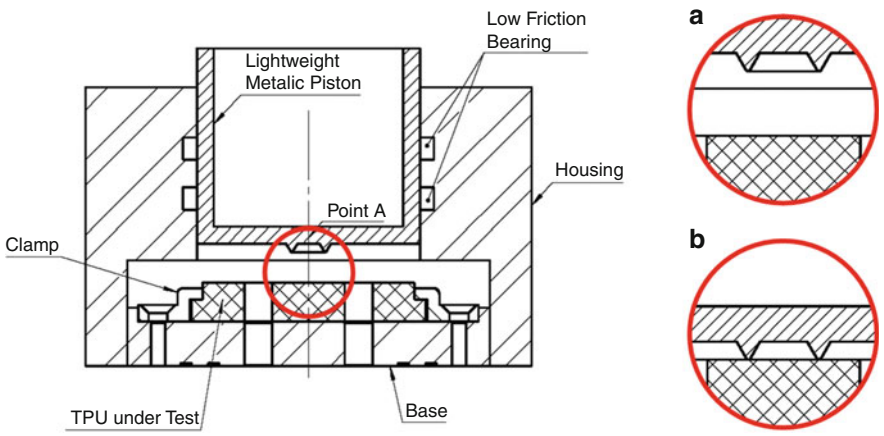

Fig. 17 Schematic sketch of the test bench for capturing "implicitly" the high strain rate behaviour of the TPU under test: (**a**) starting position, the lightweight metallic piston is about to get ejected towards the TPU specimen; (**b**) contact position, the lightweight metallic piston contacts the TPU under test with velocity v_1; after the pertinent deformation of the TPU material, the piston bounces backwards at v_2 velocity

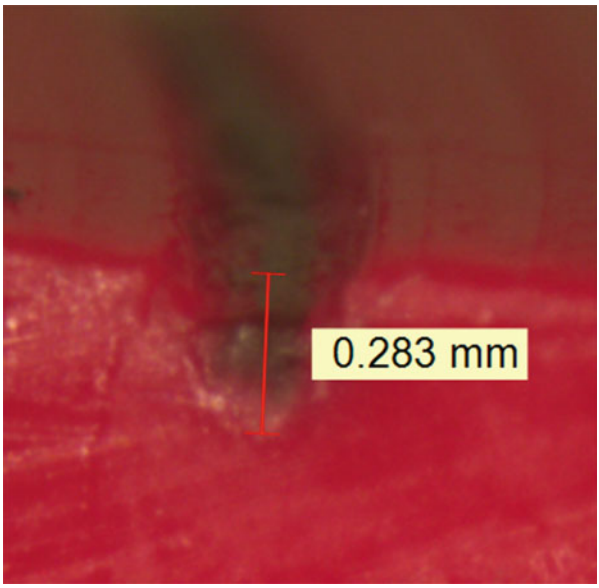

Fig. 18 Average crack length after 83 million loading cycles

The piston, while moving, Fig. 17a → Fig. 17b, is monitored by a laser vibrometer at point A. Due to this, the displacement and velocity of the piston are both measurable and readily available as acquired signals (both sampled at 1 MHz).

The measured velocity of the piston during the contact is an "implicit" expression of the high strain rate deformation of the TPU under test. Therefore, the comparison of the measured velocity with the FE-based simulated counterpart provides an independent high-level criterion to assess the ability of each of the underlying material models to capture the high strain rate behaviour of the TPU material. To achieve high accuracy for the cross-validation, the TPU material model calibration as described in Sect. 4 needs to be enriched by high strain rate experimental data (see [7] for more information). Due to symmetry, an axisymmetric and therefore time-efficient FE model is employed.

For cross-validation the test-bench system operated with a velocity $v_1 = 2.3m/s$ at RT. TPU specimens were tested for 83 million cycles in total. The tests were stopped several times in order to check crack growth at the circular penetration line. After 54 million cycles, still no crack initiation was detected. At 83 million cycles, the crack length reached 0.283 mm on average as shown in Fig. 18.

It is interesting to mention that for the current loading on the test-bench system, the crack initiation maximum tensile strains occur approximately 50mu under the TPU surface (Fig. 19 left). So crack initiation is also expected beneath the surface and not necessarily visible from the beginning. Corresponding to the tensile strain distribution is the location of the maximum ESEDEN value during contact (Fig. 19 right).

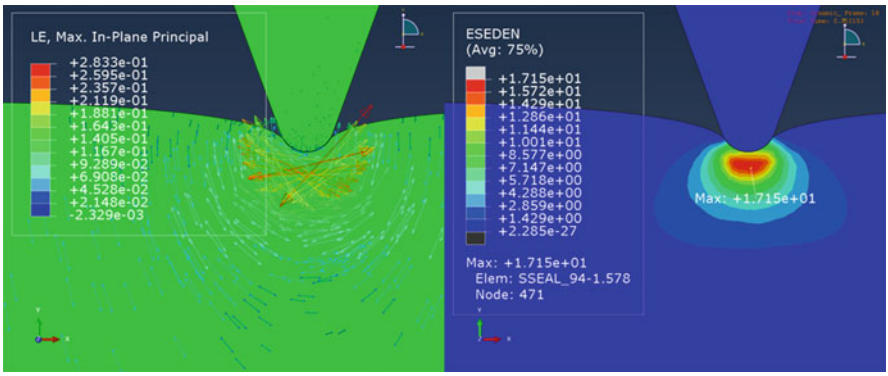

Fig. 19 Maximum tensile strains and ESEDEN during contact

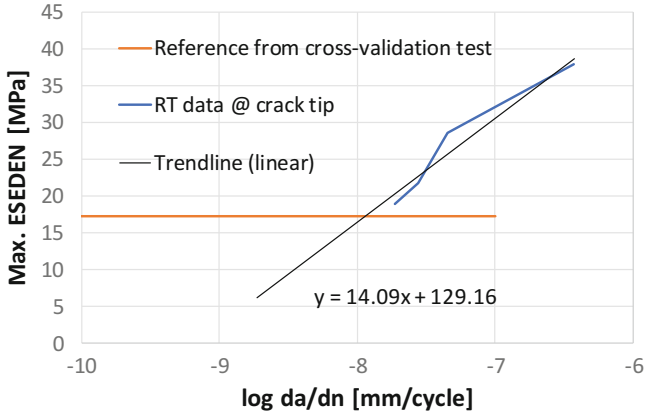

Fig. 20 Linear extrapolation of FCG curve at RT to reference data

The maximum ESEDEN value of 17.15 MPa is taken as reference for fatigue life prediction. Unlike in the previous section, it needs to be compared to maximum ESEDEN data directly at the crack tip. Figure 20 illustrates this data for low crack growth rates at RT. Since the TFA measurement with the lowest cyclic strain still yields a maximum ESEDEN value above the reference value from cross-validation, RT data in Fig. 20 is linearly extrapolated. The intersection point of the extrapolation line with the reference value from cross-validation eventually yields the related crack growth rate which under consideration of 0.283 mm crack length yields 25.2 million cycles. That means that crack initiation apparently started after 57.8 million cycles which confirms the finding that after 54 million cycles, no visible crack could be detected yet. This is a first indicator that the proposed lifetime prediction concept based on ESEDEN seems to work. An even more precise experimental quantification will be pursued in the future.

6 Conclusion and Discussion

The aim of this work was to determine how fatigue life for critical TPU components can be determined from experimental FCG results combined with the use of advanced FEA accounting for strain rate-dependent material behaviour.

The FCG analysis was done on a TFA which was adjusted and used for the cyclic loading tests of a commercially available solid TPU material. The FCG rate and the tearing energy for PS specimens were obtained accordingly. As a first result, FCG characteristics were derived from the obtained data at RT and 60°C, respectively. These plots turned out to be qualitatively quite different from what is normally seen in rubber materials which underlines the exceptional tear strength of solid TPU materials.

For the derivation of the lifetime prediction concept, the TPU material was properly calibrated and validated by FEA. Based on the validated material data, the total elastic strain energy density per element can be calculated for the TFA experiments. The FE simulation results were used to depict the maximum ESEDEN values per load case in the vicinity of the crack tip over the corresponding FCG. The resulting curves were plotted for RT and 60°C, respectively, and form the qualitative base of the proposed lifetime prediction concept under cyclic loading.

Finally, by means of a high strain rate cross-validation, the quantitative applicability of the proposed lifetime prediction concept was assessed for a mode 1 dominated cyclic loading pattern. The cross-validation results turned out to be quite promising but need to be further assessed in the future.

In general, the current fatigue life or lifetime prediction concept can be applied to further solid TPU materials which will also be considered in the future. From the authors' point of view, the proposed method provides a good balance of scientific depth (and accuracy) on one side and practical applicability on the other side. With further cross-validation experiments in place, it forms an innovative tool for competitive product development.

It must also be mentioned that the current method faces some distinct shortcomings. Currently, no information can be provided about crack initiation. This subject can form a separate field of activity in the future when considering solid TPU materials. Additionally, the fatigue life concept is not adapted to varying load cycles. This was not a primary interest of the involved industrial partner but can be relevant in many other engineering applications.

Acknowledgements This research was supported in parts by Innosuisse – Swiss Innovation Agency.

References

1. Ayoub G, Zaïri F, Naït-Abdelaziz M, Gloaguen JM, Kridli G (2014) A visco-hyperelastic damage model for cyclic stress-softening, hysteresis and permanent set in rubber using the network alteration theory. Int J Plast 54:19–33. https://doi.org/10.1016/j.ijplas.2013.08.001
2. Carleo F, Barbieri E, Whear R, Busfield JJC (2018) Limitations of viscoelastic constitutive models for carbon-black reinforced rubber in medium dynamic strains and medium strain rates. Polymers 10:988. https://doi.org/10.3390/polym10090988
3. Chai AB, Andriyana A, Verron E, Johan MR (2013) Mechanical characteristics of swollen elastomers under cyclic loading. Mater Des 44:566–572. https://doi.org/10.1016/j.matdes.2012.08.027
4. Guo Q, Zaïria F, Guo X (2018) A thermo-viscoelastic-damage constitutive model for cyclically loaded rubbers. Part I: model formulation and numerical examples. Int J Plast 101:106–124. https://doi.org/10.1016/j.ijplas.2017.10.011
5. Liu M, Hoo Fatt MS (2011) A constitutive equation for filled rubber under cyclic loading. Int J Non-Lin Mech 46:446–456. https://doi.org/10.1016/j.ijnonlinmec.2010.11.006
6. Vaikuntam SR, Bhagavatheswaran ES, Xiang F, Wießner S, Heinrich G, Das A, Stöckelhuber KW (2020) Friction, abrasion and crack growth behavior of in-situ and ex-situ silica filled rubber composites. Materials 13:270. https://doi.org/10.3390/ma13020270
7. Eberlein R, Pasieka L, Rizos D (2019) Validation of advanced constitutive models for accurate FE modeling of TPU. Adv Mater Lett 10:893–898. https://doi.org/10.5185/amlett.2019.0031
8. Qi HJ, Boyce MC (2005) Stress–strain behavior of thermoplastic polyurethanes. Mech Mater 37:817–839. https://doi.org/10.1016/j.mechmat.2004.08.001
9. Yui N, Nojima K, Sanui K, Ogata N (1985) Morphology and properties of segmented polyether poly(urethane-urea-amide). Polym J 17:969–975
10. Bergstrom JS (2015) Mechanics of solid polymers. Elsevier, London
11. Eberlein R, Pasieka L (2020) Prediction of long-term behavior for dynamically loaded TPU. Adv Mater Lett 11:1–6. https://doi.org/10.5185/amlett.2020.011458
12. Mars WV, Ellul MD (2017) Fatigue characterization of a thermoplastic elastomer. Rubber Chem Technol 90:367–380. https://doi.org/10.5254/rct.17.83780
13. Mars WV, Fatemi A (2004) Factors that affect the fatigue life of rubber: a literature survey. Rubber Chem Technol 77:391–412. https://doi.org/10.5254/1.3547831
14. Griffith AA (1921) The phenomena of rupture and flow in solid. Trans R Soc Lond 221:582–593. https://doi.org/10.1098/rsta.1921.0006
15. Stoček R, Heinrich G, Gehde M, Kipscholl R (2013) Analysis of dynamic crack propagation in elastomers by simultaneous tensile- and pure-shear-mode testing. In: Grellmann W et al (eds) Fracture mechanics & statistical mechanics, LNACM 70, pp 269–301. https://doi.org/10.1007/978-3-642-37910-9_7
16. Lake GJ, Thomas AG (1967) The strength of highly elastic materials. Proc R Soc Lond 300:108–119. https://doi.org/10.1098/rspa.1967.0160
17. Scetta G, Creton C, Ciccotti M, Heuillet P (2019) Crack propagation behaviour of polyurethane thermoplastic elastomers in cyclic fatigue. In: Proceedings of the 11th European conference on constitutive models for rubber (ECCMR 2019), June 25–27, Nantes, France
18. Faye A, Lev Y, Volokh KY (2019) The effect of local inertia around the crack-tip in dynamic fracture of soft materials. Mech Soft Mater 1:4. https://doi.org/10.1007/s42558-019-0004-2
19. Kipp ME, Sih GC (1975) The strain energy density failure criterion applied to notched elastic solids. Int J Solids Struct 11:153–173. https://doi.org/10.1016/0020-7683(75)90050-5
20. Li QM (2001) Strain energy density failure criterion. Int J Solids Struct 38:6997–7013. https://doi.org/10.1016/S0020-7683(01)00005-1
21. Eisele U, Kelbch SA, Engels H-W (1992) The tear analyzer – a new tool for quantitative measurements of the dynamic crack growth of elastomers. KGK 45:1064–1069
22. Stoček R, Heinrich G, Gehde M, Kipscholl R (2012) A new testing concept for determination of dynamic crack propagation in rubber materials. KGK 65:49–53

23. Rivlin RS, Thomas AG (1953) Rupture of rubber. I. Characteristic energy for tearing. J Polym Sci 10:291–318. https://doi.org/10.1002/pol.1953.120100303
24. Treloar LRG (1944) Stress-strain data for vulcanised rubber under various types of deformation. Trans Faraday Soc 40:59–70. https://doi.org/10.1039/TF9444000059
25. Lake GJ, Lindley PB (1966) Mechanical fatigue limit for rubber. Rubber Chem Technol 39:348–364
26. Paris P, Erdogan F (1963) A critical analysis of crack propagation laws. J Basic Eng 85:528–534. https://doi.org/10.1115/1.3656900
27. Bergstrom JS, Bischoff JE (2010) An advanced thermomechanical constitutive model for UHMWPE. Int J Struct Chang Solids 2:31–39

Adv Polym Sci (2021) 286: 203–224
https://doi.org/10.1007/12_2020_65

Published online: 29 November 2020

Cavitation in Rubber Vulcanizates Subjected to Constrained Tensile Deformation

E. Euchler, R. Bernhardt, K. Schneider, G. Heinrich, T. Tada, S. Wießner, and M. Stommel

Contents

E. Euchler (✉), R. Bernhardt, and K. Schneider
Leibniz Institute of Polymer Research, Institute of Polymer Materials, Department of Mechanics and Composite Materials, Dresden, Germany
e-mail: euchler-eric@ipfdd.de

G. Heinrich
Leibniz Institute of Polymer Research, Institute of Polymer Materials, Dresden, Germany

Technische Universität Dresden, Institute of Textile Machinery and High Performance Material Technology, Chair of Textile Technology, Dresden, Germany

T. Tada
Sumitomo Rubber Industries, Ltd., Material Research & Development HQ, Kobe, Japan

S. Wießner
Leibniz Institute of Polymer Research, Institute of Polymer Materials, Research Division Elastomers, Dresden, Germany

Technische Universität Dresden, Institute of Material Science, Chair of Elastomeric Materials, Dresden, Germany

M. Stommel (✉)
Leibniz Institute of Polymer Research, Institute of Polymer Materials, Dresden, Germany

Technische Universität Dresden, Institute of Material Science, Chair of Polymer Materials, Dresden, Germany
e-mail: stommel@ipfdd.de

Abstract The deformation and failure behavior of rubbers is significantly influenced by the chemical composition and loading conditions. Investigations on how specific loading parameters affect the mechanical behavior of rubbers are elementary for designing elastomeric products. Suitable fracture mechanical concepts describing the failure behavior of rubbers are widely accepted in industrial and academic research. However, the most common failure analyses base on macroscopic approaches which do not consider microscopic damage, although a contribution of (micro)structural changes at the network scale on the overall mechanical properties is very likely. A special phenomenon in terms of microstructural failure is cavitation due to strain constraints. Under geometrical constraints, the lateral contraction is suppressed. As a result, stress triaxiality causes inhomogeneous deformation, and internal defects, so-called cavities, appear. The formation and growth of cavities release stress and reduce the degree of constraints. Cavitation in rubbers has been studied for several decades, but the knowledge about the fundamental mechanisms triggering this process is still very limited. The present study aimed to characterize and describe cavitation in rubbers comprehensively. Hence, advanced experimental techniques, such as dilatometry and microtomography, have been used for in situ investigations on pancake specimens. Such thin disk-shaped rubber samples are characterized by a high aspect ratio. As a result, the degree of stress triaxiality is high, and the dominating hydrostatic tensile stress component causes the initiation of cavitation. Of special interest was the often suspected cavitation in unfilled rubbers. In contrast to the literature, cavitation in rubbers is not exclusively attributed to interfacial failure between the soft rubber matrix and rigid filler particles, but occurs also in unfilled rubbers. The onset of cavitation was determined precisely by highly sensitive data acquisition. Both a stress-related and an energy-based cavitation criteria were found indicating that traditional approaches predicting cavitation overestimate the material resistance against cavitation. The presented experimental methods to characterize cavitation are suitable for future studies investigating further aspects of cavitation in rubbers and other rubberlike materials, e.g., the failure behavior under dynamic loading.

Keywords Cavitation · Cavitation onset criterion · Hydrostatic tensile stress · Rubbers · Strain constraints

1 Introduction and State of the Art

The characterization and description of the mechanical behavior of rubbers is a tricky task. Even under idealized boundary conditions, such as incompressible deformation, scientists have to face challenging features, e.g., hyperelasticity. Since commercial rubber formulations are composite materials, several chemical ingredients influence the final properties as well as the processing behavior during mixing and curing. For realistic deformation scenarios, including confined geometric conditions, a lot of basic assumptions, such as the incompressibility of rubber, may not hold anymore. As a consequence, describing and modeling of rubber performance is getting even more complex. But investigations on complex loading conditions are required to achieve more reliable data for performance and lifetime prediction of rubber products.

A very specific phenomenon in the field of rubber failure is cavitation. This damaging process is characterized by the formation and growth of internal defects, so-called cavities. Although cavitation is a phenomenon that has been known since the beginning of the twentieth century [1–3], the basic mechanisms triggering this damaging process are still not fully understood. However, to improve the performance of rubber products, such as tires, sealings, bearings, or dampers, the knowledge about the deformation and failure behavior under constrained tensile deformation is essential. Due to confined geometries, rubber parts cannot contract under an applied tensile load. As a result, the hydrostatic component of the tensile stress, which is negligible under uniaxial tension, leads to internal defect growth, i.e., formation and growth of cavities. For laboratory tests, geometrical confinements can be generated using disk-shaped rubber samples fixed between two rigid sample holders made of metal or stiff plastics, e.g., polycarbonate. The critical aspect ratio of so-called pancake specimens (Fig. 1) can be quantified by the shape factor, S, which relates the loaded to the unloaded area of the rubbers sample considering its radius and thickness, r and h, respectively [4]. It should be noted that in some papers the shape factor is defined reciprocally.

$$S = \frac{\pi r^2}{2\pi r h} = \frac{r}{2h} \tag{1}$$

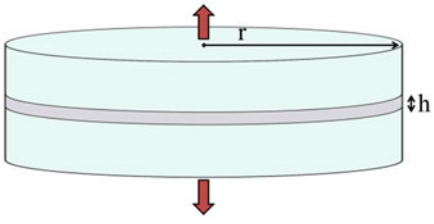

Fig. 1 Scheme of a pancake specimen consisting of two sample holders (light blue) and the rubber sample (gray) with the radius, r, and the thickness, h. The arrows (red) indicate the macroscopic loading direction

The first extensive investigation on cavitation in rubbers was performed by Gent and Lindley [4–7]. Up to now, the studies are known as poker-chip experiments. Although Gent and Lindley investigated common rubber vulcanizates, a non-rubberlike mechanical response was observed under tensile deformation. In addition, the obtained fracture surfaces exhibited cavities of different sizes and shapes, which have not been monitored before. Resting on the assumption that the onset of cavitation could be determined from the stress-strain data, a stress-related cavitation criterion, p_m, was introduced by Gent and Lindley [4]. p_m represents the maximum value of negative hydrostatic pressure occurring in the center of a stretched pancake specimen. The results of experimental and analytical investigations performed by Gent and Lindley indicated a functional relationship between p_m and the Young's modulus in uniaxial tension, E. Still, this criterion is often used to predict the cavitation onset with the following equation:

$$p_m = \frac{5}{6}E \tag{2}$$

Further studies on the cavitation phenomenon were realized using different complementary experimental techniques, such as dilatometry [8–11], acoustic measurements [12], optical analysis [13], or X-ray microtomography [14–17]. In all cases, additional information regarding the onset and progress of cavitation supported the understanding of stress-strain curves, e.g., by volumetric strain data of dilatometry. Generally, if the shape factor, S, is high, the engineering stress-strain data can be treated as equal to the hydrostatic tensile stress, σ_{HT}, versus volumetric strain, J [18]. Interestingly, most of the abovementioned studies on cavitation [4–18] are based on filler-reinforced rubbers. As a consequence, cavitation is often suspected in unfilled rubbers and mainly related to interfacial failure between soft matrix and rigid particles, such as carbon black and silica [13, 15] or zinc oxide [17]. Cavitation in unfilled rubbers has been investigated using silicones or other transparent elastomeric materials typically used as adhesives, e.g., in the glass industry. Achieved results show a clear relation between cavitation criterion, p_m, and the molecular weight, i.e., the length of polymer chains [19]. In some studies [20, 21], cavitation is described as a reversible process which is likely due to the usage of elastomeric materials with a low amount of cross-links in the network. But, since cavitation is a damaging process, it is probably related to network failure, such as polymer chain breakage [18], and, thus, irreversible. Investigations on hydrogels containing mechano-responsive functional groups, which emit photons during breakage, i.e., mechanophores, assist the latter assumption indicating mechanically induced failure of polymer chains [22, 23].

Although cavitation has been investigated for decades, the origin of cavity nucleation is still unclear. Probably, the heterogeneity of the rubber network may affect the damaging process. The network heterogeneity is influenced by the ingredients of the formulations and their distribution due to the processing, e.g., mixing and curing [24]. Additionally, voids resulting from volatile substances or impurities, such as oil or dust, can initiate cavity nucleation due to a locally lower material density and stiffness. Further aspects on cavity nucleation will be discussed in Sect. 4.3.

2 Preliminary Numerical Investigations on Strain Constraints

Independently of the rubber composition, cavitation occurs almost exclusively under constrained tension, e.g., generated due to the geometrical confinements of pancake specimens. Using the finite element (FE) software *ANSYS*, version *R19.1 Academic*, the stress situation in a pancake specimen has been analyzed. Assuming small strain, isotropy, and homogeneity, the neo-Hookean material model was chosen. The corresponding material parameters C_1 and D_1 are defined by the Lamé constants which can be revealed by the Young's modulus in tension, E, and the compression modulus, K. Since the assumption $K >> E$ can be expected also in the case of compressibility, C_1 and D_1 are expressed – according to Gent [25] – by the following equations:

$$C_1 = \frac{E}{6} \text{ and } D_1 = \frac{2}{K} \tag{3}$$

From FE simulations, stress values can be derived for selected finite elements or axes, e.g., the equator of a pancake specimen. A measure of the multiaxial stress state is the degree of stress triaxiality, η. According to Drass et al. [26], η is influenced by the triaxiality parameter, $\hbar$, which is the typically defined as the ratio of hydrostatic tensile stress and von Mises equivalent stress, σ_{HT} and σ_v, respectively [27]. Both stresses can be calculated considering the Cauchy stress tensor $\boldsymbol{\sigma} = (\sigma_x, \sigma_y, \sigma_z)$:

$$\eta = 3 * |\hbar| = 3 * \frac{\sigma_{HT}}{\sigma_v} \tag{4}$$

Theoretically, $\eta = 1$ in the case of uniaxial tension, while η tends to infinity for hydrostatic tension. Based on analytical and numerical investigations, Drass et al. [26] assessed the critical value for cavitation to be $\eta \geq 20$. In Fig. 2, η is shown as a function of the specimen's position along the equatorial plane for different shape factors, S. The critical threshold $\eta = 20$ [26] is expressed by the dashed line. Cavitation can be expected if S is sufficiently high, e.g., $S = 2.5$; otherwise the degree of stress triaxiality is too small. With increasing shape factor, the region within a pancake specimen that possibly contains cavities is increasing, which is expressed by the change in the intersection of each data curve and the critical threshold (dashed line). Thus, the width of the rim, b, surrounding the region that is covered by cavities can be determined (Table 1). The numerically obtained results regarding the width of b will be verified by surface analysis of fractured pancake specimens (Sect. 4.1).

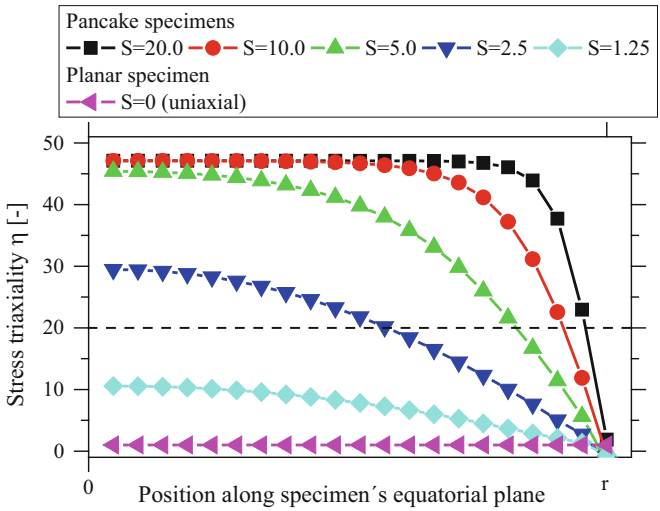

Fig. 2 FE analyses to characterize the stress triaxiality, η, along the equatorial plane of pancake specimens with different shape factors, S, while $E = 2$ MPa and $K = 20$ MPa. The dashed line represents the cavitation threshold according to Drass et al. [26]

Table 1 FE results regarding the width of the rim surrounding the region containing cavities

Shape factor	S [−]	1.25	2.5	5.0	10.0	20.0
Rim width[a]	b [mm]	–	4.3	2.0	1.0	0.5

[a]Assuming a specimen radius $r = 10$ mm

3 Experimental

3.1 Materials and Specimens

Unfilled and carbon black (CB) reinforced rubber compounds were prepared using non-crystallizing styrene-butadiene rubber (SBR), i.e., Nipol 1502, from Zeon Co., Japan. Details of the investigated rubber composition are shown in Table 2. All rubber formulations were designed and prepared by Sumitomo Rubber Industries Ltd., Japan. It is worth noting that due to the potential contribution of the rigid particles on cavitation, all compounds were prepared in the absence of zinc oxide, which is typically used as an activator for sulfur-cured rubbers [25]. The mixing process was realized in an internal mixer, and the green rubber was vulcanized to sample sheets by compression molding at 170°C. The optimized vulcanization times were defined according to the thickness and to the curing properties of the compounds estimated by a Rubber Process Analyzer from TA Instruments, USA. For the preparation of pancake specimens, disk-shaped samples were punched from sample sheets and glued between two rigid samples holders made of polycarbonate.

Table 2 Formulations of the investigated rubber compounds[a]

Sample ID	SBR	CB	Stearic acid	Antioxidants	Accelerator	Sulfur
SBR00	100	0	2.0	2.0	1.3	1.4
SBR10	100	10	2.0	2.0	1.3	1.4
SBR20	100	20	2.0	2.0	1.3	1.4
SBR30	100	30	2.0	2.0	1.3	1.4

[a]The amount of ingredients is given in parts per hundred rubbers (phr)

Table 3 Geometrical specifications of used pancake specimens

Sample ID extension[a]	Shape factor	For in situ dilatometry		For in situ microtomography	
	S [−]	r [mm]	h [mm]	r [mm]	h [mm]
2.5	2.5	10	2.0	5	1.0
5.0	5.0	10	1.0	5	0.5
10.0	10.0	10	0.5	–	–

[a]In the following, the extension will be added to the sample ID to characterize the pancake specimens explicitly

Superglue on the base of cyanoacrylate, i.e., Loctite 406™ from Henkel AG & Co. KGaA, Germany, was used to guarantee proper fixing with a low probability of interfacial failure. For the in situ experiments, different specimen geometries have been used to gain various values of the shape factor (Table 3).

3.2 Advanced Experiments

In this section, a brief introduction of the advanced experimental techniques, which have been realized to characterize cavitation in rubbers, is given. In-depth information about constructive details and optimized experimental protocols used for in situ dilatometry and X-ray microtomography can be found in another paper of the authors [28].

3.2.1 In Situ Dilatometry

A customized measuring device – a dilatometer cell – was developed and built for in situ dilatometry experiments. The principle setup of such experiments is shown in Fig. 3. Due to the optimized design of the dilatometer cell, its implementation into testing machines can be realized easily, e.g., via joint couplings. The dilatometer cell is filled with a colored fluid and connected via silicone tubes to calibrated capillaries. Due to the formation and growth of cavities, the specimen's volume will increase. The displacement of the fluid can be estimated optically by a CCD camera, type mvBlueFox from Matrix Vision GmbH, Germany, with a spatial resolution of

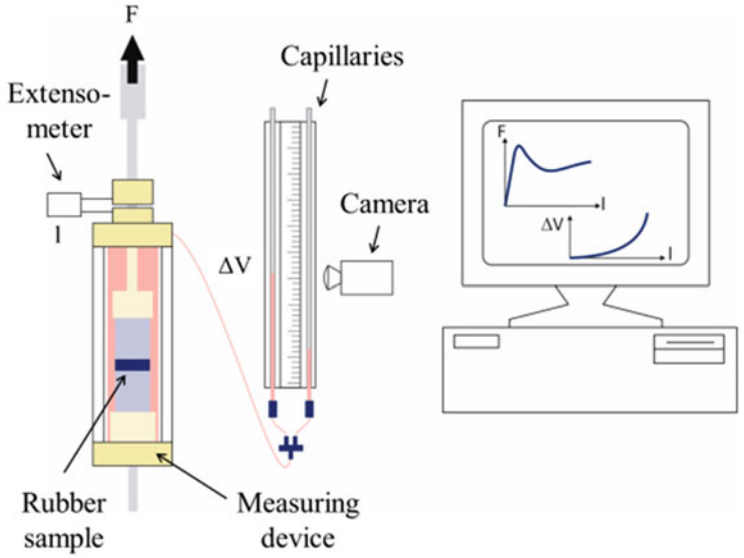

Fig. 3 Scheme of the experimental setup of in situ dilatometry. During measurements, the mechanical quantities force, F; displacement, l; and volume change, ΔV, are recorded

1,280 × 1,024 pixels with a pixel size of 5.3 µm. By using two calibrated capillaries with different inner diameters, i.e., 1.0 mm and 3.0 mm, volume change in two phases can be monitored during one measurement: (1) cavitation onset, if $\varepsilon < 0.5$, and (2) progress of cavitation until final failure, for $\varepsilon > 0.5$. The fluid flow between the capillaries can be controlled by valves. Simultaneously to the estimation of the displacement of the fluid column, force and displacement are obtained by suitable load sensors as well as an extensometer with a resolution of 0.02 µm. The experiments were performed under ambient conditions at quasi-static deformation with a loading speed of 1.0 mm/min.

3.2.2 In Situ X-Ray Microtomography (µCT)

Another customized measuring apparatus – a miniaturized tensile device – was developed and built for in situ µCT experiments. A scheme of the principle experimental setup is shown in Fig. 4.

A pancake specimen is encased by a polycarbonate vessel and attached via steel pistons to a linear actuator, type L-239.50 SD from Physik Instrumente (PI) GmbH & Co. KG, Germany. With the help of the actuator, the displacement of the pancake specimen can be controlled or measured with a resolution of 0.1 µm. The force is measured using a load sensor from burster präzisionsmesstechnik GmbH & Co KG, Germany. Force and displacement can be obtained simultaneously using customized software. The loading was performed under ambient conditions in a quasi-static

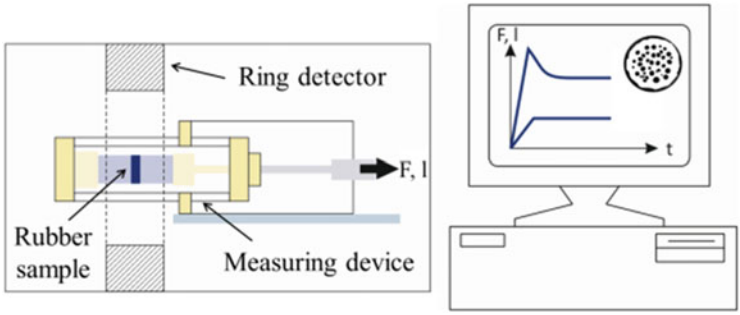

Fig. 4 Scheme of the experimental setup of in situ μCT. During measurements, the mechanical quantities force, *F*, and displacement, *l*, are recorded, and μCT images are generated

Table 4 Parameters of μCT experiments

Property	Specification
Voltage	45 kV
Current	177 μA
Rotation	360° by step of 0.12°
Pixel resolution	10 μm
Exposure time	130 ms

stepwise mode. In this study, μCT scans were realized at elevated displacement levels by X-ray tube-based microtomography using a preclinical scanner, type vivaCT 75 from Scanco Medical, Switzerland. In Table 4 the typically used parameters of the μCT experiments are summarized. The processing and evaluation of μCT data were performed using suitable software packages and tools from Scanco Medical and Java-based ImageJ.

3.2.3 Microscopy

In addition to in situ experiments, the characterization of cavitation was supplemented by surface analysis. Size distribution and shape of cavities have been studied using a digital optical microscope, type VHX 2000 from Keyence Co., Japan. Further, from Carl Zeiss NTS GmbH, Germany, a scanning electron microscope, type Ultra Plus, was used. The data evaluation was realized using open source tools of Java-based ImageJ, e.g., the "3D object counter."

4 Cavitation in Unfilled Rubbers

4.1 Cavitation Affected by the Shape Factor

Figure 5 shows typical results characterizing the deformation and failure behavior of unfilled rubber subjected to constrained tension (squares) in contrast to uniaxial tension (star). Engineering stress, σ, (filled symbols) and volumetric strain, J, (open symbols) are plotted as a function of engineering strain, ε. The data curves represent unfilled SBR with different shape factors (Tables 2 and 3). Typically, three measurements were performed for each experimental condition, but for clarity reasons the presented results are single measuring curves without error bars. The repeating tests have confirmed that the mechanical response is rather stable and the accuracy is $\pm 5\%$. While for uniaxial tension the stress-strain curve exhibits the typical "S" shape, for constrained tension the mechanical response does not display behavior that would be expected for rubbery materials. The deformation behavior due to strain constraints can be divided into four phases: (1) high stiffness in the very low strain regime, while the volumetric strain is marginal, (2) reduction of stiffness with strain and an increase in the volumetric strain, (3) dropping stress with increasing strain accompanied by a steady increase in volumetric strain, and (4) almost constant or slightly increasing stress at higher strains, while the volumetric strain increases linearly with a slope affected by the shape factor. The deformation process ends with the final failure characterized by a sudden drop in the curves. In the case of uniaxial tension, J is negligible.

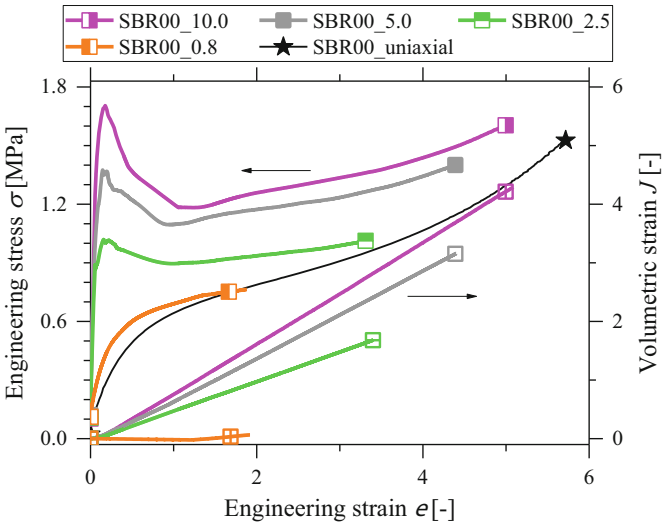

Fig. 5 Engineering stress, σ, (filled symbols) and volumetric strain, J, (open symbols) as a function of engineering strain, ε, to characterize the mechanical behavior of rubbers under different degrees of constraints (squares) and uniaxial tension (star)

Interestingly, at higher strains, the stress-strain curves obtained under constrained tension and uniaxial tension converge, which can be explained as follows. On the one side, the observed cavitation leads to stress release and, thus, reduces geometrical constraints, and the deformation becomes more and more uniaxial-like. On the other side, for initially uniaxial deformation, the progressive increase in orientation and alignment of polymer chains leads to an increase of microstructural constraints. These network constraints may cause internal damage at high strains or even just before final failure [29]. The discussion of this hypothesis will be continued in Sect. 4.4.

Fracture surface analysis of pancake specimens (Fig. 6) exhibits evidence of cavitation. The degree of constraints affects the size distribution of cavities. In general, the higher the shape factor, the higher the number of smaller cavities close to each other. In the case of SBR00_0.8, which is not shown in Fig. 6, one big cavity was monitored just before the final macroscopic failure of the specimen. Furthermore, the width of the rim surrounding the region which contains cavities is decreasing with the shape factor. This result is in good agreement with the data obtained by FE analysis (Table 1). The detailed views of cavities shown in Fig. 6 show several side cracks at the edges of single cavities indicating that cavitation can be understood as a damaging process that is driven by fracture mechanisms [30]. Additionally, the shown micrographs ensure that cavitation is not related to interfacial failure in the vicinity of the adhesive layer but occurs in the bulk of pancake specimens.

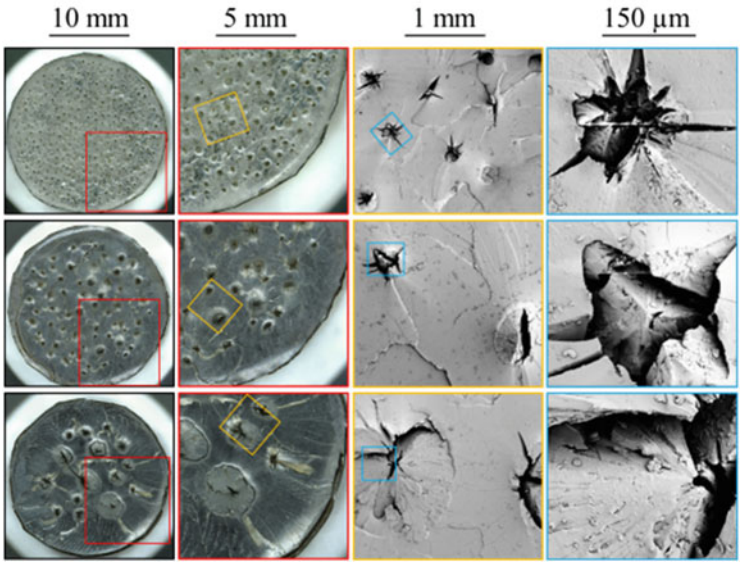

Fig. 6 Fracture surface analysis of SBR00_10.0 (top), SBR00_5.0 (middle), and SBR00_2.5 (bottom). The colored boxes mark the positions of the corresponding detailed views

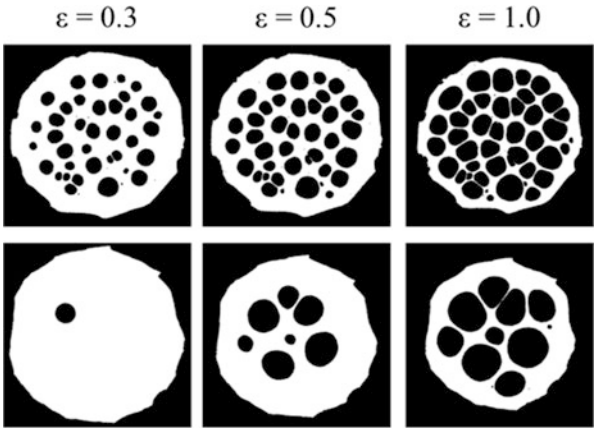

Fig. 7 Binarized μCT slices of the equatorial plane of SBR00_5.0 (top) and SBR00_2.5 (bottom) at different strain, ε. The scaling results from the initial specimen radius $r = 5$ mm

The progress of cavitation can be visualized by μCT imaging. Representatively, in Fig. 7 binarized μCT slices of the equatorial plane of a stretched pancake specimen are shown. In analogy to the results obtained by fracture surface analysis, size and number of cavities are affected by the shape factor. In Fig. 7, μCT images for $S = 5.0$ (top) and $S = 2.5$ (bottom) are compared. Furthermore, size and number of cavities increase with strain, ε, which is in agreement with the increase in volumetric strain obtained by in situ dilatometry.

Although cracks can be observed by fracture surface analysis (Fig. 6), the μCT data (Fig. 7) indicate a circular shape of cavities – or spherical in 3D. An explanation can be found considering, both, the experimental protocol and the detection limits of the μCT. By assuming that the cavity growth is controlled by crack propagation, an applied load would open up existing side cracks. However, due to the limited spatial resolution of μCT, these single side cracks cannot be separated from each other, and the contour seems to be approximately a sphere. Figure 8 illustrates the hypothetical load-controlled opening of side cracks schematically.

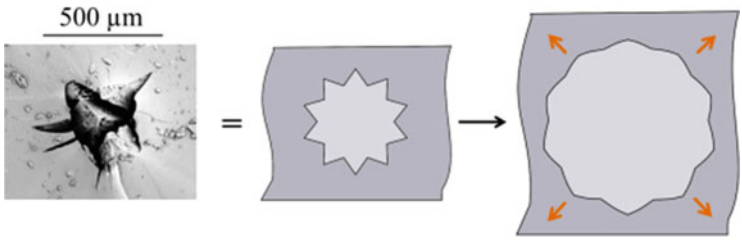

Fig. 8 Scheme illustrating the 2D expansion of starlike cavities under tension. Due to the opening of side cracks, cavities appear as spherical objects in 3D

4.2 Determination of the Cavitation Onset

The precise determination of the cavitation onset is of high interest to define a failure criterion that can be used for modeling the deformation and failure behavior of rubbers under constrained tension. Due to the detection limits of the used μCT, the early phase of cavitation cannot be evaluated by μCT imaging. Thus, the mechanical response obtained by in situ dilatometry has to be taken into account, in particular. Figure 9 shows the engineering stress, σ, and volumetric strain, J, as a function of engineering strain, ε, for SBR00_5.0. In the range of $\varepsilon \leq 0.2$, the mechanical behavior is shown for monotonic (square) and cyclic (sphere) loading. For clarity reasons, the first of three cycles for each displacement level is shown.

Owing to the deformation behavior obtained under cyclic loading, the knowledge about the cavitation process has been extended. If $\varepsilon < 0.02$, the curves show a nearly linear behavior, but after passing the critical level (K-1), the stress and volumetric strain curves exhibit hysteresis. Since for unfilled rubber internal friction processes are negligible, the hysteresis has to be attributed to an inelastic damaging process that dissipates energy [18]. The achieved results are in contrast to the approach of Gent and Lindley [4] assuming purely elastic deformation, e.g., considering Eq. (2). As a result of the cyclic and monotonic measurements performed on unfilled rubbers, the formation of the very first cavities can be determined by mechanical properties at (K-1). The other characteristic transition (K-2) corresponds to a second change in the volumetric strain curve, here, from the nonlinear to linear behavior. Interestingly, (K-2) is in good agreement with the local maximum in the engineering stress-strain curve which is often taken as the

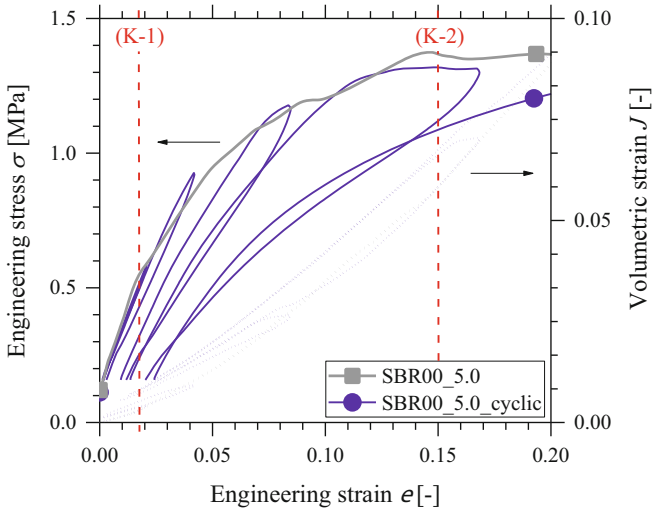

Fig. 9 Cavitation onset characterization by engineering stress, σ, and volumetric strain, J, as a function of engineering strain, ε, under monotonic (square) and cyclic (sphere) loading

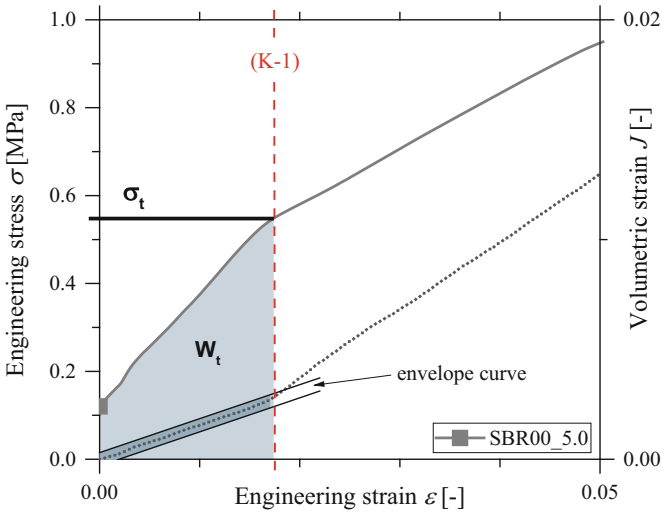

Fig. 10 Mechanical properties characterizing the cavitation onset, e.g., by σ_t and W_t, at the critical level (K-1), which is determined by the deviation of the volumetric strain curve from the defined envelope (dark gray area)

cavitation criterion, e.g., considering Eq. (2) [4]. Probably, a significantly high number of cavities has been formed at (K-2) reducing the geometrical constraints of pancake specimens by stress release.

The precise determination of (K-1) is realized by the identification of the point where the volumetric strain curve leaves the envelope range of the initially linear behavior (Fig. 10). The envelope curve is defined by the mean deviation of this linear part. The procedure to extract the characteristic material properties from dilatometry data stays the same for all investigations, i.e., considering the effect of shape factor or filler content. The absolute values of critical engineering stress, σ_t, and critical strain energy density, W_t, corresponding to cavitation onset are summarized in Sect. 6.

4.3 Nucleation of First Cavities

At strains higher than (K-1), cavities will be formed and grow with increasing strain. A remaining question remains on the origin of cavity nucleation. A material porosity with a characteristic number of intrinsic defects of finite size could be assumed [31]. If the size of these intrinsic defects is small enough, their surface tension increases the resistance against the defect opening. However, when these defects are stretched to a critical level, the surrounding network segments will bear the load until they reach the extensibility limit. Further loading would lead to the breakage of

polymer chains or cross-links. Such microfractures could explain how cavities grow and how the applied mechanical energy dissipates during cavitation. In addition, the network inhomogeneity of rubbers characterized, for example, by packing defects or the free volume [32] could trigger the formation of (sub)microscopic cavities due to inhomogeneous stress distribution through the network.

4.4 Cavity Evolution with Increasing Strain

Figure 11 shows μCT slices of the equatorial plane of a pancake specimen at elevated strain levels. While the number and size of cavities are increasing for $\varepsilon < 0.5$, the cavity number stays almost constant at high strain levels. Although the cavity size seems to increase even if $\varepsilon > 0.5$, just the thickness of walls between neighboring cavities is reduced. This effect indicates that after passing a critical load level, the geometrical constraints have been relieved; thus, cavitation is expired, and a pancake specimen containing cavities exhibits a deformation behavior comparable to uniaxial tension (Sect. 4.1).

Using μCT images, the effective cross sections of a pancake specimen have been estimated, and the true stress, σ_{true}, was calculated. In Fig. 12 the curves of σ_{true} as a function of the Hencky strain, $\ln(\lambda)$, where $\lambda = (\varepsilon + 1)$ are compared for a pristine and a preloaded pancake specimen (squares). The preloading was realized up to $\varepsilon = 1$. The preloaded and, hence, damaged pancake specimen exhibits a mechanical behavior that is comparable to that under uniaxial tension (star). Thus, the above-described hypothesis is supported further. The pristine pancake specimen is much stiffer due to the dominance of the hydrostatic tensile stress.

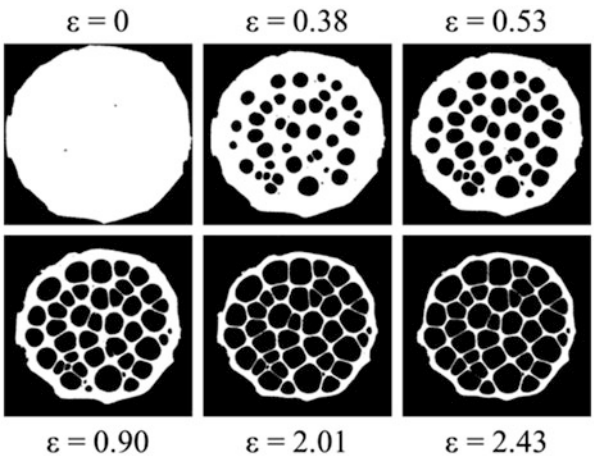

Fig. 11 Binarized μCT slices of the equatorial plane of SBR00_5.0 at different strain levels, ε. The scaling results from the initial specimen radius $r = 5$ mm

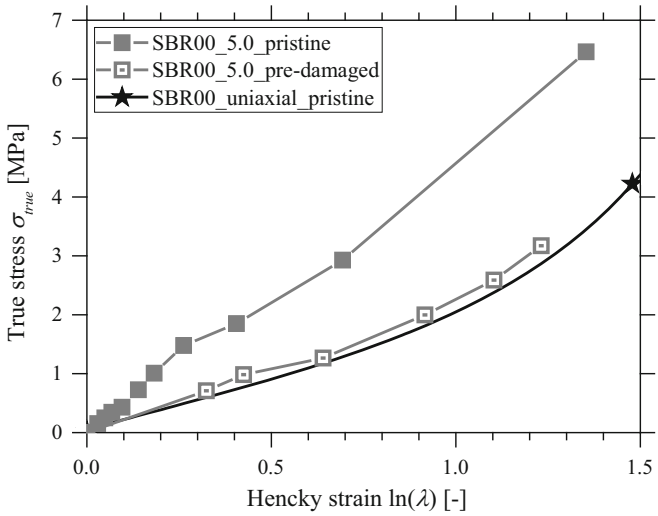

Fig. 12 True stress, σ_{true}, as a function of the Hencky strain, ln(λ), for pristine (filled square) and preloaded (open square) SBR00_5.0 pancake specimens in comparison to uniaxial tension (star)

5 Cavitation in Carbon Black Reinforced Rubbers

In the literature, cavitation in rubbers is mainly attributed to the potential interfacial failure between soft rubber matrix and rigid filler particles [4, 15]. As an important result of this study, cavitation is not exclusively related to the presence of fillers but triggered by the fracture of polymer segments in the rubber network. However, filler type and content influence the mechanical performance of rubbers immensely, and, thus, cavitation might be affected also.

Figure 13 shows representative results characterizing the deformation and failure behavior of rubbers containing different amounts of CB (Tables 2 and 3). Engineering stress, σ, (filled symbols) and volumetric strain, J, (open symbols) are plotted as a function of engineering strain, ε. Generally, with increasing CB content, the mechanical response exhibits typical features, such as higher initial stiffness, lower elongation at break, or remarkable strain hardening. The slope in the volumetric strain curve is not as much affected as in the case of the shape factor (Fig. 5).

In Fig. 14, a detailed view on the experimental data is given for $\varepsilon \leq 0.2$, and the critical levels (K-1) are marked (dashed lines). As a result, the cavitation onset properties are shifted to a higher level if the CB content is increasing. Interestingly, the first qualitative analysis suggests that the resistance against cavitation is increased due to the presence of CB. Absolute values of critical engineering stress, σ_t, and critical strain energy density, W_t, are summarized in Sect. 6.

The evolution of cavity populations influenced by the CB content can be followed by the μCT images shown in Fig. 15. For same strain levels, the number of small cavities is increasing for higher CB contents. Thus, the effect of CB content is similar

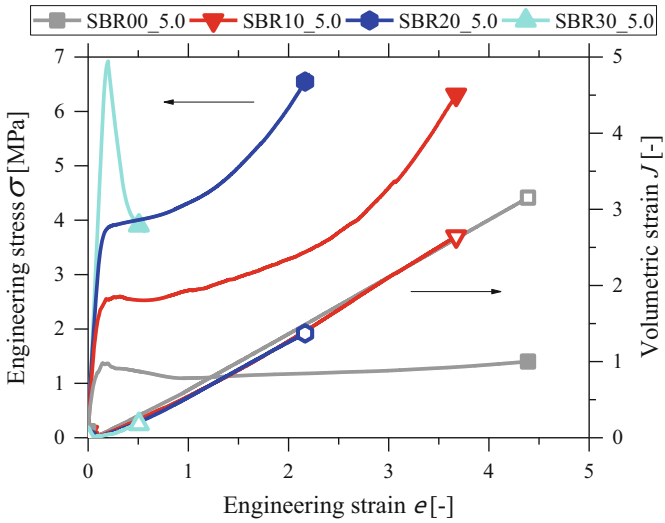

Fig. 13 Engineering stress, σ, (filled symbols) and volumetric strain, J, (open symbols) as a function of engineering strain, ε, to characterize the mechanical behavior of rubbers affected by the CB content

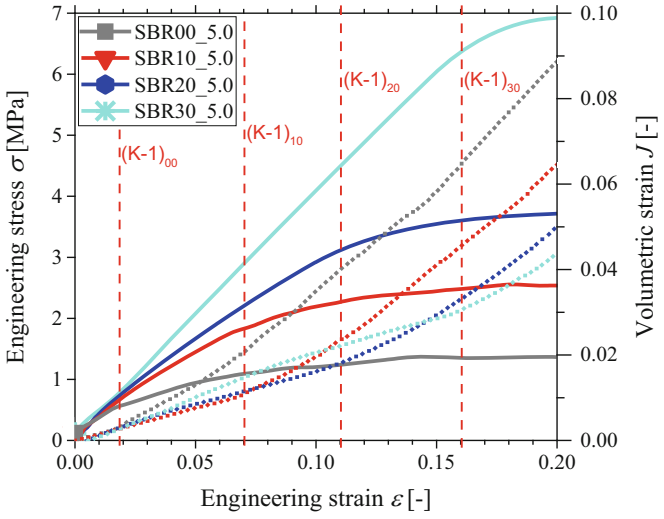

Fig. 14 Cavitation onset characterized by engineering stress, σ, (solid line) and volumetric strain, J, (dotted line) as a function of engineering strain, ε, considering different amounts of CB. The levels (K-1) are marked (dashed lines), and subscripts represent the CB content in phr

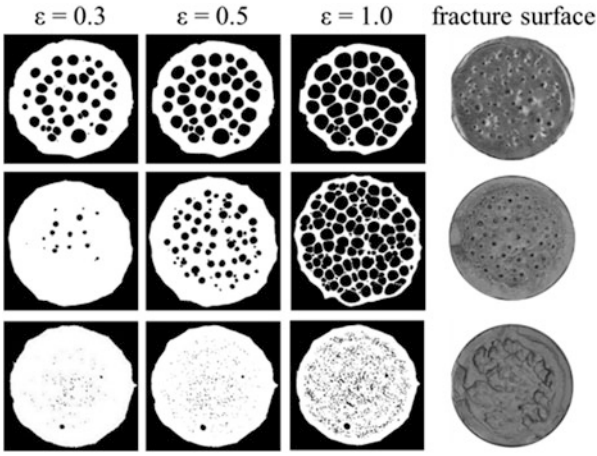

Fig. 15 Binarized µCT slices and micrographs of equatorial planes of pancake specimens at different strain levels, ε. SBR00_5.0 (top), SBR10_5.0 (middle), and SBR20_5.0 (bottom). The scaling results from the initial specimen radius $r = 5$ mm

to that observed considering the shape factor (Fig. 11). In the case of SBR20 (bottom line), the size of the cavities is too low to realize the identification of single cavities, which is again due to the detection limits of the used µCT. Probably, microscopic cavities are surrounded by tiny satellite cavities decreasing the material density locally [33]. The micrographs of the fracture surfaces shown in Fig. 15 (left) confirm that the number of small cavities is increasing with the CB content. This result can be explained by the suppressed possibility of expansion of cavities due to the presence of CB particles and agglomerates. In particular, the fracture surface of SBR20 (left bottom) does not show any cavities. Probably, the presence of a high number of tiny cavities causes the formation of small inner cracks propagating and merging inside of a pancake specimen [33], and, thus, the fracture surfaces are characterized by a certain roughness, but not by cavities.

6 Discussion on Cavitation Onset Criterions

In this study, the cavitation onset was detected precisely with the help of highly sensitive in situ dilatometry. Corresponding mechanical properties, such as critical engineering stress, σ_t, and critical strain energy density, W_t, were obtained. Table 5 summarizes the experimental results of σ_t and W_t by mean values of three measurements for each rubber formulation and shape factor (Tables 2 and 3). The corresponding standard deviations are attached. Additionally, the experimentally determined values of the Young's modulus, E, and the theoretically estimated results for p_m according to Eq. (2) are shown in Table 5.

To compare the experimental results and the prediction following the theoretical approach of Gent and Lindley [4], σ_t and W_t were normalized by the Young's modulus in tension, E. In Fig. 16, both normalized critical stress, (σ_t / E), and critical

Table 5 Mechanical properties characterizing the cavitation onset

Sample ID	S [−]	W_t [kJ/m^3]	σ_t [MPa]	p_m [MPa]	E [MPa]
SBR00_10.0	10.0	5 ± 1	0.41 ± 0.13	1.58	1.9 ± 0.1
SBR00_5.0	5.0	6 ± 0	0.53 ± 0.05	1.58	1.9 ± 0.1
SBR00_2.5	2.5	32 ± 5	0.88 ± 0.03	1.58	1.9 ± 0.1
SBR00_0.8[a]	0.8	923	0.74	1.58	1.9 ± 0.1
SBR10_5.0	5.0	79 ± 9	1.84 ± 0.02	3.00	3.6 ± 0.2
SBR20_5.0	5.0	209 ± 17	3.33 ± 0	6.50	7.8 ± 0.4
SBR30_5.0	5.0	379 ± 223	4.57 ± 2.62	13.75	16.5 ± 2.0

[a]Only one measurement has been performed

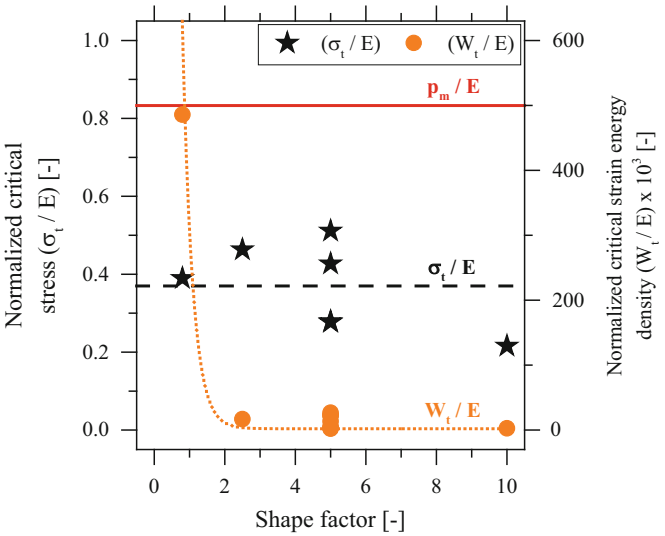

Fig. 16 Normalized critical stress, (σ_t / E), (stars) and critical strain energy density, (W_t / E), (spheres) as a function of shape factor, S. The amount of CB is considered due to the normalization by the Young's modulus, E

strain energy density, (W_t / E), are plotted as a function of the shape factor, S. The point cloud (stars) of (σ_t / E) indicates an independent critical stress level required for cavitation onset. Thus, a stress criterion is reasonable, but experimentally obtained mean value, 0.37 ± 0.11 (dashed line), is significantly lower than the value of the theoretical prediction, p_m, (solid line). As a consequence, p_m overestimates the material resistance against cavitation. Remark: σ_t represents an average value of the tensile stress and not directly the hydrostatic component. However, σ_t and p_m can be compared if the shape factor is high, because in such a case, the volumetric component of the tensile deformation is dominating, while the deviatoric component is negligible [18].

Interestingly, the data points (spheres) of (W_t / E) do not show a critical limit at the first sight (Fig. 16). Fitting the experimental data by nonlinear curve fitting tools, an exponential function (dotted line, $R^2 = 0.9263$) can be found. The choice of an exponential fit is reasonable, because, as a result, the two types of rubber failure controlled by the shape factor can be distinguished. (1) If the shape factor is low or tends to zero, a high amount of energy is required to initiate failure, while cavitation is suppressed. For uniaxial tension, the strain energy density at final failure is in the range of 10^3–10^4 kJ/m^3. (2) If $S > 1.5$, less energy is required to initiate rubber failure, which is characterized by cavitation. The plateau-like part of the fitting curve (Fig. 16) suggests an energy-based criterion for high S.

7 Conclusion and Summary

In this study, in situ experiments have been performed to study cavitation in unfilled and carbon black (CB) reinforced styrene-butadiene rubbers (SBR). The results obtained by dilatometry, X-ray microtomography, and fracture surface analysis show evidence of cavitation in unfilled rubbers, although often suspected. Furthermore, a moderate amount of CB, i.e., not higher than 30 phr, enhances the material resistance against cavitation, which is in contrast to the general impression of other studies. The achieved results suggest that cavitation is controlled by the failure behavior of network segments, such as breakage of polymer chains. Experimental results representing the cavitation onset indicate that the stress criterion is much lower compared to the often used theoretical prediction following Gent and Lindley's approach. An energy-based cavitation criterion can be found, if the shape factor is sufficiently high. In the future, further experimental work is required to extend the knowledge of cavitation in rubbers, e.g., by investigating the impact of rubber network heterogeneity. In addition, the effect of cavitation on the macroscopic crack propagation behavior should be investigated to understand the connection between rubber failure modes at different length scales.

Acknowledgments The authors thank Sumitomo Rubber Industries Ltd., Japan, for generous financial support. Also, the authors thank Dr. Vogel, Dr. Boldt, and Ms. Auf der Landwehr for providing SEM images. Ms. C. Scheibe is acknowledged for assistance in the graphical work.

References

1. Schippel HF (1920) Volume increase of compounded rubber under strain. Ind Eng Chem Res 12:33–37
2. Busse WF (1938) Physics of rubber as related to the automobile. J Appl Phys 9:438–451
3. Yerzley FL (1939) Adhesion of neoprene to metal. Ind Eng Chem Res 31:950–956
4. Gent AN, Lindley PB (1961) Internal rupture of bonded rubber cylinders in tension. Rubber Chem Technol 34:925–936

5. Gent AN, Lindley PB (1957) Internal flaws in bonded cylinders of soft vulcanized rubber subjected to tensile loads. Nature 180:912–913
6. Gent AN, Tompkins DA (1969) Surface energy effects for small holes or particles in elastomers. J Polym Sci Polym Phys Ed 7:1483–1487
7. Gent AN, Park B (1984) Failure processes in elastomers at or near a rigid spherical inclusion. J Mater Sci 19:1947–1956
8. Holt WL, McPherson AT (1937) Change of volume of rubber on stretching: effects of time, elongation, and temperature. Rubber Chem Technol 10:412–431
9. Shinomura T, Takahashi M (1970) Volume change measurements of filled rubber Vulcanizates under stretching. Rubber Chem Technol 43:1025–1035
10. Chenal J-M, Gauthier C, Chazeau L, Guy L, Bomal Y (2007) Parameters governing strain induced crystallization in filled natural rubber. Polymer 48:6893–6901
11. Hocine NA, Hamdi A, Naït Abdelaziz M, Heuillet P, Zaïri F (2011) Experimental and finite element investigation of void nucleation in rubber-like materials. Int J Solids Struct 48:1248–1254
12. Kakavas PA, Chang WV (1991) Acoustic emission in bonded elastomer discs subjected to uniform tension. II. J Appl Polym Sci 42:1997–2004
13. Tunnicliffe LB, Thomas AG, Busfield JJC (2011) Light scattering and transmission studies of nanofiller particulate size, matrix cavitation, and high strain interfacial dewetting behavior in silica-elastomer composites. J Polym Sci Part B Polym Phys 49:1084–1092
14. Bayraktar E, Antolonovich S, Bathias C (2006) Multiscale study of fatigue behaviour of composite materials by X-rays computed tomography. Int J Fatigue 28:1322–1333
15. Le Saux V, Marco Y, Calloch S, Charrier P (2011) Evaluation of the fatigue defect population in an elastomer using X-ray computed micro-tomography. Polym Eng Sci 51:1253–1263
16. Le Gorju Jago K (2012) X-ray computed microtomography of rubber. Rubber Chem Technol 85:387–407
17. Huneau B, Masquelier I, Marco Y, Le Saux V, Noizet S, Schiel C, Charrier P (2016) Fatigue crack initiation in a carbon black–filled natural rubber. Rubber Chem Technol 89:126–141
18. Dorfmann A, Fuller KNG, Ogden RW (2003) Busfield J, Muhr A (eds) Modelling dilatational stress softening of rubber in constitutive models for rubber III. CRC Press, pp 253–261
19. Cristiano A, Marcellan A, Long R, Hui C-Y, Stolk J, Creton C (2010) An experimental investigation of fracture by cavitation of model elastomeric networks. J Polym Sci Part B Polym Phys 48:1409–1422
20. Poulain X, Lefèvre V, Lopez-Pamies O, Ravi-Chandar K (2017) Damage in elastomers: nucleation and growth of cavities, micro-cracks, and macro-cracks. Int J Fract 205:1–21
21. Ono H, Nait-Ali A, Kane Diallo O, Benoit G, Castagnet S (2018) Influence of pressure cycling on damage evolution in an unfilled EPDM exposed to high-pressure hydrogen. Int J Fract 210:137–152
22. Creton C, Ciccotti M (2016) Fracture and adhesion of soft materials: a review. Rep Prog Phys 79:046601
23. Stratigaki M, Baumann C, van Breemen LCA, Heuts JPA, Sijbesma RP, Göstl R (2020) Fractography of poly(N-isopropylacrylamide) hydrogel networks crosslinked with mechanofluorophores using confocal laser scanning microscopy. Polym Chem 11:358–366
24. Valentín JL, Posadas P, Fernández-Torres A, Malmierca MA, González L, Chassé W, Saalwächter K (2010) Inhomogeneities and chain dynamics in diene rubbers vulcanized with different cure systems. Macromolecules 43:4210–4222
25. Gent A (2012) Engineering with rubber – how to design rubber components. Carl Hanser Verlag, Munich
26. Drass M, Schwind G, Schneider J, Kolling S (2017) Adhesive connections in glass structures—part I: experiments and analytics on thin structural silicone. Glass Struct Eng 3:39–54
27. Kuna M (2013) Finite elements in fracture mechanics. Springer, Berlin
28. Euchler E, Bernhardt R, Schneider K, Heinrich G, Wießner S, Tada T (2020) In situ dilatometry and X-ray microtomography study on the formation and growth of cavities in unfilled styrene-butadiene-rubber vulcanizates subjected to constrained tensile deformation. Polymer 187:122086

29. Pavlov AS, Khalatur PG (2016) Filler reinforcement in cross-linked elastomer nanocomposites: insights from fully atomistic molecular dynamics simulation. Soft Matter 12:5402–5419
30. Pourmodheji R, Qu S, Yu H (2017) Two possible defect growth modes in soft solids. J Appl Mech 85:0310011–03100110
31. Mars WV, Fatemi A (2006) Nucleation and growth of small fatigue cracks in filled natural rubber under multiaxial loading. J Mater Sci 41:7324–7332
32. Marzocca AJ, Salgueiro W, Somoza A (2013) Visakh PM, Thomas S, Chandra AK, Mathew AP (eds) Physical phenomena related to free volumes in rubber and blends in advances in elastomers II: composites and Nanocomposites. Springer, Berlin, pp 399–426
33. Yamaguchi T, Koike K, Doi M (2007) In situ observation of stereoscopic shapes of cavities in soft adhesives. EPL 77:64002

Adv Polym Sci (2021) 286: 225–244
https://doi.org/10.1007/12_2020_67

Published online: 27 November 2020

Fatigue Crack Growth vs. Chip and Cut Wear of NR and NR/SBR Blend-Based Rubber Compounds

R. Stoček, P. Ghosh, A. Machů, J. Chanda, and R. Mukhopadhyay

Contents

Abstract Tyre tread directly comes in contact with various road surfaces ranging from very smooth roads up to riding on rough road surfaces (e.g. gravel roads, roots, stalks) and is prone to damage due to cut from sharp asperities during service. As tyre experiences millions of fatigue cycles in its service life, these cuts propagate

R. Stoček
PRL Polymer Research Lab, Zlin, Czech Republic

Centre of Polymer Systems, Tomas Bata University in Zlín, Zlin, Czech Republic

P. Ghosh (✉), J. Chanda, and R. Mukhopadhyay
Hari Shankar Singhania Elastomer and Tyre Research Institute, Mysore, Karnataka, India
e-mail: pghosh@jkmail.com

A. Machů
Centre of Polymer Systems, Tomas Bata University in Zlín, Zlin, Czech Republic

continuously and lead to varied fracture processes from simple abrasion, crack growth up to catastrophic failure. In this paper firstly the complete fatigue crack growth (FCG) characteristics of rubbers from the endurance limit up to the ultimate strength and, finally, compared the data with a fast laboratory testing method determining the Chip and Cut (CC) behaviour. The study is focussed on investigation of pure natural rubber (NR) and natural rubber/styrene butadiene rubber (NR/SBR) blends, based on industrial compound formulations used for tyre tread applications. These rubbers have well-established FCG characteristics in field performance of tyre treads, with NR exhibiting the higher FCG resistance at high region of tearing energies, whereas the advantage of SBR over NR can be realized in terms of the higher fatigue threshold for SBR occurring in the low range of tearing energies. The same trend was found from the FCG analyses consisting of the complete Paris-Erdogan curve from endurance limit up to ultimate strength as well as CC behaviour determined with a laboratory Instrumented Chip and Cut Analyser (ICCA) which operates under realistic practice-like conditions and quantifies the CC behaviour using a physical parameter.

Keyword Chipping · Crack · Cutting · Fatigue · Fracture · Laboratory testing · Rubber · Tyre tread · Wear

1 Introduction

Fatigue failure is a critical issue frequently encountered by the rubber products, such as tyres, seals, dampers, conveyor belts, etc., as these products are usually exposed to cyclic dynamic stress condition in service. In the case of tyre, it is a critical safety component of a vehicle as it has to withstand against all kinds of road hazards, varied operational conditions including environmental changes (very hot to cold condition) without compromising its desired functionality. A schematic of a tyre rolling process is depicted in Fig. 1. It clearly shows that in every tyre rotation, the tread rubber elements at the tyre-road interface area are loaded for a shorter duration (~10%) followed by a longer relaxation period (~90%). Thus during rolling, tyres are exposed to special loading pattern that can be described by Gaussian pulse waveform as shown in the Fig. 1, wherein the detail of the contact between the tyre tread and the road surface is visualized. Real dynamic loading condition is defined due to proceeding of loading at the denoted region (corresponding with the tyre footprint) in the timing range of milliseconds, after that the contact is released and the zone in the tyre tread relaxes until the next contact (revolution of the tyre) proceeds. Tyre does not make perfect contact with the road over the whole footprint area. Due to the presence of the road asperity, tyre rubber-road contact area is just a few per cent of the nominal footprint contact area [1–5]. The dissipated energy significantly increases in the smallest asperity at contact regions (green dissipation fields

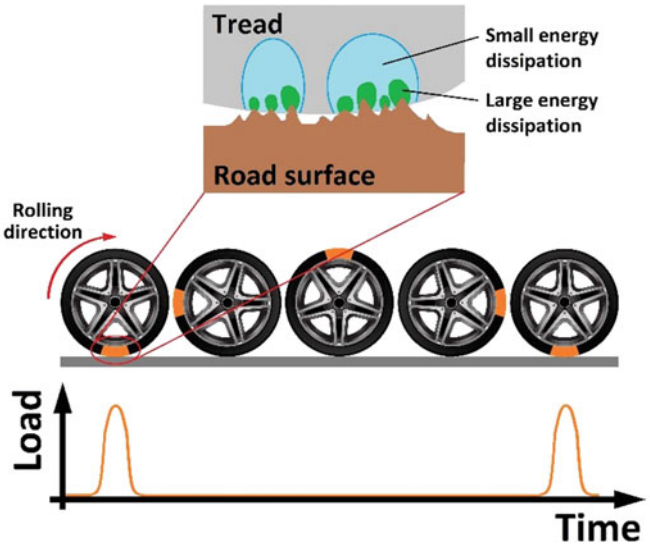

Fig. 1 Scheme of tyre rolling with the visualization of Gaussian pulse waveform and dissipation in tyre-road contact

visualized in the Fig. 1) and thus in the case of critical material value exceeding the material forces like crack driving forces can be applied; thus the fracture processes with the micro-crack initiation of the tyre tread have been started! Moreover, the micro-crack initiation is promoted due to either propagation of currently present micro-cracks in the virgin rubber matrix or due to environmental ageing by ozone and oxygen. As tyre undergoes millions of fatigue cycles, these initiated micro-cracks propagate continuously and lead to abrasion of tread, growth into macro-cracks that could lead to catastrophic failure. Therefore, exploring the fatigue damage mechanism of rubber used in tyre tread application has great significance to improve the service life of tyres. Hence, performance improvement of rubber materials with respect to fatigue damage is of paramount interest to tyre researchers.

Thus, tyre manufacturers as well as raw materials suppliers are working incessantly for improved materials that meet requirements of new generation tyres. However, introduction of any new materials in tyre production line can happen only after successful validation tests (indoor and outdoor) of tyres made with new materials. It is worth mentioning here that outdoor validation tests are quite expensive, both in terms of time as well as cost. Hence, it is necessary to devise laboratory tests that can simulate the realistic life-operating conditions of tyre and predict the performance. Ideally, predictive laboratory tests should balance accuracy, relevance and instrument productivity. It should connect to fundamental principles that show how results from a simple sheet of cured rubber are related to realistic geometry and loading conditions that occur in actual tyre use. Predictive characterization in a laboratory test set-up promises to gain complex information of the material in an early stage of development before tyre has been produced or even before designs are

finalized. Such approach promises to optimize each tyre components in terms of performance and durability. Further, it enables to fasten development times and minimize extensive tyre field tests before serial production.

The blend of natural rubber (NR) either with polybutadiene rubber (BR) or styrene butadiene rubber (SBR) is widely used in tread compound. NR/BR blend-based compounds are mainly used in truck tyre tread application, whereas NR/SBR blends find application in treads used for light truck tyres (LTT), SUV tyres (LTT) and passenger car tyres (PT) as well as for sidewall component in tyre. Although previous researchers, e.g. Refs. [6–9], have mostly reported fatigue crack growth (FCG) studies on various blend systems, where they focused on determination of stable crack growth, systematic investigation for characterization of the complex fracture fatigue behaviour from the endurance limit up to the ultimate strength is neither done theoretically nor experimentally. These phenomena are studied in isolation for various rubber or blend systems, and as mentioned above, majority of the work focused on characterization of stable crack growth characteristics and few recent studies reported investigation on the endurance limit for pure NR, SBR and BR [10, 11]. The experimental investigation of Chip and Cut (CC) resistances based on quantitative lab testing equipment of carbon black (CB)-reinforced NR, SBR and BR compounds was firstly investigated using an Instrumented Chip and Cut Analyser (ICCA) [12, 13]. Very recently, a FCG (Tear and Fatigue Analyzer) study [14] reported improvements of laboratory predictions of FCG behaviour, and their correlation to wear phenomena of truck tyre treads has been reported in [15].

NR is known for its inherent strength, its ability to withstand large deformations and resistance to FCG behaviour; however on the other side, its abrasion resistance and anti-ageing properties are poor. SBR, on the other hand, exhibits better abrasion resistance and resistance to cut initiation. Therefore, combination of NR and SBR finds vast application in various rubber products and is used as tread and sidewall component in varied tyres.

The strength of the rubber depends on its chemical structure, as well as on its viscoelastic behaviour near crack tip [16, 17]. Due to viscoelastic energy dissipation, the total energy required to propagate the crack in rubber is significantly greater than the energy associated with the endurance limit corresponding to the intrinsic strength of the molecular structure. Gent, Lindley and Thomas [18] experimentally described the fatigue fracture behaviour with a general function of the fatigue crack growth (FCG) rate, $r = da/dn$ (where da is the crack growth and dn is the increment of relevant cycle count) in dependence on the energy release rate or tearing energy, T, respectively, for rubber materials, which are loaded cyclically. Figure 2 shows the typical relationship for a rubber material in a double logarithmic diagram, known as Paris-Erdogan plot [19]. Lake and Lindley [20] firstly categorized different regions in this plot, defining different FCG behaviour. The FCG rate, da/dn, depends on the tearing energy, T, in each of the relevant regions in a characteristic manner. As long as the value of tearing energy, T, is lower than endurance limit or intrinsic strength, T_0, the FCG is independent on the dynamic loading but affected by the environmental attack. A crack operating at an energy release rate below the intrinsic

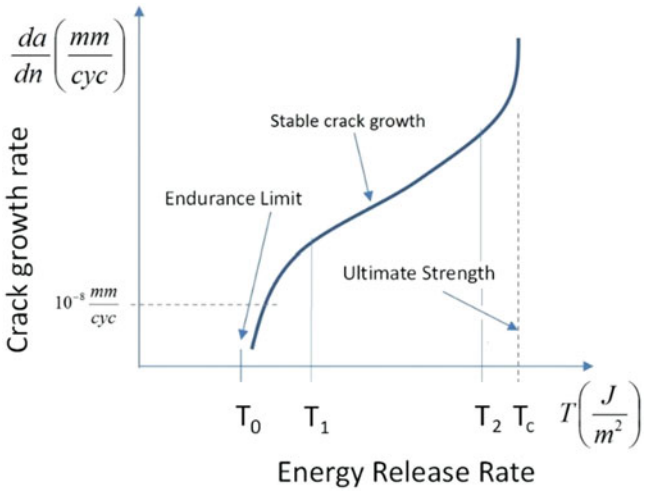

Fig. 2 Paris-Erdogan plot showing typical FCG characteristic of rubber on a log-log plot versus tearing energy

strength, T_0, can be projected to operate indefinitely without growing, since there is simply not enough energy supplied to break polymer chains at the crack tip [10]. The region of stable crack growth is located between the values of the tearing energies T_1 and T_2. This region is described with the square law defined by Paris and Erdogan in [19]:

$$T_1 \leq T \leq T_2 \rightarrow r = \frac{da}{dn} = \beta T^m, \tag{1}$$

where β and m are material constants. Finally, in the last region, the crack proceeds to the unstable fatigue growth, and the FCG rate, da/dn, becomes essentially infinite.

One practical reason for wanting to quantify the endurance limit is that it marks the lower limit of the FCG characteristic that is illustrated in Fig. 2 [21, 22]. Based on the abovementioned theorem, T_0 can be associated with intrinsic cutting energy, $S_{0,c}$ [23]. Therefore, the endurance limit or mechanical fatigue limit is very useful in product design and in fatigue analysis [24]. Few scientific publications elaborated in terms of defining the methodology for the evaluation of intrinsic strength. The pioneering work done by Lake, G. J. and O. H. Yeoh [23] is based on the cutting methods. The experimental work by Bhowmick et al. [25] reported the effect of loading of carbon black types on intrinsic strength. They analysed NR and SBR vulcanizates filled with CB varied from 10 phr (parts per hundred rubber) to 50 phr. They found that the intrinsic cutting energy increases with the increase in loading of CB irrespective of the rubber type. For N330 filled NR vulcanizates, values lie between 150 J/m^2 and 730 J/m^2, whereas SBR vulcanizates exhibited slightly higher intrinsic cutting energy, compared to NR vulcanizates at all loadings of filler. The

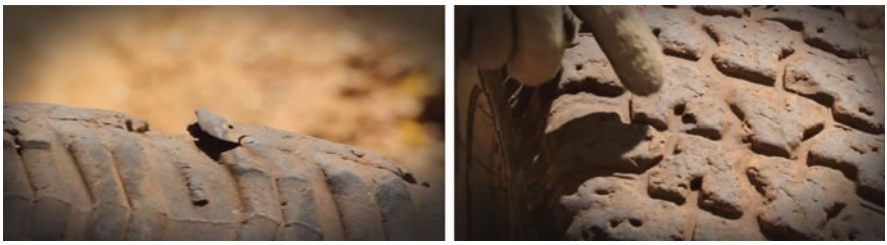

Fig. 3 Photograph of locally rupture tyre treads due to different mechanism (https://www.youtube.com/watch?v=bTnE66fvjrI)

intrinsic cutting energy varied from 360 J/m^2 for 10 phr N375 filled SBR to 1,050 J/m^2 for 50 phr filled SBR.

The pioneering work done by Rivlin and Thomas [26] on fracture mechanical study of rubber material laid the foundation of the research in this field. A considerable amount of work has been carried out on FCG characteristics in the stable crack growth region for different rubber types and varied compositions over a wide tearing energy zone. The most important results describing the general FCG behaviour of natural and synthetic rubbers have been published in Refs. [27–29]. The results show that in strain crystallizing rubber, the FCG is delayed due to strain-induced crystallization at the crack tip. On the other hand, non-strain crystallizing rubber exhibited time-dependent FCG behaviour. It was observed that the initiation of crack in synthetic rubber starts at higher tearing energy respective intrinsic strength than in NR. However, FCG in stable crack growth region shows a counter phenomenon of more rapid propagation of the crack in synthetic rubber, in comparison to the NR. Finally, the ultimate strength respective critical tearing energy, T_c, has been considered to be significantly larger in the natural rubber compared to synthetic rubbers [26]. Many researchers [27–29] have demonstrated that the critical tearing energy, T_c, does not depend on the geometry of the analysed sample and, thus, it is considered to be a material property.

In practice, due to complex and high dynamic fatigue conditions applied on the tyre, it is not possible to simply determine the complex fracture processes from the endurance limit up to ultimate strength. In service, it is mainly the final state after reaching the ultimate strength that can be qualitatively evaluated from images of failed tyres. Few practical examples of damaged tyre treads after reaching the ultimate strength are shown in Fig. 3. Both images in this figure demonstrate the CC wear; however each caused due to very different mechanism. The image shown in the left of Fig. 3 demonstrates the fracture caused by slipping, whereas the right image revealed the fracture process, caused by rolling of tyre tread over high asperities. In the scientific works Refs. [12, 13, 30], it has been clearly shown that the CC mechanism of tyre tread compound appearing under high severity conditions proceeds in the high tearing energy region close to ultimate strength.

Traditional testing methods used in the tyre industry to measure complete FCG properties in relation to real fracture processes occurring in tyres during service are

not very effective. These methods do not capture the detailed structure-property relationship which is necessary for the rational design of improved compounds for demanding applications.

Thus, the aim of this work is the quantitative determination of the complete Paris-Erdogan curve characterizing the FCG behaviour from endurance limit up to ultimate strength and, additionally, compare this behaviour with CC performance measured using a laboratory Instrumented Chip and Cut Analyser (ICCA) for pure NR as reference compound and for an industrial NR/SBR blend based compound.

2 Experimental

In this study, two industrial tyre tread rubber compounds were used. These are proprietary compounds, and hence detailed formulations are not disclosed here. However, brief compositions of these compounds are summarized below for better interpretation of the results. Out of these two compounds, one compound is based on 100 natural rubber filled with 50 phr (parts per hundred rubber) of dual filler (N220 carbon black and silica) and contains sulphur/accelerator curing system (total 1.6 phr), and other additives constitute 15 phr. Hereafter this compound will be called as NR compound. The other compound is 40–60 blend of NR & SBR filled with 66 parts dual filler (N220 carbon black and silica) and contains sulphur/accelerator curing system (total 1.9 phr), and other additives constitute (zinc oxide, stearic acid, anti-degradants, etc.) 16 phr. Hereafter this compound will be termed as NR/SBR compound.

These rubber compounds were prepared in four-stage mixing process using a laboratory scale Banbury mixture (Stewart Boling, UK) of 1.6-L capacity. In the first stage, mixing of rubbers and chemicals (except curatives) was carried out at rotor speed of 60 rpm (rotation per minute) for 5.5 min, and chamber temperature was set at 90°C. The second and third stages of mixing were performed for the duration of 5 min and 4 min, respectively, at 60 rpm. and 90°C chamber temperature. In fourth stage of mixing, curatives were mixed with the compound at 30 rpm and 70°C chamber temperature.

The required specimens for investigations were cured in a heated press (LaBEcon 300 from Fontijne Presses, Netherlands) at 160°C according to the optimum curing time *t90* + 1 min/1 mm thickness, where the *t90* has been determined from cure rheometer curves evaluated at 160°C using a Moving Die Rheometer (MDR 3000 Basic from MonTech, Germany) according to ASTM 6204.

2.1 Determination of Endurance Limit

An Intrinsic Strength Analyzer (ISA™), manufactured by Coesfeld GmbH & Co. KG, Germany, is used for estimating the endurance limit of the rubber

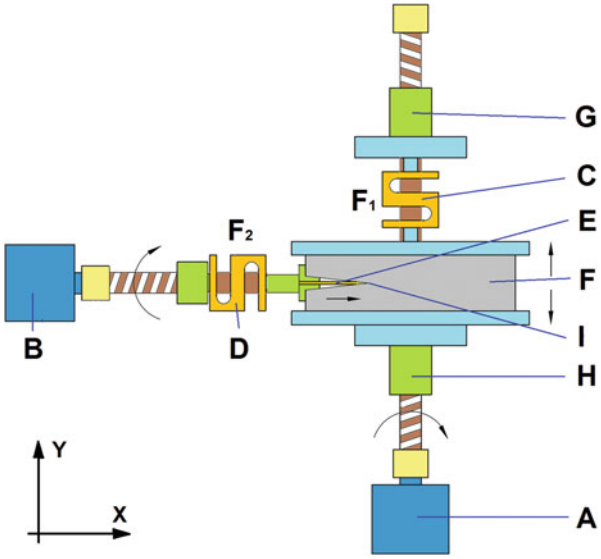

Fig. 4 Measurement principle, where (**a**), actuator of the axis Y; (**b**), actuator of the axis X; (**c**), loading cell of the axis X; (**d**), loading cell of the axis Y; (**e**), razor blade; (**f**), test specimen; (**g**), top clamping system of test specimen; (**h**), bottom clamping system of test specimen; (**i**), razor blade tip

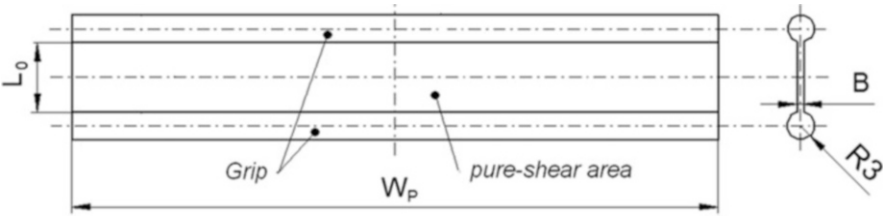

Fig. 5 Plane strain sample geometry, where $L_0 = 10$ mm, $W_P = 100$ mm and $B = 1.5$ mm (length x width x thickness)

compounds. Test methodology for endurance limit estimation is developed by Endurica LLC, USA, based on the approach of Lake and Yeoh [23].

The measuring principle of the ISA is schematically visualized in Fig. 4, and more details can be found in the previous publications Refs. [10, 11]. A plane strain (PS) tension samples (where the length of the sample is considerably lower than the width and the crack length is sufficiently long) (see Fig. 5) often labelled 'pure shear' [26, 32] is clamped to a tensile measuring station, which is instrumented to measure and control force and strain in the tension direction. The tensile set-up is symmetrical, meaning that the centre of the specimen remains in initial position during the variations of stress and/or strain. Orthogonally to the straining direction, positioned on this stable centre axis, a second actuator is located, which is also instrumented to

measure and control force and/or strain. Additionally, it is equipped with a sharp cutting blade that cuts through the sample at varied rates that are specified by the experimental protocol in Refs. [10, 11].

For the PS specimen at each applied strain before the cutting step-by-step process is applied, the tearing energy, T, is computed as the product of the strain energy density, w, and the unstrained section gauge height, L_0.

$$T = wL_0. \tag{2}$$

The strain energy density, w, in the specimen is determined as a function of strain by numerically integrating the stress-strain curve.

During the cutting by the blade, the moving force, f, is required to maintain constant rate of cutting, imparting an additional contribution to the total energy release rate, driving the crack tip. We call this the cutting energy, and its value is given by

$$F_c = \frac{f}{B}, \tag{3}$$

where B is the thickness of the specimen.

When the crack tip dissipation is sufficiently small, the cutting energy, S, for strained PS specimen, undergoing the cutting process, may be written as the sum of individual energy release rates for tearing and cutting:

$$S = T + F_c, \tag{4}$$

where T is the tearing energy and F_c is the cutting energy.

A series of consecutive measurements is performed with varied tearing and cutting energies applied. If the lowest value of $S_{0,c}$ is taken after this procedure, it is obviously the lowest energy to progress a crack with the given blade and called the intrinsic cutting energy, $S_{0,c}$.

The intrinsic strength, T_0 (endurance limit), is proportional to $S_{0,c}$, with a proportionality constant, b, which depends on the material analysed and the blade sharpness:

$$T_0 = bS_{0,c}. \tag{5}$$

The proportionality constant, b, has a value between 0.1 and 0.18 known from the work of Lake, G. J., Yeoh, O. H [23].

2.2 Determination of Stable Crack Growth

The measurements of FCG at stable crack growth region were carried out using a Tear and Fatigue Analyzer (TFA) produced by Coesfeld GmbH & Co. KG, Germany. The detailed description of the equipment can be found in Refs. [31, 32]. Mini-plane strain (mPS) specimen (Fig. 5) having dimensions $L_0 = 4$ mm, $W_p = 40$ mm and $B = 1.0$ mm is used for FCG measurements. Specimens were notched on both edges with the initial crack length $a_0 = 8$ mm based on the definition of minimal crack length in dependence on sample geometry ratio L_0/W_p as reported in Refs. [32, 33]. One set of three samples per compound has been analysed over the complete range of applied tearing energies. Finally, the Gaussian pulse waveform (see Fig. 1) of the pulse frequency 10 Hz, which corresponds with the pulse width 100 ms and loading frequency of 5 Hz at the operating temperature 70°C close to the real service conditions of tyre, has been applied for the analyses over a broad range of tearing energies, T, or strains. The analyses were performed at fully relaxing mode, where the R-ratio $=> R = 0$, which is the minimum applied stress divided by the maximum applied stress: $R = \sigma_{\min}/\sigma_{\max}$). The crack growth of each sample is monitored in situ through an image-processing system with a CCD camera. The crack contour length and the crack growth increment as well as the data of fatigue behaviour are evaluated. The resulting data finally determine the power-law defined with Eq. (1), representing the relationship between FCG rate, da/dn, over the range of tearing energies, T, where the crack grows steadily and where and the measured quantities are represented in a logarithmic scale.

2.3 Determination of Ultimate Strength

The ultimate strength has been experimentally estimated using an Intrinsic Strength Analyzer (ISA™), introduced previously and followed the above described testing protocol up to reaching the critical tearing energy, T_c. The identical pure shear rubber sample as visualized in the Fig. 5 has been used. Three sample replicates per compound have been investigated.

2.4 Determination of Chip and Cut Behaviour

Laboratory CC testing was performed on the rubber specimens using an Instrumented Chip and Cut Analyser (ICCA) manufactured by Coesfeld GmbH & Co. KG, Germany, e.g. Refs. [12, 13, 30, 34, 35]. Testing with the ICCA involves rotating the rubber sample at a selected rotational speed and impacting the sample with a stainless steel tool with specified frequency. The rotation speed, impact

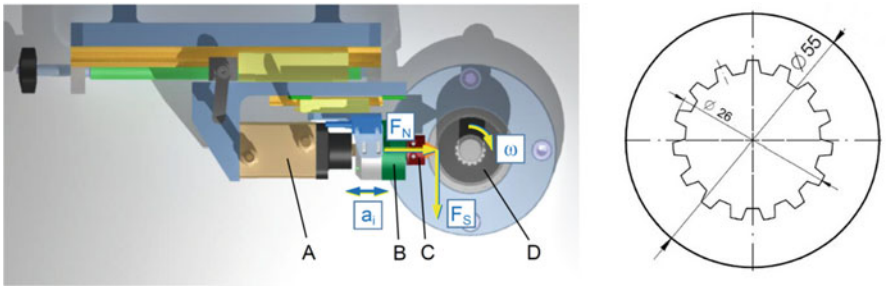

Fig. 6 Schematic of ICCA measuring principle, with pneumatic actuator (**a**); two-axis load cell (**b**); holder + impactor (**c**); and cylindrical rubber test specimen (**d**) and the rubber sample geometry with thickness of 13 mm (right)

Table 1 ICCA loading conditions

Rotation speed [rpm]	Impact normal forces [N]	Impacting frequency [Hz]	Impact time [ms]
200	70, 100, 130, 150, 170	5	200

normal force, frequency and contact (sliding) time with the rubber surface all can be independently controlled. A scheme of ICCA measuring principle is visualized in Fig. 6, left. In Fig. 6, right, the sample geometry used for the analysis is shown. The inside specific geometry of the sample is purposefully designed for assuring exact fixing of the sample in the device for maintaining constant position and prevention against the slippage during the dynamic impact. More details on impacting device, impactor geometry and description of the independent control of impact frequency and sliding time can be found in recent references [12, 13, 30, 34, 35].

As the tangential force is the resultant of impact force, which is assumed to grow proportionally with increasing roughness of the penetrated surface, thus it is taken to calculate the degree of damage for every load cycle. Therefore, the key characterization factor evaluated from a multi-channel data acquisition is the CC Damage, which is calculated using a numerical algorithm. The tangential force shows an increasing scattering as test time progresses, obviously due to the increase in roughness of the sample surface during the course of testing. For this reason, an enwrapping curve is constructed which is numerically integrated from a certain starting point $C(0)$ to a cycle count of interest, $C(n)$. Each sum will be divided by the corresponding cycle number $c(k)$ $(0 < k < n)$. This (scalar) value quantifies the CC Damage at cycle count k and is called 'CC Damage, P'. The curve P vs. cycle count (k; $k = 0$ to n) is a description of the CC behaviour under the given load conditions. More details on the numerical calculation of the CC Damage, P, can be found in previous papers [12, 30].

The CC behaviour of rubber compounds were tested at room temperature in ICCA using an impactor of 2.5 mm radius. The tests were run up to 4,000 impact cycles. Five replicates of each compound were tested. The test conditions are listed in Table 1.

3 Results and Discussion

3.1 Endurance Limit

The cutting is performed with different cutting speeds and variation of tearing energy. The goal is to acquire the cutting force without any significant viscoelastic dissipation influence and friction effects between rubber and blade on the cutting energy. In accordance with the above statement, the relationship of cutting force, *f*, versus time traces, *t*, obtained during constant rate cutting experiments, takes three forms in dependence on tearing energy: smooth rise, slip-stick and force fluctuation up to zero. In Fig. 7, cutting force (*f*)-time (*t*) traces for analysed rubbers for low (dotted) and moderate (fat) tearing energy level are presented. It is clearly visible that in the low level of tearing energies, a very dominant initial smooth rise caused by the reversible elastic deformation in NR/SBR that may be attributed to the presence of non-strain crystallizing SBR in the compound. However, in the case of NR compound, this phenomenon is much lower, which is represented with lower very first peak of the curve shown in Fig. 7, A. In moderate level of tearing energy, NR

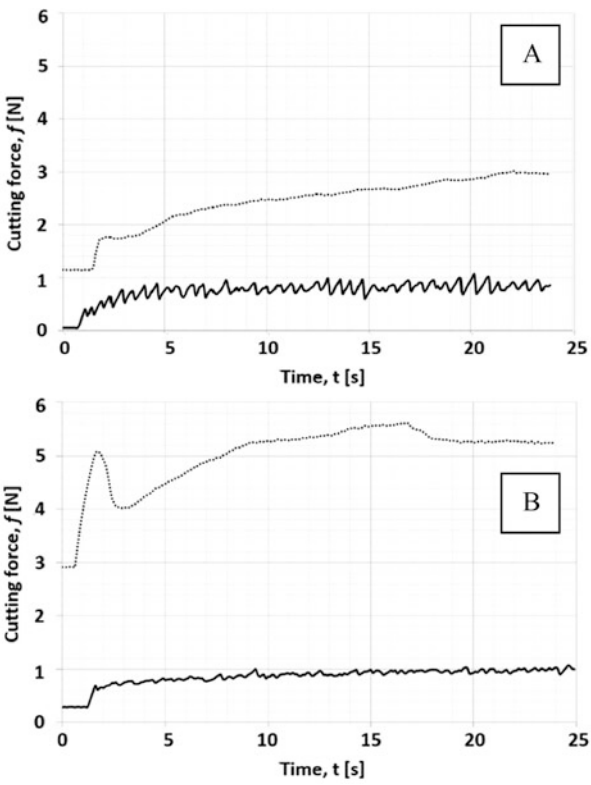

Fig. 7 Cutting force-time traces for analysed rubbers: NR (**a**), NR/SBR (**b**) for low (dotted) and moderate (fat) level of tearing energies

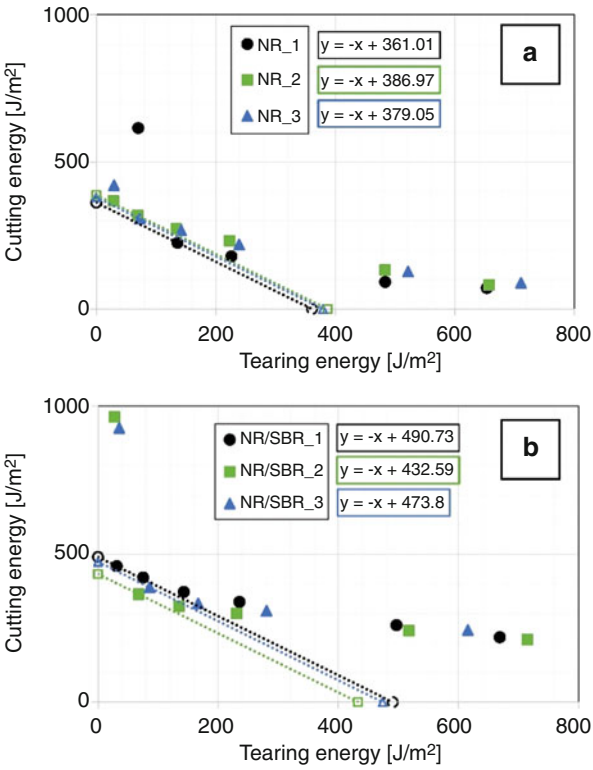

Fig. 8 Cutting energy, F_c, versus tearing energies, T, for NR (**a**) and NR/SBR (**b**) as well calculated intrinsic cutting energy, $S_{0,c}$

compound displayed stick-slip effect due to the presence of strain crystallizing property in NR, whereas the curve of NR/SBR blend is quite smooth.

Figure 8 depicts tearing energy vs. cutting energy of the rubber compounds under study. From these plots, the intrinsic cutting energy, $S_{0,c}$, of all the compounds was calculated. The simplicity of the formula in a complex nature of the various analysed compounds makes it simple to rationalize the observed dependence of intrinsic cutting energy, $S_{0,c}$, on the type of rubber used. The lower value of intrinsic cutting energy, $S_{0,c} = 376$ J/m^2 (average from three replicates), has been found for the rubber based on NR, which is caused by its strain crystallizing nature, causing the lower cutting forces over the applied range of tearing energies (see Fig. 7a). The force-time traces as depicted in Fig. 7, where the highest cutting force was determined for the NR/SBR blend containing the non-strain crystallizing SBR at lower tearing energy level, pointing out the highest elasticity of this rubber, which is reflected in terms of higher intrinsic cutting energy, $S_{0,c} = 466$ J/m^2 (average from three replicates) compare to pure NR compound.

The endurance limit, T_0, can be estimated by multiplying the intrinsic cutting strength, $S_{0,c}$ with the proportional factor, b, (see Eq. 5); in this study the factor b was chosen to be 0.13. This assumption leads to $T_0 = 49$ J/m^2 for NR and to $T_0 = 61$ J/m^2 for NR/SBR. The estimated T_0 values verify the expected trend that the addition of

SBR to NR can increase the intrinsic strength of the NR/SBR compound significantly compared to pure strain crystalizable NR compound.

3.2 Stable Crack Growth

The FCG behaviour of both compounds is plotted in Fig. 9, represented with the square-law defined in the Eq. (1), where the related material constants β, m are listed in the Table 2. Generally, the absolute value of FCG rate over the complete range of applied tearing energies is lower for the pure NR compared to NR/SBR blend. Additionally, the exponent m, defining the slope of the ability of the crack to propagate, clearly indicates superior FCG resistance by the NR compound. This is attributed to the fact that strain-induced crystallization inhibits the crack growth at higher tearing energies. The slightly higher slope, respective exponent m, was determined for the blend NR/SBR. This observation generally corresponds with the previously determined data from Lake and Lindley [20] for the FCG behaviour of natural and synthetic rubber. Finally, because of the different slopes, both curves have a theoretical crossing point at the tearing energy, $T = 0$ J/m^2.

3.3 Ultimate Strength

The critical tearing energy, T_c, was determined as the tearing energy, associated with the strain, where the crack grows without any other energy input. In Fig. 10, the

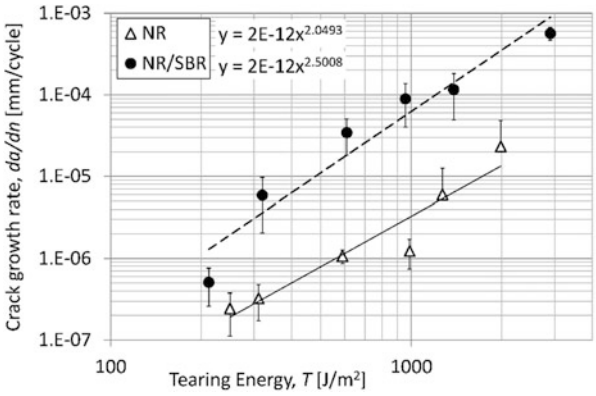

Fig. 9 FCG rate, *da/dn*, as a function of tearing energy, *T*, for the both analysed compounds

Table 2 Power-law equation and material constants determined

Material	*da/dn*	β	m
NR	2E-12x$^{2.0493}$	2E-12	2.0493
NR/SBR	2E-12x$^{2.5008}$	2E-12	2.5008

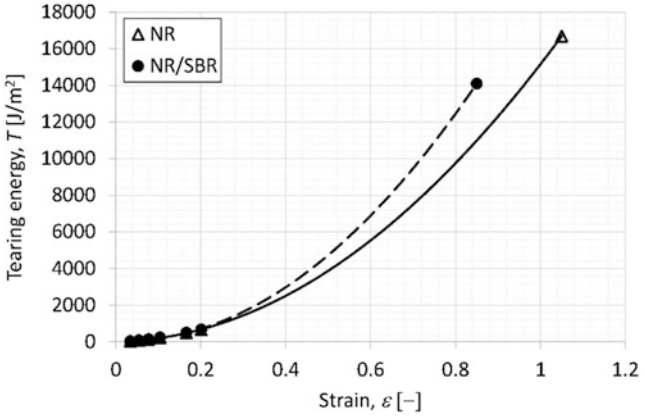

Fig. 10 Strain, ε, as a function of tearing energy, T, for analysed compounds

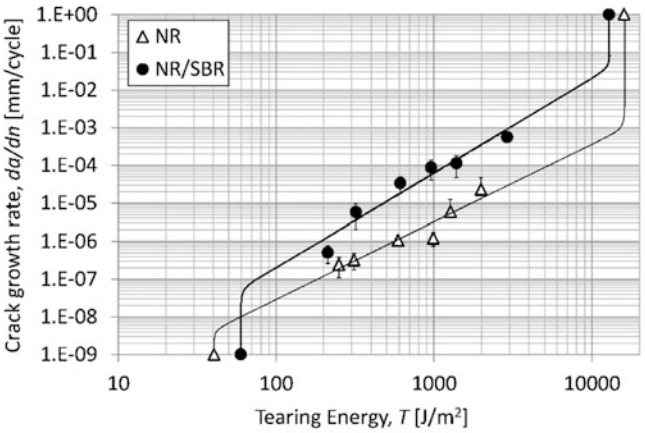

Fig. 11 Reconstructed complete FCG characteristic

critical tearing energy, T_c, demonstrates the last point of the strain vs. tearing energy function. The higher critical tearing energy $T_c = 16{,}688$ J/m^2 is exhibited by the NR-based compound compared to the critical tearing energy $T_c = 14{,}095$ J/m^2 for the NR/SBR blend.

3.4 Reconstruction of the Complete FCG Curve

Figure 11 shows the reconstructed complete FCG characteristics for both compounds. These plots contain all phases of fracture processes. The reconstruction is based on the implementation of the data determined for the endurance limits, the

stable crack growths as well as ultimate strengths evaluated in the previous paragraph.

3.5 Chip and Cut Behaviour

The results of CC tests of NR and NR/SBR compounds are shown in Fig. 12a, b, respectively. The dependence of the CC Damage, P, over the applied cycle count in the stable CC process is plotted here for four varied normal forces, F_N (see Table 1). Each curve represents an approximate polynomial function from three replicates. From this figure it can be seen that CC Damage, P, systematically increases with increase of normal force, F_N, irrespective of rubber type.

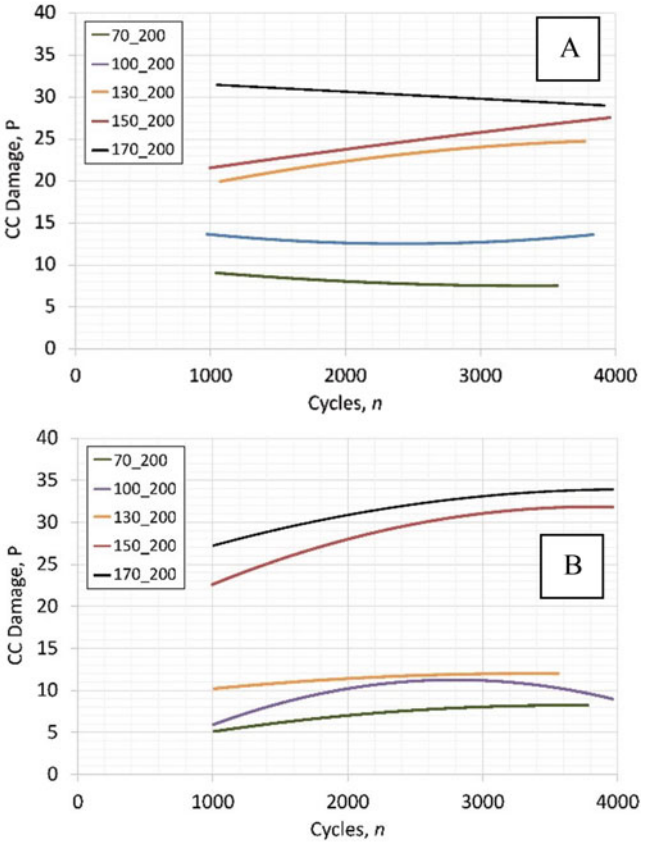

Fig. 12 CC Damage, P, versus impacting cycles for NR (**a**) and NR/SBR (**b**), whereas the labelling of the curves corresponds with the applied normal forces, F_N given in Table 1

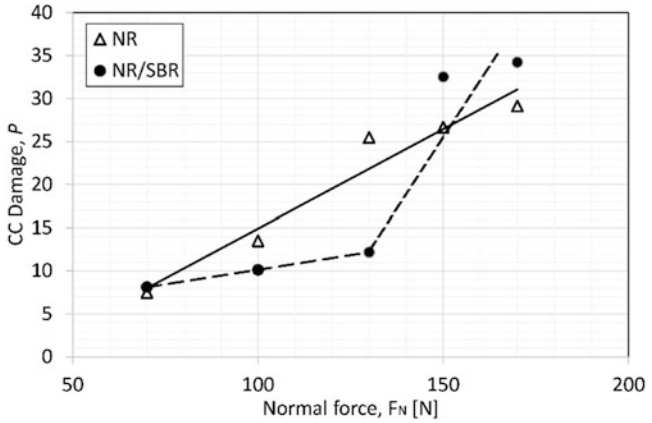

Fig. 13 CC Damage, P, versus normal forces, F_N, for both analysed compounds

The final comparison of CC Damage, P, in dependence on normal forces, F_N, for both analysed compounds is plotted in Fig. 13, where the represented P values are corresponding to the values at the very last applied cycle counts. The numerical evaluation of CC damages under different applied loading conditions gives a very clear impression of the characteristics for each type of analysed rubber. Also the comparison of NR and NR/SBR with respect to the same loading conditions shows a considerable difference in the damage development. In general, NR shows a linear increase of CC Damage for all applied normal forces. Whereas in NR/SBR blend, there is a very low and constant damage growth up to normal force of 130 N, and thereafter the slope of damage growth increased rapidly. The low damage growth at lower normal force range is due to the presence of SBR in the blend. Furthermore, it is obvious that at the low normal force level, the damage of the pure NR rubber is higher than NR/SBR, whereas at high normal force level, CC Damage, P, for NR/SBR blend remains significantly higher than that of the NR rubber. This finding is in correspondence with the previously published work [30], where more or less identical crossing behaviour for pure NR and SBR has been found. Thus, the present study confirmed the positive influence of SBR in the low level and the negative influence in the high level of normal forces on CC behaviour compared to pure NR.

It can be pointed out here that the FCG curve for the NR/SBR as shown in the Fig. 11 exhibited higher FCG rate over the complete range of applied tearing energies and shows the similar trend for CC Damage parameter at higher force level as plotted in Fig. 13.

The estimated CC Damage, P, values for both compounds can be correlated with the CC behaviour of tyres in service. It is obvious that the CC mechanism in tyre corresponds with the energy dissipation around the tip of an asperity (visualized in Fig. 1). Thus, the increase of energy dissipation as obtained experimentally is due to the increase of the normal force. A similar phenomenon of energy dissipation also takes place when a tyre runs on the roads. However, normal force or energy

dissipation varies depending on the type of roads (smooth or rough). Because of this reason, a SBR containing rubber compound performs well with respect to CC behaviour at lower normal force or tearing energy level, corresponding to terrain of low-sized asperities. This is due to the fact that SBR has a higher intrinsic strength compared to NR, whereas, at higher normal force or tearing energy level, the CC performance of SBR compound gets reversed.

Fundamentally, from the theory and ranking point of view, the determined FCG properties correspond with the CC behaviour. However, a direct quantitative derivation of the CC behaviour from the FCG characteristic is not appropriate. It is necessary to determine CC behaviour through separate CC analyses close to realistic tyre loading in service as implemented and realized using ICCA equipment.

4 Conclusion

In this paper we determined, for the first time, the complete fatigue crack growth (FCG) characteristic of rubbers from the endurance limit up to the ultimate strength and, finally, compared the data with a fast laboratory testing method determining the Chip and Cut (CC) behaviour. A series of varied experiments and unique equipment have been used for these complex analyses, whereas the endurance limit has been analysed via the determination of intrinsic strength based on the approach of Lake and Yeoh [23] using Intrinsic Strength Analyzer (ISA). The stable crack growth behaviour has been determined in situ using a Tear and Fatigue Analyzer (TFA), and the ultimate strength was determined as a final stage of the intrinsic strength measurement at the unstable region of crack growth. Finally, the CC behaviour has been determined with a laboratory Instrumented Chip and Cut Analyser (ICCA) which operates under realistic conditions and quantifies the CC behaviour using a physical parameter. The all equipment have been produced by Coesfeld GmbH & Co. KG, Germany. We have investigated carbon black (CB)-reinforced rubber based on natural rubber (NR) and natural rubber/styrene butadiene rubber (NR/SBR) blend formulations, typically used for tyre tread applications.

We found that the intrinsic strength is in fully agreement with the expected trend, i.e. the non-crystalizing SBR rubber exhibits higher threshold compared to crystalizing NR. Thus, the addition of SBR in a NR/SBR blend increases the intrinsic strength in accordance to the incorporated quantity of the synthetic rubber. The FCG rate of a NR compound is lower in the complete range of tearing energies in comparison with the NR/SBR blend. Last but not the least, a higher critical tearing energy is exhibited by NR compounds compared to NR/SBR blends. The complete FCG characteristics have been reconstructed using these data.

In accordance to the CC Damage, P, value, NR ranks higher than NR/SBR blends at lower force level, whereas the trend is reversed in the higher normal force zone. This ranking matches with the ranking of the FCG resistance of these rubber compounds.

Acknowledgments This work was supported by the Ministry of Education, Youth and Sports of the Czech Republic – DKRVO (RP/CPS/2020/004) and IGA/CPS/2020/007.

References

1. Persson B, Albohr O, Tartaglino U, Volokitin AI, Tosatti E (2005) On the nature of surface roughness with application to contact mechanics, sealing, rubber friction and adhesion. J Phys Condens Matter 17:R1–R62
2. Heinrich G, Schramm J, Müller A, Klüppel M, Kendziorra N, Kelbch S (2002) Road surface influences on braking behavior of PC-tires during ABS-wet and dry braking (in German language). Fortschritts-Berichte VDI 12:69–86
3. Grosch KA (1993) Proc R Soc Lond A274:1
4. Diserens E (2009) Calculating the contact area of trailer tyres in the field. Soil Tillage Res 103:302–309
5. Hays D (1974) The physics of tire traction, theory and experiment. Springer, Berlin
6. Hamed GR, Kim HJ, Gent AN (1996) Cut growth in vulcanizates of natural rubber, cis-polybutadiene and a 50/50 blend during single and repeated extension. Rubber Chem Technol 69:807–818
7. Lee MP (1993) Analysis of fatigue crack propagation in NR/BR rubber blend. Rubber Chem Technol 66:304–316
8. Ghosh P, Stocek R, Gehde M, Mukhopadhyay R, Krishnakumar R (2014) Investigation of fatigue crack growth characteristics of NR/BR blend based Tyre tread compounds. Int J Fract 188:9–21
9. Ghosh P, Mukhopadhyay R, Stocek R (2016) Durability prediction of NR/BR and NR/SBR blend tread compounds using tear fatigue analyser. KGK 69:53–55
10. Robertson CG, Stoček R, Kipscholl C, Mars WV (2019) Characterizing the intrinsic strength (fatigue threshold) of natural rubber/butadiene rubber blends. Tire Sci Technol TSTCA 47:292–307
11. Stoček R, Mars WV, Kratina O, Machů A, Drobilík M, Kotula O, Cmarová A (2017) Characterization of ageing effect on the intrinsic strength of NR, BR and NR/BR blends, constitutive models for rubber X – proceedings of the 10th European conference on constitutive models for rubber, ECCMR X 2017. pp 371-374
12. Stoček R, Mars WV, Kipscholl R, Robertson CG (2019) Characterisation of cut and chip behaviour for NR, SBR and BR compounds with an instrumented laboratory device. Plast Rubber Compos Macromol Eng 48:14–23
13. Robertson CG, Suter JD, Bauman MA, Stoček R, Mars WV (2020) Finite element modeling and critical plane analysis of a cut-and-chip experiment for rubber. Tire Science and Technology. In-Press
14. Wunde M, Klüppel M, Vatterott C, Tschimmel J, Lacayo-Pineda J, Schulze A, Heinrich G (2019) Verbesserung der Laborvorhersagen zum Risswachstum und Verschleiß von LKW-Reifenlaufflächen. KGK 72:72–78
15. Stocek R, Henirich G, Schulze A, Wunde M, Klüppel M, Vatterott C, Lacayo-Pineda J, Kipscholl R (2020) Chip & cut wear of truck tire treads: comparison between laboratory and real tire testing. KGK 06:51–55
16. Lake GJ, Yeoh OH (1987) Effect of crack tip sharpness on the strength of vulcanized rubbers. J Polym Sci Part B Polym Phys 25:1157–1190
17. Bhowmick AK (1988) Threshold fracture of elastomers. J Macromol Sci Polym Rev 28:339–370
18. Gent AN, Lindley PB, Thomas AG (1964) Cut growth and fatigue of rubbers. I. The relationship between cut growth and fatigue. J Appl Polym Sci:455–466

19. Paris P, Erdogan F (1963) A critical analysis of crack propagation laws. J Basic Eng Trans Am Soc Mech Eng:528–534
20. Lake GJ, Lindley PB (1965) The mechanical fatigue limit for rubber. J Appl Polym Sci 9:1233–1251
21. Lake GJ, Lindley PB (1966) Mechanical fatigue limit for rubber. Rubber Chem Technol 39:348–364
22. Andrews EH (1963) Rupture propagation in hysteresial materials: stress at a notch. J Mech Phys Solids 11:231–242
23. Lake GJ, Yeoh OH (1978) Measurement of rubber cutting resistance in the absence of friction. Int J Fract 14(5):509–526
24. Mars WV (2007) Fatigue life prediction for elastomeric structures. Rubber Chem Technol 80:481–503
25. Bhowmick AK, Neogi C (1990) Threshold tear strength of carbon black filled rubber vulcanizates. J Appl Polym Sci 41:917–928
26. Rivlin RS, Thomas AG (1953) Rupture of rubber. I. Characteristic energy for tearing. J Polym Sci 10:291–318
27. Greensmith HW, Thomas AG (1955) Rupture of rubber III. Determination of tear properties. J Polym Sci 18:189–200
28. Thomas AG (1955) Rupture of rubber II. The strain concentration at an incision. J Polym Sci 18:177–188
29. Thomas AG (1994) The development of fracture mechanics for elastomers. Rubber Chem Technol 67:G50–G60
30. Kipscholl R, Stoček R (2019) Quantification of chip and cut behaviour of basic rubber (NR, SBR). RFP Rubber Fibres Plastics 02:88–91
31. Eisele U, Kelbch SA, Engels H-W (1992) The tear analyzer – a new tool for quantitative measurements of the dynamic crack growth of elastomers. KGK 45:1064–1069
32. Stoček R, Heinrich G, Gehde M, Kipscholl R (2013) Analysis of dynamic crack propagation in elastomers by simultaneous tensile- and pure-shear-mode testing. In: Grellmann W et al (eds) Fracture mechanics and statistical mech, vol 70. LNACM, pp 269–301
33. Stoček R, Heinrich G, Gehde M, Rauschenbach A (2012) Investigations about notch length in pure-shear test specimen for exact analysis of crack propagation in elastomers. J Plast Technol 1:2–22
34. Stoček R, Mars WV, Robertson CG, Kipscholl R (2018) Characterizing rubber's resistance against chip and cut behaviour. Rubber World 257:38–40
35. Euchler E, Michael H, Gehde M, Kratina O, Stocek R (2016) Wear of technical rubber materials under cyclic impact loading conditions. KGK 69:22–26

Adv Polym Sci (2021) 286: 245–272
https://doi.org/10.1007/12_2020_74

Published online: 21 December 2020

Review on the Role of Phase Morphology and Energy Dissipation Around the Crack Tip During Fatigue Crack Propagation of Filler-Reinforced Elastomer Blends

Matthias Wunde and Manfred Klüppel

Contents

Abstract The paper reviews recent investigations of fatigue crack propagation in filler-reinforced elastomer blends based on recipes referring to truck tire tread compounds. One focus lies on viscoelastic energy dissipation effects that explain the well-known power law behavior of the crack growth rate vs. tearing energy. It is demonstrated that the crack growth rate fulfills the time-temperature superposition

M. Wunde and M. Klüppel (✉)
Deutsches Institut für Kautschuktechnologie e.V., Hannover, Germany
e-mail: Manfred.klueppel@DIKautschuk.de

principle by constructing master curves with shifting factors from viscoelastic data. In addition, energy dissipation mechanisms due to stress softening in vicinity of the crack tip are evaluated under quasi-static conditions by calculating the J-integral, which decreases significantly while approaching the crack tip. Therefore, we use combined experimental and theoretical techniques consisting of digital image correlation measurements of the strain field around the crack and calculations of the corresponding energy densities and stress fields based on a physically motivated stress-softening model of filled rubbers. A second focus lies on the role of phase morphology of carbon black (CB) filled NR/BR and NR/SBR blends in fatigue crack propagation. Therefore, the filler distribution is evaluated by an established technique referring to the variation of viscoelastic loss peaks in the glass transition regime. It is found that in NR/BR blends, almost all CB is located in the NR phase, while in NR/SBR blends, the majority of CB is located in the SBR phase. The effect of batching on the phase morphology is also considered, by mixing the NR first with CB and then blending with the second rubber phase. This leads to a more homogeneous distribution of CB in NR/SBR blends. Finally, the obtained fatigue crack growth rates of these blend systems, measured under pulsed harmonic excitations in analogy to rolling tires, are discussed on the basis of the evaluated phase morphology and filler distribution. Here, also the influence of the polymer-filler interphase on the filler distribution is considered.

Keywords Fatigue crack growth · Filled rubber blend · J-Integral · Phase morphology · Tire tread compounds · Viscoelasticity

1 Introduction

Truck tire tread compounds are mostly composed of blends of natural rubber (NR) and butadiene rubber (BR). The most important properties for truck tires are a high wear and abrasion resistance. NR due to its ability to crystallize under strain around the crack tip has the best wear resistance [1]. The crystallization stops cracks very efficiently, which is further improved by the addition of reinforcing fillers [2]. The blending with BR improves abrasion and also rolling resistance. Therefore, blends of NR and BR have a good combination of wear and rolling resistance [3]. However, the blending with SBR can improve wet traction in tires [4]. The role of phase morphology of these mostly phase-separated rubber blends in fracture and wear properties is of high technological interest for improving the overall performance of truck tire tread compounds.

For the fracture and wear of rubber goods, e.g., tire tread compounds, cracks need to be initiated and grow until final failure. Initiation of cracks arises at flaws in the composite, and, therefore, the state of mixing of elastomer compounds is essential for the lifetime of rubber goods. In carbon black filled elastomers, undispersed

agglomerates can act as flaws. Their size is governing the fatigue life, because the propagation rate increases with the size of cracks. Therefore, larger agglomerates may produce larger initial cracks which will reduce the lifetime of rubber goods significantly [5, 6]. However, when studying fracture mechanics of elastomers, the main focus is on the propagation of existing cracks in the rubber matrix. It specifies how rapidly a crack is growing under different loading conditions. The basics of fracture mechanics started with Griffith's work on glassy material [7], but after the Second World War, it was mainly developed on metals and later applied to all kind of materials [8]. For elastomers the tear resistance determined during growth of existing cracks is strongly increased by active fillers and by strain-induced crystallization [4, 9]. The improvement of crack growth resistance due to the filler increases with decreasing carbon black particle size [10]. For unfilled non-crystallizing elastomers, the crack growth behavior is inferior and depends more on the type of cross-links than on the polymeric structure [11]. The energy needed to increase the crack length of an elastomer sample is in general higher than the energy to break the respective polymer bonds in the freshly created crack surfaces. The energy to break the bonds is connected to the intrinsic strength, T_0 [70]. The difference between the energy necessary to break the sample and the energy to break the bonds can be attributed to energy dissipation around the crack tip. A linear viscoelastic theory of steady crack propagation was formulated for unfilled elastomers, which refers to the energy dissipation during the glass transition of the rubber [12–14]. It is not clear in how far similar concepts can be used for the description of fatigue crack growth (FCG) of filled elastomers, though the phenomenology appears very similar.

In the present review, we will briefly review basic theories regarding crack growth in viscoelastic materials and report about viscoelastic fingerprints during fatigue crack growth of elastomers by applying the time-temperature superposition principle. In addition, the dissipated energy around the crack tip of various filled rubber blends, with formulations close to truck tire tread compounds, is evaluated under quasi-static conditions by combining digital image correlation (DIC) measurements with the J-integral method. As a result a spatial resolution of the local energy dissipation due to stress-softening effects will be obtained. Further studies are related to various effects of blending of NR with SBR and BR, as typically used for truck tire treads, on fatigue crack propagation rates. Therefore, the phase morphology and the distribution of CB on the different phases are investigated.

2 Basic Concepts of Fracture Mechanics

2.1 Griffith Criterion

A crack in a solid does not grow by itself. To increase the crack from crack length c to $c + dc$, energy must be used to break the atomic bonds at the newly formed crack surface, $A = 2\,dc \cdot t$ (Fig. 1). The crack length, c, is given as the half contour length

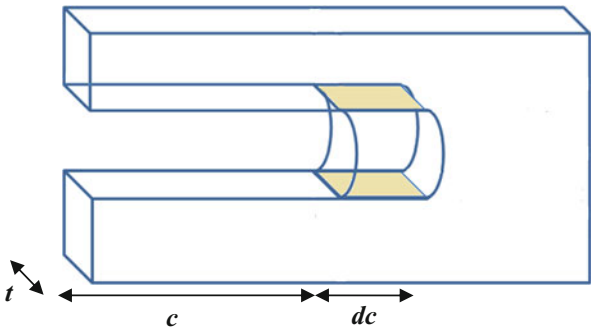

Fig. 1 Schematic drawing of a crack growing from length, c, to length, $c + dc$. The newly formed crack surfaces are shown as colored surfaces

of the crack. Therefore the surface energy, $dS = 2\,dc \cdot t \cdot \gamma_0$, is necessary to grow the crack. Here, t is the thickness of the sample and, γ_0 is the specific surface energy.

When a sample is being deformed, elastic strain energy, W, is stored. If a crack is growing, the deformed material is partially relieved, and some part of the elastic strain energy is released. According to the Griffith criterion, a crack is growing when the surface energy of the newly created surface, dS, is (over)compensated by the released elastic strain energy, $-dW$:

$$-\frac{dW}{dc} \geq \frac{dS}{dc} \tag{1}$$

Griffith calculated the released strain energy for an infinite half plate in uniaxial tension. Comparison of the surface energy increase with the elastic strain energy decrease yields growth for cracks exceeding a critical length, c^* [7].

2.2 Evaluation of Tearing Energy for Different Sample Geometries

The tearing energy, $T = -(dW/dS)_t$, denotes the characteristic energy of a material which is necessary to increase the length of a crack. If a crack is growing depends not directly on the sample geometry or the forces which are applied at the specimen borders far away from the crack tip. Important for the crack growth is the state of deformation close to the crack tip. The state of deformation is determined by the shape of the cut and the strain at the crack tip. The tearing energy for a single-edge notched tensile sample (SENT-Sample), which is deformed uniaxially, is given by [15]

$$T = \frac{2\pi}{\sqrt{\lambda}} W_{el} c \tag{2}$$

Here, λ is the strain, W_{el} is the elastic energy density far away from the crack tip, and c is the half crack contour length of the crack. The tearing energy is calculated

from the energy difference, dW, between the notched sample in comparison to the unnotched one. The $\sqrt{\lambda}$-term in the denominator was added by Clapson and Lake [16] to account for the transversal contraction of rubber at larger strain, which follows from the constant volume assumption and can be described by a Poisson's ratio, $\mu = -\ln(\lambda_2)/\ln(\lambda_1) = 0.5$. Unfilled natural rubber has a Poisson's ratio of nearly 0.5, but it is decreasing with carbon black content [17]. The Poisson's ratio is also decreasing at large strains, low temperatures, and short measurement times [18]. The decrease follows time-temperature superposition and is associated with the transition of the rubber into the glassy state [18]. Although for different sample geometries distinct formulas for the tearing energy are used, it is a material specific quantity. This has been shown by comparing the crack growth velocities of different materials [19].

When the sample is strained in one direction and the deformation in a second direction is prevented, the sample can only contract in the third direction. This is the case for the plane strain (PS) tension samples. For a sufficient long PS sample, two states, which differ only in their crack length, c, and, $c + dc$, simply differ in a volume, $ht\,dc$, being before and after the crack tip, respectively. Here, h and t are the height and the thickness of the undeformed sample, respectively. This yields a difference in strain energy, $dW = -W_{el}ht\,dc$. The tearing energy of PS samples is then

$$T = W_{el}h \tag{3}$$

Contrary to the SEN-Samples, the tearing energy for PS samples is thus independent of crack contour length c.

2.3 The J-Integral

The tearing energy considered in Sect. 2.2 is representing the global value of the energy available for surface growth of the propagating crack. In contrast, the concept of the J-integral introduced by Cherepanov and Rice [20, 21] delivers a local value of the tearing energy that may depend on the distance to the crack tip.

The J-integral is based on a path integral taking into account the 1. Piola-Kirchhoff stress tensor, P; the elastic energy density, W_{el}; and the displacement gradient, $H = (\partial U_i/\partial x_j)_{ij}$, with the element in the i-th row and the j-th column given by $\partial U_i/\partial x_j$, along a contour, Γ, around the crack tip (see Fig. 2). The first component of the J-integral, J_1, describes the local value for the tearing energy regarding straight crack propagation:

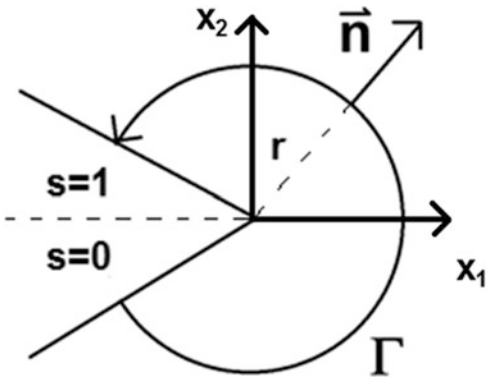

Fig. 2 Integration path $\Gamma(s)$ of the J-integral around the crack tip

$$J_1 = \oint_{\Gamma} \left[W_{el} N_1 - P_{ij} N_j \frac{\partial U_i}{\partial X_1} \right] d\Gamma \tag{4}$$

Here, $U = x\text{-}X$ is the displacement vector giving the difference between the deformed coordinates, x, and the undeformed coordinates, X. $F = I + H$ is the deformation gradient, and I is the unity matrix. The 1. Piola-Kirchhoff stress tensor is given by $P = \det(F)\sigma(F^T)^{-1}$ [22]. F^T is the transpose of the deformation gradient, F. Assuming incompressibility of the rubber leads to $\det(F)=1$. For small deformations the 1. Piola-Kirchhoff stress converges into the Cauchy stress σ. The J-integral can be described in the framework of material forces [23] with the integrand of the J-integral given by the Eshelby stress tensor [24].

For purely elastic materials, the J-integral over a closed path not containing voids or cracks is zero. In that case the J-integral surrounding the crack tip is path-independent. The only sink of the energy flux is then the crack tip. In filled elastomers also significant energy dissipation occurs far away from the crack tip due to strong nonlinearity and hysteresis. The J-integral can then capture the energy that is flowing into a small volume around the crack tip. In this region the energy is available for surface growth of the propagating crack [25, 26].

The J-integral is strictly only applicable on stationary cracks, but the concept can be generalized to growing cracks [25, 27]. One difference is that then the kinetic energy density is added to the elastic energy density, W_{el}, to build the total mechanical energy density. For nearly stationary conditions with very slowly moving cracks, the kinetic energy density is very small and can be neglected. Freund [25] examined the energy flow into a body in the x_1, x_2, t-space, in which the time, t, is regarded as additional dimension and determined the instantaneous rate of energy flow, $F(\Gamma)$, through the integration path, Γ, which both $F(\Gamma)$ and Γ depend on the instantaneous crack tip velocity, v_c. When the fields of all state variables within the contour, Γ, translate invariant with the moving crack, this so-called energy flux integral can be written as $F(\Gamma) = J \cdot v_c$.

2.4 Fatigue Crack Growth of Elastomers

In fatigue crack growth experiments, a notched sample is loaded cyclically. The excitation can be harmonic or pulsed. The crack growth is measured as crack growth, *dc*, per loading cycle, *n*. Also, for dynamic crack growth, the crack growth rate, *dc/dn*, of a crack in a material depends only on the tearing energy, *T*, and not on the sample geometry [28]. In dependence on tearing energy, three different crack growth regions can be distinguished: (1) Below the intrinsic strength, T_0, nearly vanishing crack propagation takes place. The crack growth rate, *dc/dn*, in this region is very low ($\lesssim 10^{-8}$ mm/cycle) and independent of the tearing energy but depends on the ozone concentration. The intrinsic strength, T_0, has recently been measured to 0.051 N/mm and 0.100 N/mm for NR and BR, respectively [29]. This energy values are in the order of magnitude to break the chain bonds and just above T_0, the crack growth rate increases linearly [30]. (2) In a range of intermediate tearing energies, *T*, the crack growth rate, *dc/dn*, follows a power law. This dependency is called Paris-Erdogan law [31, 32]:

$$\frac{dc}{dn} = AT^B \tag{5}$$

The log-log plot of *dc/dn* in dependence of *T* is the fatigue crack growth characteristic. In this plot the prefactor, *A*, is given as axis intercept, and the exponent *B* determines the slope. (3) Above a critical tearing energy, T_c, catastrophic tearing takes place, and the crack growth rate, *dc/dn*, becomes extremely large. The critical tearing energy, T_c, is around 100–1,000 times higher than the intrinsic strength, T_0 [28, 30]. In viscoelastic crack growth theories, the ratio between T_c and T_0 corresponds to E'_∞/E'_0, the ratio between the storage moduli at infinite, E'_∞, and zero frequency, E'_0.

2.5 Crack Propagation in Viscoelastic Solids

The stress intensity factors *K* describe the stress state at the crack tip. They depend on the loading as well as on the geometry of crack and sample. For linear (visco)elastic, homogeneous, and isotropic materials, the stress field under plane stress conditions fulfills the universal relation $\sigma(r) \cong K/\sqrt{r}$ with the distance, *r*, from the crack tip [33]. The displacement field, $u(r)$, is obtained from $\sigma(r) = E\frac{d}{dr}u(r)$ as $u(r)(\tilde{K/E})\sqrt{r}$ yielding for the tearing energy, $T = K2/E \cong \sigma\ u$, independent of *r*. The Young's modulus $E = \sigma/\varepsilon$ describes the resistance of a material to uniaxial stress, σ, at a small strain, ε.

2.5.1 Viscoelastic Crack Opening Mechanisms in Soft Adhesives

De Gennes [34] introduced the concept of crack opening mechanisms in soft adhesives to calculate the tearing energy of a simple viscoelastic solid with the frequency-dependent tensile modulus, $E^* = E_0 + (E_\infty - E_0)i\omega\tau/(1 + i\omega\tau)$. Here, ω and τ are the angular frequency and the relaxation time, respectively, and i is the unit imaginary number of the complex numbers. E^* reflects the terminal flow regime of a very slightly cross-linked (monodisperse) polymer melt just above the gel point which is often used for soft adhesives. Then the relaxation time, τ, can be identified with the reptation time of the chains which strongly varies with the molar mass, M, as $\tau_{rep} \sim M^{3.4}$ and hence can be adjusted to practical demands by moving the time scale. The real and imaginary parts of the modulus, E' and E'', respectively, of a simple viscoelastic solid are depicted in Fig. 3a. The related velocity-dependent tearing energy is shown schematically in Fig. 3b. Three regimes can be distinguished: For small or large frequencies, the system behaves like a soft or hard solid, respectively, since $E' >> E''$. The tearing energy differs and is given by $T_c = K2/E_0 \cong \sigma\, u$ for the soft solid regime and $T_0 = K2/E_\infty \cong \sigma\, u$ for the hard solid regime. Since the strain rate $\frac{d}{dt}\frac{d}{dr}u(r)\tilde{1}/\sqrt{r}$ increases significantly while approaching the crack tip, the hard solid regime is found in the vicinity of the crack tip while the soft regime is found in the outer region far away from the crack tip, provided the crack velocity is sufficiently high. In the intermediate frequency regime $\frac{E_0}{E_\infty \tau} < \omega < \frac{1}{\tau}$, the system can be approximated by a liquid with viscosity $\eta = (E_\infty - E_0)\tau \cong E_\infty \tau$ because $E' < E''$ (see Fig. 3a). The stress field is then related to the displacement field by the equation $\sigma = \eta \frac{d}{dr}\frac{du}{dt} = \eta v \frac{d^2}{dr^2}u$ which is solved by $u(r) \cong (K/v\tau E_\infty)r^{3/2}$ with v being the stationary crack velocity. Accordingly, the tearing energy increases linearly with the distance, r, from the crack tip: $T \cong \sigma u \cong \frac{K^2 r}{v\tau E_\infty} \cong \frac{r}{v\tau} T_0$ [34]. For $r \leq v\tau$ it takes the constant value, T_0, of the hard solid close to the crack tip, and for $r \geq (E_\infty/E_0)v\tau$, it takes the much larger value, T_c.

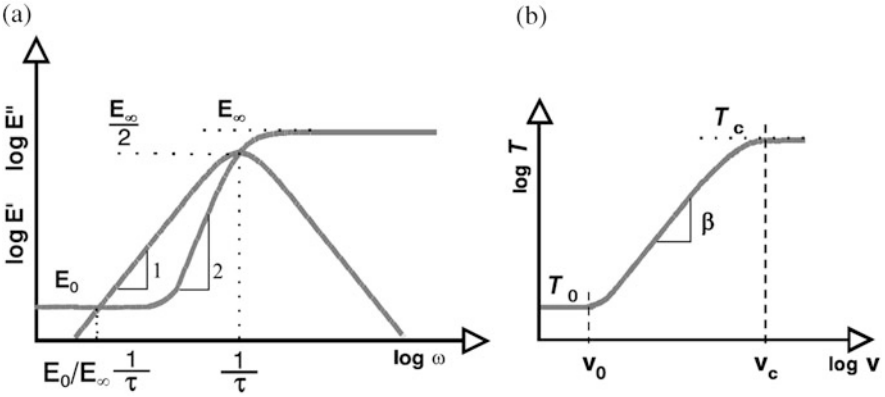

Fig. 3 Storage and loss moduli of a linear viscoelastic solid (**a**) and related velocity-dependent tearing energy (**b**)

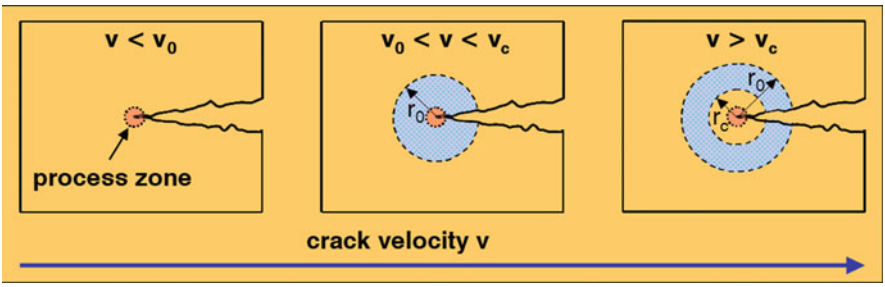

Fig. 4 Viscoelastic crack opening mechanism close to the crack tip. The blue shaded area corresponds to the regions with high energy dissipation

This indicates that for sufficient large crack velocities, when the region close to the crack tip behaves like a hard solid, only a small part of the tearing energy given by E_0/E_∞ is available at the crack tip since most of the energy is dissipated in the transition zone of the viscoelastic solid. Then, the crack contour takes a trumpetlike shape which is created as in both the soft solid regime far away from the crack tip and the hard solid regime in the vicinity of the crack tip, where the displacement, $u(r)$, is increasing proportional to $\sqrt{r}$, but in the transition regime, the displacement is varying with $r^{3/2}$ [34]. Energy dissipation around the crack tip can be neglected only for sufficient small crack velocities, $v < v_0$, where $T = T_0$. The onset of energy dissipation for soft adhesives can be evaluated as $v_0 \cong a\,(E_0/E_\infty)/\tau_{rep}$ with a being a nanoscopic length scale where chain disentanglement takes place. For $v > v_0$ the tearing energy increases linearly implying $\beta = 1$ for the exponent in Fig. 3b. For $v > v_c \cong a/\tau_{rep}$ the tearing energy reaches the final plateau value $T_c = (E_\infty/E_0)T_0$. This velocity dependence of the tearing energy is depicted in Fig. 3b. The evolution of the dissipation regime around the crack in dependence of crack velocity, v, is shown schematically in Fig. 4.

2.5.2 Viscoelastic Crack Growth in Rubber

Crack propagation in cured rubbers shows a very similar behavior as for soft adhesives though the terminal flow regime depicted in Fig. 3a disappears with increasing cross-link density. It is replaced by a rubber elastic plateau, which shows little energy dissipation. However, another relaxation transition is found at higher frequencies, the rubber-glass transition, which affects crack propagation in a similar way. The rubber-glass transition is related to a Rouse-like relaxation of the polymer strands between adjacent chain entanglements implying that the onset of energy dissipation is determined by the Rouse relaxation time, τ_{Rouse} , which scales with the square of the entanglement molar mass of the rubber, $\tau_{Rouse} \sim M_e^{\,2}$ [35]. A linear viscoelastic theory of propagating cracks in rubber was developed by Persson and Brener, which refers to the full relaxation time spectrum of the rubber in the glass transition regime [12]. The important point is that the deformation rate

compared to the bulk is significantly increasing when approaching the crack tip. Therefore, closer to the crack tip and with increasing crack velocity, v, the excitation frequency rises strongly so that the elastomer is behaving more and more glassy. This leads to a significant increase of energy dissipation around the crack tip as depicted schematically by the blue shaded area in Fig. 4. The size of the dissipation regime is determined by the two radii, $r_0 \cong v\,\tau_{\text{Rouse}}$ and $r_c \cong \left(E'_\infty/E'_0\right)^{1/\beta} v\,\tau_{\text{Rouse}}$.

The velocity dependence of the tearing energy depicted in Fig. 3b can be expressed semiempirically as [36, 37]

$$T = T_0\left(1 + \frac{E'_\infty/E'_0}{(1 + v_c/v)^\beta}\right) \tag{6}$$

Here, E'_∞ and E'_0 are the real parts of the tensile moduli in the glassy and rubbery regime, respectively, and $v_c \cong v_0\left(E'_\infty/E'_0\right)^{1/\beta}$ is the critical crack velocity where the tearing energy reaches a plateau value, $T_c \cong (E'_\infty/E'_0)T_0$, where the crack tip is behaving glassy and catastrophic crack growth takes place. For low crack growth velocities, $v < v_0$, the tearing energy, T, is given by the intrinsic strength, T_0, which is the threshold value below which no fracture occurs. It is connected to the fracture in the crack tip process zone, which is a complex region of nanoscopic size, a, where bond fracture, chain pullout, and cavity formation appear (see Fig. 4). The onset of energy dissipation can be evaluated as $v_0 \cong a/\tau_{\text{Rouse}}$. For higher crack growth velocities $v_0 < v < v_c$, the tearing energy follows a power law, $T \sim v^\beta$. The exponent β was shown to be related to the exponent, m, of the relaxation time spectrum, $H(\tau)$, in the glass transition regime [12]. This can be determined from the course of the storage modulus, E', (given by its smoothed master curve) using, e.g., the approximation method of Ferry and Williams [38]. The exponent, m, can be used to predict the exponent, $\beta = (1 - m)/(2 - m)$, of the power law increase of the tearing energy with crack velocity, v [12].

The exponent $\beta^{-1} = (2 - m)/(1 - m)$ obtained from the relaxation time spectrum for steady crack growth with constant crack velocity roughly coincides with the exponent, B, of the power law in the FCG characteristic (Paris-Erdogan law) (Eq. (5)) [36]. This indicates that viscoelastic crack opening mechanisms play also a role in FCG experiments explaining the Paris-Erdogan power law behavior (Eq. (5)). The exponent, m, in filled compounds decreases with filler loading and strength of polymer-filler interaction, predicting smaller exponents, B, with filler loading and activity, in agreement with experimental data [36]. Equation (6) was also used for a semiempirical description of the shear stress in adhesion friction that has the same velocity dependency [37]. The critical velocity, v_c, increases systematically with decreasing glass transition temperature [39], and an equivalent increase of v_c with increasing sample temperature is found. This correlates with the measured adhesion friction very well.

The viscoelastic nature of FCG in rubber becomes also apparent when measurements at different temperatures are compared, indicating that the time-temperature superposition principle is fulfilled. Figure 5a shows results of fatigue crack

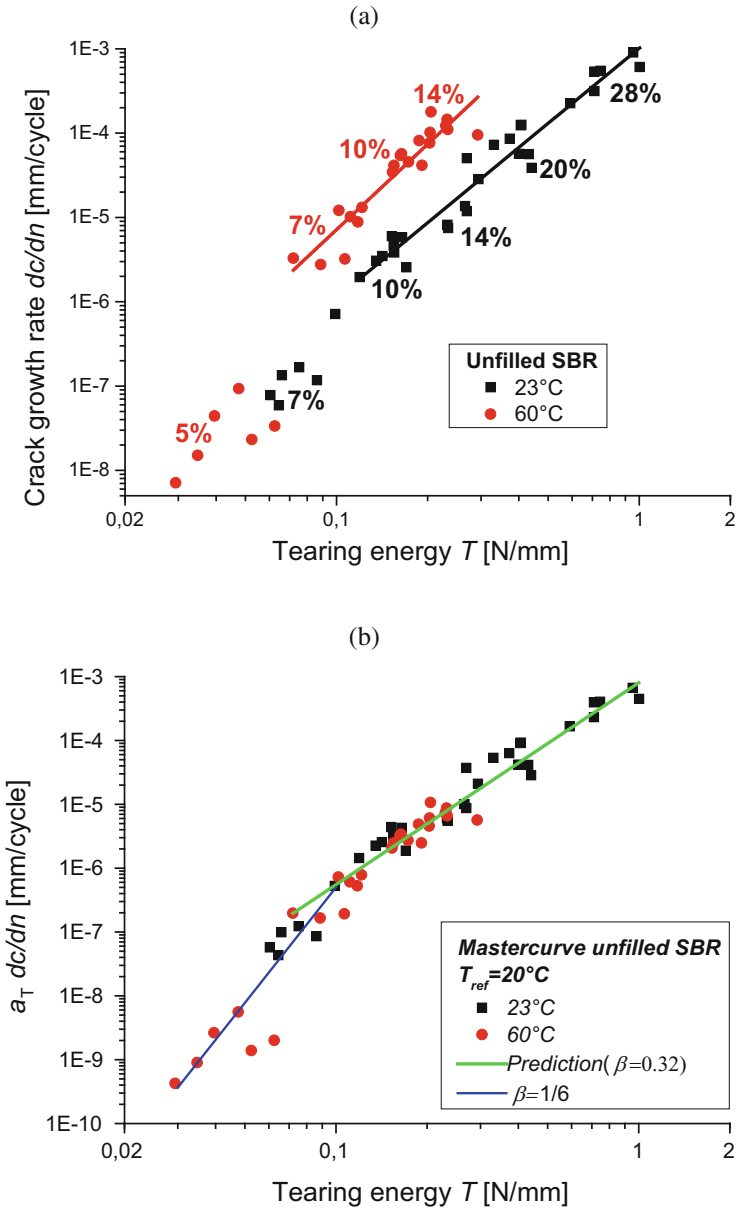

Fig. 5 Fatigue crack growth rate *dc/dn* vs. tearing energy *T* (FCG characteristics) for unfilled SBR at 23°C and 60°C (**a**) and master curve obtained by multiplying the crack growth rate *dc/dn* with the horizontal shifting factors a_T (**b**). The preload is 0.09 MPa (2 N) (from [40])

propagation of unfilled SBR with SEN-Samples at two different temperatures, 23 and 60°C [40]. The tearing energy for the cyclic tearing of unfilled SBR is calculated with Eq. (2). The (harmonic) excitation rate is low (2.5 Hz) to avoid flash temperature effects, which denotes the increased temperature close to the crack tip due to energy dissipation. Obviously, the propagation rate is about one decade smaller for measurement at 23°C. This correlates with the observation that fatigue life in unfilled SBR increases by a factor of about 10^4 when the temperature decreases from 100°C to 0°C [41, 42]. Using the WLF equation with the parameter obtained from viscoelastic master curves for the dynamic moduli, a master curve for the tearing energy in steady tearing can be established [43, 44]. The master curve in Fig. 5b demonstrates that this is also possible for fatigue crack growth. For higher tearing energies, the master curve follows a power law with exponent, $B = \beta^{-1}$, with the exponent, $\beta = (1 - m)/(2 - m) = 0.32$, obtained from the exponent, $m = 0.54$, of the relaxation time spectrum [40].

Creating master curves is possible also for filled compounds. However, in the calculation of tearing energy, a master curve is only achieved if the dynamic part of the energy density is used [40]. The dynamic energy density is the integral $\int \sigma_{dyn} d\varepsilon$, with σ_{dyn} being the dynamic energy density that neglects the preload. For both the unfilled and the filled compounds, two distinct slopes are found at high and low crack growth rates. Two distinct slopes were also reported by M. Ludwig who demonstrated that the higher slope at lower tearing energies should be used for lifetime predictions [45].

3 Experimental

3.1 Sample Preparation

The composites used in this study are polymer blends of natural rubber (SVR CV 60) blended with butadiene rubber or styrene butadiene rubber with varying proportion of the polymers and filled with 50 phr carbon black (N339). The butadiene rubber (BR) used is a high-cis butadiene rubber (Buna CB 24, Arlanxeo), and the styrene-butadiene rubber (SBR) is a solution styrene-butadiene rubber (Buna VSL 4526–0 HM, Arlanxeo) with 45 wt.% vinyl and 26 wt.% styrene groups. Neither the rubbers nor the compounds contain oil. The samples are cross-linked semi-efficiently by sulfur together with the vulcanization accelerator N-cyclohexyl-2-benzothiazole sulfenamide (CBS). The samples are compounded with the processing and vulcanization additives stearic acid and ZnO and protected against aging by N-isopropyl-N-phenyl-P-phenylenediamine (IPPD). The full recipe is shown in Table 1.

The compounds are mixed in an industrial 5 L intermeshing mixer (Werner & Pfleiderer GK 5 E) at 40 rpm for 6 min. Two different mixing techniques are used. In the standard mixing procedure, the other ingredients are inserted after 2 min mastication of the polymers. In the batching mixing procedure, the filler is blended with

Table 1 Recipe of filled rubber blends. The compounds marked with * are additionally produced with the batching mixing procedure (carbon black blended first in NR only)

Compound	NR	BR	SBR	CB	CBS	Sulfur	IPPD	ZnO	Stearic acid
N85B15	85	15	–	50	2.5	1.7	1.5	3	1
N70B30*	70	30	–	50	2.5	1.7	1.5	3	1
N55B45*	55	45	–	50	2.5	1.7	1.5	3	1
N85S15	85	–	15	50	2.5	1.7	1.5	3	1
N70S30*	70	–	30	50	2.5	1.7	1.5	3	1
N55S45*	55	–	45	50	2.5	1.7	1.5	3	1
N70B15S15*	70	15	15	50	2.5	1.7	1.5	3	1
N55B23S23	55	22.5	22.5	50	2.5	1.7	1.5	3	1

the NR only. The BR and the other ingredients are added in a second mixing stage. Leveling of the torque after mastication and after mixing indicates homogeneous mixtures. The curing system is added on a roller mill, where the compounds are handled another 7 min. Vulcanization is performed at 150°C in a heat press up to 90% of the vulcameter torque maximum (t_{90} time). The carbon black dispersion, as measured by optical dispersion analysis, is larger than 90% for all compounds.

3.2 Dynamic Mechanical Analysis

The dynamic mechanical measurements are performed in the torsion rectangular mode with strip specimen of 2 mm thickness on the dynamic analyzer ARES (Rheometrix). The dynamic moduli are measured over a wide temperature range (−115°C to +20°C) at frequency of 1 Hz and 0.5% strain amplitude. The compounds are measured after a quick cool down while heating. In the heating process, the chamber temperature is increased successively by 1°C.

3.3 Fatigue Crack Growth Analysis

The fatigue crack growth is measured at single-edge notched tensile sample (SENT-Sample) on a Tear and Fatigue Analyzer (Coesfeld GmbH & Co. KG, Germany). This machine allows a fully automatic detection of crack length for investigating ten specimens simultaneously. The crack propagation rates are measured under pulsed excitation (4 Hz, 30 ms pulse width, waveform = Gaussian pulse) at 60°C. The 15 mm broad samples with a 1 mm notch are pre-strained by 2 N and excited by varying strain amplitudes (normally between 10% and 30%). The graphical images for determination of the crack length are triggered between the pulses.

3.4 Digital Image Correlation Analysis

The displacement fields are measured by photogrammetric techniques using the digital image correlation (DIC) software ARAMIS from GOM, Germany. A fine black and white pattern is created by airbrushing the samples gently with white paint (Faskolor from Parma International). The change of the pattern when the samples are deformed is calculated into the evolution of the displacement field. The stretching of the composites is performed in a Zwick universal testing machine 1,445 at a speed of 20 mm/min. The notched PS samples are strained five times to the same maximum strain value varying between 10% and 60%. A high-speed camera is used, but only one image per second of the last deformation cycle is recorded. The spot size is approximately 20 mm $\times$ 20 mm, and the resolution is around 1000 $\times$ 1000 pixel. The image at the start of the cycle showing the smallest deformation is taken as reference configuration. Only the displacement field of the image with the highest deformation is used for evaluation. Due to the limited rate of one image per second, both the reference image and the evaluated images do not exactly correspond to the lowest and highest strains during the cycle, respectively.

4 Effect of Stress Softening on Energy Dissipation as Evaluated by the J-Integral

The J-integral allows for the consideration of energy dissipation mechanisms around the crack tip that lower the available energy for crack growth. In this section the effect of energy dissipation due to stress softening of the filled rubber blends on the available energy for crack propagation is investigated [46]. For the evaluation of the J-integral, the deformation fields around the crack tip of stretched samples have been measured by DIC. The corresponding energy and stress fields are calculated by using a recently developed model of stress softening of filled rubbers [47]. In this model the energy density is separated into two parts, an elastic part and a hysteretic part. The J-integral is evaluated at the end of the cycle, where the hysteretic contribution vanishes. The critical stress parameter σ_c of the model is set to zero. The elastic part is based on the behavior of the unfilled elastomer matrix given by the extended non-affine tube model [48], but including hydrodynamic reinforcement of the filler. The hydrodynamic reinforcement is implemented via an amplification factor X, which describes the overstretching of the elastomer due to presence and rigidity of the filler. The elastic energy density is calculated as integration of the energy density from the extended non-affine tube model multiplicated by a distribution, $P_X(X) \sim X^{-\chi}$, of amplification factors. To identify the parameters of the physically based model, multihysteresis measurements on dumbbell samples have been performed. The obtained parameters are the cross-linking modulus, G_c; the entanglement modulus, G_e; and the average number of statistical segments between trapped entanglements,

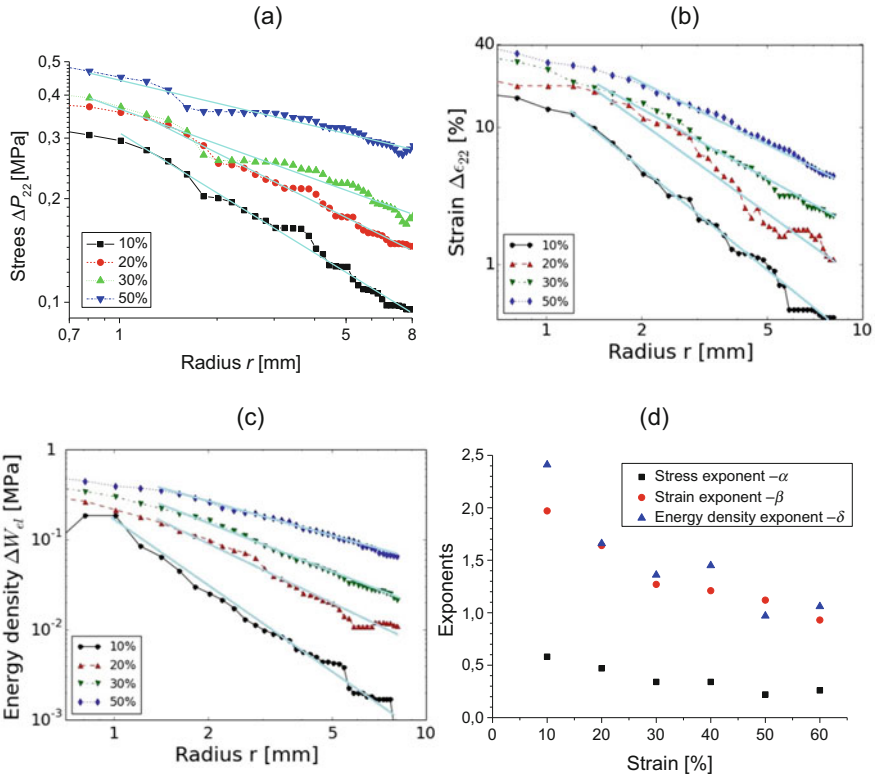

Fig. 6 Log-log plots of the stress increase $\Delta P_{22} = P_{22} - P_{\infty}$ (**a**), strain increase $\Delta\varepsilon_{22} = \varepsilon_{22} - \varepsilon_{\infty}$ (**b**), and energy density increase $\Delta W_{el} = W_{el} - W_{\infty}$ (**c**) when approaching the crack tip at $X_2 = 0$ for different strain levels, as indicated. The straight lines correspond to power law behavior with varying distance r from the crack tip. The exponents for different strains are depicted in (**d**) (from [46])

n. The filler network is characterized by the effective filler volume fraction, ϕ_{eff}; the cluster extensibility parameter, γ; and the power law exponent, χ.

Figure 6 shows results obtained for stress, strain, and energy density around the crack tip of a PS sample, which all show a power law decline toward the values far away from the crack tip. The exponents clearly differ from the exponents expected from linear elastic fracture mechanics [8]. At small strain values, the obtained exponents for strain are almost four times larger than the elastic reference value (-0.5). This indicates a stronger singular behavior due to strong stress-softening effects. At higher strain amplitudes, this is less pronounced since the level of strain is larger far away from the crack tip. This implies that less stress softening appears when approaching the crack tip. The singular behavior can only be analyzed as long the deformations can be recorded reasonably.

The J-integral Eq. (5) considers the integration on a path Γ around the crack tip over an integrand which consists of a sum of two contributions. Both contributions

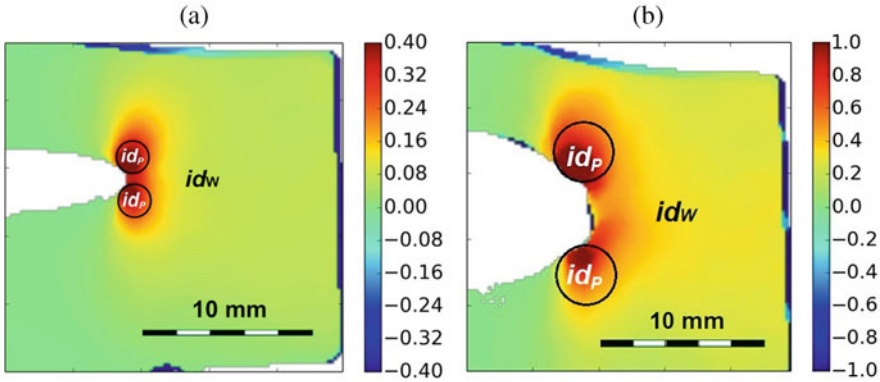

Fig. 7 Integrand of the J-integral J_I for the NR composite elongated by 20% (**a**) and 50% (**b**). The areas where the respective components id_W and id_P are dominating are indicated. J_I is calculated by Eq. (5) as integral around circular paths Γ (from [46])

depend on the integration path and the normal vector of this path. One contribution, denoted id_W, only depends on the energy density distribution. The other contribution, denoted id_P, depends on the 1. Piola-Kirchhoff stress tensor and the displacement gradients. By choosing a circular contour for Γ, the two different contributions can be visualized. The separation of the integrand yields that far away from the crack tip, the field is dominated by id_W, but close to the crack tip, id_P gives the largest contributions to the crack tip in both lateral directions. The integrand of the J-integral J_I and its distribution on id_W and id_P is shown as color code in Fig. 7 for the NR composite elongated by 20% and 50%, respectively.

The J-integral has been determined for four selected compounds and for different strain levels in dependence of the distance from the crack tip. The results are shown in Fig. 8. The J-integral is known to be path-independent for purely elastic materials. In Fig. 8 it is found to increase significantly for circular paths around the crack tip with increasing size r until a plateau is reached. The data indicate that more than 90% of the elastic energy is not available for crack growth since it is dissipated in the stress-softening area around the crack tip. For smaller strain amplitudes, the plateau value of J_I coincides with the global tearing energy T evaluated with Eq. (3). For strain amplitudes larger than 40%, the plateau value of J_I is found systematically larger than the global tearing energy T for all compounds.

5 Influence of Blend Morphology on Fatigue Crack Growth

The fatigue crack growth behavior of filled elastomer blends under specified loading conditions depends not only on the polymers and fillers used, and their respective amounts in the compound, but also on the influence of blend morphology and filler distribution. The influence of these morphological aspects on the crack propagation

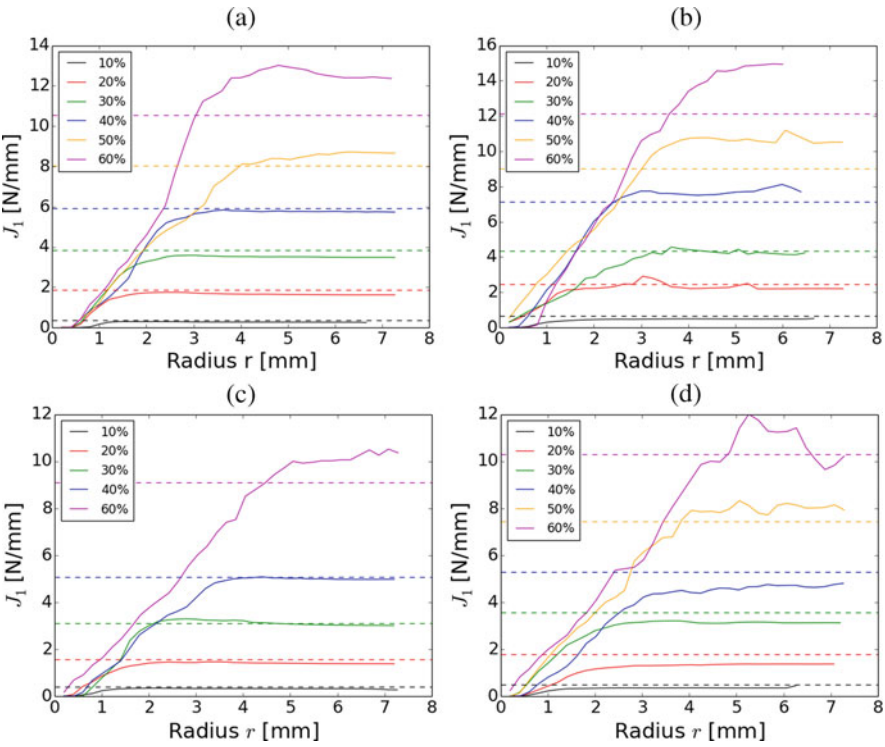

Fig. 8 J_1 for strain amplitudes between 10% and 60% for the NR composite (**a**), N55B45 (**b**), N55S45 (**c**), and N55BS23 (**d**). The global tearing energy $T = W_\infty h$ for different strain amplitudes is shown as dashed lines for comparison (from [46])

rate of blends measured by the tear fatigue analyzer has been analyzed for the compounds listed in Table 1 [49, 50]. For the blend systems marked by a star, the compounds have been mixed in two different ways: the standard mixing procedure in which the filler is added to the premixed blend and the batch mixing procedure in which the filler is added to the pure NR and then blended with the other rubbers.

5.1 Evaluation of Phase Morphology

The method used to determine the phase morphology and filler distribution in these blends relies on the increase of peak heights of the loss shear modulus, G'', due to the filler incorporated into the respective polymer phases and on the additivity of dissipated energies, whereby the dissipated energy in the blend is given by the sum of the dissipated energy in the different polymer phases. The increase of the peak heights of the loss modulus, G'', is hereby linear with the filler volume fraction ϕ_F: $G''(T_g) = G''_0(T_g) + \alpha\phi_F$. Here, G''_0, is the value of the unfilled polymer. The

peak heights of the polymer phases in an unfilled blend in comparison to the peak heights of the pure polymers can be fitted by quadratic equations. The loss modulus of the blend, G''_{blend}, is then given by $G''_{\text{blend}} = \sum_i G''_{P,i}\left(a_i + b_i\phi_i + c_i\phi_i^2\right)$. $G''_{P,\,i}$ is the loss modulus of the i-th phase. Combining the effect of the filler with the blend effect yields

$$G''_{\text{blend}} = \sum_i \left(1 + \alpha_i \frac{\phi_{F,i}}{\phi_{F,i} + \phi_i}\right) G''_{P,i}\left(a_i + b_i\left(\phi_{F,i} + \phi_i\right) + c_i\left(\phi_{F,i} + \phi_i\right)^2\right) \quad (7)$$

This equation allows for the determination of the filler volume fractions, $\phi_{F,\,i}$, in the different phases when the peak heights of the loss modulus, G'', of filled and unfilled blends and the blend ratio are known. This method has already been applied to a variety of polymer blends [51–56]. The peak heights of the different polymer phases with and without filler are compared. There are two causes for the change in peak height of G'':

1. Linear increase of peak height with filler volume fraction
2. The change of phase volume fractions due to the filler in the different phases

The phase volume fraction has a nonlinear effect on the peak height of the loss modulus, G'', and is fitted by a quadratic function. In a blend the polymer with the lower glass transition has an overproportional peak height compared to its phase volume fraction. The polymer with the higher glass transition has an underproportional peak height and yields only a significant peak above a threshold value. At this threshold the polymer phase becomes continuous. Combining these two effects allows the determination of the filler distribution in the blend.

Besides the filling of the polymer phases, also amount and filling of the interphase can be obtained. Regarding the loss modulus, G'', the interphase can be seen as increased values between both glass transition peaks. For the calculation of interphase amount and filling, the interphase is assumed to consist of the same amount of both polymers, and all properties are the average of the properties of both polymers.

In NR/SBR blends, the SBR has the higher affinity to carbon black so that the SBR phase is higher filled than the NR phase. Therefore, the filling of the SBR phase is about twice as high as the filling of the NR phase. This is shown in Fig. 9 for the standard NR/SBR blend with blend ratios 70:30 and 55:45, respectively. In the batch mixing procedure, the NR is mixed with the carbon black first. Due to the higher affinity of the SBR, also in the batch compounds, the SBR phase is higher filled than the NR phase (Fig. 10). But as the filler needs to transfer from the NR to the SBR, the filling of the SBR phase is lower compared to the compounds mixed with the standard mixing procedure. Due to the increased carbon black transfer, the interphase contains also more filler.

In NR/BR blends the BR peak height is not increasing due to the filler, indicating very little amount of filler located in the BR phase. Accordingly, the NR phase is highly filled and contains most of the carbon black. In the batch mixing procedure,

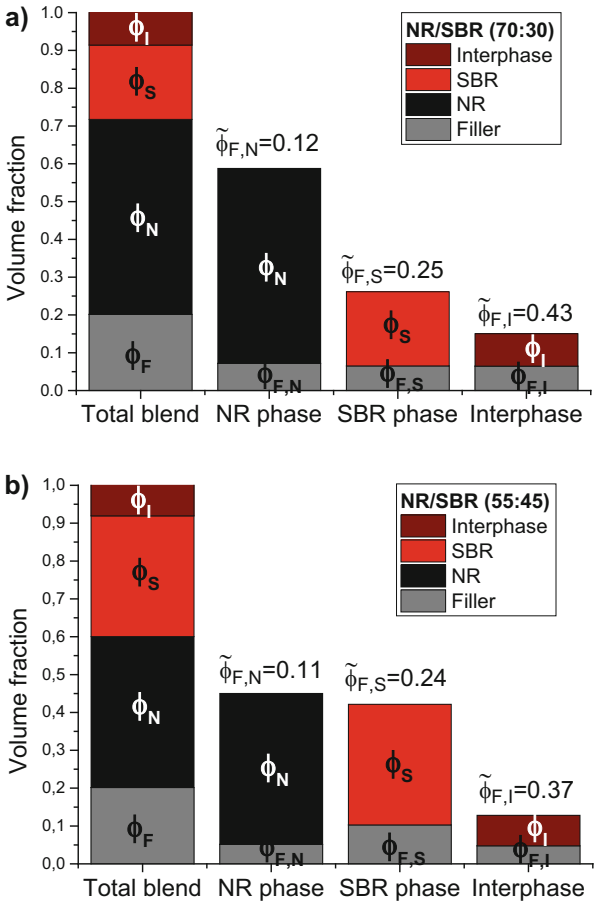

Fig. 9 Carbon black distribution in NR/SBR blend with blend ratios 70:30 (**a**) and 55:45 (**b**) both mixed according to standard procedure. The left column shows the phase proportion in the complete blend. The other columns show the amount of filler in the phases, $\phi_{F,i}$, and above the columns is given their filler volume fraction, $\tilde{\phi}_{F,i} = \phi_{F,i}/(\phi_i + \phi_{F,i})$ (from [49])

the carbon black is first mixed with the NR only. This leads to an even higher carbon black loading in the NR phase which is shown exemplary for the 70:30 blend ratio in Fig. 11. The lower filling of the BR phase can also be demonstrated by the TEM images depicted in Fig. 12. The bright BR phase contains clearly less of the dark carbon black particles than the darker NR phase.

The results concerning filler distribution in NR/BR blends, and the NR/SBR blends are summarized in Tables 2 and 3, respectively. Table 2 compares the proportions of the different phases consisting of carbon black $\tilde{\phi}_{F,i}$. In all NR/SBR blends, the SBR is higher filled than the NR phase. The BR phase in the NR/BR blends shows lower filling than the NR phase instead. The interphase in both blend systems is very highly filled. The carbon black affinity is found to be SBR $>$ NR $>$ BR. In Table 3 are shown the fractions of carbon black that are found in the different phases. For this not only the carbon black affinity but also the

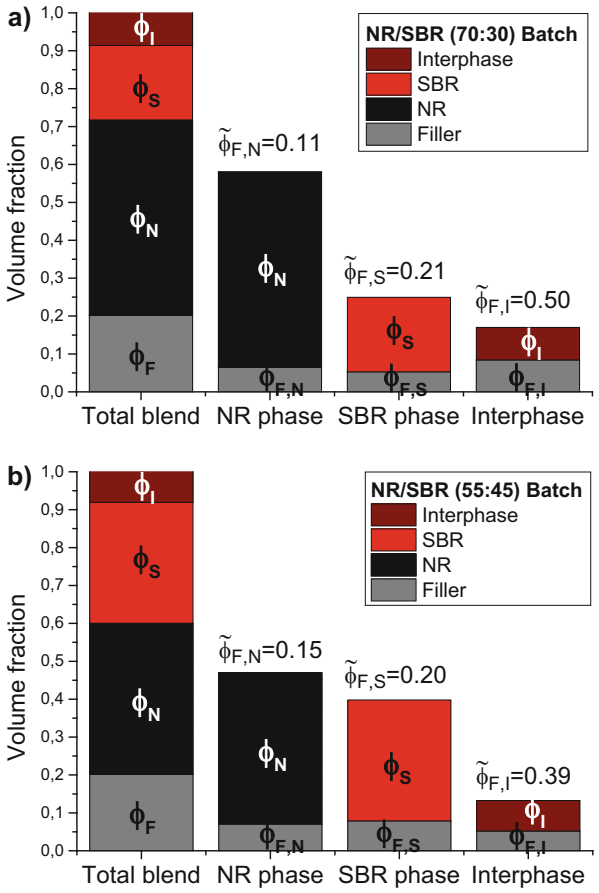

Fig. 10 Carbon black distribution in NR/SBR blend with blend ratios 70:30 (**a**) and 55:45 (**b**) both mixed according to batch mixing procedure. The left column shows the phase proportion in the complete blend. The other columns show the amount of filler in the phases, $\phi_{F,i}$, and above the columns is given their filler volume fraction, $\tilde{\phi}_{F,i} = \phi_{F,i}/(\phi_i + \phi_{F,i})$ (from [49])

size of the respective phase is decisive. So, the NR phase in the NR/SBR blends contains a substantial amount of the filler although its affinity to carbon black is low. On the contrary, the interphases, due to their small amounts, have only intermediate filler loadings, even when their affinity is very high.

In NR/BR/SBR blends, the filler is concentrated in the NR phase [57]. The thermally induced crystallization of the BR yields a second weak peak in the loss modulus, G'', which is located in the same temperature range as the NR glass transition peak [57]. This might hamper the calculation of the filler distribution in systems containing BR. The results of the filler distribution in the different blends are compared to previous findings which coincide for the NR/SBR blends fairly well [53, 54, 58–61]. These previous results were obtained by using inverse gas-liquid chromatography [58], phase-contrast optical microscopy [59, 62], combined static and dynamic modulus measurements [60], thermogravimetry on the rubber-filler gel [63], analysis of bound rubber [61], and earlier studies with the method presented in this chapter [53, 54, 64].

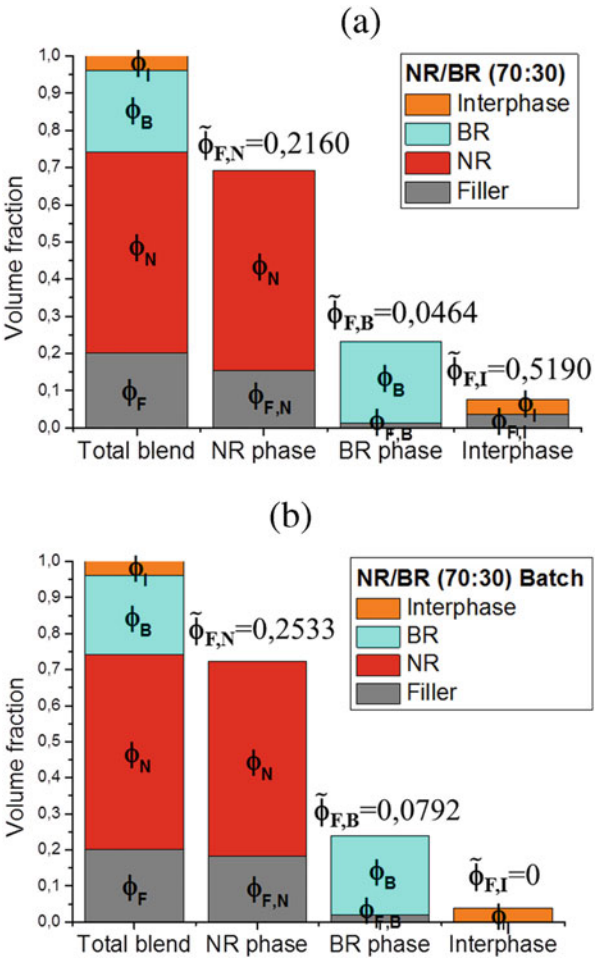

Fig. 11 Carbon black distribution in (70:30) NR/BR blends: (**a**) standard mixing procedure and (**b**) batch mixing procedure. The left column shows the phase proportion in the complete blend and the other columns show the amount of filler, $\phi_{F,i}$, in the phases. Above the columns their filler volume fraction, $\widetilde{\phi}_{F,i} = \phi_{F,i}/(\phi_i + \phi_{F,i})$, is shown (from [50])

5.2 *Fatigue Crack Growth Results*

It is well-known that the crack propagation speed in filler-reinforced rubber is much lower than that for unfilled rubbers [53, 65]. Therefore, carbon black filled rubber blends as listed in Table 1 are essential for truck tire tread compound to obtain a reasonable FCG behavior. The fatigue crack propagation behaviors of the investigated NR/BR blends and the NR/SBR blends are shown in Figs. 13 and 14, respectively. Due to the strengthening effect of strain-induced crystallization, pure

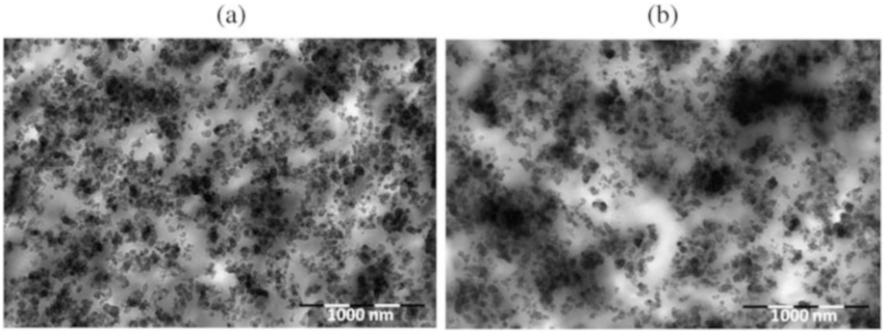

Fig. 12 TEM images of the (70:30) NR/BR blends: (**a**) standard mixing procedure and (**b**) batch mixing procedure (from [50])

Table 2 Proportion of the different phases consisting of carbon black $\widetilde{\phi}_{F,i} = \phi_{F,i}/(\phi_i + \phi_{F,i})$. ϕ_i and $\phi_{F,\,i}$ are the volume fractions of polymer and filler, respectively, that are located in phase i

Compound	Filler volume fraction			
	$\widetilde{\phi}_{F,N}$	$\widetilde{\phi}_{F,B}$	$\widetilde{\phi}_{F,S}$	$\widetilde{\phi}_{F,I}$
N85B15	0.21	0	–	0.70
N70B30	0.22	0.05	–	0.52
N70B30 batch	0.25	0.08	–	0
N55B45	0.20	0.11	–	0.60
N55B45 batch	0.26	0.14	–	0.06
N85S15	0.11	–	0.50	0.34
N70S30	0.12	–	0.25	0.43
N70S30 batch	0.11	–	0.21	0.50
N55S45	0.11	–	0.24	0.37
N55S45 batch	0.15	–	0.20	0.39

Table 3 Fraction $\phi_{F,\,i}/\phi_F$ of carbon black that is found in the different phases [%]. $\phi_{F,\,i}$ and ϕ_F are the volume fractions of filler that are located in phase i and in all phases, respectively

Compound	$\frac{\phi_{F,N}}{\phi_F}$	$\frac{\phi_{F,B}}{\phi_F}$	$\frac{\phi_{F,S}}{\phi_F}$	$\frac{\phi_{F,I}}{\phi_F}$
N85B15	90	0	–	10
N70B30	74	5	–	10
N70B30 batch	91	9	–	0
N55B45	51	20	–	29
N55B45 batch	72	26	–	1
N85S15	41	–	41	19
N70S30	36	–	32	32
N70S30 batch	32	–	26	42
N55S45	26	–	51	24
N55S45 batch	35	–	39	26

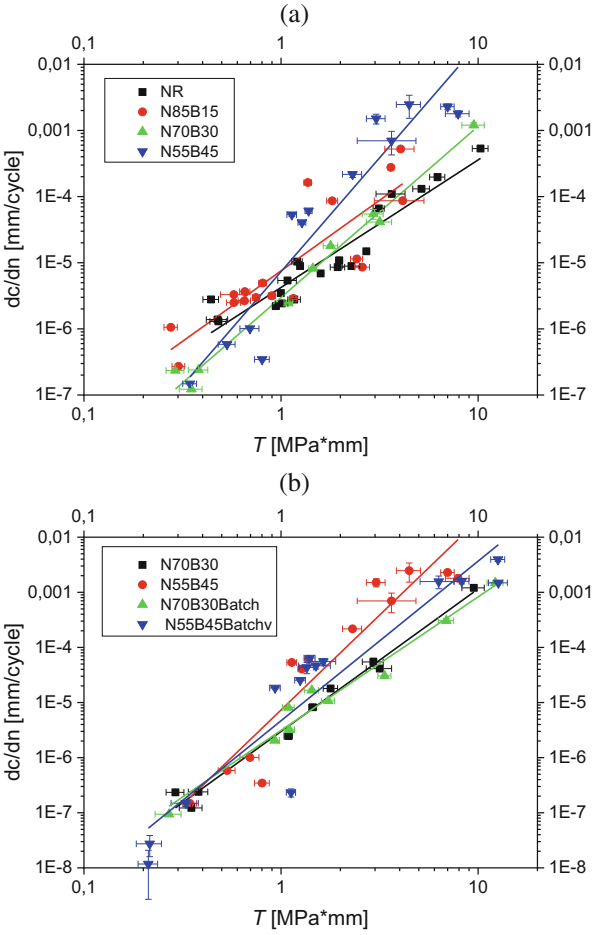

Fig. 13 Crack growth rate, *dc/dn*, vs. tearing energy, *T*: for NR/BR blends obtained with standard mixing procedure (**a**) and for NR/BR blends obtained with batch mixing procedure in comparison to the standard mixing procedure (**b**) (from [49])

NR is found to have the lowest crack propagation rates in comparison to NR blends with BR and/or SBR [66]. Increasing the SBR content leads to higher crack propagation rates for all loading intensities quantified by the tearing energy *T*. The steep slope of the N55S45Batch compound can be explained by the very low filler dispersion of this compound, which is by far lower than the other compounds. Increasing the BR content does not change the crack propagation at low tearing energies. However, for high tearing energies, the FCG rate, *dc/dn*, is strongly increasing with BR content. The crack propagation is also influenced by the mixing technique. This can be seen in the N70B30Batch compound that has lower FCG compared to the N70B30 compound mixed with the standard mixing procedure (see Fig. 13b). The higher FCG resistance of the batch is attributed to the higher filled NR phase which leads to more strain-induced crystallization of the NR at the same strain.

The Chip & Cut effect of truck tires denotes loss of tire tread material when trucks are driving on rough roads [67]. The Chip & Cut effect requires harsh conditions and

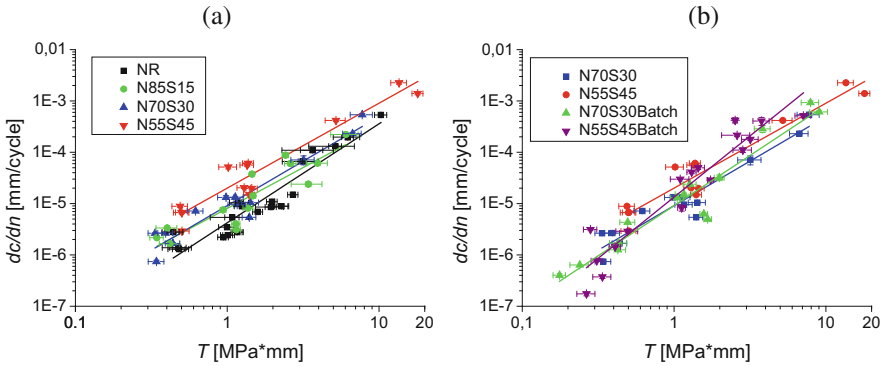

Fig. 14 Crack growth rate, *dc/dn*, vs. tearing energy, *T*: for NR/SBR blends obtained with standard mixing procedure (**a**) and for NR/SBR blends obtained with batch mixing procedure in comparison to standard mixing procedure (**b**) (from [48])

appears firstly at high tearing energy. The rating of the Chip & Cut performance of truck tire treads is based on the wear appearance after testing. These have been investigated in [68] for four selected compounds. The ranking of Chip & Cut resistance is found as NR > N55S45 > N55B23S23 > N55B45, which correlates with the ranking of the cut growth rate at high tearing energy. In particular, the crack propagation rates of N55B45 exhibit the largest values. This is probably the reason for the most pronounced Chip & Cut effect for N55B45. The results also correlate with the instrumented Chip & Cut test [69].

6 Conclusions

For the crack growth rate in viscoelastic rubber materials not the tearing energy is the decisive energy, but the part of the tearing energy that reaches the process zone. The process zone in close vicinity of the crack tip. The dissipative energy loss around the crack tip is determined with the J-integral, which is increasing from very low values for small integration radii around the crack tip toward a plateau for larger radii. The plateau value coincides roughly to the global value of tearing energy obtained with Eq. (3). The increase from low values into the plateau corresponds to the viscoelastic energy losses that do not directly affect crack growth.

Fatigue crack growth measurements at filled rubber blends show that the crack growth rate is lowest for the strain-crystallizing NR. Increasing the SBR portion in a NR/SBR blend leads to an increased crack growth for all tearing energies, and increasing the BR portion in NR/BR blends yields strongly increased crack growth for higher tearing energies. This could be connected to the Chip & Cut behavior measured in truck tire tests.

The crack growth rate of the investigated filled rubber blends is only slightly affected by the blend morphology and filler distribution in the blend, which can be manipulated, e.g., by the mixing procedure. Through a comparison of dynamical spectra from unfilled and filled blends, the filler distribution can be calculated. This calculation yields high filler loadings in the SBR phase and the interphase in NR/SBR blends, but low filler loading in the BR phase in NR/BR blends.

Acknowledgments We would like to thank our project partners Leibniz-Institut für Polymerforschung e.V. and Continental Reifen Deutschland GmbH for the very good cooperation. Continental is appreciated for mixing the compounds in industrial scale. The Deutsche Forschungsgemeinschaft (DFG) is appreciated for financial support (grant KL 1409/9-1).

References

1. Trabelsi S, Albouy P-A, Rault J (2002) Stress-induced crystallization around a crack tip in NR. Macromolecules 35:10054–10061
2. Vilgis TA, Heinrich G, Klüppel M (2009) Reinforcement of polymer nano-composites. Cambridge University Press, Cambridge
3. Grosch KA (1989) Visko-elastische Eigenschaften von Gummimischungen und deren Einfluß auf das Verhalten von Reifen. Kaut Gummi Kunst 42:745–751
4. Röthemeyer F, Sommer F (2001) Kautschuktechnologie. Carl Hanser Verlag, München
5. Huneau B, Masquelier I, Marco Y, Le Saux V, Noizet S, Schiel C, Charrier P (2016) Fatigue crack initiation in a carbon black-filled natural rubber. Rubber Chem Technol 89:126–141
6. Ludwig M, Alshuth T, El Yaagoubi H, Juhre D (2015) Lifetime prediction of elastomers based on statistical occurrence of material defects. In: Marvalová B, Petríková I (eds) Constitutive models for rubber IX. Taylor & Francis, London, pp 445–448
7. Griffith AA (1920) The phenomena of rupture and flow in solids. Philos Trans R Soc Lond Ser A 221:163–198
8. Anderson TL (1995) Fracture mechanics. CRC Press, Boca Raton
9. Eisele U (1978) Zum Einfluss der Mikrostruktur auf die Weiterreißenergie von Synthesekautschuken. Gummi Asbest Kunst 31:724–730
10. Liu C, Dong B, Zhang L-Q, Zheng Q, Wu YP (2015) Influence of strain amplification near crack tip on the fracture resistance of carbon black-filled SBR. Rubber Chem Technol 88:276–288
11. Bhowmick AK, Gent AN, Pulford CTR (1983) Tear strength of elastomers under threshold conditions. Rubber Chem Technol 56:226–232
12. Persson BNJ, Brener EA (2005) Crack propagation in viscoelastic solids. Phys Rev E 71:036123
13. Persson BNJ, Albohr O, Heinrich G, Ueba H (2005) Crack propagation in rubber-like materials. J Phys Condens Matter 17:R1071
14. Heinrich G, Klüppel M, Vilgis T, Horst T (2012) Wenn Gummi zu Bruch geht. Phys J 11:39–44
15. Holownia BP (1975) Effect of carbon black on Poisson's ratio of elastomers. Rubber Chem Technol 48:246–253
16. Kugler HP, Stacer RG, Steimle C (1990) Direct measurement of poisson's ratio in elastomers. Rubber Chem Technol 63:473–487
17. Rivlin RS, Thomas AG (1953) Rupture of rubber. I. Characteristic energy for tearing. J Polym Sci 10:291–318
18. Clapson BE, Lake GJ (1971) Truck tire groove cracking – theory and practice. Rubber Chem Technol 44:1186–1202

19. Thomas AG (1994) The development of fracture mechanics of elastomers. Rubber Chem Technol 67:50–366
20. Rice JR (1968) A path independent integral and the approximate analysis of strain concentration by notches and cracks. J Appl Mech 35:379–386
21. Cherepanov GP (1967) Crack propagation in continuous media. J Appl Math Mech 31:503–512
22. Holzapfel GA (2001) Nonlinear solid mechanics. Wiley, Chichester
23. Maugin GA (1995) Material forces: concepts and applications. Appl Mech Rev 48:213–245
24. Eshelby JD (1975) The elastic energy-momentum tensor. J Elast 5:321–335
25. Freund LB (1998) Dynamic fracture mechanics. Cambridge University Press, Cambridge
26. Zehnder AT (2012) Fracture mechanics. Lecture notes in applied and computational mechanics, vol 62, pp 33–54
27. Horst T, Heinrich G, Schneider M, Schulze A, Rennert M (2013) Linking mesoscopic and macroscopic aspects of crack propagation in elastomers. Lecture notes in applied and computational mechanics, vol 70, pp 129–165
28. Gent AN, Lindley PB, Thomas AG (1964) Cut growth and fatigue of rubbers. I. The relationship between cut growth and fatigue. J Appl Polym Sci 8:455–466
29. Robertson CG, Stoček R, Kipscholl R, Mars WV (2019) Characterizing the intrinsic strength (fatigue threshold) of natural rubber/butadiene rubber blends. Tire Sci Technol 47:78–82
30. Lake GJ, Thomas AG (1967) Physics of failure in rubber. Kaut Gummi Kunst 20:211–217
31. Paris PC, Gomez MP, Anderson WE (1961) A rational analytic theory of failure. Trend Eng 13:9–14
32. Paris PC, Erdogan F (1963) A critical analysis of crack propagation laws. J Basic Eng 85:528–533
33. Irwin GR (1957) Analysis of stresses and strain near the end of a crack traversing a plate. Trans ASME Ser E J Appl Mech 24:361–364
34. de Gennes PG (1996) Soft adhesives. Langmuir 12:4497–4500
35. Rubinstein M, Colby RH (2003) Polymer physics. Oxford University Press, New York
36. Klüppel M (2009) Evaluation of viscoelastic master curves of filled elastomers and application to fracture mechanics. J Phys Condens Matter 21:035104
37. Le Gal A, Klüppel M (2008) Investigation and modeling of rubber stationary friction on rough surfaces. J Phys Condens Matter 20:015007
38. Le Gal A, Klüppel M (2006) Investigation and modeling of adhesion friction on rough surfaces. Kaut Gummi Kunst 59:308–315
39. Williams ML, Ferry JD (1953) Second approximation calculations of mechanical and electrical relaxation and retardation distributions. J Polym Sci 11:169–175
40. Wunde M, Klüppel M (2018) Viscoelastic response during crack propagation of unfilled and filled SBR. Rubber Chem Technol 91(668):682
41. Lake GJ, Lindley PB (1964) Ozone cracking, flex cracking and fatigue of rubber. Part one: cut growth mechanisms and how they result in fatigue failure. Rubber J 146:24–30
42. Lake GJ, Lindley PB (1964) Ozone cracking, flex cracking and fatigue of rubber. Part two: technological aspects. Rubber J 146:30–36
43. Gent AN (1996) Adhesion and strength of viscoelastic solids. Is there a relationship between adhesion and bulk properties. Langmuir 12:4492–4496
44. Gent AN, Lai S-M (1994) Interfacial bonding, energy dissipation, and adhesion. J Polym Sci B Polym Phys 32:1543–1555
45. Ludwig M (2017) Entwicklung eines Lebensdauer-Vorhersagekonzepts für Elastomerwerkstoffe unter Berücksichtigung der Fehlstellenstatistik. PhD thesis, Hannover, Germany
46. Wunde M, Plagge J, Klüppel M (2019) The role of stress softening in crack propagation of filler reinforced elastomers as evaluated by the J-integral. Eng Fract Mech 214:520–533
47. Plagge J, Klüppel M (2017) A physically based model of stress softening and hysteresis of filled rubber including rate-and temperature dependency. Int J Plast 89:173–196
48. Klüppel M, Schramm J (2000) A generalized tube model of rubber elasticity and stress softening of filler reinforced elastomer systems. Macromol Theory Simul 9:742–754

49. Wunde M, Klüppel M (2017) Impact of mixing procedure on phase morphology and fracture mechanical properties of carbon black-filled NR/SBR blends. Contin Mech Thermodyn 29:1135–1148
50. Wunde M, Klüppel M (2016) Influence of phase morphology and filler distribution in NR/BR and NR/SBR blends on fracture mechanical properties. Rubber Chem Technol 89:588–607
51. Meier JG, Klüppel M, Geisler H, Schuster RH (2005) Kieselsäuregefüllte Elastomerblends durch Masterbatchtechnologie. Kaut Gummi Kunst 58:587
52. Meier JF, Klüppel M, Schuster RH (2005) Steuerung der physikalischen Eigenschaften von Elastomeren. Kaut Gummi Kunst 58:82
53. Lorenz H, Steinhauser D, Klüppel M (2013) Morphology and micro-mechanics of filled elastomer blends: impact on dynamic crack propagation. Lecture notes in applied and computational mechanics, vol 70, pp 81–128
54. Klüppel M, Schuster RH, Schaper J (1999) Carbon black distribution in rubber blends: a dynamic-mechanical analysis. Rubber Chem Technol 72:91
55. Klüppel M, Schuster RH, Schaper J (1998) Dynamischer Glasübergang in füllstoffverstärkten Kautschukblends. GAK Gummi Fasern Kunst 51:508
56. Schuster RH, Meier JF, Klüppel M (2000) The role of interphase in filler partition in rubber blends. Kaut Gummi Kunst 53:663
57. Wunde M, Klüppel M (2020) Effect of filler and blending with SBR and NR on thermally induced crystallization of high-cis BR as evaluated by dynamic mechanical analysis. Express Polym Lett 14(3):261–271
58. Schuster RH, Issel HM, Peterseim V (1996) Selective interactions in elastomers, a base for compatibility and polymer-filler interactions. Rubber Chem Technol 69:769
59. Hess WM, Scott CE, Callan JE (1967) Carbon black distribution in elastomer blends. Rubber Chem Technol 40:371–383
60. Ayala JA, Hess WM, Kistler FD, Joyce GA (1991) Carbon-black – elastomer interaction. Rubber Chem Technol 64:19–39
61. Callan JE, Hess WM, Scott CE (1971) Elastomer blends. Compatibility and relative response to fillers. Rubber Chem Technol 44:814
62. Le HH, Ilisch S, Kasaliwal GR, Radusch H-J (2008) Filler phase distribution in rubber blends characterized by thermogravimetric analysis of the rubber-filler gel. Rubber Chem Technol 81:767–781
63. Cotton GR, Murphy LJ (1988) Mixing of carbon black with rubber. Part 5. Analysis of BR/SBR blends. Kaut Gummi Kunst 41:54–58
64. Meier JF, Klüppel M, Schuster RH (2005) Steuerung der physikalischen Eigenschaften von Elastomeren. Kaut Gummi Kunst 58:82–89
65. Reincke K, Grellmann W, Klüppel M (2009) Investigations of fracture mechanical properties of filler-reinforced styrene-butadiene elastomers. Kaut Gummi Kunst 62:246–251
66. Hamed GR, Kim HJ, Gent AN (1996) Cut growth in vulkanizates of natural rubber, cis-polybutadiene, and a 50/50 blend during single and repeated extension. Rubber Chem Technol 69:807
67. Stocek R, Kipscholl R, Euchler E, Heinrich G (2014) Study of the relationship between fatigue crack growth and dynamic chip & cut behavior of reinforced rubber materials. Kaut Gummi Kunst 67(4):26–29
68. Wunde M, Schulze A, Vatterott C, Tschimmel J, Lacayo-Pineda J, Heinrich G, Klüppel M (2019) Verbesserung der Laborvorhersagen zum Risswachstum und Verschleiß von LKW-Reifenlaufflächen. Kaut Gummi Kunst 72(8):72–78
69. Stocek R, Heinrich G, Schulze A, Wunde M, Klüppel M, Vatterott C, Tschimmel J, Lacayo-Pineda J, Kipscholl R (2020) Chip & cut wear of truck tire treads: comparison between laboratory and real tire testing. Kaut Gummi Kunst 73(6):51–55
70. Robertson CG, Stoček R, Mars WV (2021) The fatigue threshold of rubber and its characterization using the cutting method. In: Heinrich G, Stoček R, Kipscholl R (eds) Fatigue crack growth in rubber materials: experiments and modelling. Springer, Heidelberg. https://doi.org/10.1007/12_2020_71

Adv Polym Sci (2021) 286: 273–296
https://doi.org/10.1007/12_2020_81

Published online: 11 December 2020

Methodology Used for Characterizing the Fracture and Fatigue Behavior of Thermoplastic Elastomers

Z. Major

Contents

Abstract The fracture and fatigue behavior of thermoplastic elastomers (TPE) is of prime practical importance for demanding engineering applications. The fatigue behavior of several TPE grades used for superior industrial application was characterized under displacement-controlled cyclic loading conditions by local strain based Wöhler curves (LSWC) and by fatigue crack growth (FCG) curves. The LSWC method is based on the determination of the local strain in diabolo-shaped cylindrical or flat specimens and the identification of cycle number-to-failure, N_f, values in the F_{max}/F_{min}-N_f diagrams. While these LSWC curves were successfully created for injection molded TPEs investigated using cylindrical specimens, the extrusion grade TPU did not reveal fatigue failure using flat specimens with 0.2 mm thickness. The LSWC curves were used for both supporting material development efforts and dimensioning cyclically loaded components. Notched Plane Strain (PS) tensile

Z. Major (✉)
Institute of Polymer Product Engineering, Johannes Kepler University Linz, Linz, Austria
e-mail: zoltan.major@jku.at

specimens were tested under displacement-controlled loading conditions and the crack length was measured optically. Tearing energy values have been calculated for the PS specimens and subsequently FCG curves were generated in terms of crack growth rate, *da/dN,* and tearing energy, *T*. The majority of the TPE grades investigated revealed extensive crack tip blunting. While the slope of the stable FCG revealed rather minor differences, the apparent fatigue threshold values were observed in the range of appr. 1.5 decades. The endurance strain limit has been estimated (1) by direct measurements in LSWC tests (2) by the determination of threshold values in the FCG curves and calculation of critical strain values and (3) by using Essential Work of Fracture (EWF) approach.

Keywords Crack tip opening displacement · Displacement control · Fatigue crack growth · Strain based Wöhler curve · Tearing energy · Thermoplastic elastomers

1 Introduction, Scope, and Objectives

The importance of thermoplastic elastomers (TPE) and more specifically the wide range of thermoplastic polyurethane elastomers (TPU) is obvious for many demanding industrial and consumer applications (e.g., automotive, medical, and electronic devices) [1–3]. It is expected that the trend of a continuous increase of the use and the variety of the formulations will be held in the near future and novel applications are expected. TPUs are exposed to complex combinations of repeated thermomechanical bulk and surface loads in these applications. Hence, the proper characterization of the long-term behavior and the prediction of the service life time along with sufficient reliability of the component is one of the key aspects for the improvement of both the recent and perspective applications. The long-term behavior is ranging from the change of the deformation properties in terms of viscoelastic parameters up to the classical fatigue failure. It is, however, somewhat surprising that in spite of the above-mentioned importance and in contrast to classical rubber compounds the characterization of the fatigue behavior is rather underrepresented in the literature [4, 5]. While the majority of the experiments are carried out only at laboratory specimen level, there are several tangible industrial applications behind these laboratory scale experiments. Our examples for fatigue relevant industrial applications of TPUs are among others seals over a wide size, service load and temperature range, large and small rolls with combined bulk and surface loading and special thin wall tubes used in novel bicycle tires. The experimental results, which are shown in this chapter have been generated in many research projects in Leoben and in Linz over the last two decades and were supported by various industry partners. However, the main focus is on the TPU grades in this study. Different TPU formulations along with some processing condition variations produced by four Austrian companies are mentioned in this paper. Due to the non-disclosure agreements the materials are not described in detail, thus they are categorized in three

Table 1 Summary of the various test series and the two main approaches

Tests	Local strain Wöhler curve (LSWC)	Fatigue crack growth (FCG)
Test series1 TPU series 1 e.g. TPU 11–18	• Injection molded and machined cylindrical diabolo-shape specimens • Monotonic and cyclic loading • Unfilled and filled TPUs	• Injection molded large (200 mm) planar tensile specimens with geometry lock • Monotonic and cyclic loading • Unfilled and filled TPUs
Test series2 TPU series 2 e.g. TPU21–28	• Machined cylindrical diabolo-shape specimens • Monotonic and cyclic loading • Unfilled TPUs and other thermoplastic elastomers	• Injection molded small (100 mm) planar tensile specimens with geometry lock • Monotonic and cyclic loading • Unfilled TPUs and other thermoplastic elastomers
Test series 3 TPU series 3	• Extruded flat thin diabolo-shape specimens (I/Q) • Monotonic and cyclic loading • Unfilled TPU	• Small planar tensile specimen from thin sheets • Monotonic and cyclic loading • Unfilled TPU

classes and finally listed in Table 1. The focus lies in this chapter on the first two TPU classes but as a special example for untypical behavior some results of TPU3x are also shortly described.

The objective of the study is the analysis and discussion of the applicability and limitation of displacement-controlled cyclic loading test methods to characterize the fatigue of thermoplastic elastomers. To answer the above questions regarding the fatigue behavior of TPEs two different methods were used in this study:

- Mechanics of materials approach: Determination of Wöhler curves in terms of local strain (LSWC).
  - Cylindrical and flat diabolo-shaped specimens were loaded under displacement-controlled cyclic loading conditions at 4–6 different displacement levels at a typical strain ratio of $R_\varepsilon = 0.1$ (maximum/minimum values of the nominal strain), but some studies are also carried out at higher R_ε ratios (i.e., 0.5). The test frequency was varied typically between 1 and 10 Hz and the majority of the tests were carried out at 23 °C (appr. 50% relative humidity). The F_{max}/F_{min} values of these tests were continuously recorded during the tests and the changes of these values were used to assign the cycle number-to-failure, N_f, values (see later Fig. 4). The displacement-controlled test with constant R_ε values resulted in altering stress ratio values.
  - Local strain distribution in the mid-section of the diabolo-shaped specimen (see Figs. 1 and 3) was determined using a proper combination of experimental mechanics and finite element simulations (FEA) methods. Local strain based Wöhler (LSWC, ε-N_f) curves were constructed by the combination of these values with relevant cycle number-to-failure values, N_f, for the TPEs investigated.

Fig. 1 Cylindrical "diabolo-type" test specimen, fixture and test setup

- Fracture mechanics approach: Determination of Fatigue Crack Growth Curves (FCG).
  - Plain strain specimens (PS) were molded, notched (see Fig. 5), and tested under displacement-controlled loading conditions typically at a nominal strain ratio of $R_\varepsilon = 0.1$. The sequences of the loading – number of load levels, cycle numbers – were varied. The test frequency was in the range of 1–10 Hz and the test was frequently performed at room temperature (RT). The local crack tip loading was characterized by tearing energy, T. The length of the typically blunted crack was optically measured and FCG rate values, da/dN were calculated and subsequently combined with the calculated tearing energy values. The tearing energy was calculated using the deformation energy values corrected with the crack length. The basic assumption was that for appropriate PS specimens no geometry factor is needed for calculating the tearing energy for sharply notched specimens [6–12]. The calculation of fracture mechanics parameters requires geometry factors for a majority of the specimens.
  - While the stable part of the crack growth curves can be used for predicting the fatigue life time, the threshold values of these curves may be used to predict the endurance strain limit, ε_e^{th} for components.

The details of above approaches and experimental techniques were described and summarized in several review papers [11–21] and further details are provided also in the experimental part of this chapter. The basics of our methodology were elaborated and described for LWSC in the Thesis Ref. [22] and for FCG curves in the Thesis Ref. [6]. There is a rather comprehensive comparison of both methods in the literature with arguments for preferred applications of both methods [13–19]. The proper control mode – load, displacement, or energy control – for robust tests is also under discussion [17, 18].

The preferences regarding these two options are summarized below:

The simplified determination of the tearing energy using notched planar tensile specimens makes the application of fracture mechanics approach simple and convenient. An FCG curve can reliably be determined over test durations of 8–24 h. These curves reveal rather low statistical variations under controlled test conditions (from specimen preparation to controlled set of all test conditions) and using proper test

devices for load and crack length measurement [6, 16–19, 21–23]. The FCG curves are sensitive to the variation of the material investigated (e.g., material formulations, processing conditions, aging). Hence, it can efficiently be used for supporting both material development and material selection efforts. There is a discussion about the proper application of these fracture toughness values measured (stable FCG rate or threshold in terms of tearing energy) to engineering design of rubber or more specifically TPE components. The proper application of fracture mechanics would require accurate determination of the shape, size, and position of crack-like defects in specific components. Sophisticated non-destructive testing (NDTE) methods are needed and the proper NDTE method should be able to determine the relevant defects size [23, 24]. There is also a room for interpretation for the definition of crack-like defect. The proper definition for practical engineering use depends on both the material and loading situation. Hence, in addition to the material qualification the main advantage of the application of fracture mechanics is a faster and more reliable measurement of relevant threshold values for crack growth initiation. These values can be used for realistically estimating the range of endurance limit values in terms of stress or strain, ε_e^{th} and can be combined with the LSWC method. While the determination of tearing energy threshold values requires several hours in the FCG tests, a statistically founded determination of the endurance limit requires several weeks using the LWSC tests (min. 4–5 undamaged specimens up to min. 5 MCycles at 5 Hz) [17, 25]. There is no perfect solution, however, for this problem and the uncertainty of the direct measurement and the estimation reliability remains a problem. A perspective solution is a data science based analysis with statistical tools.

2 Experiments

2.1 Materials

The entire experimental and modeling work consists of a many different thermoplastic elastomer grades (TPUs, TPE-As, TPOs, and other blends) as well as conventional rubber grades. More than 20 different TPU formulations along with some processing condition variations produced by four Austrian companies are mentioned in this study. These TPEs formulations represent a wide range of structures and morphologies and were produced in different processing routes. We are focusing mainly on the methodological aspects of the fatigue characterization but several influencing factors have also been studied and examples are provided. Table 1 summarizes the various test series and the two main approaches used.

The fatigue experiments were performed in two laboratories (IWpK-MUL and IPPE-JKU) using similar servohydraulic machines and other test devices [1–4, 22, 6–8].

2.2 Development of the Experimental Methodology for LSWC Curves

2.2.1 Test Specimen and Test Setup

Cylindrical diabolo-shaped specimen was designed in order to realize strain localization in a controlled volume of the specimen. The shape of this diabolo specimen is shown in Fig. 1. Special care was taken to the geometry which guaranties a locked stable fixturing of the specimen and the controlled surface roughness. These specimens can be manufactured by injection molding (rubbers and softer TPEs) or machined (harder TPUs). Some of our company partners have special expertise on the field of machining of high quality TPU seals and this expertise makes the controlled production of machined specimens possible. The fixture with the test setup is also shown in Fig. 1. The displacement control allows for the simultaneous investigation of several specimens both in a linear and a revolver configuration [22].

2.2.2 Strain Measurement and Calibration Curve

The vast majority of testing machines can perform constant amplitude displacement or force controlled cyclic tests [6, 25]. The realization of a proper local strain control (constant strain rate) is far more complicated. The combination of optical local strain measurement with the PIDF controller of new generation testing machines makes it also possible, but it is time consuming and sometimes unstable. Efforts were done to systematically perform uniaxial and biaxial monotonic tests in order to determine stress-strain relationships under constant strain rate [26]. As a practical solution, global displacement vs. local strain functions were determined in this study for the specimens investigated. While for material comparison the displacement values could also be used, the proper analysis of a component requires relevant local strain values.

Finite element simulation (FEA) was carried out to determine the strain distribution in the diabolo-type specimen and to generate a global displacement-local strain calibration curve. A proper hyperelastic material model was applied for the cylindrical specimens. The details of the selection of hyperelastic models and the experimental determination of model parameters can be found in [8, 17, 22, 26–34]. The experimental methodology used in this work and preferred from the authors involves of uniaxial, planar, and biaxial tests considering also strain rate and temperature dependences [8, 17, 22]. The model parameters are either directly implemented in FEA tools (i.e., Abaqus, SiemensNX) or additionally fitted in PolyUMod MCalibration tool (Veryst Engineering, LLC, [34]). Both above FEA and an experimental strain measurement (DIC, Aramis GOM) were applied for the flat specimen. Due to the non-linear strain distribution there are, however, several options for determining the local strain values. The FEA for cylindrical specimen is shown in

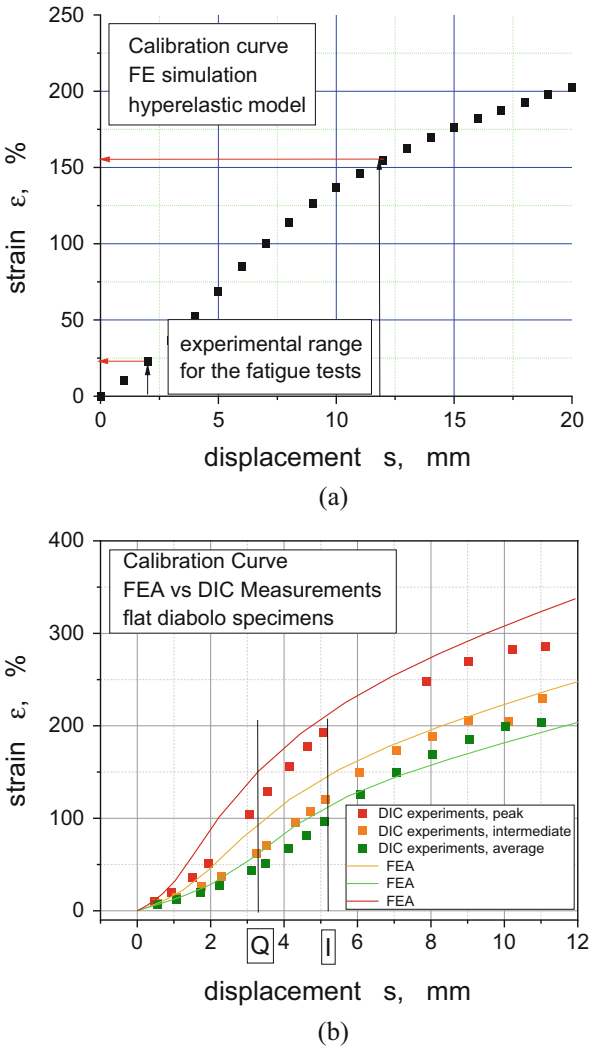

Fig. 2 Global displacement-local strain calibration curves: (**a**) cylindrical diabolo specimen using FEA and (**b**) flat diabolo specimen; comparison of FEA with experimental DIC strain analysis

Fig. 2a, a comparison of FEA with experimental DIC strain analysis is shown in in Fig. 2b for three different scenarios (peak, mid, and average).

We have been using the 95% level of the strain peak for the calibration curve. The combination of these strain values with the corresponding N_f values at various displacement levels provides the data points in the LSWC. Parameters for a typical hyperelastic model (here used Ogden model) are exemplarily shown in Table 2 for TPU11 and TPU32.

Regarding further details of the tests, for rapid material characterization and selection typically 4 displacement levels have been used and the statistical effects were neglected. For design curves, however, 5–6 levels and 3–5 specimens for each

Table 2 Parameters of the Ogden model for TPU11 and for TPU32 (I/Q)

	TPU11		TPU32-I		TPU32-Q	
Parameter	μ_i	α_i	μ_i	α_i	μ_i	α_i
1	8.575	0.907	−8.943	3.192	−71.70385	−0.6355
2	0.003	6.336	0.01275	6.91	0.0000182	10.4212
3	0.029	−3.25	25.0416	−5.88	85.83504	−1.5905

level are applied. This amount of data allows for a reliable inter and extrapolation as well as statistical analysis of the corresponding data points (ε-N_f).

2.2.3 Test Method and Data Reduction

The classical Wöhler curves were designed for stress values. The applicability of load controlled cyclic loading for cylindrical rubber specimens was characterized in the Thesis of Vezer [22] and the results and conclusions were compared with literature data [24]. Mars has also compared displacement and load controlled cyclic tests [17]. While the displacement control is robust and easy to realize, the force control is complicated for compliant materials. Furthermore, a higher data scatter of the results is expected for force controlled tests. The experiments were carried out at different displacement levels from 2 to 12 mm which corresponds to strain values of 40 to 150% (see Fig. 3) at an R_ε ratio of 0.1 at RT and usually at a test frequency of 5 Hz. The deformation and failure behavior of elastomers were influenced by a number of test and material parameters, whereas an overview can be found in [1, 6, 7, 13, 15]. The optimal situation is if the experimental devices can at least partly reproduce the loading of the real component in the selected test setup. Due to the inherent viscoelastic nature of the deformation behavior of TPUs, displacement-controlled loading generates stress relaxation. The F_{max}/F_{min} values of the cyclic tests were continuously recorded and the changes of these curves were used for assigning the cycle number-to-failure, N_f, values. A representative curve along with the definition of the optional failure values is shown in Fig. 3.

2.3 Experimental Methodology for FCG Curves

2.3.1 Test Specimen Configurations

PS specimens of larger (L_0 = 200 mm) and shorter width (L_0 = 100 mm) with a nominal aspect ratio L_0/h_0 (width/length) of 10 have been used in the FCG experiments. The test setup along with the notched planar tensile specimen geometry is shown in Figs. 4 and 5.

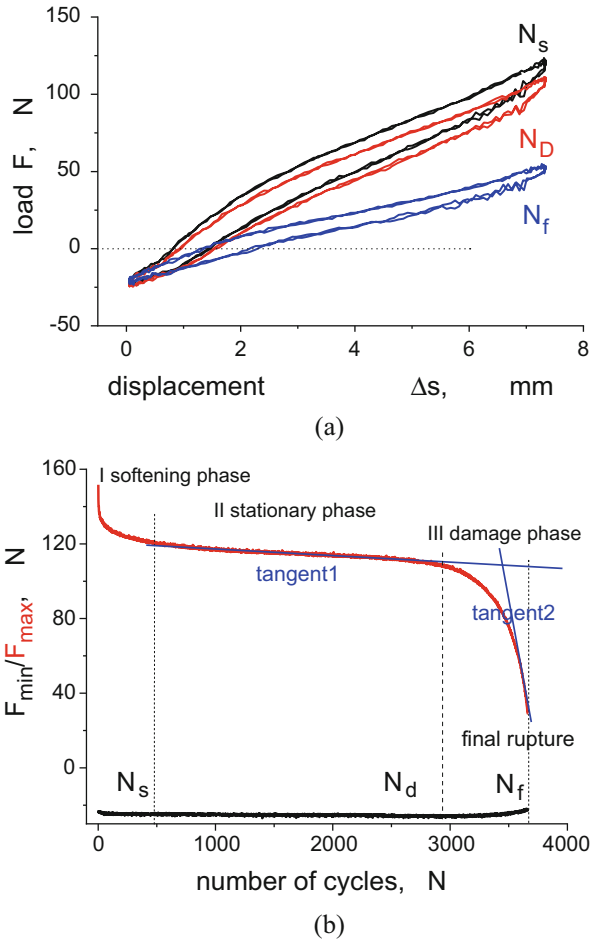

Fig. 3 (**a**) Cycle number dependence of the F_{min}/F_{max} curves and schematic representation of the determination of various cycle number-to-failure values and (**b**) representative hysteretic force-displacement curves at the end of the various deformation phases (softening, N_s, damage, N_d and final rupture, N_f) [2]

Although the faint waist is keeping usually the crack in the mid-plane, special care was taken to the straightness of the razor blade pre-crack. The initial crack length is in the same range as the height of the PS specimen (10 to 12 mm).

2.3.2 Test Method and Data Reduction

The displacement-controlled loading requires the generation of continuous crack driving forces to stable growing cracks. Hence, the displacement level is continuously increasing during these tests. The corresponding cycles within one level can be, however, varied from 1 up to several 10^4 cycles. While latter clearly reveal a fatigue character, the cycles 1 to 10 can be interpreted as semi-cyclic tests. These tests, however, can efficiently be applied for rapid material characterization.

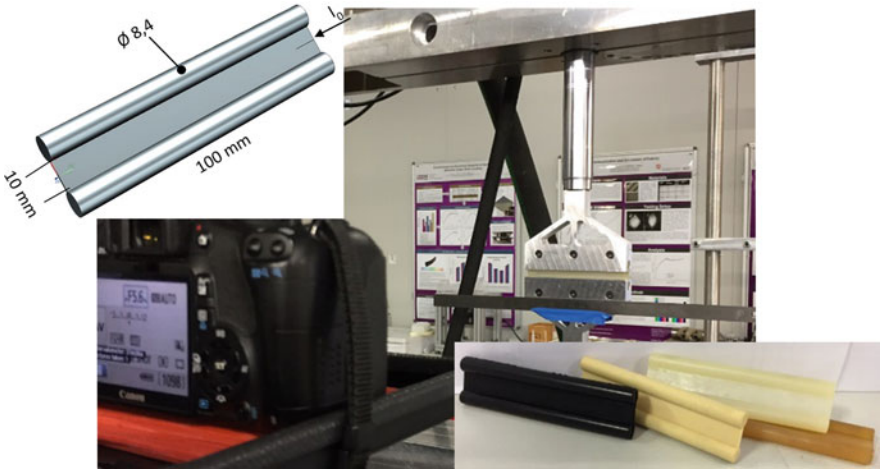

Fig. 4 PS test specimens and test setup

Fig. 5 (**a**) Notched PS test specimen of a TPU with blunted crack tip and (**b**) the local crack tip strain measured by digital image correlation (enlarged)

Sufficiently long PS specimens with sharp notch allow for the direct calculation of tearing energy without a geometry factor. The above aspect was also investigated in detail in previous works [6, 11, 19, 27, 28] and a consistent test and data reduction methodology was elaborated. Hence, tearing energy of notched PS specimens was calculated using the deformation energy values corrected with the crack length for the strain energy density, W and with the original height, h_0, using the well-known relationship without any geometry factor (a/L_0 or strain correction) [6, 11, 19]. The conventional tearing energy concept does not consider the local crack tip blunting and the corresponding local variations of strain and temperature. Additional optical strain and temperature measurement can be used to determine local strain values

around the crack tip and in the ligament [8, 35, 36]. The local deformation and strain analysis may also support the application of the J-integral approach based on the original definition of Rice [37].

3 Results and Discussion

3.1 LSWC Curves

Comparison of various elastomeric materials using injection molded specimens (test series 1) is shown in Fig. 6a. A selected set of tests for TPU11 is shown in Fig. 7b with the values of four unbroken specimens up to 3 MCycles up to a strain level of 15%.

The tests were carried out up to 3 MCycles for estimating the endurance strain limit. A comparison of the LSWC points for TPU21 and TPU22 using machined specimens is shown in Fig. 7a. Inter and extrapolation of the measured points of TPU21 for determining the fatigue life is shown in Fig. 7b.

A collection of LSWCs for three TPU grades tested is shown in Fig. 8. The materials investigated revealed significantly different failure strain from the monotonic values to the endurance strain values.

While the grade TPU21 is in the range of the majority of other materials investigated, TPU23 and 25 revealed significantly higher fatigue resistance than the other material grades. The curves are not only shifted vertically but also the slope was somewhat decreased.

The LSWC methodology was successfully applied for characterizing and comparing the fatigue behavior of various elastomers and especially various TPU grades. The investigated TPU grades revealed a wide range of critical fracture strain values under monotonic loading conditions, appr. 80% up to 220%. Correspondingly, the fatigue life curves were at different levels. This results in very different apparent endurance limit values (appr. 15% up to 80%.) up to 3 MCycles. The slope of the fatigue life curves was lightly decreased with increasing fracture strain and endurance limit strain values for TPU grades investigated. Although some deviations from this overall trend and minor differences were also observed, the trend seems to be clear; materials with high toughness in terms of critical failure strain at smooth notch of the diabolo and under monotonic loading conditions reveal also higher fatigue resistance in terms of the expected endurance strain level.

The LSWC methodology was applied with some adaptation for characterizing the deformation, failure, and fatigue behavior of thin extruded TPU materials (TPU31 and 32). Due to the extrusion a moderate anisotropy was expected. Hence, flat diabolo-shaped specimens were cut from the sheets in both directions, in extrusion (I) and transverse to extrusion (Q). These specimens were tested under monotonic, semi-cyclic, and cyclic (both LSWC and FCG) loading conditions. The comparison of the tensile, diabolo-shape, notched plane strain (PS) and double edge notched specimens (DENT) under monotonic loading is shown in Fig. 9. With increasing

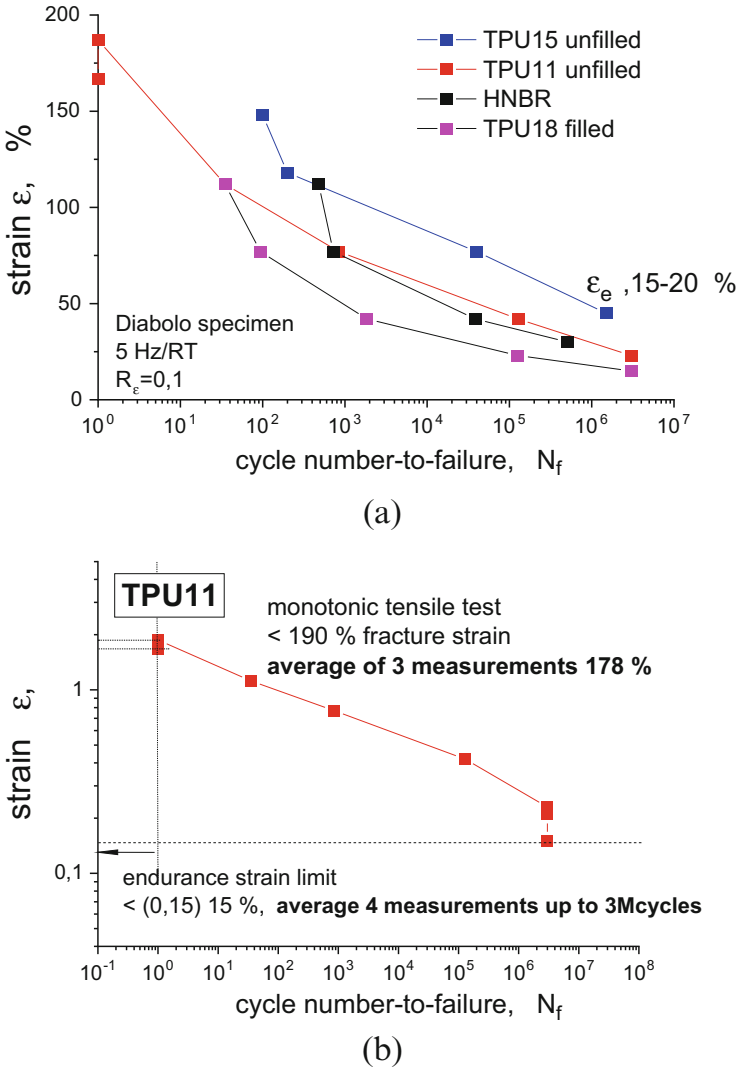

Fig. 6 LSWC results; (**a**) Comparison of various elastomers using injection molded specimens (test series 1): LSWC up to 3 MCycles and (**b**) A selected test series of the LSWC up to 3 MCycles (4 unbroken specimens)

constraint a decrease of the nominal stress and a slight change of the shape of the curves were observed. The specimens revealed high failure strain and only the DENT specimen failed in stable tearing below 200% strain. A clear but specimen configuration dependent anisotropy was also observed.

The unambiguous recognition of the onset of failure (N_f) on the F_{max}/F_{min} curves is a key prerequisite of the construction of the LSWC curves. This condition was fulfilled for all TPU and other elastomer (rubbers and other TPEs) grades testing

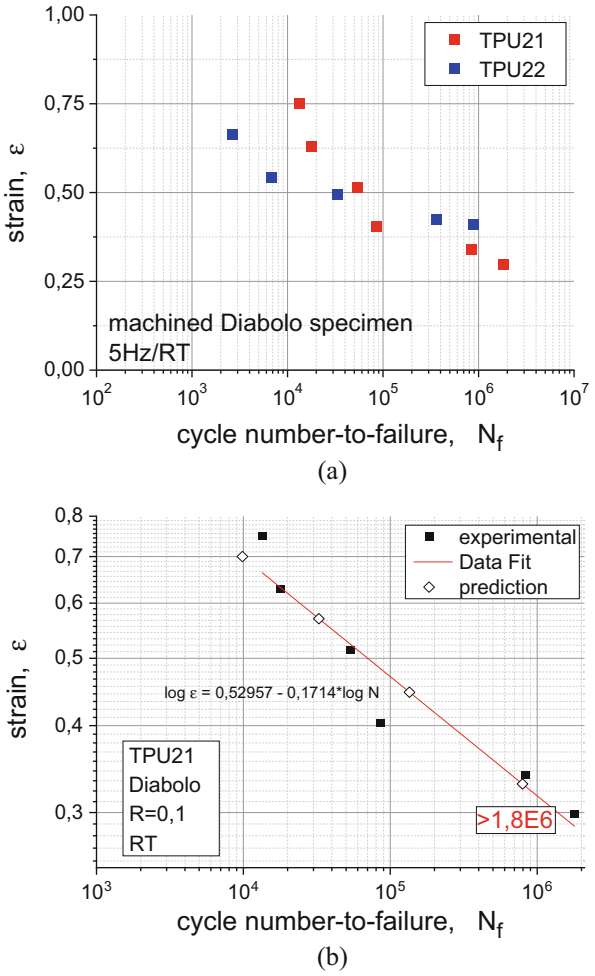

Fig. 7 LSWC results; (**a**) Comparison of the LSWC points for TPU21 and TPU22 and (**b**) Fitting of the measured points of the Wöhler curves for TPU21

both injection molded or machined cylindrical diabolo specimens. F_{max}/F_{min} curves of flat diabolo specimens are shown in Fig. 10 for specific loading conditions of two R_ε ratios (0,1 and 0,5) and at a strain level of appr 120%.

The relaxation is continuous without any sign of damage until the interruption of these tests (3 days). LSWC curves could not be constructed using the flat diabolo specimens. We faced for the first time with the fact that the application of the displacement-controlled cyclic loading is limited to ductile elastomer grades available only as thin specimens. This difficulty may, in principle, be overcome by the application of fracture mechanics approach and using sharply notched specimen configuration. Our solution with sharply notched PS and DENT specimens will be shown in the next part of this study.

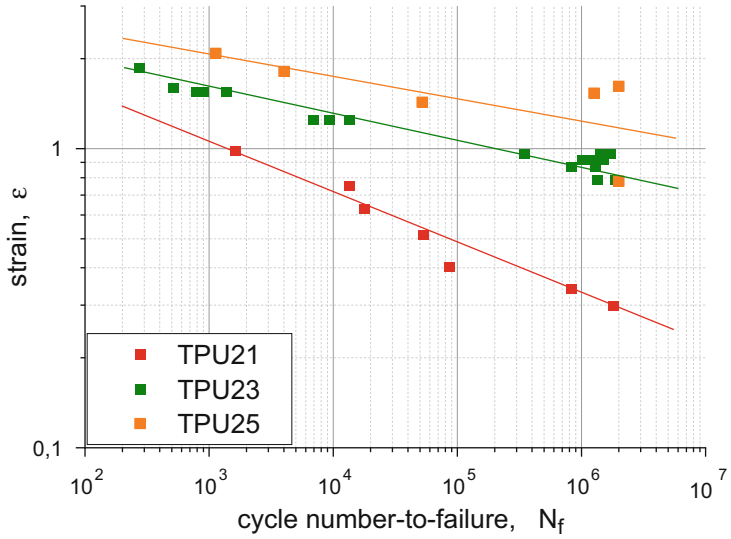

Fig. 8 Summary of the LSWC point series (ε_{max}-N_f) and the corresponding fitting curves of the three characteristically different TPU grades TPU21, 23, and 25

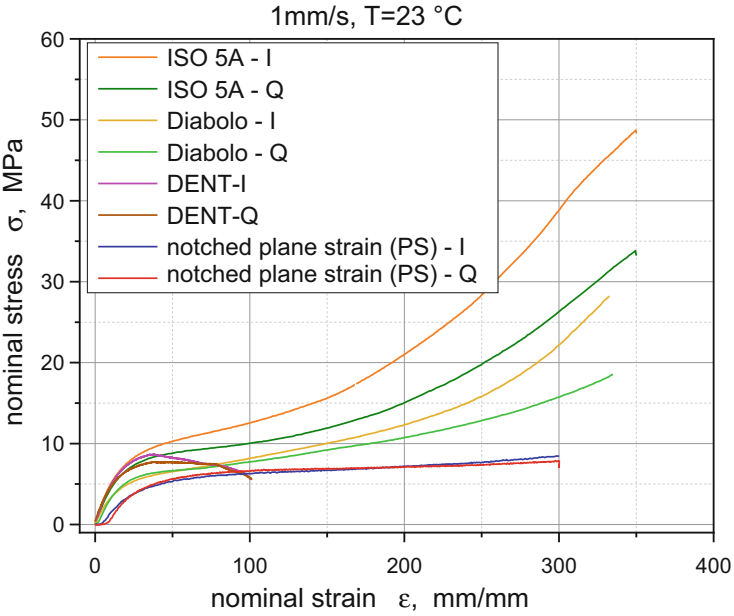

Fig. 9 Comparison of stress-strain curves for uniaxial tensile, flat diabolo (smooth notch), DENT and notched plane strain (PS) specimens for both directions (I/Q) of TPU32

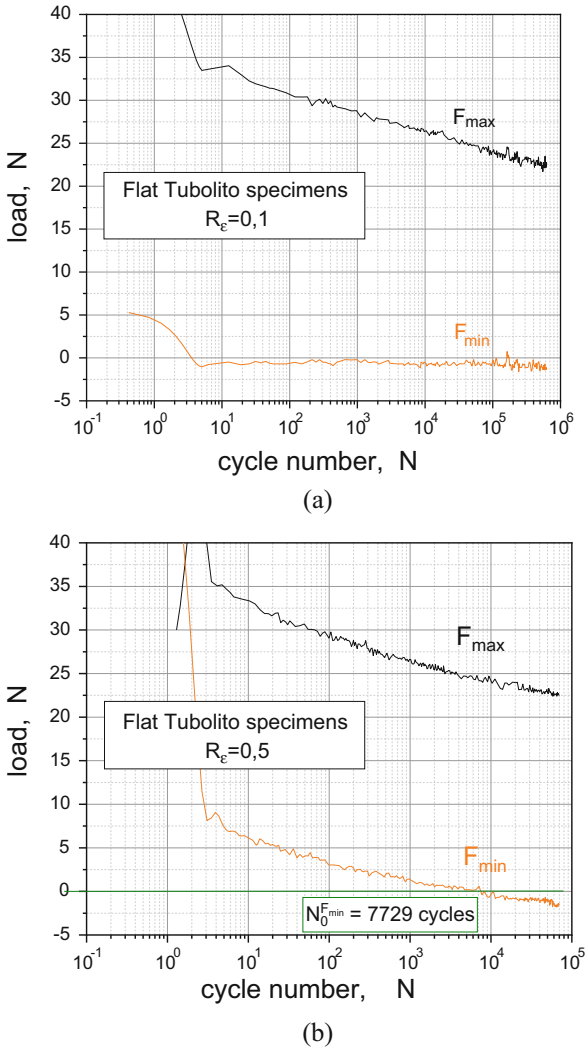

Fig. 10 F_{max}/F_{min} curves of flat diabolo specimens at $R_\varepsilon = 0.1$ and 0.5

3.2 FCG Curves

Similar to the LSWC results, selected exemplary results of all three test series will be shown along with some specific methodological issues in this section. Several unfilled and filled TPU grades were investigated using large ($L = 200$ mm) injection molded planar tensile specimens both under monotonic and cyclic loading conditions. The summary of these first tests has been reported in a previous paper [1]. From the high number of various test parameters, the influence of the test frequency and the cycle number at a specific displacement level ($N = 40$, 400, and 4,000) was investigated. The influence of the test frequency on the fatigue crack

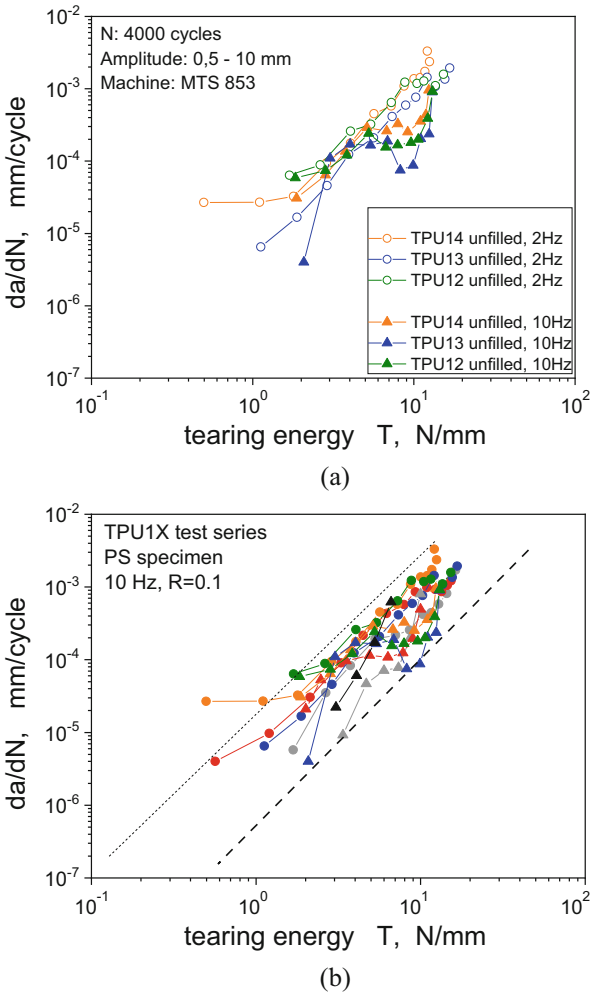

Fig. 11 FCG-T results; (**a**) Frequency dependence of unfilled TPU1xs and (**b**) Comparison of the FCG behavior of unfilled TPU1xs

growth is a key question and was previously investigated for various rubber grades in detail by Feichter [6]. It was shown that at appr. 2 Hz the test frequency dependence of the FCG curves reveals the maximum. It was speculated the below appr. 2 Hz the relaxation behaviour and above them the influence of the hysteretic heating is prominent and both may induce a distinct reduction of the crack growth resistance. The number of cycles at a specific displacement level is a practical problem. With the reduction of the cycles the duration of these test can be reduced, which is beneficial for fast material screening tests. The frequency dependence of unfilled TPU1xs is shown in Fig. 11a. The 10 Hz points are shifted to the right – lower rate at a specific tearing energy – and reveal more "less stability." This deviation from the straightness was associated with a permanent change of the continuous and discontinuous crack growth.

Comparison of the FCG behavior of unfilled TPU1xs is shown in Fig. 11b. Similar to previous investigations on rubbers [7] it was seen that the slope of the stable crack growth is rather similar, the curves are shifted from the left (corresponds to low resistance) to the right (corresponds to high crack growth resistance). Hence, the main difference is observed in the threshold level. As it was mentioned previously, TPU25 revealed an outstanding fatigue behavior in the LSWC tests. We have performed five FCG tests in order to determine the data scatter of the FCG curves. These data scatter of the FCG curves for TPU25 is shown in Fig. 12a. A comparison with a TPE-A (Pebax) grade is shown in Fig. 12b. Although the FCG resistance of TPU25 was high, the TPE-A grade revealed the highest FCG resistance (curves shifted to the right) and also a lower data scatter.

To overcome the difficulties with the LSWC based fatigue characterization of the thin TPU3x materials, the tearing energy concept was also applied. Thin sharply

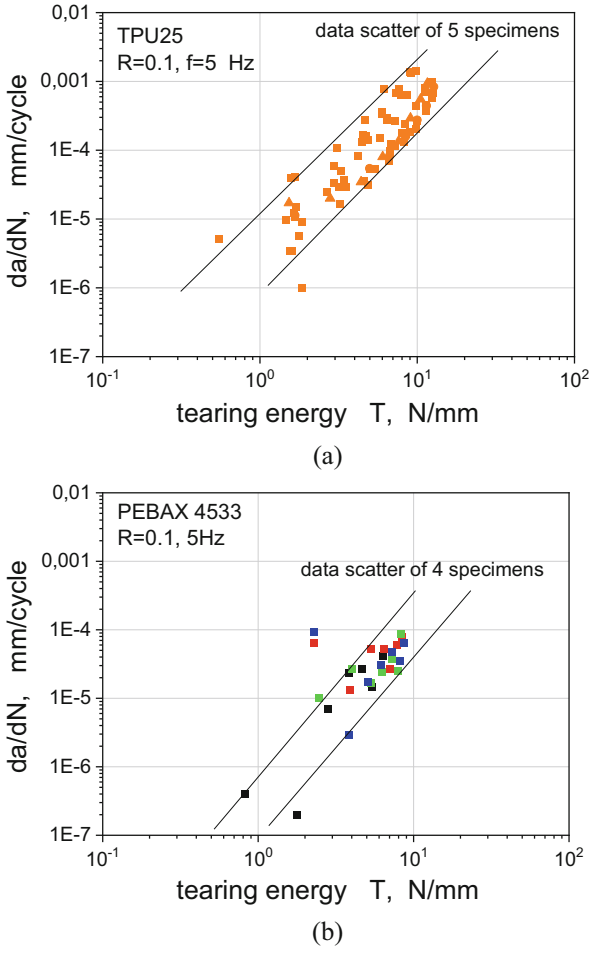

Fig. 12 FCG results; (**a**) data scatter of the FCG curves for TPU25 and (**b**) data scatter of the FCG curves for TPA (Pebax)

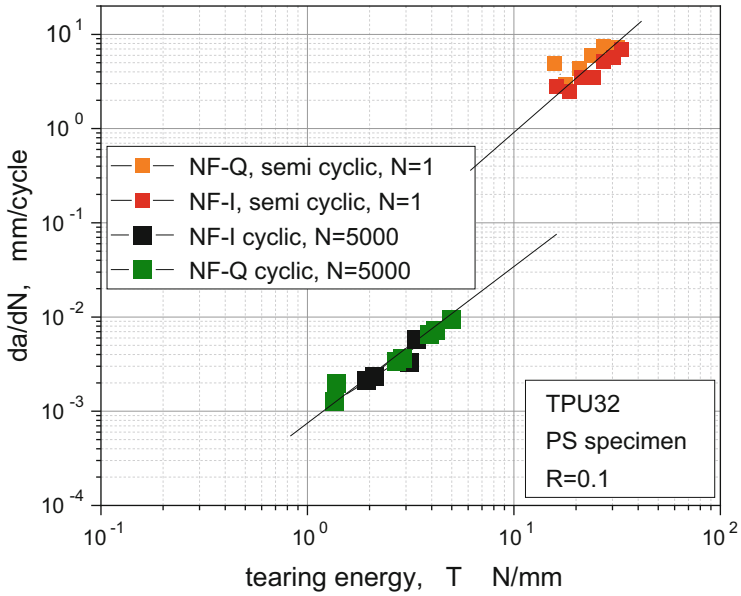

Fig. 13 Comparison of the FCG curves ($N = 1$ and 5,000 cycles/displacement level) of notched planar tensile specimens for TPU32 (Q/I)

notched small ($L = 100$ mm) PS specimens were investigated under displacement-controlled tensile loading. The sequence of this loading was varied in terms of the displacement levels and the corresponding cycle numbers applied. Comparison of the FCG curves ($N = 1$ and 5,000 cycles/displacement level) of notched planar tensile specimens for TPU32 and for both specimen orientations (Q/I) are shown in Fig. 13. The tests with 1 cycle/displacement level were used for a fast material characterization and for the accurate planning of the FCG tests. The initial sharp crack tip of the 0.3 mm thin PS specimens (see Fig. 5) was blunted after the first load cycles and a subsequent stable crack growth was observed.

As expected, the FCG curves are in different crack growth rate regimes, but reveal similar slope. The points for $N = 1$ are shifted somewhat to the left (lower resistance). We concluded that for fast screening the semi-cyclic ($1 < N < 100$) test provides reliable results with some cyclic character for material comparison. Higher cycle numbers ($N > 10^4$) are necessary for a more detailed characterization.

3.3 Estimation of the Endurance Limit Based on Threshold Values

As it was mentioned in the introduction, in spite of both the experimental and some theoretical advantages of fracture mechanics, the LSWC method reveals higher

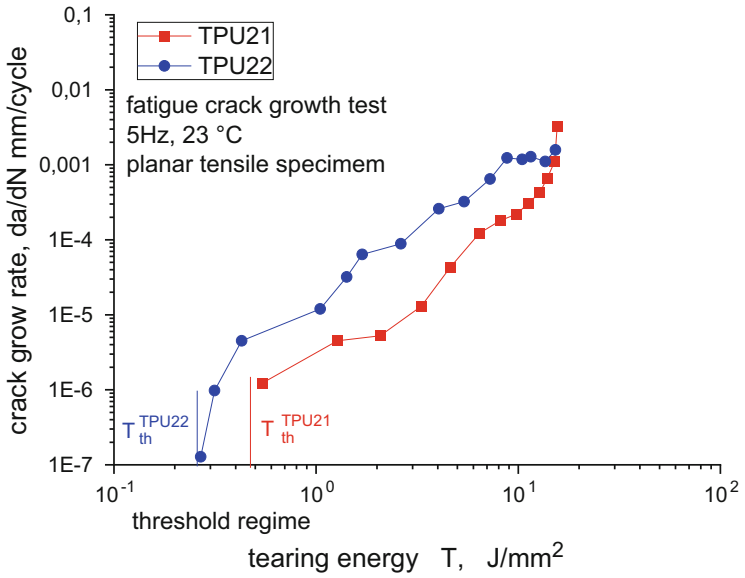

Fig. 14 FCG curves for TPU21 and TPU22 (see Fig. 9 for comparison with LSWC curves)

potential to practical application for elastomer components. Hence, the endurance limit in terms of critical strain should be estimated and rigorously appraised. There are several options for the estimation of endurance limit strain values, $\varepsilon_e{}^c$: (1) direct measurement, (2) calculation from threshold tearing energy, T_{th}, and (3) estimation from the critical CTOD, $\delta_c{}^{\text{EWF}}$, using the essential work of fracture approach.

The direct measurement is time consuming and expensive (examples up to 3 MCycles are available). Representative FCG curves are shown in Fig. 14. Special emphasis was given to the identification of the threshold values, T_{th}, in these curves. The minimum crack growth rate was measured up to 1E-7 mm/cycles, which represents a practical limit for reliable crack length measurements.

The rates, 1E-7 mm/cycles are quite fast for a long fatigue life, there are smaller values for stiffer polymers and for metals. It can be seen as a practical compromise between measurement technique and time limitations and minimum crack growth rate for a realistic and reliable estimation of physical threshold. Hence, we term as apparent engineering threshold and used for further calculations. While the crack propagation rate was similar, the curves were shifted (TPU21 > TPU22). In general, the fatigue resistance of TPU22 was somewhat lower than the fatigue resistance of TPU21 in both experiments (see Fig. 9). The expected range for the lower and upper limit of apparent threshold values, $T_{th}{}^{app}$, 0.26 to 0.6 N/mm – is shown in Fig. 14 for both TPU types investigated. The observation of all FCG curves generated based on appr. 20 elastomer grades revealed the range for this apparent threshold between 0.1 and 1 N/mm (see Figs. 13 and 14). There are some materials below and one above (i.e., TPA, appr 2 N/mm), but this is a fair range for a practical analysis.

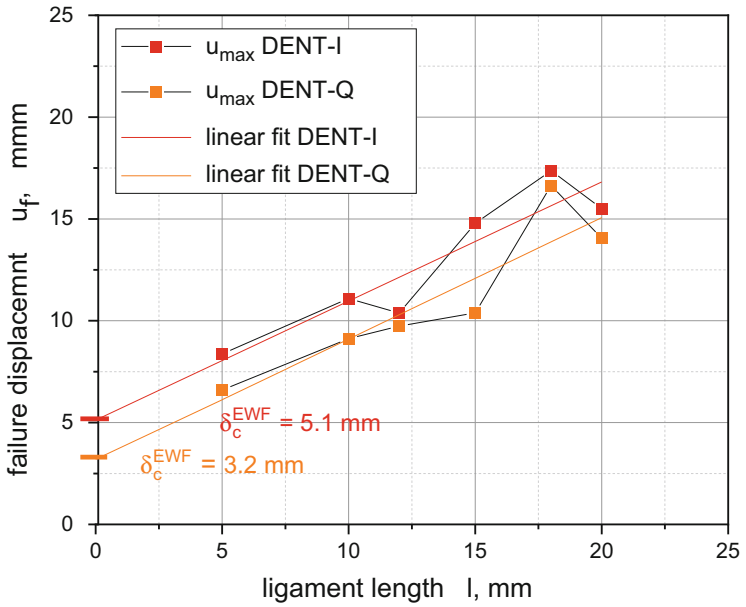

Fig. 15 Ligament length dependence of failure displacement values, u_f of thin DENT specimens. The essential work of fracture (EWF) methodology was applied to determine the critical crack tip opening displacement, δ_c^{EWF} for the TPU32 material

Critical strain values for specific tearing energy values can be calculated with the assumption of initial crack length (typical defect size). Similar calculations have been reported in the literature [38–41]. For planar tensile specimen using the corresponding critical values for W_c and σ_c (last cycle in the cyclic sequence), the critical strain, ε_c^{th}, can be calculated. Ligament length dependence of failure displacement values, u_f, for DENT specimens is shown for TPU32 (Q/I) in Fig. 15. The u_f values were determined at the maximum displacement of the load-displacement curves.

The essential work of fracture (EWF) methodology was applied to determine crack tip opening displacement (CTOD), δ_c^{EWF}, for the thin TPU32 material. The corresponding values were 5.1 mm (I) and 3.2 mm (Q). These values can be interpreted as the critical plane stress fracture toughness values in terms of displacement-based fracture mechanics parameters. This is a critical CTOD value at which a stable crack growth initiates in the plane stress state. Hence, it is a well-defined limit value for thin specimens and components. The calculation of corresponding crack tip strains and their verification with optical strain measurement makes the estimation of endurance limit values possible.

The EWF theory allows for the generation of critical crack tip opening displacement values for a plane stress situation (thin wall structures). These values can be used for calculating corresponding critical strain values at a plane stress crack tip and can be compared with optically measured strain values. The δ_c^{EWF} values from

Fig. 15 yield critical strain values in the range of 60–70% for Q and 100–120% for I specimens. This high value can be interpreted as upper bound for the endurance limit for the thin specimens. The further method development will focus on the adaptation of the EWF approach for cyclic loading conditions and to determine fatigue limit values.

4 Conclusion

In order to reduce the data scatter of the fatigue tests, the failure site should not be influenced by the gripping of the specimen. Hence, in addition to the geometry locking, the strain should be localized far from the fixture in the mid of the specimen. Cylindrical diabolo-shaped specimens along with a proper grip fulfill this requirement. The determination of local strain requires the application of a proper hyperelastic material model and the correct determination of the specific parameters needed. While the experimental verification by optical strain analysis is rather complicated for cylindrical specimens, comparable results were observed for flat diabolo-shaped specimens. The existence of a global displacement-local strain calibration curves makes an easy application of displacement-controlled cyclic tests and the construction of LSWC possible. The displacement-controlled test reveals high stability and accuracy regarding the test amplitudes over a wide test frequency and amplitude combination range.

Due to the inherent viscoelasticity of the elastomers investigated, hysteresis curves and the F_{max}/F_{min} values reveal a pronounced stress relaxation, typically with various phases. The sudden change of the F_{max} values indicates a damage in the specimen and this can be used for assigning the cycle number-to-failure, N_f values. The ε vs. N_f points have shown a rather moderate data scatter for a large number of different materials and for various test conditions (f, T, R_ε ratio). Finally, LSWC curves were generated using both molded and machined cylindrical specimens. While these values were successfully found for all elastomer grades investigated, the thin extruded TPU grades did not reveal these points and the construction of LSWC was not possible.

Local strain Wöhler curves (LSWC) can be used for supporting material selection, material development efforts and for estimating fatigue life-time of elastomeric components. The determination of the local strain is also important to the transferability of laboratory specimen level results to real components. The direct experimental determination of endurance strain values is time consuming. Our tests up to 3E6 cycles provided tendencies for apparent endurance strain values in the range of 15–80% for the elastomers investigated and are in agreement with literature [9, 41, 42].

The applicability of fracture mechanics concepts for rubbers is well-documented and described in many papers [1, 3, 11–13, 17–21, 25, 35]. The application of planar tensile specimen makes the test method and the calculation of tearing energy values simple. Modern optical measurement systems make the identification of crack tip

(also for highly blunted tip) and hence a reliable measurement of the crack length and calculation of crack growth rate possible. The fatigue crack growth curves with tearing energy were also successfully applied for thermoplastic elastomers over a wide material range and revealed clear differences regarding the investigated materials. Similar to rubber the same influence parameters could be identified and at least partly characterized.

In spite of the availability of a number of test results for elastomers, due to the lack of practical NDTE tests, the applicability of fracture mechanics to component design is rather rare. The threshold tearing energy values can be, however, used for estimating the critical endurance strain values, ε_e^{th}, and thus to complete the LSWC curves. The methodology for demanding application should consist of a proper statistical analysis of all parameters involved in the procedure. Similar to the investigations performed on various composite material and structures of the authors group [43, 44], these additional analyses with statistical methods are the next objective of the investigations for elastomers.

Acknowledgements First and foremost, it was a privilege to learn Fatigue of Metals from Prof L. Tóth (University Miskolc) and to extend to Polymer Fatigue at Prof R.W. Lang (University of Leoben). My special appreciation goes to the former PhD students Drs. Ch. Feichter, Sz. Vezér, A. Hausberger. M. Isasi and B. Schritteser in Leoben (MUL and PCCL), to the company partners Dr. T. Schwarz, Dr. Ch Lembacher and H. Müller, and to my recent colleague and research students in the field of soft materials engineering, Dr. U.D. Cakmak, Mr. J. Holzweber, Mr. M. Lackner, and Mrs. C. Emminger. The study was supported in the frame of the LIT Project (JKU, 2nd Call, 2017) "From multi-material additive manufacturing of dampers to tailored viscoelastic dissipation" (coordinator Prof. I. Graz).

References

1. Major Z, Isasi M, Schwarz T (2010) Characterization of the fracture and fatigue behavior of thermoplastic elastomer materials. Key Eng Mater 417-418:789–792
2. Major Z (2012) Applicability of displacement controlled fatigue test methods for compliant structures. In: IMEKO TC15 experimental mechanics proceedings of 11th youth symposium on experimental solid mechanics
3. Holzweber J, Müller J, Çakmak UD, Major Z (2018) Characterization and modeling of the fatigue behavior of TPU. Mater Today Proc 5:26572–26577
4. Mars WV, Ellul MD (2017) Fatigue characterization of a thermoplastic elastomer. Rubber Chem Technol 90(2):367–380
5. Eberlein R, Pasieka L (2020) Prediction of long-term behavior for dynamically loaded TPU. Adv Mater Lett 11(1):20011458
6. Feichter C (2006) Characterization of the fatigue behavior of elastomer compounds by fracture mechanics methods. PhD thesis, Montanuniversität Leoben
7. Feichter C, Major Z, Lang RW (2007) Experimental determination of fatigue crack growth behavior and surface strain distribution of 'faint waist pure shear' specimens with different crack tip radii. Rubber Chem Technol 79:712–733
8. Feichter C, Major Z, Lang RW (2006) Deformation analysis of notched rubber specimens. Strain 42:299–304

9. Seichter S, Archodoulaki VM, Koch T, Holzner A, Wondracek A (2017) Investigation of different influences on the fatigue behaviour of industrial rubbers. Polym Test 59:99–106
10. Rivlin RS, Thomas AG (1953) Rupture of rubber. I. Characteristic energy for tearing. J Polym Sci 10:291–318
11. Lake GJ (1955) Fatigue and fracture of elastomers. Rubber Chem Technol 68:435–460
12. Stoček R, Heinrich G, Gehde M, Kipscholl R (2013) Analysis of dynamic crack propagation in elastomers by simultaneous tensile- and pure-shear-mode testing. In: Grellmann W et al (eds) Fracture mechanics & statistical mech., LNACM, vol 70. Springer, Berlin, pp 269–301
13. Stadlbauer F, Koch T, Archodoulaki VM, Planitzer F, Fidi W, Holzner A (2013) Influence of experimental parameters on fatigue crack growth and heat build-up in rubber. Materials 6:5502–5516. https://doi.org/10.3390/ma6125502
14. Mars WV, Fatemi A (2001) A literary survey on fatigue analysis approaches for rubber. Int J Fatigue 24:949
15. Mars WV, Fatemi A (2003) Fatigue crack nucleation and growth in filled natural rubber. Fatigue Fract Engng Mater Struct 26:779–789
16. Aidy A, Hosseini M, Sahari BB (2019) Fatigue life modeling for elastomeric materials: a review. Int Rev Mech Eng 3(3):332–338
17. Isasi MI (2017) Fatigue stiffness loss and life prediction technique development of a real rubber automotive component by means of finite element analysis. PhD thesis, London Metropolitan University
18. Mars WV, Isasi M, Arriaga A, Plaza J (2015) Relationship between displacement and force controlled fatigue tests. In: Constitutive models for rubber IX. CRC Press, p 417
19. Stocek R, Heinrich G, Gehde M, Rauschenbach A (2012) Investigations about notch length in pure-shear test specimen for exact analysis of crack propagation in elastomers. Zeitschrift Kunststofftechnik, J Plast Technol 1:2–22
20. Eisele U, Kelbch SA, Engels HW (1992) The tear analyzer – a new tool for quantitative measurements of the dynamic crack growth of elastomers. Kautschuk Gummi Kunststoffe 45:1064–1069
21. Dedova S, Schneider K, Heinrich G (2019) Hu-neau B, Le Cam J-B, Marco Y, Verron E (eds) Energy based characterization of fracture and fatigue behaviour of rubber in complex loading conditions. Constitutive models for rubber XI. CRC Press, pp 363–367
22. Vezer SZ (2011) Characterization of the fretting fatigue behavior of engineering polymers. PhD thesis, Montanuniversität Leoben
23. Schwalbe KH (2010) Integrity of lightweight structures, a summer course. IGF Gruppo Italiano Frattura, Trieste
24. Bauman JT (2008) Fatigue, stress, and strain of rubber components. Hanser Gardner Publications, C.H. Verlag. https://doi.org/10.3139/9783446433403
25. Robertson CG, Stoček R, Kipscholl C, Mars WV (2019) Characterizing the intrinsic strength (fatigue threshold) of natural rubber/butadiene rubber blends. Tire Sci Technol TSTCA 47:292–307
26. Boyce MC, Arruda EM (2000) Constitutive models of rubber elasticity: a review. Rubber Chem Technol 73(3):504–523. https://doi.org/10.5254/1.3547602
27. Yeoh OH (1990) Characterization of elastic properties of carbon-black-filled rubber vulcanizates. Rubber Chem Technol 63:792–805
28. Yeoh OH (2001) Analysis of deformation and fracture of 'pure shear' rubber testpiece. Plastics Rubber Compos 30:389–397
29. Anand L, Parks DM (2004) Defect free fatigue, 2.002 mechanics and materials II spring supplementary note. MIT, Cambridge
30. Marckmann G, Verron E (2006) Comparison of hyperelastic models for rubber-like materials. Rubber Chem Technol 79(5):835–858
31. Ogden RW, Saccomandi G, Sgura I (2004) Fitting hyperelastic models to experimental data. Comput Mech 34:484–502

32. Çakmak UD, Major Z (2014) Experimental thermomechanical analysis of elastomers under uni-and biaxial tensile stress state. Exp Mech 54(4):653–663
33. Çakmak UD, Kallai I, Major Z (2014) Temperature dependent bulge test for elastomers. Mech Res Commun 60:27–32
34. Bergström J (2015) Mechanics of solid polymers, theory and computational modeling. Elsevier, Amsterdam
35. Stocek R, Heinrich G, Gehde M, Rauschenbach A (2012) Investigations about notch length in pure-shear test specimen for exact analysis of crack propagation in elastomers. Zeitschrift Kunststofftechnik, J Plast Technol 1:2–22
36. Feichter C, Major Z, Lang RW (2005) Influence of crack tip sharpness and radius on the strain distribution in rubbers analyzed by finite element simulation and experiments. In: Austrell PE, Kari L (eds) Constitutive models for rubber IV. A.A. Balkema Publishers, pp 89–95
37. Rice JR (1968) A path independent integral and the approximative analysis of strain concentration by notches and cracks. J Appl Mech:379–386
38. Spagnoli A, Terzano M, Brighenti R, Artoni F, Carpinteri A (2019) How soft polymers cope with cracks and notches. Appl Sci 9:1086. https://doi.org/10.3390/app9061086
39. Guo H, Li F, Wen S, Yang H, Zhang L (2019) Characterization and quantitative analysis of crack precursor size for rubber composites. Materials 12:3442. https://doi.org/10.3390/ma12203442
40. Wang X-L, Liao M-Y, Xu Y, Liu X-A (2018) Fatigue crack propagation characteristics of rubbery materials under variable amplitude loading. Results Phys 10:233–240
41. Ruellan B, Le Cam J-B, Jeanneau I, Canevet F, Mortier F, Robin E (2019) Fatigue of natural rubber under different temperatures. Int J Fatigue 124:544–557
42. Belkhiria S, Hamdi A, Fathallah R (2020) Strain-based criterion for uniaxial fatigue life prediction for an SBR rubber: comparative study and development. Proc Inst Mech Eng Part L J Mater Des Appl
43. Chung N, Major Z (2018) A fatigue prediction methodology for continuous fiber reinforced composites. In: 18th U.S. national congress for theoretical and applied mechanics, USNC-TAM conference, Chicago
44. Stelzer P, Hebertinger T, Reisecker V, Maier J, Major Z (2020) Stiffness degradation and the fatigue behavior of low-flow carbon fiber sheet molding compounds. In: Proceedings of the American society for composites – 35th technical conference, NY

Adv Polym Sci (2021) 286: 297–330
https://doi.org/10.1007/12_2020_80

Published online: 21 December 2020

About the Influence of Materials Parameters on the Ultimate and Fatigue Properties of Elastomers

L. Chazeau, J. -M. Chenal, C. Gauthier, J. Kallungal, and J. Caillard

Contents

Abstract The aim of this chapter is to revisit the historical works, mechanisms, and modeling approaches available in the field of fatigue crack growth resistance and rupture properties. After introducing the methodology developed to evaluate these properties, the impact of testing parameters such as temperature, loading speed, and pre-deformation will be highlighted. We will then review the influence of some material characteristics on rupture and crack propagation and the local mechanisms

L. Chazeau (✉), J. -M. Chenal, and J. Kallungal
Univ Lyon, INSA Lyon, CNRS, MATEIS UMR5510, Lyon, France
e-mail: laurent.chazeau@insa-lyon.fr

C. Gauthier and J. Caillard
Centre de technologies, Manufacture Française des Pneumatiques Michelin, Clermont Ferrand, France

involved. Finally, a theoretical framework primarily dedicated to the description of crack propagation under static load will be discussed that aims to underline the connection between resistance to crack growth and the ability of a material to dissipate energy.

Keywords Cyclic/static crack growth · Dissipation · Filled polymers · Mullins effect · Rupture properties · Viscoelasticity

1 Introduction

Optimizing life duration of pneumatics, seismic isolators, mechanical membranes, seals, etc. requires a good understanding of the capability of elastomers they are made of, to withstand mechanical loading and resist to crack initiation/propagation. The mechanisms of crack initiation and propagation in elastomers have been of continuous interest to the scientific community, as shown by the numerous reviews on this topic [1–6]. In addition, many recent works have been dedicated to a fine characterization of the material in the close vicinity of cracks. More recently, new fields of applications have emerged in connection with soft robotics, stretchable electronics, and bio-medical applications [7]. New ideas for the architecture of biomimetic materials with improved performance emerged [8, 9]. Recent years have thus seen the synthesis of novel elastomeric networks, such as "double networks," which appear to provide remarkable fracture properties [10]. This contributed to a renewed interest in understanding and modeling the damage and rupture of elastomeric and filled elastomeric networks [11, 12].

2 Experimental Methods and Key Features Related to Viscoelasticity

From a very general point of view, rupture appears as the consequence of the initiation and eventual propagation of one or more cracks over the entire section of the material. It can occur under a constant, monotonic, or cyclic loading or a combination of these three. Understanding crack mechanisms requires the use of microstructural characterization tools that allow to observe the process of crack appearance from the very beginning. Several studies focused on the links between the processing conditions and the presence of defects, such as cavities, aggregates, or agglomerates, from which cracks can nucleate. They are generally extended to the study of the number of cracks created under a given load scenario (monotonic or cyclic). The geometries that allow stress localization and consequently the control of the zone where cracks will appear are generally preferred (e.g., diabolo or hourglass type) [13, 14], in order to limit the observation region. Many studies use optical or

electron microscopy (SEM) to observe the surface of the specimen. The fast development of tomography now allows to access a 3-dimensional information inside the object. This one can be correlated with the strain energy necessary for the crack's nucleation and subsequent propagation that can be calculated at a macroscopic scale or locally through the characterization of strain fields inside the material (using necessarily a modeling step). It is thus possible to better understand the initiation mechanism and its link with local stress or existing flaws in the material (their morphology or their spatial distribution) [15–17]. Nevertheless, note that the estimated strain energy or the local or macroscopic critical stresses/strains to which crack initiation is related depend very much on observation tools and their resolution.

In many cases, cracks initiation is not considered as the mechanism which dictates the lifetime. Thus, many works have been rather devoted to crack propagation. Different experimental protocols and specimen geometries can be used (the most commonly used geometries are pure shear, trouser, and tensile test-pieces). This can make difficult comparison and generalization of the results. The test-piece can be strained, at a constant load force and one then measures the crack propagation velocity Vp(t). The trouser test-piece is the most suitable for this so-called crack growth tests since the stretch of the two legs can be directly related to the crack propagation velocity. Things are less straightforward on notched pure shear (PS) geometry or tensile specimens. In this case, the estimate of the propagation velocity requires a direct measurement of the crack length as a function of time. "Static cut growth test" corresponds to the measurement of the crack propagation velocity after a cut is made in a statically strained PS specimen. In the so-called fatigue crack growth tests, the notched test-piece is subjected to a cyclic loading, controlled by deformation or stress, with or without polarization. (i.e., with or without complete unloading). The stabilized propagation rate is then measured per cycle [18] for different loading levels. Such protocols are built to mimic the conditions encountered in numerous applications, where loading levels are relatively low. In these applications, the load frequencies are often significantly higher than 1 Hz. This can lead to a significant rise in temperature of the material. To avoid it, or at least to limit it, haversine type loading conditions are often used. The term "stabilized" is important: indeed, faster propagation is generally observed during the first cycles, and the crack growth rate decreases more or less rapidly towards a "stabilized" value. This is ascribed to a modification of the crack geometry (initially created from a razor cut), and of the mechanical properties of the material in its vicinity.

Whether static, monotonic, or cyclic solicitation is applied, these experiments therefore enable to relate Vp, expressed per time unit (for instance, in static crack growth experiment) or per number of cycles (in fatigue crack growth tests) to a strain energy release rate G, defined as the variation of potential energy in the specimen per advanced crack area. Note that G is noted T (for tearing energy) in many articles. The resulting Vp(G) curve is indeed considered to be independent on the geometry [18, 19], at least for those commonly used [20], if certain conditions on the geometries are fulfilled [21]. Using a Pure Shear (PS) geometry, [20, 22, 23] of

initial height h_0 submitted to a stretching λ, G associated with the propagation of a crack of length c is the product of $W(\lambda)$ by h_0, where $W(\lambda)$ is the strain energy density of the unnotched PS test-piece submitted to the same stretching. For a tensile strip geometry, the expression becomes $2kW(\lambda)c$, k being a parameter depending smoothly on λ [24, 25]. In the case of an elastic material, $W(\lambda)$ simply is the area under the loading curve of the unnotched test-piece, and G is then the stored elastic energy. The estimate is less trivial for viscoelastic material, or when the mechanical behavior irreversibly depends – over the time scale of the cycles and/or of the crack propagation – on the maximum loading (as it is the case in filled elastomers due to the Mullins effect). In fatigue crack growth test, depending on the authors, $W(\lambda)$ will then be estimated from the area under the loading curve, or under the unloading one, of a stabilized cycle. Thus, depending on the chosen option, it will include or not the energy dissipated during the cycle (this having important consequences on the interpretation of the Vp(G) curves) [26].

There is not a complete consensus in the literature on experimental protocols, whether they are used to assess the properties at break, the tearing resistance or the crack propagation characteristics. However, a generic behavior can be outlined, here introduced in the case of unfilled amorphous elastomers. Their stress and strain at break (ε_b, σ_b), often measured in tensile test, depend on the strain rate ($\dot{\varepsilon}$) and the temperature. A master curves for σ_b (corrected from entropic effects) and for ε_b can be built, as a function of $1/\dot{\varepsilon}$ [27], using temperature-dependent shift factors from the William-Landels-Ferry law for the α relaxation times. Furthermore, an envelop curve for the couple (σ_b, ε_b) with tests carried out at different speeds and temperatures can be drawn [28]. It highlights the weak rupture properties at high temperature and low velocity, and the existence of optimal temperature and strain rate conditions for the strain energy at break. The latter being related to G via the Greensmith's formula [29], this shows the dependence of the critical strain energy release rate G_c (G value for a catastrophic crack propagation) on temperature and strain rate, or in other words, on the role of the viscoelasticity in the involved processes.

$V_p(G)$ curves (or the reverse, $G(V_p)$ curves) from non-cyclic crack growth tests are found in literature with crack propagation rates which can extend over ten decades (Fig. 1) [30]. The authors estimate a tearing energy G_t (with a significant error bar), akin to G_c, when Vp reaches several m/s. In the lower or higher velocity domains, the breaking surfaces are, respectively, rough and smooth, and the velocity is approximatively or completely stable, while stick-slip occurs in the transition domain [31, 32]. These different behaviors are related to the material ability to blunt the crack tip by cavitation [33]. This mechanism involving the viscoelastic response of the material may or may not have the time to occur, depending on the propagation velocity [34]. The width of the transition domain decreases with the increase in the material crosslinking density. Note that the unstable stick-slip process may also result from a non-uniform temperature in the crack vicinity that interacts with the local viscoelasticity of the material [26]. Below G_t, two different domains can be distinguished: for G above a value named G_0, V_p roughly varies with a power law of G. Below G_0, one observes an extremely low crack propagation rate, independent

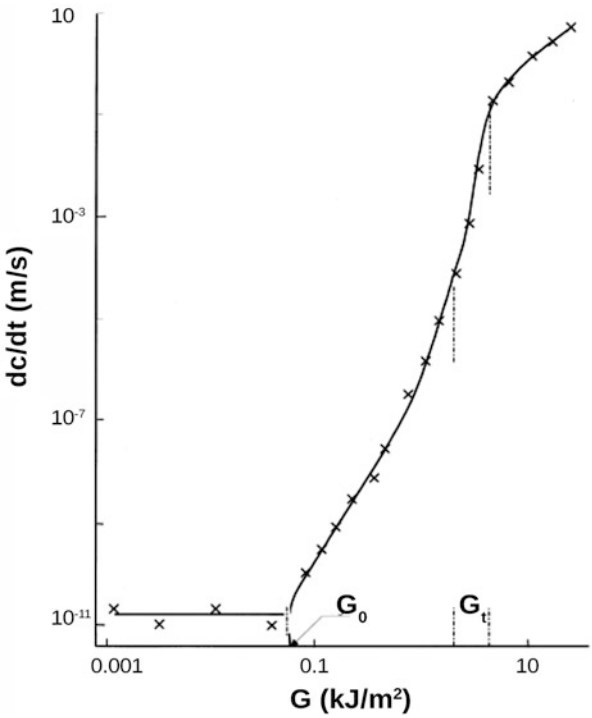

Fig. 1 Crack growth velocity (dc/dt) as a function of the strain energy release rate G for Styrene Butadiene Rubber. G_0 is the threshold energy for mechanical crack growth and G_t indicates the transition region. Figure from Ref. [30]. Reproduced with permission from Rubber Chemistry and Technology. Copyright © (2000), Rubber Division, American Chemical Society, Inc

of G, solely originating from a chemical degradation of the material at the crack tip [35]. $G(V_p,T)$ data obeys the same time-temperature equivalence as dynamic moduli and makes possible the construction of a master curve over a very large domain. Incidentally, T and V_p being given, G grows with the loss modulus. G_0 has therefore to be estimated when the viscoelastic effects are minimized. The reduction of the dissipation zone can be obtained by pushing an ultra-sharp blade into the open crack. This inspired a new efficient protocol to rapidly evaluate G_0 [36, 37]. Values are found between 20 and 100 J/m^2 [38–42]. According to Lake and Thomas [43], they correspond to the breaking energy of the chains that cross the fracture plane. When a bond breaks, the entire chain between crosslinks relaxes to zero load, making the energy dissipation proportional to the number of Kuhn segments (N) between crosslinks. Recent studies however suggest that chains rupture out of the fracture plane are also involved in the fracture energy [44] (cf. Sect. 3). Despite its simplifying assumption (perfect network without entanglement), the Lake-Thomas model predicts the right order of magnitude for G_0 in unfilled amorphous polymers and the observed dependence of G_0 on $N^{-1/2}$. Our study on γ-irradiated elastomer at different doses suggests that the model also seems to qualitatively work for materials containing a large number of dangling and soluble chains, when these are taken into account in the calculation of N [45].

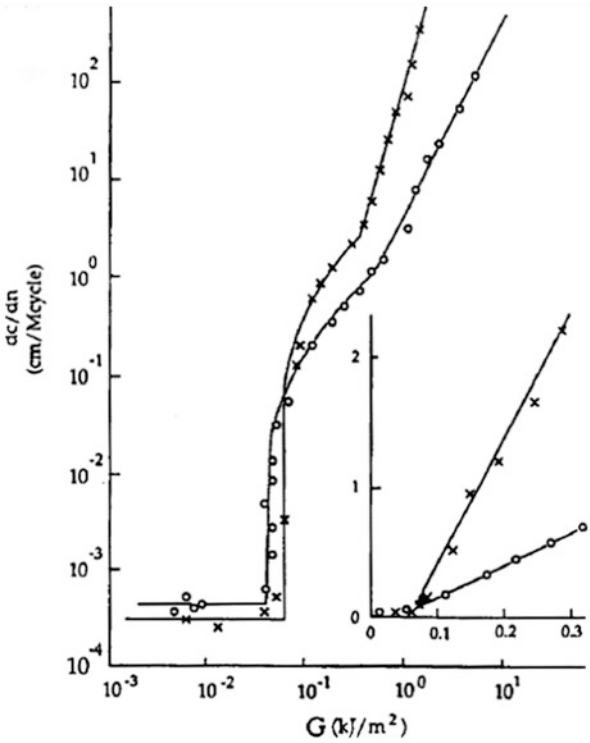

Fig. 2 Crack propagation rate as a function of the maximum energy release rate G in fatigue crack growth test for unfilled Styrene Butadiene Rubber (x) and Natural Rubber (o). From Ref. [6]. Reproduced with permission from Rubber Chemistry and Technology. Copyright © (1995), Rubber Division, American Chemical Society, Inc

Regarding fatigue crack growth tests, the curves are generally given as dc/dn (i.e., the crack growth per cycle) versus G [46]. They have a typical shape, similar to those observed for other classes of materials [47] (Fig. 2). Like for non cyclic loading, three domains are identified. At G values lower than G_0 (same meaning as previously), crack propagation is again ascribed to chemical degradation processes. Then one observes a transition on a restricted domain of G, where the $V_p(G)$ curve increases, usually according to a linear law. For higher G, dc/dn follows a Paris type law [48], i.e. is equal to $A \cdot G^{\beta}$ where A and β are material parameters. Finally, beyond a certain critical value G_c, the crack propagates in a catastrophic way, causing the sample rupture within few cycles.

As shown by Lake and Lindley [18], in the Paris domain (dc/dn $=A.\ G^{\beta}$), A decreases rapidly with the frequency increase and then stabilizes for frequencies greater than 10 cycles per minute. At low frequency, crack growth rate evolution can be deduced from the $G(V_p)$ curves obtained in static crack growth tests. For higher ones (above 1 Hz), the evolution of A suggests that this term contains a specific contribution due to the cyclic loading. Thus, the link between static and fatigue crack growth becomes more sophisticated, since the frequency both impacts the time spent at a given G and influences the bulk material viscoelastic response. In addition, the use of a positive non-relaxing loading can lead to a slowdown of the crack propagation (by a factor of up to 18 in experiments carried out at 2 Hz with Styrene

Butadiene Rubber). To explain it, Lindley [19] assumed that the dynamic component of dc/dn depends on $(G_{max} - G_{min})^{\beta}$, with β the exponent of the Paris law obtained in non-relaxing conditions. Note that at low frequency, as the static contribution of dc/dn is then preponderant, the increase in G_{min} should lead to a larger dc/dn. The influence of the temperature is more intuitive and similar to that observed in static (A increases with the temperature). Thus, as also deduced from tensile strength measurement, G_c decreases with increasing temperature. Note that the quantification of the temperature influence must be carried out so as to ensure that material ageing is avoided (precaution not always described in publications).

3 Material Parameters

3.1 The Polymer and Its Crosslinking

The strong influence of viscoelasticity in crack propagation can be retrieved in the often used expression of G as the product of G_0 and a function f (V_p, T) (cf. Sect. 4). At a macroscopic scale, the viscoelasticity impacts the evolution of the crack tip geometry during the crack advance and therefore the maximum stresses distribution in its vicinity, which causes its further propagation [36]. At the crack tip locus, for the crack to grow, the subchains immediately ahead have to be stretched enough to reach the breaking strain. Since there is internal viscosity, a force higher than that corresponding to the threshold tearing energy must be supplied. The difference between the strain energy density in the bulk and small energy density used for growth of the crack is actually used to overcome the viscosity of the rubber. Viscoelasticity also controls the appearance of other dissipative mechanisms, such as cavitation, fibrillation which may or may not appear in the crack tip and perturb its propagation. Moreover, the chain network density controls G_0 [43] and the deformation level at which strain hardening appears, which seems to decrease the radius of the crack tip and increase the stress triaxiality that promotes cavitation [49].

Thus, from a material design point of view, the key parameters for crack propagation resistance are: crosslinking density, entanglement density, presence of dangling and/or soluble chains, and the glass transition temperature of the polymer. The latter depends on the chemical nature of the polymer chains which also controls the entanglement density (via the chain persistence length), and the energy at break of their bonds. The initial length distribution of the polymer chains controls the fraction of dangling and free chains at a given crosslinking level. The ingredients, the different crosslinking recipes (sulfur, peroxide, disulfide tetramethylthiuram, etc.) and protocols (thermal curing, radiation, etc.) can also be important. Thus, for a same crosslinking density, some authors claim that "conventional" vulcanization system (sulfur/accelerator ratio > 1) leads to better breaking properties and tearing energy (with the Rivlin protocol) than efficient vulcanization system [40]. Interpretations differ on the reasons: more or less spatially homogeneous networks [50], crosslinks formed in a more or less irreversible manner, which may result in more or less built-

in/ stresses or strains [51]. Playing with the chemistry of the polymer chains, one can also create physical crosslinks. Their association/dissociation dynamics should enable a redistribution of the stresses in the elastomer network and therefore slow down the crack propagation. Studies are nevertheless necessary to confirm this. Chemical aging has also large consequences on crack resistance, since it induces, through complex chemical processes, additional crosslinks and/or chain scissions [52–55]. The characterization of molar masses between crosslinks remains however a challenge, even if it has recently benefited from advances in Nuclear Magnetic Resonance [56]. Aging can also be spatially heterogeneous, especially in sulfur vulcanized systems. Characterizing these heterogeneities is also difficult. To sum up, aging and curing conditions can lead to network structures very far from the perfect networks described in most models. This explains apparently contradictory results in the literature [45, 57].

In many cases, the network topology in elastomers results from more or less random crosslinking and/or chain scissions. Nevertheless, better control of this topology is possible [58]. Thus, toughness has been improved with elastomers made of telechelic chains with bimodal length distribution. This improvement comes from a stress redistribution due to the lower extensibility of short chains. The requirements to achieve exceptional toughness seem to be that the components have very different cross-link densities and the morphology is uniform down to the segmental level. With this idea, Buckley et al. [59] produced ethylene-propylene double networks with improved rupture properties (at constant modulus). The beneficial effect of multiple networks has also been evidenced in hydrogels [10] and in acrylate elastomers [60].

3.2 Specificity of Polymers Which Can Crystallize with Strain

The ability of the polymer for strain induced crystallization (SIC) appears to be another important parameter for crack growth resistance. All elastomers that crystallize with temperature can – under certain strain rate and temperature conditions (near their melting temperature) – crystallize under deformation [61]. Among them, poly-cis isoprene 1,4 (NR) has two advantages: a melting temperature (35°C) very close to ambient, and a reversible crystallinity which can reach several tens of %. NR crystallization kinetics [62] is slow, especially at ambient temperature. This explains, with the presence of crosslinking nodes that restrict chain diffusion, that in most cases, NR remains amorphous despite a melting temperature higher than the ambient. When the material is deformed, the chain's stretching reduces the system entropy and makes crystallization thermodynamically more favorable. Crystallites can therefore nucleate and grow, for stretch ratio usually above 4, until they reach a size limited by the presence of the crosslinking nodes. This size is small enough for the crystallites to be unstable and melt during unloading, even at room temperature. The NR SIC (and its various parameters) has been the subject of special attention in recent years [63–73] both from an experimental and theoretical points of view. SIC

leads to a significant strain hardening, explained by the creation of a network of percolating crystallites within the material (even if questions remain on this topic). It is preceded, at the very beginning of the crystallization phase, by a slight decrease in stress due to the alignment of the crystallized chains portions in the stretching direction (as this decreases the "effective" stretching of amorphous chains) [74], mostly visible at slow stretching rate.

As shown by the comparison of NR and Styrene Butadiene Rubber (SBR) data [32, 75–77], SIC is the reason for a very strong increase in strain and stress at break and a slower crack propagation velocity, in cyclic and non cycling test [78]. Unlike an amorphous polymer, in an NR Pure Shear specimen submitted to a static loading, after a short growth, the crack stops. In cyclic loading, in the Paris domain, the literature studies suggest an exponent close to 4, for an amorphous elastomer like SBR while it may be around 2 for NR. Note that these exponents can significantly vary, depending on the experimental conditions. In addition, the application of a non-relaxing loading ($G_{min} > 0$) leads to a more important slowing down of the crack propagation than with an amorphous elastomer [25]. Non-relaxing conditions also lead to crack deviations [79] (absent with unfilled amorphous elastomer). That makes less trivial the monitoring of the crack length, which may or may not include secondary cracks. All these behaviors are related to SIC which occurs at the crack tip, even at low macroscopic strain, due to the important stress concentration created by the tip geometry. Several studies investigated crystallinity at the crack tip in NR [80, 81]. In particular, Rublon et al. [14, 77] have implemented a clever method in order to map it during a dynamic test at 0.1 Hz. Directly compared to crack propagation tests performed at 2 Hz for different energy release rates G, they showed a good correlation between G, the crystallized volume, and the thickness decrease at the crack tip, which also suggests that cavitation occurs.

We have studied a conventionally vulcanized NR (noted NR1.5 on Fig. 3, with the recipe: 100 phr NR + 3Phr Sulfur +6phrPPD + 2phr stearic acid +3 phr CBS + 5phr ZnO). This material has a lower ability to crystallize than an efficiently vulcanized rubber (CBS/Sulfur concentration ratio < 1), both during cold crystallization (at $-25°C$) and during a tensile test experiment, the crystallinity being lowered by a factor of ca. 3. This may be due to a different distribution of the active chain length, and/or the presence of more grafted species on the chains which hinder their crystallization. The fatigue crack growth resistance of the material has been tested in pure shear geometry [82]. As shown in Fig. 3, in the Paris domain, at low G, the slope of the log(G)-log(V_p) curve at 0.01 Hz and at few Hz (not shown) is surprisingly large, around 3.5, i.e. close to the slope reported for amorphous materials. A new slope can however be deduced for G values above 3,500 J/m^2, which tends to be closer to the value expected for NR (around 2). The crystallization at the crack tip, measured through in situ experiments (ZnS has been used as a probe to correctly estimate the material thickness at the crack tip) is reported on Fig. 4 as a function of G. The slope change in the log(G)-log(V_p) curve corresponds to the detection of the crystallinity. Interestingly, the maximal measured crystallinity is twice larger than the maximal one measured during tensile test at rupture. As reported in literature [83, 84] and as shown by the SAXS images collected during

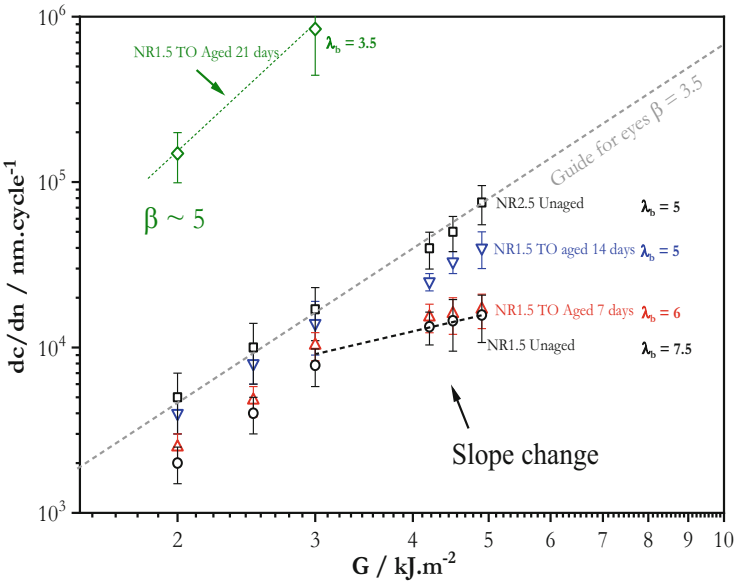

Fig. 3 Crack propagation rate as a function of the strain energy release rate G, in fatigue tests, on pure shear sample at 0.01 Hz, for aged and unaged unfilled NR. Tensile stretch at break λ_b measured in tensile test at 4.2×10^{-3} s^{-1} is also reported. Data from references [82, 84]

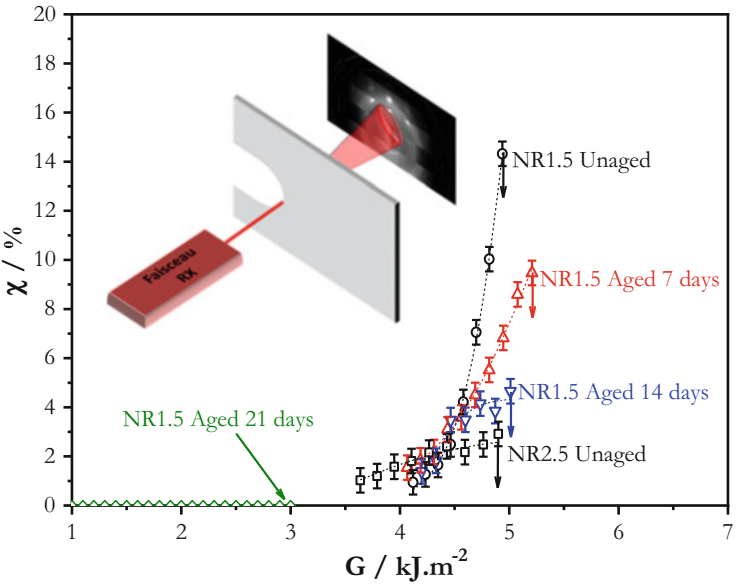

Fig. 4 Crystal volume fraction measure by SAXS in situ at the crack tip as a function of the strain energy released rate for aged and unaged NR. Measurements were performed on pure shear specimen at 1.7×10^{-3} s^{-1}. Experimental details in references [82, 84]

the WAXS measurements [84], cavities develop in the crack tip vicinity. Thus, some amorphous chains are broken and highly stretched fibrils with large crystallinity remain. A careful examination of the crack tip morphology and of the fracture surface may be of interest to confirm this. For unknown reasons, to the best of our knowledge, such studies only exist for fatigued *filled* NR or for unfilled one in non-relaxing condition [79, 85]. Even though fillers likely introduce some differences in crack propagation mechanisms, Xiang et al. conclusion can still be considered. In particular, they resume an interesting parallel, initially proposed by Zhou et al. [86], between the mechanisms induced by SIC and those occurring with double networks. At the front of the crack tip, *s*oft domains which might contain cavities, micro-cracks, and amorphous or less crystallized rubber parts alternate with hard domains of highly orientated and more crystallized ligaments. The soft domains may act like a damper to absorb energy and thus slow down the crack propagation.

The close relationship between SIC and crack propagation resistance has also been confirmed with aged NR1.5 samples whose characteristics have been deeply studied by Grasland [87]: ageing in air at 350 K enhances the heterogeneity of the spatial distribution of the crosslinks already existing in the initial material, and creates highly crosslinked domains which limit the ability for strain induced crystallization. The consequence is an increase in the crack propagation rate (Fig. 3) which is consistent with a decrease in the crystallinity measured at the crack tip (Fig. 4). Moreover, the results suggest that a minimum crystallized volume is needed to observe an inflexion on the log(G)-log(V_p) curve. This is confirmed by the study of another conventionally vulcanized elastomer, so-called NR2.5 (same recipe as NR1.5 except a doubled sulfur content). This material is more crosslinked, and therefore less crystallized than NR1.5 (Fig. 4). Its crystallization at the crack tip is too low, in the G domain explored, to lead to any slope change in the log(G)-log(V_p) curve. Moreover, for all these tested materials, the crack propagation resistance at 0.01 Hz is correlated to the energy and stretch at break, obtained from tensile test at strain rate corresponding to the maximum strain rate in the fatigue test (values reported on Fig. 3). This is quite expected if one considers that ageing did not change the intrinsic flaw at the origin of the material rupture in tensile test, and therefore that its evolution is mostly related to a change in its crack growth resistance [88].

SIC being a kinetic process [89], in "non cycling" experiments, the crack growth velocity in the domain where it is very large (above 0.1 m/s) does not depend on it [30], as SIC does not have the time to proceed. Moreover, concerning fatigue crack growth, we have found with the previous NR1.5 material that an increase in frequency by around 3 decades leads to a decrease in dc/dn by a factor 10 (Fig. 5). However, expressed in dc/dt instead of dc/dn, these data indicate a much faster crack growth which can be ascribed to a less important SIC. This is also suggested by the increase in the G value at which a change in the slope of the log(G)-log(V_p) curve is observed (this one being ascribed to a strong increase in crystallinity at the crack tip). In addition, with the NR2.5 material, one observes the decrease in the G value above which there is a fast acceleration of the crack growth rate. In other words, a higher frequency leads to a decrease in the tearing energy of this material, for which strain

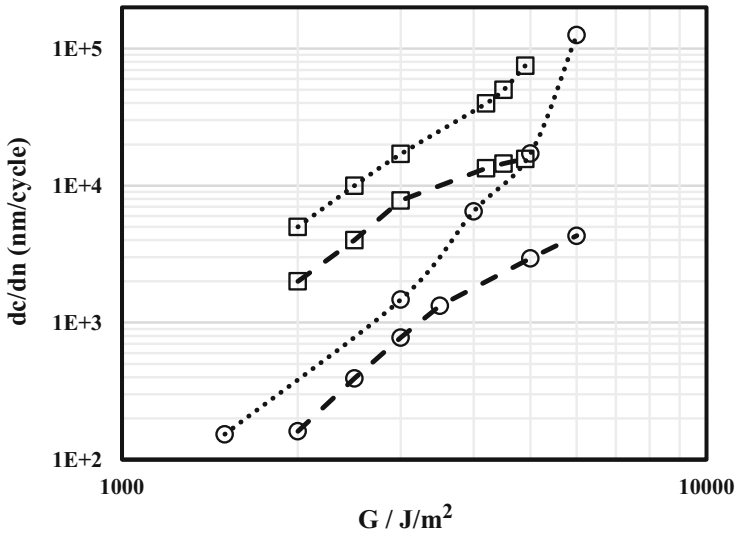

Fig. 5 Influence of the cycle frequency on the crack propagation rate as a function of the strain energy release rate for two unfilled NR (same material as in Fig. 4), unaged NR1.5 (○) and unaged NR2.5 (γ), at rate 0.01 Hz (dotted line) and around 5 Hz (---). Data from Ref. [90]

induced crystallization is so weak that it actually behaves like an amorphous material.

Going back to literature, an increase in temperature has the same consequences on SIC than an increase in frequency. Thus, both can lead to an even greater increase in the crack growth rate than in the case of amorphous elastomers, as they do more than reducing the material viscosity. However, this is dependent on the level of local deformation in the crack vicinity (i.e. on G) and, in fatigue, on the local strain rate that will result from the frequency/shape of the macroscopic cycle.

3.3 Fillers Influence

In most applications, elastomers contain reinforcing fillers. They can be of very diverse natures, the most commonly used in the rubber industry being carbon black or silica nanoparticles. Thus, elastomers are most often nano-composites, with specific viscoelastic properties [90, 91]. An abundant literature has been devoted to their nonlinear viscoelastic properties, so-called Payne effect [92]. In addition, they exhibit the so-called Mullins effect, i.e. a progressive modification of the strain-stress curve and an hysteresis during the first loading cycle which increases with the increase in the maximum strain [93]. Both Payne and Mullins effects are very dependent on the filler content and characteristics (size, aspect ratio, physico-chemical interactions with the polymer). They considerably influence the

rupture and crack resistance properties of these materials since they induce additional energy dissipation mechanisms.

Thus, the introduction of rigid nanoparticles is particularly efficient for increasing the tensile strength. Less intuitively, even though they lead to a significant amplification of local deformation in the matrix, nanofillers can also improve the elongation at break (when their content is not too large, i.e. usually below 50 phr). This is all the more remarkable given that nanofillers can form agglomerates of large sizes acting as crack initiators. Their beneficial effect for crack growth resistance is also observed on various elastomers whether these ones can or cannot crystallize under deformation [3]. The fillers, by amplifying the local strain, enable SIC and therefore a larger crystallized volume at lower macroscopic strain [94]. Nanofillers may also induce larger crystallized volume at a given G, beneficial to fatigue properties [80] (although G indirectly takes into account strain amplification). A combination of SIC and of reinforcement by nanometric fillers can also lead to tear rotation in tearing test on notched tensile specimen or trouser test-piece [95], not observed without fillers. This enables the relaxation of the local strain (or stress) which is otherwise larger at the crack tip, as shown by a sharper crack tip geometry. Thus, for Medalia [96], tear strength improvement in reinforced elastomer is even mostly associated to tear deviation rather than to energy dissipation (i.e., viscous strengthening or high strain hysteresis). In fatigue tests, more complex crack paths are also observed with fillers, which can lead, in non-relaxing conditions and with crystallizing rubber, to a complete stop of the crack propagation in the direction of the initial cut. Fillers form in the matrix a percolating network (whose connections are potentially ensured by a polymer matrix with modified mobility) which can play the role of a second network. Through decohesion mechanisms and voids formation [94, 97, 98] in the confined material in between the fillers, this network is gradually destroyed. This leads to the creation of a complex fibrillated structure [99] in which the crosslinked network of the polymer matrix is the last defense against the crack advance [100].

Several filler characteristics (shape, dispersion, polymer/filler interactions) influence the crack growth resistance in a way which depends a lot on the material processing. Bad dispersion may induce stress concentrations and micro-cracks [101], harmful to rupture properties and crack resistance. The literature indicates a positive influence of larger filler specific surface (i.e., smaller filler size) [78, 102–104] and of higher form factors (like in carbon nanotubes, graphene, graphene oxide, or nanoclays) on the resistance to crack initiation and propagation [105, 106]. Combination of nanofillers can also be used to obtain synergistic effect [107], like in the work of Xu et al. [101], who designed a compact hybrid filler network of graphene and MultiWall NanoTubes to toughen NR.

To conclude this paragraph, different mechanisms govern the fracture properties and the propagation of cracks in filled elastomers, and modeling approaches will therefore be essential to allow the evaluation of their respective contributions [5]. The next paragraph aims at devising a theoretical framework explaining crack growth and underlining the connection between resistance to crack growth and the

ability of a material to dissipate energy. Such theoretical approach can then suggest which bulk material properties should be correlated to crack growth resistance.

4 Theories Connecting Resistance to Crack Growth with Hysteresis

The models that will be reviewed in this paragraph are all built (sometimes implicitly) on the energy budget associated with a propagating crack, and were all devised for static crack growth. To the best of our knowledge, their generalization to cyclic crack growth, which seems possible due to the universality of the energy conservation principle, has not been attempted yet. The theories dedicated to isotropic linear viscoelastic materials are associated with the names of Knauss [38, 108, 109], Christensen [110, 111], De Gennes [112, 113], Hui [114], Persson [115, 116] and their coworkers. More recently, they have been extended outside this range of materials by Long [117], Qi [118], and Zhang [119]. All these theories start from the decomposition $G = \Gamma_{intrinsic} + \Gamma_{dissipation}$ with $\Gamma_{intrinsic}$ the intrinsic energy required to break molecules at the crack tip (noted G_0 in most of the experimental works, $\Gamma_{intrinsic}$ being tacitly assumed constant) and $\Gamma_{dissipation}$ the portion of G being consumed by the motion of the material surrounding the crack tip as the latter moves ahead ($\Gamma_{dissipation}$ is a peculiarity of dissipative materials). These theories aim (sometimes implicitly, as in Knauss and Hui theories) at explaining quantitatively how $\Gamma_{dissipation}$ can be deduced from the material hysteresis and the loading applied to the specimens.

4.1 Power Budget Approach

The key idea is the recognition that as a crack propagates, the stress singularity accompanying the crack tip [120] translates accordingly, so that any material point in the specimen is successively loaded and unloaded, and the hysteresis associated to this cycle participates to $\Gamma_{dissipation}$. The Fig. 6, taken from Qi [118] (see also Long [117]) draws explicitly the hysteresis associated with each horizontal "flow line": the closer this line gets to the crack plane, the greater the maximal loading, and therefore the greater the hysteresis. Indeed, by writing in detail the energy and entropy budgets of the notched specimen [118], one gets explicitly (Einstein convention of implicit summation over repeated indices being employed)

$$G = \Gamma_{intrinsic} + 2\int_0^{H_0}\int_{-\infty}^{+\infty} \varphi_p \, dXdY$$

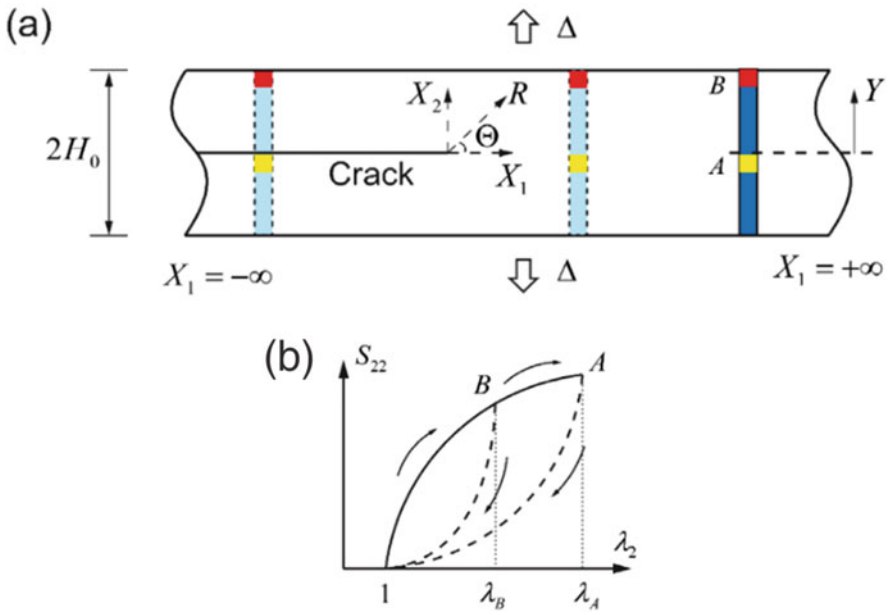

Fig. 6 (**a**) Two points A and B moving horizontally during steady state crack propagation, shown in the undeformed configuration and in a translating coordinate system centered on the crack tip. (**b**) Loading histories experienced by points A and B, illustrated by S_{22} versus λ_2 curves. The maximum stress experienced by A is larger due to stress concentration at the crack tip

$$\text{where } \varphi_p \equiv \sigma_{ij}\frac{\partial \varepsilon_{ij}}{\partial X_p} - \frac{\partial W}{\partial X_p} = \frac{\partial W}{\partial X} - \sigma_{ij}\frac{\partial \varepsilon_{ij}}{\partial X} \tag{1}$$

Here $2H_0$ is the specimen height (typically a PS specimen), X_p is the crack tip abscissa (so that $V_p = dX_p/dt$), φ_p is the dissipation associated to the crack tip motion divided by V_p, and finally $\partial/\partial X_p = -\partial/\partial X$ since we focus on the stationary regime.

Equation (1) can be further simplified by noting that the integral of φ_p over X is the total amount of energy by unit volume dissipated into heat during the matter motion from right to left, that is the mechanical hysteresis associated with this loading–unloading cycle, simply noted "hysteresis." Thus

$$G = \Gamma_{\text{intrinsic}} + 2\int_0^{H_0} \text{hysteresis}(Y)dY \tag{2}$$

It is worth underlining the *connection between this approach and the so-called configurational mechanics* [121]. Introducing the Eshelby stress tensor $\Sigma_{ij} = W\,\delta_{ij} - \sigma_{kj}\,\partial u_k/\partial X_i$, then making use of the mechanical equilibrium $\partial \sigma_{kj}/\partial X_j = 0$ and of the stress tensor symmetry, one gets

$$\frac{\partial \Sigma_{1j}}{\partial X_j} = \frac{\partial W}{\partial X_1} - \underbrace{\frac{\partial \sigma_{kj}}{\partial X_j}}_{=0} \frac{\partial u_k}{\partial X_1} - \sigma_{kj} \frac{\partial^2 u_k}{\partial X_j \partial X_1} = \frac{\partial W}{\partial X_1} - \sigma_{kj} \frac{\partial}{\partial X_1} \frac{1}{2} \left(\frac{\partial u_k}{\partial X_j} + \frac{\partial u_j}{\partial X_k} \right)$$

$$\text{that is, } \frac{\partial \Sigma_{1j}}{\partial X_j} = \frac{\partial W}{\partial X} - \sigma_{kj} \frac{\partial \varepsilon_{kj}}{\partial X} = \varphi_p \tag{3}$$

In the literature, the contributions to $\partial \Sigma_{1j}/\partial X_j$ of the various internal variables appearing in W are called "local material volume forces," up to a sign. Hence, it is demonstrated that $\Gamma_{\text{dissipation}}$ equals the integral on the whole specimen of these material forces (see also in [5] Horst et al. contribution [122]). That is, the material forces approach is equivalent to the energy and entropy budgets employed here.

4.2 Application to Isotropic Linear Viscoelastic Materials

Christensen, De Gennes, Persson and their collaborators applied these budgets to *isotropic linear viscoelastic materials*. In the sequel we will follow mostly De Gennes intuitive approach.

The material isotropy and linearity imply that the stress field satisfies the same equations as in the elastic case. Especially, the dominant term in the stress next to the crack tip is given by the well-known formulae (the so-called K-fields). Hence, if K is the stress-intensity factor, the amplitude of loading–unloading cycle at vertical coordinate Y (perpendicularly to crack axis) goes like $K / \sqrt{|Y|}$ and its wave length goes like |Y|, so its *pulsation ω goes like* $V_p/|Y|$.

Far from the crack tip, the material remains at equilibrium, i.e. it behaves like an elastic material of Young modulus E_0. So LEFM theorems apply there. Especially, computing the Rice- or $\mathcal{J}$-integral [120] *away* from the crack tip gives $G = \mathcal{J} \propto K^2/E_0$ (this integral must not be confused with compliance J introduced below).

Next, assume the cycle to be harmonic. If $E^*(\omega) = E'(\omega) + i\, E''(\omega)$ is the complex Young modulus and $J^*(\omega) = 1/E^*(\omega)$ is the complex compliance, the hysteresis at vertical coordinate Y reads

$$\text{hysteresis}(Y) \propto \frac{K^2}{|Y|} |J''(\omega)| = \frac{GE_0}{|Y|} |J''(\omega)| = \frac{GE_0}{|Y|} \frac{E''(\omega)}{|E^*(\omega)|^2} \text{ with } \omega \propto \frac{V_p}{|Y|} \tag{4}$$

Inserting this relation into Eq. (2), and noticing that $dY/Y = d\omega/\omega$, one finally gets

$$G = \Gamma_{\text{intrinsic}} + A \cdot GE_0 \int_0^{\omega_c} \frac{E''(\omega)}{|E^*(\omega)|^2} \frac{d\omega}{\omega} \text{ with } \omega_c = B \cdot \frac{\sigma_{\text{rupture}}^2 V_p}{GE_0} \tag{5}$$

A and B being some undetermined numerical constants. The boundaries of the ω-integral require some explanations. Far from the crack tip, we assumed the material to remain at equilibrium, prompting us to take $\omega_{min} = 0$. Close to the integral, the LEFM fields cannot hold when reaching the zone ahead of the crack tip where the material effectively breaks, the so-called cohesive zone, that is when $|Y| = Y_{rupture}$ such that ${\sigma_{rupture}}^2 \propto K^2/Y_{rupture}$, and we must therefore take $\omega_{max} \propto V_p/Y_{rupture}$. Persson set the A coefficient by combining the *expected value of the catastrophic tearing energy* Γ_c (G limit for infinite V_p, neglecting inertial effects, also noted G_c in experimental work) guessed by De Gennes with a "viscoelastic sum rule": some examples of such rules are provided by Eqs. (8) and (10) below.

On the one hand, when V_p grows without limit, the material close to the crack tip should reach its high frequency limit, which is the glassy plateau for the polymers. Thus, it should behave there as an elastic (brittle) material of Young modulus E_∞. Hence computing the $\mathcal{J}$-integral *close* to the crack tip gives now $\Gamma_{intrinsic} = \mathcal{J} \propto K^2/E_\infty$, with the *same* K since the dominant term in the stress field has a unique expression. Combining this relation for K with the preceding one, applicable in full generality, one gets

$$G \to \Gamma_c = \Gamma_{intrinsic} \frac{E_\infty}{E_0} \text{ when } V_p \to +\infty \tag{6}$$

The constant A appearing in (5) must be chosen so that (5) reduces to (6) for "infinite" crack growth rate.

On the other hand, if the material can be represented by a set of Kelvin solids (a spring in parallel to a damper) in *series*, the complex compliance reads

$$J^*(\omega) = \frac{1}{E_\infty} + \int_0^{+\infty} \frac{k(\tau)}{1 + i\omega\tau} d\tau = \frac{1}{E_\infty} + \int_0^{+\infty} \frac{(1 - i\omega\tau)}{1 + (\omega\tau)^2} k(\tau) d\tau \tag{7}$$

$k(\tau)\, d\tau$ is the equilibrium stiffness of the Kelvin solid of time constant τ.

Some elementary manipulations of this decomposition provide

$$\frac{1}{E_0} = J^*(\omega = 0) = \frac{1}{E_\infty} + \int_0^{+\infty} k(\tau) d\tau \text{ and thus}$$

$$\int_0^{+\infty} |J''(\omega)| \frac{d\omega}{\omega} = \frac{\pi}{2} \int_0^{+\infty} k(\tau) d\tau = \frac{\pi}{2} \left(\frac{1}{E_0} - \frac{1}{E_\infty} \right) \tag{8}$$

This latter equation is the sum rule we needed. Indeed, making $\omega_c = +\infty$ in (5) and reporting the sum rule into it, (6) will be recovered provided we choose $A = 2/\pi$. Hence the final formula

$$G = \Gamma_{\text{intrinsic}} + \frac{2}{\pi} G E_0 \int_0^{\omega_c} \frac{E''(\omega)}{|E^*(\omega)|^2} \frac{d\omega}{\omega} \text{ with } \omega_c = B \frac{\sigma_{\text{rupture}}^2 V_p}{G E_0} \tag{9}$$

ω_c can be rewritten $\omega_c = 2B\, W_{\text{rupture}}\, V_p/G$ by introducing an "equilibrium" energy of rupture $W_{\text{rupture}} \equiv \frac{1}{2}\, \sigma_{\text{rupture}}{}^2/E_0$ (the "equilibrium" adjective underlines the presence of E_0 in this expression). However, keep in mind that this W_{rupture} can, like σ_{rupture}, vary with the local temperature and strain rates at the crack tip.

The more sophisticated computations in Persson [115, 116] produced an extra $\sqrt{1 - \frac{\omega^2}{\omega_c^2}}$ factor inside the integral, with little impact on the final theoretical predictions.

4.3 Paris Law

As noted by De Gennes for a specific rheological model (a so-called Zener solid) [112, 113], and later by Persson in greater generality [115, 116], *this theory predicts the occurrence of a Paris law*, in agreement with experiments. (Strictly speaking, the Paris law originates from cyclic crack growth experiments; here, we use this terminology as a shorthand for "V_p proportional to some power of G"; as seen in the preceding chapters, such law can also be encountered experimentally in static crack growth.) This is best seen by making use of an approximate sum rule:

$$J'(\omega_2) - J'(\omega_1) = \int_0^{+\infty} \left(\frac{1}{1 + (\omega_2 \tau)^2} - \frac{1}{1 + (\omega_1 \tau)^2} \right) k(\tau) d\tau \approx \int_{1/\omega_1}^{1/\omega_2} k(\tau) d\tau$$

$$\frac{2}{\pi} \int_{\omega_1}^{\omega_2} |J''(\omega)| \frac{d\omega}{\omega} = \frac{2}{\pi} \int_0^{+\infty} \left[\tan^{-1}(\omega_2 \tau) - \tan^{-1}(\omega_1 \tau) \right] k(\tau) d\tau \approx \int_{1/\omega_2}^{1/\omega_1} k(\tau) d\tau$$

$$\Rightarrow \frac{2}{\pi} \int_{\omega_1}^{\omega_2} |J''(\omega)| \frac{d\omega}{\omega} \approx J'(\omega_1) - J'(\omega_2) \approx \frac{1}{E'(\omega_1)} - \frac{1}{E'(\omega_2)} \tag{10}$$

The first line was obtained by assuming $1/(1 + x^2) \approx H(1 - x)$ for $x \geq 0$ where H is the Heaviside step function. The second line used a similar trick, namely $(2/\pi) \tan^{-1}(x) \approx H(x - 1)$ for $x \geq 0$. The last approximation on the third line is more questionable. Reporting (10) into (9), one finally gets

$$\frac{G}{\Gamma_{intrinsic}} \approx \frac{E'(\omega_c)}{E_0} \text{ and thus}$$

$$E'(\omega) \approx E_1 \left(\frac{\omega}{\omega_1}\right)^{\alpha} \Rightarrow V_p \approx \frac{\omega_1 G}{2BW_{rupture}} \left(\frac{E_0}{E_1}\frac{G}{\Gamma_{intrinsic}}\right)^{1/\alpha} \quad (11)$$

Hence *the Paris exponent β equals* $\beta = 1 + 1/\alpha$. For $\alpha = 0.5$ (typical of Rouse dynamics), $\beta = 3$; and for $\alpha = 0.4$, $\beta = 3.5$: as noted by Persson, these values are typical of SBR in both static and cyclic crack growth. Note also that this approximation on the first line of Eq. (11) yields the same Γ_c expression as the equation from which it is derived. *Gent* [123, 124] *proposed on purely phenomenological grounds an equation similar to* (11) *to fit the results of his peeling experiments*: we thus provide here a justification of his intuition. However, Gent used $\omega_c = V_p/d$ with d some material *constant*, which should be contrasted with our d proportional to G. Actually, (11) brings theory closer to experiments as will be shown below!

4.4 Dissipation Confinement and Finite Size Effects

The theories developed by Knauss [38, 108, 109] and Hui [114] do not use *explicitly* the energy and entropy budgets. Rather, they carefully write the mechanical equilibrium of the cohesive zone, using exact results in LEFM (Kolosov-Mushkelishvili formulae and Westergaard functions applied to localized forces along crack lips). In this respect, they provide a more rigorous treatment of the problem. Yet, they yield essentially the same results: same shape for $V_p(G)$ curves, same expression for γ_c (apart for one of the four theories studied in Knauss [108, 109]), etc. This is presumably so because energy and entropy conservation remains necessarily in the background.

For instance, Hui and his coworkers demonstrate graphically [114] that *the dissipation is confined to the corona* $0.05\ V_p\ \tau_r < \text{radius} < 3.5\ V_p\ \tau_r$ where τ_r is the retardation time occurring in the creep compliance (the authors employ a Zener model) and the radius is counted from the crack tip: this region has a negligible area at low V_p and grows in size with V_p, until becoming eventually macroscopic. This explains qualitatively the trend of our $\Gamma_{dissipation}$ (recall that the r dr dθ surface element compensates the decrease of energy like 1/r). This discussion makes also clear that *the size of the specimen will impact the crack growth curves when* $V_p\ \tau_r$ *becomes comparable to it*. Indeed, so far we have ignored finite size effects, the discussion focusing on "infinite specimens." But finite size effects can be encountered experimentally, in which case the experimental results are not characteristics of the material alone. They are treated in De Gennes [112, 113], who was chiefly interested in peeling tests [1]. We will review quickly this treatment, using however a slightly more general constitutive law (see, e.g., [125] pp. 188–226):

Table 1 Main steps in the computation of the crack curve equation for a linear viscoelastic material satisfying Eq. (12)

Approximation	Soft solid	Liquid	Hard solid
Constitutive law	$\sigma = E_0\,\varepsilon$	$\sigma = (E_\infty - E_0)\,(\omega\tau)^\alpha\,\varepsilon$	$\sigma = E_\infty\,\varepsilon$
Pulsation interval	$\omega\tau < m^{-1/\alpha}$	$m^{-1/\alpha} < \omega\tau < 1$	$1 < \omega\tau$
Spatial domain	$r_s \equiv m^{1/\alpha}\,V_p\,\tau < r$	$V_p\,\tau < r < m^{1/\alpha}\,V_p\,\tau$	$r < V_p\,\tau \equiv r_h$
Stress	$\sigma = \frac{K}{\sqrt{r}}$	$\sigma = \frac{K}{\sqrt{r}}$	$\sigma = \frac{K}{\sqrt{r}}$
Displacement	$u = \frac{K\sqrt{r}}{E_0}$	$u = \frac{K\sqrt{r}}{E_\infty}\left(\frac{r}{V_p\tau}\right)^\alpha$	$u = \frac{K\sqrt{r}}{E_\infty}$
G_{local}	$G_{local} = \frac{K^2}{E_0}$	$G_{local} = \frac{K^2}{E_\infty}\left(\frac{r}{V_p\tau}\right)^\alpha$	$G_{local} = \frac{K^2}{E_\infty}$
L defining condition	$\frac{\sigma_p}{\delta} = \frac{E_0}{L}$	$\frac{\sigma_p}{\delta} = \frac{E_\infty}{L}\left(\frac{V_p\tau}{L}\right)^\alpha$	$\frac{\sigma_p}{\delta} = \frac{E_\infty}{L}$
Cohesive length	$L = \frac{E_0\delta}{\sigma_p} \equiv L_0$	$L = L_\infty{}^{\frac{1}{\alpha+1}}\left(V_p\tau\right)^{\frac{\alpha}{\alpha+1}}$	$L = \frac{E_\infty\delta}{\sigma_p} = mL_0 \equiv L_\infty$
V_p range	$V_p\,\tau < m^{-1/\alpha}\,L_0$	$m^{-1/\alpha}\,L_0 < V_p\,\tau < m\,L_0$	$m\,L_0 < V_p\,\tau$

$$E^*(\omega) = E_0 + (E_\infty - E_0)\frac{(i\omega\tau)^\alpha}{1 + (i\omega\tau)^\alpha} \tag{12}$$

In the original articles, $\alpha = 1$, but we expect $\alpha < 1$ for a glass transition. This model has three remarkable limits: soft solid at low frequencies, hard solid at high frequencies, liquid-like behavior in between. From now on, $m \equiv E_\infty/E_0 >> 1$ and we reason exclusively in *scaling* terms, so that "=" will often stand for "$\propto$". The computation of the $G(V_p)$ relation is based on the following principles.

Step 1. We have $\omega = \frac{V_p}{r}, \sigma = \frac{K}{\sqrt{r}}$ and $\varepsilon = \frac{u}{r}$ everywhere in the specimen. Thus, for each asymptotic constitutive law, we can compute its spatial domain of existence, as well as the expressions of ε, u, and $G_{local} \equiv \sigma\,u$ (the "local energy release rate") in the domain. Proceeding this way, we fill the first six lines of Table 1.

Step 2. Let L be the length of the cohesive zone. It is set by the condition $\sigma_p/\delta = \sigma(r = L)/u(r = L)$ where σ_p and δ are material constants such that $\Gamma_{intrinsic} = \sigma_p\,\delta$. Its detailed expression will therefore depend on the domain (defined as in step 1) surrounding the cohesive zone. Doing so, we obtain the next two lines of the table.

Step 3. The three expressions of L obtained in step 2 are a priori different, implying that L varies with the load applied to the specimen. One deduces from these expressions the range of crack growth rate for which each domain is immediately surrounding the cohesive zone. This leads to the last line of the table.

Step 4. Let W be the specimen size, typically a PS specimen height. The $G(V_p)$ relation is found by taking $\Gamma_{intrinsic} = G_{local}(r = L)$ and $G = G_{local}(r = W)$. Various situations can be encountered depending on how W compares with the spatial limits L, r_h (*h*ard solid *outer* radius) and r_s (*s*oft solid *inner* radius).

For an *infinite* specimen, $G = \frac{K^2}{E_0}$ and thus $\frac{G}{\Gamma_{intrinsic}} = \frac{K^2}{E_0 G_{local}(r=L)}$ in any case, since the zone near the clamps will always remain in the soft solid domain. One readily finds

$$\frac{G}{\Gamma_{intrinsic}} = \left\{ \begin{array}{c} 1 \\ m\left(\frac{V_p\tau}{L_\infty}\right)^{\frac{\alpha}{\alpha+1}} = m\left(\frac{V_p\tau}{L_\infty}\right)^{\frac{1}{\beta}} \\ m \end{array} \right\} \text{ if } \left\{ \begin{array}{c} V_p\tau < m^{-1/\alpha}L_0 \\ m^{-1/\alpha}L_0 < V_p\tau < mL_0 \\ mL_0 < V_p\tau \end{array} \right\} \quad (13)$$

Remarkably, *we end up with the same result as with our former treatment*, including the occurrence of a Paris regime characterized by the same exponent β and the same expression for Γ_c.

For a *finite* specimen however, the preceding results will stop holding once r_s reaches W. The exact consequences depend on the W value.

Assuming first $m^\beta L_0 < W$, $r_s = W$ happens only after the cohesive zone is surrounded by hard solid, so that the $G = \Gamma_c$ plateau is still observable experimentally. Once the liquid domain has reached the clamps, $\Gamma_{intrinsic} = \frac{K^2}{E_\infty}$ and $\frac{G}{\Gamma_{intrinsic}} = \frac{E_\infty G_{local}(r=W)}{K^2}$, and (13) must be supplemented by

$$\frac{G}{\Gamma_{intrinsic}} = \left\{ \begin{array}{c} \left(\frac{W}{V_p\tau}\right)^\alpha \\ 1 \end{array} \right\} \text{ if } \left\{ \begin{array}{c} m^{-1/\alpha}W < V_p\tau < W \\ W < V_p\tau \end{array} \right\} \quad (14)$$

The corresponding $G(V_p)$ curve therefore exhibits a decreasing portion after having reached the plateau of height $m\,\Gamma_{intrinsic}$. It is qualitatively consistent with results of peeling tests carried on poorly crosslinked polymers, to which this study aimed at.

This was the only situation envisaged in the original papers. Yet, it can be unrealistic in practice, since for $L_0 = 10$ nm it requires $W > 10$ mm to 10 m (!) with $m = 10^2$ to 10^3 and $\beta = 3$.

Assuming next $L_0 < W < m^\beta L_0$, $r_s = W$ now happens before the cohesive zone is surrounded by hard solid, so *the previous plateau is not observable anymore, and the material exhibits a different "effective"* Γ_c *depending on the specimen dimensions*. More precisely, the second line in (13) holds only until $V_p\,\tau = m^{-1/\alpha}\,W$ ($< m\,L_0$), where the "effective" Γ_c is attained:

$$\frac{\Gamma_c}{\Gamma_{intrinsic}} = \left(\frac{W}{L_0}\right)^{\frac{\alpha}{\alpha+1}} = \left(\frac{W}{L_0}\right)^{\frac{1}{\beta}} \quad (15)$$

For example, with $L_0 = 10$ nm, $W = 10$ mm, and $\beta = 3$ for instance, $\Gamma_c/\Gamma_{intrinsic}$ would be limited to 100. Besides, the third line in (13) must be modified.

If $m\,L_0 < W < m^\beta\,L_0$, it is replaced by

$$\frac{G}{\Gamma_{intrinsic}} = \left\{ \begin{array}{c} \left(\frac{W}{L}\right)^{\alpha} = \left(\frac{W}{L_{\infty}}\right)^{\alpha} \left(\frac{L_{\infty}}{V_p \tau}\right)^{\frac{\alpha^2}{\alpha+1}} \\ \left(\frac{W}{V_p \tau}\right)^{\alpha} \\ 1 \end{array} \right\} \text{if} \left\{ \begin{array}{c} m^{-1/\alpha} W < V_p \tau < mL_0 \\ mL_0 < V_p \tau < W \\ W < V_p \tau \end{array} \right\} \quad (16)$$

whereas if $L_0 < W < m\,L_0$, it is replaced by

$$\frac{G}{\Gamma_{intrinsic}} = \left\{ \begin{array}{c} \left(\frac{W}{L}\right)^{\alpha} = \left(\frac{W}{L_{\infty}}\right)^{\alpha} \left(\frac{L_{\infty}}{V_p \tau}\right)^{\frac{\alpha^2}{\alpha+1}} \\ 1 \end{array} \right\} \text{if} \left\{ \begin{array}{c} m^{-1/\alpha} W < V_p \tau < \left(\frac{W}{L_{\infty}}\right)^{1/\alpha} W \\ \left(\frac{W}{L_{\infty}}\right)^{1/\alpha} W < V_p \tau \end{array} \right\} \quad (17)$$

4.5 *Introducing Non-linearity in the Constitutive Equation*

Focusing exclusively on linear viscoelasticity is far too restrictive for filled polymers, which exhibit various nonlinearities at high strains as well as a supplementary source of hysteresis: Mullins effect. In the framework presented here, *the better resistance to static crack growth of a filled polymer in comparison to its unfilled homolog is attributed – at least partially – to an increase of* $\Gamma_{dissipation}$ *brought by Mullins effect*. Interestingly, as previously mentioned, the so-called multi-networks (various standard polymer networks *interpenetrated* into each other) also enjoy a high toughness and a mechanical behavior reminiscent of Mullins effect [60]. The microscopic origin of Mullins effect may be different in these two classes of materials (cavitation/decohesion in filled polymers vs. localized chains ruptures in multi-networks), but a beneficial impact of Mullins hysteresis onto $\Gamma_{dissipation}$ is expected in both cases.

Once again, this line of reasoning prompted different works [118, 119, 126]. Zhang [119] starts with the decomposition $G = \Gamma_{intrinsic} + \Gamma_{dissipation}$. $\Gamma_{dissipation}$ is assumed proportional to the "ultimate" hysteresis $H(Y_{rupture})$, where like in Eq. (5), $Y_{rupture}$ denotes the minimum height at which the material reaches there its stress at break, with a front factor homogeneous to a length. A length scale manifestly relevant to this problem is $G/W_{rupture}$. Therefore the authors were led to guess $\Gamma_{dissipation} = \alpha\, G\, h_{rupture}$ where $h_{rupture} \equiv \frac{H(Y_{rupture})}{W_{rupture}} (< 1)$. α was found by fitting the results of a campaign of Finite Element Analyses during which the material parameters describing the Mullins effect (modeled with an Ogden-Roxburgh law) and the cohesive zone were systematically varied. They obtained eventually

$$G = \frac{\Gamma_{intrinsic}}{1 - \alpha\, h_{rupture}} \text{ with } \alpha \approx 0.33 + \frac{0.034}{m/W_{rupture} + 0.045} \tag{18}$$

r, m, and β (set to 0.1 in the article) are material parameters quantifying the Mullins hysteresis: if the energy density provided during the first loading equals W, the Mullins hysteresis reads "h(W) W" where

$$h(W) = \frac{1}{r} f\left[\left(\beta + \frac{m}{W}\right)^{-1}\right] \text{ with } f(x) \equiv \frac{1}{x}\int_0^x \text{erf}(y)dy \tag{19}$$

Especially, the smaller m, the greater the hysteresis of small amplitude cycles, and thus the greater the hysteresis far from the crack tip. This remark will soon be useful.

Qi [118] *gave an analytic derivation of this result based on* Eq. (2). The maximum energy density along a line parallel to a mode I crack in a Neo-Hookean material reads $W(Y) = \frac{G}{2\pi Y}$ according to asymptotic developments. Using a slightly modified version of this expression to take far fields and Mullins softening into account, the authors reported it into (19), and (19) into (2). Proceeding this way, they obtained an α expression comparing well with (18).

Besides, *if m → 0, we noted above that the dissipation zone can extend to the clamps, so the measured G can depend on the specimen geometry*, ceasing to be an intrinsic material property. Some FEA confirmed this intuition, FEA that were themselves well reproduced by the analytic theory. $\frac{G}{\Gamma_{intrinsic}}$ appears to depend on a dimensionless parameter $\chi = \frac{2H_0}{\Gamma_{intrinsic}/W_{rupture}}$ which is the ratio of the PS specimen height to the cohesive zone length.

4.6 Experimental Tests of the Preceding Theories

Viscoelastic behavior: Knauss and his coworkers applied successfully various theories to a polyurethane. The model developed in Mueller and Knauss [38] matched well the experimental points. It relied on an analysis of the viscoelastic relaxation in the cohesive zone and its prediction read (Δa being a material constant, set to 13.4 nm by the fitting procedure):

$$G(V_p) = \frac{\Gamma_{intrinsic}}{2E_0 D(\Delta a/V_p)} \text{ where } D(t) \equiv \frac{1}{t}\int_0^t \left(1 - \frac{u}{t}\right) J(u)du \tag{20}$$

Contrary to the appearances, this result is actually quite similar to (9). Indeed, using a Kramers-Kronig relation, one can recast the denominator of (20):

$$J(t) = \frac{1}{E_0} + \frac{2}{\pi}\int_0^{+\infty} J''(\omega)\cos(\omega t)\frac{d\omega}{\omega} \Rightarrow D(t) \approx \frac{1}{2E_0} - \frac{1}{\pi}\int_0^{1/t} |J''(\omega)|\frac{d\omega}{\omega} \quad (21)$$

(We used the approximation $(1 - \cos(x))/x^2 \approx ½\, H(1 - x)$.) The only distinct feature is the constancy of Δa. So this success suggests also a success of (9).

Later [108, 109], they developed a refined version of this early model, which proved to be equally successful. In both cases, the model predicts a correct Paris exponent β. In fact, these data are consistent with the rule $\beta = 1 + 1/\alpha$: experiments suggest $\alpha \approx 0.8$ (read on master curves of dynamic moduli) and $\beta \approx 2.4$ (read on curves of V_p vs. ε_∞, ε_∞ being the macroscopic strain applied to the PS specimen, so that $G \propto {\varepsilon_\infty}^2$), in reasonable agreement with the theoretical prediction $\beta \approx 2.25$. With this material, $m \approx 1725$ MPa/2.75 MPa ≈ 627, and the predicted Γ_c ($= m\,\Gamma_0$) seems in agreement with experiment, though the final plateau is not sufficiently well observed to be categorical. Assuming $L_0 = 10$ nm for the cohesive length at low V_p, the De Gennes criterion to avoid finite size effects reads $W > 627^{2.25} \times 10\,\text{nm} = 2$ cm: it was indeed satisfied in Knauss experiments, where $W = 3.5$ cm. Incidentally, Christensen [111] also managed to fit this set of experimental results using a theory of his own, explicitly relying on an energy budget.

Saulnier [127] carried out adhesion experiments on an un-crosslinked polydimethylsiloxane (PDMS) of large molecular weight. They confirmed De Gennes predictions (with $\alpha = 1$) regarding the decrease of fracture energy at high crack growth rates – Eq. (14) – as well as the opening displacement of the crack lips: $u \propto x^{1/2}$ near the crack tip where the material behaves as a hard solid, $u \propto x^{3/2}$ farther from the crack tip where the material becomes liquid-like.

Gent [123, 124] carried out peeling tests on various crosslinked polymers of variable T_g. He found that the $G/\Gamma_{intrinsic}$ vs. V_p master curves were relatively independent of the polymer, like the $E'(\omega)/E_0$ vs. ω master curves (though to a smaller extent), and speculated, from the resemblance between these, that $\frac{G}{\Gamma_{intrinsic}} = \frac{E'(V_p/d)}{E_0}$ with d some material constant. Unfortunately the exponents of the power laws fitting the glass transition regime did not match: $\beta^{-1} = 0.3$ for the peeling energy, $\alpha = 0.6$ for the storage modulus. Trying anyway to fit the model onto experiment, he found $d \approx 0.1$ nm, or more largely $0.01\ \text{nm} < d < 1$ nm, some unrealistically low values. Besides, $\Gamma_c/\Gamma_{intrinsic}$ appears slightly greater than E_∞/E_0. But the theories explored in the preceding paragraphs point rather to $d \propto G$, implying $\frac{1}{\beta} = \frac{\alpha}{\alpha+1}$, i.e. $\beta^{-1} = 0.375$ in the present case, which is closer to experiment. One can hope that this improvement will also bring the d range towards more sensible values. In fact, this improvement could be combined with other features not addressed by the models we reviewed but envisaged by Gent: nonlinear effects near the crack tip, intermittent propagation "in a stick-slip fashion". This last feature implies that the *instantaneous* V_p can be much higher than the *average* V_p, which is the one measured: one should keep this idea in mind when considering cyclic crack growth.

Extension to cyclic crack growth and to Mullins effect dissipation: Klüppel surveyed the ability of the models we reviewed to reproduce the *cyclic* crack growth

curves measured on filled and unfilled polymer [128]. The author used crosslinked S-SBR and Ethylene Propylene Diene Monomer (1.7 phr S + 2.5 phr CBS) filled or not with 60 phr of N550 carbon black. He focused his attention on Paris law slopes, and found that the theory matched reasonably with experiment. This is particularly striking because the theory in question has been devised exclusively for static crack growth, and besides it ignores the nonlinearities and the Mullins effect typical of filled polymers. This remark suggests to check if the Paris law intercepts with the Y-axis are equally well reproduced by the theory, namely Eq. (11) with B = 1. It is an uncertain task since some key quantities ($\Gamma_{intrinsic}$ and $W_{rupture}$) are missing in the article: we must guess them and see what we get. Using notably $\Gamma_{intrinsic} \approx 50$ (resp. 100) $J.m^{-2}$ in the unfilled (resp. filled) case, we find at $G \approx 3$ $kJ.m^{-2}$, 4 Hz and ambient temperature: in unfilled S-SBR, $V_p \approx 40$ $m.s^{-1}$ theoretically vs. $V_p \approx 10$ $nm.cycle^{-1} = 40$ $nm.s^{-1}$ experimentally; in filled S-SBR, $V_p \approx 4$ $m.s^{-1}$ theoretically vs. $V_p \approx 4$ $nm.cycle^{-1} = 40$ $nm.s^{-1}$ experimentally. These estimates must be taken with caution owing to the mentioned uncertainties. Nevertheless, the discrepancy between our estimates and the measurements is such that we can consider that the theory fails to reproduce the intercept with the Y-axis of the Paris law.

Zhang [119] checked that it could reproduce by FEA the onset of crack propagation in a multi-network hydrogel considered to exhibit Mullins effect only. Constitutive law parameters were identified on cycles of increasing maximum strain applied in pure shear. The propagation threshold G was measured after various pre-strains – applied to the uncracked specimen – between 0 and the strain at break (as high as 8 here). It appears to decrease with pre-strain, reaching a plateau (400 $J.m^{-2}$) for the highest pre-strains, to be identified with the virgin $\Gamma_{intrinsic}$ (though one could argue that high pre-strains could damage enough the material to diminish its $\Gamma_{intrinsic}$). FEA results appeared to be consistent with the $G = 1{,}063$ $J.m^{-2}$ value measured with the *virgin* material. Incidentally, this experiment proves that the intrinsic resistance to crack growth represents here only 38% of G in the *virgin* state, the remaining 62% being brought by macroscopic dissipation.

Qi [118] put the pre-strain effect in equations. The line of reasoning is as follows: the horizontal strips whose strain remains below the pre-strain cannot dissipate by Mullins effect (strips close to the clamps), the dissipation being thus confined to a central strip, where it is moreover smaller than in the virgin state. These statements explain qualitatively why $\Gamma_{dissipation}$ must decrease with pre-strain: the pre-strain diminishes the capacity of the material to dissipate when a crack propagates. The agreement with experiment is even quantitative, as shown in the article.

Wunde et al. [129, 130] carried out experiments on cured CB-filled NR-based polymer blends allowing an estimation of $\Gamma_{dissipation}/G$. For the 4 mixes of the study and various macroscopic strain, they measured by Digital Image Correlation the displacement and strain fields in notched and loaded PS specimens, that they combined with the constitutive laws – modeling Mullins effect and viscoelasticity – identified independently to compute the Rice- or $\mathcal{J}$-integral on various circles C centered on the crack tip. (They considered both components of $\int_C \Sigma_{ij}\, ds_j$, but we

focus here on the sole forward component). $\mathcal{J}$ appears to increase with the circle radius R, consistently with $\mathcal{J}(R = 0) = \Gamma_{intrinsic}$ and $G = \mathcal{J}(R = +\infty)$ by construction of J and with the inequality $\Gamma_{intrinsic} < G$ for a dissipative material. Actually, the difference between these limits is $\Gamma_{dissipation}$. The analysis is complicated by a lack of resolution for $R < 0.5$ mm and by the fact that $\mathcal{J}(R = +\infty)$ becomes greater than G (computed by the Rivlin-Thomas formula) above 40% macroscopic strain. Despite these difficulties, the authors estimate that all in all, $\Gamma_{dissipation}$ represents 90% of G. These experiments also demonstrate that $\mathcal{J}$ reaches G for $R > 1$ to 5 mm (for macroscopic strains between 10 and 60%): these are macroscopic dimensions, which legitimate the qualification of $\Gamma_{dissipation}$ as a macroscopic dissipation. Especially, these dimensions demonstrate clearly that crack growth can be accompanied by energy dissipation quite far from the crack tip, where no macroscopic breakage occurs.

Slootman [44] introduced in mono- and multi-networks of polymers a known amount of a mechanophore having the property of becoming fluorescent upon breakage. The materials being transparent, they could be measured by optical confocal microscopy the spatial distribution of this fluorescence, and therefore (via an appropriate calibration) the spatial distribution of the number of broken mechanophores, and finally of overall broken bonds. These distributions were measured along the lips of a crack propagated for various loadings and temperatures. $\Gamma_{intrinsic}$ is deduced by integrating the distribution (for a unit propagated surface) and multiplying the integral by 64 $kJ.mol^{-1}$, the energetic cost of a single breakage according to Wang [131]. Most remarkably, the author demonstrated that: $\Gamma_{intrinsic}$ increases with the loading, that is with G or V_p, going from the Lake and Thomas estimate for $V_p \rightarrow 0$ up to 100 times this value at high V_p; and that the number of covalent bond scissions varies in the same proportion, with rupture occurring up to a few 100 µm far from the crack plane for the highest V_p. Especially, *$\Gamma_{intrinsic}$ cannot be treated as a material constant, as was done in the works reviewed so far, but as a function of V_p*. Notice however that Eq. (2) and the ones stemming from it can easily accommodate a V_p dependent $\Gamma_{intrinsic}$. It seems very likely that this phenomenology also applies to filled polymers, whose filler network is analogous to the first network here and whose polymer matrix is analogous to the second and third networks here. Depending on the tested Single-, Double- or Triple- Network, she found that *$\Gamma_{intrinsic}/G$ varies between a few % and a few 10%, and therefore $\Gamma_{dissipation}/G$ varies between 50 and more than 90%*.

5 Conclusion

A synthesis of the phenomenology of ultimate and crack growth properties of elastomers is not straightforward given the diversity of elastomers and used protocols. Nevertheless, the huge literature on the topic, completed by some our own experimental works, allows to well identify the different interrelated and complex

mechanisms involved in crack growth. In connection with these observations, the theories reviewed in the last part link quantitatively the resistance to crack growth to:

- the ability of the material to dissipate energy, either by viscoelasticity or by Mullins effect;
- the distribution of strain and stress around the crack tip (dictated by the constitutive law), which weights the contribution of each horizontal line to the total dissipation accompanying the crack growth;
- the break properties (limit strain/stress/energy), which define an upper bound for the dissipation integrals.

These theories have been validated experimentally in various situations. They can be useful to material designers because they allow the replacement of lengthy or sophisticated crack growth experiments by faster and simpler mechanical characterization of unnotched specimen until break, and because they offer a mean to infer what "customary" material property (moduli, break properties) to tune and in which direction to achieve an enhanced resistance to crack growth. Especially, the theories involving dynamic moduli can suggest compromises between Rolling Resistance (RR) and endurance in tires via the difference of frequency ranges relevant to each performance. This situation is reminiscent of the known compromise between RR and grip. And in fact, the analogy goes deeper: the well-known viscoelastic contribution to the friction coefficient μ is equivalent to the viscoelastic contribution in $\Gamma_{dissipation}$ (see e.g. our Eq. (9)), the role of crack tip singularity in endurance is played by road asperities in grip, and the integral over all distances Y from the crack plan is replaced in the grip case by the integral over asperity sizes and tread band depth.

Though these theories are encouraging, they still suffer of various shortcomings. The most obvious from a practical standpoint is their inability so far to handle cyclic crack growth: they have been thought for static crack growth, and their generalizations to the cyclic case is not straightforward. They also often treat $\Gamma_{intrinsic}$ and $W_{rupture}$ as material constants, although they are susceptible to vary with strain rate and thus V_p. Finally, it is highly desirable to now quantitatively relate them to the different fields measurable at the crack tip and reviewed in chapters 2 and 3 (including cavitation and degree of Strain Induced Crystallization). These missing features are as many subjects for future researches.

References

1. Creton C, Ciccotti M (2016) Fracture and adhesion of soft materials: a review. Rep Prog Phys 79:046601
2. Gent AN, Mars WV (2013) Strength of elastomers. In: The science and technology of rubber. Elsevier, Amsterdam, pp 473–516
3. Mars WV, Fatemi A (2004) Factors that affect the fatigue life of rubber: a literature survey. Rubber Chem Technol 77:391–412

4. Tee YL, Loo MS, Andriyana A (2018) Recent advances on fatigue of rubber after the literature survey by Mars and Fatemi in 2002 and 2004. Int J Fatigue 110:115–129
5. Grellmann W, Heinrich G, Kaliske M, Klüppel M, Schneider K, Vilgis TA (2013) Fracture mechanics and statistical mechanics of reinforced elastomeric blends. Springer, Berlin
6. Lake GJ (1995) Fatigue and fracture of elastomers. Rubber Chem Technol 68:435–460
7. Nonoyama T, Wada S, Kiyama R, Kitamura N, Mredha MTI, Zhang X, Kurokawa T, Nakajima T, Takagi Y, Yasuda K, Gong JP (2016) Double-network hydrogels strongly bondable to bones by spontaneous osteogenesis penetration. Adv Mater 28:6740–6745
8. Kamat S, Su X, Ballarini R, Heuer AH (2000) Structural basis for the fracture toughness of the shell of the conch Strombus gigas. Nature 405:1036–1040
9. Sen D, Buehler MJ (2011) Structural hierarchies define toughness and defect-tolerance despite simple and mechanically inferior brittle building blocks. Sci Rep 1:35
10. Gong JP, Katsuyama Y, Kurokawa T, Osada Y (2003) Double-network hydrogels with extremely high mechanical strength. Adv Mater 15:1155–1158
11. Higuchi Y, Saito K, Sakai T, Gong JP, Kubo M (2018) Fracture process of double-network gels by coarse-grained molecular dynamics simulation. Macromolecules 51:3075–3087
12. Lavoie SR, Millereau P, Creton C, Long R, Tang T (2019) A continuum model for progressive damage in tough multinetwork elastomers. J Mech Phys Solids 125:523–549
13. Laiarinandrasana L, Morgeneyer TF, Proudhon H, N'guyen F, Maire E (2012) Effect of multiaxial stress state on morphology and spatial distribution of voids in deformed semicrystalline polymer assessed by X-ray tomography. Macromolecules 45:4658–4668
14. Rublon P, Huneau B, Verron E, Saintier N, Beurrot S, Leygue A, Mocuta C, Thiaudière D, Berghezan D (2014) Multiaxial deformation and strain-induced crystallization around a fatigue crack in natural rubber. Eng Fract Mech 123:59–69
15. Kallungal J, Chazeau L, Chenal J-M, Adrien J, Maire E, Barres C, Cantaloube B, Heuillet P (2019) Methodology for 3D characterization of microstructural defects in filled polymer using X-ray tomography. In: Huneau B, Le Cam J-B, Marco Y, Verron E (eds) Constitutive models for rubber XI, 1st edn. CRC Press, pp 77–81
16. Saintier N (2001) Fatigue multiaxiale dans un élastomère de type NR chargé: mécanismes d'endommagment et critère local d'amorçage de fissure. p 225
17. Saintier N, Cailletaud G, Piques R (2006) Crack initiation and propagation under multiaxial fatigue in a natural rubber. Int J Fatigue 28:61–72
18. Lake GJ, Lindley PB (1964) Cut growth and fatigue of rubbers. II. Experiments on a noncrystallizing rubber. J Appl Polym Sci 8:707–721
19. Lindley PB (1974) Non-relaxing crack growth and fatigue in a non-crystallizing rubber. Rubber Chem Technol 47:1253–1264
20. Rivlin RS, Thomas AG (1953) Rupture of rubber. I. Characteristic energy for tearing. J Polym Sci 10:291–318
21. Roucou D, Diani J, Brieu M, Witz J-F, Mbiakop-Ngassa A (2018) Experimental investigation of elastomer mode I fracture: an attempt to estimate the critical strain energy release rate using SENT tests. Int J Fract 209:163–170
22. Thomas AG (1994) The development of fracture mechanics for elastomers. Rubber Chem Technol 67:50–67
23. Yeoh OH (2003) Fracture mechanics of bond failure in the "pure shear" test piece. Rubber Chem Technol 76:483–494
24. Greensmith HW (1963) Rupture of rubber. X. The change in stored energy on making a small cut in a test piece held in simple extension. J Appl Polym Sci 7:993–1002
25. Lindley PB (1972) Energy for crack growth in model rubber components. J Strain Anal 7:132–140
26. Carbone G, Persson BNJ (2005) Crack motion in viscoelastic solids: the role of the flash temperature. Eur Phys J E 17:261–281
27. Smith TL (1958) Dependence of the ultimate properties of a GR-S rubber on strain rate and temperature. J Polym Sci 32:99–113

28. Bueche F, Halpin JC (1964) Molecular theory for the tensile strength of gum elastomers. J Appl Phys 35:36–41
29. Kok CM, Yee VH (1986) The effects of crosslink density and crosslink type on the tensile and tear strengths of NR, SBR and EPDM gum vulcanizates. Eur Polym J 22:341–345
30. Lake GJ, Lawrence CC, Thomas AG (2000) High-speed fracture of elastomers: part I. Rubber Chem Technol 73:801–817
31. Tsunoda K, Busfield JJC, Davies CKL, Thomas AG (2000) Effect of materials variables on the tear behaviour of a non-crystallising elastomer. J Mater Sci 35:5187–5198
32. Papadopoulos IC, Thomas AG, Busfield JJC (2008) Rate transitions in the fatigue crack growth of elastomers. J Appl Polym Sci 109:1900–1910
33. Fukahori Y, Sakulkaew K, Busfield JJC (2013) Elastic–viscous transition in tear fracture of rubbers. Polymer 54:1905–1915
34. Horst T, Heinrich G (2008) Crack propagation behavior in rubber materials. Polym Sci Ser A 50:583–590
35. Mullins L (1959) Rupture of rubber – Part IX: role of hysteresis in the tearing of rubber. Trans Proc Inst Rubber Ind 35:213–222
36. Lake GJ, Yeoh OH (1978) Measurement of rubber cutting resistance in the absence of friction. Int J Fract 14:509–526
37. Robertson CG, Stoček R, Kipscholl C, Mars WV (2019) Characterizing the intrinsic strength (Fatigue threshold) of natural rubber/butadiene rubber blends. Tire Sci Technol 47:292–307
38. Mueller HK, Knauss WG (1971) The fracture energy and some mechanical properties of a polyurethane elastomer. Trans Soc Rheol 15:217–233
39. Ahagon A, Gent AN (1975) Threshold fracture energies for elastomers. J Polym Sci Polym Phys Ed 13:1903–1911
40. Bhowmick AK, Gent AN, Pulford CTR (1983) Tear strength of elastomers under threshold conditions. Rubber Chem Technol 56:226–232
41. Gent AN, Tobias RH (1982) Threshold tear strength of some molecular networks. In: Mark JE, Lal J (eds) Elastomers and rubber elasticity. American Chemical Society, Washington, pp 367–376
42. Stoček R, Stěnička M, Zádrapa P (2020) Future trends in predicting the complex fracture behaviour of rubber materials. Contin Mech Thermodyn
43. Lake GJ, Thomas AG (1967) The strength of highly elastic materials. Proc R Soc Lond Ser Math Phys Sci 300:108–119
44. Slootman J (2019) Quantitative detection of damage in soft materials using mechano-fluorescence. In: l'Ecole Supérieure de Physique et de Chimie Industrielles de la ville de Paris (ESPCI Paris)
45. De Almeida A, Chazeau L, Vigier G, Marque G, Goutille Y (2017) Ultimate and toughness properties of γ-irradiated EPDM. Eur Polym J 97:178–187
46. Kadir A, Thomas AG (1981) Tear behavior of rubbers over a wide range of rates. Rubber Chem Technol 54:15–23
47. Lake GJ, Lindley PB (1965) The mechanical fatigue limit for rubber. J Appl Polym Sci 9:1233–1251
48. Paris P, Erdogan F (1963) A critical analysis of crack propagation laws. J Basic Eng 85:528–533
49. Long R, Hui C-Y (2015) Crack tip fields in soft elastic solids subjected to large quasi-static deformation — a review. Extreme Mech Lett 4:131–155
50. Horiuchi S, Dohi H (2006) Nanoimaging and spectroscopic analysis of rubber/ZnO interfaces by energy-filtering transmission electron microscopy. Langmuir 22:4607–4613
51. Tobolsky AV, Lyons PF (1968) Tensile strength of rubbers. J Polym Sci Part 2 Polym Phys 6:1561–1566
52. Colin X, Audouin L, Verdu J (2007) Kinetic modelling of the thermal oxidation of polyisoprene elastomers. Part 3: oxidation induced changes of elastic properties. Polym Degrad Stab 92:906–914

53. Howse S, Porter C, Mengistu T, Pazur RJ (2018) Experimental determination of the quantity and distribution of chemical crosslinks in unaged and aged natural rubber, part 1: peroxide vulcanization. Polym Test 70:263–274
54. Kaidou H, Ahagon A (1990) Aging of tire parts during service. II. Aging of belt-skim rubbers in passenger tires. Rubber Chem Technol 63:698–712
55. Langley NR, Polmanteer KE (1974) Relation of elastic modulus to crosslink and entanglement concentrations in rubber networks. J Polym Sci Polym Phys Ed 12:1023–1034
56. Saalwächter K (2012) Microstructure and molecular dynamics of elastomers as studied by advanced low-resolution nuclear magnetic resonance methods. Rubber Chem Technol 85:350–386
57. Legorjujago K (2002) Fatigue initiation and propagation in natural and synthetic rubbers. Int J Fatigue 24:85–92
58. Mark JE, Tang M-Y (1984) Dependence of the elastomeric properties of bimodal networks on the lengths and amounts of the short chains. J Polym Sci Polym Phys Ed 22:1849–1855
59. Buckley GS, Fragiadakis D, Roland CM (2011) Strength enhancement from heterogeneous networks of ethylene–propylene/ethylene–propylene–diene. Rubber Chem Technol 84:520–526
60. Ducrot E, Chen Y, Bulters M, Sijbesma RP, Creton C (2014) Toughening elastomers with sacrificial bonds and watching them break. Science 344:186–189
61. Le Gac P-Y, Albouy P-A, Petermann D (2018) Strain-induced crystallization in an unfilled polychloroprene rubber: kinetics and mechanical cycling. Polymer 142:209–217
62. Candau N, Chazeau L, Chenal J-M, Gauthier C, Munch E (2016) A comparison of the abilities of natural rubber (NR) and synthetic polyisoprene cis-1,4 rubber (IR) to crystallize under strain at high strain rates. Phys Chem Chem Phys 18:3472–3481
63. Behnke R, Berger T, Kaliske M (2018) Numerical modeling of time- and temperature-dependent strain-induced crystallization in rubber. Int J Solids Struct 141–142:15–34
64. Brüning K, Schneider K, Roth SV, Heinrich G (2012) Kinetics of strain-induced crystallization in natural rubber studied by WAXD: dynamic and impact tensile experiments. Macromolecules 45:7914–7919
65. Candau N, Laghmach R, Chazeau L, Chenal J-M, Gauthier C, Biben T, Munch E (2015) Temperature dependence of strain-induced crystallization in natural rubber: on the presence of different crystallite populations. Polymer 60:115–124
66. Candau N, Chazeau L, Chenal J-M, Gauthier C, Munch E (2016) Complex dependence on the elastically active chains density of the strain induced crystallization of vulcanized natural rubbers, from low to high strain rate. Polymer 97:158–166
67. Das A, Le HH, Vuorinen J, Heinrich G (2017) Comment on "monitoring network and interfacial healing processes by broadband dielectric spectroscopy: a case study on natural rubber". ACS Appl Mater Interfaces 9:14547–14551
68. Huneau B (2011) Strain-induced crystallization of natural rubber: a review of X-ray diffraction investigations. Rubber Chem Technol 84:425–452
69. Khiêm VN, Itskov M (2018) Analytical network-averaging of the tube model: strain-induced crystallization in natural rubber. J Mech Phys Solids 116:350–369
70. Laghmach R, Candau N, Chazeau L, Munch E, Biben T (2015) Phase field modelling of strain induced crystal growth in an elastic matrix. J Chem Phys 142:244905
71. Li X, Schneider K, Kretzschmar B, Stamm M (2008) Deformation behavior of PP and PP/ZnO nanocomposites as studied by SAXS and WAXS. Macromolecules 41:4371–4379
72. Roth SV, Rothkirch A, Autenrieth T, Gehrke R, Wroblewski T, Burghammer MC, Riekel C, Schulz L, Hengstler R, Müller-Buschbaum P (2010) Spatially resolved investigation of solution cast nanoparticle films by X-ray scattering and multidimensional data set classification. Langmuir 26:1496–1500
73. Sotta P, Albouy P-A (2020) Strain-induced crystallization in natural rubber: flory's theory revisited. Macromolecules 53:3097–3109

74. Flory PJ (1947) Thermodynamics of crystallization in high polymers. I. Crystallization induced by stretching. J Chem Phys 15:397–408
75. Gent AN, Hindi M (1990) Effect of oxygen on the tear strength of elastomers. Rubber Chem Technol 63:123–134
76. Kim SG, Lee S-H (1994) Effect of crosslink structures on the fatigue crack growth behavior of NR vulcanizates with various aging conditions. Rubber Chem Technol 67:649–661
77. Rublon P, Huneau B, Saintier N, Beurrot S, Leygue A, Verron E, Mocuta C, Thiaudière D, Berghezan D (2013) In situ synchrotron wide-angle X-ray diffraction investigation of fatigue cracks in natural rubber. J Synchrotron Radiat 20:105–109
78. Hamed GR, Park BH (1999) The mechanism of carbon black reinforcement of SBR and NR vulcanizates. Rubber Chem Technol 72:946–959
79. Xiang F, Schneider K, Heinrich G (2020) New observations regarding fatigue crack paths and their fracture surfaces in natural rubber: influences of R-ratio and pre-load. Int J Fatigue 135:105508
80. Lee DJ, Donovan JA (1987) Microstructural changes in the crack tip region of carbon-black-filled natural rubber. Rubber Chem Technol 60:910–923
81. Trabelsi S, Albouy P-A, Rault J (2002) Stress-induced crystallization around a crack tip in natural rubber. Macromolecules 35:10054–10061
82. Grasland F, Chenal J-M, Chazeau L, Caillard J, Schach R (2017) Role of SIC on the fatigue properties of NR after realistic aerobic ageing. In: Lion A, Johlitz M (eds) European conference on constitutive models for rubbers X. CRC Press, Munich
83. Le Cam J-B, Toussaint E (2010) The mechanism of fatigue crack growth in rubbers under severe loading: the effect of stress-induced crystallization. Macromolecules 43:4708–4714
84. Grasland F (2018) Vieillissement du caoutchouc naturel parthermo-oxydation: Etudes de ses conséquences sur lacristallisation sous déformation, la fissuration et larupture. PhD thesis, Université de Lyon
85. Beurrot S, Huneau B, Verron E (2010) In situ SEM study of fatigue crack growth mechanism in carbon black-filled natural rubber. J Appl Polym Sci
86. Zhou W, Li X, Lu J, Huang N, Chen L, Qi Z, Li L, Liang H (2015) Toughening mystery of natural rubber deciphered by double network incorporating hierarchical structures. Sci Rep 4:7502
87. Grasland F, Chazeau L, Chenal J-M, schach R (2019) About thermo-oxidative ageing at moderate temperature of conventionally vulcanized natural rubber. Polym Degrad Stab 161:74–84
88. Grasland F, Chazeau L, Chenal J-M, Caillard J, Schach R (2019) About the elongation at break of unfilled natural rubber elastomers. Polymer 169:195–206
89. Candau N, Laghmach R, Chazeau L, Chenal J-M, Gauthier C, Biben T, Munch E (2015) Influence of strain rate and temperature on the onset of strain induced crystallization in natural rubber. Eur Polym J 64:244–252
90. Chazeau L, Gauthier C, Chenal J-M (2010) Mechanical properties of rubber nanocomposites: how, why ... and then?
91. Stöckelhuber KW, Das A, Klüppel M, Basu D (2017) Designing of elastomer nanocomposites: from theory to applications. In: Designing of elastomer nanocomposites: from theory to applications1st edn. Springer, Cham
92. Chazeau L, Brown JD, Yanyo LC, Sternstein SS (2000) Modulus recovery kinetics and other insights into the Payne effect for filled elastomers. Polym Compos 21:202–222
93. Diani J, Fayolle B, Gilormini P (2009) A review on the Mullins effect. Eur Polym J 45:601–612
94. Chenal J-M, Gauthier C, Chazeau L, Guy L, Bomal Y (2007) Parameters governing strain induced crystallization in filled natural rubber. Polymer 48:6893–6901
95. Gabrielle B, Guy L, Albouy P-A, Vanel L, Long DR, Sotta P (2011) Effect of tear rotation on ultimate strength in reinforced natural rubber. Macromolecules 44:7006–7015

96. Medalia AI (1986) Effect of carbon black on ultimate proper.Pdf. Rubber Div Am Chem Soc 60:45–60
97. Ramier J, Chazeau L, Gauthier C, Stelandre L, Guy L, Peuvrel-Disdier E (2007) In situ SALS and volume variation measurements during deformation of treated silica filled SBR. J Mater Sci 42:8130–8138
98. Zhang H, Scholz AK, de Crevoisier J, Vion-Loisel F, Besnard G, Hexemer A, Brown HR, Kramer EJ, Creton C (2012) Nanocavitation in carbon black filled styrene–butadiene rubber under tension detected by real time small angle X-ray scattering. Macromolecules 45:1529–1543
99. Le Cam J-B, Huneau B, Verron E, Gornet L (2004) Mechanism of fatigue crack growth in carbon black filled natural rubber. Macromolecules 37:5011–5017
100. Millereau P, Ducrot E, Clough JM, Wiseman ME, Brown HR, Sijbesma RP, Creton C (2018) Mechanics of elastomeric molecular composites. Proc Natl Acad Sci 115:9110–9115
101. Xu Z, Jerrams S, Guo H, Zhou Y, Jiang L, Gao Y, Zhang L, Liu L, Wen S (2020) Influence of graphene oxide and carbon nanotubes on the fatigue properties of silica/styrene-butadiene rubber composites under uniaxial and multiaxial cyclic loading. Int J Fatigue 131:105388
102. Dizon ES, Hicks AE, Chirico VE (1974) The effect of carbon black parameters on the fatigue life of filled rubber compounds. Rubber Chem Technol 47:231–249
103. Nie Y, Wang B, Huang G, Qu L, Zhang P, Weng G, Wu J (2010) Relationship between the material properties and fatigue crack-growth characteristics of natural rubber filled with different carbon blacks. J Appl Polym Sci
104. Agnelli S, Ramorino G, Passera S, Karger-Kocsis J, Ricco T (2012) Fracture resistance of rubbers with MWCNT, organoclay, silica and carbon black fillers as assessed by the J-integral: effects of rubber type and filler concentration. Express Polym Lett 6:581–587
105. Dong B, Liu C, Lu Y, Wu Y (2015) Synergistic effects of carbon nanotubes and carbon black on the fracture and fatigue resistance of natural rubber composites. J Appl Polym Sci 132
106. Zhou X, Wang L, Cao X, Yin Q, Weng G (2019) Crack resistance improvement of rubber blend by a filler network of graphene. J Appl Polym Sci 136:47278
107. Rooj S, Das A, Morozov IA, Stöckelhuber KW, Stocek R, Heinrich G (2013) Influence of "expanded clay" on the microstructure and fatigue crack growth behavior of carbon black filled NR composites. Compos Sci Technol 76:61–68
108. Knauss WG (1973) On the steady propagation of a crack in a viscoelastic sheet: experiments and analysis. In: Kausch HH, Hassell JA, Jaffee RI (eds) Deformation and fracture of high polymers. Springer, Boston, pp 501–541
109. Knauss WG (2015) A review of fracture in viscoelastic materials. Int J Fract 196:99–146
110. Christensen RM (2003) Theory of viscoelasticity.2nd edn. Dover Publications, Mineola
111. Christensen RM, Wu EM (1981) A theory of crack growth in viscoelastic materials. Eng Fract Mech 14:215–225
112. De Gennes PG (1996) Soft adhesives. Langmuir 12:4497–4500
113. De Gennes PG (1988) Fracture d'un adhésif faiblement réticulé. Comptes Rendus Académie Sci Sér 2 Mécanique Phys Chim Sci Univers Sci Terre 307:1949–1953
114. Hui C, Xu D, Kramer EJ (1992) A fracture model for a weak interface in a viscoelastic material (small scale yielding analysis). J Appl Phys 72:3294–3304
115. Persson BNJ, Albohr O, Heinrich G, Ueba H (2005) Crack propagation in rubber-like materials. J Phys Condens Matter 17:R1071–R1142
116. Persson BNJ, Brener EA (2005) Crack propagation in viscoelastic solids. Phys Rev E 71:036123
117. Long R, Hui C-Y (2016) Fracture toughness of hydrogels: measurement and interpretation. Soft Matter 12:8069–8086
118. Qi Y, Caillard J, Long R (2018) Fracture toughness of soft materials with rate-independent hysteresis. J Mech Phys Solids 118:341–364
119. Zhang T, Lin S, Yuk H, Zhao X (2015) Predicting fracture energies and crack-tip fields of soft tough materials. Extreme Mech Lett 4:1–8

120. Anderson TL (2005) Fracture mechanics: fundamentals and applications, 3rd edn. CRC Press
121. Maugin GA (1993) Material inhomogeneities in elasticity.1st edn. Chapman & Hall, London
122. Horst T, Heinrich G, Schneider M, Schulze A, Rennert M (2013) Linking mesoscopic and macroscopic aspects of crack propagation in elastomers. In: Grellmann W, Heinrich G, Kaliske M, Klüppel M, Schneider K, Vilgis T (eds) Fracture mechanics and statistical mechanics of reinforced elastomeric blends. Springer, Berlin, pp 129–165
123. Gent AN (1996) Adhesion and strength of viscoelastic solids. Is there a relationship between adhesion and bulk properties? Langmuir 12:4492–4496
124. Gent AN, Lai S-M (1994) Interfacial bonding, energy dissipation, and adhesion. J Polym Sci Part B Polym Phys 32:1543–1555
125. Haupt P (2002) Continuum mechanics and theory of materials. Springer, Berlin
126. Roucou D (2020) Caractérisation et modélisation du comportement à la déchirure de matériaux élastomères endommagés par chargement multiaxiaux. Ecole Centrale de Lille
127. Saulnier F, Ondarçuhu T, Aradian A, Raphaël E (2004) Adhesion between a viscoelastic material and a solid surface. Macromolecules 37:1067–1075
128. Klüppel M (2009) Evaluation of viscoelastic master curves of filled elastomers and applications to fracture mechanics. J Phys Condens Matter 21:035104
129. Wunde M, Plagge J, Klüppel M (2019) The role of stress softening in crack propagation of filler reinforced elastomers as evaluated by the J-integral. Eng Fract Mech 214:520–533
130. Klüppel M, Wunde M (2020) Phase morphology and frature mechanics of rubber blend. In: Heinrich G, Stocek R (eds) Fatigue crack growth in rubber materials; experiments and modelling. Springer, Berlin
131. Wang S, Panyukov S, Rubinstein M, Craig SL (2019) Quantitative adjustment to the molecular energy parameter in the Lake–Thomas theory of polymer fracture energy. Macromolecules 52:2772–2777

Adv Polym Sci (2021) 286: 331–346
https://doi.org/10.1007/12_2020_77

Published online: 19 December 2020

Influence of Plasticizers Basing on Renewable Sources on the Deformation and Fracture Behaviour of Elastomers

M. M. Rahman, K. Oßwald, B. Langer, and K. Reincke

Contents

Abstract This contribution is focused on the quasi-static and impact fracture behaviour of technical, filler-reinforced elastomer compounds containing plasticizers basing on renewable sources in various amounts. Beside the conventional plasticizer TDAE as benchmark, various plasticizer products like epoxidized rapeseed oil, rapeseed oil methyl or propyl ester, epoxidized canola oil or epoxidized ester of glycerol formal from canola oil were used. Main aims are to find products as replacement of traditional mineral oil-based plasticizers and to understand the

M. M. Rahman
Faculty of Engineering and Natural Sciences, University of Applied Sciences, Merseburg, Germany

K. Oßwald and K. Reincke (✉)
Polymer Service GmbH Merseburg, Merseburg, Germany
e-mail: katrin.reincke@psm-merseburg.de

B. Langer
Faculty of Engineering and Natural Sciences, University of Applied Sciences, Merseburg, Germany

Polymer Service GmbH Merseburg, Merseburg, Germany

interaction of polymer and plasticizer and the resulting properties, especially the deformation and fracture behaviour. It was shown that by using renewable plasticizers a comparable or better property level of technical rubber vulcanizates is possible.

Keywords Blends · Elastomers · Impact fracture · Plasticizers · R curve · Renewable

1 Introduction

Many technical elastomer products contain softening components as processing aids like stearic acid and/or plasticizers. Depending on the type and amount of such softening components, various properties of the material are more or less influenced. This means, to get finally tailor-made product properties, it is necessary to know these influencing factors. By the addition of softening components, not only hardness, but all of the mechanical and fracture mechanical properties of an elastomer material can be strongly influenced. This is a generally known and accepted fact. However, especially concerning the fracture properties of elastomers, there is a certain lack of knowledge about the impact of plasticizers.

A plasticizer is a low-molecular substance that is incorporated into a rubber mixture to improve its processability via decreasing the viscosity and reduction of the inner friction during mixing, as well as to tailor deformability and hardness of the vulcanized elastomer [1, 2]. In terms of quantitative proportion, a plasticizer is one of the most important components for the production of elastomer compounds after polymers and the fillers. A plasticizer improves in particular the low-temperature performance and elasticity of vulcanized elastomers. In addition, there are several requirements for plasticizers. They should be non-toxic, have a good compatibility with the rubber polymers, not lead to discoloration of the material, preferably have no interaction with the cross-linking chemicals (e.g. sulphur/accelerator or peroxide) and must be non-volatile during vulcanization. Frequently used plasticizers include mineral oils, synthetic esters, bio-based oils, and modified bio-based oils [3]. Mineral oil is a water-insoluble liquid of higher alkanes. According to the composition, three different types of mineral oil can be used as plasticizer: paraffinic oil, naphthenic oil, and aromatic oil. The plant-based oils are considered as sustainable and natural oils, for example, triglyceride ester of higher fatty acids [4–6]. There are some excellent results for versatile elastomers obtained with natural or modified oils, especially with epoxidized soybean oil [3], linseed oil [7], castor oil [1] or rice bran oil [8]. The most common synthetic plasticizers are phthalates, esters, alkyl sulfonic ester of phenol, and polymeric plasticizers [9]. However, the investigation of fracture mechanics behaviour on plasticized polymer has rarely been investigated by the researchers. In 1978, Brown and Stevens [10] had worked on lightly plasticized polyvinyl chloride (PVC) and performed impact-like and quasi-static tests to determine fracture toughness K_c. Di-isooctyl phthalate (DOIP) plasticizer in various amounts up to 15 wt.%

was homogenously mixed with PVC. It was found that the fracture toughness K_c under impact loading was continuously deceased with increasing amount of plasticizer, while K_c from a quasi-static fracture mechanics test showed an increasing trend with a maximum at 10 wt.% DOIP. Further, the degree of slow (interpreted as stable) crack growth was found to be dependent on the plasticizer amount. Bakar et al. [11] investigated plasticized unsaturated polystyrene resin. Various amounts of di-octyl phthalate (DOP) and tricresyl phosphate (TCP) plasticizer were used for investigation. It was found that the impact resistance as well as K_c depend on the type of plasticizer, but no reason for this was investigated. In 2014, Xie et al. [12] investigated among others the impact strength of PVC/wood compounds with plasticizers, also from renewable sources. Cardanol acetate (CA) and epoxy fatty acid methyl ester (EFAME) had been used and parallel DOP as a reference. A higher impact strength for the PVC/EFAME system was found. In [13], filler-reinforced and plasticized EPDM vulcanizates were investigated by using quasi-static and an impact-like fracture mechanics tests regarding their fracture behaviour. The plasticizers were mineral oil-based products with a varying amount of the aromatic bound carbon C/A. With increasing C/A, the resistance against initiation and propagation of a slow, stable crack changed and also the resistance against unstable crack propagation was influenced. However, no relation to the underlying chemical and physical interactions and processes was made, as it often appears in published research works on plasticized polymers. This, and the nearly completely lacking literature about fracture behaviour of elastomers with plasticizers on the basis of renewable source was motivation of this work.

Generally, low-molecular components of a rubber mixture like processing aids and plasticizers are able to migrate in the volume or out of it. An externally driven mechanical deformation of the material may influence this inner migration process. During the fracture process, this means the growth of a crack, the maximal strain and so the maximum stress concentration is around the crack tip. Thus, it is assumed that low-molecular substances like the plasticizer influence especially this region. For this reason, the type and concentration of plasticizers around the crack tip is expected to have a significant influence on the final fracture behaviour. Further, the varied loading conditions should have a crucial role influencing the fracture behaviour compared to the type and amount of plasticizers. Thus, the aim of this work is to investigate these factors. Aim of this contribution is to show the influence of different renewable plasticizers on fracture behaviour. This is focussed in a first step to the quasi-static and impact-like loading. The related experimental methods are understood as a fast and informative supplement of expensive and time-consuming cyclic fracture mechanics investigations were fatigue crack growth curves da/dn vs. tearing energy T are obtained to characterize the fatigue crack growth (FCG) [14]. Results of an earlier study [15] showed similar trends of the fracture mechanics parameters from quasi-static, impact-like, and FCG tests for carbon-black filled elastomers. Further, in [16], the threshold value of a fatigue crack growth curve T_0 was shown to be functionally related to the newly introduced intrinsic cutting energy. Latter is determined by using a specially developed equipment – the intrinsic strength tester – during a cutting test with a comparably

low speed. This means, a correlation of certain fracture mechanics parameters describing stable crack growth resistance can be expected, independent of the test conditions quasi-static or cyclic. Therefore, in addition to the understanding of the material-composition related crack processes themself and their influencing factors in plasticized elastomers, the application of the quasi-static and impact-like fracture mechanics tests could be helpful in material optimization studies in the sense of fast screening methods.

2 Determination of the Fracture Mechanics Parameters

Quasi-static fracture mechanics tests can be performed with the aim of recording crack resistance curves (R-curves) as the basis for the quantitative characterization of the materials' resistance against the initiation and propagation of a stable crack. In contrast to an unstable crack, a stable crack is growing under energy consumption and is characterized by a comparably low speed. When the external mechanical loading is stopped and no further deformation energy is transferred to the volume, a stable crack shows no further growth, as it is also the case for fatigue cracks in the linear range of a fatigue crack growth curve (Paris–Erdogan plot).

For the experimental determination of the resistance against stable crack initiation and propagation under quasi-static loading, two test procedures are possible: a single-specimen method and the multiple-specimen technique. These techniques were described in detail in [15, 17–21]. Result of these tests are crack resistance curves (R-curves). A schematic crack resistance curve from a single-specimen test is shown in Fig. 1.

The main fracture mechanics parameters as output from this test are indicated: crack initiation value J_i as the first data point of the R-curve and the crack propagation value T_J^* as the slope of the R-curve at a defined crack-opening value. The point

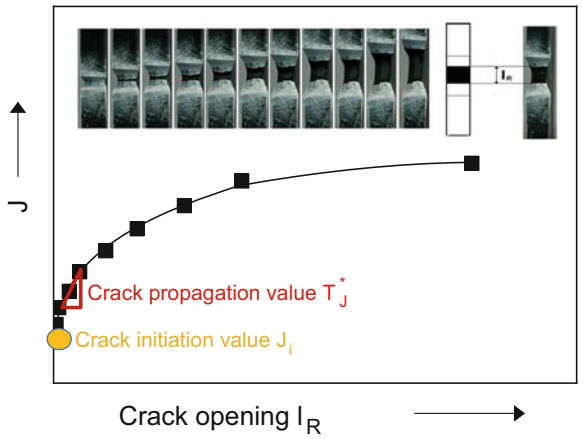

Fig. 1 Schematic representation of an R-curve from the quasi-static fracture mechanics test and an increasingly loaded specimen during a fracture mechanics test [17]

of crack initiation is determined by the observation of the notch tip by an optical system or by eye. It is defined as the point where a new crack surface is visible over the whole thickness of the specimen. In the upper part of Fig. 1, a sequence of photographs of the deformed specimen (view into the open notch) is shown. The left picture shows the state before crack initiation, the further pictures the increasing crack opening after crack initiation. Additionally, the definition of the crack-opening value l_R is shown.

The advantage of the single-specimen method is the comparatively low time- and material consumption. For the R-curve tests with application of the single-specimen method, single edge notched tension (SENT) specimens with length $L = 100$ mm, width $W = 25$ mm, and thickness $B = 6$ mm and a ratio between initial crack length a to width W of at least 0.2 should be preferred to get an appropriate stress state around the crack tip [20]. Earlier investigations [20] showed further that specimens with a minimum thickness of 6 mm should be used for such tests to exclude or at least to reduce a plane-stress state within the specimens. Also the initial gauge length l_0 and the initial notch depth a_0 influence the test results [20]. The smaller l_0 and the larger a_0 the lower the elastic deformation energy that is consumed by the specimen. As a consequence, the stress concentration at the crack tip is more pronounced and leads to an accelerated stable fracture process.

For such quasi-static fracture mechanics tests, generally, a universal testing machine is used, where the SENT specimens are loaded with a monotonically increasing load in tension leading to crack-opening mode I. The optimal test speed is between 10 mm/min and 50 mm/min. Own experiments showed that if the test speed is higher, the process of stable crack growth can be so fast/short that only a few single data pairs of J and the crack-opening value l_R can be obtained without a high-speed camera. J values are to be calculated according to [22]:

$$J = \frac{\eta U}{B\,(W - a)} \tag{1}$$

with η – geometry function, U – deformation energy up to individually defined times/deformations, B – specimen thickness, W – specimen width, and a – initial crack length (= notch depth).

At least, 6–10 single J–l_R values are necessary to display the crack resistance curve.

The notches are produced by a combination of cutting (during specimen preparation) and manual sharpening by using a thin metal blade (thickness 0.13 mm) to ensure a possibly small notch radius. For latter, the specimen is clamped and slowly loaded until a low stress and a certain opening of the pre-notch is reached. Then at the tip of the pre-notch, the metal blade notch is introduced manually. After this, the notch tip is prepared with TiO_2 powder to get a good contrast between notch (grey) new crack surface (black) and so enable the observation of the crack initiation and growth (see Fig. 1). After completion of the preparation, the test is then started at the set test speed. After the crack initiation, the distance between the edges of the original notch tip becomes larger with increasing deformation of the specimen as

the picture sequence in Fig. 1 is illustrating. This distance between the original notch edged was defined as crack opening l_R [23]. The size of it increases mainly due to elastic deformation of the material around the crack tip. From the results of multiple-specimen tests [24], it could be shown that the actual crack propagation Δa is much smaller than the crack opening l_R. However, for selected materials, a linear correlation between Δa and l_R was found [24], so that l_R is used as the damage parameter of the crack resistance curve instead of Δa.

The R-curves are analysed finally. To get a quantitative measure of the materials' resistance against stable crack propagation, the slope of the crack resistance curve T_J^* is determined. Having a non-linear function of the R-curve, it is useful to calculate the slope of it at smaller sizes of crack opening.

A second fracture mechanics test was applied in this study, the instrumented-tensile impact test. It was described in earlier publications, e.g. [19, 24] in detail and the test configuration is shown in Fig. 2.

The test is performed by using an instrumented pendulum device which allows to record load vs. time (F–t) signal during deformation of the specimen. In principle, the specimens are double-sided notched rectangular strips (DENT specimens). The size of the DENT specimens is length 64 mm × width 10 mm × plate thickness (preferably 2 mm). The pendulum hammer maximum energy was 7.5 J and a falling angle of 150° was realized, corresponding to a loading speed of 3.7 m/s. For each material, 10 single specimens were tested and the load–deformation (F–l) diagrams (calculated on the basis of the F–t diagrams) are analysed. From the analysis, measured values F_{max} and l_{max} can be determined and J values are calculated according to Eq. (1) with U is the energy up to F_{max} and the geometry function η is as follows [22]:

$$\eta = -0.06 + 5.99\left(\frac{a}{W}\right) - 7.42\left(\frac{a}{W}\right)^2 + 3.29\left(\frac{a}{W}\right)^3 \tag{2}$$

These J values are named J_d, where d means dynamic and refers to the impact-like loading during the test. J_d is interpreted as a measure of the materials' resistance against unstable crack propagation.

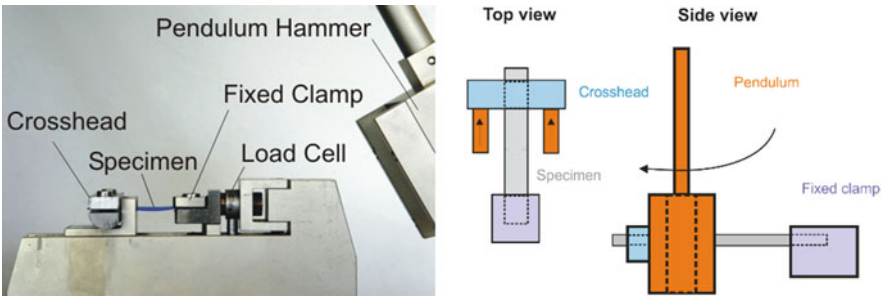

Fig. 2 Test configuration at the instrumented tensile-impact test: photograph of the clamping unit as well as sketch of the test set-up and specimen loading

3 Materials

The results presented in this contribution summarize data from different series of materials. Principally, two basic compositions were realized. Basic composition 1 was selected as follows: 115 phr polymer, 50 phr carbon black N234, 15 phr plasticizer (type variable), 3 phr zinc oxide, 1 phr stearin acid, 1.7 phr sulphur, and 3.65 phr CBS (N-Cyclohexyl-2-benzothiazyl-sulfenamid). The second basic composition for SBR, NBR, and SBR/BR vulcanizates was following: 100 phr polymer (in case of SBR/BR, blend ratio was 80/20), 40 phr carbon black N234, 0 to 37.5 phr plasticizer (type and amount variable), 3 phr zinc oxide, 1 phr stearin acid, 1,5 phr 6PPD, 1.7 phr sulphur, and 1.05 phr CBS.

The used polymers were NBR Perbunan®3445F from Lanxess Deutschland GmbH, Germany), S-SBR Sprintan™ SLR-4602 (clear grade, Trinseo Deutschland GmbH, Schkopau, Germany), and BR Buna™cis 132 (Trinseo Deutschland GmbH, Schkopau, Germany). For a comparison with the clear grade-S-SBR mixture with TDAE, one single SBR mixture (named S-25 T) was prepared by using S-SBR Sprintan™SLR-4630 (Trinseo Deutschland GmbH, Schkopau, Germany), which is extended with 37.5 phr TDAE. The composition of this mixture was the basic composition 2, but no additional plasticizer was added.

For all of the materials, as reinforcing filler, carbon black of the type Corax®N234 (Orion Engineered Carbons) was added. Main focus of the investiagations was the effect of different plasticizers:

- Treated distillate aromatic extract (TDAE) Vivatec 500 from H&R Hamburg, Germany,
- bio-oils 1 to 3 from Pilot Pflanzenöltechnologie Magdeburg e. V., Magdeburg, Germany,
- bio-oils 4 to 6 from Glaconchemie GmbH, Merseburg, Germany) (Table 1).

Zinc oxide, stearic acid, sulphur, and the accelerator CBS were from Roth Deutschland GmbH, Germany and the antioxidant 6PPD were supplied from Avokal® GmbH, Wuppertal, Germany.

The rubber compounds were prepared in a single-stage mixing process using a laboratory internal mixer Haake 300p (Thermo Haake GmbH, Germany) with adequate conditions for each recipe. Rotor speed and fill factor were kept constant

Table 1 Overview of the used plasticizers

Short name	Origin/modification	Abbreviation
Bio-oil 1	Epoxidized rapeseed oil	RE
Bio-oil 2	Epoxidized rapeseed oil methyl ester	ROME
Bio-oil 3	Epoxidized rapeseed oil propyl ester	ROPE
Bio-oil 4	Epoxidized canola oil	ECO
Bio-oil 5	Epoxidized rapeseed oil	ERO
Bio-oil 6	Epoxidized ester of glycerol formal from canola oil	EECO
TDAE	Mineral oil	TDAE

at 50 rpm and 0.70, respectively. After a mixing time of 10 min, the mixture was homogenized on a laboratory mill. For each mixture, vulcanization behaviour was characterized to determine the required vulcanization time t_{90}.

4 Dependence of the Material Properties on Plasticizer Type and Amount

4.1 Influence of Plasticizers on Mechanical and Physical Properties

It is known that the mechanical and physical properties of the vulcanizates are dependent on the type and the amount of plasticizer as well as the compatibility between plasticizer and rubber. Following, selected results of basic tests like tensile test (acc. to ISO 37), tear test (acc. to ISO 34-1), and hardness testing (acc. to DIN ISO 7619-1). As can be seen in Table 2, compared to the non-plasticized material, 15 phr of a TDAE in a carbon-black reinforced SBR vulcanizate lead to a reduction of the stress values σ_{100} and σ_{200} at 100% and 200% strain, while tensile strength σ_{max} is constant. At the same time, an increase in strain at break ε_R and a decrease in hardness can be observed. However, if bio-plasticizers based on rapeseed oil are mixed in, a slight decrease in stress values at 100% and 200% as well as tensile strength can be observed. In principle, the addition of plasticizers reduces the hardness. It can also be observed in Table 2 that the Shore A hardness of the vulcanizates containing bio-oils have the lowest hardness, whereby it does not matter which bio-oil is involved. But the characteristic values are on the same level. The reason for the difference between TDAE and bio-plasticizers is the different interaction behaviour between polymer and plasticizer molecules.

As another example, the tear resistance of an SBR/BR blend is discussed. Figure 3 shows the relationship between tear resistance T_s and the proportion of different plasticizers in a carbon-black reinforced SBR/BR blend. The tear resistance as a practically important material property can be influenced by the plasticizer more pronounced and in different ways. If TDAE or the epoxidized linseed oil (bio-oil 5) is mixed into the rubber blend, a slight reduction in tear resistance can be observed

Table 2 Summary of selected characteristic values from the tensile test and Shore A hardness values for carbon-black reinforced S-SBR compounds with 15 phr of different plasticizers (basic composition 1)

	σ_{100} (MPa)	σ_{200} (MPa)	σ_{max} (MPa)	ε_R (%)	Shore A (−)
Un-plasticized	4.37 ± 0.08	12.0 ± 0.28	17.7 ± 0.76	263 ± 10.5	71.9 ± 0.2
TDAE	2.58 ± 0.07	7.07 ± 0.21	17.5 ± 0.42	362 ± 11.5	65.0 ± 0.1
Bio-oil 1 (RE)	2.24 ± 0.03	5.84 ± 0.10	14.6 ± 1.94	373 ± 38.6	60.0 ± 0.1
Bio-oil 2 (ROME)	2.02 ± 0.02	5.30 ± 0.06	16.3 ± 0.38	425 ± 8.48	58.8 ± 0.1
Bio-oil 3 (ROPE)	2.11 ± 0.04	5.59 ± 0.10	16.8 ± 0.55	412 ± 8.16	59.5 ± 0.1

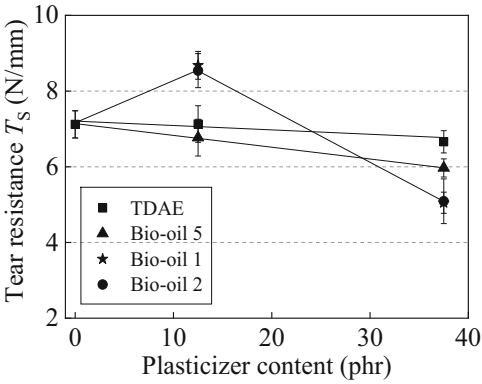

Fig. 3 Effect on the plasticizer type and content on the tear resistance for carbon-black filled SBR/BR blends (basic composition 2)

with an increase in the proportion of plasticizer. On the other hand, 12.5 phr rape seed oil epoxy (bio-oil 1) and epoxidized rape seed oil propyl ester (bio-oil 2) cause a maximum resistance to tear propagation and then reach the lowest value of all of the results at 37.5 phr.

In a multiphase blend system, plasticizers may have different solubilities in the different blend phases, which means that there could be different plasticizer concentrations in the phases. This state exists until a state of equilibrium is reached, which is present when the same chemical potential between the phases exists [22].

By the determination of the difference in solubility parameters of polymer and plasticizer and/or in surface tension, the general compatibility between polymer and plasticizer can be estimated. If there is a large difference in the surface tension values between rubber and plasticizer, there are also different chemical potentials between the phases. This difference is the driving force behind the migration of a plasticizer across the interfaces in a polymer blend system from one phase to another. The speed of migration is a function of polarity and glass-transition temperature [2]. However, the temperature also plays a major role in the migration process, because a higher temperature is associated with an increase in chain mobility. In Fig. 4, the mass loss behaviour of carbon-black reinforced SBR vulcanizates with 37.5 phr of two

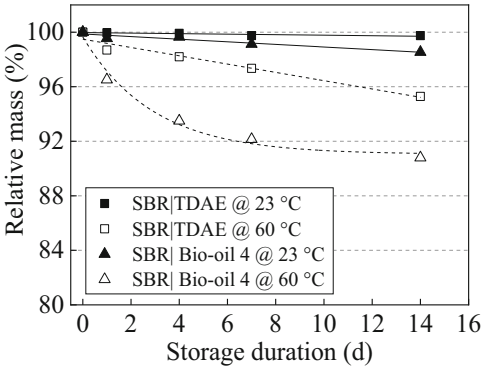

Fig. 4 Relative mass of plasticizer as a function of storage duration at different temperature for carbon-black filled SBR vulcanizates with 37.5 phr of TDAE and bio-oil 4, respectively (basic composition 2)

different plasticizers during time is shown. The samples were stored at room temperature and a higher temperature of 60°C. It can be seen that there is a certain mass loss, especially at the higher temperature, which is more pronounced for the bio-oil. Therefore, it can be expected that the bio-oil 4 basing on epoxidized canola oil migrates much easier out of the sample compared to TDAE. The related contact-angle measurements (not reported here) showed that the difference between the surface tension values of SBR|TDAE is 7.29 mN/m and between SBR|Bio-oil 4 it is much higher with 16.82 mN/m. A lower value means better compatibility between SBR and the plasticizer. Thus, a correlation between the difference in the surface tension values and the mass loss/migration is given. From the literature [25, 26], it is known that a poor compatibility between rubber and plasticizer leads to blooming effects and to changes in mechanical properties of the plasticized material. For this reason, loss in plasticizer with time should be avoided.

4.2 Influence of Plasticisers on the Fracture Behaviour

The influence of bio-based plasticizers on the materials' resistance against the initiation and propagation of a stable crack is discussed in this section. In Fig. 5, crack resistance curves (R-curves) are shown for filler-reinforced, plasticized SBR and NBR elastomers with two different amounts of the plasticizers. Generally, in Fig. 5, it can be seen that the type and the amount of plasticizer influence length, and slope of the R-curves as well as the maximum J values of the SBR and NBR vulcanizates. Because the result of the non-plasticized SBR is almost similar to previous results [14], it could be stated that the plasticizer influences the crack propagation in a positive way. This means, the level of J values of the plasticized materials is higher and also the crack opening. Different stable crack propagation behaviour of the SBR and NBR vulcanizates can be observed when the various plasticizers are used. An important reason for this are differences in polarities, as discussed above in Sect. 4.1. Due to the different polarities of SBR and NBR, not the same interaction with the used plasticizers is expected. However, depending on the plasticizer content, not the same ranking of the R-curves is given for SBR and NBR materials. This means, there must be a further factor, influencing the crack propagation. Here, the idea of an inner migration process due to the high strain and stress in front of the crack and resulting from this different friction conditions at the molecular scale may deliver one additional explanation. Therefore, future investigations should proof this inner migration process and its dependence on the stress and strain.

Concerning SBR materials with 12.5 phr plasticizers (Fig. 5a), SBR/EECO shows a higher efficiency in improving the resistance to stable crack propagation compared to the conventional plasticizer TDAE. When the plasticizer amount is enhanced to 37.5 phr, the form of R-curves of SBR/EECO and SBR/TDAE is similar, but SBR/EECO has larger crack opening (see Fig. 5b). Interestingly, the stable crack propagation behaviour of the SBR vulcanizate with 37.5 phr TDAE (mixed in) is

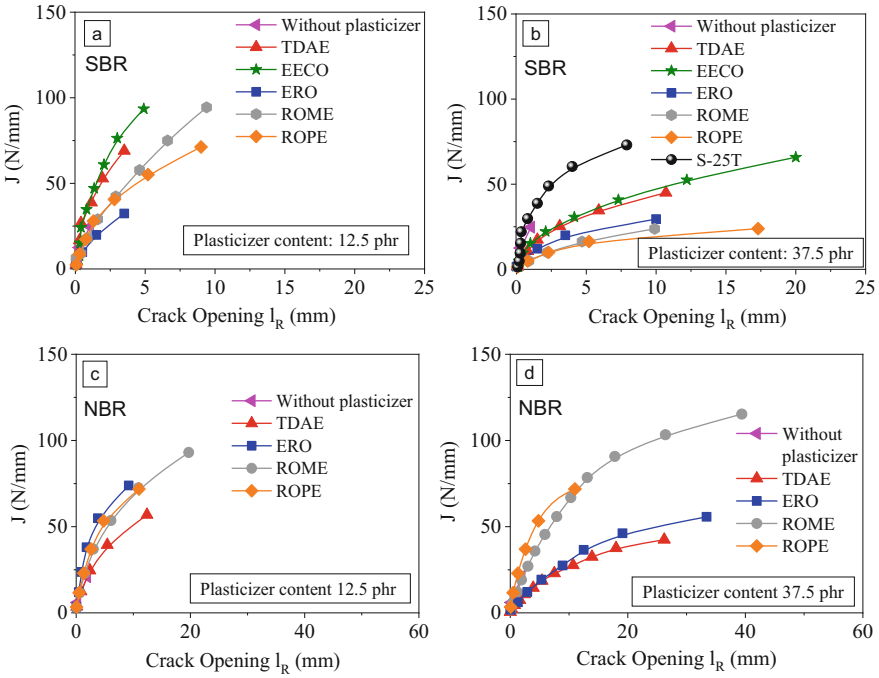

Fig. 5 Crack resistance curves J–l_R of plasticized SBR vulcanizates (**a**, **b**) and NBR vulcanizates (**c**, **d**) with 12.5 phr and 37.5 phr of different plasticizers (basic composition 2)

different to that of the SBR material S-25T, basing on an oil-extended SBR. Here, no additional plasticizer was added during mixing, but the amount of TDAE is comparable to the compound marked in red in Fig. 5a, b. S-25T vulcanizate shows highest J values. For mechanical properties (here not shown), this difference is not as pronounced. It seems that the conditions for an energy dissipation at the molecular level in S-25T are different compared to the vulcanizate with TDAE mixed in. As a consequence, the crack resistance of S-25T is higher. Also here the inner migration in the area around the crack tip can be a reason for the difference. For material S-25T it is expected that plasticizer migration is lower due to the incorporation of the plasticizer into the polymer chain.

For the NBR materials with low plasticizer content (see Fig. 5c), the crack propagation is not as different. However, with 37.5 phr (Fig. 5d), there are strong differences between ROPE, ROME, TDAE, and ERO regarding the J value level. One reason for the large crack-opening values is a higher deformability of the material, as discussed above. Therefore, a much higher elastic deformation is possible/necessary to reach a critical value in front of the crack tip. Again, the idea of the inner migration is pointed out as one possible reason for the different crack propagation. However, also the stiffness of the materials may contribute to the increase in crack resistance. If the stable crack propagation is controlled mainly by

the deformation, a decreased stiffness combined with a higher deformability would lead to a higher crack resistance.

In Fig. 6, the crack initiation values J_i and the crack propagation values of the investigated SBR and NBR materials are shown. For both polymers, the influence of the plasticizer type is much more pronounced for the crack propagation value. Further, the different plasticizers lead to different levels in crack resistance T_J* for both series. As discussed above, one reason lies in the different polarities of the polymers leading to different interaction between polymer and plasticizer.

For practical application, the crack resistance of a material should be high enough to prevent or to slow down crack propagation. As can be seen in Fig. 6a, SBR vulcanizates have a generally higher crack propagation resistance T_J* compared with NBR. However, NBR is generally known as material with a low tear and cut resistance and so it was to expect that it has a lower crack propagation resistance compared to the SBR vulcanizates. In contrast to the crack propagation, the crack initiation is higher for the non-plasticized NBR material compared to the SBR vulcanizate. However, while the crack initiation value of the SBR vulcanizates is relatively less influenced by the type of the plasticizer and the plasticizer content, in NBR this quantity is strongly reduced with plasticizer addition (Fig. 6b).

Noticeably, the SBR vulcanizate with 12.5 phr EECO shows a very pronounced maximum of the crack resistance value T_J* and a much higher value compared to the vulcanizate with TDAE (see Fig. 6a). EECO is a product having a comparatively low polar percentage [26]. The higher proportion of oleic acid [27] in the fatty acid chain of the chemical structure of EECO is one possible reason of the high level of the crack resistance and also of other mechanical properties (not shown here).

Concerning the stable crack propagation behaviour of NBR (see Fig. 6b), the bio-based plasticizers, especially ERO show excellent efficiency compared to the mineral oil-based TDAE. According to [28], the bio-based plasticizer contains OH groups that are most compatible with polar polymers like NBR. A previous study [29] had claimed that during the vulcanization of elastomeric materials, the bio-plasticizer could be co-vulcanized to the elastomer matrix, and the plasticizers

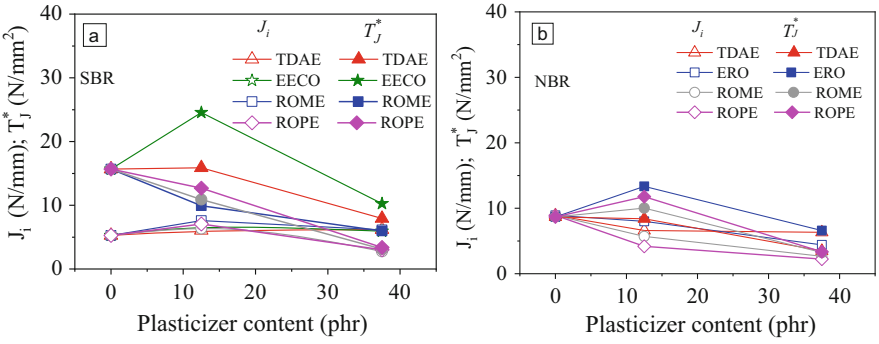

Fig. 6 Crack initiation value J_i and resistance against stable crack propagation energy T_J* of filled and plasticized SBR (**a**) and NBR vulcanizates (**b**) (basic composition 2)

may consume sulphur. In this case, the crosslink density would be reduced. This may explain also, e.g. a higher deformability. Future investigations will focus on this aspect.

Beside the quasi-static fracture mechanics investigation, also the fracture behaviour under impact-like conditions was characterized. In Fig. 7, the resistance of the materials against unstable crack propagation (J_d values, see Sect. 2) is shown for carbon-black filled SBR and NBR vulcanizates with different plasticizers.

As before, plasticizer content and plasticizer types were varied. The J_d value of non-plasticized carbon-black filled SBR is similar to previously reported results [19]. For all SBR–plasticizer combinations, the resistance against the initiation and propagation of an unstable crack becomes higher or remains constant with a plasticizer content of 12.5 phr (Fig. 7a). The further increase in plasticizer content leads to relatively strong decrease in $J_{d,}$ with exception of EECO. This vulcanizate shows a continuously increasing crack toughness. This is in contrast to the results of the quasi-static fracture mechanics test (see Fig. 6a) and can be related to the viscoelasticity. Furthermore, it is concluded that EECO leads to a much higher J_d of SBR vulcanizates than TDAE and again this shows the replacement potential of this bio-based plasticizer. The reason of the high level of crack resistance of the EECO material is still not clear. Further investigations should clarify this. Figure 7b shows the J_d values for the NBR vulcanizates in dependence on the plasticizer content and plasticizer type. The polymer type has a more significant influence on the unstable crack propagation behaviour of the compounds whenever plasticizers were the same. It appears that the addition of plasticizers increased J_d, although, at a high concentration of plasticizers, J_d decreased except for ERO. The percolating arrangement of fillers seen at the length scale of micro-dispersion, especially at a high level of filler loading, is called filler network. It is assumed that the filler dispersion and the arrangement of the filler network [30, 31] are influenced by EECO and ERO and make the carbon black more compatible with the polymer matrix.

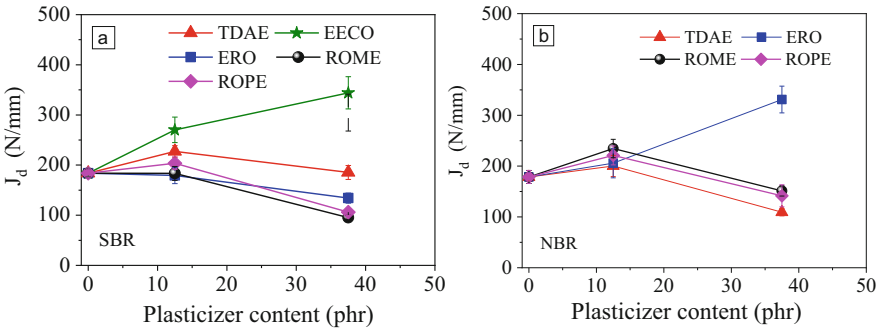

Fig. 7 Resistance against unstable crack propagation J_d of filled and plasticized SBR (**a**) and NBR vulcanizates (**b**) (basic composition 2)

5 Conclusion

This contribution deals with the mechanical and fracture mechanical behaviour of elastomeric materials containing different plasticizers from renewable sources. One aim of the investigations was to find alternatives for mineral oil-based plasticizers which are used in many technical applications. Their aromatic components may give reason for health problems when the plasticizer migrates out or comes into environment from volume loss, e.g. of tire treads. Therefore, there is a certain need to replace these components without loss in product quality. From the results, a certain potential of renewable plasticizers (bio-oils) as alternatives for conventional mineral oil-based products could be seen. For some combinations of polymer and plasticizer, the materials' resistance against crack initiation and propagation could be increased, compared to the reference. The efficiency of a plasticizer in the vulcanizates is dominated by several criteria, e.g. the polarity between polymer and plasticizer, degree of migration during vulcanization, the molecular structure, amount of the plasticizer and probably the inner plasticizer migration in the area of the fracture process zone during crack propagation leading to changed conditions at the molecular scale. For the full understanding of these interactions between polymer and plasticizer in the fracture process zone during deformation and stable crack propagation more investigations are required. The research will go on to get more insight to these physical reactions in such plasticized and filler-reinforced elastomer systems. Beside this, also chemical reactions between the various components of the material will be taken into account.

Acknowledgements The authors would like to thank the State of Saxony-Anhalt for financial support in the framework of the EFRE project (IB-LSA ZS/2019/3/97961) and the BMBF for financial support in the framework of the ZIM project: ZF4429401SL7. We would like to thank Glaconchemie GmbH and Pilot Pflanzenöltechnologie Magdeburg e. V. (PPM) for its bio-based plasticizer supply. Further, we thank Trinseo Deutschland GmbH (Schkopau) for supplying the SBR.

References

1. Raju P, Nandan V (2007) A study on the use of castor oil as plasticizer in natural rubber compounds. J Rubber Res 10(1):1–16
2. Röthemeyer F, Sommer F (2006) Kautschuktechnologie. Carl Hanser Verlag, München, Wien
3. Petrović ZS, Ionescu M, Milić J, Halladay JR (2013) Soybean oil plasticizers as replacement of petroleum oil in rubber. Rubber Chem Technol 86:233–249
4. Thomas A (2000) Fats and fatty oils. Ullmann's encyclopedia of industrial chemistry. Wiley-VCH Verlag GmbH & Co., Weinheim
5. Meier MAR, Metzger JO, Schubert US (2007) Plant oil renewable resources as green alternatives in polymer science. Chem Soc Rev 36:1788–1802
6. Wang Z, Peng Y, Zhang L, Zhao Y, Vyzhimov R, Tan T, Fong H (2016) Investigation of palm oil as green plasticizer on the processing and mechanical properties of ethylene propylene diene monomer rubber. Ind Eng Chem Res 55:2784–2789

7. Fernandez S, Kunchandy S, Ghosh S (2015) Linseed oil plasticizer based natural rubber/expandable graphite vulcanizates: synthesis and characterizations. J Polym Environ 23 (4):526–533
8. Kuriakose AP, Rajendran G (1995) Use of rice-bran oil in the compounding of styrene butadiene rubber. J Mater Sci 30(9):2257–2262
9. van Oosterhout JT, Gilbert M (2003) Interactions between PVC and binary or ternary blends of plasticizers. Part I. PVC/plasticizer compatibility. Polymer 44(26):8081–8094
10. Brown HR, Stevens G (1978) Fracture of slightly plasticized polyvinyl chloride. J Mater Sci 13:2373–2379
11. Bakar M, Djaider F (2007) Effect of plasticizers content on the mechanical properties of unsaturated polyester resin. J Thermoplast Compos Mater 20:53–64. https://doi.org/10.1177/0892705707068820
12. Xie Z, Chen Y, Wang C, Liu Y, Chu F, Jin L (2014) Effects of bio-based plasticizers on mechanical and thermal properties of PVC/wood flour composites. Bioresources 9:7389–7402. https://doi.org/10.15376/biores.9.4.7389-7402
13. Rennert M (2009) Untersuchungen zum Einfluss des Weichmacheröls auf das stabile Risswiderstandsverhalten von Elastomeren, Studienarbeit. Martin-Luther-Universität Halle-Wittenberg, Halle
14. Stoček R, Horst T, Reincke K (2017) Tearing energy as fracture mechanical quantity for elastomers. Adv Polym Sci APS 275:361
15. Reincke K, Klüppel M, Grellmann W (2009) Investigation of fracture mechanical properties of filler-reinforced styrene–butadiene elastomers. Kautsch Gummi Kunstst 62:246–251
16. Stoček R, Stěnička M, Zádrapa P (2020) Future trends in predicting the complex fracture behaviour of rubber materials. Contin Mech Thermodyn. https://doi.org/10.1007/s00161-020-00887-z
17. Grellmann W, Reincke K (2013) Technical material diagnostics – fracture mechanics of filled elastomer blends. In: Grellmann W, Heinrich G, Kaliske M, Klüppel M, Schneider K, Vilgis T (eds) Fracture mechanics and statistical mechanics of reinforced elastomeric blends. Springer, Berlin, pp 227–268
18. Reincke K, Grellmann W, Heinrich G (2006) Engineering fracture mechanics for crack toughness characterisation of elastomers. In: Proceedings of the European conference of fracture (ECF 16), Alexandroupolis, Greece, 3–7 July 2006
19. Reincke K, Grellmann W, Heinrich G (2008) Fracture mechanical investigations of filler-reinforced elastomers. In: Boukamel A, Laiarinandrasana L, Verron E (eds) Constitutive models for rubber V. Taylor & Francis Group, London, pp 221–227
20. Reincke K (2005) Bruchmechanische Bewertung von ungefüllten und gefüllten Elastomerwerkstoffen. Mensch & Buch Verlag, Berlin
21. März J (2010) Untersuchungen zur Weiterentwicklung bruchmechanischer Untersuchungsmethoden zur quantitativen Beschreibung des Deformations- und Bruchverhaltens von Elastomerwerkstoffen. Diploma thesis, Martin-Luther-Universität Halle-Wittenberg
22. Li J, Isayev AI (2018) Recent development in application of bio-based oils in elastomers. Rubber Chem Technol 91(4):719–728
23. Gerber G, Struve J (1999) Einfluß der Mischungszusammensetzung und Belastungsart auf das Versagensverhalten von Elastomeren. Kautsch Gummi Kunstst 52:400–404
24. Anderson TL (1995) Fracture mechanics. Fundamentals and application. CRC Press, Boca Raton
25. Kukreja TR, Chauhan RC, Choe S, Kundu PP (2002) Effect of the dosis and nature of vegetable oil on carbon black/rubber interactions: studies on castor oil and other vegetable oils. J Appl Polym Sci 87:1574–1578
26. Dasgupta S, Agrawal SL, Bandyopadhyay S, Chakraborty S (2007) Characterization of eco-friendly processing aids for rubber compound. Polym Test 26:489–500

27. Gallardo MA, Pérez DD, Leighton FM (2012) Modification of fatty acid composition in broiler chickens fed canola oil. Biol Res 45:149–161
28. Wypych G (2012) Effect of plasticizers on properties of plasticized materials. In: Wypych G (ed) Handbook of plasticizers2nd edn. William Andrew Publishing, Boston, pp 209–306
29. Kundu P (2002) Surface modification of carbon black by vegetable oil – its effect on the rheometric, hardness, abrasion, rebound resilience, tensile, tear, and adhesion properties. J Appl Polym Sci 84(5):993–1000
30. Kim BH, Joe CR (1989) Single specimen test method for determining fracture energy (J_c) of highly deformable materials. Eng Fract Mech 32(1):155–161
31. Reincke K, Grellmann W, Heinrich G (2004) Investigation of mechanical and fracture mechanical properties of elastomers filled with precipitated silica and nanofillers based upon layered silicates. Rubber Chem Technol 77(4):662–677

Adv Polym Sci (2021) 286: 347–376
https://doi.org/10.1007/12_2020_63

Published online: 12 December 2020

Fracture and Fatigue Failure Simulation of Polymeric Material at Finite Deformation by the Phase-Field Method and the Material Force Approach

Bo Yin, Jad Khodor, and Michael Kaliske

Contents

Abstract Failure prediction of polymeric material and structures is an important engineering task from experimental evaluation as well as from numerical simulation point of view. To investigate the fracture behavior and the fatigue failure of polymeric material, this work adopts two different numerical methodologies to

B. Yin, J. Khodor, and M. Kaliske (✉)
Institute for Structural Analysis, TU Dresden, Dresden, Germany
e-mail: michael.kaliske@tu-dresden.de

study crack initiation and propagation when the material is subjected to monotonic and cyclic fatigue loading. As a smeared crack approximation, the phase-field model does not depend on any explicit criterion to evolve cracks but yields good agreement compared to experimental validations. Another phenomenological approach to characterize crack growth based on a discrete approximation is the material force or configurational force approach, which largely depends on post-processing techniques. Both of them are developed according to the classical GRIFFITH criterion for brittle fracture. Nevertheless, regarding fatigue fracture phenomena, a fatigue induced degrading fracture toughness is assumed to evolve cracks, which basically captures the fatigue failure characteristics. This work implements these two methodologies, the phase-field approach and the material force method, into the Finite Element framework and simulates several demonstrative numerical examples, yielding good agreement by comparing to each other as well as to experimental results. Consequently, potential perspectives are proposed to close this paper.

Keywords Fatigue failure · Fracture · Material force method · Polymeric material · Phase-field modeling

1 Introduction

As one of the common failure mechanisms, reliable prediction of fracture evolution is of great importance and necessity for practical engineering applications. Especially, a number of polymers exhibit elastic nonlinearities according to experimental observations, which increase the complexities of fracture evaluation compared to classical linear elastic fracture mechanics [1–6]. According to a general understanding of structural failure, either microscopic detachment of atomic or molecular bonds and chemical chains, or macroscopic separation of material components, can lead to loss of structural integrity. In particular, numerous studies have classified two main phases of fracture in polymers, which are based on crack initiation [7–11] and crack propagation [12]. For several representative numerical models for rubber fracture, a path independent J-integral [13] can be combined with the finite element method [14, 15], which is additionally extended to rate-dependent fracture evolution in viscoelastic solids [16–18]. Addressing the numerical approximation of crack propagation, two basic classes of modelings are principally employed, namely smeared and discrete approaches discussed subsequently.

As one of the representative smeared crack approximations, the recently developed phase-field method, has been demonstrated having the capabilities to capture crack initiation, propagation as well as branching with complex characteristics. The conceptual methodology of the phase-field method is initially introduced in [19, 20] as a thermodynamical variational formulation, and is subsequently regularized in [21–24] to simulate brittle fracture. Meanwhile, in order to obtain robust and reliable fracture predictions and physical crack kinematics, several approaches are available, referring to [25–28] to name a few. In the sequel, classical brittle phase-field

modeling has been extended by incorporating several mechanical features, e.g. [29–33] for rate-dependent fracture studies, [34–38] for ductile fracture simulations, and [39–41] for anisotropic fracture analyses.

With respect to the concept of material forces or configurational forces, the approach is characterized by a non-NEWTONIAN force acting on an inclusion within an elastic homogeneous body. On the one hand, based on the theoretical studies of classical fracture mechanics, the crack tip can be understood as an inclusion, where the material force acting on is considered as the crack driving force. As a result, the energy release rate and the crack propagation direction are determined by the norm and the direction of the material force at the crack tip, respectively. On the other hand, extending to numerical simulation by means of the Finite Element approach, the crack can be approximated by a discrete representation. It is referred to [42–48] to name only a few studies. Several subsequent developments model crack propagation using the crack tip material force by employing a node splitting algorithm and an *r*-adaptivity re-meshing strategy. Furthermore, this methodology requires a prescribed initial notch to generate stress concentrations, which shows the limitation for crack initiation in the bulk material.

The scope of the work at hand intends to study fracture evolution within polymeric material by both the discrete material force method and the smeared phase-field approach. Previous work [49] has already documented these two methodologies by several demonstrative examples, which have been investigated with respect to small strains in quasi-static and transient analyses. Considering fatigue failure, the mechanism of cyclic loading induced fracture is presented in [50–52], which formulates an internal function to degrade the fracture toughness (or critical energy release rate) by an accumulative fatigue variable. As validated in [50–52], the underlaying concept has been illustrated by various numerical examples, although they only take the small strain problem into consideration. The present work is also motivated by [50–52] to extend the fatigue fracture model to finite strains for polymeric material by incorporating both the phase-field and the material force approach.

The framework of this paper is outlined as follows. In Sect. 2, the fundamental constitutive formulation of the used hyperelastic model is introduced along with a derivation of the stress tensor and the consistent tangent. Sections 3 and 4 describe the theoretical basis of the phase-field model and the material force approach and their fatigue constitutive laws, respectively. In the sequel, several representative and demonstrative numerical simulations are outlined in Sect. 5, and Sect. 6 summarizes the findings and closes the contribution with potential perspectives.

2 Constitutive Models of Polymeric Material

2.1 Kinematics and HELMHOLTZ Energy Density Function

Before covering the constitutive material models, the fundamental kinematic relations need to be introduced. Within a continuous solid Ω_0, the position vectors $\boldsymbol{X}$ and

$\boldsymbol{x}$ represent the material point in the reference and the current configuration, respectively. The motion during the deformation is denoted by $\boldsymbol{\varphi}$, which is defined as $\boldsymbol{x} = \boldsymbol{\varphi}(\boldsymbol{X}, t)$. The deformation gradient $\boldsymbol{F} = \nabla_{\boldsymbol{X}} \boldsymbol{\varphi}(\boldsymbol{X}, t)$ is one of the basic quantities for the kinematic description, where $\nabla_{\boldsymbol{X}}$ stands for the gradient operator with respect to the reference configuration. To describe the distinct volumetric and isochoric material behavior of e.g. polymeric materials, the deformation gradient $\boldsymbol{F}$ is further decomposed into

$$\boldsymbol{F} = J^{\frac{1}{3}} \bar{\boldsymbol{F}}, \tag{1}$$

where $\bar{\boldsymbol{F}}$ describes the isochoric response, and the JACOBIAN is the determinant of the deformation gradient, i.e. $J = \det(\boldsymbol{F})$. Furthermore, the right and left CAUCHY-GREEN tensors and their isochoric quantities are common strain measures for the elastic response, which are defined as

$$\boldsymbol{C} = \boldsymbol{F}^T \cdot \boldsymbol{F}, \qquad \boldsymbol{b} = \boldsymbol{F} \cdot \boldsymbol{F}^T \qquad \text{and} \qquad \bar{\boldsymbol{C}} = \bar{\boldsymbol{F}}^T \cdot \bar{\boldsymbol{F}}, \qquad \bar{\boldsymbol{b}} = \bar{\boldsymbol{F}} \cdot \bar{\boldsymbol{F}}^T, \tag{2}$$

respectively. Regarding the constitutive law, this work takes a simple NEO-HOOKEAN model [53] into account to numerically represent polymeric material at finite strains and the typical HELMHOLTZ strain energy density function with respect to the reference configuration reads

$$\varphi_0 = U(J) + \varphi_{iso}(\bar{\boldsymbol{C}}), \tag{3}$$

which consists of both the volumetric contribution $U(J)$ and isochoric contribution $\varphi_{iso}(\bar{\boldsymbol{C}})$. As commonly used functional forms, they are defined as

$$U(J) = \kappa(J - \ln(J) - 1) \qquad \text{and} \qquad \varphi_{iso}(\bar{\boldsymbol{C}}) = \frac{\mu}{2}(\bar{I}_1 - 3) \tag{4}$$

and governed by two model parameters κ and μ. The scalar quantity $\bar{I}_1$ represents the first invariant of $\bar{\boldsymbol{C}}$ or $\bar{\boldsymbol{b}}$, i.e. $\bar{I}_1 = \mathrm{tr}(\bar{\boldsymbol{C}}) = \mathrm{tr}(\bar{\boldsymbol{b}})$.

2.2 Material Stress and Consistent Tangent Tensors

Having the strain energy density function at hand, the constitutive relations can be obtained by a straightforward derivation. The KIRCHHOFF stress tensor and the consistent tangent tensor regarding the current configuration are obtained by

$$\boldsymbol{\tau}_{vol} = p\, \mathbf{1} \qquad \text{and} \qquad \boldsymbol{\tau}_{iso} = \mu \left(\bar{\boldsymbol{b}} - \frac{1}{3}\, \bar{I}_1\, \mathbf{1} \right), \tag{5}$$

and

$$\mathbb{C}_{vol} = \Big(p + s\Big)\mathbf{1} \otimes \mathbf{1} - 2p\,\mathbb{I} \qquad \text{and} \qquad \mathbb{C}_{iso} = \frac{2}{3}\,\Big(\mu\,\bar{I}_1\,\mathbb{P} - \boldsymbol{\tau}_{iso} \otimes \mathbf{1} - \mathbf{1} \otimes \boldsymbol{\tau}_{iso}\Big), \tag{6}$$

respectively. The hydrostatic KIRCHHOFF stress quantity and its corresponding modulus are obtained based on the first and the second order partial derivative of the volumetric energy density with respect to J, i.e. $p = J\ \partial_J\ U(J)$ and $s = J^2\ \partial^2_{JJ}\ U(J)$, respectively. With the definition of the KRONECKER delta δ_{ab}, the two frequently used fourth order tensors $\mathbb{I}_{abcd} = \frac{1}{2}(\delta_{ac}\delta_{bd} + \delta_{ad}\delta_{bc})$ and $\mathbb{P}_{abcd} = \mathbb{I}_{abcd} - \frac{1}{3}\delta_{ab}\delta_{cd}$ are given.

3 Fatigue Phase-Field Evolution

3.1 Phase-Field Topology

Within a continuous solid domain, the smeared approximation by the phase-field approach to model a sharp crack is a continuous and diffusive profile, which is illustrated in Fig. 1. The order parameter, namely the phase-field variable $d(\boldsymbol{X}, t)$, is a scalar quantity to identify the material state, i.e. the sound state is expressed by $d = 0$ and the fully cracked material is represented by $d = 1$. Mathematically motivated by a one-dimensional bar with an infinite length $L \in [-\infty, +\infty]$, which is assumed to be cracked at position $X = 0$, the closed form solution for a continuous phase-field according to [23] is approximated by a simple exponential function

$$d(X) = \exp\Big(-\frac{|X|}{l}\Big). \tag{7}$$

This solution is naturally bound by $0 < d \leq 1$ from the mathematical point of view. Another important quantity appearing in Eq. (7), the numerical length-scale parameter l, is employed to control the width of the transition zone between fractured and sound state. Extending to a two- or three-dimensional framework, the second order functional of the crack surface density, which is characterized by the unit mm^{-1}, is defined as

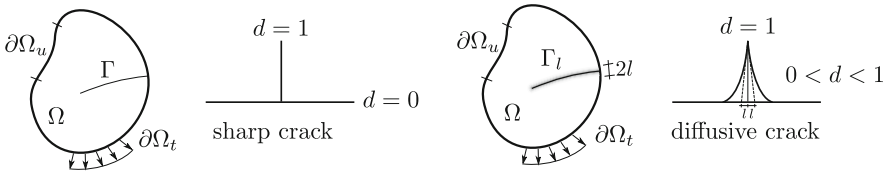

Fig. 1 Diffusive crack topology

$$\gamma_l = \frac{1}{2l}\left(d^2 + l^2|\nabla_{\boldsymbol{X}} d|^2\right), \tag{8}$$

where $\nabla_{\boldsymbol{X}}(*)$ denotes the gradient operator with respect to the reference configuration. Highlighted in [54], the realistic crack length Γ is approximately obtained by the phase-field crack length Γ_l as long as $l \to 0$, i.e.

$$\Gamma \approx \lim_{l\to 0} \Gamma_l = \lim_{l\to 0} \int_{\Omega_0} \gamma_l \, dV, \tag{9}$$

which is known as the classical Γ-convergence condition for fracture. In addition to Eq. (8) for the crack surface density function definition, other functional forms [24, 55] are alternatively used in phase-field modeling as well. Furthermore, the recent works [56, 57] have studied accuracy and reliability of phase-field modeling regarding the length-scale parameter and mesh sensitivity. The paper at hand simply chooses a conventional criterion according to [58] for finite strain problems, i.e. $h_e \leq l/2$

3.2 *Fatigue Induced Degradation of Fracture Toughness* $\mathcal{G}_c$

A number of experimental observations indicate that the instantaneous fracture toughness $\mathcal{G}_c$ depends on several factors, e.g. the strain rate in [59, 60]. Another example of rate-dependent fracture is found in polymeric materials [61], which formulates the instantaneous $\mathcal{G}_c$ as a function of the crack propagation velocity. The underlying mechanism is the different strength of the polymer chains compared to the cross-links, i.e. $\mathcal{G}_c^{links} < \mathcal{G}_c^{chain}$. Fast loading requires larger external energy to break the material, since the failure mechanism is based on the chemical bonds of the chains breaking due to lack of relaxation time. In contrast, for slow loading situations, the chain segments can be rearranged uniformly due to sufficient viscous relaxation, and the external energy is distributed to the cross-links. As a result, a lower level of external work is required to break the chemical bonds instead of the chains. In addition to rate-dependent fracture toughness [29, 61], several other approaches consider different influences on the fracture toughness, e.g. hardening dependent $\mathcal{G}_c$ for ductile fracture [30], directional dependent $\mathcal{G}_c$ for anisotropic fracture [38], and cyclic dependent $\mathcal{G}_c$ for fatigue fracture [50–52].

As an effective simplification, the rate-dependent fracture property of polymeric material is not taken into account for fatigue failure modeling. Motivated by [50–52], this work proposes a fatigue induced degradation of the fracture toughness incorporated into the phase-field method and the material force approach. An internal degradation function $\mathscr{F}$ multiplies the intrinsic $\mathcal{G}_c^0$ to obtain the instantaneous $\mathcal{G}_c$, i.e.

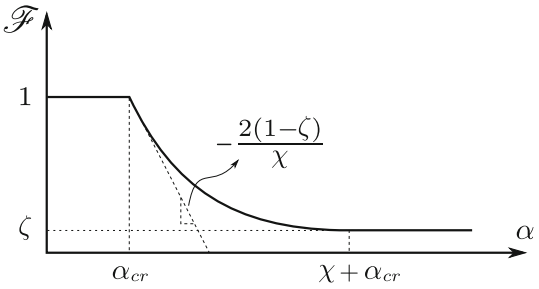

Fig. 2 Profile of fatigue induced degradation function F

$$\mathcal{G}_c = \mathscr{F}(\alpha)\ \mathcal{G}_c^0. \tag{10}$$

The degradation function $\mathscr{F}$ is defined as a functional of an internal quantity α, which is the so-called accumulative fatigue variable and is non-negatively defined. The work at hand describes this quantity as the accumulative strain energy only considering loading processes, while the strain energy at unloading cases is not included. From a mathematical point of view, the degradation function is characterized by the following properties:

$$0 \leq \mathscr{F} \leq 1, \qquad \mathscr{F}(\alpha \leq \alpha_{cr}) = 1 \qquad \text{and} \qquad \partial_\alpha \mathscr{F}(\alpha \geq \alpha_{cr}) \leq 0. \tag{11}$$

The first condition in Eq. (11) indicates the physical bounds, where the instantaneous fracture toughness $\mathcal{G}_c$ in Eq. (10) cannot exceed $\mathcal{G}_c^0$ and cannot unphysically be a negative value. The second condition introduces the threshold α_{cr} for the internal variable α to trigger the degradation function $\mathscr{F}$ as long as $\alpha_{cr} \geq \alpha$, which numerically ensures that the initial cycles do not degrade the fracture toughness. The parameter α_{cr} can be obtained by evaluating experimental investigations. The last one prescribes a monotonic decrease of $\mathcal{G}_c$ when $\alpha \geq \alpha_{cr}$. These conditions in Eq. (11) postulate a physical and reasonable conceptual understanding of the fatigue fracture mechanism.

Several alternative functional forms can be chosen to construct the degradation function $\mathscr{F}$, see [51]. In this work, a general and simple form

$$\mathscr{F} = \begin{cases} 1, & \alpha \leq \alpha_{cr}, \\ \frac{1-\zeta}{\chi^2}\left(\alpha - \alpha_{cr} - \chi\right)^2 + \zeta, & \alpha_{cr} \leq \alpha \leq \chi + \alpha_{cr}, \\ \zeta, & \chi + \alpha_{cr} \leq \alpha, \end{cases} \tag{12}$$

is employed, see Fig. 2. Specifically, χ and ζ are two key parameters to govern the quadratic degradation profile of $\mathscr{F}$. The constant χ is positively defined and the parameter ζ is characterized as the lower bound of $\mathscr{F}$, which is restricted as $0 \leq \zeta \leq 1$. Nevertheless, in order to have an effective decrease of $\mathscr{F}$, the parameter ζ in this work is set to be an infinitesimal value $0 < \zeta \ll 1$. An important reason for this mathematical property is to enhance the numerical stability of the simulation. Moreover, this algorithmic setup does not show differences compared to the solutions by setting $\zeta = 0$, since fracture will be fully evolved when the fracture

toughness $\mathcal{G}_c$ is degraded to a certain level, which is far from 0. It is noteworthy to mention that, due to the non-linearity of $\mathscr{F}$, the differentiation of $\mathscr{F}$ with respect to the internal variable α does not generally exist, except for the special case of $\alpha_{cr} = 0$. Therefore, the aforementioned $\partial_\alpha \mathscr{F} < 0$ in Eq. (11) is described based on the setup of $\alpha_{cr} > 0$, since $\partial_\alpha \mathscr{F} = 0$ is obviously when $\alpha_{cr} \leq 0$.

A number of alternatives can be employed to define the accumulative fatigue quantity α. A former assumption in [50] regarding a simple one-dimensional problem considers an accumulative strain induced fatigue degradation, which presents a simple and straightforward algorithmic setup. Nevertheless, the extension to a multi-dimensional problem yields mesh-dependent results due to the singularity of local strain measurement particularly at the crack tip. To overcome this numerical issue, the accumulated strain energy definition

$$\alpha = \int_0^{t_{n+1}} g(d)\mathfrak{H}\big(\dot{\varphi}_0^+\big)\big|\dot{\varphi}_0^+\big| \, dt \tag{13}$$

is introduced with the help of the HEAVISIDE operator $\mathfrak{H}$ to trigger time integration only at monotonic loading state, i.e. $\mathfrak{H}\big(\dot{\varphi}_0^+ \geq 0\big) = 1$ and $\mathfrak{H}\big(\dot{\varphi}_0^+ < 0\big) = 0$. It is notable that the positive energy term φ_0^+ is known as the phase-field driving force, which is determined depending upon the energy split mechanism for the phase-field evolution. The algorithmic setup of the volumetric-deviatoric split together with the phase-field degradation function $g(d)$ are discussed in Sect. 3.3 in detail. Outlined in [51], this definition characterizes the fatigue feature independent of the mean load of a cycle. Furthermore, a numerical approach to obtain the time integration of α in Eq. (13) significantly reduces the complexity, which is approximated as

$$\alpha_{t_{n+1}} = \alpha_{t_n} + \int_{t_n}^{t_{n+1}} g(d)\mathfrak{H}\big(\dot{\varphi}_0^+\big)\big|\dot{\varphi}_0^+\big| \, dt \approx \alpha_{t_n} + \Delta t \Big[g(d)\mathfrak{H}\big(\dot{\varphi}_0^+\big)\big|\dot{\varphi}_0^+\big| \Big]_{t_{n+1}}. \tag{14}$$

The time increment is given as $\Delta t = t_{n+1} - t_n$. The energy rate is further expanded as

$$\begin{aligned} \dot{\varphi}_0^+ &= \frac{\partial \varphi_0^+}{\partial \boldsymbol{b}} : \dot{\boldsymbol{b}} = \frac{\partial \varphi_0^+}{\partial \boldsymbol{b}} : \big(\boldsymbol{l} \cdot \boldsymbol{b} + \boldsymbol{b} \cdot \boldsymbol{l}^T\big) \\ &= \left(2 \, \frac{\partial \varphi_0^+}{\partial \boldsymbol{b}} \cdot \boldsymbol{b}\right) : \boldsymbol{l} = \boldsymbol{\tau}_0^+ : \boldsymbol{l}, \end{aligned} \tag{15}$$

where the spatial velocity gradient is $\boldsymbol{l} = \dot{\boldsymbol{F}} \cdot \boldsymbol{F}^{-1}$. In the sequel, as a straightforward expansion, the stepwise increment of the spatial velocity gradient is approximately $\Delta \boldsymbol{l} = \Delta t \, \dot{\boldsymbol{F}} \cdot \boldsymbol{F}^{-1} = \Delta \boldsymbol{F} \cdot \boldsymbol{F}^{-1}$, leading to the stepwise energy increment as $\Delta \varphi_0^+ = \boldsymbol{\tau}_0^+ : \Delta \boldsymbol{l}$. As a result, the internal variable α in Eq. (14) is updated as

$$\alpha_{t_{n+1}} \approx \alpha_{t_n} + g(d)\mathfrak{H}\big(\Delta \varphi_0^+\big)\big|\Delta \varphi_0^+\big|. \tag{16}$$

3.3 Governing Equations of the Coupled Problem

The constitutive law for the fatigue phase-field evolution is obtained based upon the energy balance. The total internal energy density consists of the strain energy density to drive and not drive the phase-field evolution, e.g. φ_0^+ and φ_0^-, as well as the fracture energy density φ_Γ within an isotropic solid domain Ω_0, reading

$$\mathcal{Q} = \int_{\Omega_0} \Big(g(d)\varphi_0^+ + \varphi_0^- \Big)\, dV + \int_{\Omega_0} \varphi_\Gamma \, dV, \tag{17}$$

where the function $g(d)$ in Eq. (17) prescribes the degradation of the elastic strain energy to evolve the phase-field. Slightly different from the function $\mathscr{F}$, the phase-field degradation function $g(d)$ is characterized by the following properties:

$$g(0) = 1, \qquad g(1) = 0, \qquad \partial_d\, g(d) \leq 0 \qquad \text{and} \qquad \partial_d\, g(1) = 0. \tag{18}$$

The first two conditions in Eq. (18) prescribe the mathematical limits of the sound and broken states, respectively. The two other conditions describe a monotonic degradation during the fracture evolution procedure. Particularly, at a fully broken state, $\partial_d\, g(1) = 0$ circumvents the elastic driving force in Eq. (17). An early proposal in [21] gives a quadratic function $g(d) = (1-d)^2$, which satisfies all properties in Eq. (18). In the sequel, several other alternatives are studied in [27, 62, 63] as well.

A classical volumetric-deviatoric split regarding the strain energy degradation according to Amor et al. [25] is applied in this work, which decomposes the total strain energy into positive and negative parts to identify a proper driving force for the phase-field evolution. By using the Heaviside operator $\mathfrak{H}$ again, the positive and negative energy densities are defined as

$$\varphi_0^+ = \mathfrak{H}(J-1)U(J) + \varphi_{iso} \qquad \text{and} \qquad \varphi_0^- = \Big(1 - \mathfrak{H}(J-1)\Big)U(J), \tag{19}$$

to distinguish the volume compression or expansion state, respectively. In addition to the volumetric-deviatoric split algorithm, several other alternatives are also available, see [26–28] to name only a few.

According to [51], the accumulative fracture energy density for fatigue phase-field modeling is defined as

$$\varphi_\Gamma = \int_0^{t_{n+1}} \mathscr{F}(\alpha)\; \mathcal{G}_c^0 \left(\frac{\partial \gamma_l}{\partial d}\dot{d} + \frac{\partial \gamma_l}{\partial \nabla_{\boldsymbol{X}} d} \nabla_{\boldsymbol{X}} \dot{d} \right) dt. \tag{20}$$

Thus, the rate of the fracture energy density yields

$$\dot{\varphi}_\Gamma = \mathscr{F}(\alpha)\ \mathcal{G}_c^0 \left(\frac{\partial \gamma_l}{\partial d} \dot{d} + \frac{\partial \gamma_l}{\partial \nabla_{\boldsymbol{X}} d} \nabla_{\boldsymbol{X}} \dot{d} \right). \tag{21}$$

In the sequel, the balance of energy fundamentally exists

$$\frac{D\mathscr{K}}{D\,t} + \mathscr{P}_{int} = \mathscr{P}_{ext}, \tag{22}$$

where the kinetic energy and the external power quantities are defined by

$$\mathscr{K} = \int_{\Omega^0} \frac{1}{2}\, \rho_0\, \dot{\boldsymbol{U}} \cdot \dot{\boldsymbol{U}}\, dV \quad \text{and} \quad \mathscr{P}_{ext} = \int_{\Omega^0} \mathfrak{B} \cdot \dot{\boldsymbol{U}}\, dV + \int_{\partial\Omega^0} \mathfrak{T} \cdot \dot{\boldsymbol{U}}\, dA, \tag{23}$$

respectively. The derivative with respect to time is denoted by $D(*)/D\,t$ in Eq. (22). The material density, velocity, body force, and surface traction quantities are expressed by ρ_0, $\dot{\boldsymbol{U}}(= D\,\boldsymbol{U}/D\,t)$, $\mathfrak{B}$ and $\mathfrak{T}$ with respect to the reference configuration, respectively. The internal power $\mathscr{P}_{int}$ in Eq. (22) is obtained as

$$\begin{aligned}
\mathscr{P}_{int} &= \frac{DQ}{Dt} = \int_{\Omega^0} \left\{ \left(g(d) \partial_{\boldsymbol{F}}\, \varphi_0^+ + \partial_{\boldsymbol{F}}\, \varphi_0^- \right) : \dot{\boldsymbol{F}} + \partial_d\, g(d) \varphi_0^+\, \dot{d} + \dot{\varphi}_\Gamma \right\} dV \\
&= \int_{\Omega^0} \left\{ \left(g(d) \boldsymbol{P}^+ + \boldsymbol{P}^- \right) : \dot{\boldsymbol{F}} + \partial_d\, g(d) \varphi_0^+\, \dot{d} + \mathscr{F}(\alpha)\ \mathcal{G}_c^0 \left(\frac{\partial \gamma_l}{\partial d} \dot{d} + \frac{\partial \gamma_l}{\partial \nabla_{\boldsymbol{X}} d} \nabla_{\boldsymbol{X}} \dot{d} \right) \right\} dV \\
&= \int_{\partial\Omega^0} \left\{ \mathfrak{N} \cdot \left(g(d) \boldsymbol{P}^+ + \boldsymbol{P}^- \right) \right\} \cdot \dot{\boldsymbol{U}}\, dA - \int_{\Omega^0} \left\{ \nabla_{\boldsymbol{X}} \cdot \left(g(d) \boldsymbol{P}^+ + \boldsymbol{P}^- \right) \right\} \\
&\quad \cdot \dot{\boldsymbol{U}}\, dV + \int_{\partial\Omega^0} \left\{ \mathcal{G}_c^0\, \mathscr{F}(\alpha)\, \frac{\partial \gamma_l}{\partial \nabla_{\boldsymbol{X}} d} \cdot \mathfrak{N} \right\} \dot{d} dA + \int_{\Omega^0} \left\{ \partial_d\, g(d) \varphi_0^+ \right. \\
&\quad \left. + \mathscr{F}(\alpha)\ \mathcal{G}_c^0 \left(\frac{\partial \gamma_l}{\partial d} - \nabla_{\boldsymbol{X}} \left(\frac{\partial \gamma_l}{\partial \nabla_{\boldsymbol{X}} d} \right) \right) - \mathcal{G}_c^0\, \nabla_{\boldsymbol{X}} \mathscr{F}(\alpha) \cdot \frac{\partial \gamma_l}{\partial \nabla_{\boldsymbol{X}} d} \right\} \dot{d} dV,
\end{aligned} \tag{24}$$

where the quantities $\boldsymbol{P}^\pm = \partial_{\boldsymbol{F}}\, \varphi_0^\pm$ are known as the first Piola–Kirchhoff stress tensors and $\mathfrak{N}$ represents the normal vector outward the solid surface. The divergence operator with respect to the reference configuration is denoted by $\nabla_{\boldsymbol{X}} \cdot (*)$. By inserting Eqs. (23) and (24) into Eq. (22), the governing equations for the coupled phase-field problem are obtained as

$$\begin{aligned}
\rho_0 \ddot{\boldsymbol{U}} - \nabla_{\boldsymbol{X}} \cdot \left(g(d) \boldsymbol{P}^+ + \boldsymbol{P}^- \right) - \mathfrak{B} = \boldsymbol{0} \quad &\text{in } \Omega_0 \quad \text{and} \quad \mathfrak{N} \cdot \left(g(d) \boldsymbol{P}^+ + \boldsymbol{P}^- \right) \\
&= \mathfrak{T} \quad \text{at } \partial\Omega_0
\end{aligned} \tag{25}$$

and

$$\begin{aligned} \partial_d\, g(d)\varphi_0^+ + \mathscr{F}(\alpha)\,\frac{\mathcal{G}_c^0}{l}\left(d - l^2\,\Delta_{\boldsymbol{X}} d\right) - \mathcal{G}_c^0\, l\,\nabla_{\boldsymbol{X}}\mathscr{F}(\alpha)\cdot\nabla_{\boldsymbol{X}} d &= 0 \quad \text{in } \Omega_0, \\ \mathscr{F}(\alpha)\,\nabla_{\boldsymbol{X}} d\cdot\mathfrak{N} &= 0 \quad \text{at } \partial\Omega_0, \end{aligned} \tag{26}$$

with respect to the elastic response and the phase-field evolution, respectively, where the LAPLACIAN operator is denoted by $\Delta_{\boldsymbol{X}}(*)$. Certainly, the governing equation of the elastic response can also be written regarding the current configuration alternatively as

$$\rho\ddot{\boldsymbol{u}} - \nabla_{\boldsymbol{x}}\cdot\left(g(d)\,\boldsymbol{\tau}^+ + \boldsymbol{\tau}^-\right) - \mathfrak{b} = \boldsymbol{0} \quad \text{in } \Omega \text{ and } \mathfrak{n}\cdot\left(g(d)\,\boldsymbol{\tau}^+ + \boldsymbol{\tau}^-\right) = \mathfrak{t} \text{ at } \partial\Omega. \tag{27}$$

The symbols $\nabla_{\boldsymbol{x}}\cdot(*)$, $\ddot{\boldsymbol{u}}$, $\mathfrak{n}$, $\mathfrak{b}$, and $\mathfrak{t}$ are accordingly updated to describe the operation in the current configuration.

Furthermore, in order to avoid numerical healing during phase-field evolution, another history variable is employed to define the phase-field driving force according to [26], rewriting Eq. (26) as

$$\begin{aligned} \partial_d\, g(d)\mathscr{H} \quad &+\mathscr{F}(\alpha)\,\frac{\mathcal{G}_c^0}{l}\left(d - l^2\,\Delta_{\boldsymbol{X}} d\right) - \mathcal{G}_c^0\, l\,\nabla_{\boldsymbol{X}}\mathscr{F}(\alpha)\cdot\nabla_{\boldsymbol{X}} d = 0, \\ &\text{where} \quad \mathscr{H} = \underset{\tau\le t_{n+1}}{\text{Max}}\ \varphi_0^+(\boldsymbol{F},\tau) \end{aligned} \tag{28}$$

is defined. Thus, a monotonically increasing phase-field is numerically achieved, leading to irreversible damage in the material. In the contribution at hand, this regularization is employed for the fatigue phase-field approach. Additionally, appropriate DIRICHLET boundary conditions for the phase-field degree of freedom can also be re-defined as soon as the material is assumed to be cracked, i.e. $d \ge 0.9999$. Thus, the driving force does not depend on the history variable $\mathscr{H}$ and is calculated promptly at current step $\varphi^+_{0,t_{n+1}}$. For the detailed algorithmic setup, it is referred to [64].

4 Fatigue Failure by the Material Force Method

4.1 Fundamentals of the Material Forces Approach

Material forces or configurational forces are non-NEWTONIAN forces acting on a flaw within a body such as a crack tip or an inclusion. The movement of an inclusion within an elastic homogeneous body is studied by ESHELBY's thought experiment [65]. The energy variation due to a movement $\delta\boldsymbol{X}$ of the inclusion is defined as

$$\delta\Phi = \boldsymbol{F}^{\text{mat}} \cdot \delta\boldsymbol{X}, \tag{29}$$

where $\boldsymbol{F}^{\text{mat}}$ is the material force acting on the inclusion. The material force is computed by carrying out a surface integral around the inclusion

$$\boldsymbol{F}^{\text{mat}} = \int_{\partial\Omega^0} \boldsymbol{\Sigma} \cdot \bar{\mathfrak{N}}\, dA \quad \text{and} \quad \boldsymbol{\Sigma} = \varphi\, \boldsymbol{I} - \boldsymbol{F}^T \cdot \boldsymbol{P}, \tag{30}$$

where $\bar{\mathfrak{N}}$ represents the normal vector outward the surface $\partial\Omega^0$ surrounding the inclusion. The Eshelby stress tensor and the first Piola–Kirchhoff stress tensor are denoted by $\boldsymbol{\Sigma}$ and $\boldsymbol{P}$, respectively. The term φ is the free strain energy. In the fracture mechanics context, the direction of the material force vector acting on the crack tip and its direction are used to determine the crack propagation direction and the energy release rate, respectively.

The local balance of linear momentum for a quasi-static case is defined as

$$\nabla_{\boldsymbol{X}} \cdot \boldsymbol{P} + \mathfrak{B} = \boldsymbol{0}, \tag{31}$$

where $\mathfrak{B}$ are body forces. A covariant pull-back operation by multiplying Eq. (31) by $\boldsymbol{F}^T$ from the left yields

$$\boldsymbol{F}^T \cdot (\nabla_{\boldsymbol{X}} \cdot \boldsymbol{P}) + \boldsymbol{F}^T \cdot \mathfrak{B} = \boldsymbol{0}. \tag{32}$$

Applying the product rule to Eq. (32) leads to

$$\boldsymbol{P} : \nabla_{\boldsymbol{X}}\, \boldsymbol{F} = \nabla_{\boldsymbol{X}} \cdot \left(\boldsymbol{F}^T \cdot \boldsymbol{P}\right) - \boldsymbol{F}^T \cdot (\nabla_{\boldsymbol{X}} \cdot \boldsymbol{P}). \tag{33}$$

The gradient of the free energy φ is expressed by

$$\nabla_{\boldsymbol{X}} \varphi(\boldsymbol{F}, \boldsymbol{X}) = \frac{\partial \varphi}{\partial \boldsymbol{F}} : \frac{\partial \boldsymbol{F}}{\partial \boldsymbol{X}} + \frac{\partial \varphi}{\partial \boldsymbol{X}}\Big|_{\text{exp}}. \tag{34}$$

The quantity $\frac{\partial \varphi}{\partial \boldsymbol{X}}\Big|_{\text{exp}}$ is the explicit derivative of the strain energy density function with respect to the position $\boldsymbol{X}$, which vanishes in case of a homogeneous body. Substituting Eq. (33) in Eq. (34) results in

$$\nabla_{\boldsymbol{X}} \cdot (\varphi\, \boldsymbol{I}) = \nabla_{\boldsymbol{X}} \cdot (\boldsymbol{F}^T \cdot \boldsymbol{P}) + \boldsymbol{F}^T \cdot \mathfrak{B} + \frac{\partial \varphi}{\partial \boldsymbol{X}}\Big|_{\text{exp}}. \tag{35}$$

Due to the relation $\nabla_{\boldsymbol{X}}\, \varphi = \nabla_{\boldsymbol{X}} \cdot (\varphi\, \boldsymbol{I})$, the strong form of balance of energy momentum is written

$$\nabla_{\boldsymbol{X}} \cdot \boldsymbol{\Sigma} + \boldsymbol{B} = \boldsymbol{0} \quad \text{and} \quad \boldsymbol{B} = -\boldsymbol{F}^T \cdot \mathfrak{B} - \frac{\partial \varphi}{\partial \boldsymbol{X}}\Big|_{\text{exp}}, \tag{36}$$

where $\boldsymbol{B}$ is the configurational volume force. Multiplying Eq. (36) by an arbitrary test function $\boldsymbol{\eta}$ according to the GALERKIN method and performing integration by parts yields

$$\int_{\partial\Omega^0} (\boldsymbol{\Sigma} \cdot \bar{\mathfrak{N}}) \cdot \boldsymbol{\eta}\, dA - \int_{\Omega^0} \left(\boldsymbol{\Sigma} : \nabla_{\boldsymbol{X}}\, \boldsymbol{\eta} + \boldsymbol{B} \cdot \boldsymbol{\eta} \right) dV = 0. \tag{37}$$

Performing a direct GALERKIN discretization over the whole continuum, nodal material forces are evaluated as

$$\boldsymbol{F}^{I,\text{mat}}_{\text{node}} = -\sum_{e=1}^{k} \int_{\Omega_e^0} \boldsymbol{\Sigma} \cdot \nabla_{\boldsymbol{X}}\, N^I dV_e + \sum_{e=1}^{k} \int_{\Omega_e^0} \boldsymbol{B}\, N^I\, dV_e + \sum_{e=1}^{ksur} \int_{\partial\Omega_e^0} \boldsymbol{\Sigma} \cdot \bar{\mathfrak{N}}\, N^I dA_e, \tag{38}$$

where N^I is the shape function regarding the node I and k is the number of elements connected to the node. The index *ksur* is the number of surface elements connected to the node I. Further details related to the calculation of nodal material forces can be found in the work of MÜLLER and MAUGIN [48].

4.2 Fatigue Crack Propagation by Material Force Approach

In this section, the process of fracture toughness degradation is discussed. According to GRIFFITH [1], the criterion for crack propagation is defined as

$$\mathcal{G} - \mathcal{G}_c^0 = 0, \tag{39}$$

where $\mathcal{G}$ is the energy release rate and $\mathcal{G}_c^0$ is defined previously as the fracture toughness. Using the material force approach, $\mathcal{G}$ is replaced by the norm of the material force acting on the crack tip $\left\|\boldsymbol{F}^{\text{mat}}_{\text{crack}}\right\|$. When the body is subjected to cyclic loading, the crack propagates despite $\left\|\boldsymbol{F}^{\text{mat}}_{\text{crack}}\right\|$ being smaller than the fracture toughness. To characterize this phenomenon, a modified GRIFFITH criterion is introduced as

$$\left\|\boldsymbol{F}^{\text{mat}}_{\text{crack}}\right\| - \mathscr{F}(\alpha)\ \mathcal{G}_c^0 = 0, \tag{40}$$

where $\mathscr{F}(\alpha)$ is the degradation function introduced in Eq. (12). Similar to Eq. (13), α is evaluated as

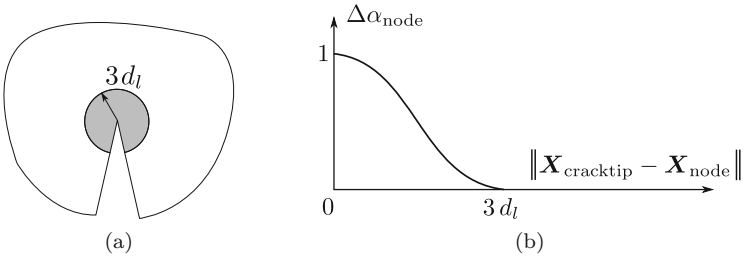

Fig. 3 (**a**) Crack tip zone and (**b**) regularization effect of the distance at the crack tip on the surrounding nodes

$$\alpha = \int_0^{t_{n+1}} \mathfrak{H}(\dot{\gamma})\ |\dot{\gamma}|\ dt, \tag{41}$$

where $\gamma = \left\|\boldsymbol{F}^{\text{mat}}_{\text{crack}}\right\|$. Hence, α is numerically accumulated as

$$\alpha_{n+1} = \alpha_n + \Delta\alpha \quad \text{and} \quad \Delta\alpha = |\gamma_{n+1} - \gamma_n|\ \mathfrak{H}\left(\frac{\gamma_{n+1} - \gamma_n}{\Delta t}\right). \tag{42}$$

Furthermore, to address the issue of mesh sensitivity, a particular regularized accumulation around the crack tip nodes is employed, which reads

$$\Delta\alpha_{\text{node}} = \exp\left(-\frac{\|\ \boldsymbol{X}_{\text{cracktip}} - \boldsymbol{X}_{\text{node}}\ \|^2}{2\ d_l^2}\right)\ \Delta\alpha_{\text{cracktip}}, \tag{43}$$

where d_l is the distribution parameter, $\Delta\alpha_{\text{node}}$, $\boldsymbol{X}_{\text{node}}$ and $\Delta\alpha_{\text{cracktip}}$, $\boldsymbol{X}_{\text{cracktip}}$ are the accumulation increment and the reference coordinates at the surrounding nodes and the crack tip node, respectively. The regularized accumulation is a typical numerical approach to avoid the issue of mesh dependency, which is applied within the so-called fatigue zone depicted in Fig. 3. It can be seen from Fig. 3 that only the nodes within a distance 3 d_l at the crack tip are significantly affected by the distribution. Nevertheless, the influence of the nodes out of the distance 3 d_l can be simply neglected according to the fact $0 < \exp\left(-\frac{(3\ d_l)^2}{2\ d_l^2}\right) \ll 1$.

5 Numerical Simulations

5.1 Tearing Failure of a Thin Polymeric Film

The first example studies a three-dimensional out-plane tear test by the phase-field method to demonstrate the capability of the fracture simulation of the polymeric material at large deformation. It is noteworthy that the fictitious material is assumed

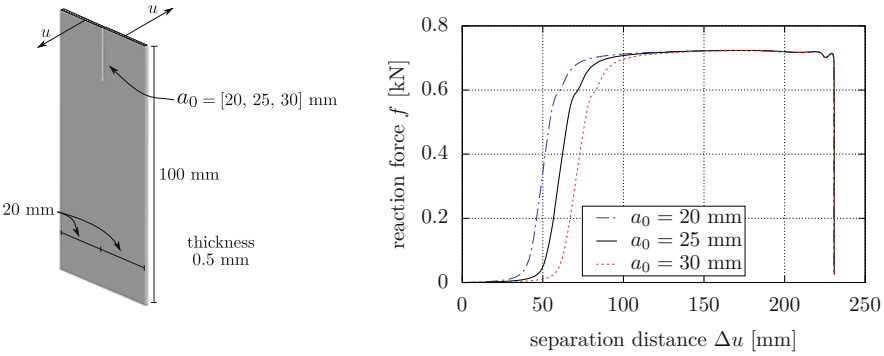

(a) Geometrical setup

(b) Numerically obtained load-separation curves

Fig. 4 (**a**) Geometry and loading setup of the three-dimensional tear test and (**b**) relationship between the external load and the separation distance regarding different initial crack length

to be a kind of soft rubber, which is not validated here by real experimental investigations. Similar investigations have been studied in [30] by considering a simplified half geometry, where the polymeric material is characterized as visco-elastic and eventually shows rate-dependent fracture behavior. Nevertheless, this example does not consider the inelastic material property. The three-dimensional boundary value problem is depicted in Fig. 4a. Two upper edges (right and left) are fully bound and subjected to external loads, which are completely opposite to each other. A discrete crack is prescribed vertically at the middle of the upper region. Three finite element models with different initial crack lengths are discretized by 16,140, 16,150, and 16,160 uniform 8-node brick elements and the mesh size is $h_e = 0.5$ mm. The model parameters of the material are given as $\kappa = 1.96$ MPa, $\mu = 0.134$ MPa, $\mathcal{G}_c^0 = 1.22\ N/\text{mm}^2$, and the length-scale parameter is $l = 1.2$ mm. Deactivating the fatigue constitutive evolution of the present phase-field modeling, the threshold simply is set $\alpha_{cr} \approx \infty$ for the degradation function $\mathscr{f}$.

Three simulations with different initial crack lengths, e.g. $a_0 = [20, 25, 30]$ mm, are performed. Particularly, the phase-field crack evolution is shown in Fig. 5 at four different loading states. To achieve a vivid visualization, the damaged material, e.g. $d \geq 0.95$, is blanked by post-processing, which appropriately models crack propagation. It is necessary to point out that the out-plane tear fracture consists of three phases, namely crack initiation, stable crack propagation, and eventually unstable propagation up to final failure. These three distinct features are also evaluated by the relationship of loading regarding the separation distance, see Fig. 4b. The initially prescribed crack cannot transfer any resistance, hence, the reaction forces measured at the loading edges are close to zero along with increasing the separation distance. As long as the element at the prescribed discrete crack tip is largely deformed and the elastic energy is sufficient enough to evolve the local phase-field variable from 0 to 1, the smeared crack starts to initiate and the reaction force starts to increase as well up to a certain amplitude. In the sequel, the smeared phase-field crack propagates stably and the reaction force keeps approximately the

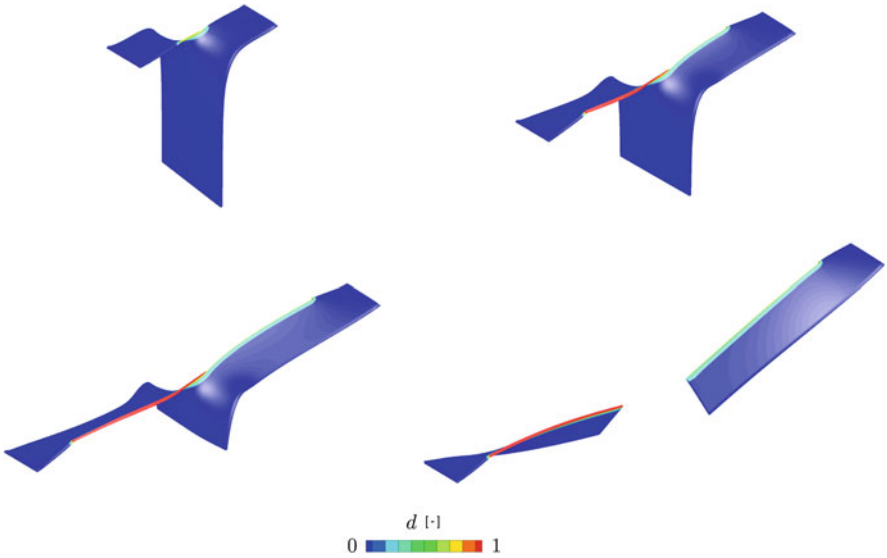

Fig. 5 Phase-field crack evolution of the three-dimensional tear test by blanking the data $d \geq 0.95$

same amplitude up to a certain length, where the numerical crack propagation becomes unstable and ends up with rupture. Meanwhile, it can be observed that the three different setups obtain similar maximum separation distances at failure. Nevertheless, their phase-field crack initiations are dissimilar due to different initial notch lengths.

An important finding is that the elements at the crack tip largely deform before fully losing stiffness, which has a significant impact on the solution with respect to the numerical convergence. Particularly in terms of a comparatively large loading increment at one single step, the sudden loss of stiffness even strongly distorts the element shapes, consequently yielding nonphysical negative JACOBIAN quantities at the integration points. As a result, the simulation does not converge anymore and aborts easily. Therefore, to overcome this numerical issue, smaller loading increments for each step are required, especially for the situation of unstable crack propagation.

5.2 Tension Failure of a Double-Notch Specimen

This example compares the phase-field method and the material force approach by studying a benchmark of polymer fracture, which is experimentally conducted by HOCINE [15] to estimate the critical fracture energy. In the sequel, this problem is numerically studied by the material force method and the phase-field model in [66, 67], respectively, and good agreement is obtained compared to the insight of

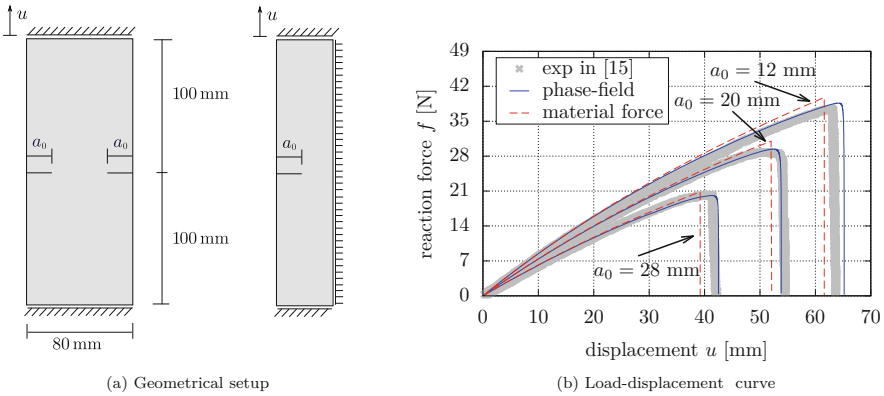

(a) Geometrical setup (b) Load-displacement curve

Fig. 6 (**a**) Geometrical setup of the two-dimensional notched specimen and its simplified half model due to symmetry and (**b**) comparison of the load-displacement relations obtained by the phase-field model and the material force approach to the experimental results in [15] regarding tension fracture of styrene butadiene rubber

[15]. Regarding the constitutive law, [66] uses the ARRUDA–BOYCE model and [67] adopts the NEO-HOOKEAN formulation, whose energy functions read

$$\varphi_0 = \kappa(J - \ln J - 1) + \mu N \left(\lambda_r \mathscr{L}^{-1}(\lambda_r) + \ln \frac{\mathscr{L}^{-1}(\lambda_r)}{\sinh \mathscr{L}^{-1}(\lambda_r)} \right) \tag{44}$$

and

$$\varphi_0 = \frac{\mu}{\beta} \left(J^{-\beta} - 1 \right) + \frac{\mu}{2} (\mathrm{tr}(\boldsymbol{C}) - 3) \tag{45}$$

with additional material parameters N and β, respectively. The notations $\lambda_r = \sqrt{\mathrm{tr}(\bar{\boldsymbol{C}})/3N}$ and $\mathscr{L}^{-1}$ express the stretch and inverse LANGEVIN function, respectively. To carry out an explicit comparison of both methodologies, this work reproduces the fracture process by using the HELMHOLTZ energy density function in Eqs. (3) and (4).

The two-dimensional setup of the boundary value problem is depicted in Fig. 6a. Several symmetrically notched specimens with three initial crack lengths $a_0 = [12, 20, 28]$ mm are investigated. The bottom edge is fully fixed and the top one is fixed by a vertically upward displacement, which leads to monotonic tensile failure. Due to the symmetric geometry, loading as well as boundary conditions, only half of the original specimen is analyzed by applying an appropriate boundary condition. Three finite element models are approximately discretized by 12, 880 4-node quadratic elements. The potentially cracked regions are discretized by finer meshes with an element size $h_e = 0.5$ mm. The model parameters are given as $\kappa = 5.89$ MPa, $\mu = 0.61$ MPa, $\mathcal{G}_c^0 = 2.67$ N/mm^2 and the length-scale parameter for the phase-field evolution is $l = 1.6$ mm. As aforementioned, without triggering fatigue evolution, the threshold of the degradation function $\mathscr{F}$ is simply set $\alpha_{cr} \approx \infty$.

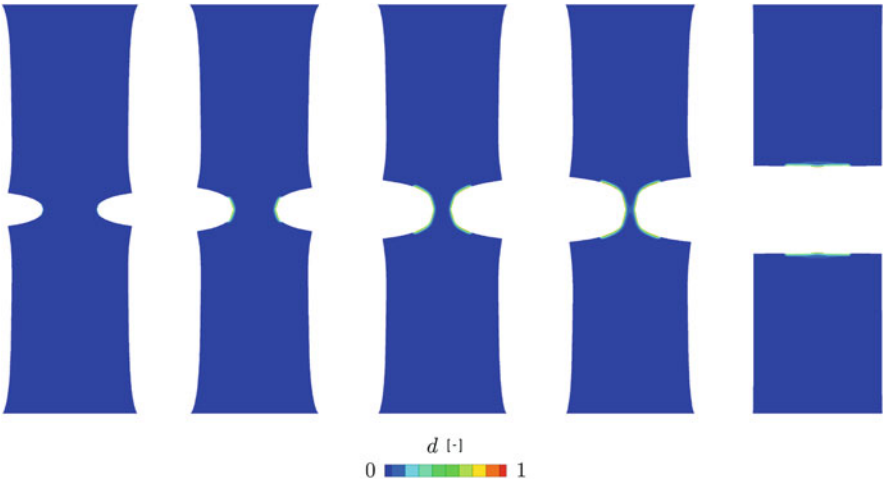

Fig. 7 Fracture evolution by the phase-field method and blanking the phase-field $d \geq 0.95$

Fig. 8 Fracture evolution by the material force method combined with a node splitting technique

The fracture evolution based on the geometrical setup with $a_0 = 20$ mm is shown in Fig. 7 for phase-field modeling and in Figs. 8 and 9 for the material force nodal splitting algorithm. Regarding the phase-field crack approximation, fully evolved cracks are assumed at $d \geq 0.95$ and the post-processing technique blanks the material with the phase-field value $d \geq 0.95$ to show a vivid crack initiation and propagation up to complete separation. With respect to the material force approach, the crack propagates in an unstable manner at maximum displacement, where the instantaneous energy release rate reaches or exceeds the critical value. Nevertheless, this numerical instability can be addressed by several algorithmic treatments, e.g. the arc-length method. Different from the phase-field blanking technique, the material

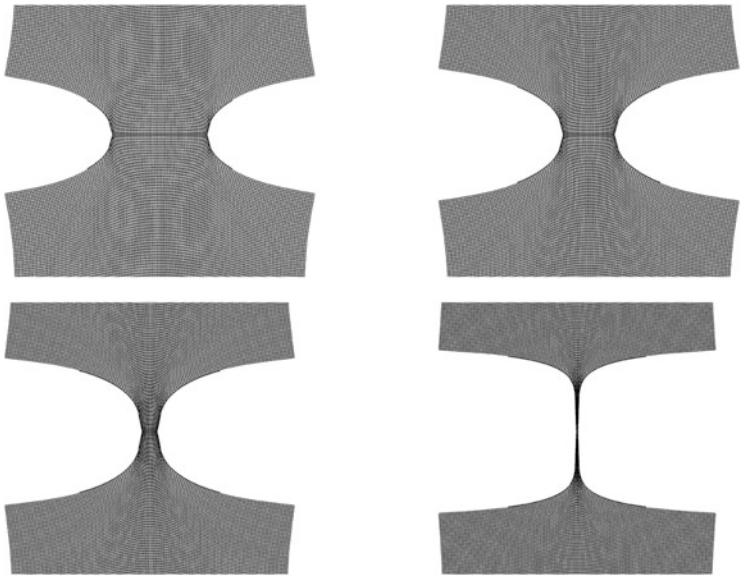

Fig. 9 Magnified plot of the fracture zone (for full specimen see Fig. 8)

force simulation yields an explicit crack evolution according to the nodal duplicating strategy. Moreover, the load-displacement graphs obtained by numerical simulations are compared to the experimental evaluation in Fig. 6b for all specimen geometries. It can be observed that the peak loads and the fracture displacements are properly predicted by both methodologies. The fact of a smaller initial notch leading to larger overall strength is validated. Meanwhile, the brittle failure behavior is represented by a sudden drop of the resultant force along with rapid and unstable crack growth. Nevertheless, the phase-field simulations always show a slight softening behavior before brittle fracture. Reducing the length-scale parameter can effectively remedy such phenomena, but an increasing computational effort is accordingly required. As a conclusion, these results are sufficient to demonstrate the capabilities of both methods for polymeric failure simulation.

5.3 Fatigue Failure of a Notched Cyclically Loaded Polymer by Phase-Field Modeling

This numerical simulation studies fatigue fracture of a fictitious polymeric specimen with assumed material parameters by the presented fatigue phase-field model. Based on the aforementioned description, the cyclic loading induced failure mechanism is the result of the locally degrading fracture toughness $\mathcal{G}_c$ along with the increasing accumulative fatigue history α. A two-dimensional boundary value problem is

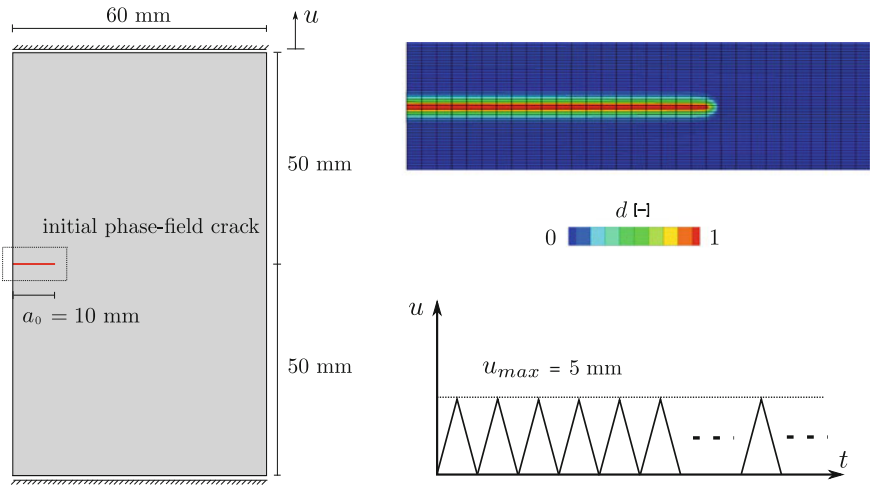

Fig. 10 Geometrical setup of the two-dimensional specimen by a prescribed phase-field crack to approximate the initial notch and the cyclic loading function

analyzed with the geometry and loading setup shown in Fig. 10. An initial horizontal notch with the length $a_0 = 10$ mm is introduced at the left edge of the specimen. Different from the setups in Sects. 5.1 and 5.2 using the discrete crack to represent the initial notch, this example alternatively describes the discrete notch by means of an initial phase-field crack, where the nodes of the cracked elements are prescribed by the phase-field boundary condition $d = 1$. The specimen is fully fixed at the bottom edge and the top one is subjected to a vertically upward displacement. It is necessary to point out that compression induced fracture is not included in the scope of the work at hand. For simplicity, only tensile cyclic loading is subjected to the upper boundary of the specimen, where the loading function is depicted in Fig. 10. The finite element model consists of 9, 720 4-node quadratic elements, where the potential cracked region is discretized by the element size 0.1×0.5 mm^2. The model parameters of the material are given as $\kappa = 2.96$ MPa, $\mu = 0.152$ MPa, $\mathcal{G}_c^0 = 4.36$ N/mm^2 and the length-scale parameter is $l = 0.5$ mm. The threshold to trigger the degradation function $\mathscr{F}$ is set to $\alpha_{cr} = 0.06$, where the degradation profile of $\mathscr{F}$ is governed by the two parameters $\chi = 1.66$ and $\zeta = 0.001$.

As a reference, fracture by a monotonic tensile loading is also simulated and the results are shown in Figs. 11a and b with respect to the phase-field crack evolution and the load-displacement curves, respectively. It can be observed that the maximum displacement for monotonic loading induced fracture is around $u_{\max} \approx 38$ mm, where the total deformation approximately reaches 38% of its vertical dimension. Therefore, the cyclic displacement with the amplitude $u = 5$ mm, which only leads to 5% deformation, is insufficient to yield brittle fracture at the beginning when $\mathcal{G}_c$ is not significantly reduced yet. As a result, the crack starts to initiate after 22 cycles and to propagate 1 mm after 46 cycles. In the sequel, the phase-field crack proceeds

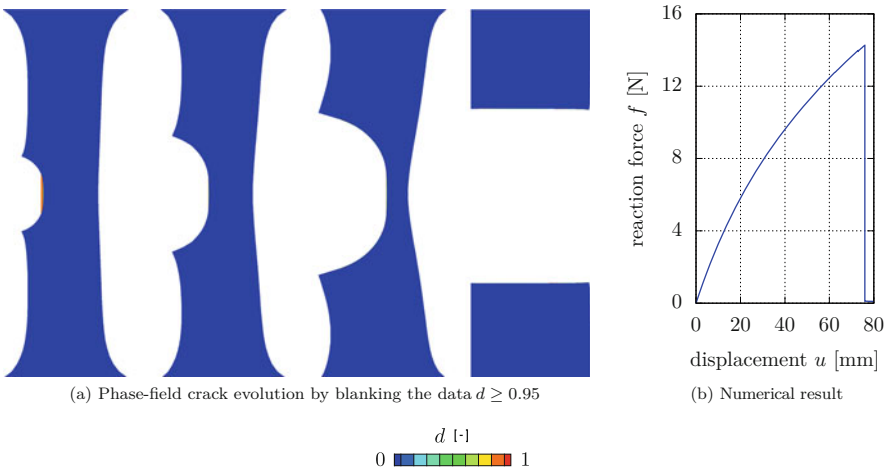

(a) Phase-field crack evolution by blanking the data $d \geq 0.95$ (b) Numerical result

Fig. 11 Brittle fracture obtained by monotonic tension loading, (**a**) phase-field fracture evolution and (**b**) numerically obtained load-displacement graph

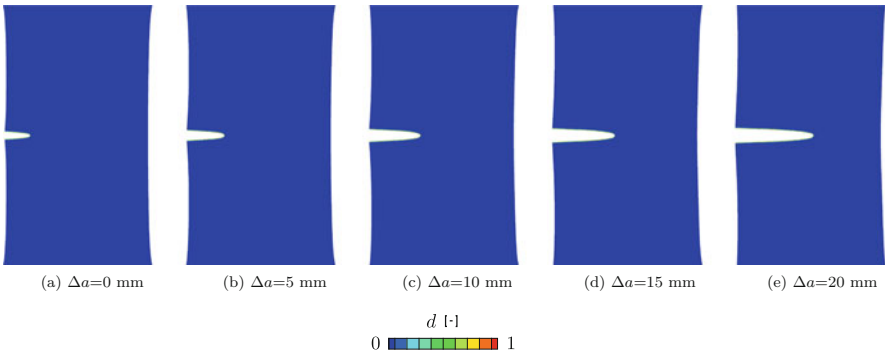

(a) Δa=0 mm (b) Δa=5 mm (c) Δa=10 mm (d) Δa=15 mm (e) Δa=20 mm

Fig. 12 Phase-field crack propagation at different loading cycles, (**a**) for crack initiating at $N_{cyc} = 22$ cycles and (**b**)–(**d**) for certain lengths with regard to $N_{cyc} = [188, 323, 430, 524]$ cycles, respectively

to propagate up to 20 mm after 524 cycles, where the phase-field crack profile at different cycles is shown in Fig. 12. In particular, at cycle $N_{cyc} = 524$ with an evolved crack length Δa=20 mm, the phase-field crack tip and the degradation function $\mathscr{F}$ are shown in detail in Fig. 13. It can be seen that the damaged elements with $d \geq 0.9999$ are significantly deformed. Meanwhile, the degradation function $\mathscr{F}$ also reduces to the lower bound, i.e. $\mathscr{F} = b$. Another interesting finding is that the phase-field crack is subsequently evolved into two or three rows of damaged elements (see Figs. 13 and 14b for the crack tip), which is different from the initial setup (only one row of damaged elements represents a crack, see Fig. 14a). This

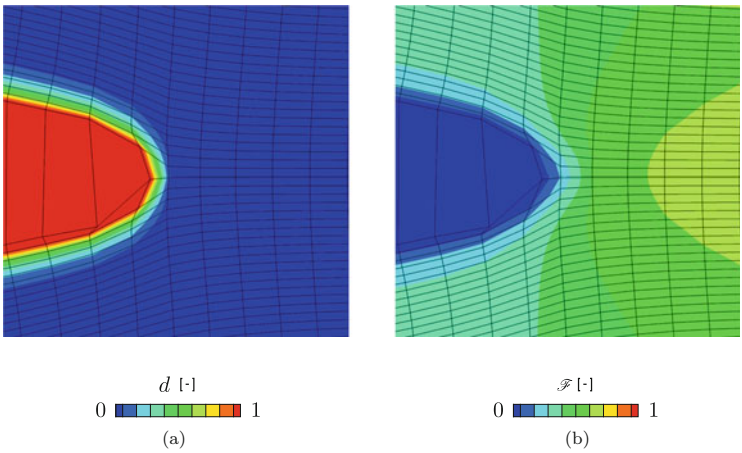

Fig. 13 Distribution of the phase-field variable and the fatigue degradation function around the crack tip at $N_{cyc} = 524$, crack length Δa=20 mm. (**a**) Phase-field d. (**b**) Function F

feature, which yields a slightly broadening crack profile during the phase-field evolution, is quite common among the numerical simulations of general phase-field modeling. Nevertheless, as long as the mesh is sufficiently refined compared to the specimen's dimensions, the overall crack pattern is still characterized as a thin and concentrated phase-field distribution.

The reaction forces at maximum displacement $f_{u_{\max}}$ as well as the crack length increments are evaluated with respect to the loading cycles, see Fig. 15a. As can be predicted, along with increasing loading cycles, the crack length Δa shows a stepwise increment, meanwhile, the reaction force $f_{u_{\max}}$ decreases quadratically. It is necessary to point out that the crack length increment cannot be obtained by an explicit algorithm, since the crack tip is not robustly determined due to the diffusive transition of phase-field variables ($0 < d < 1$). Hence, the work at hand approximates the crack tip as long as the phase-field variable reaches $d \geq 0.95$ at the vicinity of crack tip.

Furthermore, this example also studies the classical Paris law of fatigue fracture. However, due to the finite strain formulation, the stress intensity factor of small strain problems [51] cannot be used. Therefore, in order to achieve a simple evaluation, the approximated energy release rate $\mathcal{G}$ based on the implicit energy difference algorithm is employed in this example. This methodology is numerically implemented into the in-house post-processing technique. The numerical definition of the energy release rate reads

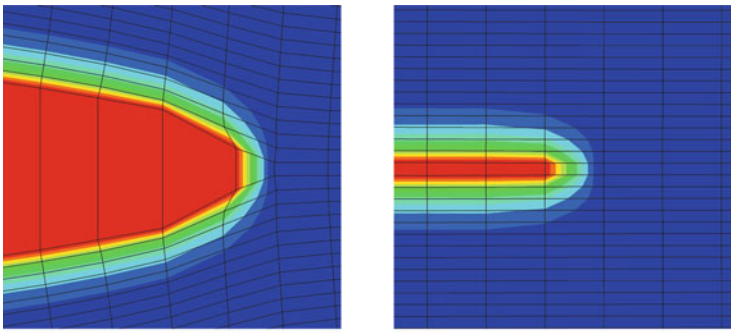

(a) Deformed and undeformed shape at Δa=0 mm

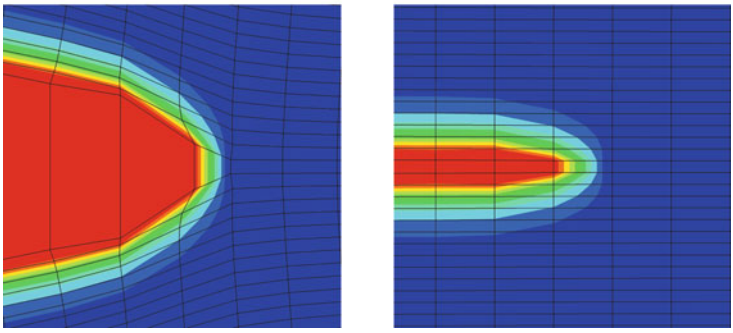

(b) Deformed and undeformed shape at Δa=5 mm

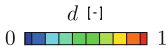

Fig. 14 The fully cracked material (**a**) is initially represented by only one row of damaged elements, nevertheless, (**b**) is diffusively evolved to more rows of damaged elements

$$\begin{aligned}\mathcal{G} &\approx \frac{\int_{\Omega^0}\varphi^{int}\,dV\big|_{a^{n+1},u_{\max}} - \int_{\Omega^0}\varphi^{int}\,dV\big|_{a^{n},u_{\max}}}{\Delta a} \\ &= \frac{\int_{\Omega^0}\left(g(d)\varphi_0^+ + \varphi_0^-\right)\,dV\big|_{a^{n+1},u_{\max}} - \int_{\Omega^0}\left(g(d)\varphi_0^+ + \varphi_0^-\right)\,dV\big|_{a^{n},u_{\max}}}{a^{n+1} - a^n},\end{aligned} \tag{46}$$

where the current and previous crack lengths are denoted by a^{n+1} and a^n, respectively. The internal effective strain energy density $\varphi^{int} = g(d)\varphi_0^+ + \varphi_0^-$ is integrated all over the entire reference volume Ω^0, where the maximum loading ($u = u_{\max}$) is applied for different crack lengths. Based on this algorithmic manipulation, Fig. 15 shows the characteristics of PARIS law by investigating the relationship of $\log_{10}(\Delta a/\Delta N_{cyc})$ versus $\log_{10}(\mathcal{G})$, which has shown a stable crack propagation before rupture. Furthermore, to demonstrate robustness of the phase-field crack, a reference problem by considering an equivalent real crack model is employed for comparison. The numerical treatment is described as follows:

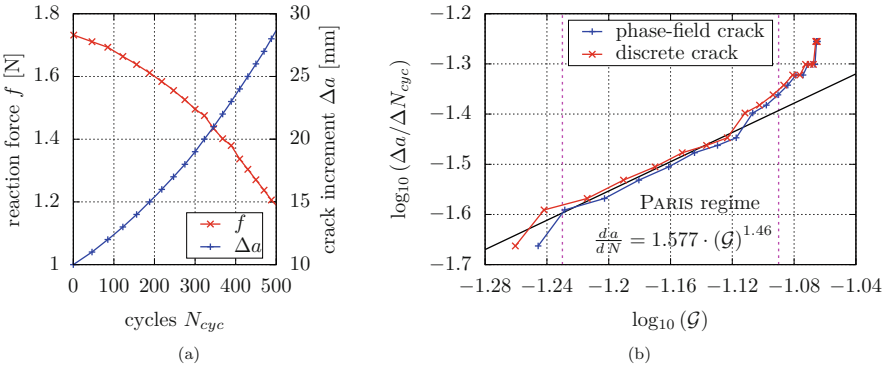

Fig. 15 (**a**) The measured reaction forces $f_{u_{\max}}$ as well as the crack length increment Δa with respect to the loading cycles and (**b**) the relationship of fatigue crack growth rate for polymeric material

- according to the phase-field fatigue solution, an approximated crack length is determined;
- a new geometry with a discrete crack is modeled with the aforementioned crack length;
- subjecting the loading to the FE model up to $u = u_{\max}$, the strain energy is subsequently integrated within the whole volume.

Thus, the energy release rate can be alternatively calculated independent of the phase-field profile. Nevertheless, the data Δa and ΔN_{cyc} are still obtained from the phase-field simulation. According to this comparison between the smeared phase-field crack and the discrete crack, the differences have shown the numerical errors of the phase-field crack approach. As aforementioned, the initial crack is prescribed by only one row of damaged elements, while the subsequent fracture evolution broadens the crack profile up to two or three rows of damaged elements. Hence, comparatively more strain energy is degraded through the phase-field degradation function $g(d)$ compared to the case with only one row of elements to represent the crack. Nevertheless, Fig. 15 does not show significant differences, and the tendencies are in good agreement to each other, which roughly captures the Paris law for fatigue fracture investigation. Paris law is approximately obtained as $d\,a/d\,N = 1.577 \cdot (\mathcal{G})^{1.46}$. As a result, the capabilities of the phase-field method for fatigue fracture evolution in polymeric material are demonstrated.

5.4 *Fatigue Analysis of a Notched Cyclically Loaded Specimen by the Material Force Method*

This example examines a double edge notched specimen subjected to cyclic loading by the present material force method. The aim of this study is to demonstrate the

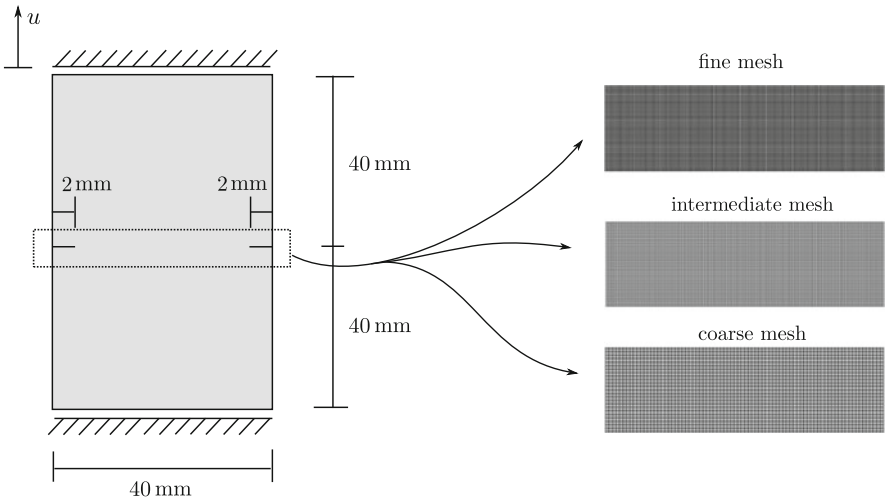

Fig. 16 Geometrical setup of the specimen and different FE models along the possible crack path

numerical capabilities of the fatigue material force method, instead of parametric studies. Therefore, the calibration of model parameters according to experimental investigations is not considered in the work at hand. The geometrical setup and the boundary conditions of the two-dimensional boundary value problem are illustrated in Fig. 16. The material constants are given as $\kappa = 0.667$ MPa, $\mu = 0.4$ MPa, $\mathcal{G}_c^0 = 4$ J/mm^2, $\chi = 0.5$, $\zeta = 0.001$, and $\alpha_{cr} = 5$. The regularization parameter is $d_l = 1$ mm. Only cyclic tensile loading is applied with a maximum displacement $u_{\max} = 4$ mm and minimum displacement $u_{\min} = 0$ mm. To investigate the effect of the distribution function, the crack path region is discretized using uniform meshes. As shown in Fig. 16, three different numerical discretizations with the size of possibly cracked elements as 0.25 mm $\times$ 0.25 mm, 0.15 mm $\times$ 0.15 mm, and 0.125 mm $\times$ 0.125 mm are taken into account, which end up with a total of 2,260, 6,650, and 9,280 elements, respectively.

To investigate the effect of the regularized accumulation explained in Eq. (43) depending upon the element size, a mesh sensitivity study is performed. The simulations including and excluding the regularized accumulation are depicted in Fig. 17. It can be observed in Fig. 17a that the number of loading cycles to failure increases almost twice by decreasing the element size around the crack path from 0.25 mm $\times$ 0.25 mm to 0.125 mm $\times$ 0.125 mm. This behavior is reasonable since the number of nodes along the crack path doubled, i.e. from 73 nodes for coarse mesh to 146 nodes for the fine mesh. In other words, the crack propagates along more nodes in the fine mesh than in the coarse mesh. Since the degradation is applied only at the crack tip and without affecting the surrounding nodes, the fatigue life doubles for the fine mesh. It is obvious from Fig. 17b that the fatigue crack propagation using the regularized accumulation is independent of the element size. Evaluating the simulation results from the coarse to fine mesh, the fatigue life increases from 378, 391 to

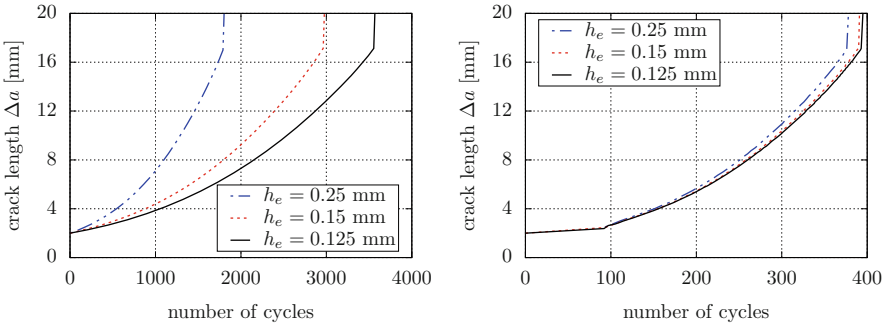

Fig. 17 Numerical results for the mesh sensitivity study by (**a**) without and (**b**) with the regularized accumulation

Fig. 18 Double logarithmic plot of crack growth rate per cycle versus material force

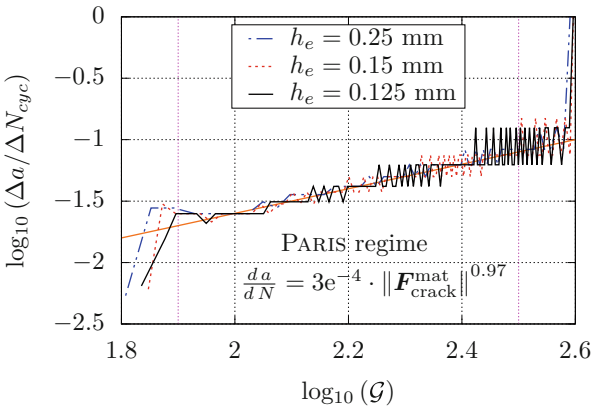

395 cycles, which shows a converging tendency for the fatigue life prediction. A finer mesh seems not to improve the numerical validation anymore.

The last investigation of this example is to obtain the classical PARIS law numerically. Similar to the algorithm presented in Sect. 5.3, a double logarithmic plot of the crack growth rate per cycle $\frac{da}{dN}$ versus $\left\|\boldsymbol{F}^{\text{mat}}_{\text{crack}}\right\|$ is shown in Fig. 18. According to the demonstration, the material force approach can properly depict the PARIS regime. The obtained PARIS law can be approximately expressed as

$$\frac{da}{dN} = C\left\|\boldsymbol{F}^{\text{mat}}_{\text{crack}}\right\|^{m}, \tag{47}$$

where $C = 3 \times 10^{-4}$ and $m = 0.97$. Furthermore, to simulate realistic engineering tasks, the model parameter of the degradation function and regularized accumulation are necessary to be further studied.

6 Conclusions

Within this work, fracture and fatigue failure of polymeric material are simulated by two approaches, e.g. the smeared phase-field model and the discrete material forces method. The theoretical foundation of these two methodologies are based upon the classical GRIFFITH criterion for brittle fracture, which characterizes that the crack starts to evolve as long as the energy release rate reaches the fracture toughness. The model parameter, the fracture toughness, is assumed to be a material constant and dependent on the material type with regard to brittle fracture. The paper at hand has successfully demonstrated the simulation of brittle fracture of polymeric material by representative numerical examples. Even comparing to experimental investigations expected good agreement is obtained.

Nevertheless, extending to fatigue failure predictions, a degrading fracture toughness is introduced to model crack growth due to cyclic loading. This novel conceptual mechanism, which is motivated by [50–52], still satisfies the general GRIFFITH criterion at the vicinity of the crack tip. This work extends the proposal of [50–52] to finite strain problems by both phase-field and material force approaches. Meanwhile, an alternative fatigue degradation function, which is dissimilar to [51], is also applied and demonstrated to capture the fatigue fracture behavior appropriately. Furthermore, for the material force approach, the accumulative internal fatigue variable has been defined as the norm of the material force at the crack tip, which differs from the internal energy type quantity defined in the phase-field modeling, yielding promising numerical results.

The work at hand only takes hyperelastic material properties into account. However, this is not sufficient for polymeric material in general, since most materials are characterized by both elastic and viscous properties simultaneously. Hence, further work is necessary to include rate-dependent features or other inelastic behaviors, to achieve a more general and comprehensive consideration of the failure prediction of polymeric materials.

References

1. Griffith AA (1921) The phenomena of rupture and flow in solids. Philos Trans R Soc Lond A 221:163–198
2. Gol'Dstein R, Salganik R (1974) Brittle fracture of solids with arbitrary cracks. Int J Fract 10:507–523
3. Pons AJ, Karma A (2010) Helical crack-front instability in mixed-mode fracture. Nature 464:85–89
4. Cooke ML, Pollard DD (1996) Fracture propagation paths under mixed mode loading within rectangular blocks of polymethyl methacrylate. J Geophys Res Solid Earth 101:3387–3400
5. Amestoy M, Leblond J (1992) Crack paths in plane situations-II. Detailed form of the expansion of the stress intensity factors. Int J Solids Struct 29:465–501

6. Lazarus V, Buchholz FG, Fulland M (2008) Comparison of predictions by mode II or mode III criteria on crack front twisting in three or four point bending experiments. Int J Fract 153:141–151
7. Gent AN, Lindley PB (1959) Internal rupture of bonded rubber cylinders in tension. Proc R Soc A 249:195–205
8. Gent AN, Park B (1984) Failure processes in elastomers at or near a rigid spherical inclusion. J Mater Sci 19:1947–1956
9. Ball JM (1982) Discontinuous equilibrium solutions and cavitation in nonlinear elasticity. Philos Trans R Soc Lond A 306:557–610
10. Lake GJ, Lindley PB (1965) Role of ozone in dynamic cut growth of rubber. J Appl Polym Sci 9:2031–2045
11. Robertson CG, Stoček R, Kipscholl C, Mars WV (2019) Characterizing the intrinsic strength (fatigue threshold) of natural rubber/butadiene rubber blends. Tire Sci Technol 47:292–307
12. Knauss WG (2015) A review of fracture in viscoelastic materials. Int J Fract 196:99–146
13. Rice JR (1968) A path independent integral and the approximate analysis of strain concentration by notches and cracks. J Appl Mech 35:379–386
14. Hocine NA, Abdelaziz MN, Mesmacque G (1998) Experimental and numerical investigation on single specimen methods of determination of J in rubber materials. Int J Fract 94:321–338
15. Hocine NA, Abdelaziz MN, Imad A (2002) Fracture problems of rubbers: J-integral estimation based upon η factors and an investigation on the strain energy density distribution as a local criterion. Int J Fract 117:1–23
16. Schapery RA (1984) Correspondence principles and a generalized J integral for large deformation and fracture analysis of viscoelastic media. Int J Fract 25:195–223
17. Kroon M (2011) Steady-state crack growth in rubber-like solids. Int J Fract 169:49–60
18. Kroon M (2014) Energy release rates in rubber during dynamic crack propagation. Int J Solids Struct 51:4419–4426
19. Ambrosio L, Tortorelli VM (1990) Approximation of functionals depending on jumps by elliptic functionals via convergence. Commun Pure Appl Math 43:999–1036
20. Francfort GA, Marigo JJ (1998) Revisiting brittle fracture as an energy minimization problem. J Mech Phys Solids 46:1319–1342
21. Bourdin B, Francfort GA, Marigo JJ (2000) Numerical experiments in revisited brittle fracture. J Mech Phys Solids 48:797–826
22. Hakim V, Karma A (2009) Laws of crack motion and phase-field models of fracture. J Mech Phys Solids 57:342–368
23. Miehe C, Welschinger F, Hofacker M (2010) Thermodynamically consistent phase-field models of fracture: Variational principles and multi-field FE implementations. Int J Numer Methods Eng 83:1273–1311
24. Pham K, Amor H, Marigo J, Maurini C (2011) Gradient damage models and their use to approximate brittle fracture. Int J Damage Mech 20:618–652
25. Amor H, Marigo JJ, Maurini C (2009) Regularized formulation of the variational brittle fracture with unilateral contact: Numerical experiments. J Mech Phys Solids 57:1209–1229
26. Miehe C, Hofacker M, Welschinger F (2010) A phase field model for rate-independent crack propagation: Robust algorithmic implementation based on operator splits. Comput Methods Appl Mech Eng 199:2765–2778
27. Steinke C, Kaliske M (2019) A phase-field crack approximation approach based on directional stress decomposition. Comput Mech 63:1019–1046
28. Storm J, Supriatna D, Kaliske M (2020) The concept of Representative Crack Elements (RCE) for phase-field fracture - Anisotropic elasticity and thermo-elasticity. Int J Numer Methods Eng 121:779–805
29. Yin B, Steinke C, Kaliske M (2020) Formulation and implementation of strain rate dependent fracture toughness in context of the phase-field method. Int J Numer Methods Eng 121:233–255
30. Yin B, Kaliske M (2020) Fracture simulation of viscoelastic polymers by the phase-field method. Comput Mech 65:293–309

31. Shen R, Waisman H, Guo L (2019) Fracture of viscoelastic solids modeled with a modified phase field. Comput Methods Appl Mech Eng 346:862–890
32. Schänzel LM (2015) Phase field modeling of fracture in rubbery and glassy polymers at finite thermo-viscoelastic deformations. Ph.D. thesis. Universität Stuttgart
33. Loew PJ, Peters B, Beex LAA (2019) Rate-dependent phase-field damage modeling of rubber and its experimental parameter identification. J Mech Phys Solids 127:266–294
34. Ambati M, Gerasimov T, De Lorenzis L (2015) Phase-field modeling of ductile fracture. Comput Mech 55:1017–1040
35. Miehe C, Hofacker M, Schänzel L, Aldakheel F (2015) Phase field modeling of fracture in multi-physics problems. part II. coupled brittle-to-ductile failure criteria and crack propagation in thermo-elastic-plastic solids. Comput Methods Appl Mech Eng 294:486–522
36. Kuhn C, Noll T, Müller R (2016) On phase field modeling of ductile fracture. Surv Appl Math Mech 39:35–54
37. Borden MJ, Hughes TJR, Landis CM, Anvari A, Lee IJ (2016) A phase-field formulation for fracture in ductile materials: Finite deformation balance law derivation, plastic degradation, and stress triaxiality effects. Comput Methods Appl Mech Eng 312:130–166
38. Yin B, Kaliske M (2020) A ductile phase-field model based on degrading the fracture toughness: Theory and implementation at small strain. Comput Methods Appl Mech Eng 366:113068
39. Gültekin O, Dal H, Holzapfel GA (2018) Numerical aspects of anisotropic failure in soft biological tissues favor energy-based criteria: A rate-dependent anisotropic crack phase-field model. Comput Methods Appl Mech Eng 331:23–52
40. Teichtmeister S, Kienle D, Aldakheel F, Keip MA (2017) Phase field modeling of fracture in anisotropic brittle solids. Int J Non-Linear Mech 97:1–21
41. Yin B, Kaliske M (2020) An anisotropic phase-field model based on the equivalent crack surface energy density at finite strain. Comput Methods Appl Mech Eng 369:113202
42. Gurtin ME (2000) Configurational forces as basic concepts of continuum physics. Springer, New York
43. Kienzler R, Herrmann G (2000) Mechanics in material space: with applications to defect and fracture mechanics. Springer, Berlin
44. Maugin GA (1995) Material forces: Concepts and applications. Appl Mech Rev 48:213–245
45. Maugin GA (2010) Configurational forces: thermomechanics, physics, mathematics, and numerics. CRC Press, Boca Raton
46. Miehe C, Gürses E (2007) A robust algorithm for configurational-force-driven brittle crack propagation with R-adaptive mesh alignment. Int J Numer Methods Eng 72:127–155
47. Braun M (1997) Configurational forces induced by finite-element discretization. Proc Estonian Acad Sci Phys Math 35:379–386
48. Müller R, Maugin GA (2002) On material forces and finite element discretizations. Comput Mech 29:52–60
49. Steinke C, Özenç K, Chinaryan G, Kaliske M (2016) A comparative study of the r-adaptive material force approach and the phase-field method in dynamic fracture. Int J Fract 201:97–118
50. Alessi R, Vidoli S, De Lorenzis L (2018) A phenomenological approach to fatigue with a variational phase-field model: The one-dimensional case. Eng Fract Mech 190:53–73
51. Carrara P, Ambati M, Alessi R, De Lorenzis L (2020) A framework to model the fatigue behavior of brittle materials based on a variational phase-field approach. Comput Methods Appl Mech Eng 361:112731
52. Seiler M, Linse T, Hantschke P, Kästner M (2020) An efficient phase-field model for fatigue fracture in ductile materials. Eng Fract Mech 224:106807
53. Holzapfel GA (2000) Nonlinear solid mechanics: A continuum approach for engineering. Wiley, Chichester
54. Borden MJ, Hughes TJR, Landis CM, Verhoosel CV (2014) A higher-order phase-field model for brittle fracture: Formulation and analysis within the isogeometric analysis framework. Comput Methods Appl Mech Eng 273:100–118

55. Alessi R, Ambati M, Gerasimov T, Vidoli S, De Lorenzis L (2018) Comparison of phase-field models of fracture coupled with plasticity. Advances in computational plasticity: A book in honour of D. Roger J. Owen, pp 1–21
56. Zhang X, Vignes C, Sloan SW, Sheng DC (2017) Numerical evaluation of the phase-field model for brittle fracture with emphasis on the length scale. Comput Mech 59:737–752
57. Mandal T, Nguyen VP, Wu JY (2019) Length scale and mesh bias sensitivity of phase-field models for brittle and cohesive fracture. Eng Fract Mech 217:106532
58. Hofacker M (2013) A thermodynamically consistent phase field approach to fracture. Ph.D. thesis. Universität Stuttgart
59. Bischoff PH, Perry SH (1991) Compressive behaviour of concrete at high strain rates. Mater Struct 24:425–450
60. Fineberg J, Gross SP, Marder M, Swinney H (1992) Instability in the propagation of fast cracks. Am Phys Soc 45:5146–5154
61. Özenç K (2016) Approaches to model failure of materials by configurational mechanics: theory and numerics. Ph.D. thesis, Technische Universität Dresden
62. Borden MJ (2012) Isogeometric analysis of phase-field models for dynamic brittle and ductile fracture. Ph.D thesis. The University of Texas at Austin
63. Kuhn C, Schlüter A, Müller R (2015) On degradation functions in phase field fracture models. Comput Mater Sci 108:374–384
64. Kuhn C (2013) Numerical and analytical investigation of a phase field model for fracture. Ph.D. thesis. Technischen Universität Kaiserslautern
65. Eshelby JD (1951) The force on an elastic singularity. Philos Trans R Soc Lond 244:87–112
66. Özenç K, Kaliske M (2014) An implicit algorithm to assess the failure mechanism of elastomeric continua. Int J Numer Methods Eng 100:669–688
67. Miehe C, Schänzel LM (2014) Phase field modeling of fracture in rubbery polymers. Part I: Finite elasticity coupled with brittle failure. J Mech Phys Solids 65:93–113

Adv Polym Sci (2021) 286: 377–420
https://doi.org/10.1007/12_2020_76

Published online: 12 January 2021

Viscoelastic Crack Propagation: Review of Theories and Applications

N. Rodriguez, P. Mangiagalli, and B. N. J. Persson

Contents

Abstract We review a theory of crack propagation in viscoelastic solids. We consider both cracks in infinite systems and in finite-sized systems. As applications of the theory we consider two adhesion problems, namely pressure sensitive

N. Rodriguez
BD Medical-Pharmaceutical Systems, Prefillable Systems, Franklin Lakes, NJ, USA

P. Mangiagalli
Sanofi Vitry, Vitry-sur-Seine, France

B. N. J. Persson (✉)
PGI-1, Research center FZ Jülich, FZ Jülich, Germany
e-mail: b.persson@fz-juelich.de

adhesives and the ball-flat adhesion problem. We also study crack propagation in the pig skin dermis, which is of medical relevance, and rubber wear in the context of tires.

1 Introduction

The cohesive strength of solids usually depends on crack-like defects, and the energy to propagate cracks in the material. Similarly, the strength of the adhesive bond between two solids is usually determined by the energy to propagate interfacial cracks. Here we are interested in crack propagation in viscoelastic materials, such as rubber [1–19]. This topic is of great importance, e.g., the wear of tires or wiper blades resulting from the removal of small rubber particles by crack propagation [20].

In this article we will review a theory for crack propagation in viscoelastic solids. We will consider crack propagation in both infinite-sized solids and finite-sized solids. The latter is also relevant for rubber wear where small particles (often micrometer sized) are removed from the rubber surface by the high tensile stresses, which exist in the asperity contact regions during sliding. We will also consider interfacial crack propagation, which is important for adhesion. As applications of the theory we consider: (a) adhesion for the sphere-flat contact problem, and for pressure sensitive adhesives; (b) crack propagation in the skin dermis as may be relevant for intradermal fluid injection; and (c) rubber wear for the case of a tread block sliding on a road surface.

2 Theory of Crack Propagation in Viscoelastic Solids

Rubber wear usually involves crack propagation in the bulk of the material (see Fig. 1a). For a bulk crack, the stress and strain are usually very high close to the crack tip, and nonlinear effects, involving the breaking of strong covalent bonds, chain pull-out, and cavity formation, will occur close to the crack tip. This region of space is denoted the crack tip process zone. The detailed nature of the crack tip process zone is still a research topic, especially in cases involving heterogeneous media.

Another important set of applications involves interfacial crack propagation, e.g., between rubber materials and a hard countersurface (see Fig. 1b). In this case the strain and stresses at a crack tip can be much smaller, in particular if the interaction at the interface is dominated by the weak van der Waals interaction. In this case nonlinear viscoelastic effects may occur only in a very small region close to the crack tip where the bond breaking occurs.

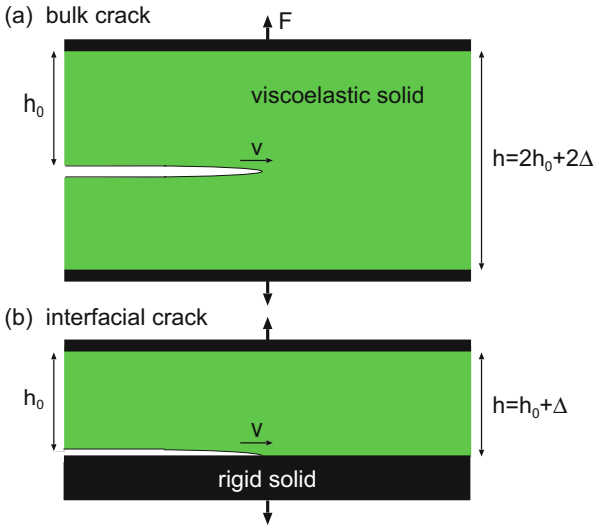

Fig. 1 (**a**) Crack propagation in the bulk of a viscoelastic solid (cohesive crack propagation), and (**b**) at the interface between a viscoelastic solid and a countersurface (adhesive crack propagation)

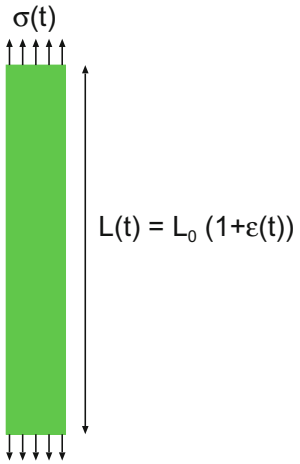

Fig. 2 The length of a strip of rubber exposed to the stress $\sigma(t)$ will fluctuate as $L(t) = L_0(1 + \varepsilon(t))$, where L_0 is the unperturbed length and $\varepsilon(t)$ the strain at time t

2.1 Viscoelastic Modulus

Assume that a rectangular block of a linear viscoelastic material is exposed to the stress $\sigma(t)$. This will result in a strain $\varepsilon(t)$ (see Fig. 2). If we write

$$\sigma(t) = \int_{-\infty}^{\infty} d\omega \; \sigma(\omega) e^{-i\omega t},$$

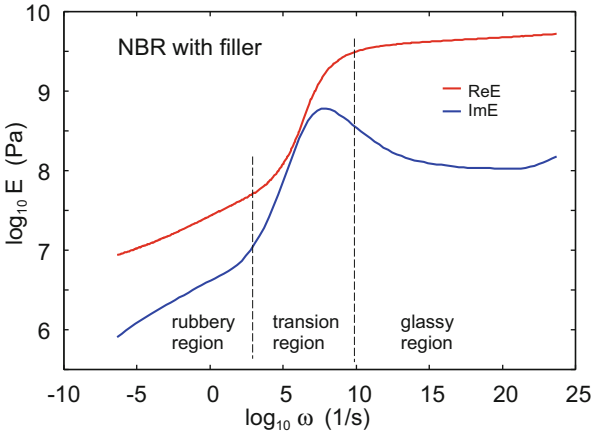

Fig. 3 The real and the imaginary parts of the viscoelastic modulus as a function of frequency ω (log–log scale). For an NBR rubber compound with filler at $T = 20^{\circ}\mathrm{C}$

$$\varepsilon(t) = \int_{-\infty}^{\infty} d\omega\ \varepsilon(\omega) e^{-i\omega t},$$

then

$$\sigma(\omega) = E(\omega)\varepsilon(\omega). \tag{1}$$

For viscoelastic materials like rubber, the viscoelastic modulus $E(\omega)$ is a complex quantity, where the imaginary part is related to energy dissipation (transfer of mechanical energy into the random thermal motion). In a typical case $E(\omega)$ depends on the frequency as indicated in Fig. 3 (log–log scale). For low frequencies (or high temperatures), the rubber responds as a soft elastic body (rubbery region) with a viscoelastic modulus $E(\omega)$ of order $\approx$1 MPa for the rubber used in tires, or for the human skin dermis, or $\approx$1 kPa for the weakly crosslinked rubber used in pressure sensitive adhesives. At very high frequencies (or low temperatures), it is behaves as a stiff elastic solid (glassy region) with the viscoelastic modulus $E(\omega)$ of order $\approx$1 GPa. In the transition region it exhibits strong internal damping, and this is the region important for energy loss processes, e.g., involved in rubber friction. In this context the loss tangent $\mathrm{Im}E(\omega)/\mathrm{Re}E(\omega)$ is very important and is shown in Fig. 4.

The viscoelastic modulus $E(\omega)$ is a causal linear response function. This implies that the real and the imaginary parts of $E(\omega)$ are not independent functions, but given one of them, one can calculate the other one using a Kramers–Kronig equation [21]. One can also derive sum rules, and the most important in the present context is

$$\frac{1}{E_0} - \frac{1}{E_1} = \frac{2}{\pi}\int_0^{\infty} d\omega \frac{1}{\omega}\mathrm{Im}\frac{1}{E(\omega)}, \tag{2}$$

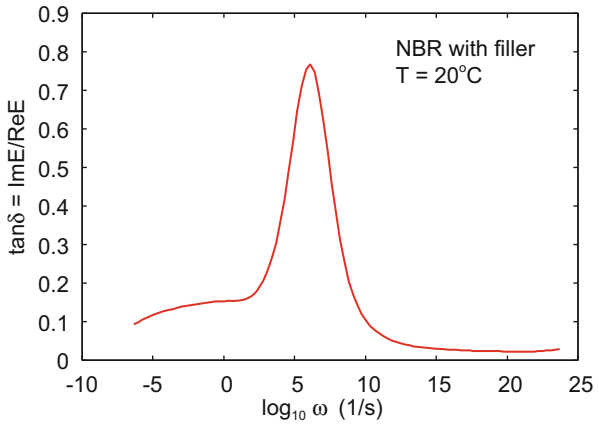

Fig. 4 The loss tangent $\tan\delta = \mathrm{Im}E/\mathrm{Re}E$ as a function of the logarithm of the frequency ω. For the NBR rubber compound shown in Fig. 3 at $T = 20^{\circ}\mathrm{C}$

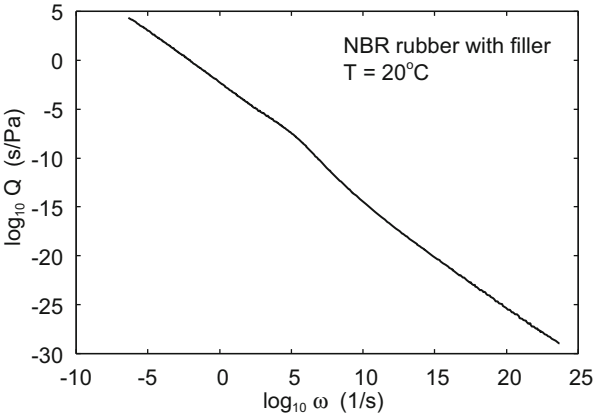

Fig. 5 The crack loss function $Q(\omega) = (1/\omega)\mathrm{Im}[1/E(\omega)]$ as a function of the logarithm of the frequency ω. For the NBR rubber compound shown in Fig. 3 at $T = 20^{\circ}\mathrm{C}$

where $E_0 = E(0)$ is the static ($\omega = 0$) modulus, and $E_1 = E(\infty)$ the modulus for infinite high frequency $\omega = \infty$. The function

$$Q(\omega) = \frac{1}{\omega}\mathrm{Im}\frac{1}{E(\omega)} \tag{3}$$

occurring in the integral in (1) is very important in viscoelastic crack propagation, and we will denote it as the crack loss function. It is shown in Fig. 5 for the same rubber compound (acrylonitrile butadiene [NBR] with filler particles) as in Figs. 3 and 4. Note that $Q(\omega)$ decays monotonically with increasing frequencies and is hence largest in the rubbery region in spite of the small magnitude of the damping in this frequency region. This has important implications for the finite-sized effect in rubber crack propagation (see below).

2.2 Opening Crack in Infinite Solid

We consider first an opening crack in an infinite viscoelastic solid characterized by the viscoelastic modulus $E(\omega)$, which depends on the frequency ω. Consider a crack loaded in tension (mode I) (see Fig. 1). The energy dissipated per unit time and unit length of the crack line, P, is given by

$$P = \int d^2x \, \dot{\varepsilon}_{ij}\sigma_{ij}, \tag{4}$$

where $\dot{\varepsilon}_{ij}$ is the strain rate tensor and σ_{ij} the stress tensor (summation over repeated indices is implicitly understood). For an opening crack, the stress field close to the crack tip has the universal form (also for a viscoelastic solid):

$$\sigma(\mathbf{x}, t) \approx \frac{K}{(2\pi|\mathbf{x} - \mathbf{v}t|)^{1/2}}, \tag{5}$$

where K is the stress intensity factor and $\mathbf{v}$ is the velocity of the crack tip. Using (4) and (5) and the relation (1) between stress and strain, one can calculate [8]

$$P = vK^2 \frac{2}{\pi} \int_0^{\omega_c} d\omega F(\omega) Q(\omega), \tag{6}$$

where we have introduced a high-frequency cut-off $\omega_c = 2\pi v/a$, where a is the radius of the crack tip. The function:

$$F(\omega) = \left[1 - \left(\frac{\omega}{\omega_c}\right)^2\right]^{1/2}. \tag{7}$$

Now, let us consider the energy conservation condition relevant to the crack propagation. In the present case, the elastic energy stored in the solid in front of the crack tip is dissipated at the crack tip. The flow of elastic energy into the crack is given by vG (where G is the crack propagation energy per unit surface area), which must equal the fracture energy term vG_0 (the energy dissipated in the crack tip process zone) plus the bulk viscoelastic dissipation term P given by (6). Energy conservation gives

$$vG = vG_0 + P. \tag{8}$$

Using (6) and (8) gives

$$G = G_0 + K^2 \frac{2}{\pi} \int_0^{\omega_c} d\omega F(\omega) Q(\omega).$$

Using the standard relation $G = K^2/E_0$ from the theory of cracks [22], we obtain

$$G = \frac{G_0}{1 - E_0 \frac{2}{\pi} \int_0^{\omega_c} d\omega F(\omega) Q(\omega)}. \tag{9}$$

Equation (9) depends on the cutoff length a and (9) is of limited practical importance unless we have a way of determining this length. Experiments have shown that the crack tip radius in polymers increases with increasing speed of the crack tip [10]. We choose a equal to the radius of the crack tip, which we determine as follows. The stress at the crack tip must be equal to the stress necessary to break the atomic bonds at the tip in order for the tip to propagate. If σ_c denotes this stress, which is a characteristic property of the material in question, we obtain, from (5),

$$\sigma_c = \frac{K}{(2\pi a)^{1/2}}, \tag{10}$$

where a depends on the crack tip velocity. Combining this with $G = K^2/E_0$ gives

$$G = \frac{2\pi a \sigma_c^2}{E_0}. \tag{11}$$

Combining (9) and (11) gives

$$\frac{a_0}{a} = 1 - E_0 \frac{2}{\pi} \int_0^{\omega_c} d\omega F(\omega) Q(\omega), \tag{12}$$

where $\omega_c = 2\pi v/a$ and $a_0 = E_0 G_0/(2\pi\sigma_c^2)$. Since ω_c depends on a, this is an implicit equation for $a = a(v)$. Thus the theory gives both the (velocity-dependent) radius of the crack tip, $a(v)$, and the crack propagation energy, $G(v) = G_0 a(v)/a_0$.

For large crack tip velocities, $G(v) \approx G_0 E_I/E_0$ or $a(v) \approx a_0 E_I/E_0$. The ratio between the high- and low-frequency modulus, E_I/E_0, is typically very large, e.g., $\sim$1000 for the rubber in Fig. 3. Hence for large crack tip velocity, the denominator in (9) will almost vanish. Thus any small error in the evaluation of the integral will result in big numerical error for $G(v)$ and $a(v)$. For numerical accuracy reason, it is therefore useful to rewrite (12) using the relation (2). If we eliminate E_0 in (12) using (2), we get

$$\frac{a_0}{a} = 1 - \frac{E_1 \frac{2}{\pi} \int_0^{\omega_a} d\omega \frac{1}{\omega} F(\omega) \mathrm{Im} \frac{1}{E(\omega)}}{1 + E_1 \frac{2}{\pi} \int_0^{\infty} d\omega \frac{1}{\omega} \mathrm{Im} \frac{1}{E(\omega)}}. \tag{13}$$

Since $E(\omega)$ typically varies with ω over very many decades in frequency, for the numerical evaluation of the integrals in (13) it is convenient to write (see [9]) $\omega = \omega_0 e^{\xi}$, so that if ω varies over ~30 decades, ξ varies only by a factor ~100.

2.3 Numerical Results

We now present some numerical results for the dependency of the crack propagation energy $G(v)$ on the crack tip velocity. We first consider the highly idealized three-element viscoelastic model shown in Fig. 6. The low-frequency modulus $E(0) = E_0$ and the high-frequency modulus $E(\infty) = E_1$ and the viscosity η are indicated in the figure. Real rubber materials have a very wide range of relaxation times while the present model is characterized by a single relaxation time τ. However, this model has been used in most model studies so far and is therefore a good test case.

Figure 7 shows the crack propagation energy G (in units of adiabatic value G_0) as a function of the crack tip speed v (in units of a_0/τ) (log–log scale) for the three-element viscoelastic model shown in Fig. 6. In the calculation we have assumed $E_1/E_0 = 100$ and that is the reason for why G/G_0 increases from 1 to 100 with increasing crack tip speed.

The results presented in Fig. 7 are virtually identical to the numerical results obtained by Greenwood using the Barenblatt process zone model [11]. This shows that the detailed nature of the process zone is not very important as the present study uses a completely different description of the process zone (just a cut-off radius $a(v)$) than in the Barenblatt model where a linearly extended process zone is used. The advantage of the present approach is that it can trivially be applied to real materials using the measured viscoelastic modulus $E(\omega)$.

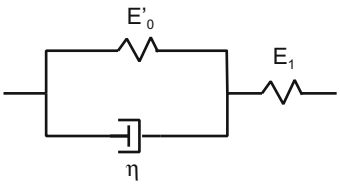

Fig. 6 Three-element viscoelastic model used in model calculation of the crack propagation energy $G(v)$. The low-frequency modulus $E(0) = E_0 = E_0' E_1/(E_0' + E_1)$ and the high-frequency modulus $E(\infty) = E_1$ and the viscosity η are indicated

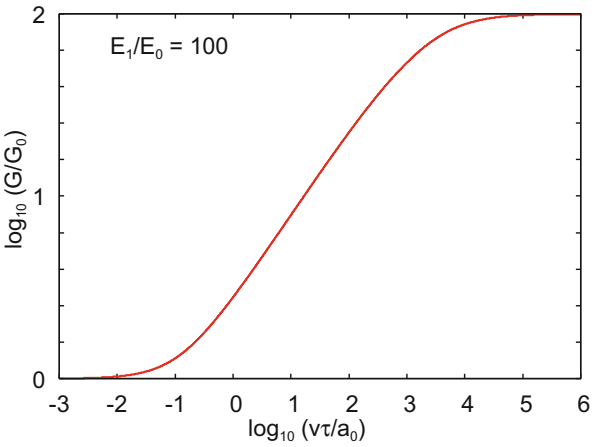

Fig. 7 The crack propagation energy G (in units of adiabatic value G_0) as a function of the crack tip speed v (in units of a_0/τ) (log–log scale) for the three-element viscoelastic model shown in Fig. 6

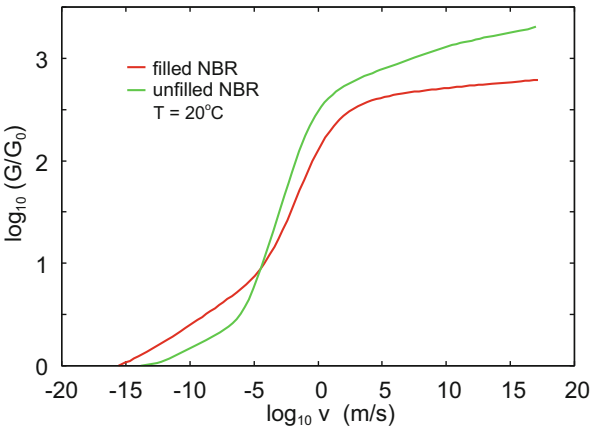

Fig. 8 The crack propagation energy G (in units of adiabatic value G_0) as a function of the crack tip speed v (log–log scale) for filled and unfilled NBR rubber at $T = 20^{\circ}$C. In the calculations we have used the measured low-strain viscoelastic modulus (shown in Fig. 3 for the filled NBR compound)

To illustrate this, in Fig. 8 we show the crack propagation energy G (in units of adiabatic value G_0), as a function of the crack tip speed v (log–log scale) for filled and unfilled NBR rubber at $T = 20^{\circ}$C. In the calculations we have used the measured low-strain viscoelastic modulus (shown in Fig. 3 for the filled NBR compound). For the unfilled compound, $E_1/E_0 > 1000$, and this explains the large increase in $G(v)$ with increasing crack speed.

2.4 *Opening Crack in Finite Solid*

Most theories of cracks in viscoelastic solids assume an infinite large system [4, 5, 8, 9, 12, 13, 23]. A few studies exist for the slab geometry [24–29], where the solid is infinite in the x-direction but finite in the perpendicular z-direction, say with

thickness h_0 (see Fig. 1). If the surfaces $z = 0$ and $z = h_0$ are clamped, the stress field from the crack tip in a slab is screened by the solid walls, in which case the slab geometry is similar to a finite solid with linear size $L \approx h_0$, and the results presented below are approximately valid also for the slab geometry.

The viscoelastic energy dissipation is determined by an integral over the relevant frequencies of the crack dissipation function $Q(\omega)$. We show $Q(\omega)$ for a typical case in Fig. 5. The biggest contribution to the integral over frequencies of $Q(\omega)$ will be from the lowest frequency region in spite of the fact that in this region the loss tangent $\tan\delta$ is very small. Hence, any effect that influences the low-frequency part of the viscoelastic modulus can have a big impact on the crack propagation energy. One such influence is finite-sized effects.

The theory described in Sect. 2.2 (see also [8, 9, 12, 13]) is for an opening crack in an infinite viscoelastic media. The theory predicts that as the crack tip velocity $v \to \infty$, the crack propagation energy $G \to (E_1/E_0)G_0$, where G_0 is the crack propagation energy as $v \to 0$, where no viscoelastic energy dissipation takes place. The high- and low-frequency modulus, E_1 and E_0, respectively, both are real and can be obtained from the complex viscoelastic modulus $E(\omega)$ as the frequency $\omega \to \infty$ and $\omega \to 0$, respectively.

For an infinite solid, there will always be a region far enough from the crack tip where the solid can be considered as purely elastic and characterized by the static (or low-frequency) modulus $E_0 = E(\omega = 0)$. This follows from the observation that if the crack tip propagates with the velocity v the time-dependent deformations of the rubber at a distance r from the crack tip are characterized by the frequency $\omega = v/r$. Thus, as $r \to \infty$ we get $\omega \to 0$. However, all solids have a finite extent, say with linear dimension L. In this case $r < L$ and hence $\omega > v/L$. It follows that for high crack tip speed, the frequency ω will be very large *everywhere*, and the rubber will be in the glassy, purely elastic, state everywhere in the solid. Hence in this limiting case there is no viscoelastic energy dissipation, i.e., $G(v) \approx G_0$ for large enough v. This is not the case for infinite solids where $G(v) = (E_1/E_0)G_0$ for large enough v.

Here we will study how the finite size of real solid objects influences the crack propagation energy. For example, consider the pull-off of a rubber ball from a flat surface. This can be considered as a circular opening crack propagating toward the center of the circular contact region. Let L be the linear size of the contact area. The region where the viscoelastic crack propagation theory is valid is limited to distances from the crack tip $a < r < L$, where a is the crack tip radius. Some time-dependent deformations of the rubber will occur also for $r > L$ in this case, but only for $r < L$ the stress field (as a function of r) has the inverse square-root singular nature characteristic of crack-like defects. When the crack tip moves with the velocity v, the viscoelastic spectra will be probed in the frequency range $2\pi v/L < \omega < 2\pi v/a$. We denote $\omega_L = 2\pi v/L$ and $\omega_a = 2\pi v/a$.

We can (approximately) use the theory for viscoelastic crack propagation in an infinite medium also for a finite system of linear size L by using the following procedure: We replace the measured viscoelastic modulus $E(\omega)$ with another modulus $\tilde{E}(\omega)$ where $\mathrm{Im}\tilde{E}^{-1}(\omega) = \mathrm{Im}E^{-1}(\omega)$ for $\omega > \omega_L$ and $\mathrm{Im}\tilde{E}^{-1}(\omega) = 0$ for $\omega < \omega_L$.

This implies that viscoelastic energy dissipation will only occur for distances from the crack tip $r < L$. Given $\mathrm{Im}\tilde{E}^{-1}(\omega)$, we obtain $\mathrm{Re}\tilde{E}^{-1}(\omega)$ using a Kramers–Kronig relation [21], which holds for all causal linear response functions. We can choose the high-frequency modulus (which is real) $\tilde{E}_1 = E_1$, but the static (or low-frequency modulus) $\tilde{E}_0 > E_0$, which is expected to be of order $\tilde{E}_0 \approx \mathrm{Re}E(\omega_L)$.

To obtain $G(v)$ for a finite-sized solid, we replace $E(\omega)$ in (13) with $\tilde{E}(\omega)$ defined so that $\mathrm{Im}\tilde{E}^{-1}(\omega) = \mathrm{Im}E^{-1}(\omega)$ for $\omega > \omega_L$ and $\mathrm{Im}\tilde{E}^{-1}(\omega) = 0$ for $\omega < \omega_L$. We get

$$\frac{a_0}{a} = 1 - \frac{E_1 \frac{2}{\pi} \int_{\omega_L}^{\omega_a} d\omega \frac{1}{\omega} F(\omega) \mathrm{Im} \frac{1}{E(\omega)}}{1 + E_1 \frac{2}{\pi} \int_{\omega_L}^{\infty} d\omega \frac{1}{\omega} \mathrm{Im} \frac{1}{E(\omega)}}. \tag{14}$$

Note that as $v \to 0$ and $v \to \infty$, $a \to a_0$ and $G \to G_0$.

Figure 9 shows the viscoelastic enhancement factor G_{open}/G_0 as a function of the crack-tip speed for the rheological model shown in Fig. 6. Results are shown for the system sizes $L = 1$ μm, 1 cm, and for infinite system.

Figure 10 shows the viscoelastic enhancement factor G_{open}/G_0 as a function of the crack tip speed for filled NBR at $T = 20^{\circ}$C. Results are shown for the system sizes $L = 1$ μm, 1 cm, and for infinite system. The system size $L = 1$ cm is typical for the sample size used in studies of the crack propagation in macroscopic rubber samples and is clearly not equivalent to the infinite sample size. The reason for the strong finite-sized effects is that the function $Q(\omega)$ decreases monotonically with increasing frequencies, making the integrals in (14) very sensitive to the lower cut-off

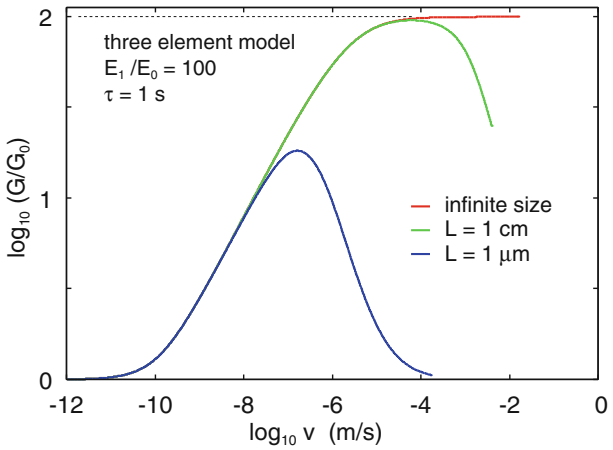

Fig. 9 The viscoelastic enhancement factor G_{open}/G_0 as a function of the crack-tip speed for the rheological model shown in Fig. 6. Results are shown for the system sizes $L = 1$ μm, 1 cm, and for infinite system

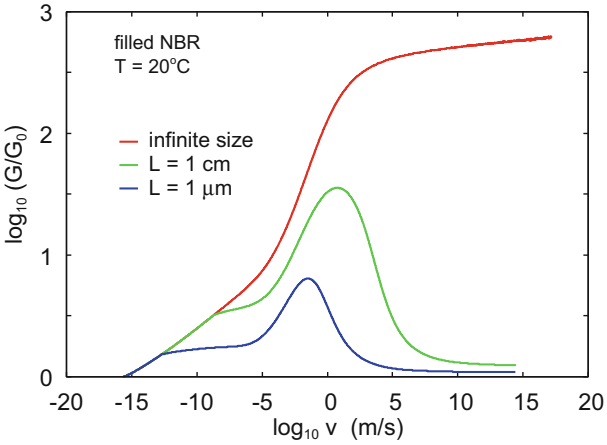

Fig. 10 The viscoelastic enhancement factor G_{open}/G_0 as a function of the crack tip speed for filled NBR at $T = 20^{\circ}C$. Results are shown for the system sizes $L = 1$ μm, 1 cm, and for infinite system

frequency ω_L determined by the size of the system. Note that for the finite-sized sample there is a maximum in the $G(v)$-curve, corresponding to an instability in the crack tip motion.

Note that for the three-element model used in Fig. 9 finite sized effects are less important than for real rubber materials as in Fig. 10. This must reflect the differences in the viscoelastic properties of real rubber materials then in the three-element model. Thus, real rubber materials are characterized by a very broad distribution of relaxation times typically extending over more than 10 decades in time compared to the single relaxation time characterizing the three-element rheological model.

2.5 *Role of Temperature*

The crack propagation energy $G(v, T) = G_0(1 + f(v, T))$ depends strongly on the temperature. The viscoelastic factor $1 + f(v, T)$ depends on temperature via the temperature–frequency shift factor a_T since $f(v, T) = f(va_T, T_0)$, where T_0 is a reference temperature with $a_{T_0} = 1$. Thus, increasing the temperature shifts the factor $1 + f(v, T)$ to higher sliding speeds. The factor $G_0 = G_0(v, T)$ depends also on the crack tip speed and the temperature because breaking the bonds in the crack tip process zone is a thermally activated, stress-aided process [30, 31]. This temperature effect is particularly important for low-energy bonds, e.g., for weak adhesive bonds [30–33].

In a recent study [34] using fluorogenic mechanochemistry with quantitative confocal microscopy mapping, it was found how many and where covalent bonds are broken as an elastomer fractures. The measurements reveal that bond scission

near the crack plane can be delocalized over up to hundreds of micrometers and can increase G_0 by a factor of ≈100 depending on temperature and stretch rate, pointing to an intricated coupling between strain rate-dependent viscous dissipation and strain-dependent irreversible network scission. These findings show that energy dissipated by covalent bond scission accounts for a much larger fraction of the total fracture energy than previously believed.

At low crack tip speed, the temperature will everywhere be close to surrounding (background) temperature, but for a fast moving crack tip, the energy dissipated close to the crack tip will not have time to diffuse away resulting in a higher temperature close to the crack tip. Including this temperature increase in the theory is a complex topic addressed in [12, 13, 35].

We note that it is possible to reformulate (14) as an integral over temperature rather than frequency, which is useful if the viscoelastic modulus has been measured only as a function of temperature for one frequency. Assume that the viscoelastic modulus has been measured as a function of temperature for the frequency $\omega = \omega_1$, i.e., $E(\omega_1, T)$ is known. Let T_1 denote the temperature of interest so that (14) takes the form:

$$\frac{a_0}{a} = 1 - \frac{E_1 \frac{2}{\pi} \int_{\omega_L}^{\omega_a} d\omega \frac{1}{\omega} F(\omega) \mathrm{Im} \frac{1}{E(a_{T_1}\omega)}}{1 + E_1 \frac{2}{\pi} \int_{\omega_L}^{\infty} d\omega \frac{1}{\omega} \mathrm{Im} \frac{1}{E(a_{T_1}\omega)}}. \tag{15}$$

where $E(a_{T_1}\omega) = E(\omega, T_1) = E(a_{T_1}\omega, T_0)$. Next, let us write $\omega = \omega_1 a_T / a_{T_1}$. We consider T as the new integration variable and get

$$d\omega \frac{1}{\omega} = dT (\ln a_T)',$$

where $(\ln a_T)' = d(\ln a_T)/dT$. Denoting the solution to $\omega_a = \omega_1 a_T / a_{T_1}$ as T_a and to $\omega_L = \omega_1 a_T / a_{T_1}$ as T_L, we can write (15) as

$$\frac{a_0}{a} = 1 - \frac{E_1 \frac{2}{\pi} \int_{T_a}^{T_L} dT \, (-\ln a_T)' \, F(T) \mathrm{Im} \frac{1}{E(T)}}{1 + E_1 \frac{2}{\pi} \int_{0}^{T_L} dT \, (-\ln a_T)' \, \mathrm{Im} \frac{1}{E(T)}}, \tag{16}$$

where $E(T) = E(a_{T_1}\omega, T_0) = E(a_{T_1}[\omega_1 a_T / a_{T_1}], T_0) = E(a_T \omega_1, T_0) = E(\omega_1, T)$ and

$$F(T) = \left[1 - \left(\frac{\omega_1}{\omega_a} \frac{a_T}{a_{T_1}}\right)^2\right]^{1/2}. \tag{17}$$

2.6 Closing Crack

When an opening crack propagates in the bulk of a viscoelastic solid the breaking of the bonds in the crack tip process zone is usually an irreversible process: the broken (dangling) bonds formed during the crack opening react quickly with molecules from the atmosphere, or with mobile molecules in the solid. Hence if the external crack driving force is removed, no closing crack propagation involving the reformation of the original bonds will occur. However, for interfacial crack propagation, the situation may be very different. Thus, in many cases rubber binds to a countersurface mainly with the weak and long-ranged van der Waals bonds. In this case the bonds broken during crack opening and the bonds formed during crack closing may be very similar.

For an opening crack in a viscoelastic solid, energy conservation requires that $vG = vG_0 + P$, i.e., $G > G_0$. For a closing crack, the energy conservation condition gives

$$vG = vG_0 - P,$$

so that $G < G_0$. Physically, the energy gained by the binding of the solids at the crack interface is in part lost as viscoelastic energy dissipation inside the solid. For an opening crack, as the crack speed $v \to \infty$ we have $G/G_0 \to E_1/E_0$ but for a closing crack $G/G_0 \to E_0/E_1$. The latter result is most easily understood by considering the simple crack problem shown in Fig. 11.

Figure 11 shows a fast moving opening crack (a) and closing crack (b) in a thin viscoelastic slab under tension. In case (a) the slab is elongated by $L_0\varepsilon$, and we wait until a fully relaxed state is formed before inserting the crack. Thus the elastic energy stored in the strip C of width Δx is $\sigma\varepsilon L_0 \Delta x/2 = E_0\varepsilon^2 L_0 \Delta x/2$. For a fast moving crack, in the present finite-sized setup (L_0 is finite), there will be negligible viscoelastic

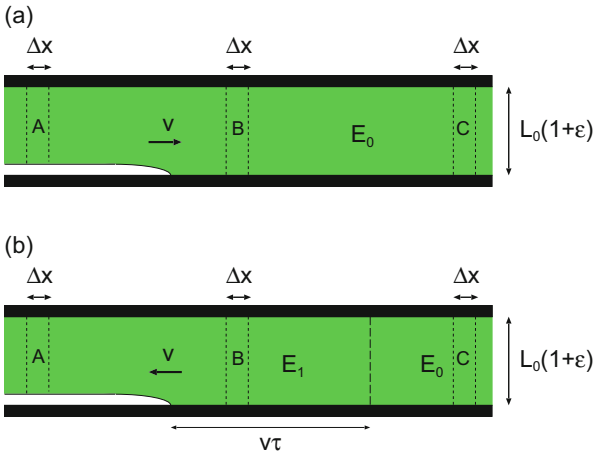

Fig. 11 Fast moving opening crack (**a**) and closing crack (**b**) in thin viscoelastic slab under tension. In (**a**) negligible viscoelastic energy dissipation occurs and the crack propagation energy is given by the energy to break the interfacial bonds, $G \approx G_0$. In (**b**) viscoelastic energy dissipation occurs and the effective crack propagation energy $G \approx (E_0/E_1)G_0$ is reduced by a factor E_0/E_1 (see text for details)

energy dissipation in the solid and $G \approx G_0$ is determined by the energy conservation condition $G_0 \Delta x = E_0 \varepsilon^2 L_0 \Delta x/2$ or $G_0 = E_0 \varepsilon^2 L_0/2 = \sigma_0^2 L_0/(2E_0)$. The fact that $G \approx G_0$ in this case is a finite-sized effect (for an infinite system we would instead get $G = (E_1/E_0)G_0$).

For the closing crack (case (b)), the situation is different: For a fast moving crack, the strip A is quickly elongated when it approaches the crack tip, which requires a large stress $\sigma = E_1 \varepsilon$ determined by the high-frequency modulus E_1. Since the crack moves very fast, the stress in the strip will remain at this large value even when the crack tip has moved far away from the strip as in position B. However, due to viscoelastic relaxation the stress will finally arrive at the relaxed value $\sigma = E_0 \varepsilon$ as at position C. The time this takes depends on the nature of the viscoelastic relaxation process, e.g., for a process characterized by a single relaxation time τ, a time $t > \tau$ (and distance $s > v\tau$) would be needed to reach the relaxed state. During this relaxation, mechanical energy is converted into heat. Since the crack tip is far away from the region where this relaxation process takes place, it does not know about it, and the interfacial binding energy is converted into elastic energy in the rapid stretching of the strip in the process going from strip position A to B. Thus $G_0 \Delta x = E_1 \varepsilon^2 L_0 \Delta x/2$. However, the crack propagation energy G refers to the relaxed state configuration so that $G \Delta x = E_0 \varepsilon^2 L_0 \Delta x/2$. Thus $G = E_0 \varepsilon^2 L_0/2 = (E_0/E_1) E_1 \varepsilon^2 L_0/2 = (E_0/E_1) G_0$.

Using the Barenblatt description of the crack tip process zone, Greenwood has shown that for an infinite sized system $G_{\text{open}} G_{\text{close}} \approx G_0^2$. Thus if we write the opening crack tip propagation energy as

$$G_{\text{open}} = [1 + f(v, T)] G_0, \tag{18}$$

then

$$G_{\text{close}} \approx \frac{G_0}{1 + f(v, T)}. \tag{19}$$

Thus we can use the theory presented in Sect. 2 to predict the crack propagation energy also for closing cracks. However, the theory for closing cracks in viscoelastic solids is still not fully understood, e.g., for a fast moving crack, a region of compressible stress occurs close to the crack tip for which no physical explanation exists [16, 17].

The results presented here are crucial for adhesion involving viscoelastic solids, e.g., rubber materials. Thus in a typical case no adhesion can be detected when two solids are squeezed in contact (closing crack propagation), but strong adhesion is observed during separation (opening crack propagation). One well-known case is the contact involving adhesive tape: when the tape is pushed in contact, no adhesion can be detected, but during separation, a strong adhesion force prevail. In general these are several reasons for contact hysteresis (e.g., related to roughness or chain inter-diffusion), but in many cases the most important effect is viscoelasticity.

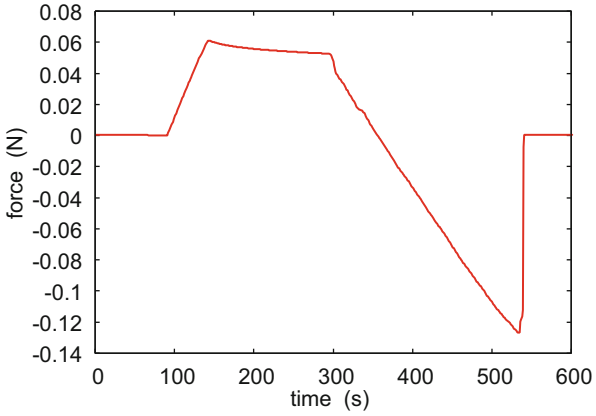

Fig. 12 The interaction force between a glass ball (diameter $2R = 2.5$ cm) moved in contact with a pressure sensitive adhesive film (double-sided adhesive tape attached to a smooth glass surface) and then removed. The approach and retraction speed is 36 μm/s. Note the strong adhesion hysteresis: no adhesion is observed during approach, but a strong adhesion (corresponding to the work of adhesion $G \approx 2$ J/m^2) is observed during pull-off

As an example illustrating contact hysteresis effects, in Fig. 12 we show the interaction force between a glass ball (diameter $2R = 2.5$ cm) moved in contact with a pressure sensitive adhesive film (double-sided adhesive tape attached to a smooth glass surface) and then removed. The approach and retraction speed is 36 μm/s. Note the strong adhesion hysteresis: no adhesion is observed during approach, but a strong adhesion (corresponding to the work of adhesion $G \approx 2$ J/m^2) is observed during pull-off.

2.7 *Implications for Sliding Friction*

When a rubber block slides on hard and rough substrate surface, such as an asphalt or concrete road surface, the rubber-road contact will in general not be complete, but it will consist of many small asperity contact regions. The contact area is usually a very small fraction of the nominal contact area, e.g., for a tire it may be only ~ 1 cm^2. A very important contribution to the friction force is derived from the interaction between the rubber molecules and the road surface in the area of real contact. For clean surfaces, two different (adhesive) contributions to the frictional force have been considered, namely from the opening crack on the exit side of the asperity contact region (see Fig. 13) [36, 37] and from bonding–stretching–debonding process within the area of real contact [38, 39]. If the typical diameter of a contact region is L, one can show that the contribution from the opening cracks gives a contribution to the frictional shear stress given by (see Fig. 12) $\tau_f \approx (G_{open} - G_{close})/L$.

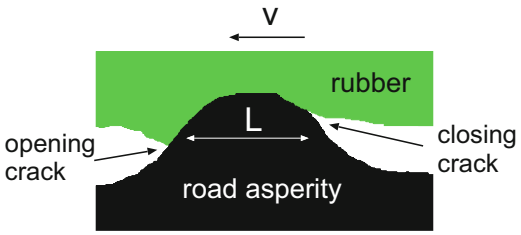

Fig. 13 A rubber block in contact with a road asperity. We assume that the contact region is circular with the diameter $L = 2r_0$. During sliding (speed v), a closing crack is observed on the entrance side and an opening crack on the exit side. During sliding the distance Δx the dissipated energy in an asperity contact region $(G_{\text{open}} - G_{\text{close}})L\,\Delta x$. The dissipated energy can also be written as $\tau_{\text{f}}\pi r_0^2\Delta x$, where τ_{f} is an effective frictional shear stress, giving $\tau_{\text{f}} \approx (4/\pi)(G_{\text{open}} - G_{\text{close}})/L$

For a rubber tread block sliding on an asphalt road surface, contact mechanics calculations (including adhesion) [40, 41] show that the lateral size of a typical asperity contact region is of order $L \approx 1$ μm. For this case, it was shown in [42] that the maximum of the frictional shear stress derived from crack-opening, is about $10 - 20$ times smaller than the adhesive contribution to the friction needed to explain measured friction data. We conclude that the contribution to the friction from the opening crack propagation cannot explain the observed magnitude (or velocity dependency) of the shear stress acting in the area of real contact. This suggests another origin for the main contribution to the friction from the area of real contact. In [43, 44] it was proposed that molecular bonding–stretching–debonding process [38, 39] in the area of real contact can explain the observed magnitude (and velocity dependency) of the contribution to the friction from the area of real contact.

If the asperity contact regions would be much smaller than ∼1 μm, the crack opening contribution to the friction could be much more important and may dominate the adhesive contribution. Furthermore, the adhesive contribution to rolling friction on a smooth rubber surface, and the friction associated with Schallamach waves, are both determined by the crack opening (and closing) contribution [45].

2.8 Role of Surface Roughness

Surface roughness has a big influence on interfacial crack propagation. For very soft rubber compounds, like pressure sensitive adhesives, the pull-off force is proportional to the relative area of real contact A/A_0. We illustrate this in Fig. 14, which shows the squeeze-together force and the pull-off force between a pressure sensitive adhesive film, attached to a smooth glass plate, and a glass ball. Note that the pull-off force is proportional to the applied normal force (see Fig. 15), which we attribute to the fact that the area of real contact is proportional to the normal force. Thus due to surface roughness the adhesive film (see Fig. 16) makes only partial contact with the

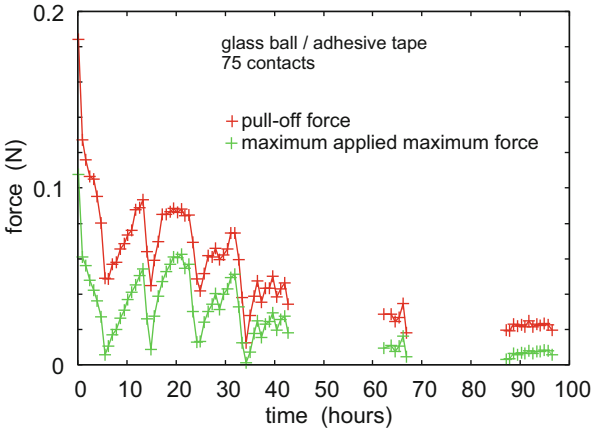

Fig. 14 The pull-off force (red) and the maximum applied squeezing force (green) as a function of time during repeated contacts (75 contacts) between a glass ball (diameter 2.5 cm) and an adhesive tape attached to a smooth flat glass plate. Based on force–time curves such as shown in Fig. 12. Note that the pull-off force is proportional to the applied squeezing force (see Fig. 15)

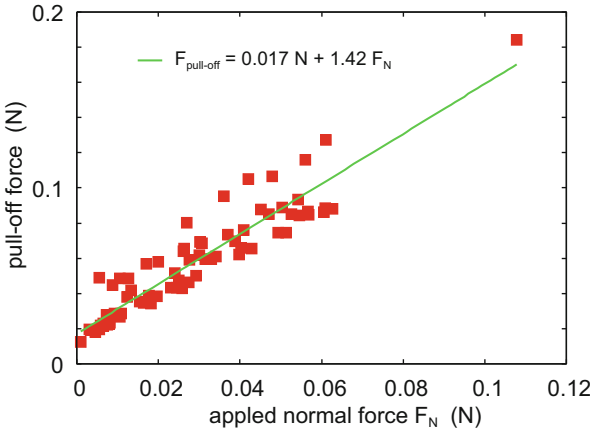

Fig. 15 The pull-off force between a glass ball and an adhesive tape as a function of the maximum applied squeezing force. Based on the data shown in Fig. 14

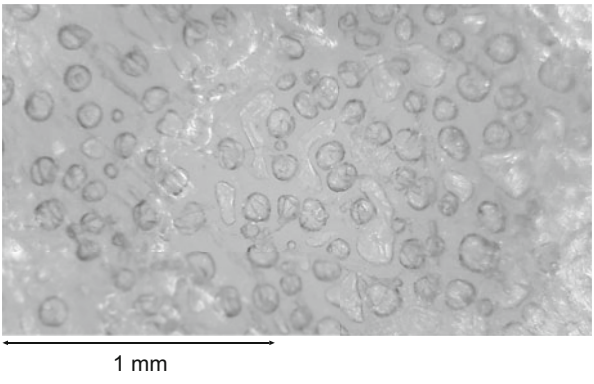

Fig. 16 Optical picture of the double-sided adhesive film (tesa 5338) (attached to a smooth glass plate) used in the adhesion experiments. Note the surface roughness. Single-sided adhesive films give very smooth surface if pulled rapidly (but a rough surface if pulled very slowly), while the present film gives a rough surface independent of the pull-off speed

glass ball in the nominal contact area, and the effective crack propagation energy for opening crack

$$G \approx (A/A_0)G_{\text{open}}(v),$$

where A/A_0 is the relative contact area at the rim of the nominal contact area at the point of snap-off (where the opening crack speed is v). The crack propagation energy (also denoted the work of adhesion) $G_{\text{open}}(v)$ is the interfacial crack propagation energy for smooth surfaces.

For a thick rubber film, the pull-off force is given by the Johnson–Kendall–Roberts theory

$$F_{\text{pull-off}} = \frac{3\pi}{2}RG.$$

If the elastic modulus of the rubber compound is high enough, the effective crack propagation energy G must be corrected for the elastic energy stored when the rubber surface is bent to make contact with the substrate

$$G \approx [(A/A_0)G_0 - U_{\text{el}}](1 + f(v, T)),$$

where U_{el} is the elastic energy per unit surface area due to the surface roughness. Thus if the roughness is big enough, $(A/A_0)G_0 \approx U_{\text{el}}$, the pull-off force will vanish.

3 Applications

3.1 Pulling Adhesive Tape

A pressure sensitive adhesive tape typically consists of a soft (weakly crosslinked) rubber film (with tacky additives) on a stiffer polymer film, e.g., of polyester type. In recent studies of peeling of adhesive tapes [46–49], the crack propagation energy $G(v)$ was measured as a function of the peeling velocity v. Thus, for example, peeling of the 3M Scotch 600 tape, which consists of a polymer film covered by a thin $d \approx 20$ μm (acrylic) adhesive film, resulted in a $G(v)$ function very similar in form to what is shown in Fig. 10, with a maximum around $v_{\text{m}} \approx 0.1$ m/s. For peeling velocities $v < v_{\text{m}}$, the crack tip process zone is very complex involving cavitation and stringing, and $G_0(v)$ is likely to depend on the crack tip speed. Thus for $v < v_{\text{m}}$ the velocity dependency of $G(v)$ will depend not only on the bulk viscoelastic energy dissipation but also on $G_0(v)$, which was considered as a constant above.

The complex processes occurring close to the crack tip for low peeling velocities result in a very rough rubber surface, which appears white due to light scattering from the surface inhomogeneities [50]. However, high peeling speeds result in a much smoother (and transparent) rubber film. This indicates a much simpler crack

tip process zone for $v > v_m$. Thus, the theory developed above may be directly applied to $v > v_m$. In this velocity region the decrease in $G(v)$ may result from the finite thickness of the adhesive film as predicted by the theory above. This is expected for a thin film, but not for an infinite system where $G(v)$ increases monotonically with the crack tip speed (see Figs. 7 and 8). This origin of a maximum in the $G(v)$ curve was already suggested by de Gennes [51].

Let us present some numerical results for a pressure sensitive (acrylic) rubber compound used in an earlier study (see [52]). Figure 17 shows the viscoelastic modulus as a function of frequency (log–log scale) for a pressure sensitive adhesive denoted by A in [52]. (a) shows the real and imaginary parts of E and (b) ImE/Re $E = \tan\delta$. Figure 18 shows the logarithm of the (horizontal) frequency–temperature shift factor a_T as a function of the temperature for the same compound.

Using the viscoelastic modulus in Fig. 17 and assuming a $L = 20$ μm thick rubber film, in Fig. 19 we show the calculated viscoelastic enhancement factor G_{open}/G_0 as a function of the crack tip speed for the pressure sensitive adhesive A, for the temperatures $T = 20°C$ (red lines), 30°C (green lines), and 40°C (blue lines). The

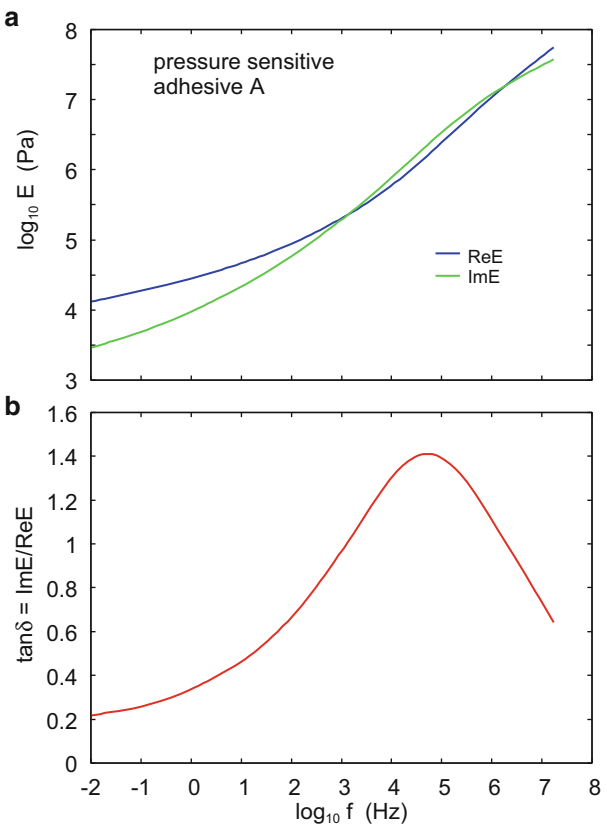

Fig. 17 The viscoelastic modulus as a function of the logarithm of the frequency for the pressure sensitive adhesive A used in [52]. (**a**) shows the real and imaginary parts of E (log-scale) and (**b**) ImE/Re $E = \tan\delta$

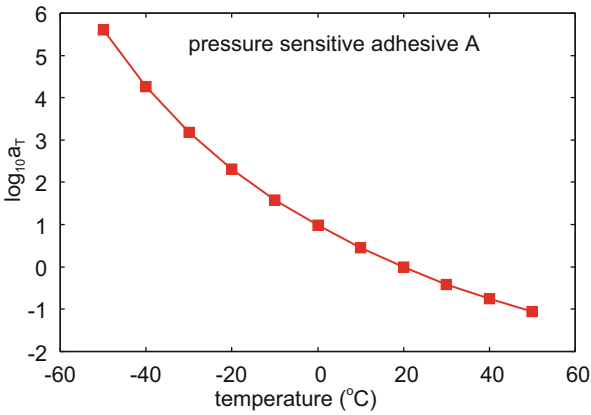

Fig. 18 The logarithm of the (horizontal) frequency–temperature shift factor a_T as a function of the temperature for the pressure sensitive adhesive A

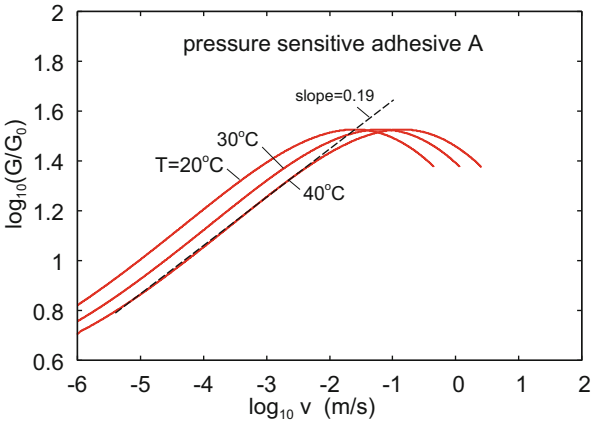

Fig. 19 The viscoelastic enhancement factor G_{open}/G_0 as a function of the crack tip speed for the pressure sensitive adhesive A, for the temperatures $T = 20^{\circ}$C (red lines), 30°C (green lines), and 40°C (blue lines). The results are shown for the system sizes (film thickness) $L = 20$ μm

slope of the curve and the velocity where $G(v)$ is maximum is close to what is observed in [46, 47].

The maximum of the $G(v)$ curve in the experiments presented in [46, 47] is about 100 J/m^2. We have found that at the maximum $G/G_0 \approx 30$. So this implies $G_0 \approx 3$ J/m^2. This is much bigger than the adiabatic work of adhesion $\Delta\gamma = \gamma_1 + \gamma_2 - \gamma_{12}$, which probably is around 0.05 J/m^2 (because of the inert backing of the tape). So G_0 is increased by a factor of $\sim$60 or so compared to the adiabatic case. We attribute this to the cavitation and stringing in the crack tip process zone.

3.2 Ball-Flat Adhesion: Role of Finite-Sized Effects

Here we compare the theory prediction with a ball-flat pull-off (adhesion) experiment [53–64]. Adhesion experiments are typically performed by moving a spherical ball (radius R) in and out of contact with a substrate. This type of experiments can be analyzed using the Johnson–Kendall–Roberts (JKR) theory, which predict the pull-off force $F_{\text{pull-off}} = (3\pi/2)GR$, where G is the work of adhesion. The work of adhesion is the energy per unit surface area to propagate an interfacial (opening or closing) crack. Hence, for viscoelastic solids such as rubber, there will be a viscoelastic contribution to G given by the theory above: $G/G_0 = 1 + f(v, T)$, where G_0 is the work of adhesion in the adiabatic limit (crack speed $v \to 0$).

Here we are interested in a hard ball in contact with a flat rubber surface. In a typical adhesion experiment, the ball radius R is of order a few mm, and the diameter of the area of contact when the pull-off instability occurs of order ~0.1 mm. The linear size $L \sim 0.1$ mm of the contact region (at the point of the onset of snap-off) determines the size of the region in space where the stress field exhibits the inverse square-root (singular) behavior expected as a function of the distance away from the tip of crack-like defects.

Figure 20 shows the calculated [from (6)] viscoelastic enhancement factor G_{open}/G_0 as a function of the temperature for the crack tip speed $v = 10$ μm/s. The system size $L = 0.1$ mm. Results are shown for unfilled and filled (20.4 Vol.% carbon black) Hydrogenated Nitrile Butadiene Rubber (HNBR) rubber (red solid and dashed lines, respectively) and for a tread compound (blue curve). The glass transition temperatures of the HNBR and tread compounds are − 16°C and − 32°C, respectively.

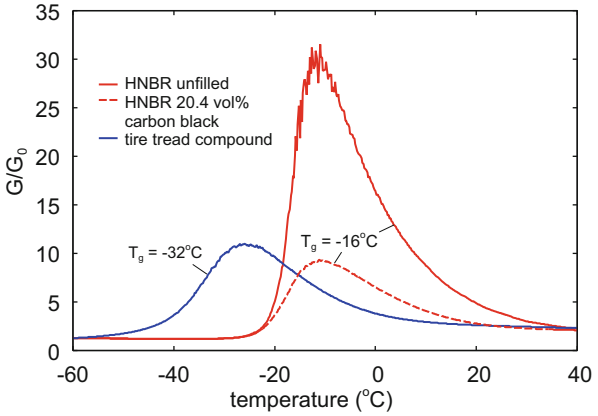

Fig. 20 The viscoelastic enhancement factor G_{open}/G_0 as a function of the temperature for the crack tip speed $v = 10$ μm/s. The system size $L = 100$ μm as is the typical diameter of the contact between a ball and a flat surface in JKR [59] adhesion experiments. Results are shown for unfilled and filled (20.4 Vol.% carbon black) HNBR (red solid and dashed lines, respectively) and for a tread compound (blue curve). The glass transition temperatures of the HNBR and tread compound are − 16°C and − 32°C, respectively

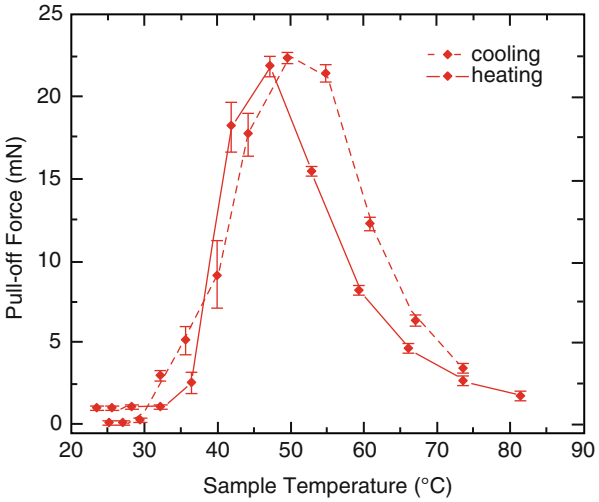

Fig. 21 The pull-off force as a function of temperature for a glass ball with radius $R = 1.5$ mm first squeezed in contact with a flat surface of a (photopolymerizable) acrylic polymer ($T_g = 53^\circ$C) and then pulled-off with the speed $v_z \approx 10$ μm/s. From [60]

Let us compare the results in Fig. 20 with the experimental results obtained in [60] for a silica-glass ball with radius $R = 1.5$ mm first squeezed in contact with a flat surface of an acrylic polymer and then pulled-off with the speed $v_z \approx 10$ μm/s. We will assume that both surfaces are perfectly smooth. The acrylic polymer surfaces are produced by photopolymerization with the polymer confined between two smooth glass plates. The glass ball is also expected to be very smooth, but no information about the surface roughness was given in [60].

The acrylic polymer used in Fig. 21 has a much higher glass transition temperature than the HNBR rubber used in the calculations ($T_g = 53^\circ$C compared to -16°C for HNBR), which will result in a shift of the adhesion curve along temperature axis, but the temperature dependency of the pull-off force (which is proportional to G) for the acrylic polymer is very similar to the temperature dependency on the work of adhesion for unfilled HNBR. In particular, both the full width at half maximum (FWHM) (about 20°C) and the asymmetry of the peak in the pull-off force and the work of adhesion are nearly the same. This is indeed expected because the change in the viscoelastic modulus from the rubbery region to the glassy region is nearly the same for both polymers (from ≈3 MPa to ≈2 GPa). We also note that the viscoelastic enhancement in the pull-off force observed in the experiment (roughly $15 - 30$) is very similar to what the theory predicts. Unfortunately, the (complex) frequency-dependent modulus $E(\omega)$ for the acrylic polymer was not reported on in [60] so no detailed comparison between theory and experiment is possible.

3.3 *Crack Propagation in the Pig Skin (Dermis), with Application to Intradermal Injections*

The delivery of a drug product through body tissue (muscle, skin, or organ tissue) is one of the most common routes of delivery for therapeutic drug products. Delivery into the skin layers includes injections in the sub-cutaneous space, which has growing interest, due to its applications to patient self-injection for chronic diseases like diabetes. Intra-dermal injection, targeting the space between the outer skin layer (epidermis) and the sub-cutaneous space, is of particular interest for vaccines, due to its potential to elicit a stronger immune response. To understand the fundamentals of injections, we need to consider the tissue as a media composed of cells, extracellular matrices, and interstitial fluids [65, 66]. The drug delivery depends on the permeability of the tissue as well as the compatibility between the injecting fluid and the interstitial fluids.

The majority of the studies analyzing the fundamentals of how the drug is delivered into the tissue use porous elastic models where the drug product diffuses through the tissue by permeability. The use of Darcy's and Brinckman's diffusion equations is a common practice [67].

Here we consider the injection of fluid in the pig dermis. The dermis consists of a three-dimensional crosslinked network of elastic fibers (collagen, elastin) surrounded by an amorphous gel-like (water-rich) substance (containing mucopolysaccharides, chondroitin sulfates, and glycoproteins). The gel-like substance provides lubrication for collagen fibers, which indicate that the bonding interaction between the elastic fibers and the gel-like substance may be relatively weak, and a likely region for crack to propagate during fluid injection.

We propose that the fluid injection in the dermis is similar to hydraulic fracturing (also called fracking), used in oil and gas exploration, involving the fracturing of an inhomogeneous material (here the dermis) by a pressurized liquid. In the present case, because of the low elastic modulus the skin dermis, the pressurized fluid will separate the cracked surfaces giving fluid filled cavities in the skin. Because of the permeability of the dermis, the fluid is diffusing away from the fluid filled cavities, but the speed of this process will depend on the compatibility of the injected fluid and the interstitial fluids.

3.3.1 Viscoelastic Modulus of the Dermis

The experimental study uses pig skin where the dermis is relative thick, see Fig. 22. The specimen used in the experiment was bought from the butcher and used 1 day after the pig was killed. The viscoelastic modulus was measured in tension mode using a DMA Q800 from TA Instruments. From the skin specimen, we have cut out a sample of the dermis removing first the subcutis and the epidermis. We used stripes of the dermis with rectangular cross section, 4.5×2.5 mm, and length of 7–12

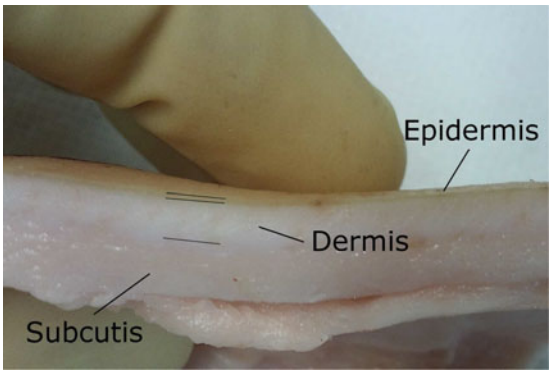

Fig. 22 Picture of the pig skin used in the experiment with the different skin layers as indicated. For the experiment, we have cut out pieces of the dermis of the skin

mm. One problem is that the viscoelastic properties of the specimen change with time, e.g., due to the loss of fluid evaporating to the atmosphere. As we cannot control the humidity in the DMA Q800, this effect may have the largest influence on the results. In order to minimize this effect, we have covered the sample with liquid pork fat prior to the experiment. The fat has been produced by heating up some of the pig skin in an oven for some time.

To measure the viscoelastic modulus, the specimen gets excited with different frequencies in tensile mode at different temperatures. The applied strain amplitude is chosen to be rather small (0.5% strain) to avoid nonlinear effects. The temperature range covered starts at 40°C down to − 50°C. The results have then been shifted to obtain a smooth master curve. This is found to be rather complicated as their is a strong change when the temperature is around − 10°C.

The first measurement is done at a constant temperature of 40°C while the frequency is changed in steps from 25 to 0.25 Hz. Later, the temperature is decreased by 10°C and the experiment repeated until − 50°C is reached. We have shifted the imaginary part of the viscoelastic modulus to obtain a smooth master curve. This time–temperature shifting procedure is often used for rubber-like materials but may not hold accurately for the dermis.

Figure 23 shows the real and imaginary parts of the elastic modulus as a function of frequency (log–log scale) of the pig dermis. Figure 24 shows the shift factors obtained by shifting the imaginary part of the viscoelastic modulus as to obtain the (smooth) master curve shown in Fig. 23. We have also plotted $\ln a_T$ as a function of $1/T$, where T is the absolute temperature (Kelvin) (not shown). We have found that, to a good approximation, $a_T = b e^{-\varepsilon/k_B T}$, with the activation energy $\varepsilon \approx 2.5$ eV.

Preliminary analysis of pig skin dermis using deferential scanning calorimetry indicates several thermal transitions within the physiological temperature range 0–40°C. Further analysis is ongoing to determine their relation to the viscoelastic behavior of the dermis.

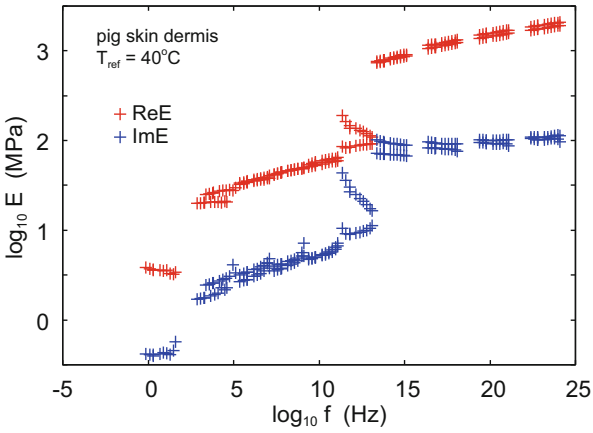

Fig. 23 Real and imaginary parts of the elastic modulus of the pig dermis for with fat covered pig skin samples. The experiment started at $T = 40^{\circ}$C and ended at $T = -50^{\circ}$C after $\sim$2 h

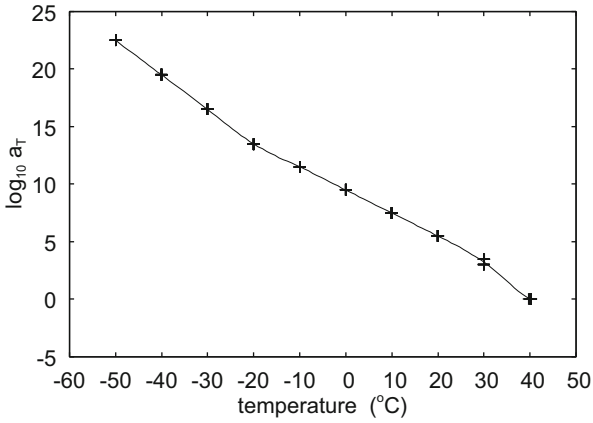

Fig. 24 The shift factors obtained by shifting the imaginary part of the low-strain viscoelastic modulus so that a smooth master curve is observed (shown in Fig. 23). The reference temperature chosen is 40°C

3.3.2 Crack Propagation in the Dermis

We have measured the energy per unit area for crack propagation in the pig skin dermis. The experiments were conducted in an Instron tensile bench, model 5542 equipped with pneumatic grippers set to a pressure of 20 psi. The samples consisted of $w \approx 2.0 - 2.5$ cm-wide strips of skin where a crack was initiated by a razor blade cut in the dermis region of the skin, see Fig. 25. We measured the $F(v)$ as a function of the crack tip speed v (Fig. 26). Neglecting the elastic energy stored in the skin, the work $FS \approx GwS$ (where S is the length of the crack). Using this equation in Fig. 27, we show G as a function of the crack tip speed. Note that there is only a weak increase in G with the speed v and no systematic temperature dependency.

The crack propagation energy $G = G_0(1 + f(v, T))$, where $1 + f(v, t)$ is the viscoelastic enhancement factor and G_0 (which also depends on v and T) the contribution from the crack tip process zone to the crack propagation energy. In Fig. 28 we show

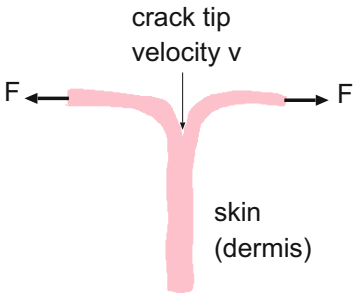

Fig. 25 The crack propagation energy $G \approx F/w$, where w is the width of the strip

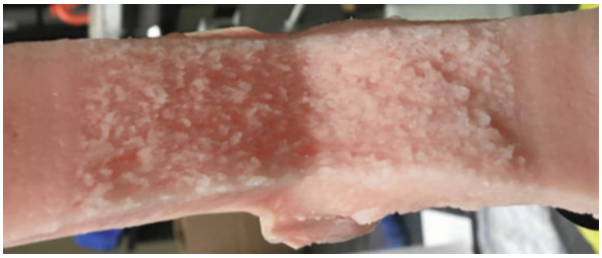

Fig. 26 Crack propagation in the pig dermis results in a rough surface

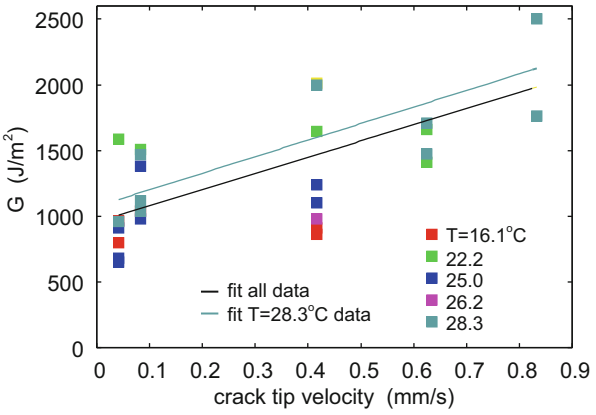

Fig. 27 Crack propagation energy $G(v)$ in the dermis of pig skin for different temperatures and crack tip velocities

the calculated viscoelastic enhancement factor $G(v)/G_0 = 1 + f(v, T)$ as a function of the logarithm of the crack tip speed. In the calculation we have used the viscoelastic modulus of the pig dermis shown in Fig. 23 and the shift factor from Fig. 24. Results are shown for $T = 16.1$, 22.2, and 28.3°C and taking into account the finite-sized effect with $L = 1$ cm of order the thickness of the dermis. For the crack speeds shown in Fig. 27, the factor $1 + f(v, t)$ is approximately temperature and velocity independent. Taking into account the magnitude of $1 + f(v, t)$, we conclude that $G_0(V)$ on the average increases from ≈200 J/m^2 for $v < 0.1$ mm/s to ≈400 J/m^2 for $v \approx 1$ mm/s.

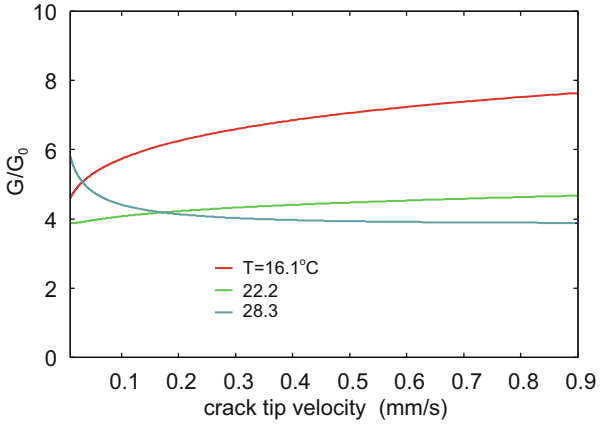

Fig. 28 The viscoelastic enhancement factor $G(v)/G_0 = 1 + f(v, T)$ as a function of the logarithm of the crack tip speed. In the calculation we have used the viscoelastic modulus of the pig dermis shown in Fig. 23 and the shift factor from Fig. 24. Results are shown for $T = 16.1$, 22.2, and 28.3°C and taking into account the finite-sized effect with $L = 1$ cm of order the thickness of the dermis

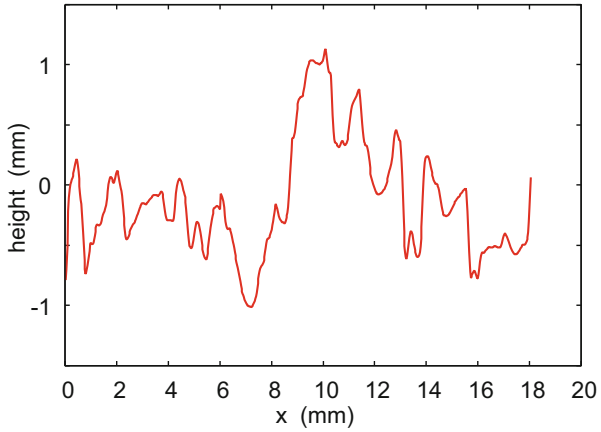

Fig. 29 Topography (line scan) of pig skin dermis surface after crack propagation

3.3.3 Surface Roughness of Dermis Crack Surfaces

The roughness resulted from the pig skin crack propagation was studied using a Keyence VR 5200 3D measurement system. The scanned area was 20 mm × 20 mm. The dermis crack surfaces exhibit strong surface roughness as shown in Fig. 26. Figure 29 shows that the amplitude of the height fluctuations is about 1 mm. In Fig. 30 we show the calculated two-dimensional (2D) surface roughness power spectrum. Including only the wavenumber region shown in the figure, the surface

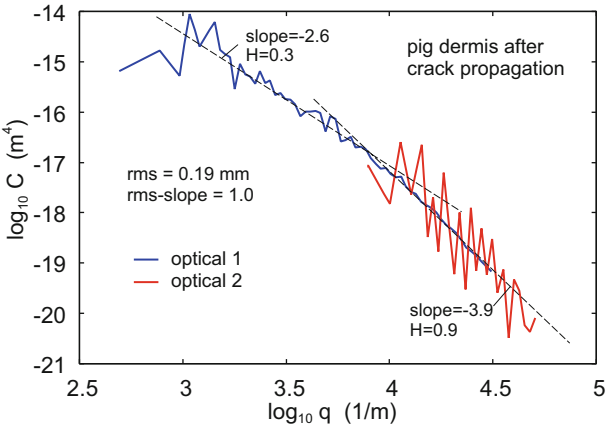

Fig. 30 The 2D surface roughness power spectrum of pig skin dermis surface after crack propagation

has the root-mean-square (rms) roughness amplitude of 0.19 mm and the rms-slope of 1.0.

Note that the slope of the power spectrum curve (on the log–log scale) changes for $q = 2\pi/\lambda$, $\lambda \approx 1$ mm, from -2.6 to -3.9. We associate the region $q < 2\pi/\lambda$ with the large (mm-sized) protruding structures, which can be seen in Fig. 26, which probably are domains of the soft extracellular matrix detached from the highly elongated fibril network (collagen and elastin) in the crack tip process zone. Thus, the morphology of the cracked surface (see Fig. 26) suggests that the (strong) fibril component of the dermis is not homogeneously distributed but is separated by relative large regions of the soft matrix. This will have important implications for the crack propagation in the dermis during fluid injection (see Sect. 3.3.5).

The roughness found on the cracked surfaces in Fig. 26 is consistent with the crack propagation energy shown in Fig. 27. Thus, experiments have shown that when a strip of dermis is elongated in tension, the maximum tensile stress before the dermis break is $\sigma_c \approx 2$ MPa (see [66]). The amplitude of the surface roughness created on the cracked surfaces in Fig. 26 is about $d \approx 1$ mm (typically $\approx$5 times higher than the rms roughness amplitude). Thus one expects the crack propagation energy to be $G_0 \approx \sigma_c d/2 \approx 1000$ J/m^3, which is consistent with Fig. 27.

3.3.4 Intradermal Fluid Injection

We have measured the injection of deionized water in the pig belly dermis (see Fig. 34). The water was injected using a 1 mL glass syringe with a barrel with inside cross section area $A \approx 30$ mm^2. The syringe's needle was a 29 gauge with 184 μm inner diameter and 340 μm outer diameter. The injection depth was 6 mm. The injection setup was mounted in an Instron tensile bench model 5542 to control the speed and injected volume.

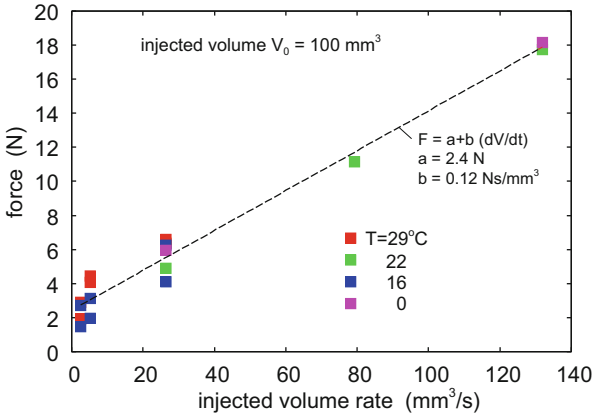

Fig. 31 The dependency on the force needed to inject a fluid in the pig dermis on the volume injection rate

The total force applied to the rubber stopper is $F_{\text{tot}} = F_{\text{f}} + F_{\text{vis}} + Ap$, where F_{f} is the friction force between the rubber stopper and the glass barrel, F_{vis} the force (due to the water viscosity) needed to squeeze the fluid through the needle, and Ap the force to inject the fluid in the dermis (p is the water pressure in the dermis, and A the barrel inner cross-section area). The friction force between the rubber stopper and the glass barrel F_{f} and the viscous force needed to squeeze the fluid through the needle F_{vis} were measured before and after injecting fluid in the skin dermis. The so obtained force was subtracted from the total force F_{tot} needed to inject the fluid in the dermis. Figure 31 shows the dependency of the effective injection force Ap on the volume injection rate $\dot{V}$. The total injected volume is $V_0 = 100$ mm^3. Note that the injection force tends to increase linearly with the injection rate and is nearly independent of the temperature.

3.3.5 Theory and Analysis of the Experimental Data

Here we will study the fluid pressure p necessary in order to inject fluid into the dermis of the skin. We will calculate p as a function of the size of the injected fluid volume and as a function of the speed of fluid injection. We will assume that the fluid forms a roughly ellipsoidal-shaped volume with height h and radius R, see Fig. 32. Thus the fluid volume $V \approx 4\pi R^2 h/3$. We consider an equilibrium situation and determine R and h by minimizing the total potential energy U_{tot}. We have

$$U_{\text{tot}} = -Fu + G\pi R^2 + \frac{1}{2}E\left(\frac{h}{R}\right)^2 \kappa R^3.$$

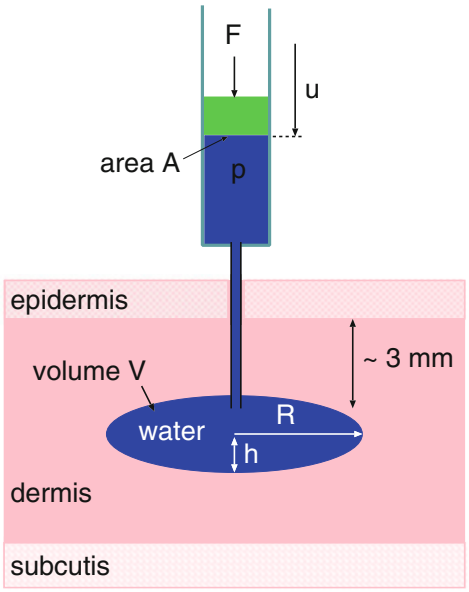

Fig. 32 Fluid injection into the skin

The first term is the potential energy of the loading mass acting on the stopper, which is squeezing the fluid into the skin. The second term is the energy to break the bonds on the surface area πR^2, and the last term is the elastic energy stored in the system when bending the surfaces (by the amounts h) in the area πR^2 so it can occupy the fluid volume $V \approx 4\pi R^2 h/3$. This term can be understood as the strain energy density $\sigma\varepsilon/2 = E\varepsilon^2/2$ integrated over the volume where the strain is finite. The strain is of order h/R and the volume of order R^3. The factor κ is the number of order unit, which depends on the location of the dermis relative to the skin surface, and also on the exact skin elastic properties such as the elastic modulus and thickness of the epidermis (the skin top layer) and subcutis (see Fig. 22).

We assume that the fluid (water) is incompressible so that fluid volume conservation requires

$$V = Au = \frac{4\pi}{3} R^2 h. \tag{20}$$

Using this equation and $F = pA$, we can write

$$U_{\text{tot}} = -\frac{4\pi}{3} R^2 hp + G\pi R^2 + \frac{1}{2} E \left(\frac{h}{R}\right)^2 \kappa R^3. \tag{21}$$

Minimizing with respect to h and R gives

$$-\frac{4\pi}{3} R^2 p + Eh\kappa R = 0, \tag{22}$$

$$-\frac{8\pi}{3}Rhp + G2\pi R + \frac{1}{2}Eh^2\kappa = 0, \tag{23}$$

which gives

$$h = \left(\frac{4\pi}{3\kappa}\frac{GR}{E}\right)^{1/2}, \tag{24}$$

$$p = \left(\frac{3\kappa}{4\pi}\frac{EG}{R}\right)^{1/2}. \tag{25}$$

Using (20) and (24), we obtain the volume of injected fluid

$$V = \beta R^{5/2}, \tag{26}$$

where

$$\beta = \frac{4\pi}{3}\left(\frac{4\pi}{3\kappa}\frac{G}{E}\right)^{1/2}. \tag{27}$$

Assume that fluid is injected at a constant volume per unit time so that $V(t) = \dot{V}t$. If the injection occurs during the time period $0 < t < t_0$, we get the injected volume $V(t_0) = V_0 = \dot{V}t_0$. The time averaged force

$$\langle F\rangle = \frac{1}{t_0}\int_0^{t_0} dt\ F(t) = \frac{1}{V_0}\int_0^{V_0} dV\ F(V). \tag{28}$$

We get

$$F = Ap = \left(\tfrac{3\kappa}{4\pi}EG\right)^{1/2}AR^{-1/2} = \alpha AR^{-1/2}, \tag{29}$$

where

$$\alpha = \left(\tfrac{3\kappa}{4\pi}EG\right)^{1/2}. \tag{30}$$

Combining (26) and (29) gives

$$F = \alpha\beta^{1/5}AV^{-1/5}. \tag{31}$$

Assume now first that E and G can be treated as constants independent of the injection rate $\dot{V}$, i.e., independent of the crack tip velocity $\dot{R}$. In this case, using (28) and (31), we get

$$\langle F\rangle = \frac{1}{V_0}\int_0^{V_0} dV\ \alpha\beta^{1/5}AV^{-1/5} = \frac{5}{4}\alpha\beta^{1/5}AV_0^{-1/5}. \tag{32}$$

Note that the force depends very weakly on the injected volume (or injection time), e.g., doubling the injection time results in a change in a reduction in the force with $\approx$13%. In reality $G(v)$ increases with increasing crack tip speed $v = \dot{R}$, and since $R = (V/\beta)^{2/5}$, we get $\dot{R} = (2/5)\beta^{-2/5}V^{-3/5}\dot{V}$. Thus the crack speed decreases with increasing time as $t^{-3/5}$, which will reduce $G(v)$ with increasing time.

Let us compare (32) with the experimental results shown in Fig. 31. The dermis has nonlinear viscoelastic properties, and the Young's modulus E in the equations above must be considered as an effective modulus obtained for the typical strain $\approx h/R$ involved in the cavity formation. If we use $E = 5$ MPa and $G = 1000$ J/m^2 and assume R a few mm using (24), we get a strain h/R of order unity. For such large strain, the effective modulus $E = 5$ MPa appears reasonable [66]. Using this E modulus for $V_0 = 100$ mm^3 and $A = 30$ mm^2, we get $\langle F\rangle \approx 18$ N. This is similar to the observed injection force for the highest injection rate. However, the dependency of the calculated $\langle F\rangle$ on the injection rate $\dot{V}$ (via the dependency of G and E on the crack tip speed) is weaker than observed. Thus, we note that the strain rate $\approx \dot{R}/R$ varies with the radius R but is typically $\approx 0.1 - 10$ s^{-1} as $\dot{V}$ varies from the smallest to the highest value in Fig. 31. This corresponds to an increase in the E-modulus with only a factor of $\sim$2. Thus, most of the dependency of $\langle F\rangle$ on the injection rate must be due to the crack propagation energy G. We conclude that at least for the lowest injection rates in Fig. 31 the fluid injection will not result in a breaking of all components of the dermis material, and the crack propagation energy G will be much smaller than used above but may increase rapidly with increasing injection rate. Our present understanding of the fluid injection process is illustrated in Fig. 33.

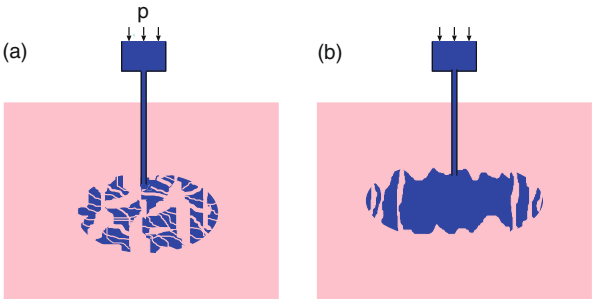

Fig. 33 Two limiting models of fluid injection. The dermis is assumed to consist of two components: a soft (gel-like) matrix and a network of elastic fibers, which break only at very high tension force. (**a**) If the pressure in the fluid is not too high, it will generate cracks in the soft matrix, or at the interface between the soft matrix and the fibers, forming a complex network of fluid filled and connected regions, while the fiber network is intact but stretched. (**b**) The fluid pressure is so high (e.g., as a result of very high injection rate) that also the fiber network break, resulting in crack propagation in the dermis similar to in the model study reported on in Sect. 3.3.2

Figure 33 shows two limiting models of fluid injection. The dermis is assumed to consist of two components: a soft (gel-like) matrix and a network of elastic fibers, which break only at very high tension force. If the pressure in the fluid is not too high, it will generate cracks in the soft matrix, or at the interface between the fibers and the gel matrix, forming a complex network of connected fluid filled regions, while the fiber network is intact but stretched (see Fig. 33a). In Fig. 33b it is instead assumed that the fluid pressure is so high (e.g., as a result of very high fluid injection rate) that also the fiber network breaks, resulting in crack propagation in the dermis similar to in the model study reported on in Sect. 3.3.2. In practical applications the case (a) is likely to occur.

After injection of the fluid, resulting (from interfacial crack propagation) in a complex network of pressurized fluid filled regions, a slower process will take place where the fluid diffuses into the skin dermis. This latter phase involves the skin permeability and is governed by the (Darcy's and Brinkman's) diffusion equation and by poroelastic fluid dynamics. This can be a slow process as manifested by the fact that after injecting the fluid and removing the needle, the fluid pressure in the cavity is high enough to allow some fluid to leak to the surface of the skin where it forms small water droplets (see Fig. 34). We note that after the needle is removed, the dermis and especially the epidermis (which is elastically much stiffer than the dermis) will elastically rebound and tend to close the hole formed by the needle, but Fig. 34 shows that the fluid pressure is high enough to allow some fluid leakage to the skin surface.

3.4 Rubber Wear

Rubber wear is a complex topic. Here we are interested in a rubber block sliding on a a rigid substrate with surface roughness on different length scales, e.g., a tire tread

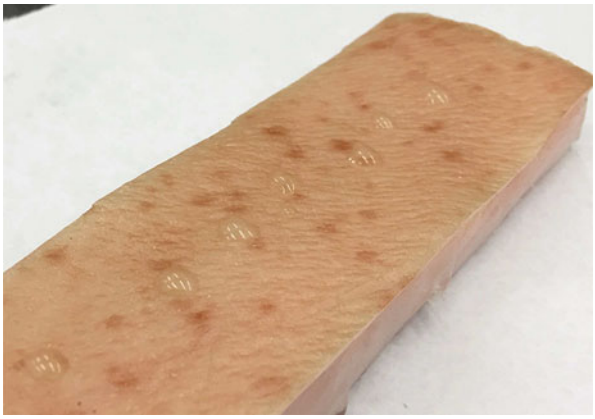

Fig. 34 After injecting the fluid and removing the needle, the fluid pressure in the cavity is high enough to allow some fluid to leak to the surface of the skin where it forms small water droplets

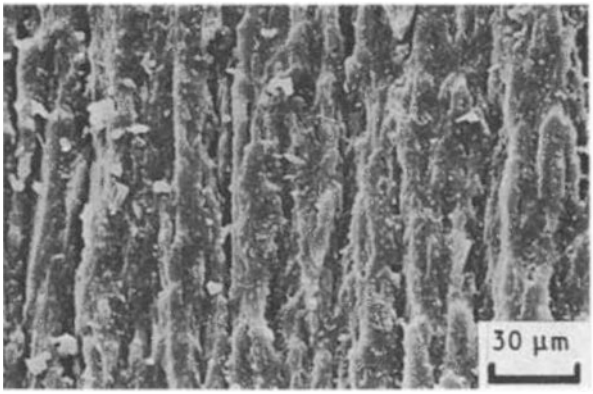

Fig. 35 Wear tracks on rubber surface

block on a concrete surface. There are several different limiting wear modes depending on the chemical composition of the rubber compound, the sharpness of the surface roughness, the composition of the atmospheric gas, the temperature, and the sliding speed. Thus, at low temperature or for very sharp roughness (large rms slope and kurtosis), the wear may involve cutting the rubber surfaces forming linear wear tracks on the rubber surface (see Fig. 35). This would result in rapid wear. Some rubber compounds tend to wear while forming a smear layer on the countersurface, which may reduce the wear rate with increasing contact time (if slid repeatedly over the same surface area). Other compounds may wear at a constant rate by formation of small rubber wear particles (dry rubber dust). This latter wear mode appears to be most important for tires and will be considered in the following.

There is at present no accurate theory to predict the wear rate of rubber materials. Here we will discuss several aspects that must be taken into account in any realistic model of rubber wear.

3.4.1 Multiscale Crack Propagation

Rubber wear on road surfaces is a multiscale phenomenon. All surfaces of solids have roughness on different length scales. The best picture of this is that a big asperity has smaller asperities on top of it, and the smaller asperities have even smaller asperities on top of them, and so on. When a rubber block is sliding on a surface with multiscale roughness, the contact will in general not be complete, but the contact area will decrease continuously as the magnification increases and new shorter wavelength surface roughness is observed. If the rubber makes contact with an asperity and D is the width of the contact region, then the deformation (and stress) field will extend into the rubber block a distance of order D. The elastic energy (temporally) stored in the volume element D^3 can drive a crack in the surface region

only if the crack extends into the rubber over a length less than D. Thus different stages in the propagation of a crack will involve the surface roughness of different wavelength, and a crack extending a distance D into the rubber can only be driven further by road asperities of similar (or larger) size as the crack length D.

In order for a rubber wear particle to form, a crack cannot just propagate into the rubber surface, but it must "turn around." The distribution of sizes of wear particles has been studied experimentally by collecting the particles generated from a tire in rolling contact (with some small slip) with a road surface [68, 69]. The probability distribution of wear particle sizes (effective diameter D) was found to be exponential

$$P(D) = l^{-1} e^{-(D-D_1)/l}, \tag{33}$$

which is normalized so that

$$\int_{D_1}^{\infty} dD\, P(D) = 1.$$

Here D_1 is the smallest wear particle diameter observed, which was found to be ≈4 μm. Using (33), the average volume of a wear particle $\approx \pi l^3$.

In [20] a theory was developed, which gives a probability distribution of the form (33) in which the distance l was interpreted as the crack mean free path. That is, it was assumed that after an average distance l the crack abruptly changed direction, e.g., by hitting into a filler particle cluster, or some other impenetrable inhomogeneity. For the rubber used in the experimental study of [68], $l \approx 16$ μm.

3.4.2 Frictional Shear Stress

Rubber wear result from the frictional shear stress the rubber is exposed to when sliding on a countersurface. At the exit side of asperity contact regions, large tensile stress may develop, which can drive cracks in the rubber surface region (see Fig. 36). Thus, rubber wear and rubber sliding friction are closely connected phenomena.

When a rubber block is sliding on hard countersurface with roughness on many length scales, the apparent rubber–substrate contact area will depend on the magnification. At the magnification ζ, only the roughness with wavenumber $q < q_0\zeta$ can be observed. Here q_0 is the wavenumber of the most long wavelength roughness component. Using the Persson rubber friction theory [70], in Fig. 38 we show the relative area of contact A/A_0 (where A_0 is the nominal contact area) as a function of the logarithm of the magnification for the sliding speed $v = 1$ cm/s. The result is for a rubber tread compound used in a passenger car tire, assuming the nominal contact pressure $p_0 = 0.3$ MPa and the temperature $T = 20^{\circ}$C. In the calculation we have used the surface roughness power spectrum shown in Fig. 37.

As the magnification increases, the contact area decreases and the normal contact stress increases. Since the normal force is constant, we have $F_N = p_0 A_0 = p(\zeta)A(\zeta)$ or $p(\zeta) = p_0 A_0/A(\zeta)$. As we increase the magnification, the contact pressure and the

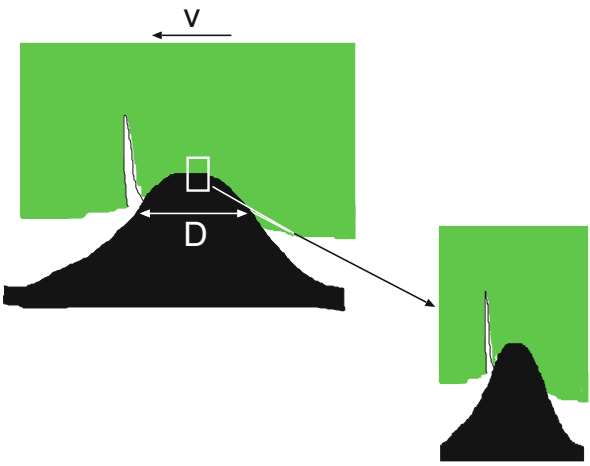

Fig. 36 Big asperities drive big cracks in the rubber, and small asperities on top of bigger asperities drive small cracks. The stress field of an asperity extends a distance into the rubber of order the width of the contact region

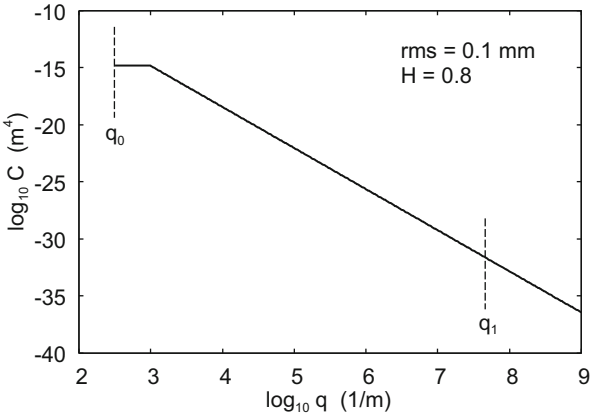

Fig. 37 The surface roughness power spectrum used in the friction calculations. The surface is assumed to be self-affine fractal with the Hurst exponent $H = 0.8$ and the rms roughness 0.1 mm. The vertical dashed line is the large wavenumber cut-off q_1 used in the friction calculations. Including all the roughness with wavenumber $q < q_1$ results in a surface with the rms slope 1.3

effective frictional shear stress $\tau(\zeta) = \mu F_N / A(\zeta) = \mu p(\zeta)$ will increase and finally, if the surface is rough enough, the shear stress becomes so high as to break the bonds in the rubber. In the friction theory we assume this to occur at the point where including all the roughness with wavenumber $q = q_0\zeta < q_1$ results in an rms-slope of 1.3. This choice of cut-off is a condition obtained by analyzing a lot of experimental data, but there is no rigorous theoretical argument for this cut-off. In fact, understanding how to determine the large wavenumber cut-off in the rubber friction calculation is a very important but unsolved problem. However, we are convinced that on very rough surfaces, such as asphalt or concrete road surfaces, the cut-off is related to the onset of strong wear as outlined above. We believe at the magnification $\zeta_1 = q_1/q_0$ continuous cutting of the rubber surface by the road asperities occurs, as observed at much

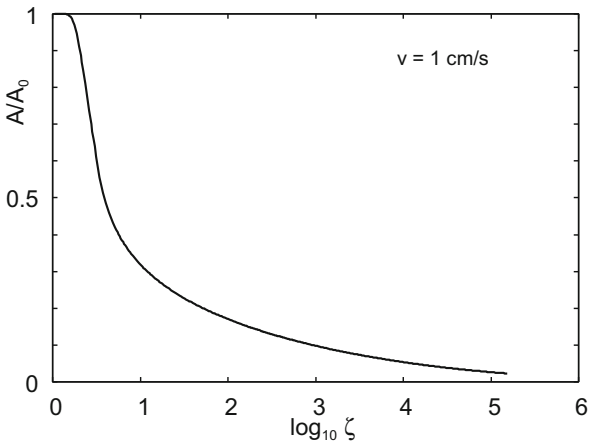

Fig. 38 The relative area of contact A/A_0 (where A_0 is the nominal contact area) as a function of the logarithm of the magnification for sliding speed $v = 1$ cm/s. The nominal contact pressure $P_0 = 0.3$ MPa and the temperature $T = 20°C$

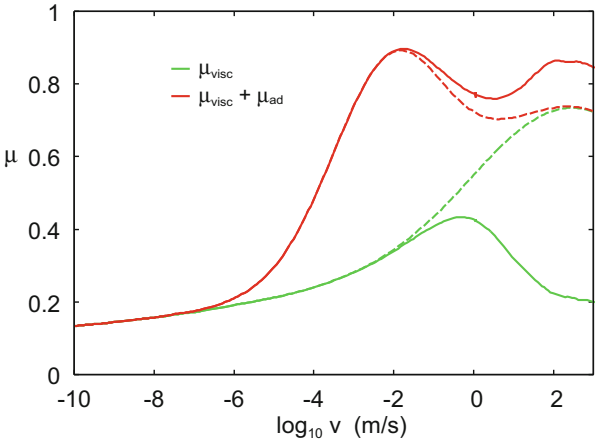

Fig. 39 The viscoelastic contribution to the friction coefficient μ_{visc} (green lines) and the total friction coefficient $\mu = \mu_{visc} + \mu_{ad}$ (where μ_{ad} is the adhesive contribution, i.e., the contribution from the area of real contact). The solid and dashed lines are with and without the flash temperature. The nominal contact pressure $P_0 = 0.3$ MPa and the background temperature $T = 20°C$

larger length scale in Fig. 35 (which occurs at low temperature or for much sharper roughness).

For the same system as used in Fig. 38 (rubber tread compound for a tire), in Fig. 39 we show the viscoelastic contribution to the friction coefficient μ_{visc} (green lines) and the total friction coefficient $\mu = \mu_{visc} + \mu_{ad}$ (where μ_{ad} is the adhesive contribution, i.e., the contribution from the area of real contact). The solid and dashed lines are with and without the flash temperature.

3.4.3 Size-Dependent Crack Propagation Energy

We have argued that on surfaces with large roughness during slip strong rubber wear of the type seen in Fig. 35 will always occur at short enough length scale, and it will act as an effective cut-off in calculating the rubber friction (see Sect. 3.4.2). This would typically result in rubber wear particles of micrometer size. However, larger rubber wear particles may also form, but they result not from interaction with one road asperity, but as a result of a cumulative influence of many accounts with road asperities. There are two reasons for this: as the length scale increases (or the magnification decreases), the asperity stress decreases while simultaneously the crack propagation energy (at a given crack tip velocity) increases. In this case, every time an asperity slides over a crack it will result in a small movement of the crack tip, and finally to the detachment of a rubber particle. This process is denoted as fatigue wear. Given the time-dependent stress acting on the rubber surface from the road asperities, one can estimate the fatigue wear rate from the knowledge how the asperity stress field and the (velocity-dependent) crack propagation energy change with the length scale (or magnification). The former is given by the rubber friction theory and the latter by the theory of crack propagation, or both quantities can be obtained from experiments.

As an illustration, Fig. 40 shows the measured crack tip displacement Δx (in mm) per cycle, as a function of the amplitude of the oscillating energy release rate [71] (for other similar measurements, see [72]). In the experiment the crack (in natural rubber) is exposed to an oscillating external stress field, which simulates the oscillations in the stress observed by a crack in the surface region of a rubber block as it is sliding over road asperities. If T is the oscillation time period (in the present case of order 1 s), one can define an average crack tip velocity $v = \Delta x/T$. In this way Fig. 40 is closely related to the crack tip $G(v)$ function. Indeed, if the crack tip velocity v is plotted as a function of G, one obtains a curve very similar to that shown in Fig. 40. To illustrate this, in Fig. 41 we show the calculated relation between v and G for unfilled NBR rubber for a system of size $L = 1$ cm. We show the curve only up to the maximum of $G(v)$ as there is no stable solution for larger G.

Finally, as pointed out before, the crack propagation curve $G(v)$ depends on the system size so measurements of the $G(v)$ relation (or the relation between the maximum energy release rate and the crack growth rate, Fig. 40) for a macroscopic system cannot be directly applied to the very small cracks, which prevail at an early stage in the crack propagation phase. In Fig. 41 we illustrate this with the calculated crack propagation energy for the tread rubber used in the friction study in Sect. 3.4.2. We show the results for an infinite system (red lines), and for finite-sized systems with linear size $L = 1$ cm (green) and $L = 1$ μm (blue), and for the temperatures $T = 20$, 30, and 40°C (Fig. 42).

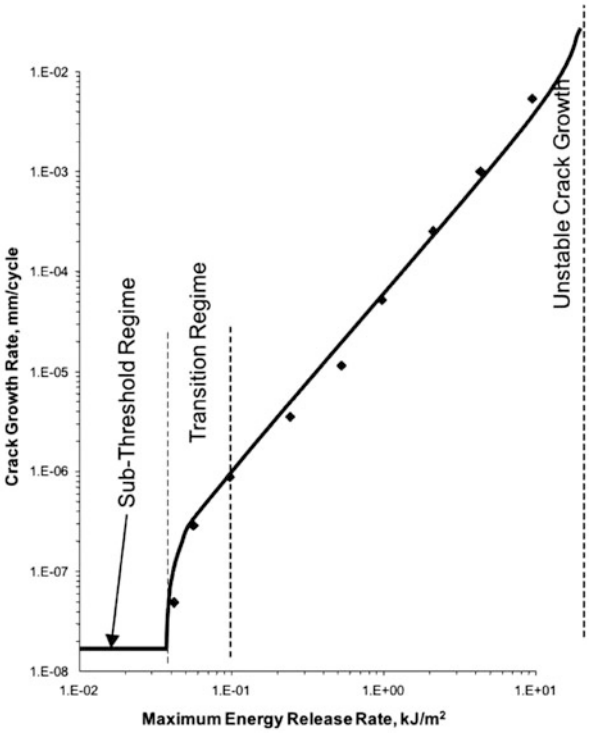

Fig. 40 Crack growth in unfilled natural rubber. The rubber sample is exposed to an oscillating strain with the period $T = 0.5$ s. The minimum of the energy release rate is zero. In each stress cycle, the crack extends by a distance Δx so the effective crack tip speed $v = \Delta x/T$. Adapted from [71]

3.4.4 Discussion

Crack propagation in rubber involves several effects not discussed above but which are important in practical applications. For very slowly moving cracks, the bond breaking at the crack tip is influenced by atmospheric gases such as oxygen or ozone [73]. This chemical bond breaking results in a crack speed, which is nearly independent of the driving stress for small stress. Another effect is strain crystallization. Some types of rubber, like natural rubber, undergo crystallization when exposed to large strain [74]. The crystalline state is mechanically stronger than the amorphous state, which will increase the crack propagation energy. However, strain crystallization requires some time to occur, and if the driving stress is changing (fluctuating) fast enough, there may be no time for crystallization to occur. But if the fluctuating stress never vanishes, e.g., $\sigma(t) = \sigma_0 + \sigma_1 \cos\omega t$ with $\sigma_0 > \sigma_1$, then some crystallization may always occur at the crack tip. Finally we note that if sliding occurs in one preferable direction, a wear or abrasion pattern may form on the rubber surface [75], usually consisting of periodic parallel ridges orthogonal to the sliding direction. When a wear pattern form, it will influence (usually increase) the wear rate.

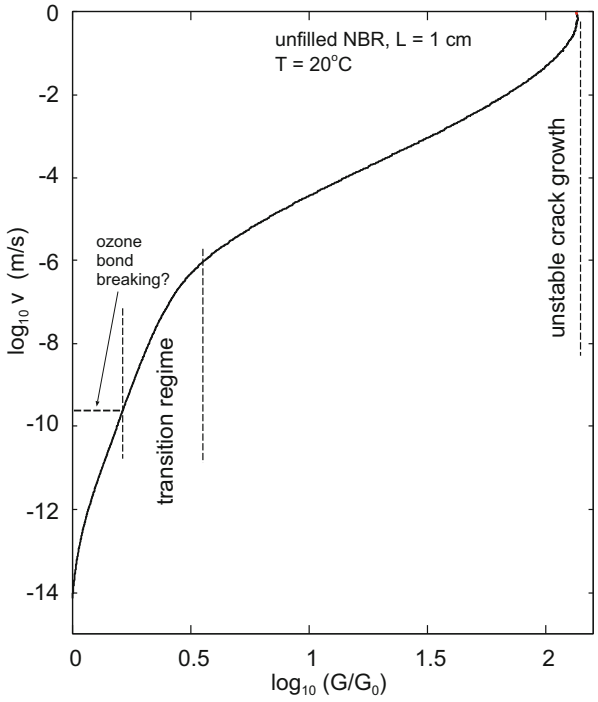

Fig. 41 Crack growth in unfilled NBR rubber

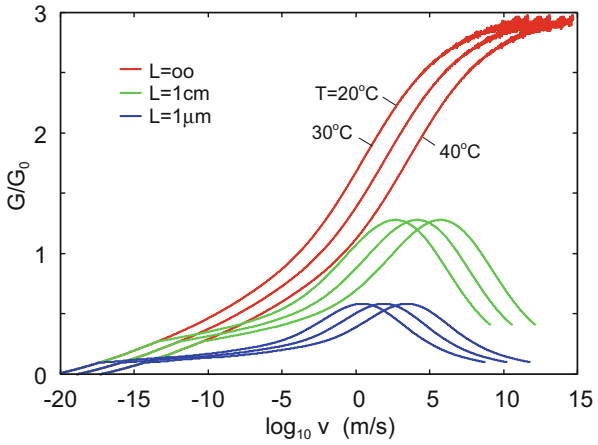

Fig. 42 The crack propagation energy G for an infinite-sized system (red lines), and for finite-sized systems with linear size $L = 1$ cm (green) and $L = 1$ μm (blue). Results are given for the temperatures $T = 20$, 30, and 40°C

4 Summary and Conclusion

We have reviewed a theory for crack propagation in viscoelastic solids. We have considered opening and closing cracks and finite-sized effects. The theory was applied to pressure sensitive adhesives, the ball-flat adhesion problem, intradermal fluid injection, and rubber wear.

Acknowledgements We thank Anand Jagota for useful comments on the manuscript. We thank Boris Lorenz (Continental, Singapore) for the DMA measurements of the pig skin dermis. We thank William Peabody (Keyence Corporation of America, NJ, USA) for the measurements of the roughness profile of the pig dermis crack surface. We thank A. Tiwari for the pull-off force measurements on pressure sensitive adhesive film.

References

1. Knauss WG (2015) A review of fracture in viscoelastic materials. Int J Fract 196:99
2. Schapery RA (1975) Int J Fract 11:549
3. Knauss WG, Dietmann H (1970) Int J Eng Sci 8:643
4. Greenwood JA, Johnson KL (1981) Philos Mag A 43:697
5. Hui CY, Xu DB, Kramer EJ (1992) J Appl Phys 72:3294
6. Gent AN (1996) Langmuir 12:4492
7. de Gennes P-G (1988) C R Acad Sci Paris 307:1949
8. Persson BNJ, Brener EA (2005) Phys Rev E 71:036123
9. Persson BNJ, Albohr O, Heinrich G, Ueba H (2005) J Phys Condens Matter 17:R1071
10. Hui C-Y, Jagota A, Bennison SJ, Londono JD (2003) Crack blunting and strength of soft elastic solids. Proc R Soc Lond A 459:1489
11. Barenblatt GI (1962) Adv Appl Mech 7:55
12. Carbone G, Persson BNJ (2005) Phys Rev Lett 95:114301
13. Carbone F, Persson BNJ (2005) Eur Phys J E 17:261
14. Creton C, Ciccotti M (2016) Rep Prog Phys 79:046601
15. Sun TL, Luo F, Hong W, Cui K, Huang Y, Zhang HJ, King DR, Kurokawa T, Nakajima T, Gong JP (2017) Macromolecules 50:2923
16. Baney JM, Hui CY (1999) J Appl Phys 86:4232
17. Greenwood JA (2004) J Phys D Appl Phys 37:2557
18. Greenwood JA (2007) J Phys D Appl Phys 40:1769
19. Greenwood JA, Johnson KL, Choi S-H, Chaudhury MK (2008) J Phys D Appl Phys 42:035301
20. Persson BNJ (2009) J Phys Condens Matter 21:485001
21. Lorenz B, Pyckhout-Hintzen W, Persson BNJ (2014) Polymer 55:565
22. Bertram Broberg K (1999) Cracks and fracture. Academic Press, New York
23. Saulnier F, Ondarcuhu T, Aradian A, Raphaël E (2004) Macromolecules 37:1067
24. Mueller MK, Knauss WG (1971) J Appl Mech 38(Series E):483
25. Barber M, Donley J, Langer JS (1989) Phys Rev A 40:366
26. Xu DB, Hui CY, Kramer EJ (1992) J Appl Phys 72:3305
27. Rahulkumar P, Jagota A, Bennison SJ, Saigal S (2000) Int J Solids Struct 37:1873
28. Rahul-Kumar P, Jagota A, Bennison SJ, Saigal S, Muralidhar S (1999) Acta Mater 47:4161
29. Seshadri M, Saigal S, Jagota A, Bennison SJ (2007) J Appl Phys 101:093504
30. Thanawala SK, Chaudhury MK (2000) Langmuir 16:1256
31. Persson BNJ (1998) J Phys Condens Matter 10:10529

32. Persson BNJ (1998) Phys Rev Lett 81:3439
33. Persson BNJ (1999) J Chem Phys 110:9713
34. Slootman J, Waltz V, Yeh CJ, Baumann C, Göst R, Comtet J, Creton C (2020) arXiv preprint arXiv:2006.09468
35. D'Amico F, Carbone G, Foglia MM, Galietti U (2013) Eng Fract Mech 98:315
36. Le Gal A, Klüppel M (2008) J Phys Condens Matter 20:015007
37. Lang A, Klüppel M (2017) Wear 380:15
38. Schallamach A (1963) Wear 6:375
39. Persson, BNJ, Volokitin AI (2006) Eur Phys J E 21:69
40. Persson BNJ (2006) Surf Sci Rep 61:201
41. Persson BNJ, Sivebaek IM, Samoilov VN, Zhao K, Volokitin AI, Zhang Z (2008) J Phys Condens Matter 20:395006
42. Tiwari A, Dorogin L, Tahir M, Stöckelhuber KW, Heinrich G, Espallargas N, Persson BNJ (2017) Rubber contact mechanics: adhesion, friction and leakage of seals. Soft Matter 13:9103
43. Lorenz B, Oh YR, Nam SK, Jeon SH, Persson BNJ (2015) J Chem Phys 142:194701
44. Persson BNJ, Lorenz B, Shimizu M, Koishi M (2017) Multiscale contact mechanics with application to seals and rubber friction on dry and lubricated surfaces. In: Designing of elastomer nanocomposites: from theory to applications. Advances in polymer science, vol 275, pp 103–156
45. Roberts AD, Thomas AG (1975) The adhesion and friction of smooth rubber surfaces. Wear 33:45
46. Dalbe M-J, Santucci S, Cortet P-P, Vanel L (2014) Soft Matter 10:132
47. Villey R, Creton C, Cortet P-P, Dalbe M-J, Jet T, Saintyves B, Santucci S, Vanel L, Yarusso DJ, Ciccotti M (2015) Soft Matter 11:3480
48. Barquins M, Ciccotti M (1997) Int J Adhes Adhes 17:65
49. Afferrante L, Carbone G (2016) J Mech Phys Solids 96:223
50. Persson BNJ, Kovalev A, Wasem M, Gnecco E, Gorb SN (2010) EPL 92:46001
51. de Gennes P-G (1996) Langmuir 12:4497
52. Persson BNJ, Albohr O, Creton C, Peveri V (2004) J Chem Phys 120:8779
53. Kendall K (2001) Molecular adhesion and its applications: the sticky universe. Kluwer Academic, New York
54. Tiwari A, Dorogin L, Bennett AI, Schulze KD, Sawyer WG, Tahir M, Heinrich G, Persson BNJ (2017) Soft Matter 13:3602
55. Lorenz B, Krick BA, Mulakaluri N, Smolyakova M, Dieluweit S, Sawyer WG, Persson BNJ (2013) J Phys Condens Matter 25:225004
56. Krick BA, Vail JR, Persson BNJ, Sawyer WG (2012) Tribol Lett 45:185
57. Persson BNJ, Albohr O, Creton C, Peveri V (2004) J Chem Phys. 120:8779
58. Chaudhury MK, Weaver T, Hui CY, Kramer EJ (1996) J Appl Phys 80:30
59. Johnson KL, Kendall K, Roberts AD (1971) Proc R Soc Lond A 324:301
60. Lakhera N, Graucob A, Schneider AS, Kroner E, Arzt E, Yakacki CM, Frick CP (2013) Int J Adhes Adhes 44:184
61. Dorogin L, Tiwari A, Rotella C, Mangiagalli P, Persson BNJ (2018) J Chem Phys 148:234702
62. Rodriguez N, Dorogin L, Chew KT, Persson BNJ (2018) Tribol Int 121:78
63. Dorogin L, Persson BNJ (2018) Soft matter 14:1142
64. Dorogin L, Tiwari A, Rotella C, Mangiagalli P, Persson BNJ (2017) Phys Rev Lett 118:238001
65. Pissarenko A, Yang W, Quan H, Brown KA, Williams A, Proud WG, Meyers MA (2019) Acta Biomater 86:77
66. Zak M, Kuropka P, Kobiel M, Dudek A, Kuratewicz KK, Szotek S (2011) Acta Bioeng Biomech 13:37
67. Swartz MA, Fleury ME (2007) Annu Rev Biomed Eng i 9:229
68. Dannis ML (1974) Rubber Chem Technol 47:1011
69. Khafidh M, Schipper DJ, Masen MA, Vleugels N, Dierkesa WK, Noordermeer JWM (2019) Wear 428–429:481

70. Persson BNJ (2001) J Chem Phys 115:3840
71. Lake GJ, Lindley PB (1965) J Appl Polym Sci 9:1233
72. Wunde M, Klüppel M (2018) Rubber Chem Technol 91:668
73. Layer RW, Lattimer RP (1990) Rubber Chem Technol 63:426
74. Brüning K, Schneider K, Roth SV, Heinrich G (2013) Polymer 54:6200
75. Schallamach A (1954) Proc Phys Soc London Sect B 67:883

Adv Polym Sci (2021) 286: 421–444
https://doi.org/10.1007/12_2020_75

Published online: 21 December 2020

Dissipative Heating, Fatigue and Fracture Behaviour of Rubber Under Multiaxial Loading

S. Dedova, K. Schneider, M. Stommel, and G. Heinrich

Contents

Abstract Nowadays, different concepts to investigate the crack propagation in rubber materials are used. Most of them are based on the investigation of uniaxial loaded specimens and without taking into account the dissipative aspects of deformation.

S. Dedova (✉) and K. Schneider
Leibniz-Institut für Polymerforschung Dresden, Dresden, Germany
e-mail: dedova@ipfdd.de

M. Stommel
Leibniz-Institut für Polymerforschung Dresden, Dresden, Germany

Technische Universität Dresden, Institut für Werkstoffwissenschaft, Dresden, Germany

G. Heinrich
Leibniz-Institut für Polymerforschung Dresden, Dresden, Germany

Technische Universität Dresden, Institut für Textilmaschinen und Textile Hochleistungswerkstofftechnik, Dresden, Germany

Rubber parts are used for different kinds of applications like tires, vibration damper, sealing parts, gaskets, diaphragms, etc. These parts are often subjected to multiaxial cyclic loading during operation. To utilize the whole mechanical potential of the rubber, it is necessary to investigate and characterize the material and crack behaviour under application relevant conditions.

This study will work out that regardless of the deformation state (equibiaxial, asymmetrical biaxial, "pure shear", uniaxial) the same amount of energy is dissipated if the amount of the equivalent strain (von Mises) is equal.

The present paper investigates, how different states of deformation possibly differently triggers the competitive dissipative processes of the material with the aim, to work out the different amount of dissipative effects as a function of the deformation state. It will be further shown how these effects influence the situation at the crack tip during cyclic loading. The correlations between von Mises equivalent strain, dissipative heating and crack propagation were analysed and used for the characterization of the material behaviour at the crack tip.

It is shown how the dissipated energy can be estimated and how the data describe the heating of the and the heat transfer to the surrounding in detail. The dissipated conditions in the whole sample and in the vicinity of the crack tip correlate with the crack behaviour. The dependence of the crack growth rate and thermal state at the crack tip from the von Mises strain is discussed in detail.

A physically motivated model approximates the strain at the crack tip and, finally, estimates the relationship between strain, energy dissipation and temperature state of the rubber material in the vicinity of the crack tip.

The used rubber is a solution-SBR loaded with 50 phr carbon black. The experiments were performed on a biaxial test machine from Coesfeld GmbH & Co. KG. The measurements were done using an optical digital image correlation (DIC) system ARAMIS from GOM, Germany, to measure and analyse the strain. The thermal behaviour was determined by infrared thermography from InfraTec, Germany.

Keywords Crack tip · Dissipative heating · Fatigue · Fracture · Multiaxial testing · Rubber

1 Introduction

Fracture and fatigue behaviour are mostly characterized using two concepts: (1) the global concept of classical tear fatigue analysis (TFA [1, 4–12]) and (2) the local concept, known as a J-integral method [2, 3, 13–17].

The global concept is mostly used for the analysis of fatigue and fracture behaviour, while the local concept is an alternative due to its suitability for the case of deviation of crack growth from the orthogonal direction to the main strain and its independence from specimen geometry.

It is known that the two above concepts are developed initially for elastic materials, where next to the process zone of the crack no energy dissipation appears. But in the case of rubber there is in general a dissipation during deformation, which can be rather well described by the viscoelasticity of the rubber.

In previous works [18, 19] we presented a procedure which enables an energetic description of the deformation and damage process and a separation of elastically stored and dissipated energy components.

The present study is an extension of the previous work, with an improved description of the thermal behaviour of the whole sample, and vicinity of the crack tip. The estimation of the energy dissipation near the crack tip, the dependence of the crack grow behaviour on different multiaxial loaded cases (equibiaxial, asymmetrical biaxial, "pure shear") are investigated in this study with respect to temperature and strain distribution. The experiments are performed using a biaxial test device (Coesfeld GmbH & Co. KG) ([20], http://products.coesfeld.com/WebRoot/WAZ/Shops/44402782/5238/4E9A/BB18/5A3B/993E/D472/521A/76A8/61-490_Biaxtester_engl.pdf. Status 06.2020) to replicate almost realistic multiaxial loading conditions. A short description of the equipment and the used evaluation procedures can be found more detailed in the previous publications [18, 19].

2 Energetic Characterization of Hysteresis Behaviour at Multiaxial Loading Conditions

For a better understanding of the behaviour of rubber material containing cracks, it is necessary to consider various effects that result in dissipation of energy.

With mechanical load of rubber material, mechanical energy (or work) is induced. This energy is not stored in the material in total and cannot be recovered during subsequent unloading. A certain part of the energy is dissipated by dissipative heating, crack initiation and propagation in the molecular network. This leads to a hypothesis that not only different but also competitive dissipative processes occur in a rubber material.

In the first step, it is useful to separate the amount of dissipation according to crack propagation from the amount of viscoelastic dissipative effects. Due to the inhomogeneous deformation of a material containing a crack, it is helpful to characterize initially the viscoelastic behaviour of the uncracked material under homogeneous loading conditions. These information are used to describe the inhomogeneous deformed state of the cracked rubber.

One component of the viscoelastic behaviour – the elastic one – can be recovered and is measured by using the unloading path of the load cycle. Contrarily, the dissipative one is determined by subtracting the energies of the loading and the unloading path of the load cycle. The dissipative part of energy causes an increase in temperature in the material [18, 21]. Externally supplied energy during the loading

splits into thermal energy, saved in the material and into heat which is transferred to the surrounding.

For the material containing a crack (case of inhomogeneous strain situation), energy dissipation is not only located in the crack tip, leading to a local temperature peak, but they are also distributed across the whole deformed viscoelastic material.

The energy density, *w,* of a volume element will be changed per load cycle under an external load according to:

$$\Delta w = \oint \sigma_{ij} d\varepsilon_{ij} = \oint \sigma_{ij} d\lambda_{ij}, \tag{1}$$

$\sigma_{ij}$is the applied stress and ε_{ij} is the applied strain, where i and j are the tensor component indices. In this work engineering stress and engineering strain will be used, which are defined as:

$$\sigma = \frac{F}{S_0}, \text{and } \varepsilon = \frac{L - L_0}{L_0},$$

here F is the loading force, S_0 is the initial cross-section, L and L_0 are the length at the current and initial deformation, respectively. The stretch ratios are defined as $\lambda = \varepsilon + 1$.

According to the first law of thermodynamics (energy conservation) the energy balance of the load cycle can be written as

$$\Delta w + \Delta q = \Delta u_{\text{therm}} + \Delta u_{\text{pot}} + \Delta w_{\text{kin}} + \Delta w_{\text{irrev}}, \tag{2}$$

here Δw is the mechanical work applied per volume element (during one closed loading cycle according to Eq. (1)), Δq is the thermal energy (heat) per volume element, $\Delta u_{\text{therm}} = \rho\, c_p \Delta T$ is the change in the thermal part of the internal energy per volume element using ρ, c_p and $\Delta\ T$ as density, specific heat and temperature difference of the cycle. $\Delta u_{\text{pot}} = 0$ is the change in the elastically stored potential energy per volume element and it equals zero, as we assume no change of the potential energy between the beginning and the end of the cycle, $\Delta w_{\text{kin}} = 0$ is the change of the kinetic energy per volume element, which equals zero in the case of a closed loading cycle, and Δw_{irrev} is the irreversible energy loss per volume element due to the creation of a new crack surface that equals also zero if the crack does not grow.

In a two-dimensional planar approximation for a volume element of the sample with the thickness d_0 it follows for a closed load cycle

$$\oint \sigma_{ij} d\varepsilon_{ij} d_0 + \Delta q d_0 = \rho\, c_p\, \Delta T d_0. \tag{3}$$

The heat, Δq, supplied to an incompressible volume element, dV with twice the surface $dA = dxdy$, the initial thickness, d_0, and the actual thickness, d, respectively,

during a closed load cycle follows a simple linear expression for the heat exchange according to

$$\Delta q = -\frac{2}{dV}\int \alpha\, dA(T - T_0)\, dt = -\frac{2}{d_0}\int \alpha\, \lambda_x\, \lambda_y\, (T - T_0)\, dt, \tag{4}$$

where

$$dV = dx_0 \cdot dy_0 \cdot d_0 = dA \cdot d = dx \cdot dy \cdot d = \lambda_x \cdot \lambda_y \cdot dA_0 \cdot d \tag{5}$$

and the initial surface area is dA_0.

Here α is the heat transfer coefficient and *2* in the numerator of Eq. (4) refers to both sides of the sample (upper and lower surfaces in the case of the biaxial test), where the heat is exchanged, assuming comparable heat transfer on the upper and the lower side of the sample. T is the temperature of the volume element under consideration and T_0 the temperature of the environment. The integration runs over the whole load cycle. Then the heat transfer coefficient can be estimated for a closed load cycle using the separately estimated specific heat capacity by

$$\alpha = \frac{d_0\left(\oint \sigma\, d\varepsilon - \rho\, c_p \Delta T\right)}{2\int \lambda_x \lambda_y * (T - T_0) dt}. \tag{6}$$

An alternative approach to estimate the heat transfer coefficient, α, by the time constant of free cooling of a dissipative heated sample [18, 19] turned out to be inappropriate, because the convective heat transfer of an unmoved sample is strongly different to the situation of a dynamically deformed sample.

Now, the knowledge of α enables the estimation of the energy density for different kinds of energy over the whole loading–unloading cycle, as long as there is no crack propagation observed.

Especially, the changes in the density of the potential energy can be estimated as

$$\Delta u_{\text{pot}} = -\Delta w - \Delta q + \Delta u_{\text{therm}}$$

$$\Delta u_{\text{pot}} = -\int_{\varepsilon_0}^{\varepsilon} \sigma\, d\varepsilon - 2\int_{t_0}^{t} \alpha\, \lambda_x \lambda_y\, (T - T_0)\, dt + \int_{T_0}^{T} \rho\, c_p\, dT. \tag{7}$$

To analyse these effects in the case of multiaxial loading, independent of individual load axes, the von Mises strain was chosen as an equivalent value.

For the comparison of the different loaded samples from the estimated field of engineering strains the von Mises equivalent strain was calculated under the assumption of incompressibility and plane strain conditions in the x-y plane as

$$\varepsilon_{\mathrm{M\_equ}} = \exp\left(\sqrt{\frac{4}{3}\left(\left(\ln\lambda_{\mathrm{major}}\right)^2 + \ln\lambda_{\mathrm{major}} * \ln\lambda_{\mathrm{minor},1} + \left(\ln\lambda_{\mathrm{minor},1}\right)^2\right)}\right) - 1$$

with $\lambda_{\mathrm{major,minor},1} = 1 + \frac{\varepsilon_x+\varepsilon_y}{2} \pm \sqrt{\left(\frac{\varepsilon_x+\varepsilon_y}{2}\right)^2 - \left(\varepsilon_x\varepsilon_y - \varepsilon_{xy}^2\right)}$ and

$$\lambda_{\mathrm{minor2}} = \frac{1}{\lambda_{\mathrm{major}}\,\lambda_{\mathrm{minor},1}}. \tag{8}$$

Here are λ_{major}, $\lambda_{\mathrm{minor},\ 1}$, $\lambda_{\mathrm{minor},\ 2}$ are the major and minor strain ratios, respectively.

Under the condition of incompressibility there is no change in volume. Directly measurable (using ARAMIS software) von Mises strain is used, which is proportional to the Euclidean norm of the deviatoric part of the strain tensor.

The crack tip field, i.e. the stresses and strains in the vicinity of a crack tip (the so-called process zone), is of fundamental importance, it determines the processes taking place in this region [22]. To approach the strain at the crack tip in an appropriate way, the optically estimated strain was approximated assuming a decay proportional to the square root of the distance from the crack tip, similar to the common stress decay at a crack tip. Additionally, it is assumed that a constant critical value of the strain is reached in a region with the radius of r_{cr} around the crack tip. So the strain was approximated as

$$\varepsilon_M = \varepsilon_{M0} + \frac{a}{\sqrt{r + r_{cr}}} \tag{9}$$

with the reference strain, ε_{M0}, within a critical radius, r_{cr}, around the crack, within that the strain is limited to a critical value of

$$\varepsilon_{cr} = \varepsilon_{M0} + \frac{a}{\sqrt{r_{cr}}} \text{ or } a = \sqrt{r_{cr}} * (\varepsilon_{cr} - \varepsilon_{M0}). \tag{10}$$

In this way, finally the critical strains, ε_{cr}, and thus a critical radius, r_{cr}, will be determined to characterize the processes at the crack tip.

3 Materials and Experimental Procedure

3.1 Materials and Sample Preparation

The investigations were carried out with an oil-extended solution styrene butadiene rubber (SSBR) with a composition summarized in Table 1. The samples were vulcanized for 10 min at 160°C with sulphur as crosslinker.

Table 1 The composition of investigated material

Ingredient	SSBR with 50 phr CB
SSBR Buna VSL 4526-2 HM[a]	137.5
CB Corax N330	50
Zinc oxide (Red seal)	3
Stearic acid	2
Vulkanox 4020 (6PPD)	1
Sulphur	1.5
Vulkacit CZ (CBS)	1.5
Luvomaxx DPG	2

[a]The SBR contains 27.3% by weight oil, so that the rubber content is the reference value of 100, with 50 phr (parts per hundred rubber) of carbon black

3.2 Experimental Setup

The experiments were done using a Biaxial Tester (Coesfeld GmbH & Co. KG; Dortmund, Germany) at Leibniz-Institut für Polymerforschung Dresden (IPF) ([20], http://products.coesfeld.com/WebRoot/WAZ/Shops/44402782/5238/4E9A/BB18/5A3B/993E/D472/521A/76A8/61-490_Biaxtester_engl.pdf. Status 06.2020). For the tests square specimens with a framing bulge for a form fit in a clamping system were taken. The bulge was cut between each individual clamp to increase the homogeneity of the strain fields. The data of the samples are summarized in Table 2.

The strain in the flat samples was estimated by the displacement of the clamps. The optical camera (JAI BM-500 GE) and the illumination (LQ-LADB875-30°/95RL) were controlled together with the motors and the displacement–force sensors by a software from Coesfeld. The optical frame rate was 1 Hz with a resolution of 0.08 mm/pix.

Subsequent optical analyses of strain fields were done by DIC using software ARAMIS from GOM, Germany. A 19 x 19 pix facet size with 15 pix distance was chosen for the optical evaluation. This empirical set value depends on the combination of such factors as picture resolution and quality of stochastic patterns. A random pattern was applied on the samples by an airbrush. To ensure that the pattern adheres at high strains and can be evaluated accordingly the paint was mixed with a latex paint 2/1.

Table 2 Dimensions of the investigated samples and properties of the material

Initial thickness	mm	1.85
Initial length	mm	77
Initial width	mm	77
Diameter of the bulge	mm	5.5
Density	g/cm^3	1.099
Heat capacity, estimated by DSC	J/g K	1.665

3.2.1 Thermography

Parallel to the mechanical measurement and the optical recording of strain fields a 2D-temperature measurement was done using an IR-camera VarioCam from InfraTec, Germany, with the lens MWIR f/2.0 f = 50 mm. The frame rate was 20 Hz with a resolution of 0.37 mm/pix. The total field of view is 45,052 mm^2. For the analysis the IRBIS Software was used. The temperature measurement together with the displacement and force measurement enables in the case of homogeneous deformation according to (3), (5) and (7) the time-dependent estimation of the locally stored and dissipated energy.

The complete setup is shown in Fig. 1. The arrangement is described in more detail in [20, 23].

The optical camera was placed perpendicular to the specimen surface. The axis of the thermal camera has to be tilted in relation to the perpendicular axis to enable a simultaneous measurement of the strain and temperature field with both cameras.

To avoid metallic reflexes, which could influence the observed temperature data, the clamps were covered by white paper. Additionally, it was checked and verified that the illumination of the sample and the tilted arrangement of the IR camera did not have a relevant impact on the measured temperature field. The calibration of the thermal camera for the black and the patterned specimen was double-checked with a thermocouple. There was no influence of the pattern on the estimated temperature and the temperature values of the IR-system found.

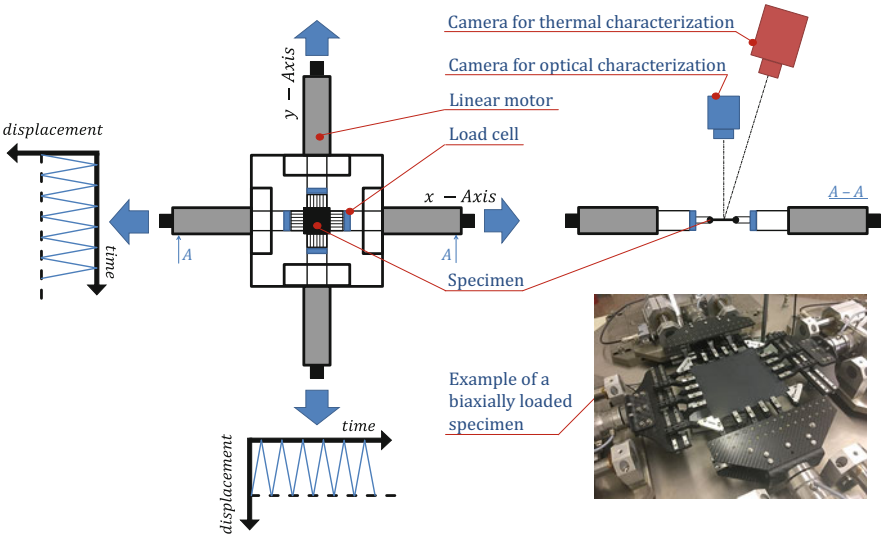

Fig. 1 Scheme of experimental setup. Left: principle structure of Biaxial Tester (top view); right: lateral view with principal positions of optical and thermal (IR) camera; at the bottom right: clamping system with specimen at max strain

3.2.2 Experimental Procedure

Generally, two types of experiments were performed:

1. Estimation of properties under homogeneous stretching conditions (unnotched sample).
2. Characterization of a notched sample following the crack propagation behaviour (notched sample).

Firstly, all samples were preloaded equibiaxially up to 120% strain with 1 Hz by a triangular waveform for 30 cycles in order to eliminate the Mullins effect ("demullinization"). The state after demullinization was defined as the initial/reference state for further measurements.

Afterwards, before each dynamic loading, the specimens were loaded quasi-statically at a speed of 0.1 mm/s (approx. 0.13%/s) up to the maximum displacement of the particular experiment. This loading step is used for following optical the strain field changes from beginning up to target (maximum) strain during loading process.

Finally, the dynamic part of the experiment was done at 1 Hz under a triangular waveform using the following 4 regimes: equibiaxial (EB), asymmetrical biaxial (AB), "pure shear" (PS) and for the unnotched case also uniaxial (UA) tension. A triangular loading was used to enable a comparison of the experiments with previous own tensile tests done with constant strain rate (DIN 53504:2017–03).

During the tests the technical strain is estimated by $\varepsilon_i = \Delta l_i / l_{i,\,0}$. 300 load cycles were applied (corresponding 300 s) on the unnotched samples at each strain value in accordance with Table 3 to reach the thermally stable state (temperature plateau).

At 120% strain the samples failed before reaching the thermally stable state [19].

In the case of notched samples 1,000 load cycles were applied to reach a stable crack propagation. Here the applied strain was limited (Table 3) because at higher values the samples failed in an instable way (spontaneous total fracture at the initial cycles).

The upper loading point for cyclic loading corresponds to the maximum target elongation for the current experiment. The lower point of loading corresponds to zero force. The general schedule of experiment and the specimen is shown in Fig. 2.

Table 3 Experimental details

Triangular load	Unnotched samples (homogeneous stretch conditions)		Notched samples (inhomogeneous stretch conditions)	
1 Hz	Cycles	Main strain = strain amplitude	Cycles	Main strain = strain amplitude
EB ($\varepsilon_x = \varepsilon_y$)	300	30, 60, 90%	1,000	15, 20, 25, 30, 35%
AB ($\varepsilon_x = 2\varepsilon_y$)	300	30, 60, 90%	1,000	15, 20, 25, 30, 35%
PS ($\varepsilon_x = x$; $\varepsilon_y = 1$)	300	30, 60, 90%	1,000	15, 20, 25, 30, 35%
UA ($\varepsilon_x = x$)	300	30, 60, 90%	–	–

[a]Here ε_x – main strain; ε_y–minor strain

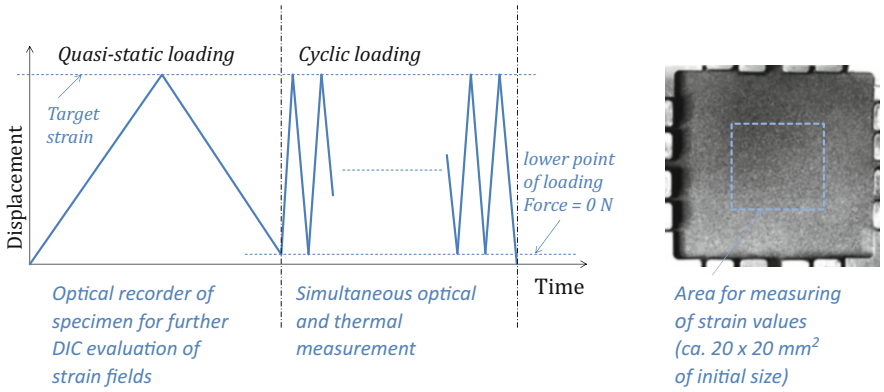

Fig. 2 Left: Schematic time schedule of the experiments; Right: Image of a specimen with the marked area for measuring the strain values

According to the permanent set of the specimens the strain at the lower loading point was slightly increasing with the maximum strain.

An experimental speciality is that during the first 10 cycles the self-adaptive controller of the Biaxial Tester is stabilizing the periodic loading procedure. During this period of the experiments the strain values are not precisely the prescribed values and, therefore, they are disregarded.

4 Results and Discussion

4.1 Mechanical Characterization of Homogeneous Deformed Samples

The strain measurements were calibrated optically before the first loading cycles. A specimen stretched up to 90% in EB, AB and PS mode is shown exemplarily in Fig. 3. Hereby the technical strain is estimated optically vs. the strain estimated by the displacement of the clamps.

The optical strain values were measured in the middle region of the sample of about 20 x 20 mm^2 of initial size. The mean value from this region was used for the investigation of the relationship between optical strain and technical strain.

To characterize the stress–strain behaviour in the different loading regimes, the curves of the last cycle are shown in Fig. 4.

For each experiment, the dissipated energy density was calculated by performing the integration according to Eq. (1). The dependence of the dissipated energy density in dependence of the loading conditions vs. individual and von Mises equivalent strain is shown in Fig. 5.

It was found that the dissipated energy per volume and per cycle correlates well with the von Mises equivalent strain. This strain is quite homogeneous over nearly

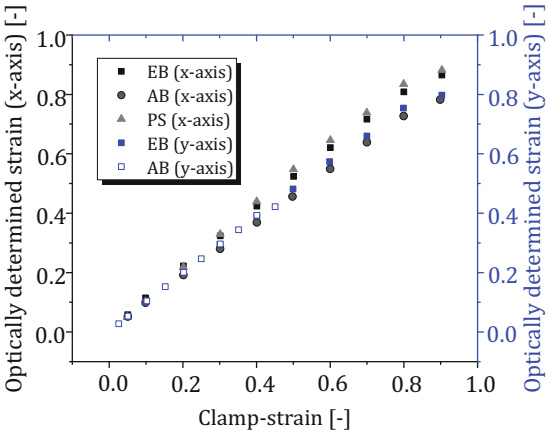

Fig. 3 Relation between the optically determined strain to the clamp-strain, determined by the displacement of the clamps

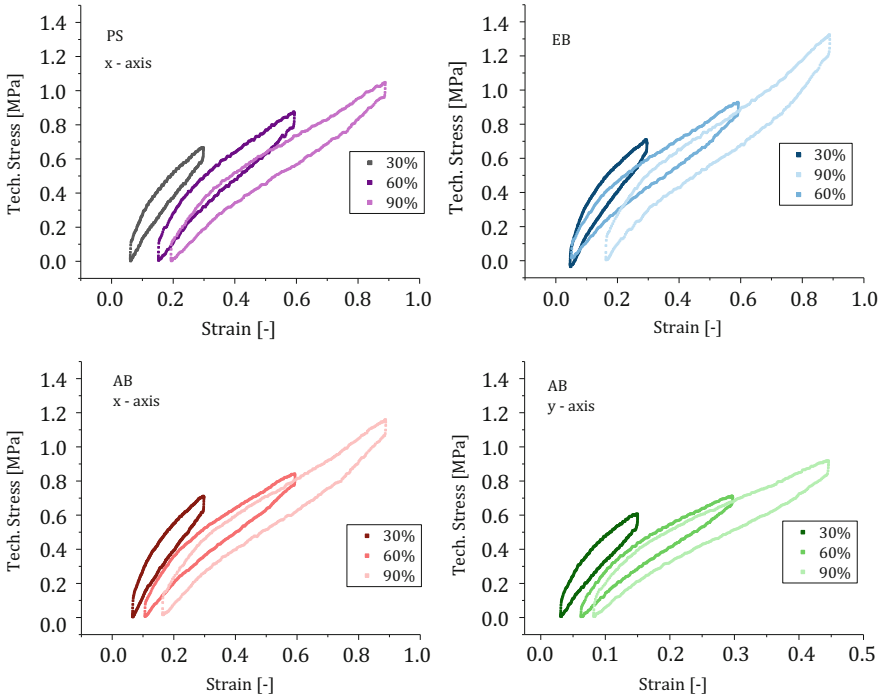

Fig. 4 Stress–strain curves of the last cycle for different loading conditions, SBR50, unnotched samples

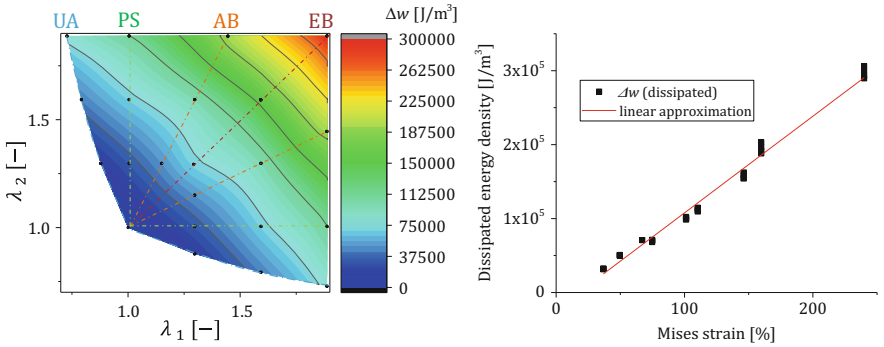

Fig. 5 Dissipated energy density of the last dynamical loading cycle of unnotched samples at different loading conditions (left) vs. von Mises equivalent strain (right)

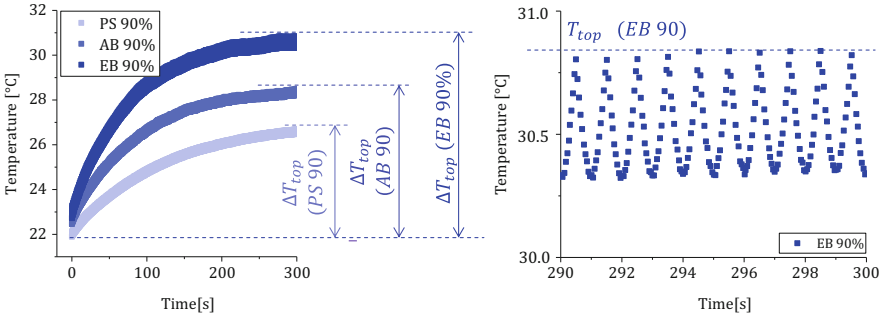

Fig. 6 Example of dissipative heating curves for different loading conditions with main strain 90%; Left: Whole time regime, Right: final 10 cycles of EB loading behaviour zoomed out

the whole EB stretched sample, thus the temperature distribution is quite homogeneous.

By cyclic loading of unnotched samples, the samples were heated by internal dissipation. The overall thermal behaviour can be approximated with an exponential function, see Fig. 6, left. In detail the global trend is superimposed by the heating during the individual cycles, see Fig. 6, right.

On the right diagram of Fig. 6 the temperature for individual cycles shows no linear behaviour with respect to the deformation, where the triangular waveform (linear deformation) has been applied. This temperature profile originates from the hysteresis and the non-linear stress–strain behaviour of the samples.

For each individual cycle it is now possible to estimate the coefficient of heat transfer according to Eq. (6). In Fig. 7 the coefficient of heat transfer is shown for the different loading regimes over the actual sample temperature.

It was found that the coefficient of heat transfer, α, is strongly dependent on the overall deformation of the sample. Obviously, the sample movement changes the conditions of heat transfer by local convection via the moving air at the surface.

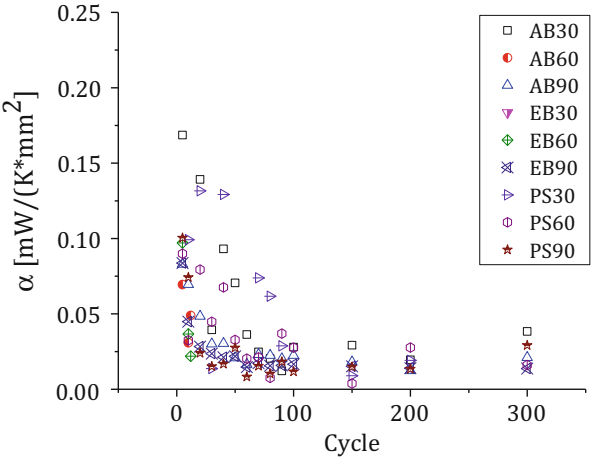

Fig. 7 Heat transfer coefficients, estimated for different loading regimes and amplitudes or sample temperatures, respectively

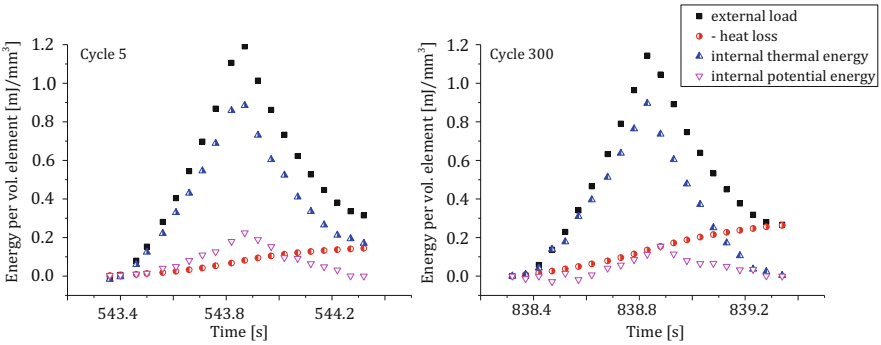

Fig. 8 Components of supplied energy and internal energy during a 5th and 300th loading cycle at the EB loading regime of $\varepsilon_x = \varepsilon_y = 90\%$

Generally, the coefficient of heat transfer stabilizes after about 100 cycles in the range of 0.02... 0.04 mW/Kmm^2.

Using the locally estimated coefficients of heat transfer, the kinds of the internal energy were estimated. Figure 8 shows the components at the beginning and end of the complete loading process (using the EB90 specimen as an example), namely for the 5th and the 300th cycle.

It can be seen from Fig. 8 that only a certain amount of the applied mechanical energy can be recovered, another portion is used to increase the internal energy or is transmitted as heat to the surrounding, respectively. During a deformation cycle only a small amount of applied energy is elastically stored as potential energy. The

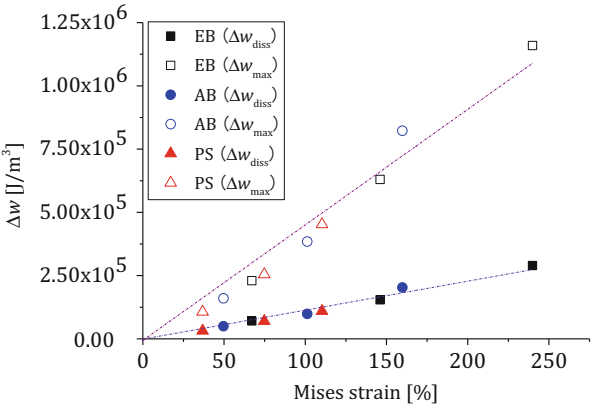

Fig. 9 Maximum input of mechanical energy density during the last loading cycle at different loading regimes in dependence of the von Mises equivalent strain (open symbols) and dissipated energy density during the whole cycle (filled symbols)

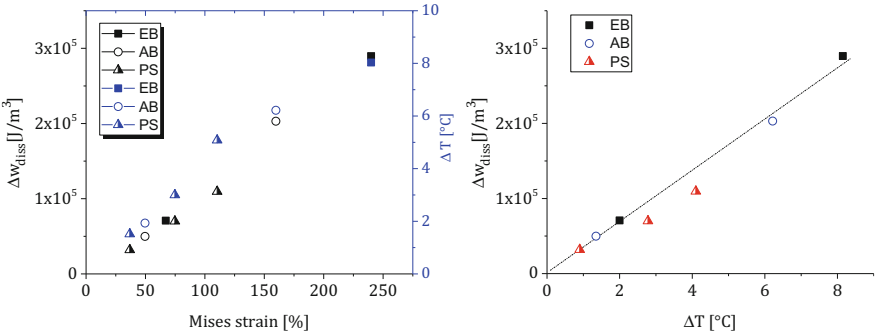

Fig. 10 Dependence of Δw and equilibrium temperature difference, ΔT,from von Mises strain (left); correlation of Δw and equilibrium temperature difference, ΔT (right)

individual kinds of internal energy correlate also for different loading regimes quite good with the von Mises equivalent strain, see Fig. 9. The results in Fig. 9 suggest that the amount of mechanical and dissipated energy density does not depend on the deformation mode provided that the amount of the von Mises strain is equal.

The small amount of potential energy which is elastically stored is much smaller than the thermally stored amount.

Figure 10 shows the correlations between von Mises strain, dissipated energy density Δw and temperature differenceΔT. It can be seen that the Δw andΔT show an almost linear dependence of von Mises strain and remain once again independent of the deformation mode (PS, AB or EB). Between the Δw values andΔT an almost linear trend is also observed.

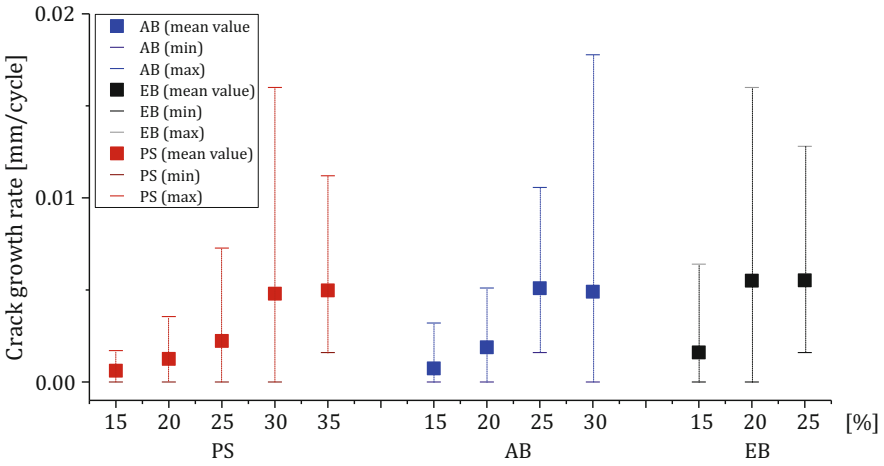

Fig. 11 Crack grow rate at varied strain; mean strain equals strain amplitude

4.2 Properties Under Inhomogeneous Stretching and Crack Propagation

4.2.1 Crack Growth Rate

By optical analysis of the crack propagation during cyclic loading the crack growth rate was evaluated for the different loading conditions, namely varied deformation modes (AB, EB, PS) and varied strain amplitudes (from 15% up to 35% strain of x-axis) (see Table 3, notched samples). The crack length was measured each 50 cycles. For the load conditions of AB 35% and EB 30% and 35% the crack growth was instable. The specimens have been totally ruptured during the first loading and it was not possible to estimate a crack growth rate subsequently. The results are presented in Fig. 11. The bars represent differences in the crack growth rate over the intervals of each 50 cycles. The stable crack growth has been defined due to an experiment that lasted minimally 150 cycles.

The trend for different loading conditions shows the increase of the crack growth rate in parallel to the load level. The mean values of load conditions PS 30% and 35%, AB 25% and 30%, and EB 20% and 25% stay on the comparable level. At the other loading levels a clear increase of crack growth rate with the loading amplitude is found. Relatively large error bars show that the crack growth was not always continuous. But with regard to the whole process the scatter of the values remains relatively low (between 0 and 0.018 mm/cycle).

4.2.2 Development of Maximum Temperature Near the Crack Tip

During a stable crack growth the temperature of the sample and the maximum temperature, $T_{max,}$ near the crack tip was estimated by IR thermography. The global heat build-up curves can be approximated by an exponential function, as it would be expected from the fundamental solution of the heat conduction equation, describing the T_{max} of the individual loading cycles, see Fig. 12.

The slight deviations of T_{max} temperature at the given cycle on the extrapolating exponential behaviour seem to correlate to the real steps of crack growth.

Figure 13 shows the crack growth rate in dependence on the difference of the T_{max} with respect to the surrounding. Each point refers to an experiment with the relevant loading conditions described above. According to the different loading regimes different samples were used. There is a nearly linear dependence of the log of crack growth rate from the temperature difference, independent of the type of loading.

4.2.3 Strain and Temperature at the Crack Tip

If one measures strains by DIC the measured strain field is always dependent on the size and distance of the used facets with the random pattern on the surface of the sample. Therefore, the strain at the crack tip cannot be estimated directly. On the other side, the IR-images does not have this restriction. Here it is generally possible to estimate the temperature directly at the crack tip on the flat side of the specimen and also within the crack tip. But here, according to the changed geometry and mainly the reduced thickness the surface-to-bulk ratio is changed and so also the heat transfer to the surrounding. According to the remarkably increased temperature at the crack tip additionally the heat exchange within the sample must be taken into account. So the maximum temperature reflects neither the dissipated energy nor the strain at the crack tip, respectively.

Figure 14 shows an example of the temperature vs. the von Mises strain along the ligament (= path of prospective crack propagation in an initial notch) for the sample EB25. While the slope of the curve for strains up to about 80% is nearly linear, it reduces drastically according to the above described reasons for higher strains. The other investigated systems show similar behaviour.

Figure 15 shows the strain field, estimated by ARAMIS, and the temperature field for the specimen EB25. The reference temperature was 23°C. During cyclic loading of a notched sample, an inhomogeneous strain field and temperature field will be induced on the specimen near the crack tip (area A). At a certain distance from the crack tip, strain and temperature remain close to the constant value according to the homogenously deformed sample (area B). On the bottom the approximated and extrapolated strain along the ligament according to Eq. (9) is shown. Modelling the strain at the ligament for the different geometries gives satisfying results with an $\varepsilon_{M0} = 0$ for the different loading situations with identical $\varepsilon_{cr} = 300$ [%] and different

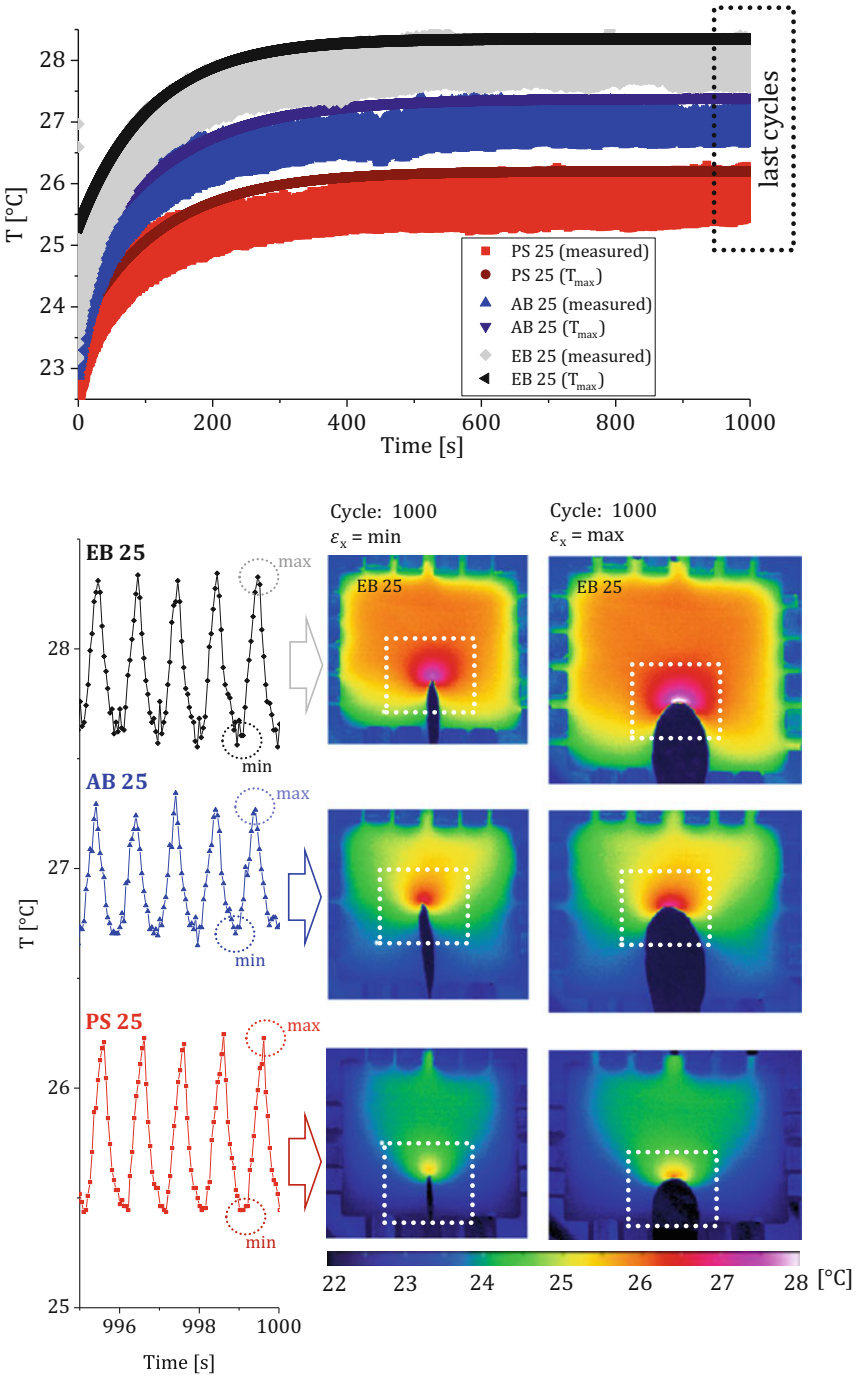

Fig. 12 Top: Maximum temperature at the crack tip of a cyclically loaded (25% strain) notched PS, AB and EB-specimen; bottom: the change of the temperature field between loading and unloading position at the last cycles

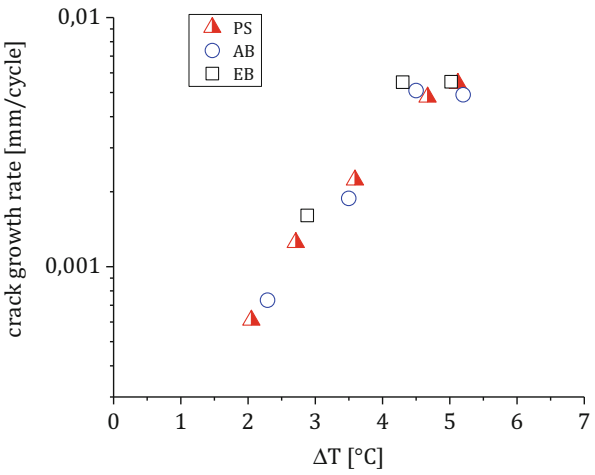

Fig. 13 Crack grow rate (mean value, log-scale) vs. temperature amplitude of T_{max} near the crack tip during stable crack growth

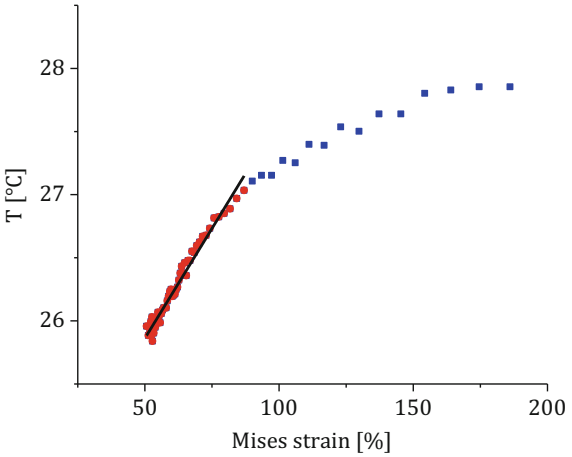

Fig. 14 Surface temperature of the EB25 sample vs. the von Mises strain along the ligament (prospective crack path)

values for r_{cr}. Here it is shown that the value of ε_{cr} has only a very small influence on the approximation, its real determination is therefore only conditionally meaningful. Conversely, the approximation is very strongly dependent on r_{cr}. Insofar r_{cr} is relevant for further discussion.

The temperature and measured values of von Mises strain and extrapolation of the strain to the crack tip at the crack tip region (area A) are shown in Fig. 16.

In Fig. 17. the dependence of the logarithm of crack growth rate on the von Mises strain and the dependence of the critical value, r_{cr}, on the von Mises strain of the homogeneous area *B* are shown.

It is obvious that the crack growth rate and the critical value r_{cr} increase with the von Mises strain in the homogeneously deformed region. In addition, there are

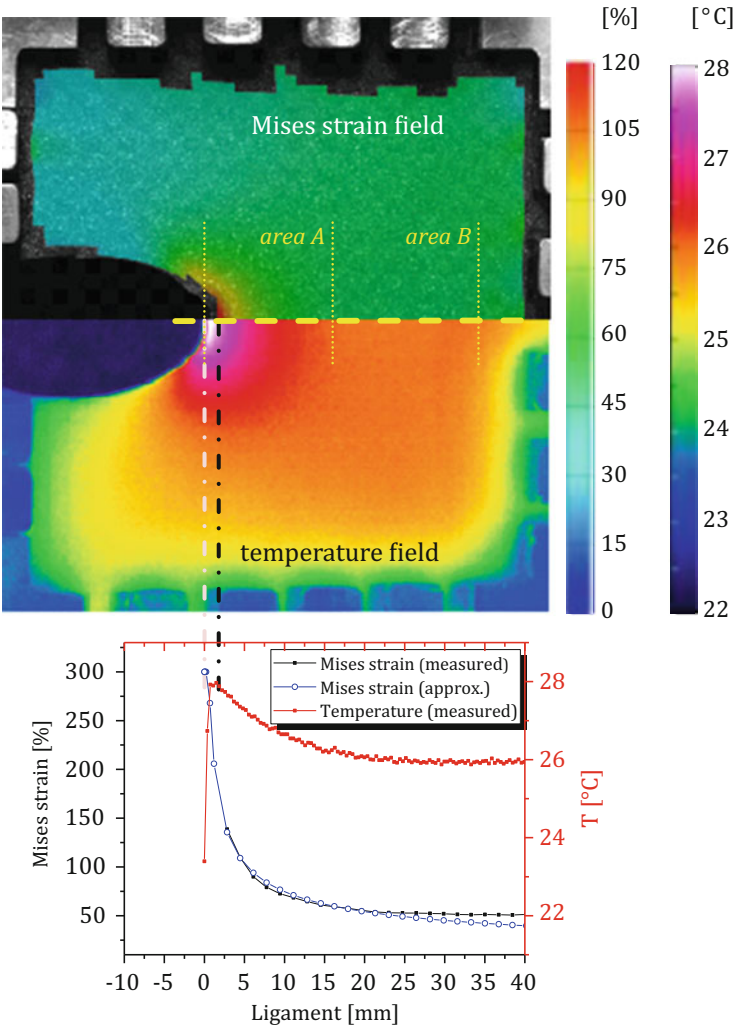

Fig. 15 Pre-cracked sample EB25 with propagating crack and illustration of region A and B on the von Mises equivalent strain and temperature field, and the ligament (yellow dashed line)

differences in the nature of the load, which will have to be investigated in detail in the future.

In Fig. 18 the dependence of ΔT on the von Mises strain in the homogeneously deformed region is shown. The correlation shows the nearly linear trend independent of the loading conditions.

The used model for the extrapolation means that there is a critical strain at the crack tip, but a different size of this critical range.

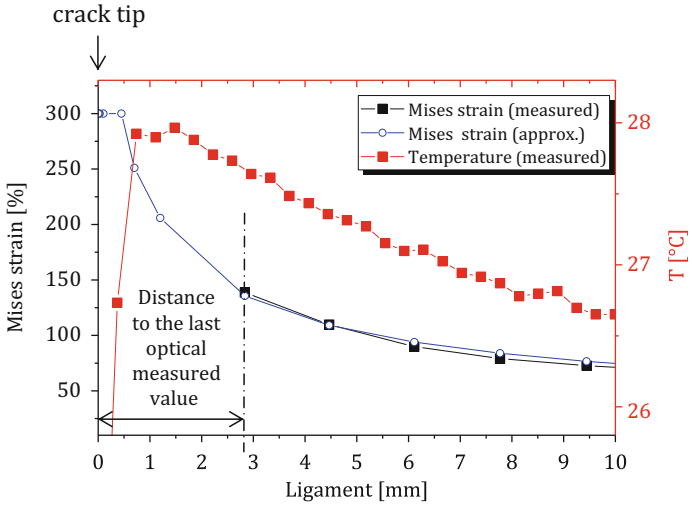

Fig. 16 Crack tip region (area A): temperature and von Mises strain, measured values and extrapolation of the strain to the crack tip

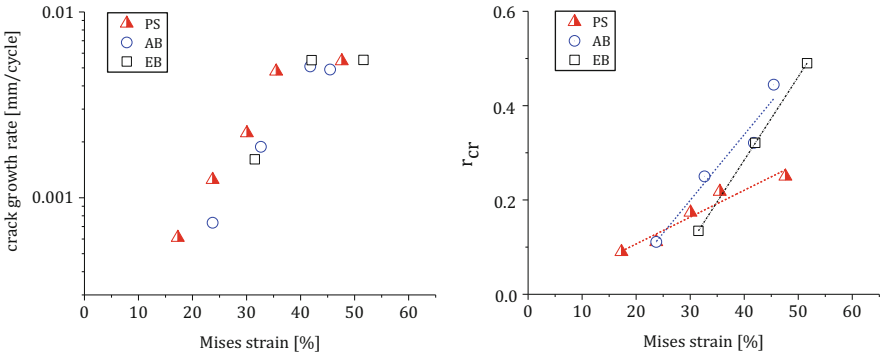

Fig. 17 Left: Dependence of the crack growth rate (mean value, decadic log-scale) on the von Mises strain in the homogeneous deformed area *B*; Right : dependence of the critical value r_{cr} on the von Mises strain in the homogeneous deformed area *B*

The temperature situation on the crack tip correlates with the crack growth rate, but for a quantitative evaluation it will be necessary to improve the evaluation of the thermal measurements.

The characterization of the situation close to the crack tip needs further measurements. It will be necessary to improve the model-based extrapolation of the strain at the crack tip to estimate the size of this critical strained region.

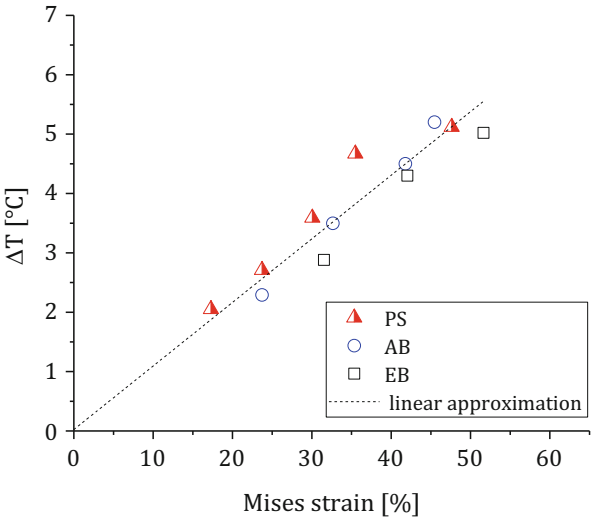

Fig. 18 Dependence of the ΔT of the crack tip on the von Mises strain in the homogeneously deformed area (area *B*)

5 Conclusions

In the present study a combined mechanical and thermal analysis of rubber under complex loading conditions was presented. The experiments were performed on SSBR with 50 phr carbon black. For homogeneous deformation and cyclic loading a strong correlation between von Mises strain and the dissipated energy within the material was found. According to a thermal model it was possible to correlate the energy dissipation to the surface temperature of the sample.

For strain estimation at the crack tip it is necessary to model the strain for the ligament at the sample surface to the crack tip, because the last measured grid points of the optical evaluation are far away from the crack tip. This extrapolation is quite well possible by a physical-motivated function (Eq. 10). It enables the description of the strain with the assumption of an ultimate strain at the crack tip. The size of the region of this ultimate strain depends on the global strain in the homogeneously deformed samples. It is in the range below 0.5 mm. This size correlates with the estimated crack growth rate.

Using the relation between strain and energy dissipation enables to extrapolate the nominal temperature resp. energy dissipation at the crack tip. The deviation from the real measured temperature close to the crack tip is caused by changed cooling behaviour compared to the flat sample.

According to the linear relation between von Mises strain and energy dissipation in the homogeneous deformed specimen, there is also a linear dependence of the log crack growth rate from the locally dissipated energy.

Although the resolution of IR thermography is much better than the local strain estimation by image correlation techniques, it cannot directly be used for the characterization of crack propagation.

Acknowledgements Kristina Eichhorn, Dan Pornhagen and Eric Schlötke are acknowledged for their support at the experiments, Dr. Jan Domurath for helpful discussion with respect to data evaluation.

References

1. Rivlin RS, Thomas AG (1952) Rupture of rubber. I. Characteristic energy for tearing. J Polym Sci X(3):291–318
2. Cherepanov GP (1967) Crack propagation in continuous media. PMM 31(3):476–488
3. Rice JA (1968) Path independent integral and the approximate analysis of strain concentration by notches and cracks. J Appl Mech 35:379–386
4. Mars WV, Fatemi A (2002) A literature survey on fatigue analysis approaches for rubber. Int J Fatigue 24:949–961
5. Gent AN, Lindley PB, Thomas AG (1964) Cut growth and fatigue of rubbers. I. The relationship between cut growth and fatigue. J Appl Polym Sci 8:455–466
6. Stadlbauer F (2013) Einfluss des Rußfüllgrades von Elastomeren auf Aspekte der Ermüdung in Zug-Druck-Belastung. KGK 7-8:37–42
7. Stocek R, Kratina O, Ghosh P, Malac J, Mukhopadhyay R (2017) Grellmann W, Langer B (eds) Influence of thermal ageing process on the crack propagation of rubber used for tire application. Springer, Berlin, pp 351–363
8. Marano C, Boggio M, Cazzoni E, Rink M (2014) Fracture phenomenology and toughness of filled natural rubber compounds via the pure shear test specimen. Rubber Chem Technol 87 (3):501–515
9. Schieppati J, Schrittesser B, Wondracek A, Robin S, Holzner A, Pinter G (2018) Impact of temperature on the fatigue and crack growth behavior of rubbers. Proc Struct Integr 13:642–647
10. Xiang F, Schneider K, Heinrich G (2020) New observations regarding fatigue crack paths and their fracture surfaces in natural rubber: influences of R-ratio and pre-load. Int J Fatigue 135:1–13
11. Stocek R, Stanicka M, Zadrapa P (2020) Future trends in predicting the complex fracture behaviour of rubber materials. Continuum mechanics and thermodynamics. Springer, Berlin
12. Stoček R, Heinrich G, Gehde M, Kipscholl R (2013) Analysis of dynamic crack propagation in elastomers by simultaneous tensile- and pure-shear-mode testing. In: Grellmann W et al (eds) Fracture mechanics and statistical mechanics of reinforced elastomeric blends. LNACM, vol 70. Springer, Berlin, pp 269–301
13. Wunde M, Klüppel M, Vatterott C, Tschimmel J, Lacayo-Pineda J, Schulze A, Heinrich G (2019) Verbesserung der Laborvorhersagen zum Risswachstum und Verschleiß von LKW-Reifenlaufflächen. KGK 10:72–78
14. Wunde M, Plagge J, Klüppel M (2019) The role of stress softening in crack propagation offiller reinforced elastomers as evaluated by the J-integral. Eng Fract Mech 214:520–533
15. Nguyen TD, Govindjee S, Klein PA, Gao H (2005) A material force method for inelastic fracture mechanics. J Mech Phys Solids 53:91–121
16. El Yaagoubi M, Juhre D, Meier J, Kröger N, Alshuth T, Giese U (2018) Lifetime prediction of filled elastomers based on particle distribution and the J-integral evaluation. Int J Fatigue 112:341–354
17. Caimmi F, Calabrò R, Briatico-Vangosa F, Marano C, Rink M (2015) J-integral from full field kinematic data for natural rubber compounds. Strain 51:343–356
18. Dedova S, Schneider K, Heinrich G (2017) Influence of dissipative specimen heating on the tearing energy of elastomers estimated by global and local characterization methods. In: Lion A, Johlitz M (eds) Constitutive models for rubber X. CRC Press, pp 219–224

19. Dedova S, Schneider K, Heinrich G (2019) Energy based characterization of fracture and fatigue behaviour of rubber in complex loading conditions. In: Huneau B, Le Cam J-B, Marco Y, Verron E (eds) Constitutive models for rubber XI. CRC Press, pp 363–367
20. Dedova S, Schneider K, Heinrich G (2018) Biaxial testing system for high static and dynamic loading of elastomers and its application. KGK 6:85–90
21. Plagge J, Spratte T, Wunde M, Klüppel M (2017) Thermo-mechanical properties of strain-crystallizing elastomer nanocomposites. In: Lion A, Johlitz M (eds) Constitutive models for rubber X. CRC Press, pp 489–494
22. Gross D, Seelig T (2011) Bruchmechanik. Springer, Berlin
23. Schneider K, Calabro R, Lombardi R, Kipscholl C, Horst T, Schulze A, Dedova S, Heinrich G (2017) Grellmann W, Langer B (eds) Characterisation of the deformation and fracture behavior of elastomers under biaxial deformation. Springer, Berlin, pp 335–349

Adv Polym Sci (2021) 286: 445–466
https://doi.org/10.1007/12_2020_66

Published online: 26 November 2020

Determination of the Loading Mode Dependence of the Proportionality Parameter for the Tearing Energy of Embedded Flaws in Elastomers Under Multiaxial Deformations

R. J. Windslow, T. W. Hohenberger, and J. J. C. Busfield

Contents

Abstract In this paper, the relationship between the tearing energy and the far-field cracking energy density (CED) is evaluated for an embedded penny-shaped flaw in a 3D elastomer body under a range of loading modes. A 3D finite element model of the system is used to develop a computational-based fracture mechanics approach which is used to evaluate the tearing energy at the crack in different multiaxial loading states. By analysing the tearing energy's relationship to the far-field CED, the proportionality parameter in the CED formulation is found to be a function of stretch and biaxiality. Using a definition of biaxiality that gives a unique value for each

R. J. Windslow
Schlumberger, Ltd., Rosharon, TX, USA

T. W. Hohenberger and J. J. C. Busfield (✉)
Queen Mary University of London, School of Engineering and Materials Science, London, UK
e-mail: j.busfield@qmul.ac.uk

loading mode, the proportionality parameter becomes a linear function of stretch and biaxiality. Tearing energies predicted through the resulting equation show excellent agreement to those calculated computationally.

Keyword Biaxiality · Cracking energy density · Elastomer · Fracture · Multiaxial · Tearing energy

1 Introduction

Researchers during the early twentieth century suggested that stress concentrations at flaws were the root cause of fracture. However, analytical modelling found that the maximum stress of an elliptical crack approached infinity (a physical impossibility) as the radius of the crack tip tended towards zero [1]. To overcome this problem, Griffith proposed evaluating the local energy field at the crack tip rather than the more complex stress field [2]. Griffith's premise was that the release of strain energy as a crack propagated was equivalent to the surface energy required to form the new fracture surfaces. Therefore, a crack would only propagate if the resulting release of strain energy was in excess of the surface energy requirements to create the new faces. This proved successful for brittle materials but did not translate to elastomers as dissipative effects caused the released strain energy to significantly exceed the surface energy.

Realising the issue, Rivlin and Thomas extended Griffith's approach to make it more applicable to elastomers and other polymers [3]. This was achieved by introducing a critical energy release rate, above which the crack would grow independent of the test piece geometry. The critical energy release rate, or tearing energy, T, is equivalent to the rate of change in strain energy, U, of the sample, divided by the increase in area of one of the newly formed fracture surfaces, A. Under the assumption that the sample was held at constant length, l, the energy contribution due to external work could be negated Eq. (1):

$$T = -\left(\frac{\mathrm{d}U}{\mathrm{d}A}\right)_l \tag{1}$$

Rivlin and Thomas also showed that the tearing energy could be applied globally to the system or locally about the crack tip. This allowed them to develop analytical solutions to quantify the tearing energy in edge cracked samples when deformed in pure shear and uniaxial tension. One of the key derivations was for the single edge notched tension, SENT, test piece. Owing to the introduction of the crack, the SENT test piece can be divided into three regions: two far-field regions under uniform deformation and a complex energy region influenced by the crack (Fig. 1). Through the use of a proportionality parameter, k, Rivlin and Thomas defined the tearing

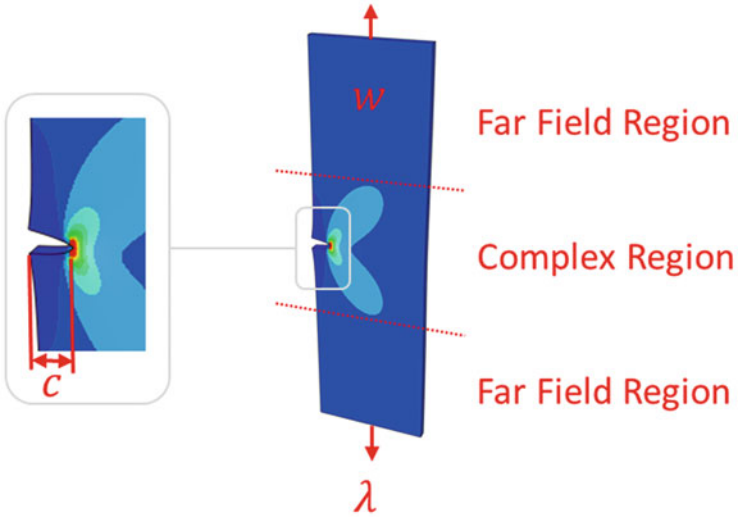

Fig. 1 Strain energy density field in a SENT test piece under uniaxial tension

energy available for a given crack length, c, and strain energy density, SED or w, in the far-field region Eq. (2):

$$T = 2kwc \tag{2}$$

One of the barriers for this approach was suitably defining the proportionality parameter, k. Through experimentation, Greensmith showed that it was loosely dependent upon the far-field principal stretch, λ, decreasing from $k = 3$ at small strains to $k(\lambda = 3) = 2$ [4]. Later Lindley used finite element analysis (FEA) to define this constant in terms of the principal stretch Eq. (3) [5]. His expression broadly agreed with Greensmith's results:

$$k = \frac{2.95 - 0.08(1 - \lambda)}{\sqrt{\lambda}} \tag{3}$$

At a similar time, Lake attempted to use symmetry conditions to adapt Rivlin and Thomas' SENT solution to the tearing energy at a centrally positioned flaw in a thin sheet under uniaxial tension [6]. He found the proportionality parameter related to the far-field principal stretch through π Eq. (4). The value of the proportionality parameter is relatively similar regardless of whether it is expressed through Eq. (3) or Eq. (4). Due to this researchers typically use the simpler form, Eq. (4), for both edge and central cracks. However, it is worth noting that Klüppel and coworkers have published experimental data from SENT test pieces that suggests the factor of π is too high, so they replaced it with a front factor that ranged from 1.2 to 3.1 [7]. In any

case, Eqs. (3) and (4) are only suitable when the global system is under uniaxial tension and for small to moderate strains, $1 \leq \lambda \leq 3$:

$$k = \frac{\pi}{\sqrt{\lambda}} \tag{4}$$

Alternative expressions to make Eq. (2) suitable for multiaxial deformations at finite strains have been proposed. Yeoh observed that under far-field tension, an embedded penny-shaped flaw became elliptical [8]. He deduced that for a flaw of initial radius (i.e., half-length), c, which under deformation formed an ellipse of length, $2a'$, and height, $2b'$, the proportionality parameter would be a function of the geometry, the SED in the far-field region and the Cauchy stress, σ_y, acting against the flaw opening Eq. (5). The model showed good agreement against tearing energy values calculated using computational-based fracture mechanics up to 100% strain in uniaxial and planar tension; however, it provided a poor fit in equibiaxial tension:

$$k = \frac{\sigma_y \pi b'}{4wc} \tag{5}$$

An alternative approach has been presented, and gained traction, in which the load mode dependence of the fracture process is accounted for by scaling the far-field energy variable to represent only the portion that is actually available for release upon fracture. The approach consequently assumes the proportionality factor is independent of loading mode [9]. The scaled far-field energy variable is referred to as the cracking energy density (CED) or w_c. For a flaw in a linearly elastic material, the CED has been quantified in terms of the stress tensor, $\boldsymbol{\sigma}$; the incremental strain tensor, $\mathrm{d}\boldsymbol{\varepsilon}$; and a unit vector normal to the crack plane, $\vec{r}$:

$$\mathrm{d}w_c = \left(\vec{r}^{\,\mathrm{T}}\boldsymbol{\sigma}\right) \cdot \left(\mathrm{d}\boldsymbol{\varepsilon}\vec{r}\right) \tag{6}$$

More recently, a large strain formulation for the CED based upon the Ogden hyperelastic model has been derived in terms of the second Piola-Kirchhoff principal stresses, S_i; the principal stretches, λ_i; and the orientation, θ, of the void with respect to the principal axes of stress [10, 11]:

$$\begin{aligned} \mathrm{d}w_c = {} & \frac{\lambda_1 S_1 \cos^2\theta}{\cos^2\theta + \left(\frac{\lambda_1}{\lambda_2}\right)^2 \sin^2\theta}\mathrm{d}\lambda_1 + \frac{\lambda_2 S_2 \sin^2\theta}{\cos^2\theta + \left(\frac{\lambda_1}{\lambda_2}\right)^2 \sin^2\theta}\mathrm{d}\lambda_2 \\ & - \frac{\lambda_1 \lambda_2^3 S_2 \sin^2\theta}{\cos^2\theta + \left(\frac{\lambda_1}{\lambda_2}\right)^2 \sin^2\theta}\mathrm{d}\lambda_3 \end{aligned} \tag{7}$$

In Eq. (7), λ_1 and λ_2 are assigned as maximum and mid-principal stretches, respectively. The CED is one of the most important breakthroughs in fracture

mechanics for elastomers since Rivlin and Thomas' initial paper from 1953. There is a large body of work which physically validates the CED as a useful tool for evaluating fracture in elastomers, particularly in fatigue analysis [12–15]. In these works, fatigue tests have been run on a range of geometries using different loading modes. In each, the CED has been found to be the best current fatigue criterion for unifying cycles to failure from different loading modes into a single Wöhler curve. Nevertheless, there has yet to be a full study which demonstrates that the proportionality parameter, assumed constant in the CED approach, is truly independent of the loading mode, particularly for embedded flaws.

A partial study has been carried out as part of the initial CED paper; however, it did not directly compare the results against pure fracture mechanics [9]. In the paper, the tearing energy for an embedded flaw under uniaxial, planar and equibiaxial deformations was calculated using the proportionality constant defined by linear elastic fracture mechanics (LEFM) for an axisymmetrical embedded flaw under uniaxial tension. The proportionality constant was then assumed to be independent of loading mode, with the load mode dependence being accounted for through the CED. The predicted tearing energies were then compared against values from a previous paper [8], which had used pure fracture mechanics to study the tearing energy under these loading modes. As the earlier paper had evaluated a central crack in a flat sheet, a different problem case, the results were compared by normalising the tearing energy values from the equibiaxial and planar states against the predictions from the uniaxial state. The normalised values from the two cases were in rough, although not exact, agreement and hence formed a good start for evaluating the tearing energy in multiaxial cases. Nevertheless, the work could not directly indicate whether the tearing energy was suitably predicted for the embedded flaw case. It only showed that the tearing energy's load mode dependence was similar between the two cases.

There have been a couple of papers which have used pure fracture mechanics to determine the tearing energy of an embedded flaw using the far-field energy [16, 17]. In both these papers, the tearing energy was represented through Eq. (8) which is an adaption of Eq. (2) from its flat sheet form into an expression more suited to an embedded penny-shaped crack. Neither of these papers used the CED; rather the SED was used with the proportionality parameter's definition accounting for the load mode dependence. In one of these papers, multiple deformation modes were studied, with proportionality constants being derived for uniaxial and equibiaxial loading [16]. In the other paper, only uniaxial deformations were studied. Neither of these studies accounted for the proportionality parameter's dependence on the loading mode in a manner that is broadly general for different loading modes:

$$T = \frac{3}{2\pi} kwc \tag{8}$$

In this paper, the relationship between the tearing energy and the far-field CED is evaluated for an embedded penny-shaped flaw in a 3D elastomer body under a range of loading modes. A 3D finite element model of the system is developed

before a computational-based fracture mechanics approach is used to evaluate the tearing energy at the crack in a range of multiaxial states. By analysing the tearing energy's relationship to the far-field CED, a stretch-dependent proportionality parameter is determined for each loading mode. From this, it is shown that the CED approach does not fully account for the load mode dependence of the proportionality parameter; however, a simple relationship for this parameter is deduced from the biaxiality of each loading mode. To proceed, Eq. (8) is adapted to replace the SED variable with the CED as shown in Eq. (9). To differentiate between the proportionality parameters in each equation, a subscript 'c' is used for the CED variant:

$$T = \frac{3}{2\pi} k_c w_c c \tag{9}$$

2 Material Model

The simulations use two carbon black-filled elastomers, a nitrile rubber (NBR) and an ethylene-propylene-diene-monomer (EPDM) rubber, both of which were supplied by Clwyd Compounders. The elastomers were characterised at 23°C using uniaxial tension dumbbell, uniaxial compression button and rectangular planar tension test piece geometries. The nominal gauge dimensions of the dumbbells were 25 × 6 × 2 mm. The nominal diameters and heights of the buttons were 25 and 12.5 mm, respectively. The buttons were compressed on their axial surfaces but free to radially expand. The nominal gauge dimensions of the planar test pieces were 150 ×15 × 2 mm. Each test was carried out at 1% strain per second. Three repeats were carried out per test with the median profile being used to calibrate hyperelastic material models. The test data were then fitted to second-order Ogden hyperelastic functions, wherein the elastomers were treated as fully incompressible (Fig. 2). The model's derived fitting parameters, μ_i and α_i, are provided in Table 1. Although it is not shown in the figure, the model's behaviour in equibiaxial tension has been confirmed to be realistic. It is worth noting that Abaqus, the FEA solver used for the modelling work, has a slightly different definition of the Ogden model compared to Ogden's original formulation [18]. Abaqus' formulation is given in Eq. (10). N is the model order, and λ_i's are principal stretches:

$$w = \sum_{i=1}^{N=2} \frac{2\mu_i}{{\alpha_i}^2} \left({\lambda_1}^{\alpha_i} + {\lambda_2}^{\alpha_i} + {\lambda_3}^{\alpha_i} - 3 \right) \tag{10}$$

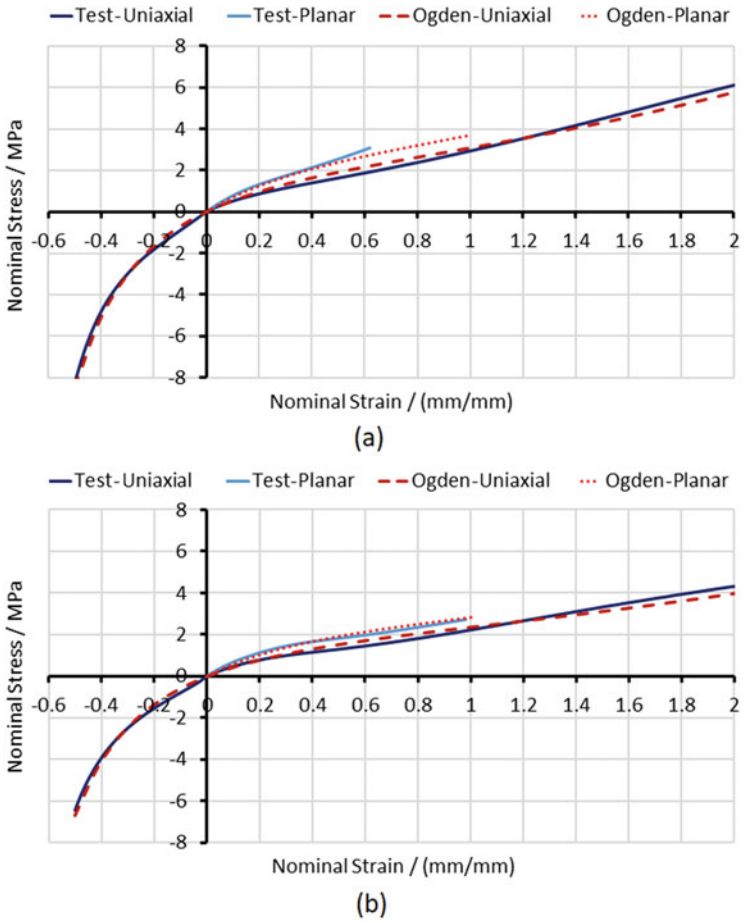

Fig. 2 Fit of the second-order Ogden hyperelastic material models to the elastomers' test data for (**a**) NBR and (**b**) EPDM

Table 1 Second-order Ogden material model parameters for the two elastomers

Elastomer	μ_1 / MPa	α_1	μ_2 / MPa	α_2
NBR	0.540	3.341	1.490	−0.232
EPDM	0.338	3.272	1.327	0.089

3 FEA Model Development

To study the embedded void case, a quartile section of a 2 × 2 × 2 mm cube was modelled in Abaqus with a penny-shaped crack at its centre. The penny-shaped crack was created using the seam interaction function. Symmetry boundary conditions were applied at the internal faces of the quartile section such that it behaved as

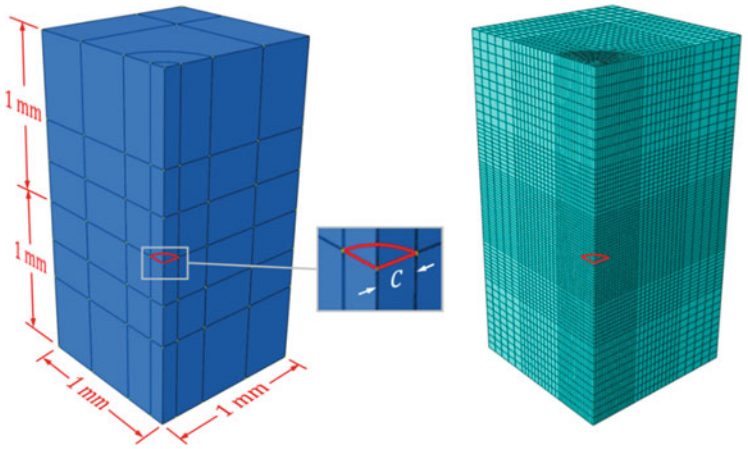

Fig. 3 Modelled quartile system with the embedded penny-shaped crack of length c

if part of the whole cube. Displacement boundary conditions were applied to the cube's external faces to impose desired deformation modes. The model was meshed using first-order hex hybrid elements with enhanced hourglassing control. As the key energy fields were in the complex region around the crack tip, the mesh density was biased towards this region. Mesh convergence found that 37,800 elements formed a suitable mesh density for capturing the strain energy stored in the system. The model is shown in Fig. 3.

The computational-based energy balance fracture mechanics approach was used to evaluate the tearing energy [19]. This approach is essentially the direct application of Eq. (1); therefore, it is extremely accurate provided the mesh density is fine enough to capture the strain energy stored in the global system. To apply, the system is modelled through the desired deformation process multiple times, wherein in each re-simulation, the crack's length has been incrementally increased. This builds a relationship between the strain energy stored in the system with the crack's surface area for a given stretch. The gradient of this plot is the rate at which energy is released by the crack propagating which, as per Eq. (1), is the tearing energy. In this work, for each loading mode modelled, the unit cube was re-simulated with the crack's radius, c, varying from 0.1 mm to 0.3 mm in 0.025 mm increments. As only a quarter of the system was modelled, in each case the strain energy was multiplied by 4 to determine the strain energy in the system as a whole before the tearing energy was calculated.

The tearing energy was evaluated for six loading modes. These were the typical loading modes – uniaxial, planar and equibiaxial – and three intermediate biaxial states somewhere between planar and equibiaxial deformation. In each of the loading modes, the crack would undergo a Mode I 'opening'-type fracture. As such, simple shear was not studied here. A helpful approach that can be used to

Table 2 Comparison of the biaxiality definitions

Loading modes	Principal stretches			Biaxialities, B	
	λ_1	λ_2	λ_3	Eq. (11)	Eq. (12)
Equibiaxial ($\lambda = \lambda_1 = \lambda_2$)	2.0	2.0	0.25	1.0	−2.0
Equibiaxial ($\lambda = \lambda_2 = \lambda_3$)	0.25	2.0	2.0	−0.5	−2.0
Equibiaxial ($\lambda = \lambda_1 = \lambda_3$)	2.0	0.25	2.0	−2.0	−2.0
Uniaxial tension ($\lambda = \lambda_1$)	2.0	0.707	0.707	−0.5	−0.5

Table 3 Biaxialities of the loading modes modelled

Loading mode	Biaxiality, B	CED/SED
Uniaxial	−0.50	1.000
Planar	−1.00	1.000
Complex 1	−1.25	0.857
Complex 2	−1.50	0.714
Complex 3	−1.75	0.595
Equibiaxial	−2.00	0.500

characterise the loading modes of incompressible elastomers is to define a measure of biaxiality, B, such that $\lambda_2 = {\lambda_1}^B$ and $\lambda_3 = {\lambda_1}^{-(1+B)}$ [9]:

$$B = \frac{\log \lambda_2}{\log \lambda_1} \tag{11}$$

For the current purposes, there is a slight issue with this definition of the biaxiality in that it does not account for the load mode equivalencies exhibited by elastomers. As shown in Table 2, three different biaxiality values occur with the same loading mode, depending on the direction of loading. More concerning, however, is that the same biaxiality value is achieved for uniaxial tension in the λ_1 axis as equibiaxial tension in the λ_2 and λ_3 axes. Other definitions of biaxiality have been proposed [20], but the authors chose to resolve this issue with a subtle adjustment of Eq. (11). By referring to the maximum and minimum principal stretch components, λ_{max} and λ_{min} in Eq. (12), each loading mode has a unique biaxiality, regardless of the direction of loading as shown in Table 2. This arrangement assumes that the crack is initially perpendicular to the max stretch direction, which is typically the orientation that generates the largest tearing energy in literature [10]:

$$B = \frac{\log \lambda_{min}}{\log \lambda_{max}} \tag{12}$$

The biaxialities of the loading modes modelled in this work are given in Table 3. The CED/SED values provided were calculated using the small strain CED solution given by Zine et al. Eq. (13) and are used purely to illustrate the load mode dependence of the energy release [10]. In the equation ν is Poisson's ratio:

$$\frac{w_c}{w} = \frac{(B\nu + 1)\cos^2\theta + \left(B^2 + B\nu\right)\sin^2\theta}{B^2 + 2B\nu + 1} \tag{13}$$

As the fracture process is studied to high strains, the finite-strain formulation provided in Eq. (7) is used to numerically calculate the CEDs in this study. It should be noted that the redefinition of the biaxiality does not alter the CED/SED ratio for a given loading mode; rather the values correlate with previous findings for the same loading modes [9, 10].

4 FEA Results

The energy fields in the deformed cubes are shown in Fig. 4 for the different loading modes. The flaw deformed to different extents depending on which loading mode was used, and maximum strain governed the stability of the model. As such the uniaxial and planar deformations were studied up to $\lambda_{max} = 3.0$, the three intermediate states were studied up to $\lambda_{max} = 2.5$, and the equibiaxial case was studied up to $\lambda_{max} = 2.0$. In each case the tearing energy was evaluated at ten evenly spaced increments over the deformation.

For each loading mode, the strain energy was plotted against the surface area of one face of the undeformed crack under constant stretch. These profiles were fitted with fourth-order polynomials, which were then differentiated to give the tearing energy for the given crack area (Fig. 5a). Plotting the tearing energy against the crack's radius for a range of stretches results in the expected linear relationship between the crack's length and tearing energy (Fig. 5b).

Once the tearing energy was known for the given deformations, the proportionality parameters could be determined by rearranging the tearing energy equations.

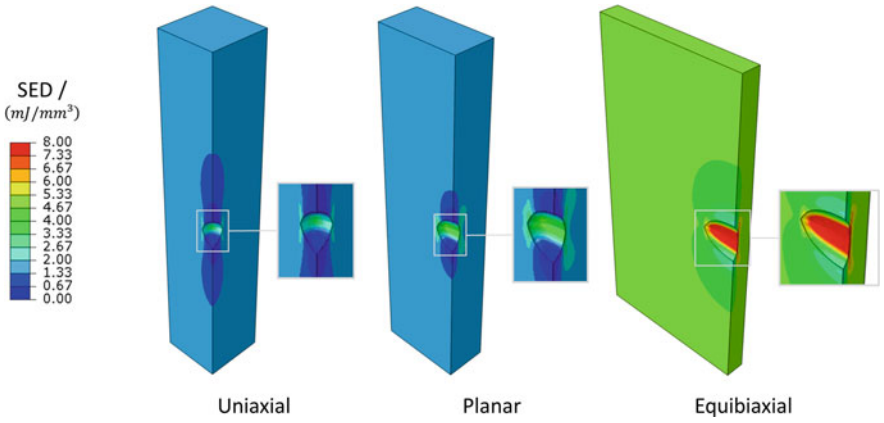

Fig. 4 SED fields in deformed cubes under uniaxial, planar and equibiaxial loading at a stretch of $\lambda_{max} = 2$

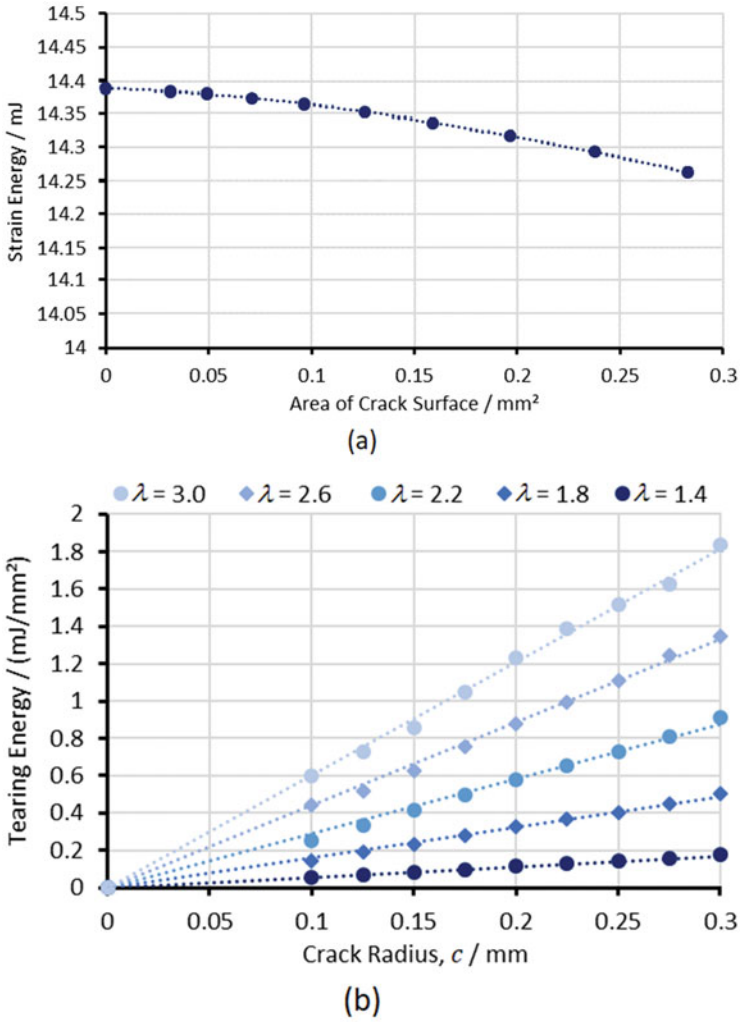

Fig. 5 (**a**) Energy release in NBR as the crack grows during uniaxial extension with $\lambda = 2$; (**b**) effect of stretch on the tearing energy of NBR during uniaxial extension

For each case, two sets of proportionality parameters were calculated, one based on Eq. (8) where the tearing energy was defined in terms of the SED and another defined in terms of the CED Eq. (9). These will be referred to as k and k_c, respectively, and are defined through Eqs. (14a) and (14b):

$$k = \frac{T}{c} * \frac{1}{w} * \frac{2\pi}{3} \tag{14a}$$

$$k_c = \frac{T}{c} * \frac{1}{w_c} * \frac{2\pi}{3} \tag{14b}$$

For both equations, the *T*/*c* term is the gradient formed by plotting *T* vs. *c* and then fitting a linear trendline to the data points (Fig. 5b). For each of the loading modes, the proportionality parameter was determined for each stretch value that was simulated, allowing careful study of the parameter's load mode dependence. This dependence was compared in terms of the SED and CED (Fig. 6), which reveals an important result. Although the initial purpose of the CED was to remove the load mode dependence of the proportionality parameter for a given SED, the figures

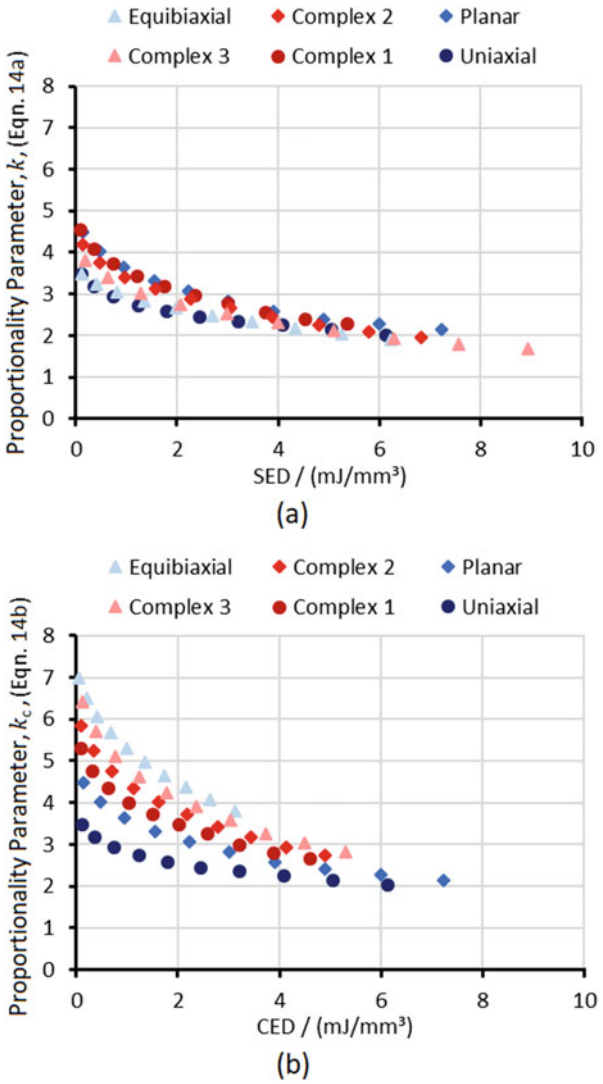

Fig. 6 Relationship between the proportionality parameter and the (**a**) SED and (**b**) CED for NBR

suggest that this is not the case; rather, CED causes the profiles to actually spread. It should be noted that as these profiles are plotted against the SED and CED, the power terms of the chosen strain energy function are likely to influence how the profiles stretch along the horizontal axis. The hyperelastic model dictates the rate of energy storage with stretching and biaxiality; as such, the correlation of the profiles may vary when different strain energy functions or fitting parameters are used.

In Fig. 7 the proportionality parameters' dependence on the stretch is compared for both cases, SED and CED. The uniaxial and planar responses are identical

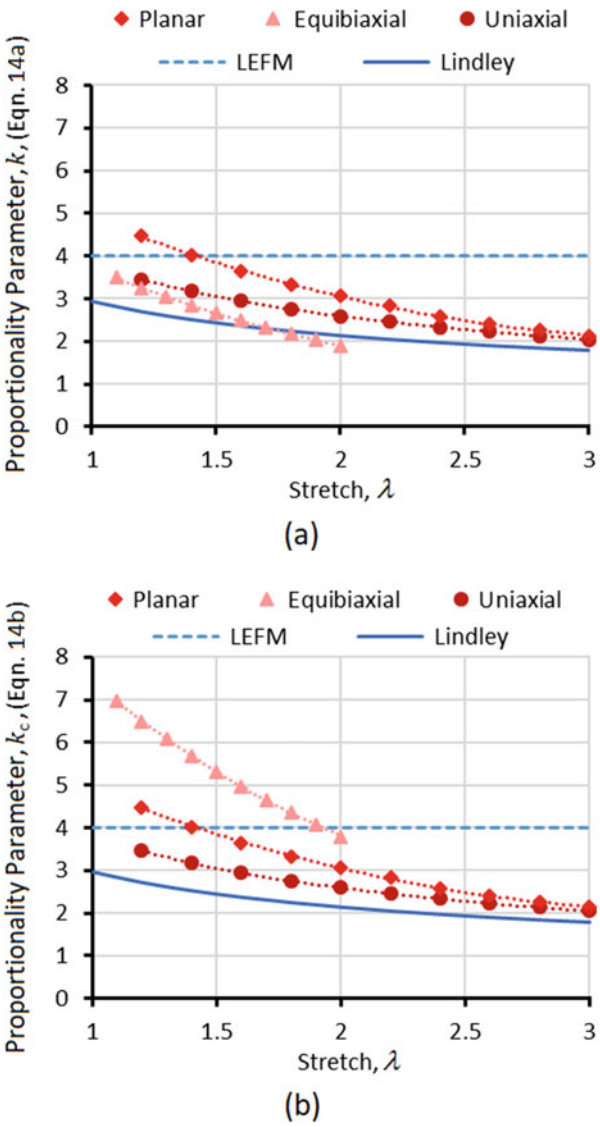

Fig. 7 Relationship between the proportionality parameter and the stretch when calculated using the (**a**) SED and (**b**) CED in NBR

because $w_c/w = 1$ for these load cases. The proportionality parameters calculated for the uniaxial and equibiaxial cases, defined through the SED, show very good agreement with previous research [16, 17]. For the uniaxial case at low strains, $k = 4$ which corresponds to the LEFM solution, whilst the overall profile matches those found previously. The equibiaxial data also corresponds with that of Gough and Muhr, who found the SED proportionality parameter varied from $k(\lambda = 1) = 4$ to $k(\lambda = 1.6) = 2$ [16]. Again, when plotting the proportionality parameter in terms of the stretch, using the CED heightens the load mode dependence of the proportionality parameter. Nevertheless, this may actually be beneficial as it causes the separate profiles to all converge towards $k = 2$ at $\lambda \geq 3$. This does not occur with the SED, particularly for the equibiaxial case.

The convergence of the proportionality parameter for the CED case is similar to the SENT case wherein Greensmith noted that it decreased from $k = 3$ at small strains to $k(\lambda = 3) = 2$, as shown by the Lindley profile plotted in the Figs. 5 and 6. In both cases, SENT and embedded flaw, the tearing energy appears to be directly related to the CED at $\lambda \geq 3$; that is, k_c tends towards a constant value as strain increases. It is only at lower strains, $\lambda \leq 3$, that $k_c = k_c(\lambda)$ (as opposed to $k_c =$ constant) is required to properly proportion the far-field CED to the tearing energy. As noted by Gough and Muhr [16], it appears that reducing the biaxiality (or, equivalently, tending towards an equibiaxial loading state) increases the proportionality parameter's dependence on the stretch.

For central and edge flaws in flat sheets, both Lake and Lindley found that the proportionality parameter varied with the inverse of the square root of the stretch ratio [6, 7]. In the present work, this is assumed for the embedded flaw as well. As such, the proportionality parameter calculated using the CED is plotted against this relation. There is a complication in determining which stretch component to use, particularly for the biaxial deformation states. Considering that in each case the fracture process is being driven by λ_{max}, it is chosen for the abscissa in Fig. 8 for the different loading modes and elastomers.

For both elastomers, the profiles form identical linear relationships for the given loading modes. The interesting point is that the ordering of the profiles, in terms of their gradients and y-intercepts, is related to the loading modes' biaxialities. The profiles become steeper as the biaxiality decreases, but all converge to the same point at $\lambda_{max} = 3$ (i.e., $\lambda_{max}^{-0.5} \approx 0.58$). As such, the proportionality parameter forms a linear relationship to the inverse square root of the max principal stretch, through gradient, m, and y-intercept, b:

$$k_c = \frac{m}{\sqrt{\lambda_{max}}} + b \tag{15}$$

Plotting the gradient, m, and y-intercept, b, of these profiles against the biaxiality of the loading modes yields two linear relationships (Fig. 9). This linear relationship would not be seen if the tearing energy was represented through the SED rather than the CED. From these two profiles, a new general definition of the proportionality

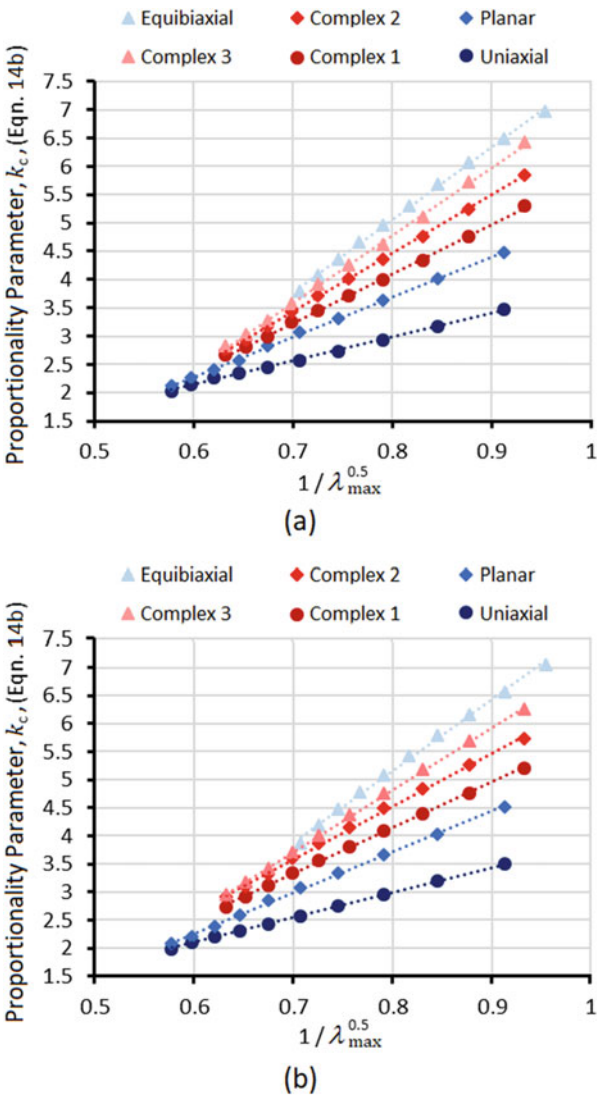

Fig. 8 Relationship between the CED proportionality parameter and the inverse square root of the max stretch term in (**a**) NBR and (**b**) EPDM

parameter can be defined, for use with the CED, in terms of the loading mode biaxialities.

The gradient and y-intercept themselves form linear relationships to the biaxiality, resulting in:

$$m = m_{\mathrm{m}} B + b_{\mathrm{m}} \tag{16a}$$

$$b = m_{\mathrm{b}} B + b_{\mathrm{b}} \tag{16b}$$

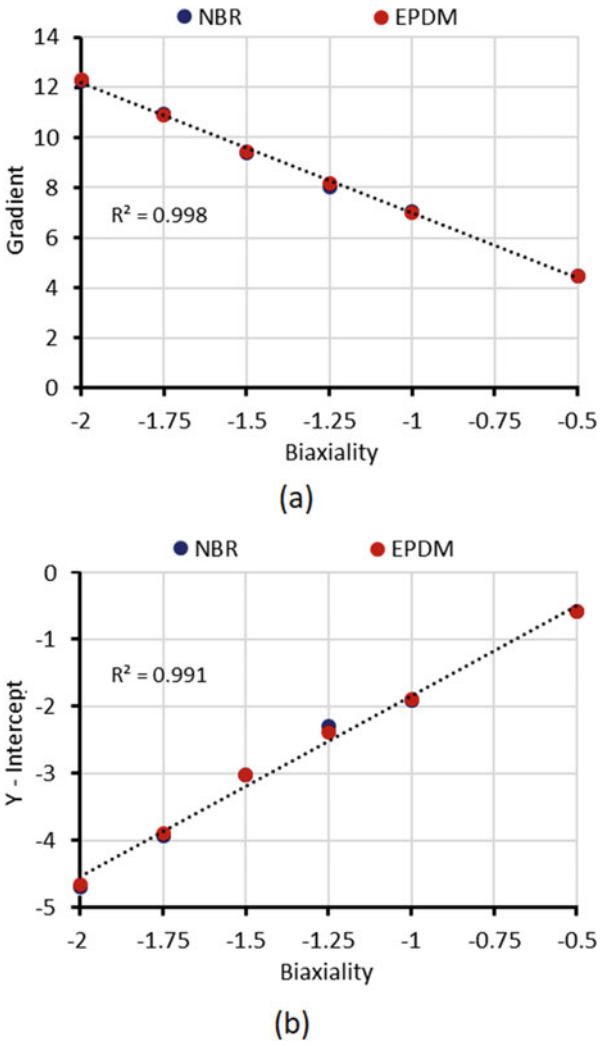

Fig. 9 Relationship between the biaxiality and the (**a**) gradients and (**b**) y-intercepts of the profiles in Fig. 8

Here, m_m and b_m are the gradient and y-intercept of the linear profile found in Fig. 9a by plotting the gradient, m, of Eq. (15) against the biaxiality. Similarly, m_b and b_b are the gradient and y-intercept of the linear profile found in Fig. 9b by plotting the y-intercept, b, of Eq. (15) against the biaxiality. Combining these with Eq. (15) defines the proportionality parameter in terms of the biaxiality:

$$k_c = \frac{m_m B + b_m}{\sqrt{\lambda_{max}}} + (m_b B + b_b) \tag{17}$$

In turn, this presents a new form of Eq. (9) that is suitable for calculating the tearing energy in embedded flaws under multiaxial deformations:

$$T = \frac{3}{2\pi}\left(\frac{m_{\mathrm{m}}B + b_{\mathrm{m}}}{\sqrt{\lambda_{\max}}} + (m_{\mathrm{b}}B + b_{\mathrm{b}})\right)w_{\mathrm{c}}c \tag{18}$$

For this particular case, the values of m_{m}, b_{m}, m_{b} and b_{b} define the tearing energy through Eq. (19), where for simplicity it is useful to incorporate the $3/2\pi$ term in the proportionality parameter such that the tearing energy is given by:

$$T = \left(\frac{(0.884 - 2.486B)}{\sqrt{\lambda_{\max}}} + (1.293B + 0.375)\right)w_{\mathrm{c}}c \tag{19}$$

5 Discussion

The correlation between the tearing energy calculated from the FEA model and the tearing energy predicted through Eq. (19) is compared in Fig. 10. For each of the six loading modes, the tearing energy was calculated at five stretches, evenly spaced over the strain range. For example, the uniaxial data was evaluated over the following stretches: 1.4, 1.8, 2.2, 2.6 and 3.0. Furthermore, at each stretch the data was evaluated for each of the nine crack lengths modelled, $0.1 \leq c \leq 0.3$. The combined data is presented in the figures and grouped to the different loading modes. The tearing energy values predicted from the equation correlate extremely well to those predicted by FEA, particularly considering that this is for multiple crack lengths, stretches and loading modes.

It is worth noting that the introduction of a proportionality parameter is ultimately an approximate solution. Rivlin and Thomas introduced the factor as a way to relate the far-field energy to the local energy field about the crack – similar to the use of a stress intensity factor in LEFM. That said, capturing the proportionality parameter's load mode dependencies, as demonstrated in this work, is highly beneficial for applying theoretical fracture mechanics to more complex engineering components.

Calculating the tearing energy of a 3D flaw using a global approach also leads to an approximate solution, even when solidly based in fracture mechanics such as with the energy balance approach. Both the energy balance and heuristic equation-based approaches provide a single tearing energy value for the crack. In 3D cases, where the deformation of an initially circular crack geometry becomes an ellipsoid with three unique axes, the tearing energy is nonuniform around the crack's circumference. Nevertheless, a singular 'averaged' tearing energy value is likely a reasonable predictor of fatigue life, particularly when trying to optimise the design of an engineering component.

As explained in the introduction, the CED was developed to remove the need for a variable proportionality parameter whilst still allowing a derated tearing energy to be predicted from the far-field parameters. Whilst CED had been demonstrated to work well on 2D cases, it had not been validated for 3D cases. The present study

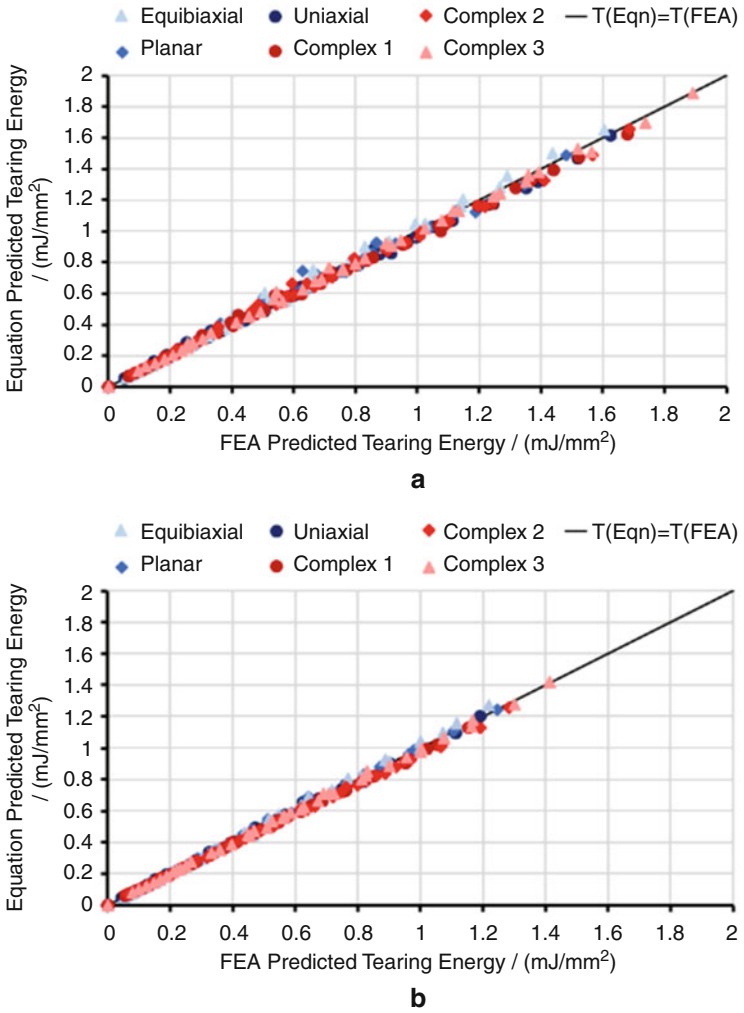

Fig. 10 Correlation between tearing energy predicted through Eq. (19) and by computational-based fracture mechanics for the different loading modes for (**a**) NBR and (**b**) EPDM

suggests that CED is still superior to SED in predicting fracture, but it works best with a proportionality parameter that is a function of the loading mode. In fact, CED appears to amplify the loading mode dependencies (see Fig. 6), but this does not necessarily complicate the construction of a proportionality parameter that depends on the loading mode, particularly when the biaxiality definition in Eq. (12) is used.

Other key findings from this paper are the linear relationships in Fig. 9 that allow the proportionality parameter to be defined through the loading mode biaxialities. It is probable that these relationships define the geometric non-linearity of the crack and its influence on the tearing energy, or, in other words, how the application of

strain alters the crack tip geometry and tearing energy at the crack. There is likely a second non-linearity related to the material behaviour: how the rate of energy storage varies with loading mode. The gradients found by plotting Eqs. (16a) and (16b) may depend on the strain energy function and related model parameters, thereby controlling the material non-linearity of the fracture process. In this particular paper, the hyperelastic functions for both elastomers yielded similar profiles; hence, a single gradient sufficed. Future studies should investigate how the material models' parameters affect the gradient of these profiles and determine whether they are indeed related to the material non-linearity aspect of the fracture process.

Finally, this work suggests that CED should be further explored with 3D simulations and testing. In particular, CED predicts fracture that is based on a single value for the tearing energy, whereas more generally the tearing energy can vary around a crack tip. To better assess the effect of this variation, future simulation work in 3D should use a local fracture mechanics approach at the crack tip to determine how maximum, minimum and average tearing energies relate to the CED.

6 Conclusions

Building on work in the 1920s, the first generally useful analytical model for the fracture of rubber was developed in the 1950s. It suggested that tearing energy could be deduced from crack geometry and far-field strain energy that was released upon crack propagation. The model included a proportionality parameter, k, sometimes assumed constant, to scale the tearing energy in much the same way that stress concentration factors arise in the fracture of linear elastic solids. Early refinements of this model proposed specific forms of $k = k(\lambda)$, but only with partial success as proper accounting for the load mode dependence of rubber fracture was elusive. The introduction of cracking energy density was a significant breakthrough because it addressed loading mode sensitivities in a more general manner. It did so by scaling a system's total strain energy to the portion that was actually available to drive fracture. The model adopted a constant proportionality parameter from LEFM, but it has nevertheless been useful, especially for 2D analysis.

The present work provides a 3D finite element study of tearing energy and CED for an embedded flaw with multiaxial loads at finite strain. At a given stretch, tearing energy is found to be linearly related to crack length as expected. However, the proportionality parameter in the CED formulation is found to be variable, albeit in a predictable way. Using a definition of biaxiality that gives unique values for a given loading mode, the proportionality parameter becomes a linear function of biaxiality. This gives a simple analytical expression to relate tearing energy to CED, and it can be readily adopted for engineering design. Future work should extend this work to address (1) deformations that are not pure, for instance, simple shear; (2) the effects of variation in tearing energy and geometry around the crack tip circumference; and (3) the influence of the hyperelastic material model and related parameters.

Acknowledgements The authors would like to thank Schlumberger for funding and supporting this research. They would also like to thank Clwyd Compounders for providing the elastomers used.

References

1. Inglis CE (1913) Stresses in a plate due to the presence of cracks and sharp corners. Trans Inst Nav Arch 55:219–239
2. Griffith AA (1921) The phenomena of rupture and flow in solids. Philos Trans R Soc A Math Phys Eng Sci 221:163–198
3. Rivlin RS, Thomas AG (1953) Rupture of rubber. I Characteristic energy for tearing. J Polym Sci 10:291–318
4. Greensmith HW (1963) Rupture of rubber. X. The change in stored energy on making a small cut in a test piece held in simple extension. J Appl Polym Sci 7:993–1002
5. Lindley PB (1972) Energy for crack growth in model rubber components. J Strain Anal Eng Des 7:132–140
6. Lake GJ (1970) Application of fracture mechanics to failure in rubber articles, with particular reference to groove cracking in tyres. In: International conference yield, deformation and fracture of polymers. Plastics and Rubber Institute, Cambridge
7. Klüppel M, Huang G, Bandow B (2008) Evaluation of tearing energy of elastomer materials. Kautschuk, Gummi, Kunststoffe 61:656–659
8. Yeoh OH (2002) Relation between crack surface displacements and strain energy release rate in thin rubber sheets. Mech Mater 34:459–474
9. Mars WV (2006) Heuristic approach for approximating energy release rates of small cracks under finite strain, multiaxial loading. In: Coveney VA (ed) Elastomers and components: service life prediction – progress and challenges, 1st edn. Woodhead Publishing, Sawston, pp 91–111
10. Zine A, Benseddiq N, Naït AM, Aït HN, Bouami D (2006) Prediction of rubber fatigue life under multiaxial loading. Fatigue Fract Eng Mater Struct 29:267–278
11. Ayoub G, Naït-Abdelaziz M, Zaïri F, Gloaguen JM, Charrier P (2011) A continuum damage model for the high-cycle fatigue life prediction of styrene-butadiene rubber under multiaxial loading. Int J Solids Struct 48:2458–2466
12. Mars WV, Fatemi A (2005) Multiaxial fatigue of rubber: part I: equivalence criteria and theoretical aspects. Fatigue Fract Eng Mater Struct 28:515–522
13. Mars WV, Fatemi A (2006) Analysis of fatigue life under complex loading: revisiting Cadwell, Merrill, Sloman, and Yost. Rubber Chem Technol 79:589–601
14. Ayoub G, Naït-Abdelaziz M, Zaïri F (2014) Multiaxial fatigue life predictors for rubbers: application of recent developments to a carbon-filled SBR. Int J Fatigue 66:168–176
15. Poisson JL, Méo S, Lacroix F, Berton G, Hosséini M, Ranganathan N (2018) Comparison of fatigue criteria under proportional and non-proportional multiaxial loading. Rubber Chem Technol 91:320–338
16. Gough J, Muhr AH (2005) Energy release rates for small cracks in rubber components. In: Austrell P-E, Kari L (eds) Constitutive models for rubber IV: proceedings of the fourth European conference on constitutive models for rubber, 1st edn. Taylor & Francis Group, London, pp 51–57
17. Yeoh OH (2006) Strain energy release rates for some classical rubber test pieces by finite element analysis. In: Coveney VA (ed) Elastomers and components: service life prediction – progress and challenges, 1st edn. Woodhead Publishing, Sawston, pp 75–89
18. Ogden RW (1972) Large deformation isotropic elasticity - on the correlation of theory and experiment for incompressible rubberlike solids. Proc R Soc A Math Phys Eng Sci 326:565–584

19. Asare S, Busfield JJC (2011) Fatigue life prediction of bonded rubber components at elevated temperature. Plast Rubber Compos 40:194–200
20. Wadham-Gagnon M, Hubert P, Semler C, Paidoussis MP, Vezina M, Lavoie D (2006) Hyperelastic modeling of rubber in commercial finite element software (ANSYS). In: Proceedings of the SAMPE '06: creating new opportunities for the world economy

Adv Polym Sci (2021) 286: 467–492
https://doi.org/10.1007/12_2020_79

Published online: 11 December 2020

Microfocused Beam SAXS and WAXS Mapping at the Crack Tip and Fatigue Crack Propagation in Natural Rubber

Quentin Demassieux, Daniel Berghezan, and Costantino Creton

Contents

Abstract We investigated crack propagation in cyclic fatigue in filled (50 phR of N347 carbon black), highly crosslinked, natural rubber pure shear samples and, in parallel, mapped in detail the microstructure present at the crack tip with a microfocused X-ray synchrotron beam. We acquired data by wide-angle X-ray scattering (WAXS) to characterize strain-induced crystallization (SIC) and by small-angle X-ray scattering (SAXS) to detect nano-cavitation. Crack propagation

Q. Demassieux and C. Creton (✉)
Laboratoire de Sciences et Ingénierie de la Matière Molle, ESPCI Paris, PSL University, Sorbonne University, CNRS, Paris, France
e-mail: Costantino.creton@espci.psl.eu

D. Berghezan
Michelin Research Center, Ladoux, Clermont-Ferrand, France

experiments were carried out for a range of maximum energy release rates during the cycles varying from 1 to 4 kJ/m^2. Each material was tested at two temperatures: room temperature and 100°C and in new and aged conditions (10 days at 100°C in an inert atmosphere). We found that although significantly less SIC at the crack tip was present at the crack tip at 100°C, the resistance to crack propagation under cyclic loading was barely affected. In aged samples SIC at the crack tip was significantly lower than in new samples at room temperature, and was not detectable at all in aged samples at 100°C. The crack propagation rate, however, only increased with aging for the more crosslinked sample at 100°C and never increased catastrophically. Finally, a few percent of nano-cavities were detected at the crack tip and the comparison of X-ray transmission and digital image correlation suggested the presence of a significant fraction of large cavities at the very crack tip. In conclusion while strain-induced crystallization in NR may be affecting fatigue resistance we could not establish a quantitative correlation between the volume crystallized at the crack tip and the crack propagation rate in cyclic fatigue.

Keywords Cavitation · Crack propagation · Crystallization · Fatigue · Mechanical properties · Natural rubber · X-ray scattering

1 Introduction

Although strain-induced crystallization (SIC) is a very well-known and well-studied phenomenon in natural rubber (NR) several questions remain in terms of its role as a toughening mechanism. In this study we explore in more detail, and for realistic carbon black filled materials, the connection between the occurrence of strain-induced crystallization at the crack tip and the propagation of a crack in cyclic fatigue.

To follow up on our earlier study carried out in uniaxial tension, we focus here on highly crosslinked NR obtained with a sulfur based conventional curing chemistry, and 50 phr (17 vol%) of highly reinforcing carbon black filler. Such materials are found between steel plies of the carcass of a truck tire. The need to bond to the steel cord is imposing high levels of added sulfur and therefore a high crosslink density that makes the rubber less fatigue resistant [1].

In addition we compare two different conditions of cyclic fatigue: room temperature and 100°C, representative of highway driving, and two sets of materials: pristine materials and the same materials exposed to non-oxidizing aging conditions at a temperature of the order of 100°C for 10 days.

Several authors have argued that the unique capability of NR to crystallize at high strains is crucial to prevent cracks from propagating in cyclic fatigue since crystallization occurs at the crack tip [2–4]. The two key arguments behind this conclusion are the superior fatigue *resistance* of NR at high strains relative to non-crystallizing rubbers and the strong reinforcing effect of the superposition of a permanent tensile strain over the cyclic fatigue testing.

However, to the best of our knowledge no study directly compared crack propagation in fatigue results with the extent of SIC at the crack tip on the same samples. In particular, for crack proapgation tests performed at high temperature and for samples after thermal aging.

SIC was observed at the crack tip in several studies by Lee & Donovan [5], Trabelsi et al [6], Brüning et al. [7, 8], Rublon et al. [2, 9, 10], and Zhou [11], while nano-cavitation at the crack tip of a filled rubber was only observed by Zhang et al. [12] and Brüning et al. [8]. No observations of SIC or cavitation were made at high temperature.

The size of the crystallized zone appeared highly dependent on the material formulation, the macroscopic stretch ratio at the time of observation, and, for cyclic tests, the frequency and lowest stretch ratio of the cycles. As the choice was made to only perform observations of static cracks, these last two parameters are irrelevant.

In our previous publication we showed that in the filled natural rubbers used in this study, at high strains, both strain-induced crystallization and cavitation can be observed [13]. Given that the strain level at the crack tip is likely to exceed the critical strain to crystallize and in some cases to cavitate, we hypothesized that these mechanisms would be observable in NR in the last 200 μm in front of the crack tip.

The first purpose of the in situ tests was to test if the crystallization and cavitation observed at the crack tip were consistent with the observations made in tensile tests. The second and more important objective was to test the hypothesis that a larger crystallized zone leads to a better fatigue resistance and hence to a lower fatigue crack growth dc/dn at fixed applied maximum energy release rate, G.

2 Materials and Methods

2.1 Materials and Sample Preparation

Vulcanized NR samples were kindly provided by Michelin. The unvulcanized NR had an average molar mass M_w = 1,300 kg/mol and a polydispersity index, PDI = 3.9. The filler was CB N347 and was introduced into the rubber matrix at the 50 phr (parts of weight per hundred parts of rubber) level corresponding to a volume fraction of 17.3%. The density of the matrix and the filler are $\rho = 0.92$ g/cm^3 and $\rho = 1.8$ g/cm^3. The composition of the materials used is summarized in Table 1. Samples were prepared in the following way: all ingredients except vulcanizing agents were first mixed in a lab scale Haake internal mixer. The vulcanization agent was then incorporated in a calendaring machine following a procedure developed by Michelin. The sheet was then cut into pieces into a mold and put in an oven at 150°C for vulcanization. The vulcanization time for each material was optimized with a rheological measurement at 150°C. Finally, samples were removed from the molds, and air-cooled. Samples had a 40 mm effective length and a 4 mm by 2–2.5 mm cross section.

Table 1 Material composition

Material	NR50	NR50 S-
NR	100	100
CB N 347 (phr)	50	50
CB N 347 (vol%)	17.3	17.3
6PPD	2	2
Stearic acid	2	2
ZnO	5	5
DCBS	1	0.5
Sulfur	6	3
ν (mol/cm^3)	2.5×10^{-4}	1.5×10^{-4}
M_c (kg/mol)	9	15

For the aging process the samples were placed in a nitrogen filled and sealed bag and kept for 10 days into an oven at 110°C. These samples will be referred to as A10 in the following.

2.2 Cyclic Fatigue Testing

The testing device used for the characterization of crack propagation under cyclic fatigue was an MTS hydraulic device located in the Michelin laboratory. The device has a 60 mm displacement range, a 2,000 N load cell and can perform tests up to a frequency of 80 Hz. A sealed bag can enclose the sample. The temperature inside the testing chamber is regulated by an oil bath and liquid nitrogen. The O_2 inside the oven can be controlled. In this study, the tests were performed with a pure N_2 atmosphere, to prevent any oxidative aging in the samples tested. A binocular is mounted outside the testing chamber and a window allows to follow the propagation of the crack without opening the testing chamber. The binocular is equipped with a sight and fixed on a micrometric position sensor, to measure the position of the crack with maximal accuracy.

The sample used on this device is a so-called pure shear sample as commonly called in crack propagation tests in fatigue and applies a plane strain loading to most of the sample except at the edges. The useful section is 13 mm high, 157 mm long, and 2 mm thick as shown in Fig. 1. The large aspect ratio of the useful section ensures a near pure shear state in the uncracked sample: the principal elongations are (λ, 1, 1/λ). In such a sample, the energy release rate measured during crack propagation can be expressed as the simple product of the density of stored elastic energy, W, and the height of the sample, h_0:

$$G = Wh_0 \tag{1}$$

The complete process used to obtain the crack propagation curve of a material necessitated two samples of each material. A first sample was left uncracked and

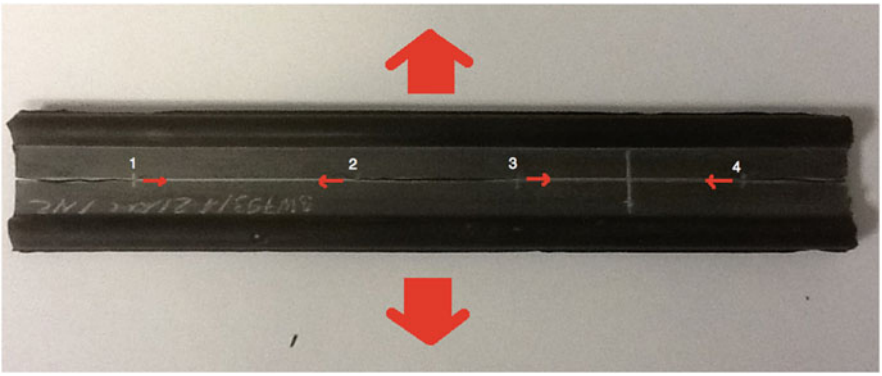

Fig. 1 Pure shear sample used for the characterization of crack propagation in fatigue

used to characterize the relation between the strain, ε, and the stored elastic energy, W. The second sample was used for the crack propagation step. The test was controlled in displacement, using a half cycle sinusoidal signal shape followed by a half-period resting time. This particular shape was chosen to mimic the load encountered during a tire cycle, as the loading occurs each time the observed section encounters the road. The choice was made to control the strain rate to a maximum of 10 s^{-1}. The consequence being that the frequency of the test was decreased when G (and the deformations) increased.

To obtain the relation $W(\varepsilon)$,a virgin pure shear sample was mounted on the MTS. After stabilization of the temperature, the sample was cycled for 1,000 cycles, with a strain greater than any strain used afterward, to accommodate the material and remove the Mullins effect. The characterization of the energy release rate was then performed: 1,000 cycles were done at each strain level and the last 10 cycles were recorded to calculate $W(\varepsilon)$.

After the characterization of the energy release rate, a new sample was mounted and cycled for 1,000 cycles with a strain of 115%, to remove the Mullins effect. The oven was then opened, and three cracks were cut into the sample with a razor knife: one crack of 20 mm on each side and one of 30 mm in the middle, for a total of four crack tips.

Finally, the sample was cycled between $\varepsilon = 0$ and the strain necessary to obtain the desired G. The test was stopped to periodically measure the position of the four crack tips. At the beginning of the fatigue test, the observed crack propagation rate decreases with time, as the crack formed by a sharp knife evolves to a more blunt form. The test was continued until the speed is stabilized, and the crack propagation rates measured for the four crack tips were then averaged to obtain the final value of dc/dn(G). All samples showed a Power Law regime that could be fitted by a power law of the type: $dc/dn = \alpha \times G^{\beta}$.

2.3 Design of the Crack Tip Characterizations

2.3.1 Sample Preparation

The choice of a sample size and geometry to carry out the characterization of the structure at the crack tip was decided based on a balance between ease of use and relevance to fatigue experiments. Several different sample geometries were used in the past to carry out X-ray or digital image correlation mapping at a crack tip in filled rubbers. Among them can be mentioned simple cuts on the edge of a tensile sample [5–7], cuts inside films [11], and, more commonly in recent studies, cuts made in pure shear samples [1, 14–18]. The advantage of the latter geometry for this study is clear, since the same geometry is commonly used to evaluate the rate of crack propagation in fatigue of rubbers at fixed applied G.

However, the pure shear geometry used for the fatigue experiment is not suitable for X-ray scattering experiments. The size, and the load required to deform it, requires to carry a large tensile machine to the beamline [2]. Instead the choice was made to use a scaled down version of the pure shear sample with a useful section of 6 mm high by 1 mm thick and a 40 mm length [19]. Each sample was then split in to two 20 mm long samples, to fit the clamps designed for the X-ray scattering experiment.

As the height of the sample is different, the relationship between strain and energy release rate was also different compared to that of the pure shear sample and a correction was applied relative to the values measured for pure shear samples.

Before any crack was introduced, each sample was cycled 1,000 times to $\varepsilon = 66\%$ to remove the Mullins effect in the bulk. A side crack about 7 mm long was then introduced in each sample and the sample was cycled 5,000 times at a given strain to create a fatigue crack.

The choice of the value of ε (and the corresponding G) was made to match values of G. The G for cyclic fatigue was chosen to be below the critical energy release rate $\Gamma_{c,}$ where the crack propagates in a single cycle, for all materials and environmental conditions: G = 1,000 J/m^2. All samples carried to the X-ray experiment were fatigued at that energy release rate.

After the fatigue step always done at 23°C, all samples were characterized by X-rays at a crack opening corresponding to G = 1,000 J/m^2, but the samples able to bear more strain were also observed at higher values of applied G meaning that while ε was kept in all cases under 66%, local amplification of the strain at the crack tip may have locally reactivated some Mullins damage.

2.3.2 Test Set-up for DIC and X-Ray Scattering

The tensile stage used for both digital image correlation (DIC) and X-ray scattering was the same: a Deben micro-tensile stage, with a 10 mm displacement amplitude and a 200 N load cell. As strain is applied using a rotating screw, the strain rate was

limited to low values and all X-ray measurement were made on static cracks. This is a limitation, since the crack propagation experiments are dynamic, and it was shown in previous studies that the strain rates and frequency can affect both crack speed and strain-induced crystallization [18, 20–22]. However, the characterization of SIC and cavitation in uniaxial tests [13] was made at very low strain rates, which makes the comparison between uniaxial tests and crack tip tests easier.

To carry out the X-ray experiments, the sample was mounted vertically. A heating system by conduction was also developed for the high temperature tests. Four 100 Ω resistors in a parallel circuit were fixed on the four parts of the clamps, and a simple 30 V table generator was used to heat the sample. The clamps and sample were isolated from the stage using two Teflon mounts between the clamps and the stage. The whole set-up, while simple, is transportable, and ex situ tests showed that high temperatures were achievable quickly, and that only 19 V was required to reach 100°C.

2.4 DIC Experiments

The images acquired for DIC were processed with Correli^{LMT} software, a digital image correlation program that runs on Matlab. For more information about the program, the reader is invited to refer to the work of Mzabi [1, 19] and specialized reviews [23]. The region of the image where the calculation was made (ROI) was split into boxes. Correli^{LMT} uses a minimization of the gray level difference to track the displacement of each box center. The size of the box used was either 16 pixel or 32 pixels. While a data visualization module is included in Correli^{LMT}, a manual post-treatment of the displacements field provided was made.

2.5 In Situ Mapping of Fatigue Crack Tips

2.5.1 Scanned Fields and Beam Parameters

The energy release rate applied to the sample for the fatigue experiments before scanning was G = 1,000 J/m^2, while the X-ray beam scanning of the samples was carried out at different crack openings corresponding to a maximum of G = 4,000 J/m^2. These relatively low values of stretch λ as well as the observation made by digital image correlation suggested to only image a very small area at the crack tip. The beamline used for the crack tip experiment was ID-02 at ESRF and the type of microfocused beam used was similar to what was described by Zhang et al. [17].

The beam used had a 0.0995 nm wavelength (12.45 keV). The data for both WAXS characterization of SIC and SAXS observation of cavitation were acquired in two successive scans. A long exposure (1 s) scan is used to acquire both the WAXS data and the high q region of the SAXS data on two separate detectors. A short

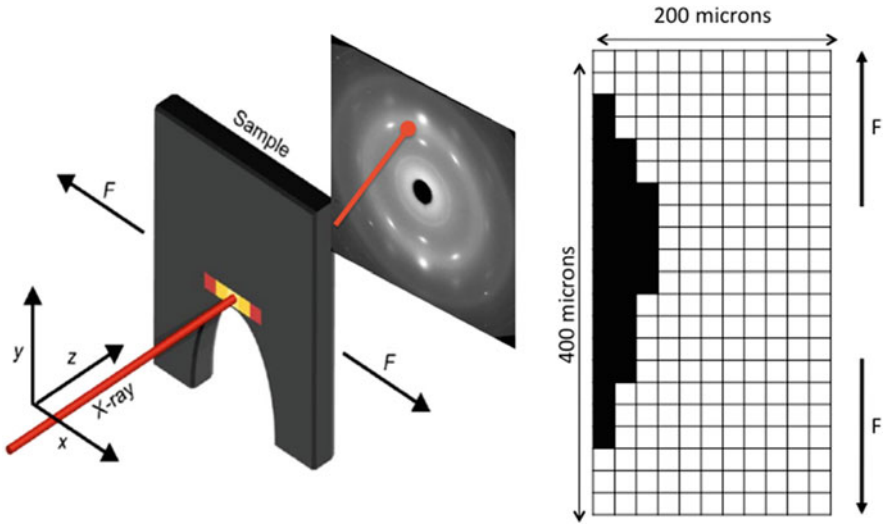

Fig. 2 Schematic view of the experiment set-up and scanned area for in situ X-ray mapping of the crack tips

exposure (0.01–0.02 ms) scan was then used to acquire the low q region of the SAXS data. The two SAXS images are then merged following a previously published procedure [13]. The sample to detector distance for WAXS acquisition was 10 cm, and 10 m for SAXS. The scattering vector q is defined as $4\pi/\lambda \sin(\theta)$ where 2θ is the scattering angle. In those conditions the accessible q range was between 0.006 and 0.5 nm^{-1}.

Since this beamline allows to focus the beam to a 20 μm size, the choice was made to scan over a 200 μm length along the crack propagation direction, and 400 μm along the tensile direction. The scanned area, presented on Fig. 2, extended 200 μm on each side of the crack tip point in the tensile direction. If the origin is placed at the crack tip, in the crack direction, the scan was performed from −40 to 160 μm. The mapping of the sample on the scan field is done by moving the table where the tensile stage is mounted. This movement is operated with a step motor with a micrometric precision. The scanning points are spaced by 20 μm, and a 21 by 11 lattice (231 points) covers the scanned area. Finally, a scan in the crack direction between −400 and 1,600 μm is made using a 200 μm step. This scan is solely used to measure the local thickness of the sample using the attenuation of the beam.

2.5.2 Construction of the Crystallinity and Cavitation Maps at the Crack Tip

The patterns acquired were corrected and analyzed following a previously published procedure [13]. While the methodology to compute the scattering invariant Q for

cavities detection was the same as in previously published work [13, 17], a word has to be said about the calculation of the crystallinity index. The detector used for WAXS detection proved to be very noisy. The methodology used in [13] (subtracting a profile integrated around an amorphous direction to one integrated around the tensile direction) could not be used here. The following method was used to compute the crystallinity index. First, the local tensile direction was found by identifying the angle between the tensile direction and the [200] and [120] peaks. The intensity was then integrated at +/− 5° around that direction. Due to the detector characteristics, the resulting profile was very noisy. Since the easiest peak to separate from the noise is the [200], the profile was fitted in the amorphous region. The crystallinity index is defined as the ratio between the integrated area between the fit of the amorphous and the intensity over the 200 peak.

The results of the processing are a value of crystallinity index and variation of scattering invariant for each 20 μm × 20 μm region. The local mappings were constructed by assigning theses values to the position where they were taken. The boundary of the crack was then determined by defining where the attenuation of intensity was lower than 10%. Finally, the maps were smoothened using a median filter of diameter 3: each value was replaced by the median value among the observed point and its immediate neighbors. It is noteworthy that the generated maps are in the deformed configuration. The maps offer an easy and quick qualitative comparison between experiments. However, to achieve more quantitative comparisons, 1D profiles were also generated by averaging in the tensile direction the value of the crystallinity index or the variations of the scattering invariant. The results are then presented as a function of the distance to the crack tip.

3 Results

3.1 Effect of Crosslinking Density

The measurement of the crack propagation rate of the two differently crosslinked materials (NR50 and NR50 S-) are shown on Fig. 3: dc/dn propagation curves for the NR50 and the NR50S-. Note that for the low values of G, the test was performed at 65 Hz for ~10 days to obtain a sufficient number of cycles to visualize crack advance with precision.

The values of the fitted power laws ($dc/dn = \alpha \times G^{\beta}$) are reported in Table 2 and show that the less crosslinked material has a higher coefficient and a lower slope. The consequence is that it performs poorly at low energy release rates, and better at high energy release rates. The same evolution was observed on filled SBRs by Mzabi et al. [1].

The critical energy release rate Γ_c increases significantly when the crosslink density is reduced. Although this is a well-known result in threshold conditions (Γ_0) [24–26], to the best of our knowledge no study specifically focused on the evolution of Γ_c with crosslink density in NR, but this result can be related to the

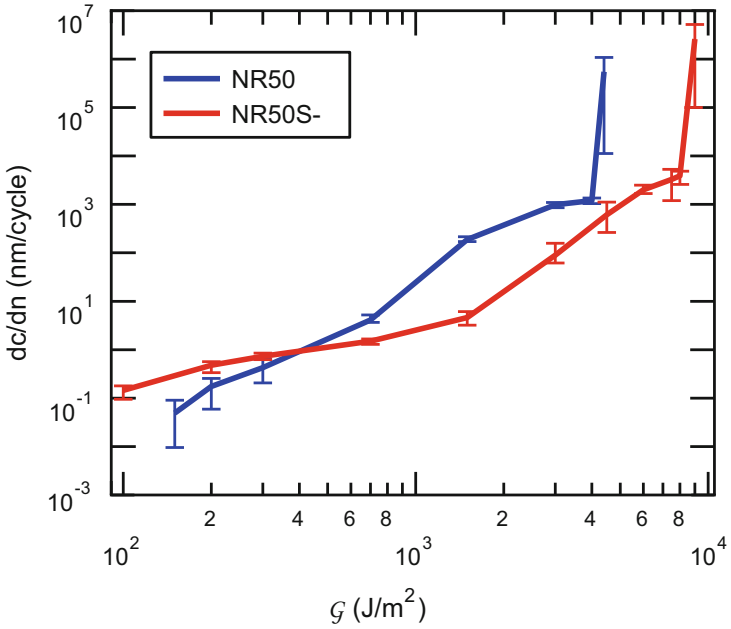

Fig. 3 dc/dn propagation curves for the NR50 and the NR50S-

Table 2 Coefficients of the fitted power law α and β in the first regime of propagation, and Γ_c values. R^2 characterizes the quality of the fit

Material	α (nm/cycle)	β	R^2	Γ_c (J/m^2)
NR50	5.8×10^{-9}	3.20	0.987	4,400
NR50S-	7.8×10^{-7}	2.41	0.937	9,000

observation made on the stress at break for pre-cut NR materials by Hamed et al. [27].

Figure 4 shows the comparison of the crystallization maps and profiles at G = 2,000 and 3,000 J/m^2 with the reference NR50 material.

The NR50S- seems to crystallize over a slightly bigger area than the NR50, and achieve higher values of crystallinity at the crack tip. As at these values of energy release rate, dc/dn is lower for NR50S-, X-ray mapping of the crack tip is consistent with a protective role played by strain-induced crystallization.

3.2 *Effect of Temperature*

The effect of temperature on fatigue crack propagation is shown on Fig. 5 and coefficient values are listed in Table 3. Interestingly, and contrary to what could be expected from strain-induced crystallization arguments, both filled materials do not

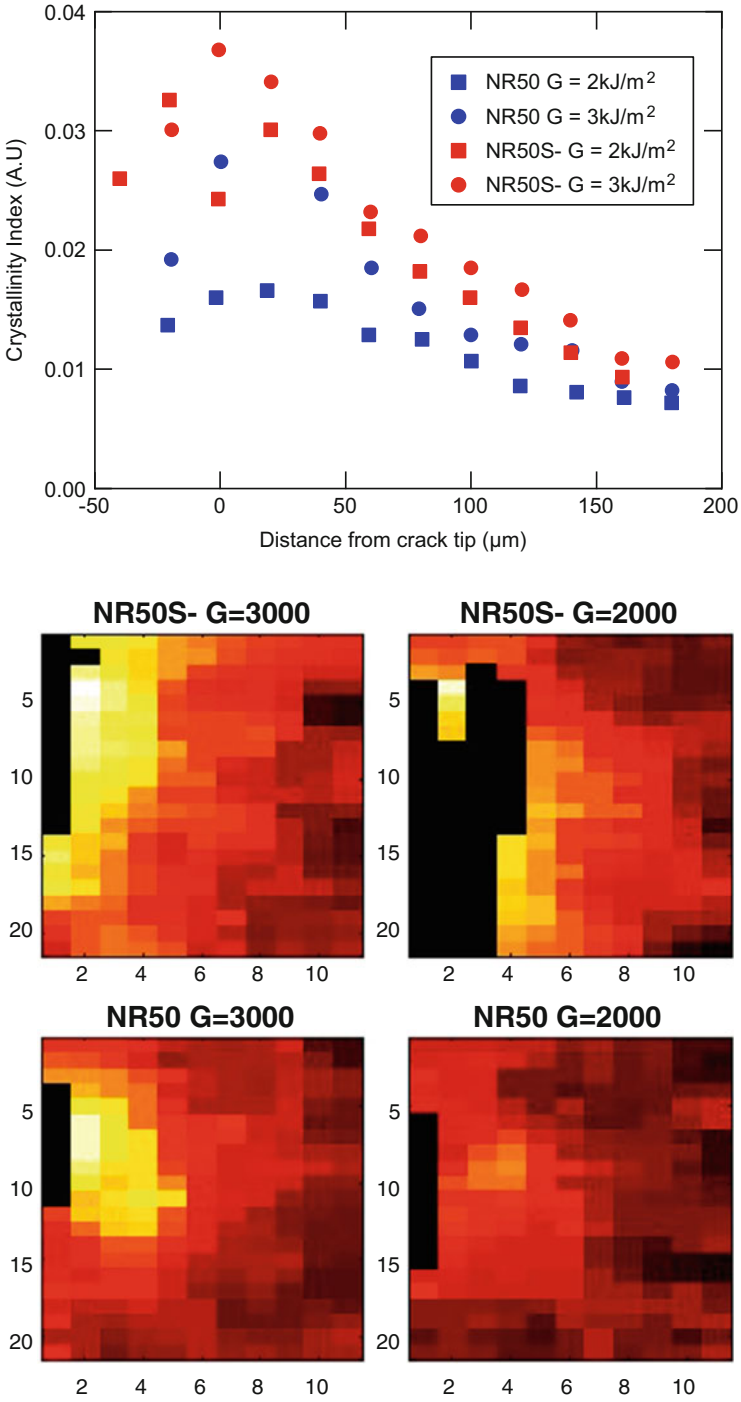

Fig. 4 Comparison between the crystallinity index maps and profiles of NR50 and NR50S- at G = 2000 and G = 3,000 J/m^2. (**a**) 1D profiles and (**b**) 2D maps at the crack tip

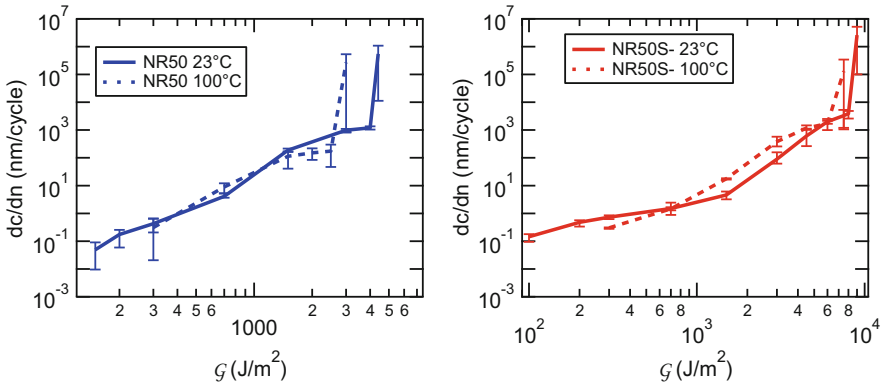

Fig. 5 Effect of temperature on the crack propagation curves for NR50 and NR50S-

Table 3 Coefficient of the power law in the first regime of propagation, and Γ_c values

Material	α (nm/cycle)	β	R^2	Γ_c (J/m^2)
NR50 (23°C)	5.8×10^{-9}	3.20	0.987	4,400
NR50 (100°C)	1.0×10^{-8}	3.08	0.987	3,000
NR50S- (23°C)	7.8×10^{-7}	2.41	0.937	9,000
NR50S- (100°C)	3.5×10^{-9}	3.12	0.982	7,500

show a significant increase of the crack propagation rate at 100°C relative to 23°C. However, their critical energy release rate Γ_c is lower at high temperature.

This evolution is somewhat similar to what was observed by Rublon [9, 18]. However, it differs from the observations of Young [28–30] and Kaang [31]. They observed for the materials they tested a slight increase in dc/dn over the range of energy release rate investigated. The degree of crosslinking and type of filler were, however, different.

Following the protocol described in the experimental section we mapped by microbeam focused WAXS the degree of crystallinity of the NR50 and NR50S- near the crack tip at 23°C and 100°C. In order to detect crystallinity over a sufficient volume near the crack tip, the samples fatigued for 5,000 cycles at 23°C and G = 1 kJ/m^2 were strained statically in the X-ray beam (at 23°C and 100°C) up to an applied G of 3 kJ/m^2 for the NR50 and 4 kJ/m^2 for the NR50S-. Figures 6 and 7 show, respectively, the effect of an elevation of temperature from 23°C to 100°C on both NR50 and NR50S-. As expected from previously published results in uniaxial tension [13], the two materials show indeed a clearly reduced crystallinity at the crack tip at 100°C, but some crystallinity remains observable. To the best of our knowledge these are the first results on SIC at the crack tip at high temperature for filled NR. Comparing Figs. 6 and 7 with Fig. 5, it is clear that the raw amount of crystallinity present at the crack tip cannot be considered as a quantitative indicator of the resistance to crack propagation in fatigue of the material. The presence of a small amount of crystallinity at the crack tip may be enough to modify the singularity induced by the crack.

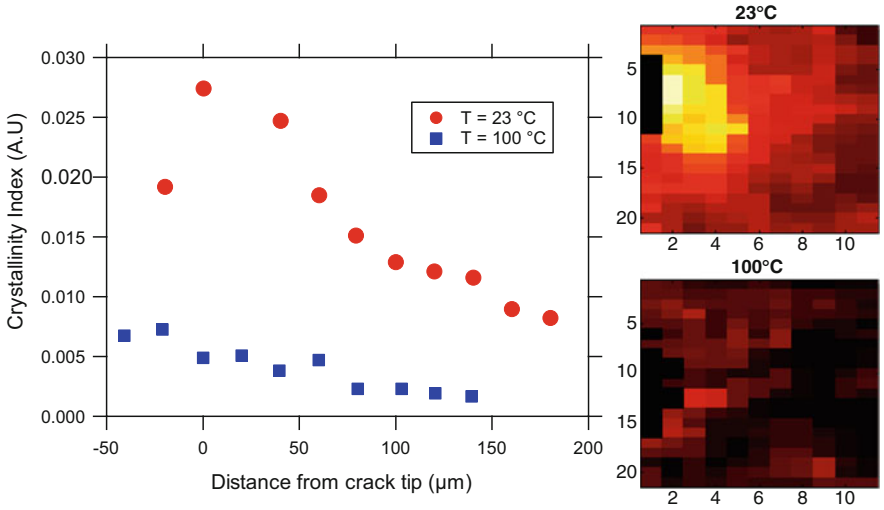

Fig. 6 Comparison of the crystallinity profiles and maps for the NR50 at G = 3,000 J/m^2 at 23°C and 100°C

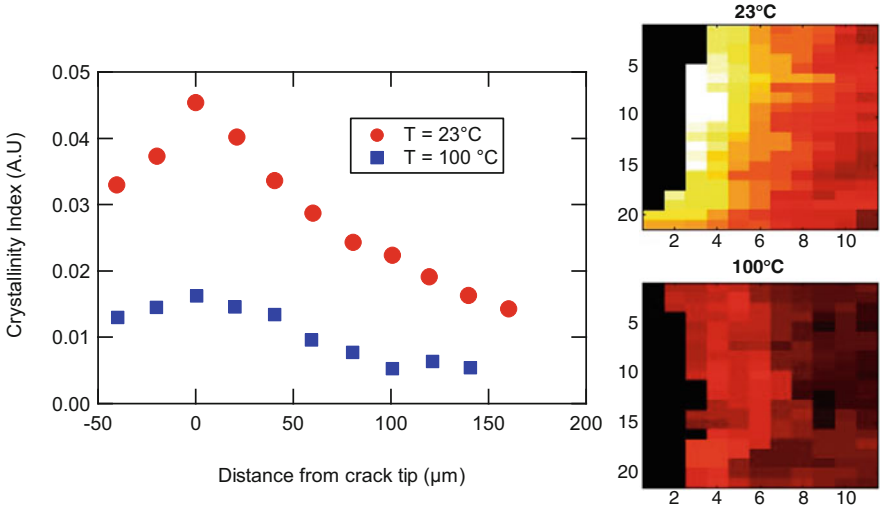

Fig. 7 Comparison of the crystallinity profiles and maps for the NR50S- at G = 4,000 J/m^2 at 23°C and 100°C

3.2.1 Effect of Aging

As mentioned in the introduction, non-oxydative aging has rarely been tested before this study. The following results are therefore even harder to compare to existing results. Figure 8 presents the difference between the crack propagation curves of new

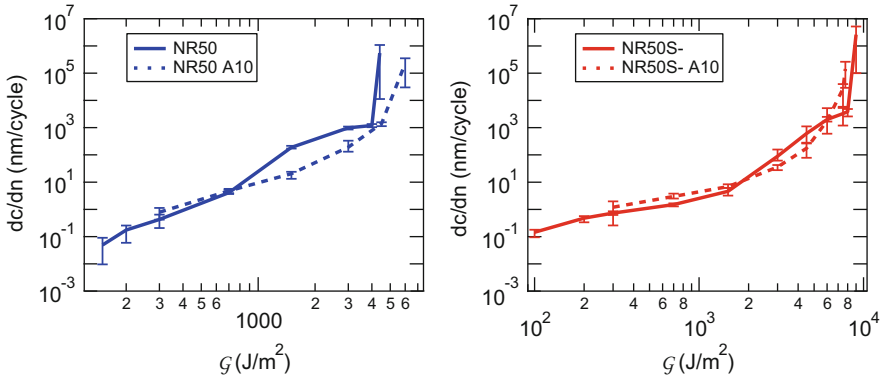

Fig. 8 Crack propagation curves for new and aged materials at room temperature (23°C)

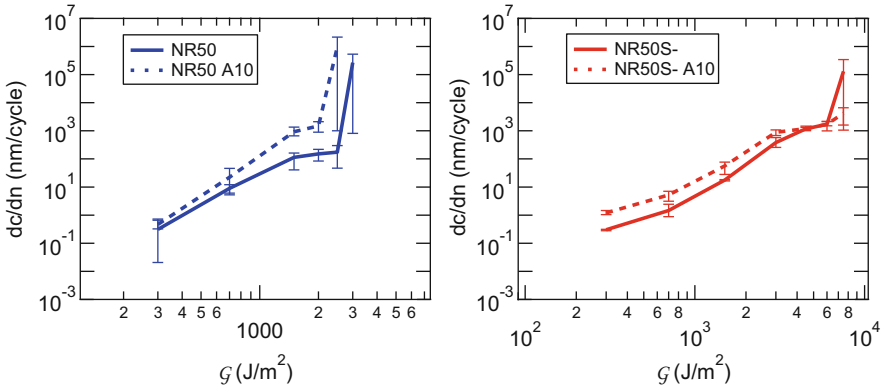

Fig. 9 Crack propagation curves for new and aged materials at high temperature (100°C)

and aged materials at room temperature, while Fig. 9 presents the same results at high temperature. The "new" samples are the same shown in Figs. 3 and 5 and the aged samples were aged at 110°C in inert atmosphere for 10 days.

At room temperature, the aged NR50 has a slightly increased Γ_c (6 kJ/m^2 vs 4.4 kJ/m^2) and performs slightly better for $800 < G < 4{,}000$ J/m^2). However, the behavior of NR50S- is mostly unchanged by aging.

A 100°C, the aged NR50 has now an inferior performance than the unaged material, with a higher dc/dn and lower Γ_c. The propagation rate measured of the less crosslinked NR50S- is still mostly unaffected by aging.

These results suggest that several competing mechanisms may be involved and it is difficult to isolate a unique mechanism that would explain the modification of the fatigue properties of aged materials. The case of NR50 seems the most interesting, since the effect of aging is inversed by the elevation of temperature.

The results obtained on the same materials in uniaxial tension [13] laid the first experimental proofs that thermal non-oxydative aging significantly reduces the

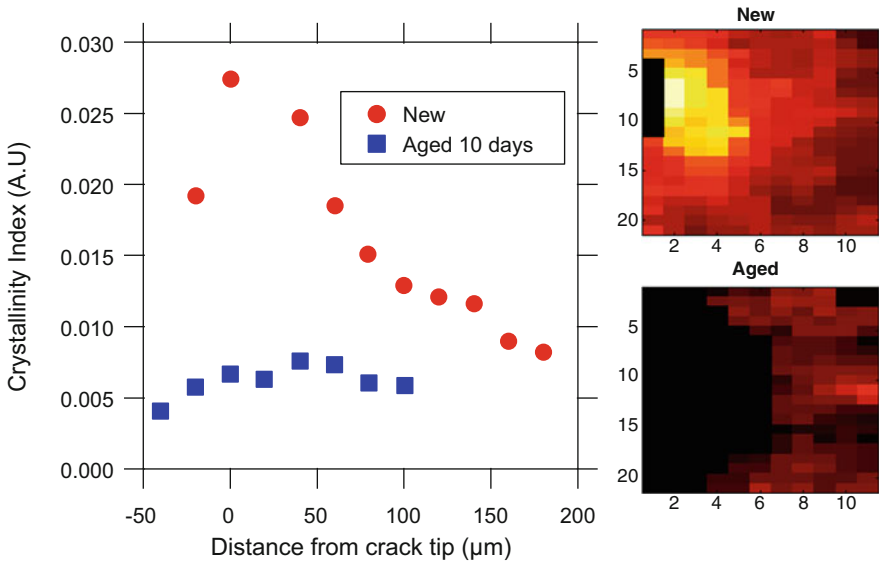

Fig. 10 Comparison of the crystallinity maps of NR50 at 23°C and G = 3,000 J/m^2, for both new and aged materials

ability of the material to crystallize in natural rubber. The effect of aging observed at the crack tip is qualitatively the same. Figure 10 shows the effect of aging on the crystallinity at the crack tip of a NR50 sample at room temperature. The crystallinity in the aged sample appears almost absent. The same qualitative evolution can be observed for NR50S- on Fig. 11. Since NR50S crystallizes more than NR50 before aging at the same applied G, and was mapped at a higher applied G, the level of crystallinity after aging is more present than for the NR50.

The combination of aging and high testing temperature effectively removes any observable crystallinity from the crack tip. Figure 12 shows the crystallinity of fresh and aged NR50S- at 100°C, and confirms that no crystallinity is visible in these conditions within the spatial resolution of the experiment.

Similarly to what was discussed in the previous section about the effect of the temperature, the observed reduced crystallinity at the crack tip after aging and the comparison between Figs. 8, 10, 11 and 12 casts doubt on the real role played by strain-induced crystallization in the outstanding fatigue properties of filled natural rubber since the two NR50 showed fatigue properties slightly improved at room temperature after aging, while degraded at high temperature.

Since the decrease in crystallinity was observed both at room and high temperature, strain-induced crystallization cannot be the sole contributor to the excellent fatigue properties of natural rubber. At room temperature, the reduced crystallinity may be offset by a beneficial evolution of the crosslinking due to aging. The uniaxial tension studies of the same materials (aged and unaged) showed that aging reduces

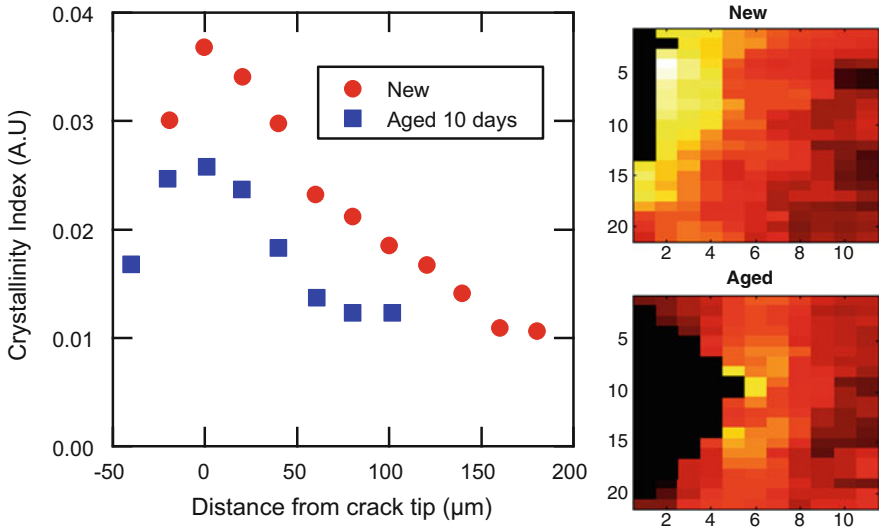

Fig. 11 Comparison of the crystallinity maps of NR50S- at 23°C and G = 3,000 J/m^2, for both new and aged materials

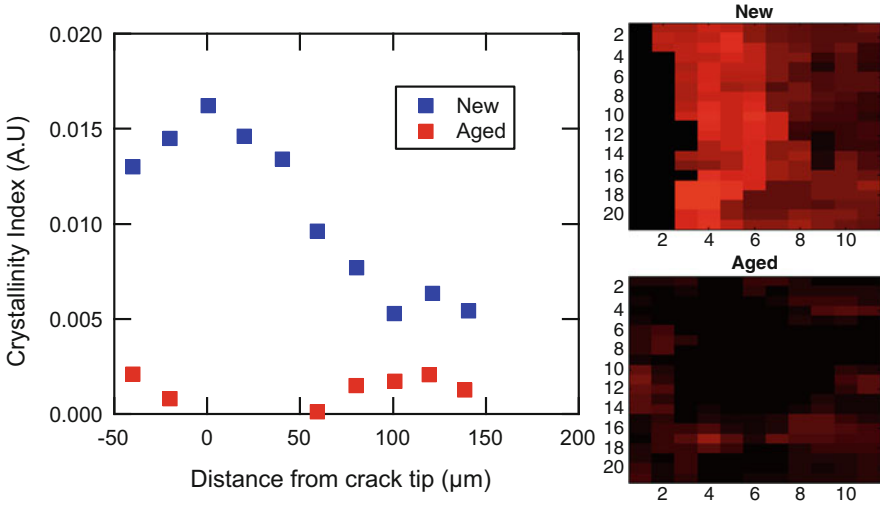

Fig. 12 Comparison of the crystallinity maps of NR50S- at 100°C and G = 4,000 J/m^2, for both new and aged materials

the crosslink density [13] and less crosslinked rubbers display better fatigue properties in threshold [24–26] and in non-threshold conditions.

The effect of aging on fatigue properties seems therefore to be a balance between the reduced crystallinity and the reduced crosslink density. This interpretation seems to further illustrate the importance of the presence of a little crystallization at the

crack tip. At room temperature, the low crystallinity remaining after aging has enough impact on the fatigue properties for the reduced crosslink density to offset the expected increased crack growth rates. At 100°C, however, no crystallinity is detected and the reduced crosslinking cannot offset the loss of properties due to the higher test temperature.

3.3 On the Presence of Cavities at the Crack Tip

Up to this point we presented correlations between the presence of SIC at the crack tip, applied energy release rate G and rate of crack propagation dc/dn in cyclic fatigue. By using results of SIC obtained in uniaxial tension to interpret our data, we implicitly assumed that the stress state at the crack tip could be assimilated to uniaxial tension.

Yet far from the crack tip the stress state of our samples may be close to pure shear. The details of the local stress state may be important for the presence or not of cavities upon loading. While in uniaxial tension the nano-cavities due to the presence of filler in sufficient amount, do not reopen upon reloading [32], they were observed at the crack tip after cyclic loading in non-crystallizable SBR and with similar sample geometries by Zhang et al. [17], suggesting therefore that the stress state near the crack tip may have some biaxial component.

Using displacement fields measured by digital image correlation at the crack tip, the value of λ_1 and λ_2 can be obtained, where λ_1 is the tensile direction. These values can be then used to qualify the mechanical state near the crack tip and define a biaxiality index I_{BA} inspired by the work of Samaca et al. [15].

$$I_{BA} = 1 - 2\frac{\log(\lambda_2)}{\log(\lambda_1)} \tag{2}$$

The value of I_{BA} is 0 for a uniaxial state and 1 for a pure shear state. Figure 13 presents the mapping of the value of the index for the NR50. The first observation is that far from the crack tip, the value of the index is 0.8, which means that the sample is not purely in a pure shear state. This is probably the result of the shortened mini pure shear sample: the aspect ratio of the effective area is a bit too short to ensure a complete pure shear state. Approaching to the crack tip, the state progressively becomes close to uniaxial. Finally, on the sides of the crack, it becomes purely uniaxial, while at the very crack tip, a biaxial state reappears.

This state of biaxial stress up to a close distance from the crack tip does introduce a degree of triaxiality and should favor cavitation. Figure 14 shows the 2D map of the value of the normalized SAXS scattering invariant Q/Q(0) around the crack tip for the less crosslinked NR50S- at room temperature and at an applied G of 4,000 J/m^2 where Q(0) is the value at $\lambda = 1$. As discussed in a previous publication the value

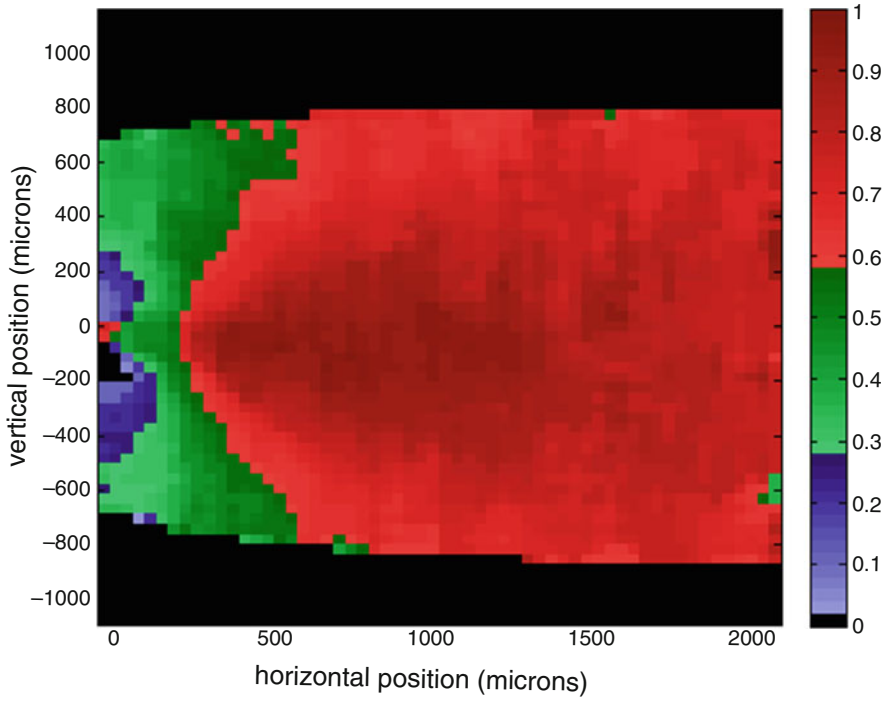

Fig. 13 Mechanical state at the crack tip of a NR50 sample, G = 3,000 J/m^2. The index I_{BA} displayed is equal to 1 for a true pure shear state and to 0 for a pure uniaxial tensile state

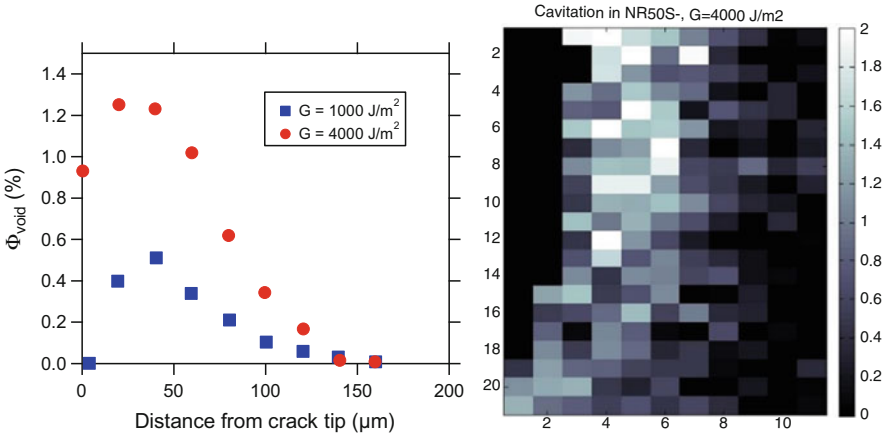

Fig. 14 Void volume fraction around the crack tip for a NR50S- sample at room temperature and at two values of G

of Q/Q(0) is directly proportional to the volume fraction of nano-cavities present in the material [12].

The data shows that there is an increase in scattering invariant over an area slightly smaller but comparable to the size of the area where SIC is observed. At an applied G = 4,000 J/m^2 the level of cavitation is important and based on previous publications [12, 17, 32, 33], the volume fraction of nano-cavities should reach a few percent. However and interestingly the 1D scans of Fig. 14 also show that cavitation is clearly observed even at the level of energy release rate where the sample was fatigued before the scattering experiment: G = 1,000 J/m^2. The presence of a biaxial stress state must create enough hydrostatic stresses to reopen cavities at each cycle [32].

Surprisingly the nanovoid volume fraction seems to decrease slightly right at the crack tip. This may be due to the fact that the cavities detected by a change in scattering invariant are only the cavities in the range of length scales accessible on the SAXS detector. The presence of the beamstop prevents the observation of any object bigger than 300 nm. The observed decrease in the volume fraction of nano-cavities in the last microns could be linked to a growth of the average cavity size near the crack tip.

3.4 Comparison between Digital Image Correlation (DIC) and X-Ray Absorption: Mapping the Thickness at the Crack Tip

An additional information that can be obtained by SAXS for each scan is the thickness traversed by the beam, and by comparing this value with the value that can be inferred by DIC by assuming incompressibility, an estimate of the volume fraction of voids (without any assumption on size) can be obtained.

The thickness T traversed by the beam and the attenuation of the beam are linked by the following equation, derived from the Beer–Lambert law:

$$T = \mu \ln\left(\frac{\mathrm{IC}_1}{R\mathrm{IC}_2}\right) \tag{3}$$

where μ is a material constant, IC_1 is the measured intensity of the beam before the sample, IC_2 is the intensity of the transmitted beam, and R is a calibration factor to account for the difference between the two detectors. Hence the relative variation of the thickness of material traversed by the X-ray beam only depends on the attenuation of the beam itself.

Conversely, 2D digital image correlation can be used map the thickness by assuming that the material is incompressible (This approximation is valid out of the 150 μm cavitation zone but is obviously incorrect at the very crack tip, where the material cavitates as shown from SAXS) and that the 2D strain field is invariant

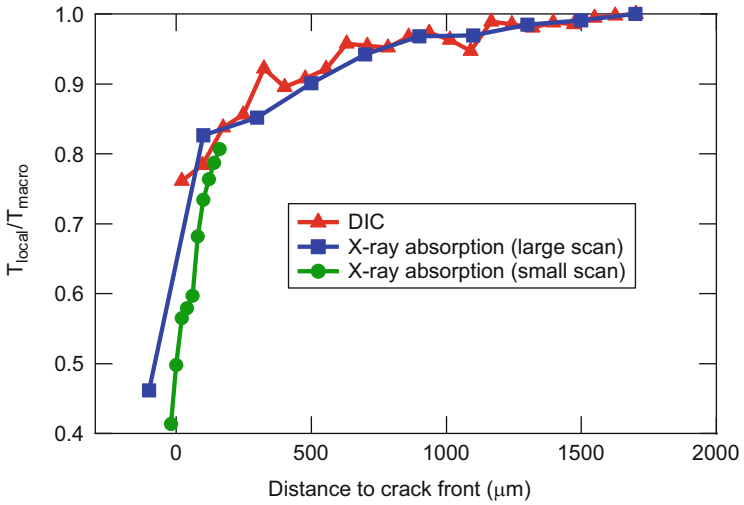

Fig. 15 Calculated thickness of the NR50S- at G = 4,000 J/m^2 using both X-ray attenuation and DIC fields assuming incompressibility (no voids)

through the thickness of the sample. Under these assumptions, the thickness variation $T_{\text{local}}/T_{\text{macro}}$ can be expressed as a function of the principal stretch ratios λ_1 and λ_2 as:

$$\frac{T_{\text{local}}}{T_{\text{marco}}} = \frac{1}{\lambda_1 \lambda_2} \tag{4}$$

Figure 15 shows the calculated thickness variations based on both DIC and X-ray transmission experiments for the NR50S- sample at G = 4,000 J/m^2. The 2 mm scan in the crack direction of the X-ray experiment was used for the comparison with the full field of observation of the digital image correlation.

Far from the crack tip (1,600 μm to 200 μm ahead of the crack), the two fields seem to match almost perfectly. However, in the last 200 μm in front of the crack, where the X-ray scans are performed, a significant drop in predicted thickness is observed by the X-ray scan.

Two explanations are possible for this observed thickness decrease:

- The material probed by X-ray presents an important volume fraction of void, reducing the attenuation of the beam.
- The stretch ratios are much larger than what is measured by DIC (because of the poor spatial resolution of the method near the singularity), causing the abrupt thinning of the sample.

Both explanations are plausible since large scale cavitation very near the crack tip is consistent with the SEM images of NR crack tips [34], and the presence of oriented fibrils near the crack front. Higher stretch ratios are also probable, since

the degree of crystallinity observed at the crack tip suggests that the local extension ratios are indeed higher than what is measured by DIC. It should be noted, however, that some of the discrepancy between DIC and X-rays may be also due to the fact that the crack front is not exactly parallel to the beam.

Alternatively, the local value of λ_1 in the fibrils can be estimated using the relation between stretch ratio and crystallinity index obtained in uniaxial tension [13]. As the method to calculate the index used in the crack tip experiment differs from the one used in uniaxial tension, the uniaxial data for that sample were reprocessed with the crack tip method to obtain a relation $\chi(\lambda_1)$.

The crystallinity index χ found at the crack tip for the NR50S- is 0.0457, and the corresponding λ_1 value is 3.6. The void volume fraction in the fibrillar zone Φ can now be estimated using the attenuation value at the crack tip. In a uniaxial mechanical state, the thickness T_f of the fibrillated material can be expressed as:

$$T_f = \frac{1}{\sqrt{\lambda_1}} \tag{5}$$

The corresponding void volume fraction is then evaluated using the difference between the measured thickness using the X-ray attenuation T_{local} and T_f:

$$T_{local} = (1 - \Phi)T_f \tag{6}$$

which brings

$$\Phi = 1 - \frac{T_{local}}{T_f} \tag{7}$$

The estimated value of the volume fraction of voids Φ for the NR50S- at 4000 J/m^2 at the crack tip is $\Phi = 0.42$.

Based on these results, a plausible scenario schematically described on Fig. 16 can be proposed for this experimental condition: at the very crack tip, nano-cavities formed in the region of triaxial stress grow to a macroscopic size, and the bulk structure of the material transforms into a fibrillar structure. In that fibrillated zone, the void volume fraction is high and the fibrils are highly stretched forming a lozenge like shape (see SEM image) and some strain-induced crystallinity may be present in these highly stretched fibrils. However, the region a bit further from the crack tip does not fibrillate and the level of strain achieved there is not sufficient to activate SIC.

The presence of cavities at the very crack tip and the formation of a fibrillar structure maybe also present for other conditions and in particular at high temperature. Since we never observe a catastrophic decrease in crack propagation rate even at 100°C in aged materials where we do not detect any SIC, we hypothesize that a small amount of SIC in the fibrillar region may be sufficient to stabilize it and prevent bond scission during the multiple cycles of the fatigue tests. However, this is

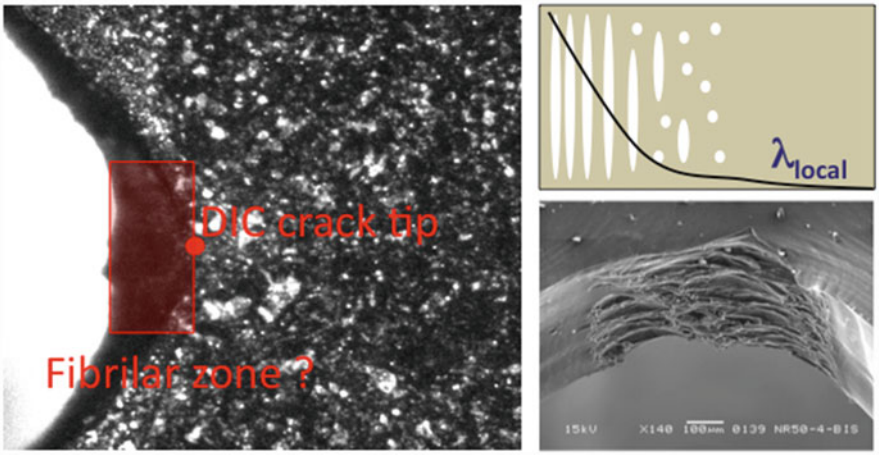

Fig. 16 Left: zoom on the image used for DIC of NR50S- at G = 1,000 J/m^2. Top right: schematic view of the cavitation to fibrillation process. Bottom right: SEM image of a NR50 fatigued for 400 cycles at G = 1,410 J/m^2, taken from (4)

highly speculative and other mechanisms than SIC may be active to slow crack propagation.

4 Conclusions

We have carried out systematic WAXS and SAXS experiments to detect and map strain-induced crystallization and cavitation at the crack tip of samples of highly crosslinked and carbon black filled natural rubber, that were previously used to propagate a crack in cyclic fatigue. In parallel systematic experiments of crack propagation in cyclic fatigue were carried out over a wider range of applied energy release rates for the same materials and conditions.

The scattering experiments carried out near the crack tip of open static cracks with a 20 µm spatial resolution, demonstrated that at the energy release rates applied typically in fatigue experiments (1–4 kJ/m^2), a crystallized volume is present at the tip of the crack. Due to the low strains applied, this crystallized volume is much smaller than previously reported sizes [2, 6, 7], as it extends to a maximum of 200 µm ahead of the crack.

The set-up developed allowed to perform comparisons between the crystallized volumes and crack propagation rates dc/dn. The main results can be summarized as follows:

- *Effect of crosslink density*: a reduced crosslink density increases the size of the crystallized zone and increases the maximum degree of crystallinity present at a given energy release rate. It does also reduce dc/dn at the same applied G.

- *Effect of temperature*: the elevation of the fatigue test temperature (and observation temperature for SIC) from 23°C to 100 strongly decreases the amount of crystallinity observed. Some crystallization is, however, still observable at the crack tip at 100°C. Interestingly dc/dn is almost the same for both temperatures and for nearly the whole range of applied G.
- *Effect of thermal aging*: aging in N_2 atmosphere also strongly decreases the observed crystallinity at the crack tip. The combination of aging and high temperature effectively removes any detectable crystallinity. However dc/dn stays the same at 23°C and decreases slightly with aging at 100°C.

Therefore, a direct correlation between the extent of SIC at the crack tip and the rate at which a crack propagates in fatigue could not be established based on these results.

Yet the presence of a few percent of nano-cavities was observed at the crack tip on a volume slightly smaller than the crystalline volume in the less crosslinked material. In addition, the comparison of the real thickness of the sample, using the attenuation of the X-ray beam, and the thickness obtained from extrapolating DIC measurements assuming incompressibility shows that the material observed had likely a fibrillar structure with a much larger (~40 vol%) volume fraction of voids. The nano-cavities observed with SAXS probably cohabits with cavities of much greater size to form the fibrillar structure. Since even with aged samples at 100°C, where no SIC is detected, the fatigue resistance is not catastrophically bad, we hypothesize that the fibrils in those regions very near the crack face may have therefore a much higher actual strain and still crystallize. Such crystallized fibrils may be very hard to detect because of the 3-dimensional nature of the open crack face but nevertheless play a crucial role in fatigue by reducing the probability of fibril failure during the repeated loading cycles and hence reducing dc/dn. However, in the absence of direct detection by WAXS, this remains speculative and other mechanisms may be at play.

Acknowledgements We wish to thank the help of the staff at the ID-02 beamline of the ESRF in Grenoble and in particular Dr. Theyencheri Narayanan, in charge of the beamline who was of invaluable help in setting up the line and data acquisition system so that the experiments could be done as efficiently as possible. We also gratefully acknowledge the company Michelin for financial support and for many helpful discussions on the results. For the fatigue testing we thank Fabien Vion-Loisel and his team at Michelin.

References

1. Mzabi S, Berghezan D, Roux S, Hild F, Creton C (2011) A critical local energy release rate criterion for fatigue fracture of elastomers. J Polym Sci Polym Phys 49:1518–1524
2. Rublon P, Huneau B, Saintier N, Beurrot S, Leygue A, Verron E, Mocuta C, Thiaudière D, Berghezan D (2013) In situ synchrotron wide-angle X-ray diffraction investigation of fatigue cracks in natural rubber. J Synchrotron Radiat 20:105–109

3. Mars WV, Fatemi A (2004) Factors that affect the fatigue life of rubber: a literature survey. Rubber Chem Technol 77:391–412
4. Tee YL, Loo MS, Andriyana A (2018) Recent advances on fatigue of rubber after the literature survey by Mars and Fatemi in 2002 and 2004. Int J Fatigue 110:115–129
5. Lee DJ, Donovan JA (1987) Microstructural changes in the crack tip region of carbon-black-filled natural rubber. Rubber Chem Technol 60:910–923
6. Trabelsi S, Albouy P-A, Rault J (2002) Stress-induced crystallization around a crack tip in natural rubber. Macromolecules 35:10054–10061
7. Brüning K, Schneider K, Roth SV, Heinrich G (2013) Strain-induced crystallization around a crack tip in natural rubber under dynamic load. Polymer 54:6200–6205
8. Brüning K, Schneider K, Heinrich G (2013) In-situ structural characterization of rubber during deformation and fracture. In: Grellmann W, Heinrich G, Kaliske M, Klüppel M, Schneider K, Vilgis T (eds) Fracture mechanics and statistical mechanics of reinforced elastomeric blends, vol. 70. Lecture notes in applied and computational mechanics. Springer, Berlin, pp 43–80
9. Rublon P, Huneau B, Verron E, Saintier N, Beurrot S, Leygue A, Mocuta C, Thiaudière D, Berghezan D (2014) Multiaxial deformation and strain-induced crystallization around a fatigue crack in natural rubber. Eng Fract Mech 123:59–69
10. Beurrot-Borgarino S, Huneau B, Verron E, Rublon P (2013) Strain-induced crystallization of carbon black-filled natural rubber during fatigue measured by in situ synchrotron X-ray diffraction. Int J Fatigue 47:1–7
11. Zhou W, Li X, Lu J, Huang N, Chen L, Qi Z, Li L, Liang H (2014) Toughening mystery of natural rubber deciphered by double network incorporating hierarchical structures. Sci Rep 4:7502
12. Zhang H, Scholz AK, de Crevoisier J, Vion-Loisel F, Besnard G, Hexemer A, Brown HR, Kramer EJ, Creton C (2012) Nanocavitation in carbon black filled styrene butadiene rubber under tension detected by real time small angle X-ray scattering. Macromolecules 45:1529–1543
13. Demassieux Q, Berghezan D, Cantournet S, Proudhon H, Creton C (2019) Temperature and aging dependence of strain-induced crystallization and cavitation in highly crosslinked and filled natural rubber. J Polym Sci B Polym Phys 57:780–793
14. Le Cam J-B, Toussaint E, Dubois O (2012) Effect of thermal cycles on the deformation state at the crack tip of crystallisable natural rubber. Strain 48:153–156
15. Samaca Martinez JR, Toussaint E, Balandraud X, Le Cam JB, Berghezan D (2015) Heat and strain measurements at the crack tip of filled rubber under cyclic loadings using full-field techniques. Mech Mater 81:62–71
16. De Crevoisier J (2012) Analyse multi-échelles de la fatigue des élastomères : définition et identification de l'endommagement en pointe de fissure. Université Pierre et Marie Curie, Paris
17. Zhang H, Scholz AK, de Crevoisier J, Berghezan D, Narayanan T, Kramer EJ, Creton C (2015) Nanocavitation around a crack tip in a soft nanocomposite: a scanning microbeam small angle X-ray scattering study. J Polym Sci B Polym Phys 53:422–429
18. Rublon P (2013) Multiscale experimental study of fatigue crack growth in natural rubber. Ecole Centrale de Nantes (ECN) (ECN) (ECN) (ECN)
19. Mzabi S (2010) Caractérisation et analyse des mécanismes de fracture en fatigue des élastomères chargés. Université Pierre et Marie Curie, Paris
20. Candau N, Chazeau L, Chenal J-M, Gauthier C, Ferreira J, Munch E, Rochas C (2012) Characteristic time of strain induced crystallization of crosslinked natural rubber. Polymer 53:2540–2543
21. Candau N, Laghmach R, Chazeau L, Chenal J-M, Gauthier C, Biben T, Munch E (2015) Influence of strain rate and temperature on the onset of strain induced crystallization in natural rubber. Eur Polym J 64:244–252
22. Candau N, Chazeau L, Chenal J-M, Gauthier C, Munch E (2016) A comparison of the abilities of natural rubber (NR) and synthetic polyisoprene cis-1,4 rubber (IR) to crystallize under strain at high strain rates. Phys Chem Chem Phys 18:3472–3481

23. Hild F, Roux S (2006) Digital image correlation: from displacement measurement to identification of elastic properties – a review. Strain 42:69–80
24. Bhowmick AK, Gent AN, Pulford CTR (1983) Tear strength of elastomers under threshold conditions. Rubber Chem Technol 56:226–232
25. Bhowmick AK (1986) Tear strength of elastomers over a range of rates, temperatures and cross-linking tearing energy spectra. J Mater Sci 21:3927–3932
26. Bhowmick AK (1988) Threshold fracture of elastomers. J Macromol Sci C28:339–370
27. Hamed GR, Rattanasom N (2002) Effect of crosslink density on cut growth in gum natural rubber vulcanizates. Rubber Chem Technol 75:323–332
28. Young DG (1990) Application of fatigue methods based on fracture mechanics for tire compound development. Rubber Chem Technol 63:567–581
29. Young DG, Danik JA (1994) Effects of temperature on fatigue and fracture. Rubber Chem Technol 67:137–147
30. Young DG (1985) Dynamic property and fatigue crack propagation research on tire sidewall and model compounds. Rubber Chem Technol 58:785–805
31. Kaang S, Jin YW, Huh Y-i, Lee W-J, Im WB (2006) A test method to measure fatigue crack growth rate of rubbery materials. Polym Test 25:347–352
32. Zhang H, Scholz AK, Vion-Loisel F, Merckel Y, Brieu M, Brown H, Roux Sp, Kramer EJ, Creton C (2013) Opening and closing of nanocavities under cyclic loading in a soft nanocomposite probed by real-time small-angle X-ray scattering. Macromolecules 46:901–913
33. Zhang H, Scholz AK, Merckel Y, Brieu M, Berghezan D, Kramer EJ, Creton C (2013) Strain induced nanocavitation and crystallization in natural rubber probed by real time small and wide angle X-ray scattering. J Polym Sci B Polym Phys 51:1125–1138
34. Beurrot S, Huneau B, Verron E (2010) In situ SEM study of fatigue crack growth mechanism in carbon black-filled natural rubber. J Appl Polym Sci 117:1260–1269